N22

NUREG/CR-6471, Vol. 1
PNNL-11143

Characterization of Flaws in U.S. Reactor Pressure Vessels

Density and Distribution of Flaw Indications in PVRUF

Prepared by
G.J. Schuster, S.R. Doctor, P.G. Heasler

Pacific Northwest National Laboratory

Prepared for
U.S. Nuclear Regulatory Commission

AVAILABILITY NOTICE

Availability of Reference Materials Cited in NRC Publications

NRC publications in the NUREG series, NRC regulations, and *Title 10, Energy,* of the *Code of Federal Regulations,* may be purchased from one of the following sources:

1. The Superintendent of Documents
   U.S. Government Printing Office
   P.O. Box 37082
   Washington, DC 20402–9328
   <http://www.access.gpo.gov/su_docs>
   202–512–1800

2. The National Technical Information Service
   Springfield, VA 22161–0002
   <http://www.ntis.gov/ordernow>
   703–487–4650

The NUREG series comprises (1) technical and administrative reports, including those prepared for international agreements, (2) brochures, (3) proceedings of conferences and workshops, (4) adjudications and other issuances of the Commission and Atomic Safety and Licensing Boards, and (5) books.

A single copy of each NRC draft report is available free, to the extent of supply, upon written request as follows:

Address: Office of the Chief Information Officer
Reproduction and Distribution
Services Section
U.S. Nuclear Regulatory Commission
Washington, DC 20555–0001
E–mail: <GRW1@NRC.GOV>
Facsimile: 301–415–2289

A portion of NRC regulatory and technical information is available at NRC's World Wide Web site:

<http://www.nrc.gov>

All NRC documents released to the public are available for inspection or copying for a fee, in paper, microfiche, or, in some cases, diskette, from the Public Document Room (PDR):

NRC Public Document Room
2121 L Street, N.W., Lower Level
Washington, DC 20555–0001
<http://www.nrc.gov/NRC/PDR/pdr1.htm>
1–800–397–4209 or locally 202–634–3273

Microfiche of most NRC documents made publicly available since January 1981 may be found in the Local Public Document Rooms (LPDRs) located in the vicinity of nuclear power plants. The locations of the LPDRs may be obtained from the PDR (see previous paragraph) or through:

<http://www.nrc.gov/NRC/NUREGS/SR1350/V9/lpdr/html>

Publicly released documents include, to name a few, NUREG-series reports; *Federal Register* notices; applicant, licensee, and vendor documents and correspondence; NRC correspondence and internal memoranda; bulletins and information notices; inspection and investigation reports; licensee event reports; and Commission papers and their attachments.

Documents available from public and special technical libraries include all open literature items, such as books, journal articles, and transactions, *Federal Register* notices, Federal and State legislation, and congressional reports. Such documents as theses, dissertations, foreign reports and translations, and non-NRC conference proceedings may be purchased from their sponsoring organization.

Copies of industry codes and standards used in a substantive manner in the NRC regulatory process are maintained at the NRC Library, Two White Flint North, 11545 Rockville Pike, Rockville, MD 20852–2738. These standards are available in the library for reference use by the public. Codes and standards are usually copyrighted and may be purchased from the originating organization or, if they are American National Standards, from—

American National Standards Institute
11 West 42nd Street
New York, NY 10036–8002
<http://www.ansi.org>
212–642–4900

N22

NUREG/CR-6471, Vol. 1
PNNL-11143

Characterization of Flaws in U.S. Reactor Pressure Vessels

Density and Distribution of Flaw Indications in PVRUF

Manuscript Completed: September 1998
Date Published: November 1998

Prepared by
G.J. Schuster, S.R. Doctor, P.G. Heasler

Pacific Northwest National Laboratory
Richland, WA 99352

D.A. Jackson, NRC Project Manager

Prepared for
Division of Engineering Technology
Office of Nuclear Regulatory Research
U.S. Nuclear Regulatory Commission
Washington, DC 20555-0001
NRC Job Code L1099 and W6275

NUREG/CR-6471, Vol. 1 has been reproduced from the best available copy.

For sale by the U.S. Government Printing Office
Superintendent of Documents, Mail Stop: SSOP, Washington, DC 20402-9328
ISBN 0-16-049841-4

Abstract

Characterization of Flaws in U.S. Reactor Pressure Vessels is a multi-volume report. Volume 1, this document, gives the results of a non-destructive examination conducted at the Oak Ridge National Laboratory's Pressure Vessel Research User Facility (PVRUF) on a vessel fabricated for a canceled nuclear power plant. Volume 2, in preparation, will document the results of Pacific Northwest National Laboratory's (PNNL's) destructive validation of the flaw rates in the PVRUF evaluation.

A nondestructive evaluation was made of the fabrication flaws in an unused U.S. nuclear reactor pressure vessel. The examination was conducted at the Oak Ridge National Laboratory's Pressure Vessel Research User Facility (PVRUF) on a vessel fabricated for a canceled nuclear power plant of a pressurized water reactor (PWR) design. The inspections were made using the fieldable, real-time Synthetic Aperture Focusing Technique for Ultrasonic Testing (SAFT-UT) system developed by PNNL under sponsorship of the U.S. Nuclear Regulatory Commission. Twenty linear meters of weldment were inspected by SAFT-UT, including the entire circumferential beltline weld of the vessel. Ten different inspection modes were used, including five different modes specifically selected for the inspection of the inner 25 mm (1.0 in.) of the vessel wall.

There were 2500 detectable indications in the SAFT-UT inspections of the PVRUF vessel. The largest number of these, 982, were found at the clad-to-base metal interface, but 978 of these were less than 2 mm (0.08 in.) in size. In the near surface zone, the weld metal contained 98 detectable planar indications. The density of indications was four times higher in the weldment than in the base metal. The distribution of the empirical data provided enough information to apply a parametric model of the cumulative flaw rate to six different subsets of the data, and to obtain reasonable confidence bounds on the results. Recommendations are given for validating the indication rates by selective destructive analysis, to provide the necessary high quality flaw statistics for use in fracture mechanics calculations, such as those used in pressurized thermal shock (PTS) analysis.

Contents

		Page
Abstract		iii
Executive Summary		xv
Acknowledgments		xvii
Glossary and Abbreviations		xix
1	Introduction	1.1
1.1	Reasons for Estimating Fabrication Flaw Rates	1.1
1.2	Principal Objectives	1.2
1.3	Secondary Objectives	1.2
1.4	Flaws of Concern to Reactor Pressure Vessel Integrity	1.2
2	Description of Reactor Pressure Vessel Material	2.1
2.1	Differences Between PWRs and BWRs	2.1
2.2	Fabrication Methods	2.1
2.3	Materials	2.2
2.4	Weld Procedures	2.2
2.5	Description of PVRUF	2.3
2.6	Categorization of RPVs	2.3
3	SAFT-UT Measurements of RPV Material	3.1
3.1	SAFT-UT Equipment Configuration at PVRUF	3.1
3.2	Measurement Plan for PVRUF	3.1
3.3	Calibration of SAFT-UT Inspections	3.2
3.4	Scanning Procedure and Vessel Coordinate System	3.3
3.5	Amount of Material Inspected	3.4
4	Analysis Methods	4.1
4.1	Detection of Indications at PVRUF	4.1
4.2	Clustering of Detections	4.4
4.3	Sizing and Characterizing Indications at PVRUF	4.4
5	Results of the Analysis of SAFT-UT Inspections at PVRUF Vessel	5.1
5.1	Analysis of SAFT-UT Images	5.1
5.2	Indications in the Near-Surface Zone	5.1
5.2.1	Indications in the Near-Surface, Weldment	5.1
5.2.2	Indications in the Near-Surface, Heat Affected Zone	5.2
5.2.3	Indications in the Near-Surface, Base Metal	5.2
5.2.4	Clad and Clad-to-Base Metal Interface	5.2

Page

5.3 Indications Outside the Near Surface Zone 5.4

5.3.1 Indications in the Weldment 5.4
5.3.2 Indications in the Heat Affected Zone 5.5
5.3.3 Indications in the Base Metal 5.5

6 Distribution of Indications of Flaws in SAFT-UT Data 6.1

6.1 Joint Frequency Distribution of Indications in the Near Surface Zone 6.1
6.2 Joint Frequency Distribution of Indications Outside the Near Surface Zone 6.2

7 Estimates of SAFT-UT Performance 7.1

7.1 Probability of Detecting a Flaw 7.1
7.2 Sizing Error 7.1
7.3 False Call Probability 7.1

8 Flaw Rate Estimates 8.1

8.1 Use of SAFT-UT Performance Data 8.1
8.2 Method of Estimation: Maximum Likelihood 8.2
8.3 Maximum Likelihood Using the Weibull Distribution 8.2
8.4 Data Requirements for the Estimation Method 8.3
8.5 Near Surface Zone Flaw Rate Estimates 8.3
8.6 Outside the Near Surface Zone Flaw Rate Estimates 8.5
8.7 Comparison to Other Published Flaw Rate Estimates 8.6

9 Discussion of Flaw Rate Estimates 9.1

9.1 SAFT-UT Flaw Indications and Inspections During Fabrication 9.1
9.2 PVRUF Flaw Rates and the Marshall Distribution 9.1

10 Validation Plan 10.1

10.1 Removal of Material from PVRUF for Destructive Testing 10.1
10.2 Selection of Indications for Destructive Testing 10.1

11 Reliability Requirements for ISI Systems 11.1

11.1 Quantitative Model of Inservice Inspection 11.1
11.2 Scenarios for Evaluating Different Aspects of Inspection Capability 11.2

11.2.1 Perfect Inspection Scenario 11.3
11.2.2 Imperfect Detection Scenario 11.3
11.2.3 Imperfectly Calibrated POD Scenario 11.3
11.2.4 Imperfect Sizing Scenario 11.4
11.2.5 Imperfectly Calibrated Sizing Scenario 11.4

11.3 Flaw Distribution Function 11.4

Page

11.4 Results from Scenario Evaluations 11.5

11.4.1 Base Case Scenario Results 11.5
11.4.2 Imperfect Detection Scenario Results 11.5
11.4.3 Imperfectly Calibrated POD Scenario Results 11.6
11.4.4 Imperfect Sizing Scenario Results 11.6
11.4.5 Imperfectly Calibrated Sizing Scenario Results 11.7

11.5 Recommended Requirements for ISI 11.7

12 Conclusions 12.1

13 Recommendations 13.1

14 References 14.1

Appendix A – SAFT-UT Images of the Most Significant Flaws A.1
Appendix B – Inspections of the Midland Vessel B.1

Figures

		Page
1.1	Significant flaws for vessel fracture from pressurized thermal shock events	1.6
1.2	Significant flaws for vessel fracture from low temperature over pressurization events	1.7
1.3	Effects of surface length on fracture evaluation	1.8
1.4	Effects of subsurface flaw location and orientation on fracture evaluation	1.9
1.5	Effect of cladding on fracture evaluation	1.10
1.6	PTS flaws of equivalent severity	1.11
2.1	Typical PWR with internals	2.5
2.2	General schematic for PVRUF vessel showing weld identification numbers and configuration	2.6
2.3	Photograph of the PVRUF vessel from the outside	2.7
2.4	Photograph of the PVRUF vessel from the inside	2.7
3.1	Block diagram of SAFT-UT field system as configured at PVRUF	3.5
3.2	SAFT-UT data acquisition and display system as configured for PVRUF	3.5
3.3	Instrument platform and scanner pendulum showing center pivot	3.6
3.4	Insonification for inspection mode 1, near surface normal beam	3.6
3.5	Insonification for inspection mode 2, near surface 70° L wave at 0° skew	3.7
3.6	Insonification for inspection mode 3, near surface 70° L wave at 90° skew	3.7
3.7	Insonification for inspection mode 4, near surface 70° L wave at 180° skew	3.7
3.8	Insonification for inspection mode 5, near surface 70° L wave at 270° skew	3.8
3.9	Insonification for inspection mode 6, full volume 45° S wave at 0° skew	3.8
3.10	Insonification for inspection mode 7, full volume 45° S wave at 90° skew	3.8
3.11	Insonification for inspection mode 8, full volume 45° S wave at 180° skew	3.9
3.12	Insonification for inspection mode 9, full volume 45° S wave at 270° skew	3.9
3.13	Insonification for inspection mode 10, full volume normal beam	3.9

Page

3.14 SAFT-UT scanner attached to the calibration block for calibration of inspection modes 6 through 9, 45° S wave inspections 3.10

3.15 SAFT-UT scanner attached to the calibration block for calibration of inspection mode 10, normal beam 3.10

3.16 Signal strength from 1/4 thickness side drilled hole in calibration block for inspection mode 1 ..... 3.11

3.17 Signal strength from 1/4 thickness side drilled hole in calibration block for inspection modes 2 through 5 ..... 3.11

3.18 Time variable gain curve for modes 6 through 9, 45° S wave inspections 3.12

3.19 Signal strength after TVG amplification from 1/4 thickness side drilled hole in calibration block for inspection modes 6 through 9 ..... 3.12

3.20 Signal strength after TVG amplification from 1/2 thickness side drilled hole in calibration block for inspection modes 6 through 9 ..... 3.13

3.21 Signal strength after TVG amplification from 3/4 thickness side drilled hole in calibration block for inspection modes 6 through 9 ..... 3.13

3.22 Time variable gain curve for mode 10, full volume normal beam 3.14

3.23 Signal strength after TVG amplification from 1/4 thickness side drilled hole in calibration block for inspection mode 10 ..... 3.14

3.24 Signal strength after TVG amplification from 1/4 thickness side drilled hole in calibration block for inspection mode 10 ..... 3.15

3.25 Signal strength after TVG amplification from 3/4 thickness side drilled hole in calibration block for inspection mode 10 ..... 3.15

4.1 Near surface detection record 4.5

4.2 Full volume detection record 4.6

4.3 Embedded, compact time-of-flight shape 4.7

4.4 Embedded, broadened time-of-flight shape 4.8

4.5 Tip signal pattern showing two wave packets in the proper orientation for tip signals from a vertically oriented planar reflector 4.9

4.6 Surface wave pattern showing two wave packets in the proper orientation for re-radiation from a round trip of a volumetric flaw 4.10

4.7 Coin shape near the clad-to-base-metal interface 4.11

4.8 Normal beam shape below the clad-to-base-metal interface 4.12

Page

4.9 Shape of indications in the clad-to-base-metal interface 4.13

4.10 Detection of a cloud-like shape 4.14

4.11 Distance matrix for the clustering of detections from different inspection modes 4.15

4.12 Multimodal detection sheet for one portion of the weldment 4.16

4.13 Characterization work sheet for one indication 4.17

5.1 Mode 1 detection of planar indication #1 in the near surface zone 5.8

8.1 Typical probability of detection curve 8.8

8.2 Confidence bounds on model parameters for sample size of 3 ..... 8.8

8.3 Cumulative flow rate function with 95% confidence bounds for a sample size of 3 ..... 8.9

8.4 Confidence bounds on model parameters for sample size of 15 ..... 8.9

8.5 Cumulative flaw rate function with 95% confidence bounds for a sample size of 15 ..... 8.10

8.6 Parameter estimates with confidence bounds for simple Weibull fit to the SAFT-UT data of 9 planar indications in the near surface weldment 8.10

8.7 Estimate of cumulative flaw rate function with 95% confidence interval for simple Weibull fit to the SAFT-UT data of 9 planar indications in the near surface weldment 8.11

8.8 Parameter estimates with confidence bounds for simple Weibull fit to the SAFT-UT data of 21 planar indications in the near surface base metal. 8.11

8.9 Estimate of cumulative flaw rate function with 95% confidence interval for simple Weibull fit to the SAFT-UT data of 21 planar indications in the near surface base metal 8.12

8.10 Parameter estimates with confidence bounds for simple Weibull fit to the SAFT-UT data of 26 planar indications in the weldment below the near surface 8.12

8.11 Estimate of cumulative flaw rate function with 95% confidence interval for simple Weibull fit to the SAFT-UT data of 26 planar indications in the weldment below the near surface 8.13

8.12 Parameter estimates with confidence bounds for simple Weibull fit to the SAFT-UT data of 14 planar indications in the heat affected zone below the near surface. 8.13

8.13 Estimate of cumulative flaw rate function with 95% confidence interval for simple Weibull fit to the SAFT-UT data of 14 planar indications in the heat affected zone below the near surface. 8.14

8.14 Parameter estimates with confidence bounds for simple Weibull fit to the SAFT-UT data of 7 volumetric indications in the base metal below the near surface 8.14

Page

8.15 Estimate of cumulative flaw rate function with 95% confidence interval for simple Weibull fit to the SAFT-UT data of 7 volumetric indications in the base metal below the near surface 8.15

8.16 Parameter estimates with confidence bounds for simple Weibull fit to the SAFT-UT data of 31 planar indications in the base metal below the near surface 8.15

8.17 Estimate of cumulative flaw rate function with 95% confidence interval for simple Weibull fit to the SAFT-UT data of 31 planar indications in the base metal below the near surface 8.16

11.1 Impact of pressure vessel flaws on structural integrity 11.8

11.2 Imperfectly calibrated POD scenario 11.8

11.3 Flaw distribution functions λ_1, λ_2, λ_3, λ_4, λ_5, and λ_6 from PVRUF 11.9

11.4 Flaw distribution functions: solid curves represent true functions, dashed curves represent found functions for λ_1, λ_2, λ_3, λ_4, λ_5, and λ_6. σ_s = 1 mm is used 11.10

Tables

		Page
1.1	Nomenclature for estimating cumulative flaw rates	1.2
2.1	Summary of base material volumes and areas in the PVRUF vessel	2.4
2.2	Summary of weld volumes in the PVRUF vessel	2.4
3.1	SAFT-UT inspection plan for PVRUF	3.2
3.2	Step sizes and sampling rates for SAFT-UT inspections of the beltline weld in PVRUF	3.3
3.3	Amount of material inspected by SAFT-UT at PVRUF	3.4
4.1	Detection rule statements	4.3
5.1	Planar indications in the weldment of the near-surface	5.2
5.2	Volumetric indications in the weldment of the near-surface	5.2
5.3	Planar indications in the heat-affected zone of the near-surface	5.3
5.4	Volumetric indications in the heat-affected zone of the near-surface	5.3
5.5	Planar indications in the base metal of the inner surface zone	5.3
5.6	Volumetric indications in the base metal of the inner surface zone	5.4
5.7	Planar indications in the cladding and in the clad-to-base metal interface	5.4
5.8	Volumetric indications in the cladding and in the clad-to-base metal interface	5.5
5.9	Planar indications in the weldment	5.5
5.10	Volumetric indications in the weldment	5.6
5.11	Planar indications in the heat-affected zone	5.6
5.12	Planar indications in the base metal	5.7
5.13	Volumetric indications in the base metal	5.7
6.1	PVRUF: Number of near surface indications by category	6.2
6.2	PVRUF: Number of indications outside the near-surface zones by category	6.3
7.1	POD for advanced procedures from fits to PISC-II data	7.2

Page

7.2 Estimated POD for SAFT-UT inspections of the Midland blocks 7.2

7.3 True-state table for through-wall extent 7.2

8.1 Maximum likelihood fits run to determine sample size 8.4

8.2 Parameter confidence bound widths for different sample sizes 8.4

8.3 PVRUF flaw rate function parameters 8.6

8.4 Published flaw rate function parameters 8.6

8.5 PVRUF estimates of cumulative indication rates from Weibull fits to the indication frequencies 8.7

8.6 Published estimates of cumulative flaw rates for weldment using Weibull fit 8.7

10.1 Location of the largest indications along the weld, near surface zone 10.2

10.2 Location of the largest indication along the weld outside the near surface zone 10.2

11.1 Flaw distributions from PVRUF 11.5

11.2 RMSE for base case 11.5

11.3 RMSE (imperfect detection)/RMSE (base case) 11.6

11.4 RMSE (imperfectly calibrated POD)/RMSE (imperfect detection) 11.6

11.5 RMSE (imperfect sizing)/RMSE (base case) 11.6

11.6 RMSE (imperfect calibrated sizing)/RMSE (imperfect sizing) 11.7

Executive Summary

This report contains the results of a nondestructive examination of an unused U.S. nuclear reactor vessel for material fabrication flaws. This is Volume 1 of a multi-volume set where the second volume contains the results of a destructive validation of the indications reported here. Volume 2 contains descriptions of the removal of material from the PVRUF vessel, the conduct of confirmatory NDE techniques and metallographic analysis, and the confirmation of flaw rates for the vessel.

In this volume, we provide a description of the examination that was conducted at the Oak Ridge National Laboratory's Pressure Vessel Research User Facility (PVRUF) on a vessel fabricated for a canceled nuclear power plant. Under the sponsorship of the U.S. Nuclear Regulatory Commission, PNNL conducted a sequence of inspections using the Synthetic Aperture Focusing Technique for Ultrasonic Testing (SAFT-UT) for the purpose of detecting and characterizing zones containing any fabrication (preservice) flaws.

Twenty linear meters of weldment were inspected by SAFT-UT, including the entire beltline weld of the vessel. Ten different inspection modes were used, including 5 inspections specifically selected to examine the inner 25 mm (1.0 in.) of the vessel wall. The 10 inspection modes produced complementary information on the size, type, location, and density of the indications of flaws in the vessel. The added value of each modality was demonstrated in detection and characterization of the indications as described in this report. The calibration and vessel scanning procedures were routinely and successfully applied during the 18 months of data collection at PVRUF. The image quality of the SAFT-UT inspections was very high because of the fine sample spacing specified in the measurement plan and the careful execution of the calibration and scanning procedure.

Among the principal findings of this report are the 2500 detectable indications in the SAFT-UT inspections of the PVRUF vessel. Only these inspection results are included here. Where sizing results are reported, the SAFT-UT sizing rules were used to conservatively size indication zones to insure that all potentially large flaws would be included in the validation plan. Confirmations obtained by destructive tests, construction radiographs, or complementary NDE techniques are not included in this report.

At the start of the SAFT-UT inspections of the PVRUF vessel, PNNL expected that 80% of the indications would be small, that is, on the order of 2 mm (0.08 in.) in through-wall size. This was based on experience gained from the inspections of the Midland vessel. The data presented in this report show that 97% of the indications were less than 2 mm in through-wall size in the near surface zone, that is, within 25 mm of the inner surface of the PVRUF vessel. For the remainder of the vessel, that is, the portion outside the near surface zone, the data show that 80% of the indications were smaller than 4 mm (0.16 in.) in through-wall size. The rate of false detections in the analysis is expected to be low, because the detection rules were developed from the high correlation of SAFT-UT indications with flaws validated by destructive tests of material removed from the Midland vessel (see Appendix B).

The distribution of the empirical data provided enough information to apply a parametric model of the cumulative flaw rate to six different subsets of the data, and obtain reasonable confidence bounds on the results. It was possible to extract distinct distributions for the weldment and the base metal in the near surface zone. A comparison of these two distributions shows significantly higher indication rate in the weldment compared to the base metal in the near surface zone. It was also possible to extract different distributions for the weldment, heat affected zone, and base metal in the portion of the vessel outside the near surface zone (i.e., beyond 25 mm from the inner surface). These distributions also show a significantly higher indication rate in the heat-affected zone and weldment than in the base metal.

For the near surface zone, the comparison of indication distributions for the weldment and base metal reveals a greater estimated density of indications in the weldment. For all planar flaws, the density ratio is 4 to 1 for the weldment compared to the base metal in the near surface zone. This ratio increases to 28 to 1 when only the indications larger than 6 mm are considered. This is a reasonable result, because planar flaws include cracks and lack of fusion in the weld, and the base metal is

thought to contain mostly volumetric flaws with little through-wall extent. It is expected that validation of the SAFT-UT indications by means of destructive testing will provide valuable metallographic data on the nature of flaws in the two distinct populations.

For the portion of the vessel outside the near surface zone, comparisons of the indication distributions for the weldment, heat-affected zone, and base metal shows greater estimated densities of indications in the heat-affected zone and weldment. For all planar flaws, the density ratio is 4 to 1 for the weldment compared to the base metal. For all planar flaws, the density ratio is 8 to 1 for the heat-affected zone compared to the base metal. It was expected that the mid-wall portion of the base metal would contain a population of volumetric flaws with little through-wall extent. A determination of the nature of the larger SAFT-UT indications in the outside the near-surface portion of the vessel wall can significantly add to our understanding of the distribution of fabrication flaws in reactor pressure vessels.

This report contains estimated flaw rate functions for six different subsets of the SAFT-UT indications, along with confidence bounds. A principle conclusion of this project is that the flaw densities predicted by the SAFT-UT inspections are significantly greater in all six cases than those predicted by a Marshall distribution of flaws (Marshall, 1982). This difference is explained by the higher sensitivity of the inspections reported here compared to those employed during the Marshall Study. The Marshall distribution was developed in the 1970s and was based on the best inspection results of that time.

The inspection effectiveness of reactor pressure vessels for the mid-1970s has been quantified by the Plate Inspection Steering Committee Phase I (PISCI) studies. The inspection effectiveness of RPVs based on use of high sensitivity inspections has been quantified by the performance of advanced techniques in the Programme for the Inspection of Steel Components Phase 2 (PISCII).

In this report, recommendations are given for validating the indication rates by selective destructive analysis to provide the high quality flaw statistics necessary for probabilistic fracture mechanics analysis, such as pressurized thermal shock (PTS) analysis. The inspection data provided enough indications to estimate the six different indication rates in the reactor pressure vessel (RPV). These indication rates, after validation, can be used as the flaw rates for the PVRUF RPV and for other vessels that were fabricated using similar procedures.

Volume 2, in preparation, will provide the results of the destructive validation: the confirmed flaw density and distribution. Although these results have not yet been published, the principle findings of the destructive validation are: the 2500 indications in the SAFT-UT data are flaws; the flaws are mostly less than 4 mm (0.16 in.) in size (as predicted); the fusion lines of the structural weld with the base metal contain an elevated concentration of vertical planar discontinuities; flaws greater than 8 mm (0.32 in.) in size are associated with repairs; and the flaws are complex (a combination of cracks, lack of fusion, slag, and voids). What is chiefly not supported by the destructive validation test is the applicability of one of the sizing rules. The sizing rule in question states that two isolated, vertically oriented ultrasonic echoes can be explained by the presence of one crack and the echoes indicate the top and bottom of that crack. The application of this rule is confounded by the fact that the concentration of small flaws on the fusion line creates signals that are not easily distinguished from crack tips of a large crack. Specifically, some of the larger SAFT-UT indications reported in these NDE results will be characterized as two small flaws in the destructive examinations reported in Volume 2.

Acknowledgments

The authors would like to acknowledge the contribution of Mr. Robert Bowey in the fabrication of SAFT-UT data acquisition equipment for use at PVRUF and the contributions of Mr. Steven Minister and Ms. Marlana Campbell in the analysis of the SAFT-UT data. The authors would like to thank the cooperative staff at the Oak Ridge National Laboratory, in particular Dr. William Pennel, Mr. Fred Jackson, Dr. Daniel McGuire, and Mr. Paul Burns for providing support during the SAFT-UT inspections of the PVRUF vessel. Mr. Jeff Prior, Mr. Robert (Moe) Schoefield, and Mr. Luke Sunwoo did an outstanding job of operating the SAFT-UT system at ORNL and providing very accurately documented data for PNNL to use.

The authors wish to thank Cathy Stephens and Marsha Brehm for assistance in preparing this manuscript.

The authors thank the U.S. Nuclear Regulatory Commission, Office of Nuclear Regulatory Research for supporting this work and in particular the NRC program managers, Ms. Deborah A. Jackson, Mr. Craig A. Hrabal, Dr. Joseph Muscara, and Mr. Allen L. Hiser, Jr.

Glossary and Abbreviations

BWR. Boiling Water Reactor. A nuclear reactor in which the coolant is water, maintained at such a pressure as to allow it to boil and form steam.

Butt weld. The structural welds in RPVs (piping, etc.). This includes the RPVs circumferential and axial welds but does not include the cladding weldments.

Base metal. The metal that composes the RVP plates or forged rings. RPV plates (e.g., alloy A533B) and forged rings (e.g., A508) are assembled into an RPV by butt-welding.

Cumulative flaw rate. The density of flaws greater than a specified size.

False call. The characterization of a blank unit of material as flawed or cracked.

Flaw. An imperfection or unintended discontinuity in a material. A void, porosity, inclusion, lack of fusion or crack that is physically distinct from the metallic microstructure.

Flaw density. The number of flaws per unit length, area, or volume.

Flaw depth size. See through-wall extent.

Flaw distribution. The number of flaws measured in separate categories.

Flaw rate. The flaw density expressed as a function of flaw through-wall extent.

Fusion line. One of two lines, on the cross-section of the weld, that form the boundary between the weld metal and the base metal.

Heat-affected zone (HAZ). A portion of the base metal (adjacent to the weld) whose microstructure is altered by heat deposited during welding.

Indication (of a flaw). The response or evidence of a flaw from the application of NDE. For ultrasonic NDE, a coherent packet of (ultrasonic) energy that is characterized as originating from a flaw.

Inclusion. A foreign solid, (e.g., slag, scale, oxide, or non-metallic substance) entrapped in the base metal or weld metal.

LTOP. Low temperature over-pressurization.

Lack of fusion. Lack of metallic bond between weld passes or between a weld pass and the base metal.

LWR. Light water reactor. Either of two nuclear fission reactor designs (see BWR and PWR) that heat water as a means of power production.

Marshall Distribution. A cumulative flaw rate in the weld metal of RPVs. See Marshall 1982.

Midland vessel. The Consumers Power Unit 2 reactor vessel. See Babcock & Wilcox 1989.

Near-surface zone. The first 25mn (1.0 inch) of RPV material from the cladding's wetted surface.

Outside the near-surface zone. The remainder of vessel wall when the near-surface zone is excluded.

PVRUF vessel. The Pressure Vessel Research User's Facility vessel, at Oak Ridge National Laboratory, was a PWR vessel from a cancelled U.S. plant. See Pennel 1989.

Planar flaw. A flat two-dimensional flaw in a plane other than parallel to the surface of the component. In this study, it includes a crack or lack of fusion that is oriented vertically in the vessel.

POD. Probability of Detection. the expected value for the fraction of flawed or cracked units of material that will be found to be flawed or cracked by an inspection system.

Porosity. A group of voids located in close proximity to each other.

PWR. Pressurized Water Reactor. A nuclear reactor in which the coolant is water, maintained at such a pressure as to keep it from boiling.

PTS. Pressurized Thermal Shock.

RPV. Reactor Pressure Vessel.

Ring down. An ultrasonic term that refers to the period of time, following excitation of the transmit transducer, when acoustic interference is present at the receiver.

SAFT-UT. Synthetic Aperture Focusing Technique for Ultrasonic Testing. See Doctor 1995.

Size. See through-wall extent.

Through-wall extent. The maximum dimension, normal to the surface of the component, of the rectangle circumscribing the flaw.

Void. A volume of gas entrapped in the vessel material.

Volumetric flaw. A three-dimensional flaw such as a void, porosity, or inclusion without vertical orientation in the vessel.

Weld profile. The shape of the weldment when sectioned across the weld.

Wiebull Distribution. A distribution that has been used extensively to deal with such problems as reliability and life testing. The continuous random variable "s" has a Weibull Distribution, with parameters α and β, if its density function is given by

$$f(s) = \alpha\beta s^{\beta-1} e^{-\alpha s^{\beta}} \qquad S>0$$

$$= 0, \qquad \text{elsewhere}$$

where $\alpha > 0$ and $\beta > 0$.

1 Introduction

The U.S. Nuclear Regulatory Commission initiated a program at the Pacific Northwest National Laboratory (PNNL) with the major objective of estimating the rate of occurrence of fabrication flaws in U.S. light-water reactor pressure vessels (RPVs). In this study, RPV material was examined using a state-of-the-art ultrasonic inspection system, the Synthetic Aperture Focusing Technique for Ultrasonic Testing (SAFT-UT), to detect and characterize flaws created during fabrication.

This chapter discusses those flaw characteristics that are predicted by fracture mechanics calculations to be important for vessel integrity. Design and fabrication information on RPVs is presented in Chapter 2, especially on the subclass of vessels used in pressurized water reactors (PWRs), along with the specifications for the vessel inspected in this program. Chapter 3 specifies the measurements performed by SAFT-UT and includes a description of the SAFT-UT equipment and the calibration procedures. The analysis of the SAFT-UT inspections is described in Chapter 4, and example indications are presented to explain the process of detecting and characterizing the ultrasonic images produced by SAFT-UT. Chapter 5 discusses the most significant indications in the inspection and documents their important features. The distributions of the indications in those categories important for vessel integrity are presented in Chapter 6. Chapter 7 describes the tests measuring the performance of SAFT-UT as it pertains to probability of detection and sizing error, which are necessary inputs for calculating flaw rates. Chapter 8 presents the methodology for fitting a parametric rate function to the distribution of indications in the SAFT-UT measurements. Chapter 9 describes the validation plan for the characterized indications in the SAFT-UT data. Chapter 10 explains the ISI reliability requirements needed to predict flaw rates in vessels. The conclusions and recommendations that were derived from this program are given in Chapters 11 and 12. Further reference is provided in Chapter 13. The SAFT-UT images of the most significant flaws can be found in Appendix A.

Previous work has been included here. The analysis-before-test document was integrated into this report and the details of the inspections of the material removed from the Midland vessel are included as Appendix B.

Volume 2 of this report, in preparation, will document the results of the destructive validation of the SAFT-UT indications. As of this writing, the destructive validation is largely completed and the principle findings are: the 2500 SAFT-UT indications are flaws; the flaws are mostly small (as predicted), and the fusion line between the weld and the base metal contains an elevated concentration of small vertical planar discontinuities; flaws greater than 8mm in size are associated with repairs; and the flaws are complex (a combination of cracks, lack of fusion, slag, and voids).

What is chiefly not supported by the destructive analysis in the analysis of SAFT-UT indications presented here is the applicability of one of the sizing rules. The elevated concentration of small discontinuities on the weld fusion line created signals that are difficult to distinguish from crack tips. Consequently, the reader should expect the sizes of some of the flaws to be amended in Volume 2.

1.1 Reasons for Estimating Fabrication Flaw Rates

Estimates for flaw rates are an important input to structural assessments by probabilistic fracture mechanics, such as those relating to the Pressurized Thermal Shock (PTS) scenario. The PTS issue can be an important factor in questions pertaining to plant life extension for some plants. Computer codes such as the VISA code (Simonen, et al. 1986a) require accurate estimates of the flaw rates in the reactor vessel to determine the likelihood of a vessel failure during a PTS event. The majority of past work in probabilistic fracture mechanics (PFM) considered cracks to be expressed in terms of a single crack size parameter (size in the depth dimension). A two-dimensional crack is much more realistic but considerably more complex. Some PFM codes are capable of treating a two-dimensional crack, and are based on the assumption that a two-dimensional crack is a semi-elliptical surface crack.

These codes can provide the capability of considering more realistic and specific flaw rate information, but because of the lack of empirical data on fabrication flaw distributions, conservative assumptions are made about the initial flaw size distribution, aspect ratios, and

through-wall locations. Studies (Simonen et. al. 1986a, Simonen and Khaleel 1995) have shown that the probability of vessel failure is sensitive to: the location of the flaw in the vessel (i.e., near surface versus interior of the vessel wall); the flaw type (e.g., cracks, lack of fusion, porosity, inclusions, etc.); and the flaw aspect ratio (i.e., flaw length as well as depth). Therefore, it would be useful to have flaw rate estimates that are based on empirical data.

Future work, in NRC JCN W6275, will measure flaw density and distribution in material removed from the Shoreham, River Bend Unit 2, and Hope Creek Unit 2 vessels. These distributions, together with information on vessel fabrication techniques will be used to produce generalized flaw density and size distributions for application to the entire population of vessels of all classes. An existing statistical and weld process model, as developed by Chapman (1993) in the U.K., is being evaluated for its ability to predict vessel-specific flaw densities and size distributions for use with and comparison to in-service inspection (ISI) results from operating reactors. The data from this project will be used to benchmark and calibrate Chapman's predictive model. A calibrated predictive model, such as the one developed by Chapman, is expected to provide, when used with ISI data, a means of extrapolating the flaw rates from this project to the entire population of vessels in the U.S.

1.2 Principal Objectives

This program concentrated on estimating six different flaw rates in one reactor pressure vessel, the Pressure Vessel Research User Facility (PVRUF) vessel located at Oak Ridge National Laboratory. The PVRUF vessel is a PWR vessel that was fabricated by Combustion Engineering but never put into service. The pressure vessel manufacturing was started in 1978 and completed in 1982. It is constructed from A533B alloy steel.

At the start of this study, six different flaw rates were proposed that were all combinations of the two flaw types of interest (planar and volumetric) and three different locations (near surface, weldment, and base metal) as illustrated in Table 1.1. The three locations referred to in the table are defined as follows: "Near Surface" designates the region within 25 mm (1 in.) of the inner surface of the vessel wall. "Weldment" includes all welded material not within 25 mm of the inner surface and also the heat-affected zone of the base metal. "Base Metal" refers to all base metals not within 25 mm of the inner surface and outside the heat-affected zone. The heat-affected zone is the zone within the base metal that undergoes structural changes but does not melt during welding.

Table 1.1 Nomenclature for estimating cumulative flaw rates

Location	Flaw type: Planar	Flaw type: Volumetric	Units
Near Surface	$\Lambda_{sp}(s)$	$\Lambda_{sv}(s)$	# flaws/m^2
Weldment	$\Lambda_{wp}(s)$	$\Lambda_{wv}(s)$	# flaws/m^3
Base Metal	$\Lambda_{pp}(s)$	$\Lambda_{pv}(s)$	# flaws/m^3

s = flaw depth (cm)

The **cumulative flaw rate function**, $\Lambda_{kj}(D)$ describes the average number of flaws of type j greater than size D that occur in a unit of material in location k. For example, $\Lambda_{sp}(15)$ describes how many planar flaws with a depth greater than 15 mm would occur in a square meter of material within 25 mm of the inner surface. By definition, the negative of the derivative of the cumulative function represents the desired flaw rate function. This estimation problem is often discussed in terms of both the flaw rate and the cumulative rate. It is important to recognize that once one is determined, the other can be computed.

1.3 Secondary Objectives

The SAFT inspection produced flaw length information, so it is possible to consider flaw rate functions that depend on flaw length as well as on flaw depth. However, reliable estimation of such a two-dimensional function requires more data than needed to estimate the six flaw rates proposed. Nevertheless, estimates are made of both length and depth from the produced inspection data.

1.4 Flaws of Concern to Reactor Pressure Vessel Integrity

Characteristics of the fabrication flaws in reactor pressure vessels are necessary inputs for fracture calculations to assess reactor pressure vessel integrity. Fracture mechanics calculations are typically based on idealized flaws with worst-case characteristics. It is implied that "fracture mechanics flaws" often represent or approximate the significant flaws in the real vessel, which may have irregular and random features.

The majority of SAFT-UT indications in vessel inspections come from several categories of naturally occurring

flaws. These flaws do not, in general, correspond to the hypothetical and worst-case flaws that are usually assumed for purposes of fracture mechanics calculations. This analysis of SAFT-UT inspections focused on detecting and characterizing indications that approximate the idealized flaws of fracture mechanics models. Some categories of natural flaws are as follows.

Base metal flaws, which are present in the original plate or forging prior to vessel assembly and welding. Typical flaws of this type would be inclusions and laminations, which are most often encountered in the mid-wall region of the vessel cross-section, and with orientations parallel to the surfaces of the finished vessel.

Underclad cracks, which are produced by the heat input and stresses associated with the welding process used to apply the cladding to the inner surface of the vessel. These cracks will be in the base metal, initiating from the clad-to-base metal interface. Typical cracks are shallow in depth. The susceptibility of RPVs to such cracking depends on the particular grade of vessel steel and the welding process used to clad the vessel. If cracks are present in a given vessel, then there are likely to be a large number of such cracks.

Cracks in the cladding itself, which can be produced by stress corrosion cracking. These cracks will be shallow, but if conditions are right, they could occur in large numbers for a given vessel.

Welding flaws, which can occur either within the weld metal itself, or within the heat-affected-zone of the base metal. These flaws could occur anywhere within the thickness of the welded cross-section. Because root passes for welds are often made using special procedures, a bimodal distribution for such flaws can be postulated. The flaw distributions used in fracture mechanics calculations for RPVs tend to focus on welding and heat-affected zone flaws. In these calculations, the flaws are typically treated in a worst-case fashion, by assuming that the flaws are at the inner surface of the vessel.

In this study, we are interested in reporting flaw sizes and flaw locations that have the greatest impact on vessel integrity. Vessel failure modalities are described here because they determine which features of the measured flaw population are significant.

The pressurized thermal shock (PTS) and low-temperature over pressurization (LTOP) transients are two of the most important scenarios for reactor pressure vessel failure. Both of these events have been addressed in fracture mechanics calculations, and both contribute significantly to RPV failure probability. The PTS event produces high cooling within the inner vessel wall with associated high tensile thermal stresses and low fracture toughness in this region. Thus, small flaws near the clad inner surface are of primary concern.

The LTOP event has quite different characteristics. There are essentially no thermal stresses, and the stresses from internal pressure are relatively uniform through the wall of the vessel. During LTOP events, the entire vessel wall is also rather uniformly at low temperatures; in some cases these temperatures approach the lower shelf portion of the material's toughness-versus-temperature curve. Therefore, with relatively uniform distributions of both tensile stresses and fracture toughness, a flaw anywhere within the vessel wall could impact vessel integrity. However, buried flaws remain much less significant than surface flaws.

Results of fracture mechanics calculations predict the probability that the event of interest will cause vessel failure, but also for purposes of this discussion indicate the sizes and locations of flaws that are most likely to cause such failures. Two sets of calculations are discussed here, which address the bounding events of PTS and LTOP. The PTS case corresponds to a sudden cooling of a vessel starting from its initial state at operating temperature, whereas the LTOP events consists of a rapid increase in pressure for a vessel starting from a cold shutdown condition. PTS events present a severe challenge to vessel integrity but only to the inner region of the vessel wall. The stress levels for LTOP events are at more modest values, but the entire vessel wall is challenged at low temperatures, where the vessel material has relatively low resistance to brittle fracture.

Both the PTS and LTOP transients are more than postulated events, because both have actually occurred on several occasions at operating reactors. However, on all such occasions, the vessels have survived undamaged, because critical conditions of flaw size and material embrittlement did not exist at the time of the event for the particular vessels of concern.

PTS calculations have been performed in a previous study using the VISA-II computer code (Simonen et al. 1986b). Figure 1.1 shows histograms plotted from the results of these VISA-II calculations. The plots show the depths and locations of the flaws that were the root cause of the simulated vessel failure. The flaw location is defined as the distance from the inner tip of the flaw to the inner surface of the vessel. The Octavia flaw distribution

(Vesely, 1978) was assumed for these calculations, as well as a large flaw length relative to flaw depth. Flaws were assumed to be distributed uniformly or randomly through the vessel wall.

For PTS events, the calculations indicate that flaws situated outside the inner 30% of the vessel wall contribute little to RPV failure probability. Also, flaw depths greater than about 25% of the vessel thickness contribute little to failure probability, because the thermal stresses do not extend that far into the vessel. On the other hand, small flaws of depth less than 10% of the vessel wall make a substantial contribution. For PTS conditions, flaws as small as 6 mm (0.25 in.) can make a sizable contribution to the overall vessel failure probability.

LTOP calculations have been performed in a previous study using the VISA-II computer code (Simonen et al. 1986b) and assuming a severe pressure excursion at low temperature (as might occur during reactor startup). The assumed conditions for the selected LTOP example had a relatively high initial value of ductile brittle transition temperature and a low level of radiation damage. The vessel material was essentially on the lower shelf of the fracture toughness versus temperature curve during the LTOP event. The objective was to define a limiting case with relatively little variation of fracture toughness through the vessel wall. This case, although not representative of most LTOP situations, serve as a contracting bounding case relative to the conditions of PTS events. Figure 1.2 shows histograms plotted from the VISA-II results, presenting statistics on the depths and locations of the flaws that caused the simulated vessel failures for the LTOP event. Unlike the PTS scenario, flaw depths of less than 10% of the vessel wall thickness are relatively unimportant for LTOP failures. Rather, it is the somewhat larger flaws in the range of 10% to 30% of wall thickness that contribute the most toward vessel failure under LTOP conditions. Flaws greater than 30% of wall thickness contribute less to the probability of vessel failure, because they are much less likely to occur.

For the example LTOP event addressed here, the calculations show that flaws situated within the outer part of the vessel wall should be of concern, in addition to flaws near the inner surface. Figure 1.2 indicates that about half the calculated vessel failures are due not to surface flaws, but to flaws within the interior of the vessel wall. The other half of the calculated failures are due to flaws near surfaces of the vessel (inner and outer 10% of the wall thickness). In this regard, a given flaw within the inner 10% of the wall is about four times as likely to cause a vessel failure as the same flaw located elsewhere in the vessel wall. The results also show a similar but less severe sensitivity to flaws within the outer 10% of the vessel wall.

Deterministic calculations of stress intensity factors for PTS conditions have been reported by Simonen, Johnson, and Simonen (1985), and these results supplement the insights gained from probabilistic fracture mechanics calculations. Of particular interest in this discussion are flaws near the inner surface of the vessel, and the localized stress states that exist near the interface between the cladding and the base metal.

Figures 1.3 to 1.5 shows plots of calculated stress intensity factors Ki for various flaw configurations. For purposes of predicting the potential for brittle fracture, the factors have been normalized with respect to the governing fracture toughness at the tip of the crack. All calculations accounted for the stress state induced by the differential thermal expansion of the cladding relative to the base metal. The irradiated fracture toughness of the cladding was assumed to be the same as that for the base metal. Calculations were for the Rancho Seco transient, and for the same vessel parameters as described above for the probabilistic calculations. Figure 1.3 shows the relationship between flaw length and flaw depth on calculated stress intensity.

Figure 1.4 indicates that cracks parallel to the vessel surface have no impact on vessel integrity. In fact, these results show negative stress intensity factors, meaning that cracks will tend to close rather than open. It should be noted that these results address the embrittled region of the vessel beltline, and may not apply to other parts of the vessel with more complex states of stress.

There are significant driving forces that propagate small cracks that are entirely within the cladding, cracks that extend only slightly into the base metal, or base metal cracks at the interface with the cladding, Figure 1.5. Vessel integrity is quite sensitive to such cracks, and improved information on both the number and sizes of cracks in cladding is therefore desirable. Nondestructive Evaluation (NDE) examinations should include detailed examinations of the cladding, and the base metal region adjacent to the cladding. It should be noted that underclad cracks for Case 2 of Figure 1.5 can grow into the clad metal, which (unlike Case 3) is assumed to have the same low level of toughness as the base metal.

Figure 1.6 shows various flaws (shown to scale on a cross-section of a vessel wall) that has the same significance relative to vessel fracture in a PTS event. Clearly, a

long shallow crack extending through the cladding, shown at left, has a disproportionate impact on vessel integrity, although it may be of relatively small size. By comparison, a much larger subsurface crack, shown at right, is no more severe than the shallow crack through the cladding. Other evaluations of PTS have often observed an insensitivity to crack size, once the threshold crack size is exceeded. The comparisons depicted in Figure 1.6 support this observation.

Summing up, it is evident that a high priority should be given to detecting and characterizing flaws near the inner surface of the vessel (by size, shape, orientation, etc.). Within this region, flaws as small as 6 mm (0.25 in.) in depth can be significant, including flaws within the cladding. In addition, flaws within the remainder of the vessel wall should be detected and characterized. Somewhat larger flaws in this region, approximately 20 mm and greater, contribute to vessel failure in probabilistic fracture mechanics (PFM) calculations of LTOP events.

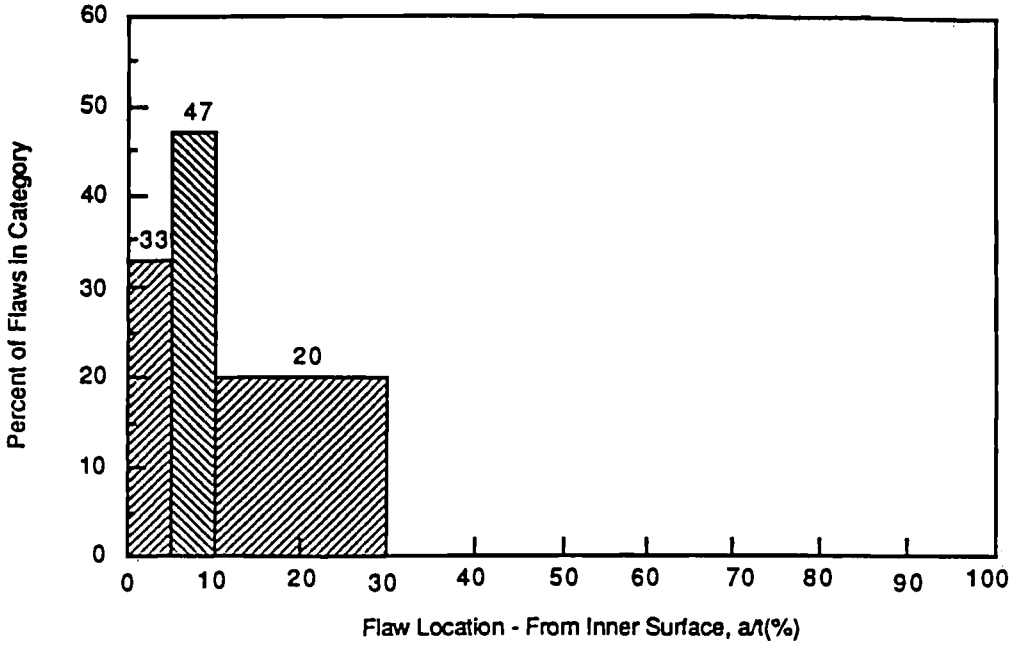

(a) Contribution of Various Flaw Locations to Vessel Fracture Probability

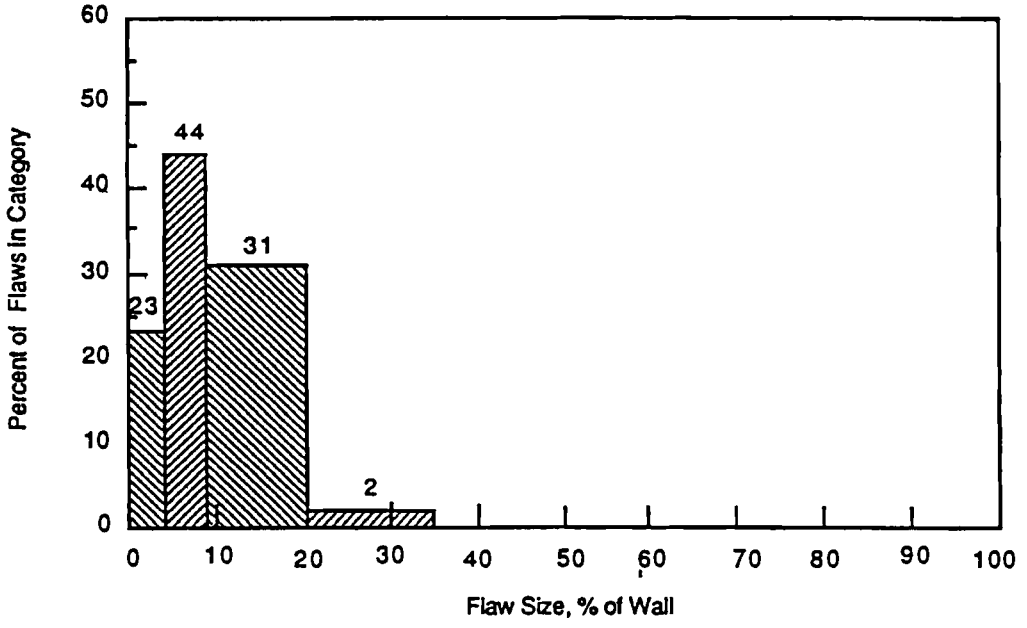

(b) Contribution of Various Flaw Sizes to Vessel Fracture Probability

Figure 1.1 Significant flaws for vessel fracture from pressurized thermal shock events (Simonen 1984)

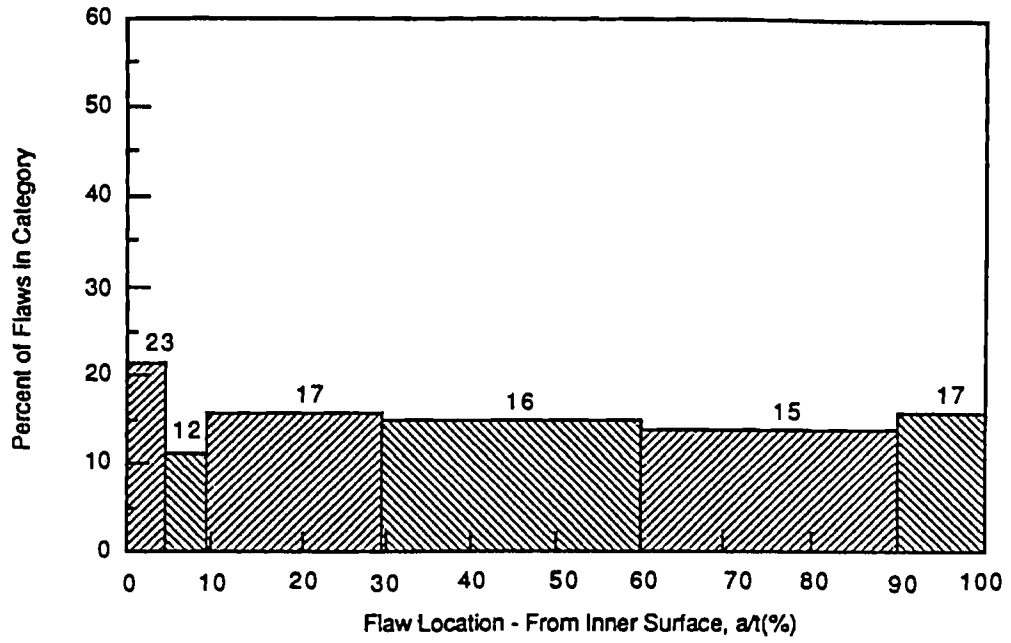

(a) Contribution of Various Flaw Locations to Vessel Fracture Probability

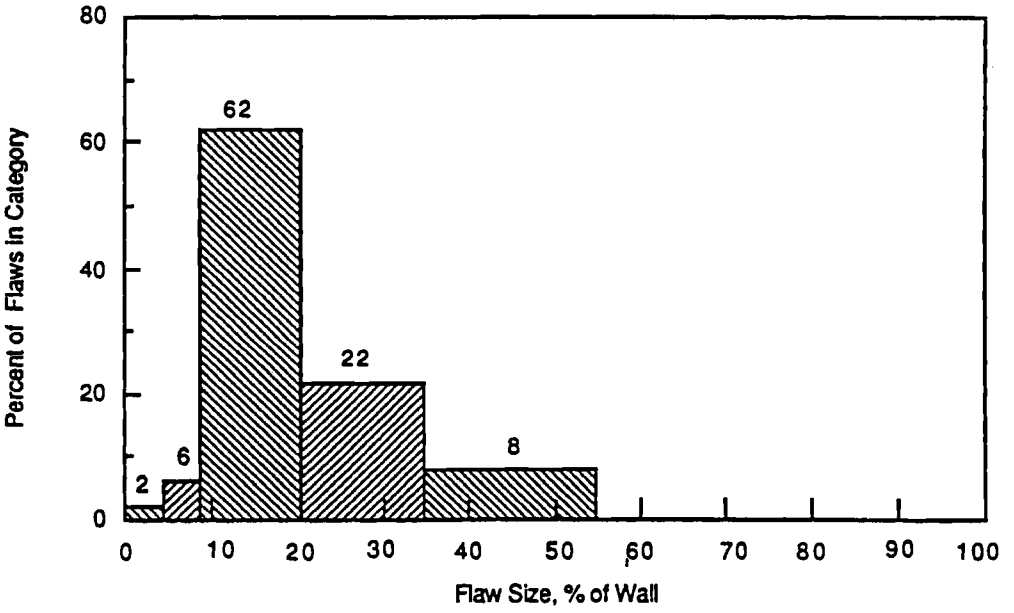

(b) Contribution of Various Flaw Sizes to Vessel Fracture Probability

Figure 1.2 Significant flaws for vessel fracture from low temperature over pressurization events (Simonen 1984)

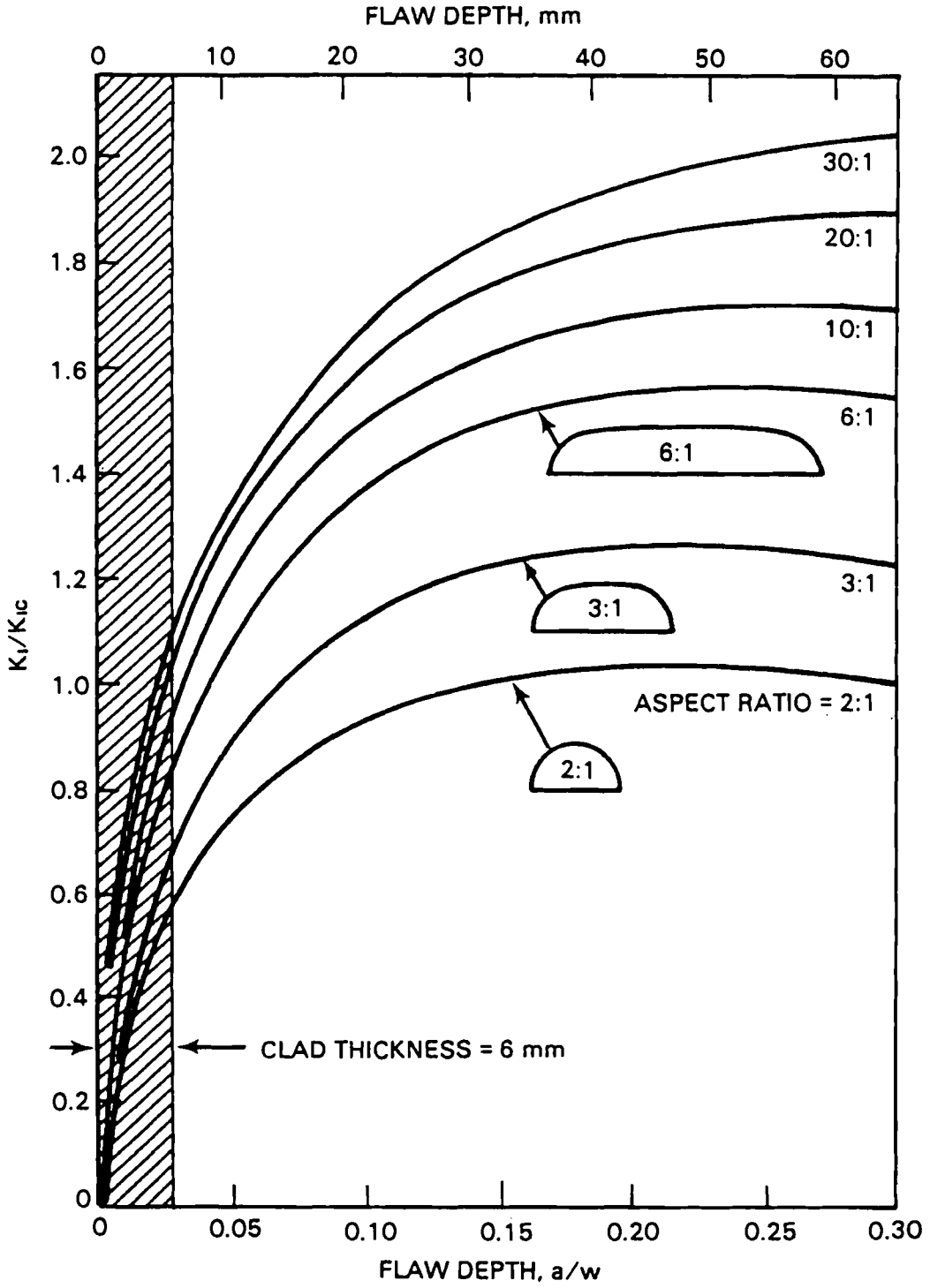

Figure 1.3 Effects of surface length on fracture evaluation (Simonen 1984)

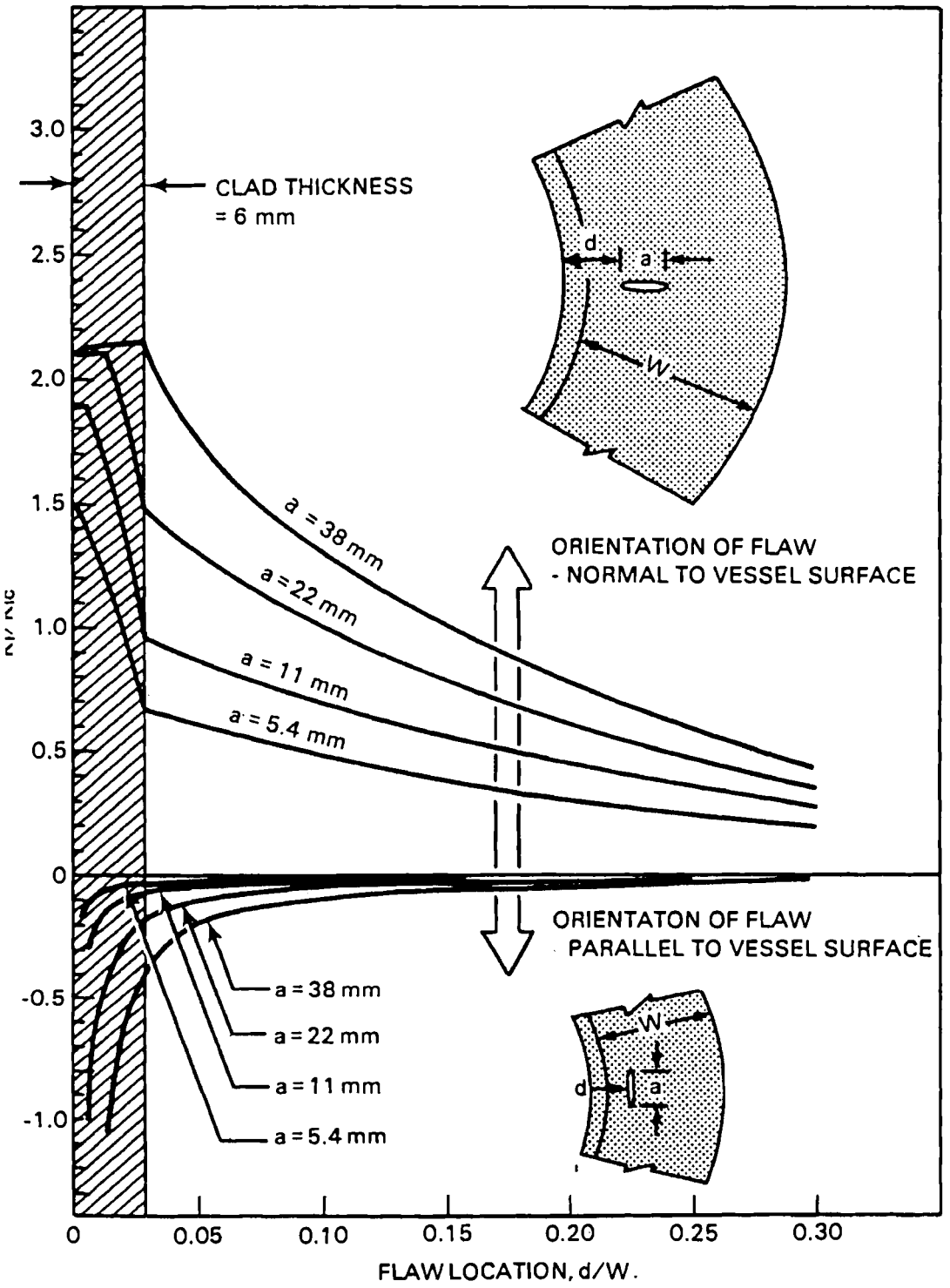

Figure 1.4 Effects of subsurface flaw location and orientation on fracture evaluation (Simonen 1984)

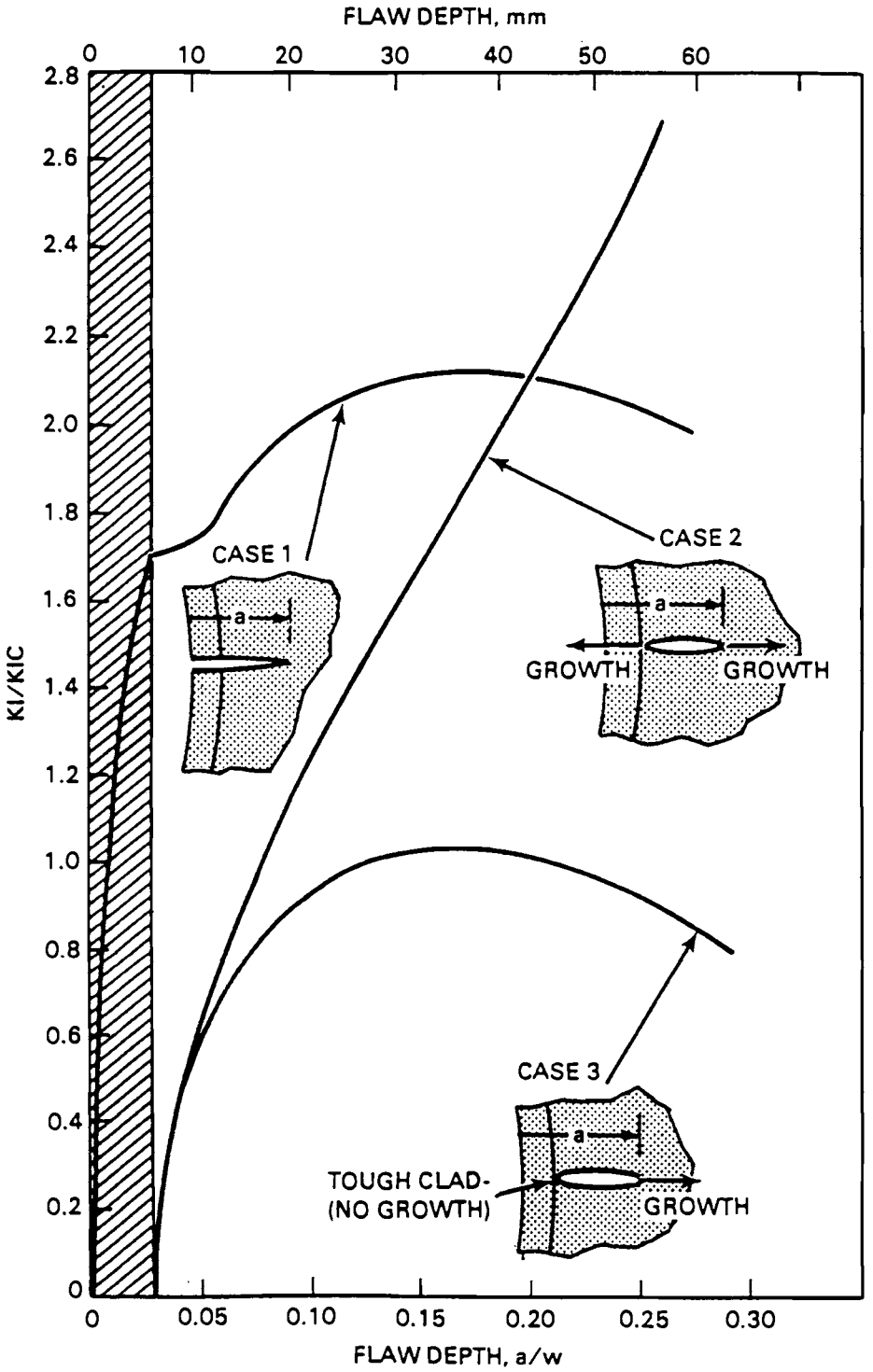

Figure 1.5 Effect of cladding on fracture evaluation (Simonen 1984)

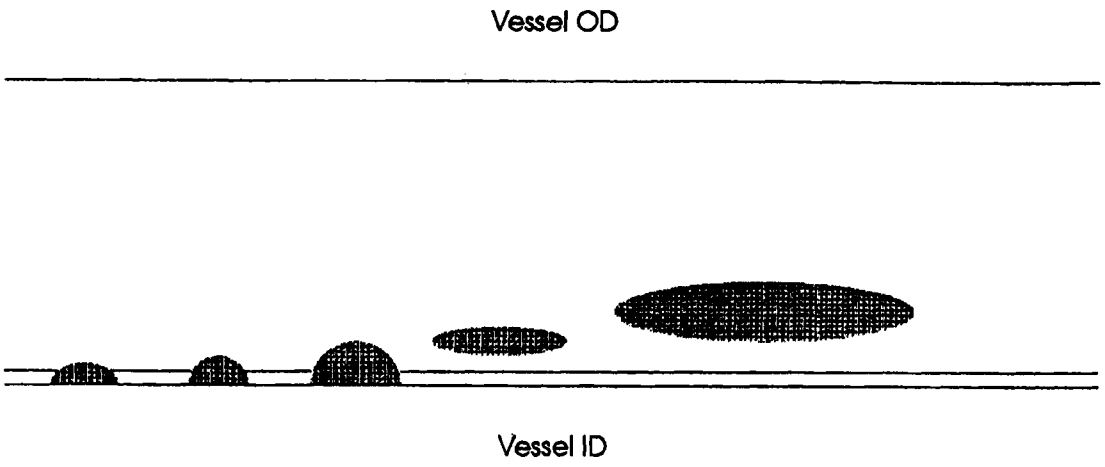

Figure 1.6 PTS flaws of equivalent severity

2 Description of Reactor Pressure Vessel Material

The reactor vessel is the most critical component in the light water reactor primary pressure boundary, since a loss of integrity will uncover the reactor core. Vessel integrity is of particular concern in PWRs because of the high coolant pressures, the high neutron doses, the limited make-up rate for lost coolant, and the event scenarios that challenge the integrity of the RPV.

For BWRs, the recent BWR Owners Group (BWROG) program on vessels and internals has performed analysis for various vessel failure scenarios. This work has found that the failure probabilities are much lower for the circumferential welds than for the axial or longitudinal welds. BWR vessel integrity is being driven by the structural integrity of axial or longitudinal shell course welds and the associated fabrication flaws in these welds (EPRI, 1995).

This program concentrated on measuring the fabrication flaws in two PWR reactor pressure vessels: the PVRUF vessel, and blocks removed from the Midland vessel (see Appendix B). The PVRUF vessel was fabricated by Combustion Engineering (CE) but was never put into service. Manufacture of the vessel was completed in 1982 and it is constructed from A533B alloy steel. The shell courses were fabricated from rolled and welded plate. About 30 similar reactor vessels in service in the U.S. were fabricated by CE out of A533B material.

The Midland vessel was fabricated by Babcock and Wilcox. The shell courses of the Midland vessel were fabricated out of forged rings by piercing a large ingot of A508 steel and rolling it until a ring of the proper shape was obtained. There are approximately 12 operating PWRs in service in the U.S. that were manufactured by B&W out of A508 material.

The estimates obtained in this study may be applied to the general population of reactors, but corrections must be made, depending on how similar the specific reactor is to the sub-population we have investigated. One way of accomplishing this is through coordination with work in progress on other NRC programs. Future work, in NRC JCN W6275, will gather information on vessel fabrication techniques for use in producing generalized flaw density and size distributions for application to the entire population of vessels or to classes of vessels. An existing statistical model, as developed by Chapman (1993) in the U.K., is being evaluated for its ability to predict vessel-specific flaw densities and size distributions for use with and comparison to in-service inspection (ISI) results from operating reactors. The data from this project will be used to benchmark and calibrate Chapman's predictive model. A calibrated predictive model such as the one developed by Chapman is expected to provide, when used with ISI data, a means of extrapolating the flaw rates from this project to the entire population of vessels in the U.S.

2.1 Differences Between PWRs and BWRs

Figure 2.1 illustrates a typical pressurized water reactor (PWR) pressure vessel and internals. A 1000-MWe class vessel is about 4.32 m (170 in.) in diameter and 13.7 m (45 ft.) high; the wall is about 228.6 mm (9 in.) thick.

The PWR system uses external steam generation and separation, so the PWR vessel is much shorter than the BWR vessel. The PWR system does not use internal jet pumps; hence, the PWR vessel has a smaller diameter than the BWR RPV. The PWR operates at a higher pressure, typically 15.5 MPa (2250 psi), and a temperature of 288-316°C (550-600°F). Accordingly, the PWR wall thickness is significantly greater than that of the BWR, to accommodate the higher operating pressure.

Vessel integrity is of particular concern in PWRs because of the high coolant pressures and high neutron doses. The problem of radiation embrittlement is reduced in BWRs because of their larger diameters, their lower pressures, more sources of water to cover the core, and the greater amount of water shielding the shell from the reactor core. However, radiation damage in BWR vessels could become a limiting factor, depending on material chemistries and accumulated fluence. Most BWR vessels have an end-of-life fluence ($E > 1$ MeV) of about 5×10^{17} n/cm^2 compared to a typical end-of-life fluence for a PWR vessel of about 1×10^{19} n/cm^2.

2.2 Fabrication Methods

Similar techniques have been used to fabricate BWR and PWR RPVs. Some PWR vessels have been constructed entirely from forged rings, flanges, and nozzles. The Midland vessel was fabricated in this manner. Alternatively, rolled and welded plate have been used to fabricate the

shell courses, and forgings for the flanges and nozzles. The PVRUF vessel was fabricated in this way. All BWR vessels have used the latter construction, with shell courses of rolled and welded plate.

For the rolled and welded construction practice, the first step in the fabrication sequence is to hot-form plate into 120° segments. Three 120° segments are then welded together into a shell course. The shell courses are typically clad with austenitic stainless steel weldment using either the multiple wire or strip cladding submerged arc welding process.

Three shell courses typically make up the cylindrical portion of a PWR. The upper shell course is usually thicker than the intermediate and lower shell courses. The additional thickness is required to reduce the stresses associated with the nozzle penetrations. Nozzle forgings are then welded into large diameter holes in the nozzle shell course. The vessel's upper flange is welded to the top of the nozzle shell course, and the intermediate shell course is welded to the bottom of the nozzle shell course, forming one of two vessel subassemblies. Following welding, a manually applied cladding layer is deposited on the zone around the weld in order to link the cladding already existing on the two shell courses.

The second vessel subassembly consists of the lower shell course and the bottom head. The final steps are to weld the upper and lower subassemblies together and stress relieve the assembly. Fabrication of the top head is conducted in a similar manner.

A forged vessel is constructed in a similar fashion, except that the shell courses are one-piece ring forgings. This construction technique avoids longitudinal weldments and generally requires between three and five forged rings to construct a reactor vessel.

2.3 Materials

Reactor vessel steel plate specifications have evolved since the beginning of the commercial nuclear power industry. The original steels selected, A212 and A302B, were in widespread use in the construction of fossil-fueled power plant components. All of the plates are low-alloy ferritic steels. A212 was used only in the very early plants, which are now decommissioned. A much more widely used material, A302B, is a carbon-manganese-molybdenum steel that was used in the quenched and tempered condition. With the increasing size of RPVs, greater hardenability was needed. The addition of nickel to the A302B composition provided the necessary increased hardenability to achieve the desired mechanical properties. This steel was initially known as A302B Modified. Later, it became the present grade A533B Class 1, which is the most widely used material for construction of RPVs.

In 1973, ASME Code and ASTM developed limits that were placed on the percentage of copper and phosphorus permissible for use in the beltline region of RPVs, where the neutron flux is high. The influence of weld chemistry on embrittlement were first addressed in Regulatory Guide 1.99, Revision 1 (U.S. NRC, 1979) and later updated in Revision 2 (U.S. NRC, 1988). The reduction of copper and phosphorus served to minimize the sensitivity of the steel to radiation embrittlement. The steel of choice was A533 for the beltline region. The current ASME Code and ASTM requirements for beltline materials in the reactor vessel for a new plant specify that the content of residual elements such as copper, phosphorus, sulfur, and vanadium should be controlled to low levels. However, in selecting the optimum amount of nickel allowed, its deleterious effect on radiation embrittlement should be balanced against its beneficial metallurgical effects and its tendency to lower the initial reference temperature for the unirradiated vessel material.

Pressure vessel forging materials have also evolved with time. The material used most extensively for RPV flanges, nozzles, and rings has been A508 Class 2 steel. Production problems were encountered with this material, in that underclad cracks occurred with certain cladding procedures. Application of strip cladding tended to produce small cracks on the order of several millimeters in depth in some of the heat-affected zones. It was eventually discovered that the presence of chromium in this forged material was the root cause of the cracking. Such cracking has never been observed in the A533B Class 1 plate material or the submerged arc weld metal. To eliminate underclad cracking, A508 Class 3 material is now used in place of A508 Class 2.

2.4 Weld Procedures

Full-thickness welding is required to assemble the shell courses, the nozzle forgings, the flange forgings, the top and bottom heads, and any internal or external support pads. The most frequently used technique is the automatic submerged arc welding procedure. The materials consumed in this welding process are a manganese-molybdenum-nickel filler wire and a granulated flux that

minimizes atmospheric contamination and provides ingredients to form a slag to remove oxides during the welding process. The type of flux material is important because the mechanical properties of the weldment can differ, depending on what flux is used. Welds made by Babcock & Wilcox employed Linde 80 flux which typically gives lower values of upper-shelf Charpy V-notch properties than other fluxes. Combustion Engineering (CE) and Chicago Bridge & Iron used Linde 0091, 1092, and 124 fluxes; these three fluxes produce similar mechanical properties.

Narrow-gap submerged arc welding is a variant of this welding technique used primarily for circumferential seam welds. The benefit of this variation is reduced weld metal volume and fabrication time. However, their upper shelf energy values are statistically and physically distinct on the basis of flux type (ABB-CE, 96)

Manual welding was used frequently for complex configurations, for repairs of base material, or for areas of weld buildup. A shielded metal arc (SMA) welding procedure was used in such instances. The SMA electrode is a wire coated with a bonded flux, typically an E8018 electrode.

The electroslag welding technique was used for full-thickness welds in some of the earlier BWR pressure vessels. This technique provides high deposition rates. Because of their coarse-grained cast microstructure, electroslag welds must be austenitized, quenched, and tempered in a manner similar to the treatment for the base metal.

All interior surfaces of the PWR vessel were clad with austenitic stainless steel to inhibit general corrosion and the buildup of radioactive crud. BWR vessels were clad below the steam-water interface. Three cladding processes were used. Automatic submerged arc welding with an SMA electrode was used when possible due to its high deposition rate. The process used either multiple wires or strip electrodes of Type 308 or 309 stainless steel. In areas where an automatic process was not possible, shielded metal arc or gas tungsten arc welding were utilized.

2.5 Description of PVRUF

The PVRUF pressure vessel was assembled by Combustion Engineering for a nuclear power plant that was never completed and its general configuration is illustrated in Figure 2.2. The pressure vessel has a diameter of 4.39 m (173 in.), a height of approximately 13.34 m (525 in.), and is made out of A533B material. The wall thickness of the pressure vessel varies from one region to the next, but around the beltline it is 22 cm (8.6 in.).

Table 2.1 shows the amount of base material in the PVRUF vessel. This table gives the volume and surface area for base material by vessel section (see Figure 2.2 for the relative location of each vessel section). Table 2.2 shows the amount of weldment in the PVRUF. This table gives the linear amount of weld in each section of PVRUF. Figure 2.2 identifies the welds by number. Figure 2.3 is a photograph of the PVRUF from the outside as it lay on its side during the inspections by SAFT-UT. Figure 2.4 is a photograph of the inside of the PVRUF vessel showing the instrument platform used for the SAFT-UT measurements.

2.6 Categorization of RPVs

Information is needed on the RPV fabrication characteristics in order to develop a basis for extrapolating flaw distribution estimates obtained from SAFT-UT inspections of the PVRUF RPV to the general population of RPVs in service. Useful information includes vessel history, methods of fabrication, welding processes, heat treatments, repairs during fabrication, plate and weld material types, and the preservice inspection results.

The Electric Power Research Institute (EPRI) has assembled a material chemistry database for RPVs. The database is intended to aid in the resolution of RPV radiation embrittlement/life extension issues, and does not contain information on RPV fabrication methods and procedures. However, it does contain design information on operating RPVs. The plant name, utility company name, vessel supplier, date of commercial operation, edition of the Code followed during vessel fabrication, shell materials, vessel ID, shell thickness, and cladding thickness are given in the database.

In response to generic letter 92-01, the Nuclear Regulatory Commission (NRC) has gathered a substantial amount of fabrication, chemical property, and fracture toughness information on RPV materials, plates, and welds. A Reactor Vessel Integrity Data Base was prepared under sponsorship of the NRC Office of Nuclear Reactor Regulation. This database was also assembled to address RPV radiation embrittlement/life extension issues, and is very useful for categorizing RPVs.

Table 2.1 Summary of base material volumes and areas in the PVRUF vessel

Assembly	Dimensions	Volume (m^3)	Area (m^2)
Upper Head	2.18 m Ri, 2.37 m Ro, 18.8 cm wall clad = 6 mm	11.95	57.98
Upper Shell:			
Shell	3.22 mm OD long, 4.34 m ID	9.80	71.79
Inlet Nozzle	4 Noz, 1.21 m OD, .71 m ID, 1.05 m long	4.48	15.57
Outlet Nozzle	4 Noz, 1.21 m OD, .75 m ID, .98 m long	2.50	11.75
Total Upper Shell:		28.68	157.09
Inter. Shell	4.37 m ID, 4.81 m OD, 2.67 m long	8.50	36.63
Lower Shell	4.37 m ID, 4.81 m OD, 2.67 m long	8.50	36.63
Bottom Head	2.24 m R, 13.4 cm wall	8.54	59.41
Total		54.22	289.75

Table 2.2 Summary of weld volumes in the PVRUF vessel

Weld no. description	Length (m)	X-Sect. (m^2)	Volume (m^3)
Weld-1 Dome to torus	10.74	0.0055	0.0585
Weld-2 Torus to flange	12.47	0.0043	0.0543
Weld-3 Flange to upper shell	13.62	0.0082	0.1115
Weld-4 Upper shell to inter. shell	13.73	0.0067	0.0925
Weld-5 Inter. shell to lower shell	13.73	0.0075	0.1025
Weld-6 Lower shell to bottom head torus	13.73	0.0040	0.0547
Weld-7 Bottom head torus to bottom head dome	10.73	0.0040	0.0427
Weld-8 Upper shell axial welds (3X)	9.66	0.0075	0.0725
Weld-9 Inter. shell axial welds (3X)	8.00	0.0057	0.0454
Weld-10 Lower shell axial welds (3X)	8.00	0.0057	0.0454
Weld-11 Nozzle welds:			
Inlet nozzles	18.67	0.6932	0.1901
Outlet nozzles	16.13	0.5966	0.1636
Totals	149.24		1.0339

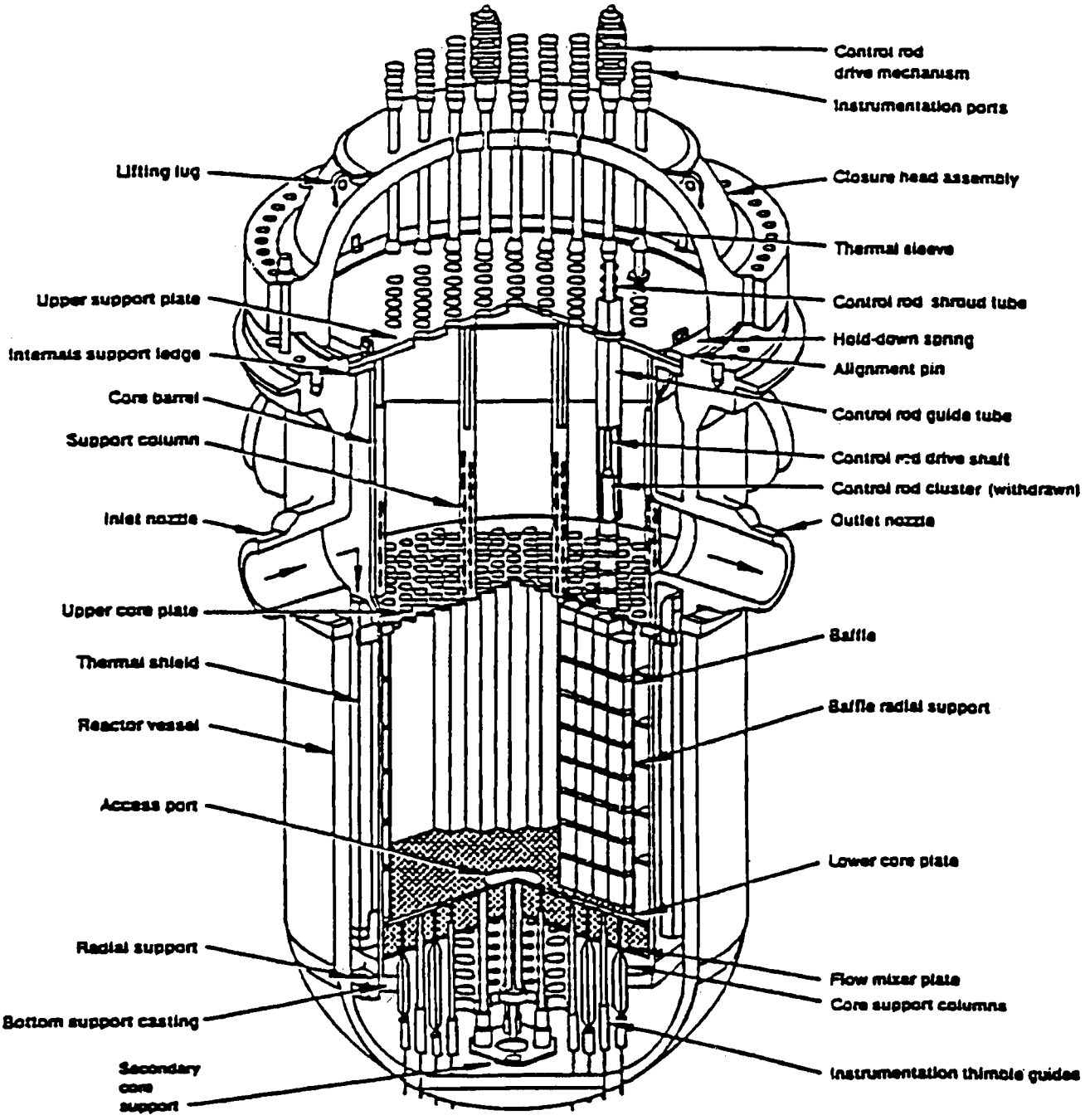

Figure 2.1 Typical PWR with internals (Luk 1993)

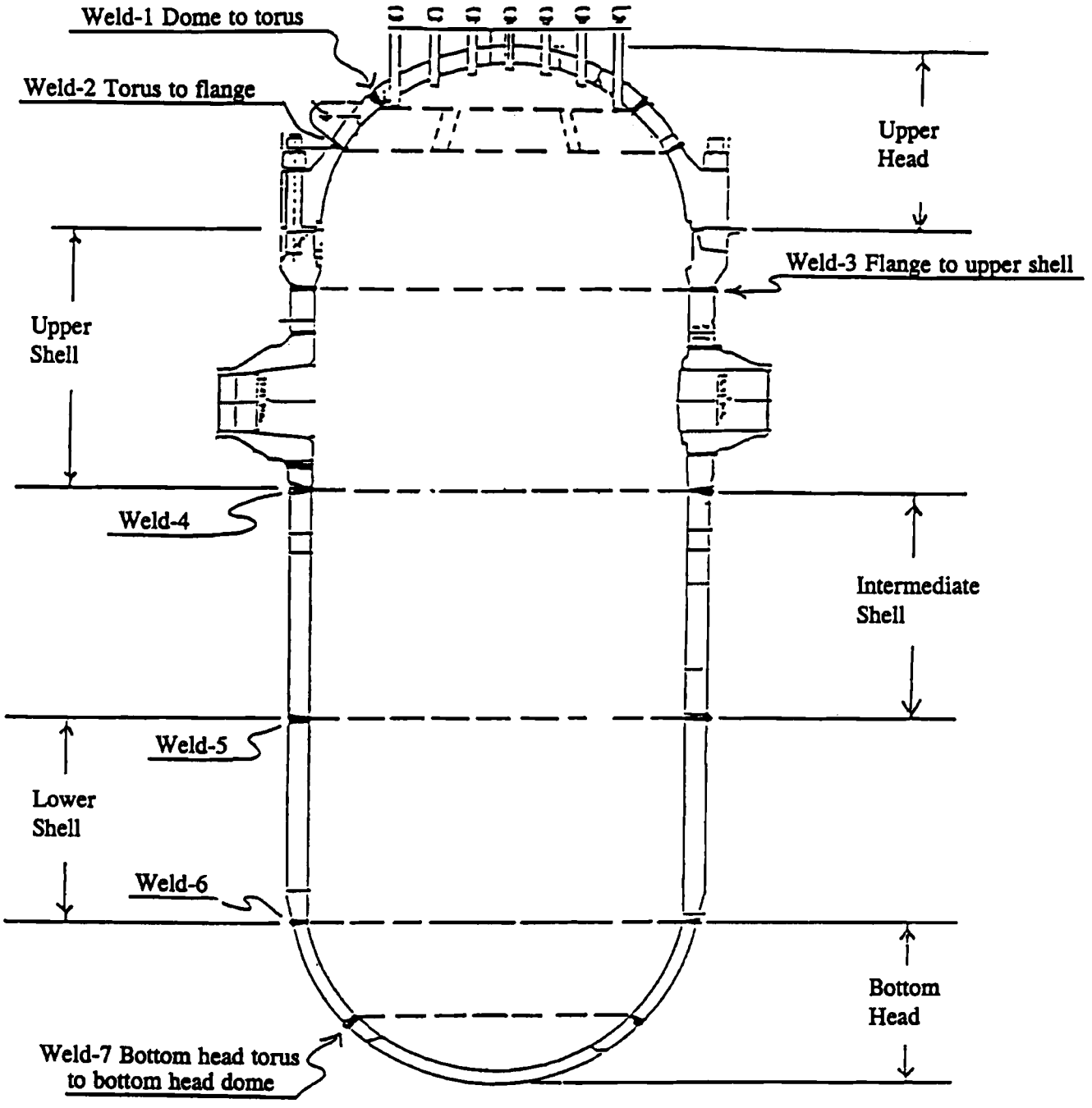

Figure 2.2 General schematic for PVRUF vessel showing weld identification numbers and configuration

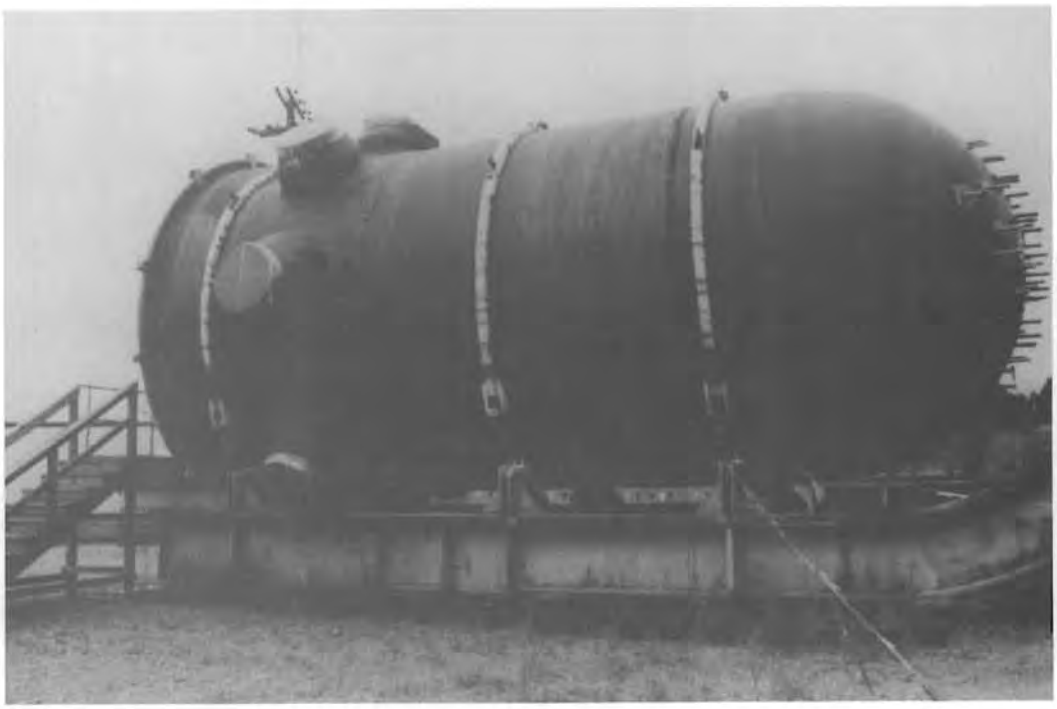

Figure 2.3 Photograph of the PVRUF vessel from the outside

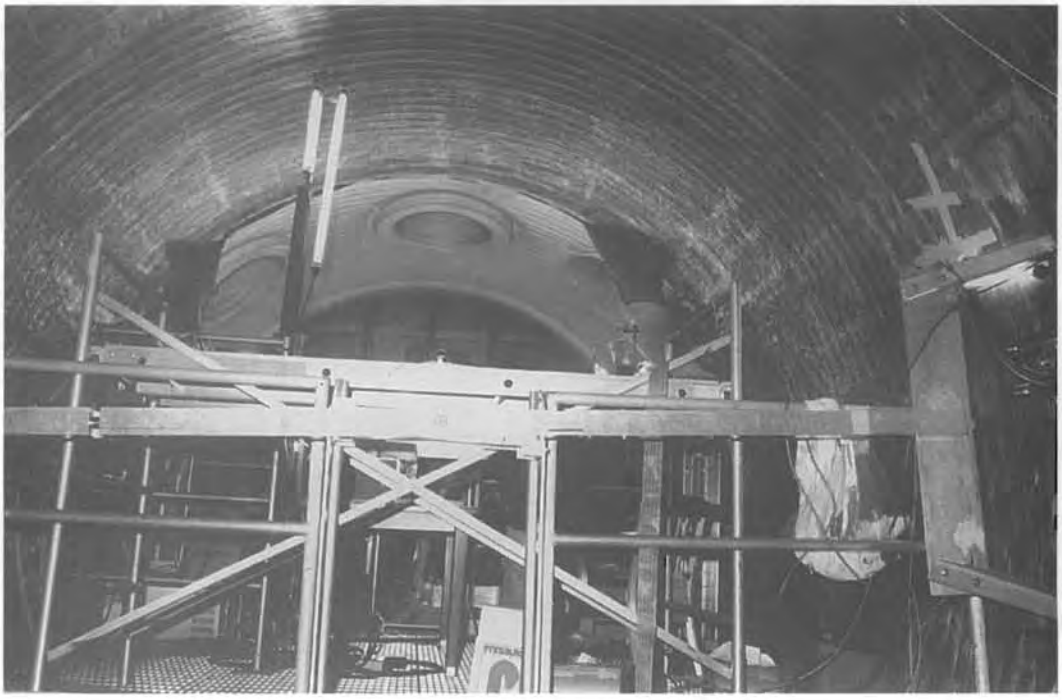

Figure 2.4 Photograph of the PVRUF vessel from the inside

3 SAFT-UT Measurements of RPV Material

The SAFT-UT field system is an excellent choice for evaluating fabrication flaws in nuclear pressure vessel material due to its validated high probability of detection of small flaws and its proven sizing accuracy for flaws in thick-section steel. The high performance of this system in this application is due to its focal properties.

In SAFT-UT, data is collected over a large area, using a small transducer with a diverging sound field. This technique, synthetic aperture focusing, has an advantage over physical focusing techniques in that the resulting image is full-volume focused over the entire inspection area. Traditional physical focusing techniques provide focused images only over a limited zone at the depth of focus of the lens. In SAFT-UT, digital signal processing of the data reproduces the focal properties of a large focused transducer.

Within a regional aperture, the coherent summation for each image point involves shifting a locus of A-scans by predicted time delays, and summing the shifted A-scans (digitized ultrasonic transients). Each picture element (pixel) is thus based on a spatial average of a number of points to produce the final value for display. Spatial averaging produces a second benefit of SAFT, an enhanced signal-to-noise ratio, suitable for detection and characterization of small reflectors in heavy section steel. For a complete description of the SAFT-UT system see Doctor et al., 1995.

3.1 SAFT-UT Equipment Configuration at PVRUF

In the development and evaluation of SAFT-UT technology, an important goal has been to improve the reliability of the inspection of reactor pressure vessels. Based on the experience with the Midland RPV blocks (see Appendix B), the SAFT-UT system was upgraded to better cope with the large volume of data that results from this kind of inspection, and to provide faster and more accurate scans.

A redesigned SAFT-UT system was assembled for the PVRUF inspections, and a block diagram is shown in Figure 3.1. A Compaq 486/25 personal computer performs the data acquisition and a Sun Microsystems graphics workstation performs the SAFT processing and data display. A photograph of the SAFT-UT data acquisition and display system at PVRUF is shown in Figure 3.2. Figure 3.3 shows the instrument platform inside the vessel, with the cross-vessel scanner track support assembly that was built to enable fast and convenient repositioning of the scanner track.

3.2 Measurement Plan for PVRUF

The inspection plan for the PVRUF vessel was based on previous SAFT-UT results on material from the Midland vessel, the condition of the PVRUF vessel (especially the clad surface roughness), and the necessity for off-line analysis of the SAFT-UT data. Previous use of SAFT-UT indicated that small flaws could be expected, and that 10 different ultrasonic inspection modes would be needed to characterize the ultrasonic indications. The surface conditions of the PVRUF vessel were typical of U.S. RPVs (based on visual inspection by PNNL staff of the cladding on other RPVs and on knowledge of U.S. clad fabrication processes). The roughness of the clad surface limited the scanning speed. Data analysis was performed at PNNL.

One of the principal findings of the SAFT-UT inspection of material removed from the Midland reactor pressure vessel was that most of the flaws (80%) were less than 2 mm (0.08 in.) in through-wall extent. That was one of the reasons for operating the SAFT-UT system with high spatial sampling rates. Because the SAFT-UT system's lateral resolution is sufficient to show flaw features on the order of one wavelength, the step sizes were set to one half of one wavelength in both the X and Y scanner directions. This had the effect of producing smooth images of the flaws, with the best capacity to separate small flaws that may be close together.

Ultrasonic inspection of the PVRUF vessel was conducted. Table 3.1 specifies the ten inspection modes. Five of the modes were used for inspection of the inner 25 mm (1.0 in.) of the vessel wall. A 4-MHz, dual-element, normal-beam transducer was used in inspection mode #1 to provide sensitivity to volumetric flaws (porosity and slag inclusions) near the inner surface of the vessel. Figure 3.4 shows the insonification pattern in mode 1. A 2-MHz, dual-element, 70° angle-beam

Table 3.1 SAFT-UT inspection plan for PVRUF

Inspection no. / type	Beam (skew) direction	Frequency, MHz	Y length, cm (in.)	X length, cm (in.)	File size, MB
Near-surface zone inspections					
1 / Normal beam	NA	4.0	23 (9)	23 (9)	22
2 / 70°, L-wave	+X	2.0	23 (9)	23 (9)	8
3 / 70°, L-wave	+Y	2.0	23 (9)	23 (9)	8
4 / 70°, L-wave	-X	2.0	23 (9)	23 (9)	8
5 / 70°, L-wave	-Y	2.0	23 (9)	23 (9)	8
Inspection of the base-metal weld					
6 / 45°, S-wave	+X	1.5	23 (9)	28 (11)	80
7 / 45°, S-wave	+Y	1.5	23 (9)	23 (9)	75
8 / 45°, S-wave	-X	1.5	23 (9)	28 (11)	80
9 / 45°, S-wave	-Y	1.5	23 (9)	23 (9)	75
10 / Normal beam	NA	5.0	23 (9)	12.7 (5)	157

transducer was used in modes 2 through 5 to provide sensitivity to planar flaws (cracks or lack of fusion) that may be oriented along or across the weld. Figures 3.5 through 3.8 show the insonification patterns using the 70° L wave transducer.

In a similar fashion, additional five inspection modes were used to detect and characterize indications in the vessel material located more than 25 mm (1.0 in.) below the inner vessel surface. A 1.5-MHz, 45° angle beam shear transducer was used in inspection modes 6 through 9 to provide sensitivity to planar flaws that may be oriented along or across the weld. Figures 3.9 through 3.12 show the insonification patterns for the 45° S-wave inspection modes. A 5-MHz normal-beam transducer was used in inspection mode 10 to provide sensitivity to volumetric flaws. Figure 3.13 shows the insonification domain for the mode 10 inspection.

Table 3.1 also shows the scanning details and file sizes for the different SAFT-UT inspection modes. The five inspections of the upper 25 mm of the vessel wall had 23 x 23 cm (9 x 9 in.) scanning apertures. The five inspections of the base metal weld had apertures and file sizes listed in the table. Table 3.2 shows the step sizes and sampling rates for the PVRUF inspections.

Staff of the Oak Ridge National Laboratory (ORNL) were trained in the proper operation of the SAFT-UT system and collected all the data, with relatively little PNNL oversight. The inspections started with the beltline weld. This is the circumferential weld between the intermediate and lower shell courses of the vessel, labeled weld #5 in Figure 2.2. After the beltline weld, the circumferential weld between the intermediate and upper shell course (weld #4) was inspected. The SAFT-UT system worked very well, but after inspecting 20.3 m (800 linear in.) of weld, 50 GBytes of data, and 18 months of operation the SAFT-UT system needed repair in order to do further inspection. We would have liked to conduct more inspections, but our data indicated that a sufficient number of indications had been detected; so the data acquisition task was ended.

3.3 Calibration of SAFT-UT Inspections

Calibration of the SAFT-UT system was performed when the system was turned on and when the transducers were changed. For calibration, the SAFT-UT scanner was moved to the calibration blocks that were made available for the calibration procedure. SAFT-UT inspection modes 1 through 5 used PNNL calibration block #1-2A-5B-1 and inspection modes 6 through 10 used PVRUF block #196-103. Figure 3.14 shows a photograph of the scanner attached to the calibration block for calibration of modes 6 through 9. The three side drilled holes for 45° S wave calibration are visible in the photograph. Figure 3.15 shows a photograph of the scanner attached to the calibration block for calibration of mode 10.

For ease of operation, a computerized calibration procedure was provided to the inspection team. The computerized procedure first prompts the operator for the transducer type.

Table 3.2 Step sizes and sampling rates for SAFT-UT inspections of the beltline weld in PVRUF

No.	Y length, cm (in.)	Y step, cm (in.)	X length, cm (in.)	X step, cm (in.)	Sample rate MHz
1	23 (9)	0.08 (0.03)	23 (9)	0.08 (0.03)	25
2	23 (9)	0.15 (0.06)	23 (9)	0.15 (0.06)	12
3	23 (9)	0.15 (0.06)	23 (9)	0.15 (0.06)	12
4	23 (9)	0.15 (0.06)	23 (9)	0.15 (0.06)	12
5	23 (9)	0.15 (0.06)	23 (9)	0.15 (0.06)	12
6	23 (9)	0.10 (0.04)	28 (11)	0.10 (0.04)	6
7	23 (9)	0.10 (0.04)	23 (9)	0.10 (0.04)	6
8	23 (9)	0.10 (0.04)	28 (11)	0.10 (0.04)	6
9	23 (9)	0.10 (0.04)	23 (9)	0.10 (0.04)	6
10	23 (9)	0.06 (0.025)	13 (5)	0.06 (0.025)	25

Normal Beam, full volume:
KB-A, #M21240, 0.25" diameter, 5 MHz.
-or-
KB-A, #M21241, 0.25" diameter, 5 MHz.

Normal Beam, near surface:
Sigma, #2001-89001, dual element, 4 MHz.

Angle Beam, near surface:
RTD 70, L wave, #84-23, dual element, 2 MHz.

Angle Beam, full volume:
KB-A, #17275, 45°, S wave, .375" dia., 1.5MHz
-or-
KA-A, #15124, 45°, S wave, .375" dia., 1.5MHz

After the transducer type is selected, the computerized procedure retrieves the established gain settings for the data acquisition electronics and starts the transducer excitations on the side drilled holes in the calibration blocks. The signal level for each of the side drilled holes was checked and documented for the selected transducer. The documentation included a photograph of the signal level on an oscilloscope.

Figure 3.16 shows the signal strength from the 1/4 thickness side drilled hole in the PNNL calibration block for the near surface normal beam transducer used in SAFT-UT inspection mode 1. The signal strength of the transducer signal from this reflector was reproduced to calibrate each transducer type at the start of a set of inspections. Figure 3.17 shows the signal strength from the 1/4 thickness side drilled hole in the PNNL calibration block for the near surface angle beam transducer used in inspection modes 2 through 5.

Figure 3.18 shows the electronic distance-amplitude correction (DAC) that was applied to the signal from the full volume angle beam transducer. This correction was applied with a time varying gain (TVG) amplifier that produced the gain slopes shown in the figure. This electronic DAC curve was maintained for all inspections with the full volume angle beam transducer. Figures 3.19 through 3.21 show the signal strengths from the calibration block after the time variable gain amplifier applied the electronic DAC.

Figure 3.22 shows the electronic distance-amplitude correction (DAC) that was applied to the signal from the full volume normal beam transducer. Figures 3.23 through 3.25 show the signal strengths from the calibration block after the time variable gain amplifier applied the electronic DAC.

3.4 Scanning Procedure and Vessel Coordinate System

After the calibration of the transducer, the computerized data acquisition procedure prompted for the inspection mode (1 through 10) and for the starting coordinate of the scanner on the weld's circumference. The file name for the inspection data was constructed from the inspection mode and the starting circumferential coordinate. For example, "5s1_360" identified the file as an inspection of weld 5, using mode 1, and starting at circumferential PNNL coordinate 9.144 m (360 in.).

PNNL's inspection coordinate system for the beltline weld was measured along the weld's inside diameter, starting with 0.0 inches at the bottom dead center as the

vessel lay on its side. The weld coordinate increased clockwise with the observer facing the back (or bottom) of the vessel. The weld center line had been marked with punch marks on the clad surface by the manufacturer of the vessel. PNNL marked the weld circumference with triple punch marks every 203 mm (8.0 in.) starting at the bottom of the vessel. The coordinate across the weld was measured as a positive or negative distance from 0.0 inches at the weld center line, with positive being closer to the vessel entrance (flange side).

PNNL's inspection coordinate system for the circumferential weld between the intermediate and upper shell courses was not the same as for the beltline weld, because of the inside diameter change from the intermediate to upper shells. The scanner track was moved to the entrance (flange) side of the weld in order to accommodate the smaller inside diameter of the upper shell course, and the coordinate system was changed as follows. The weld coordinate increased counter clockwise with the observer facing the back (or bottom) of the vessel. The weld center line was punch marked in the same way as the beltline weld. The coordinate across the weld was measured as a positive or negative distance from 0.0 inches at the weld center line, with positive being closer to the vessel entrance (flange).

3.5 Amount of Material Inspected

SAFT-UT was used to inspect all of the beltline weld and approximately half of the weld of the intermediate to upper shell course for a total of 20 meters (800 inches) of inspected weld in 10 inspection modes. Table 3.3 lists the volumes and surface areas for the SAFT-UT inspection at PVRUF, based on the nominal cladding thickness of 6 mm and the weld cross sections from the construction drawings.

Table 3.3 Amount of material inspected by SAFT-UT at PVRUF

Near surface zone	
Clad	0.027 cubic meters
Clad-to-Base Metal Interface	4.6 sq. meters (surface area)
Weld	0.0082 cubic meters
Heat-affected Zone	0.005 cubic meters
Base Metal	0.075 cubic meters
Deeper zone	
Weld	0.19 cubic meters
Heat-affected Zone	0.051 cubic meters
Base Metal	0.90 cubic meters for angle beam
	0.28 cubic meters for normal beam

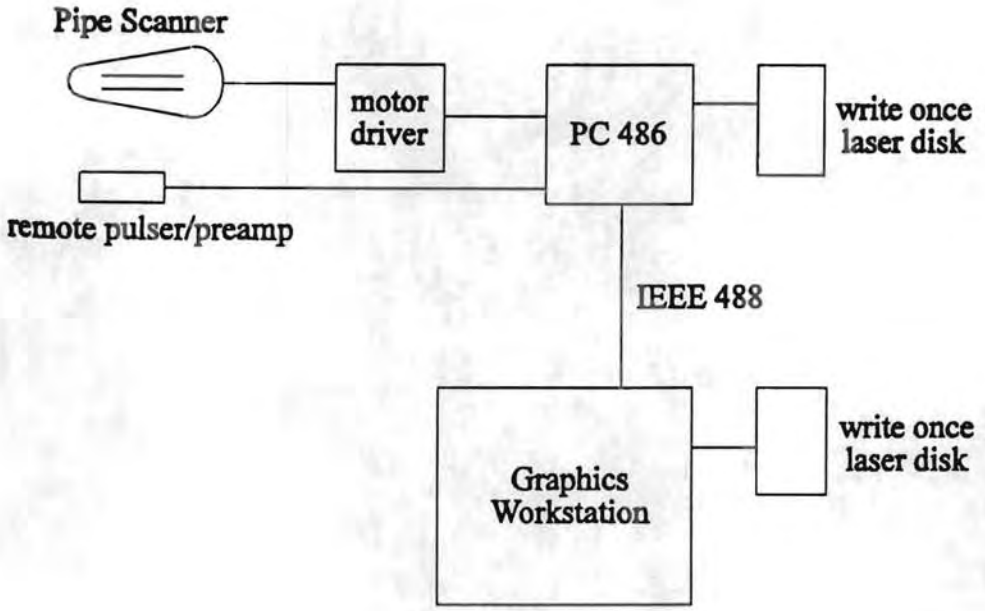

Figure 3.1 Block diagram of SAFT-UT field system as configured at PVRUF

Figure 3.2 SAFT-UT data acquisition and display system as configured for PVRUF

Figure 3.3 Instrument platform and scanner pendulum showing center pivot

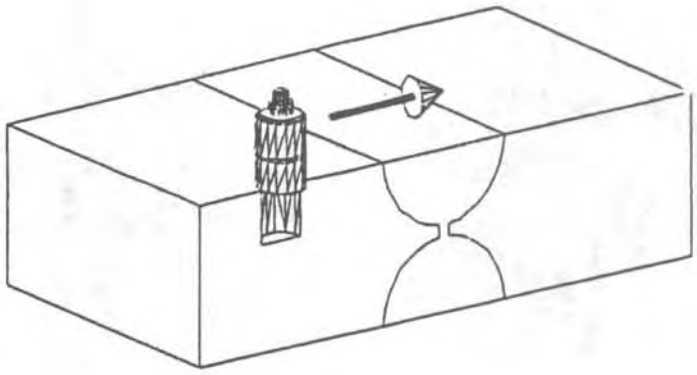

Figure 3.4 Insonification for inspection mode 1, near surface normal beam

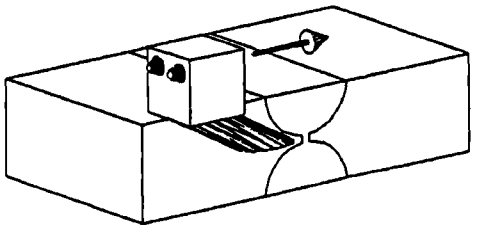

Only Inspects Upper 25 mm Across the Weld

Figure 3.5 Insonification for inspection mode 2, near surface 70°L wave at 0° skew

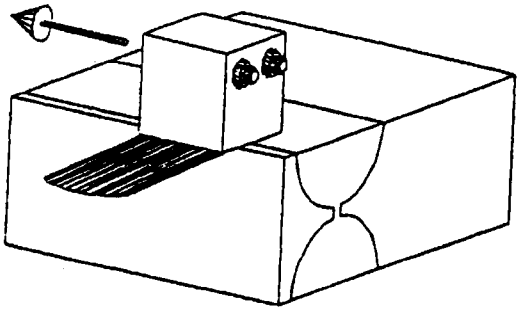

Only Inspects Upper 25 mm

Figure 3.6 Insonification for inspection mode 3, near surface 70°L wave at 90° skew (along the weld)

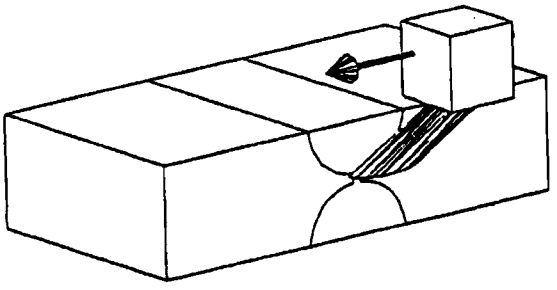

Only Inspects Upper 25 mm

Figure 3.7 Insonification for inspection mode 4, near surface 70°L wave at 180° skew (across the weld)

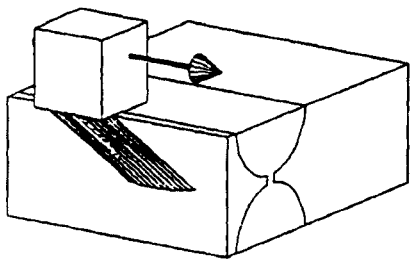

Only Inspects Upper 25 mm

Figure 3.8 Insonification for inspection mode 5, near surface 70°L wave at 270° skew (along the weld)

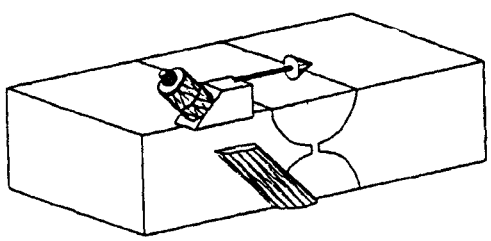

Upper 12 mm Not Inspected

Figure 3.9 Insonification for inspection mode 6, full volume 45°S wave at 0° skew

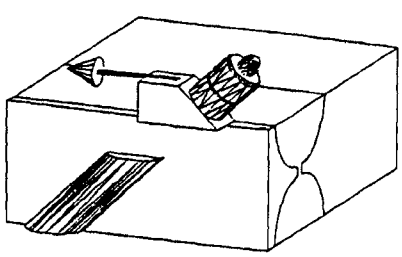

Upper 12 mm Not Inspected

Figure 3.10 Insonification for inspection mode 7, full volume 45°S wave at 90°skew

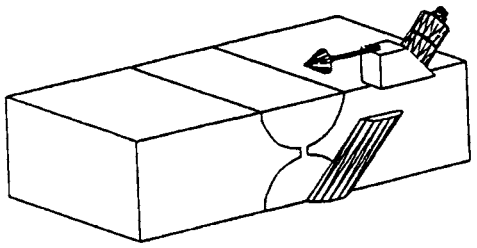

Upper 12 mm Not Inspected

Figure 3.11 Insonification for inspection mode 8, full volume 45°S wave at 180° skew

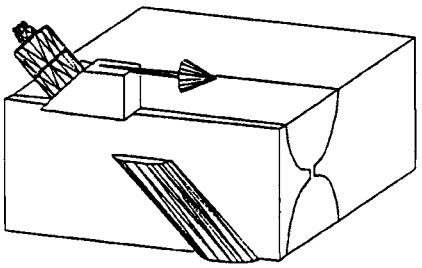

Upper 12 mm Not Inspected

Figure 3.12 Insonification for inspection mode 9, full volume 45°S wave at 270° skew

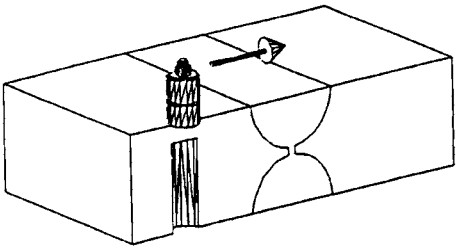

Upper 12 mm Not Inspected

Figure 3.13 Insonification for inspection mode 10, full volume normal beam (full volume, normal beam)

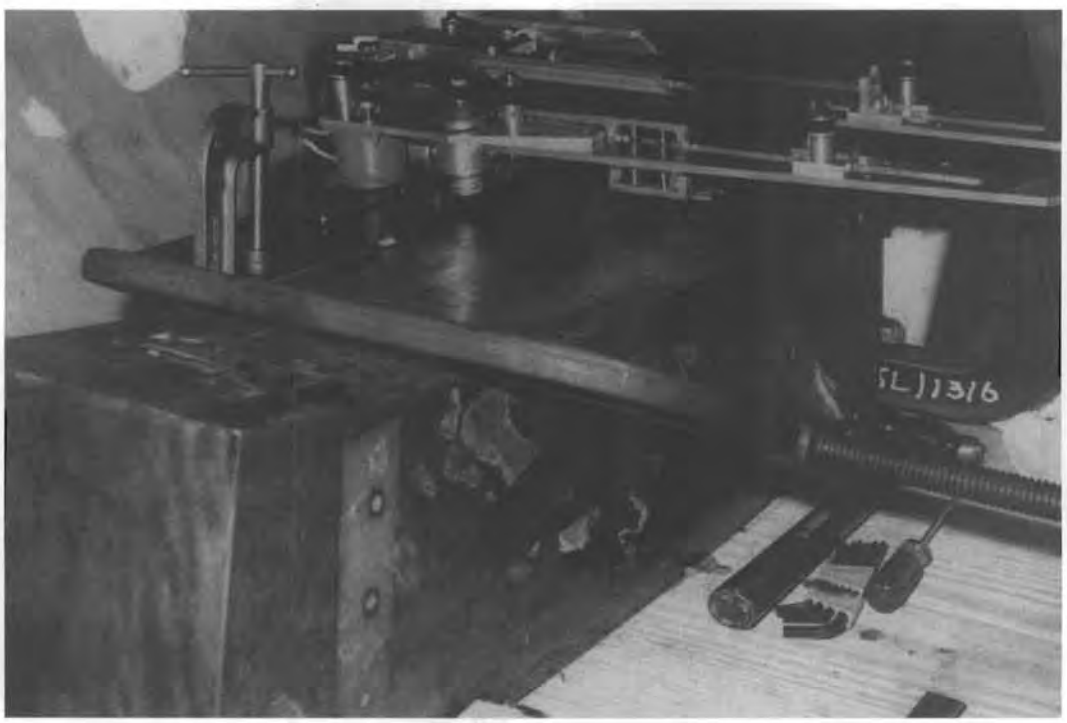

Figure 3.14 SAFT-UT scanner attached to the calibration block for calibration of inspection modes 6 through 9, 45°S wave inspections

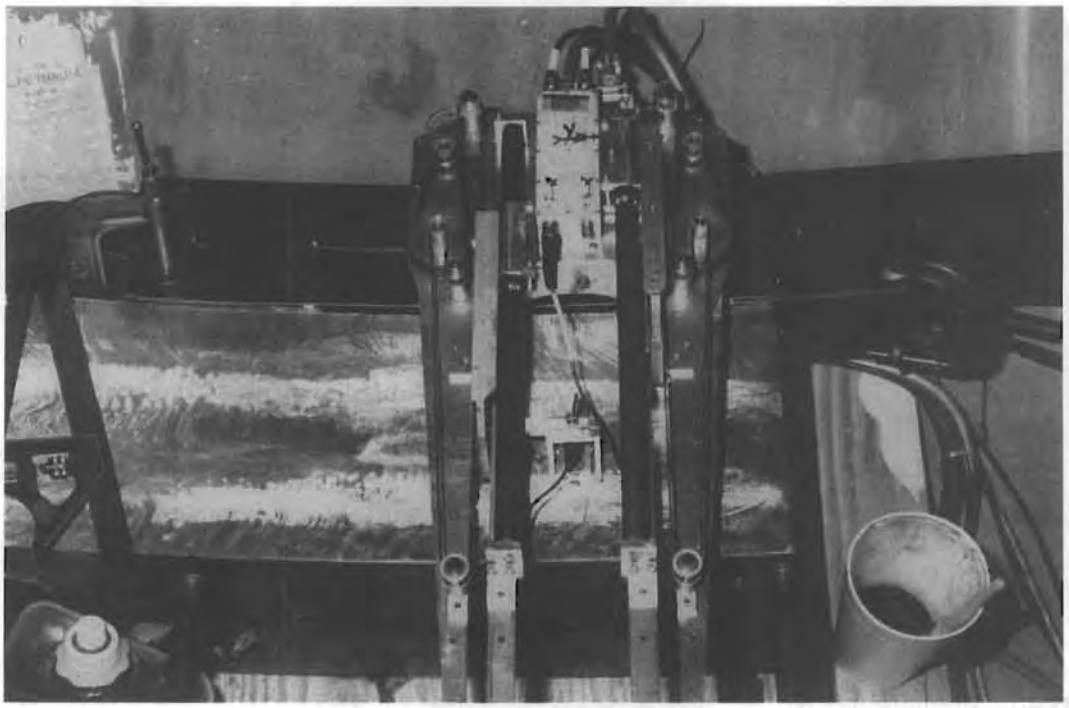

Figure 3.15 SAFT-UT scanner attached to the calibration block for calibration of inspection mode 10, normal beam

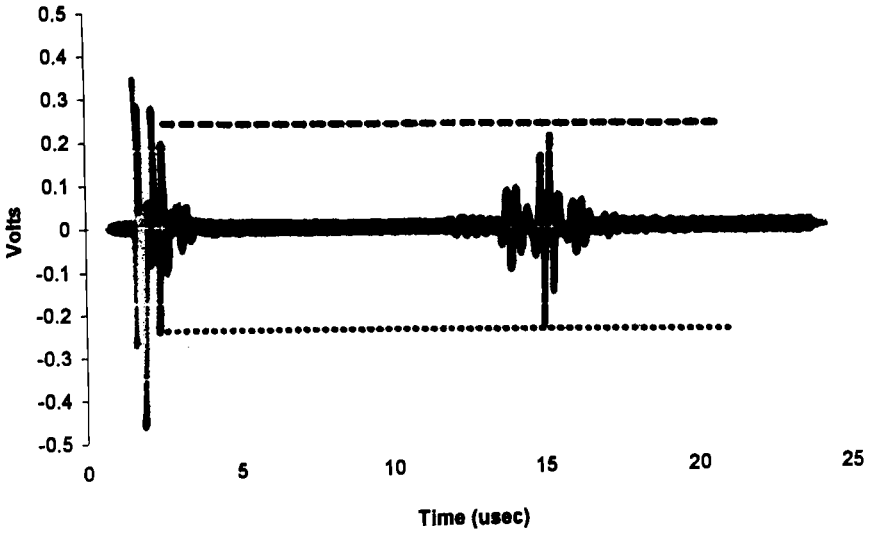

Figure 3.16 Signal strength from 1/4 thickness side drilled hole in calibration block for inspection mode 1

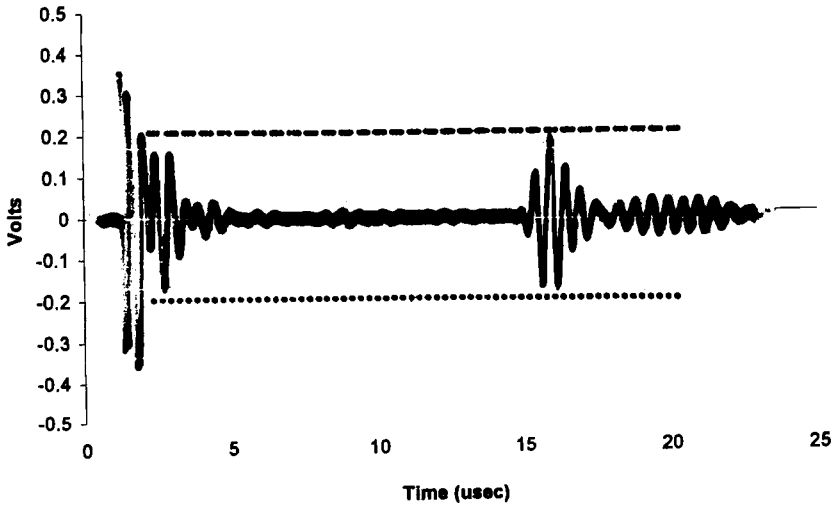

Figure 3.17 Signal strength from 1/4 thickness side drilled hole in calibration block for inspection modes 2 through 5

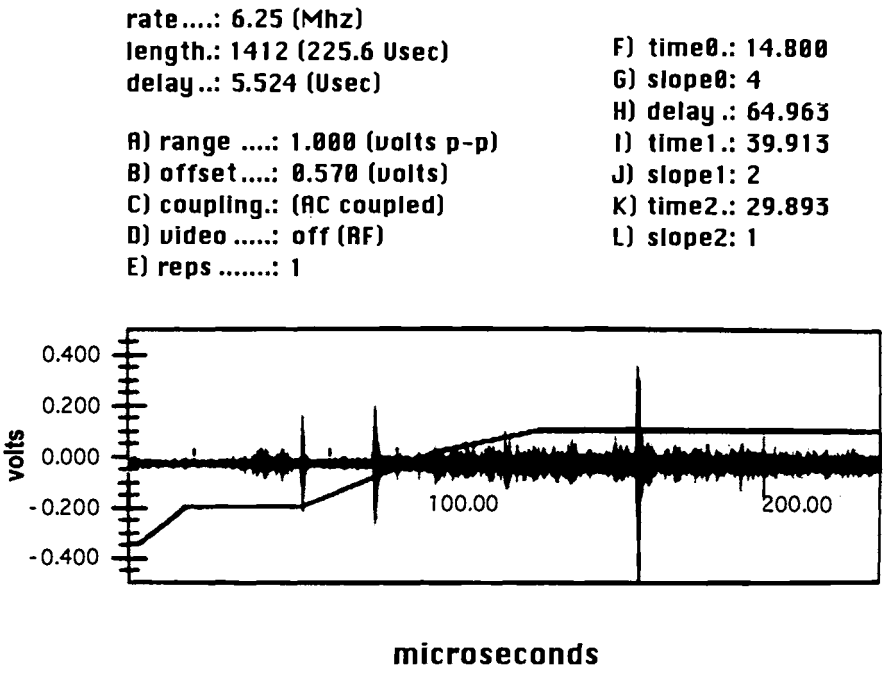

Figure 3.18 Time variable gain curve (TVG) for modes 6 through 9, 45°S wave inspections

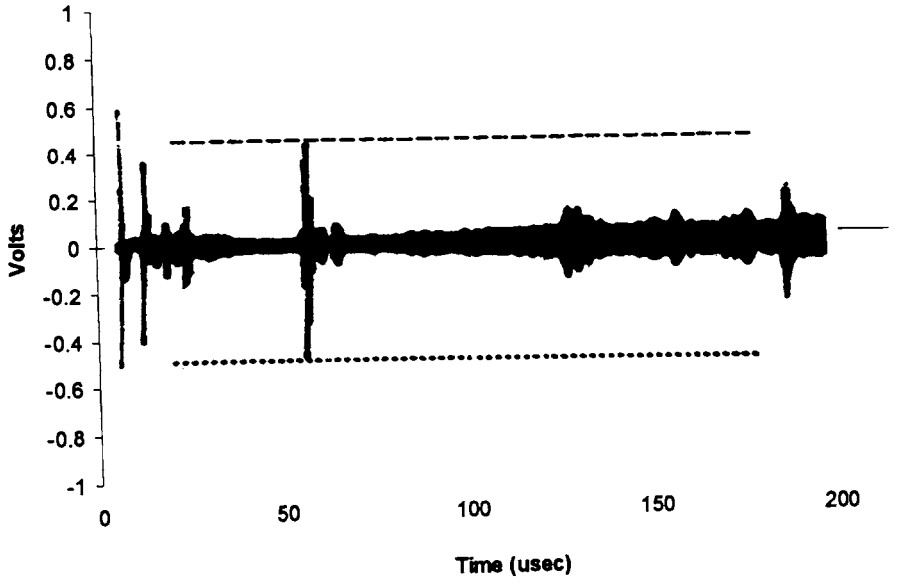

Figure 3.19 Signal strength after TVG amplification from 1/4 thickness side drilled hole in calibration block for inspection modes 6 through 9

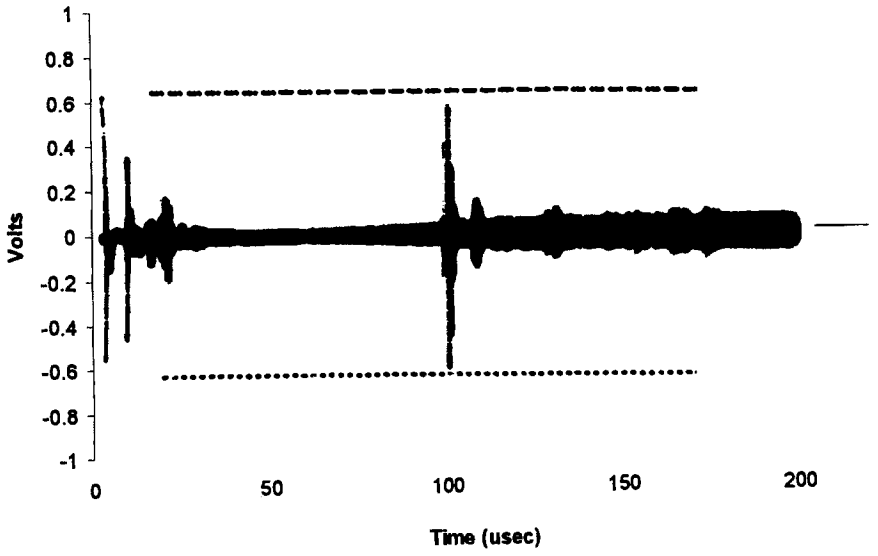

Figure 3.20 Signal strength after TVG amplification from 1/2 thickness side drilled hole in calibration block for inspection modes 6 through 9

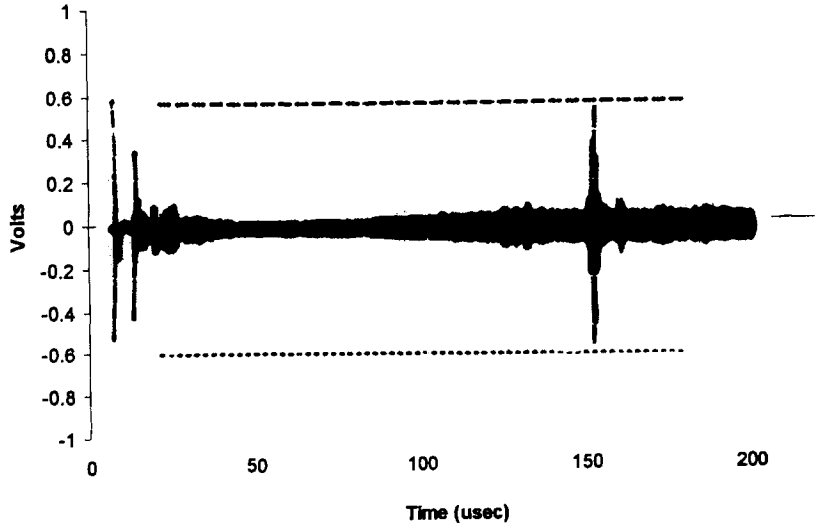

Figure 3.21 Signal strength after TVG amplification from 3/4 thickness side drilled hole in calibration block for inspection modes 6 through 9

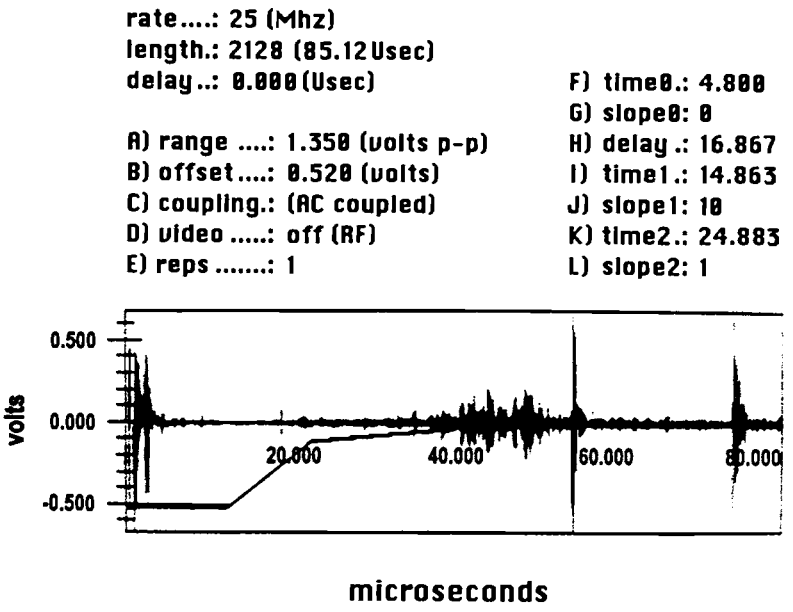

Figure 3.22 Time variable gain curve for mode 10, full volume normal beam

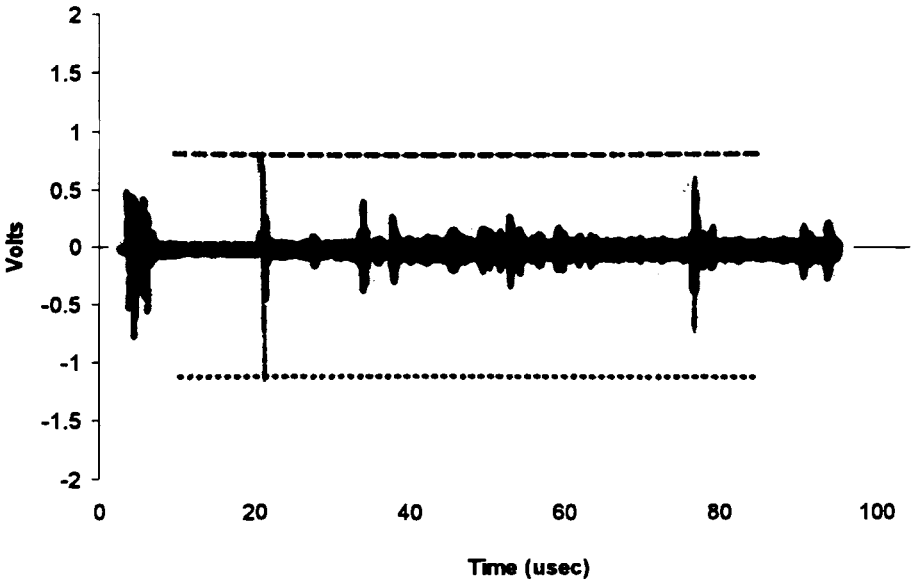

Figure 3.23 Signal strength after TVG amplification from 1/4 thickness side drilled hole in calibration block for inspection mode 10

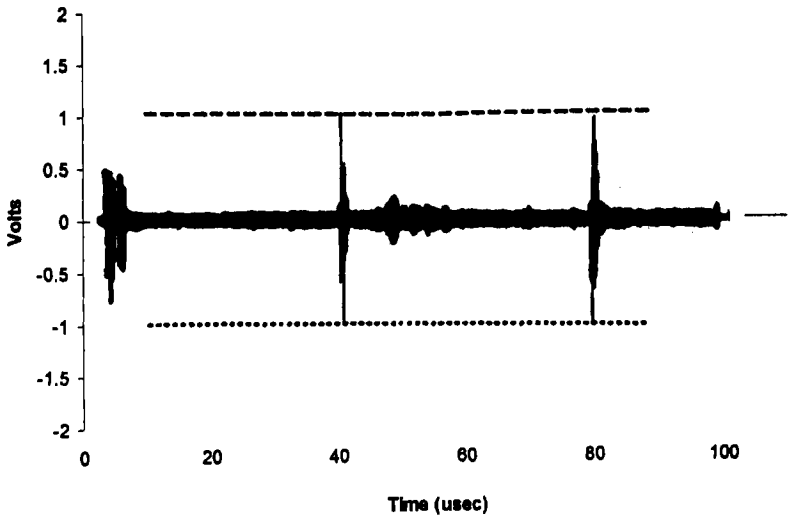

Figure 3.24 Signal strength after TVG amplification from 1/4 thickness side drilled hole in calibration block for inspection mode 10

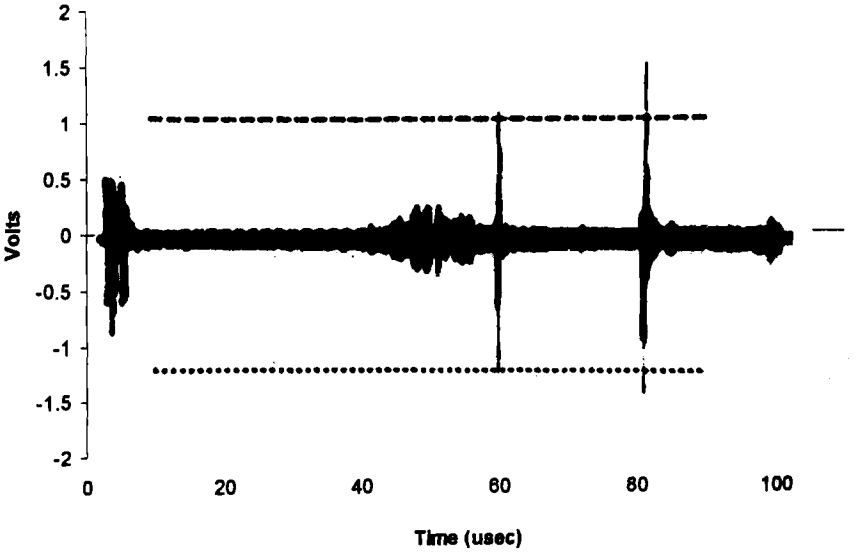

Figure 3.25 Signal strength after TVG amplification from 3/4 thickness side drilled hole in calibration block for inspection mode 10

4 Analysis Methods

In this chapter we describe the data presentation software and the analysis process that was uniformly applied to the SAFT-UT inspections of the PVRUF vessel. The inspection data was imaged on a graphics workstation, and a set of rules was applied to the images to detect and characterize the flaw indications. The rule statements are defined in this chapter, with examples of their application.

4.1 Detection of Indications at PVRUF

Rules were developed and used to detect about 2500 flaw indications in the SAFT-UT data from the PVRUF vessel. The first step in the detection process is the recognition of objects in an image of the ultrasonic volumetric data. An object in an ultrasonic image is defined to be a collection of adjacent pixels (picture elements) that form a recognizable shape.

The brightness and shape of an object are the two most important properties used in recognition that an indication may be a flaw. The location of the object, its proximity to other objects, and the surrounding random noise are also used in the recognition rules.

The joining of objects that are closely spaced (by applying proximity rules) into an indication of a flaw, and the separation of objects into indications of multiple flaws is the second most important step in the detection process. Small flaws on the order of 1 to 2 mm (0.04 to 0.08 in.) in size are expected in the SAFT-UT data, and such closely spaced small flaws should be resolved into separate indications. On the other hand, large flaws are known to produce an indication in ultrasonic data that is composed of separate closely spaced ultrasonic objects, and rules are required to correctly classify them as single large flaws.

After the identification of an indication as one or more objects in the volumetric data, the location of the center of the indication is recorded. The center locations are used in the characterization step to fuse detections in the different inspection modes into a single characterized indication. Ultimately, the location of the characterized indication is an important input in determining its significance to vessel integrity. The appropriate method of estimating the center of the indication depends on the kind of object(s) making up the indication. The rules that define this process are described in the following.

Estimates of the through-wall extent (depth size) of the indications are recorded in the detection process. This measurement is made because only the most significant flaws in the SAFT-UT data need to be fully characterized. The measurement of through-wall extent is used to rank order the indications for full characterization.

The signal-to-noise ratio is sometimes useful in detection. The signal level and the noise level are recorded in the detection process according to a set of rules. The signal level or the signal-to-noise ratio may become important later on in the characterization of PVRUF data. For example, a destructive validation may indicate that the ratio is a valuable discriminant of flaw type.

Spreadsheets were used to document the results of the detection of indications in the SAFT-UT data from the PVRUF vessel. The detection procedure examines each file for detectable indications. The inner 25 mm (1.0 in.) of the vessel is examined first, and then the remaining deeper portion (25 mm to 225 mm) is analyzed. The results are entered in separate spreadsheets because the procedures and rules are different for the two cases.

Figure 4.1 is a typical spreadsheet format of a near surface detection record. The entries are organized by row and each entry (row) has a number, filename, position (X, Y, and Z), estimates of through-wall extent (DZ) signal level (S), noise level (N); and comment. For the near surface detection procedure, 10 files are analyzed for detectable indications (one file for each of the 10 inspection modes). Each of the 10 files has at least one entry in the spreadsheet. If the inspection file is missing or does not contain any detectable flaws, then the filename is entered with a comment of "no file" or "no calls." The position of each detectable indication is recorded in the spreadsheet to within ± 0.25 mm according to a procedure described below. The estimate of though-wall extent is made as a part of the detection process because this is one of the most significant characteristics, and provides a way of rank ordering the detections for full characterization. The signal and noise level fields may be used to select indications of different signal strengths for validation in the destructive test plan. The comment field is used to record the method of estimating through-wall extent, other variables of the detection process that do not have a dedicated field in the spreadsheet, or observations about a

particular indication that should be documented and considered in the evaluation process.

Figure 4.2 shows a full volume detection record and provides the second example of a detection spreadsheet. This one uses the five inspections of the deeper portion (25 mm through 225 mm) of the vessel. Except for the reduced number of inspections compared to the near surface spreadsheet, the fields and entries of both spreadsheets are the same. The procedure of detecting the deeper indications is different and described below.

The first step in the detection of flaw indications is object recognition in the computer generated images. The object recognition rules are listed in Table 4.1. The table lists a rule name, the rule statement, and a reference to an example SAFT-UT image.

In practice, the images resulting from ultrasonic inspections are typically cluttered with noise. This is especially true for small fabrication flaws in thick section steel, because of the high gain used to amplify the weak signals from small flaws deep in the steel. It should be noted here that the measurement plan called for the detection of small flaws in order to estimate the fabrication flaw distribution. Therefore, the test protocol was set up and run at the highest sensitivity possible without saturating the signals from the flaws. Consequently, the images are noisier than would normally be obtained from an inspection designed to ASME code requirements.

Figure 4.3 shows an example of an unbroadened time of flight (TOF) shape produced by a small embedded reflector. This isolated shape is found in the transducer's side view projection. The wave packet has the 3/2 wavelength width characteristic of the transducer's broadband response. This pattern is generated by the movement of the transducer's angled beam pattern across the small embedded flaw. The SAFT-UT inspections of the Midland block (see Appendix B) confirmed that most of these shapes are detectable as indications of embedded flaws, but, in a tight wave packet such as this one, there is little information about the size of the reflector.

These tight wave packets can be produced by the top of a volumetric flaw (slag or porosity) or by the top or bottom of a planar flaw (crack or lack of fusion in the weld). For each recognized object of this kind, an entry is made in a detection spreadsheet. The through-wall extent of these indications is estimated to be less than one half wavelength of the ultrasound in the material. For detectable echoes with isolated wave packets below the clad-to-base-metal interface and above 10 mm (0.39 in.) in 70°L inspections, the through-wall extent is estimated at 1.5 mm (0.06 in.) (½ wavelength).

Figure 4.4 shows an example of an embedded, broadened TOF Shape. In this case, the wave packet is broadened from the impact-limited case in Figure 4.3, and the broadening can be used to estimate the size (through-wall extent) of the indication. The through-wall extent of the indication is estimated to be the width of the wave packet less three halves of one wavelength. These are small flaws, and a conservative approach in this analysis is to consider the width to be an indicator of the top and bottom of a small planar flaw. The top of a planar flaw will have, for the transducer used, a 3/2 wavelength response; so the size is estimated to be the wave packet width minus the transducer response.

Figure 4.5 shows an example of a tip signal pattern where two wave packets are in the proper orientation for tip signals from a vertically oriented planar flaw. When ultrasound is incident on the top or bottom of a vertically oriented discontinuity, the sound is diffracted and a weak signal can sometimes be detected from both ends of the discontinuity. Thus, pairs of TOF shapes can be generated from the top and bottom (tip signals) of planar flaws separated vertically by the size of the flaw (through-wall extent), so the pair is detected as one indication.

Figure 4.6 shows an example of two wave packets in the proper orientation for creeping wave re-radiation from a round trip of a volumetric flaw. Volumetric flaws, such as slag inclusions or porosity, can produce a pair of TOF shapes separated along the insonification direction by the time of flight of one round trip of the flaw's circumference.

Figure 4.7 shows an example of a coin (semi-circular or elliptical) shape near the inner surface of the vessel. Underclad cracks will have a large aspect ratio, distinguishing them from near-surface inclusions, and often producing a coin shape in the transducer end view of angle beam inspections.

Figure 4.8 show a normal beam echo below the clad-to-base-metal interface. These shapes are detectable as indications of a flaw when the signal-to-noise ratio is greater than 6 dB. The application of this rule does not greatly affect the size distribution of flaws, because normal beam indications do not produce a measurement of

Table 4.1 Detection rule statements

Rule name	Rule statement	Example
Unbroadened TOF	An isolated unbroadened TOF shape is detectable as a flaw. Through-wall extent is estimated to be less than one half wavelength.	Figure 4.3
Broadened TOF	An isolated broadened TOF shape is detectable as a flaw. Through-wall extent is estimated to be the width of the wave packet less three-halves of the wavelength.	Figure 4.4
Tip Pattern	A pair of vertically aligned TOF shapes is detectable as the top and bottom of one flaw. Through-wall extent is estimated from the vertical component of the distance between the two TOF shapes.	Figure 4.5
Reradiation	A pair of TOF shapes that are aligned along the sound path are detectable as one flaw. Through-wall extent is estimated from the time-of-flight of one round trip of the flaw circumference, assuming a cylindrical shape for the flaw.	Figure 4.6
Coin Shape	A coin shape is detectable as an underclad flaw. Through-wall extent is estimated based on analyst judgement.	Figure 4.7
Normal Beam	An indication in a normal beam inspection is detectable as a flaw when the signal-to-noise ratio exceeds 6 dB. Through-wall extent estimates are not made from normal beam inspections.	Figure 4.8
Clad-to-Base Metal	Indications in the clad-to-base metal interface are detectable as flaws when their amplitude exceeds 30 percent of full scale. Though-wall extent estimates are usually less than 2 mm for these indications.	Figure 4.9
Cloud-Like	Tight clusters of TOF shapes are detectable as one indication. Through-wall extent is sometimes estimated from the loss-of-signal in several modes.	Figure 4.10

through-wall extent. Detections in normal beam inspections are used to locate and characterize an indication as volumetric, or to separate volumetric flaws that may be close to one another.

The physical basis for the normal beam rule derives from the SAFT-UT inspections of the Midland blocks. The echoes from flaws in normal beam inspections are distinguishable from noise sources, based on image structure and clustering patterns. The destructive analysis of Midland block 1-8 showed that the echoes with signal-to-noise ratios down to 6dB in the SAFT-UT data correlated well with the actual positions of the flaws.

Figure 4.9 represents a detection of an object located in the clad-to-base-metal interface. These shapes are detectable as indications of a flaw when their amplitudes are greater than 30 percent of full scale. The application of this rule requires that the calibration of the probes be maintained. The spreadsheet contains the amplitude for the detected indications, so that adjustments can be made in the detections after destructive validation.

The physical basis for this rule also derives from the SAFT-UT inspections of the Midland blocks. The echoes from flaws at the clad-to-base-metal interface using RTD 70° L probes do not produce a shape that distinguishes them from echoes due to interface roughness. The destructive analysis of Midland block 1-8 showed that the echoes with amplitudes greater than 30 percent of full scale in the SAFT-UT data correlated with the positions of the destructed flaws.

Figure 4.10 shows an example of a cloud-like indication. These indications are recognized from the tight cluster of TOF shapes. The through-wall extent of a cloud-like indication is sometimes estimated from the loss of signal in several modes.

4.2 Clustering of Detections

A significant portion of the indications detected in the first pass through the SAFT-UT inspections will be multiple detections of the same indication. In principle, a flaw in the vessel could be detected 10 different times, once in each of the 10 inspection modes. The method for clustering the detections from the individual inspections into a reduced detection list, where multiple detections of the same indication are identified and recorded, is discussed below.

Figure 4.11 shows the distance matrix for the 14 indications detected in the first pass through the 10 inspection modes in one portion of the PVRUF weldment. The distance matrix is used to identify multiple detections of the same indication. It tabulates the calculated Euclidian distances of the indications from each other. The matrix shows that indications 2 and 11 are close (distance = 2 mm [0.08 in.]) and that 3 and 12 are also close (distance = 4.2 mm [0.17 in.]). This information is passed to the multimodal detection sheet described below.

Figure 4.12 shows the multimodal detection sheet for the 14 indications shown in the distance matrix of Figure 4.11. Zone 2 in the multimodal detection sheet shows that indications 2 and 11 are now considered to be two detections of the same indication. Zone 3 shows indications 3 and 12 are considered to be two detections of the same indication. The 14 indications are thus reduced to 12.

4.3 Sizing and Characterizing Indications at PVRUF

SAFT-UT sizing rules were created to conservatively size indication zones to ensure that all potentially larger flaws would be included in the validation plan.

After the number of original detections is reduced by identifying the multiple detections of the same indication, a characterization is performed on the largest of the indications from the reduced list. Figure 4.13 shows the characterization worksheet for one indication. There were three detections of this indication in the first pass in modes 1, 2, and 4; where mode 1 is the near surface normal beam inspection, and modes 2 and 4 are near surface 70° L wave inspections. The first step in the characterization is to review the other modes to determine if a confirmation of the indication can be found by increasing the detection sensitivity. In the example, a confirmation was found in mode 5 and a comment was made identifying the entry as a confirmation. The characterization worksheet contains the information from the detection sheets plus additional information from the characterization steps.

In the characterization of the largest indications, the length and width of the indication is estimated from the loss of signal (LOS) in each of the modes where an estimate can be made. The spreadsheet uses the location of the indication to calculate whether the indication is in the weldment, base metal, heat affected zone, or cladding-using a formula derived from the weld cross section.

The spreadsheet also records whether the indication is volumetric or planar. An indication is always considered planar if tip signals are identified. In most cases, a normal beam detection is evidence of a volumetric indication.

	A	B	C	D	E	F	G	H	I	J	K	L	M
1	511												
2	#	Filename		X	X2	Y	Y2	Z	DZ	S	N	COMMENTS:	CBI
3													
4	1	5s0	8	2.2		5.62		0.44		179	80		
5	2	5s0	8	-2.15		1.42		0.46		206	65		
6	3	5s0	8	-1.95		2.37		0.43		205	80		
7	4	5s1	8									There are 3 echoes in the CBI with signal levles of 100 counts or more.	
8	5	5s1	8									There is 1 echoes below the CBI with signal levels of 80 or more.	
9	6	5s2	8	3.54		6.08		0.21	0.06	108	15	Since this call is in the CBI, DZ is the minimum.	0.27
10	7	5s2	8	4.2		6.02		0.24	0.06	105	15	Since this call is in the CBI, DZ is the minimum.	0.27
11	8	5s2	8	4.02		0.44		0.24	0.06	103	15	Since this call is in the CBI, DZ is the minimum.	0.27
12	9	5s2	8	-1.38		6.14		0.61	0.07	15	5	DH=.25,DZ=DH-3/2(lambda)	
13	10	5s2	8	-0.42		2.84		0.67	0.06	12	4	DH=.21,DZ=DH-3/2(lambda), DZ=Minimum.	
14	11	5s2	8	1.86		1.52		0.56	0.06	25	8	DH=.24,DZ=DH-3/2(lambda), DZ=Minimum.	
15	12	5s3	8	-0.3		0.99		0.24	0.06	120	22	Since this call is in the CBI, DZ is the minimum.	0.27
16	13	5s3	8	0.72		7.59		0.24	0.06	101	30	Since this call is in the CBI, DZ is the minimum.	0.27
17	14	5s4	8									No file	
18	15	5s5	8	-1.08		-0.28		0.24		117	45	Since this call is in the CBI, DZ is the minimum.	0.27
19	16	5s5	8	-1.08		-0.76		0.21		109	45	Since this call is in the CBI, DZ is the minimum.	0.27
20	17	5s5	8	-0.66		-0.88		0.24		101	45	Since this call is in the CBI, DZ is the minimum.	0.27
21	18	5s6	8									No calls (shapes).	
22	19	5s7	8									No calls (shapes).	
23	20	5s8	8	2.3		4.64		1	0.04	57	25	DH=.12, DZ=DH-3/2(lambda), DZ=Minimum.	
24	21	5s9	8									No calls (shapes).	

Figure 4.1 Near surface detection record. The filename columns follow the protocol described in Section 3.2. The column labeled "X" is given in inches from the weld centerline. "Y" is the distance along the weld, also in inches. "Z" is the distance in inches from the clad surface. "DZ" is the through-wall extent of the irradiation in inches. The column "S" is the signal level in digitizer units (0-255). "N" is the noise level, also in digitizer units.

RECORD OF ECHOES											
#	Filename		X	X2	Y	Y2	Z	DZ	S	N	Comments
1	5s6	104	0.16		103.52		3.2	0.08	21	5	DH=0.2, DZ=DH-.12
2	5s6	104	-0.24		101.92		2.97	0.46	20	4	Tip pattern echo.
3	5s6	104	-0.08		97.04		3.2	0.07	18	5	DH=0.19, DZ=DH-.12
4	5s6	104	0.8		95.44		9.08	0.04	24	5	DH=0.16, DZ=DH-.12 (Possible aperture limited).
5	5s6	104	4.48		96.96		8.14	0.05	15	5	DH=0.17, DZ=DH-.12
6	5s6	104	-0.32		102.96		2.94	0.36	14	4	Tip pattern echo, but tip signals are broader than usual, possible two seperate indications.
7	5s6	104	-0.16		98.72		3.2	0.08	13	4	DH=0.2, DZ=DH-.12
8	5s6	104	0.56		97.28		4.17	0.04	18	7	DH=0.15, DZ=DH-.12
9	5s8	104	0.62		102.48		2.06	0.04	17	2	DH=0.15, DZ=DH-.12
10	5s8	104	-0.34		102.88		2.46	0.3	15	3	Tip pattern echo.
11	5s8	104	-0.34		101.92		2.91	0.05	21	4	DH=0.17, DZ=DH-.12
12	5s8	104	-0.26		96.96		3.06	0.05	20	5	DH=0.17, DZ=DH-.12
13	5s8	104	0.86		99.84		4.94	0.08	16	6	DH=0.2, DZ=DH-.12
14	5s9	104	-2.18		93.84		4.03	0.12	15	7	DH=0.17, DZ=DH-.12

Figure 4.2 Full volume detection record. The file name columns follow the protocol described in Section 3.2. The column "X" gives the distance in inches from the weld centerline. "Y" is the distance along the weld in inches. "Z" is the distance in inches from the clad surface. "DZ" is the through-wall extent of the irradiation in inches. The column "S" is the signal level in digitizer units (0-255). "N" is the noise level also in digitizer units.

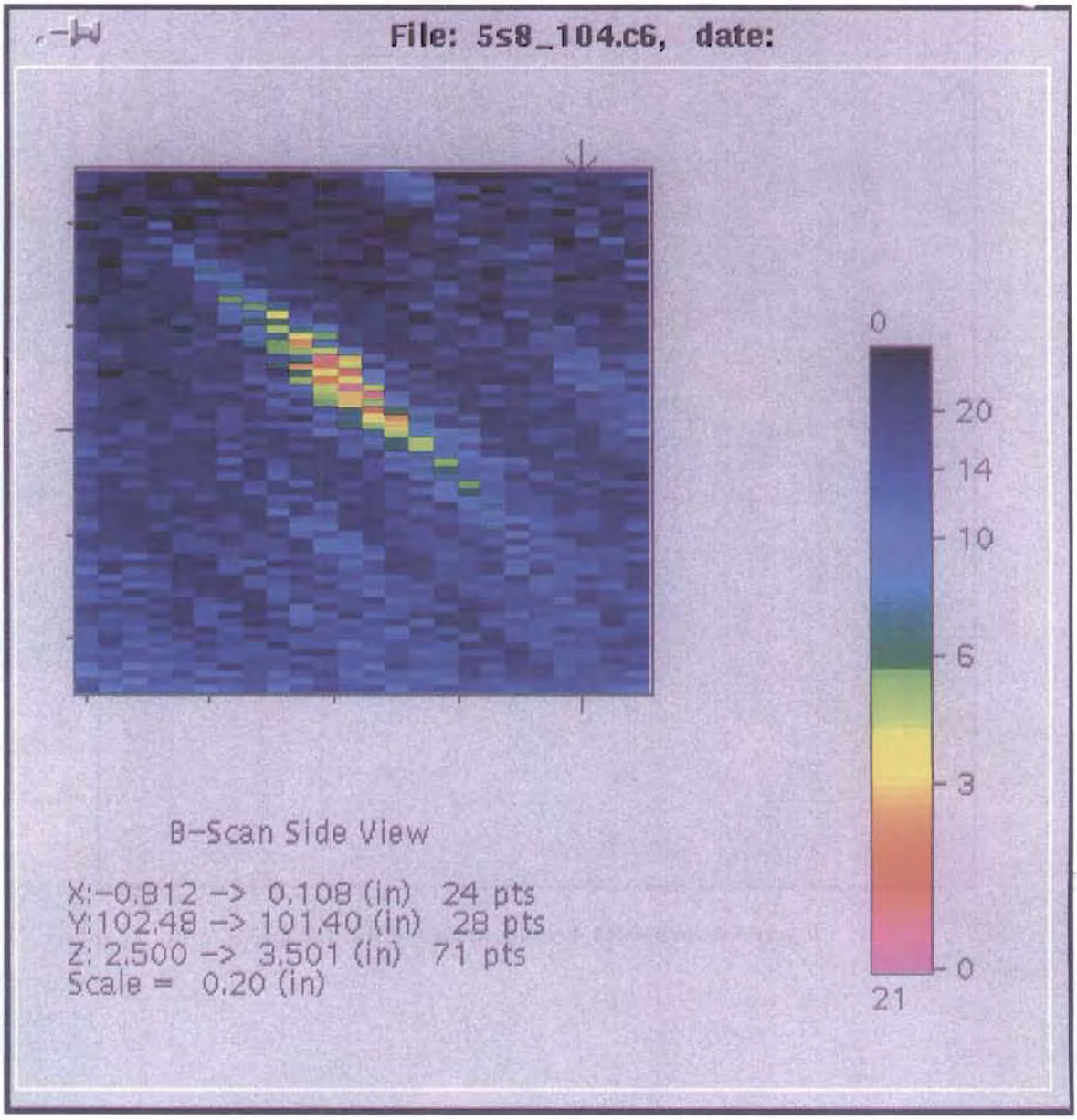

Figure 4.3 Embedded, compact time-of-flight shape

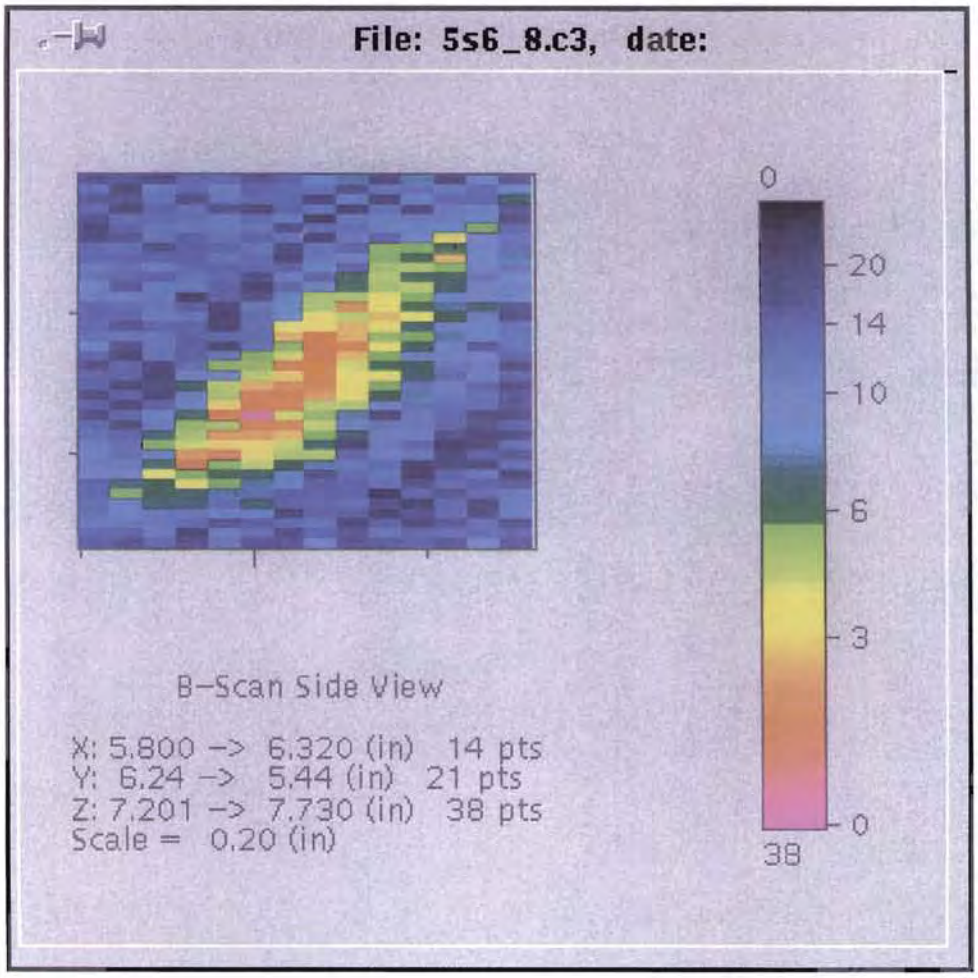

Figure 4.4 Embedded, broadened time-of-flight shape

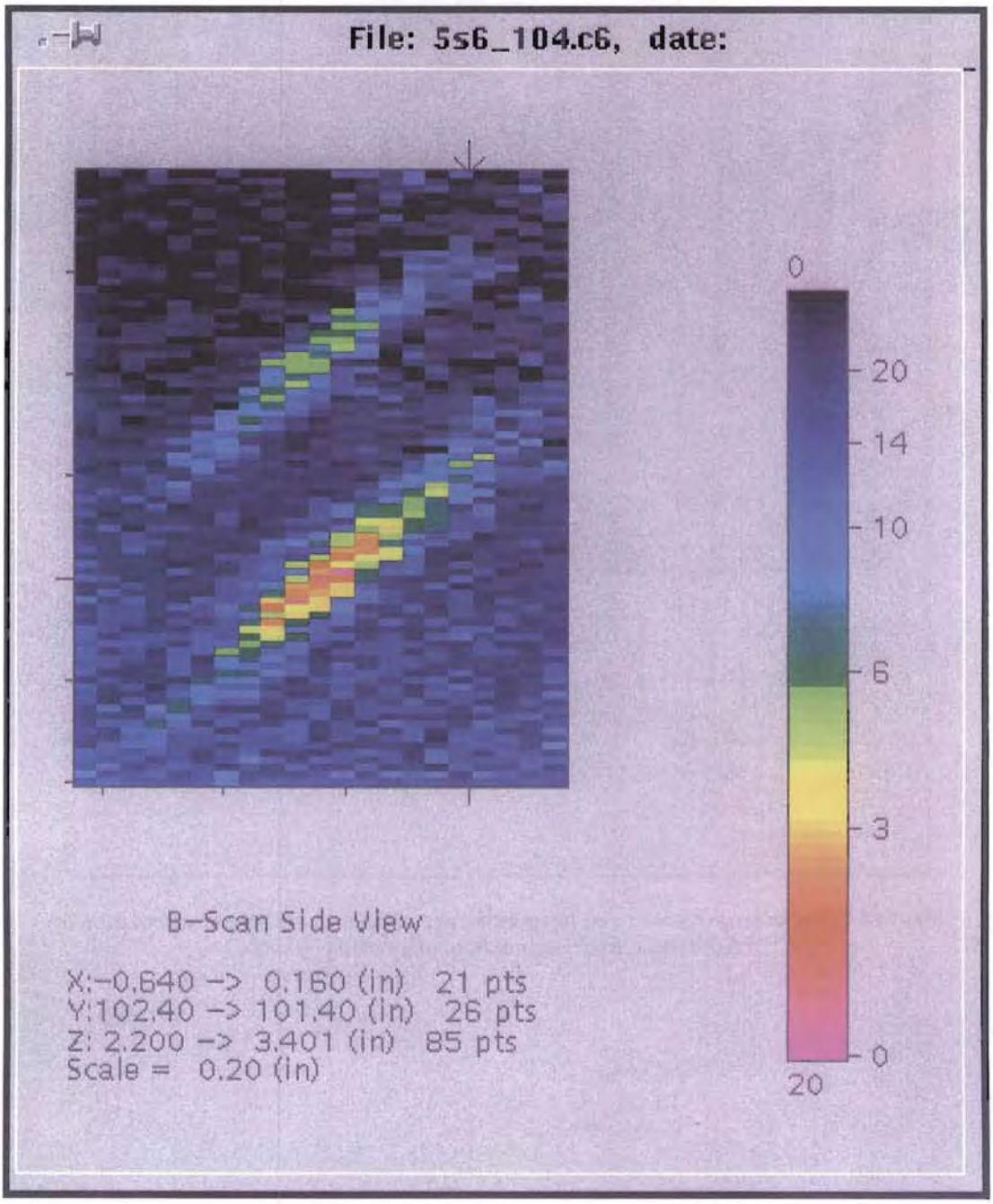

Figure 4.5 Tip signal pattern showing two wave packets in the proper orientation for tip signals from a vertically oriented planar reflector

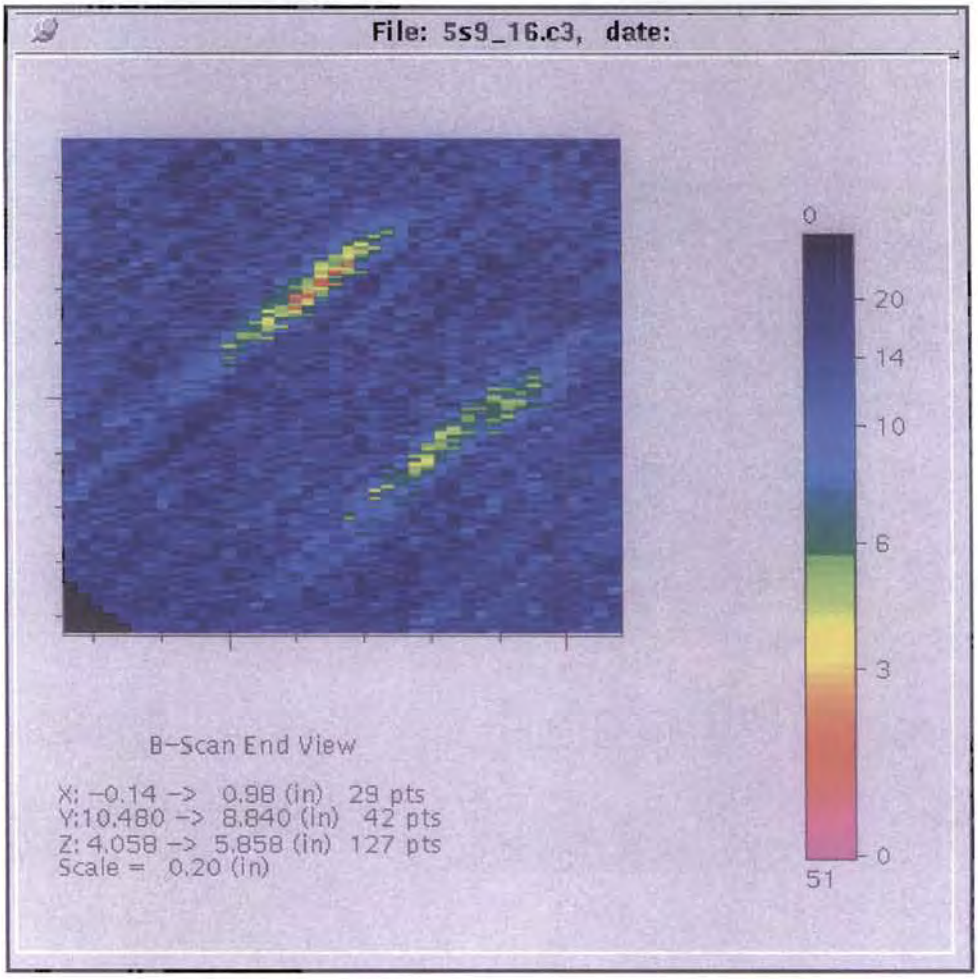

Figure 4.6 Surface wave pattern showing two wave packets in the proper orientation for re-radiation from a round trip of a volumetric flaw

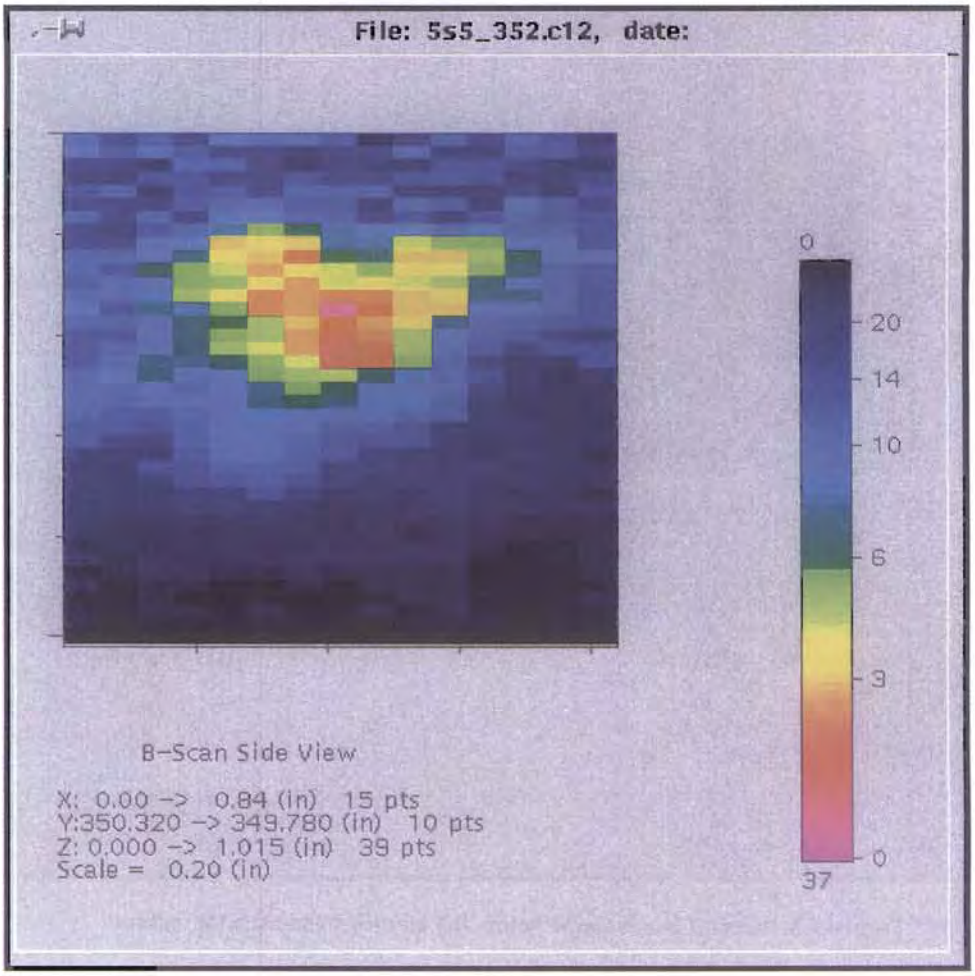

Figure 4.7 Coin shape near the clad-to-base-metal interface

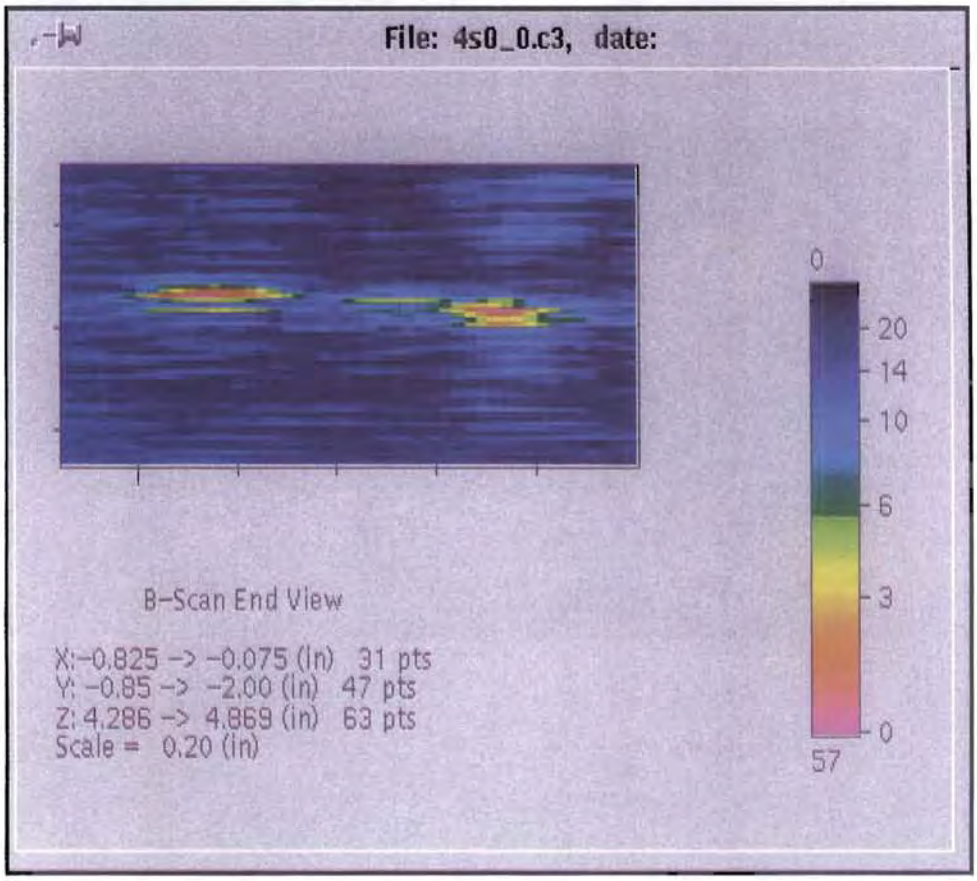

Figure 4.8 Normal beam shape below the clad-to-base-metal interface

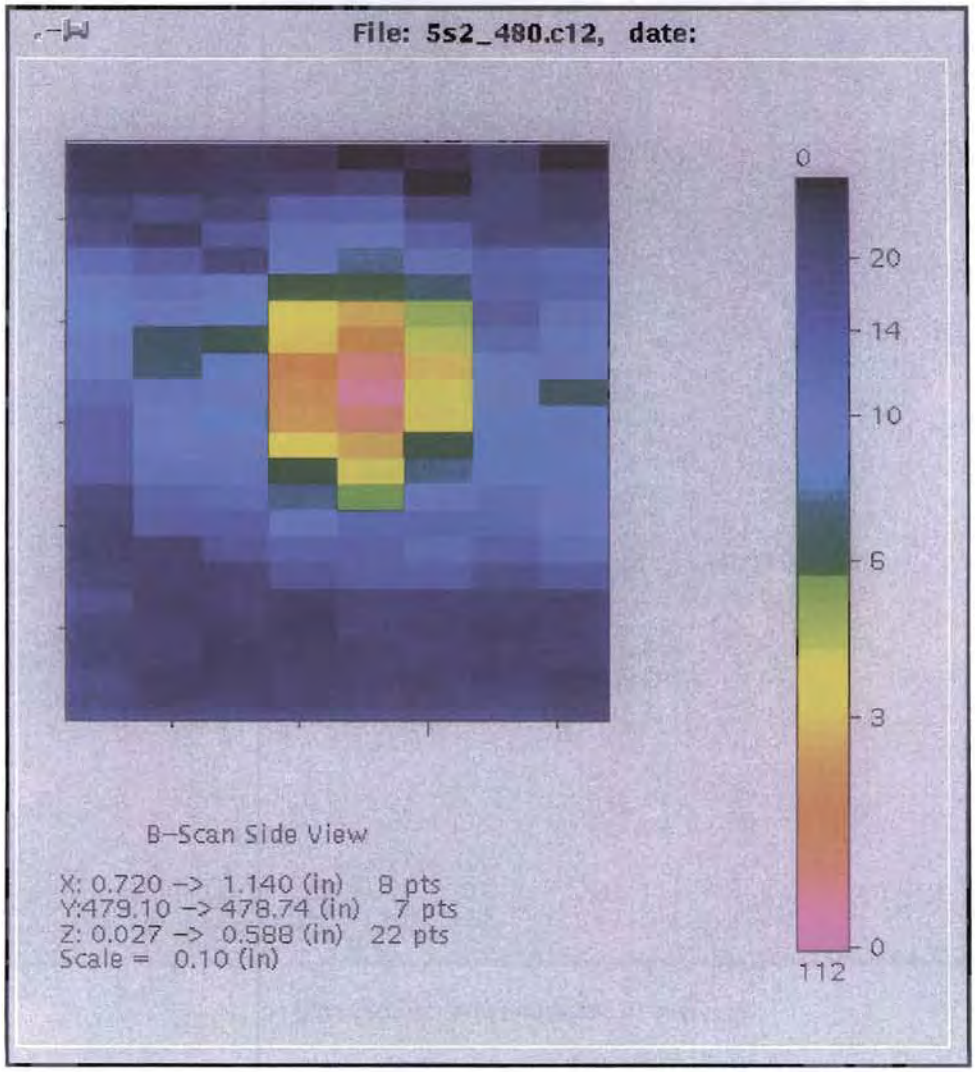

Figure 4.9 Shape of indications in the clad-to-base-metal interface

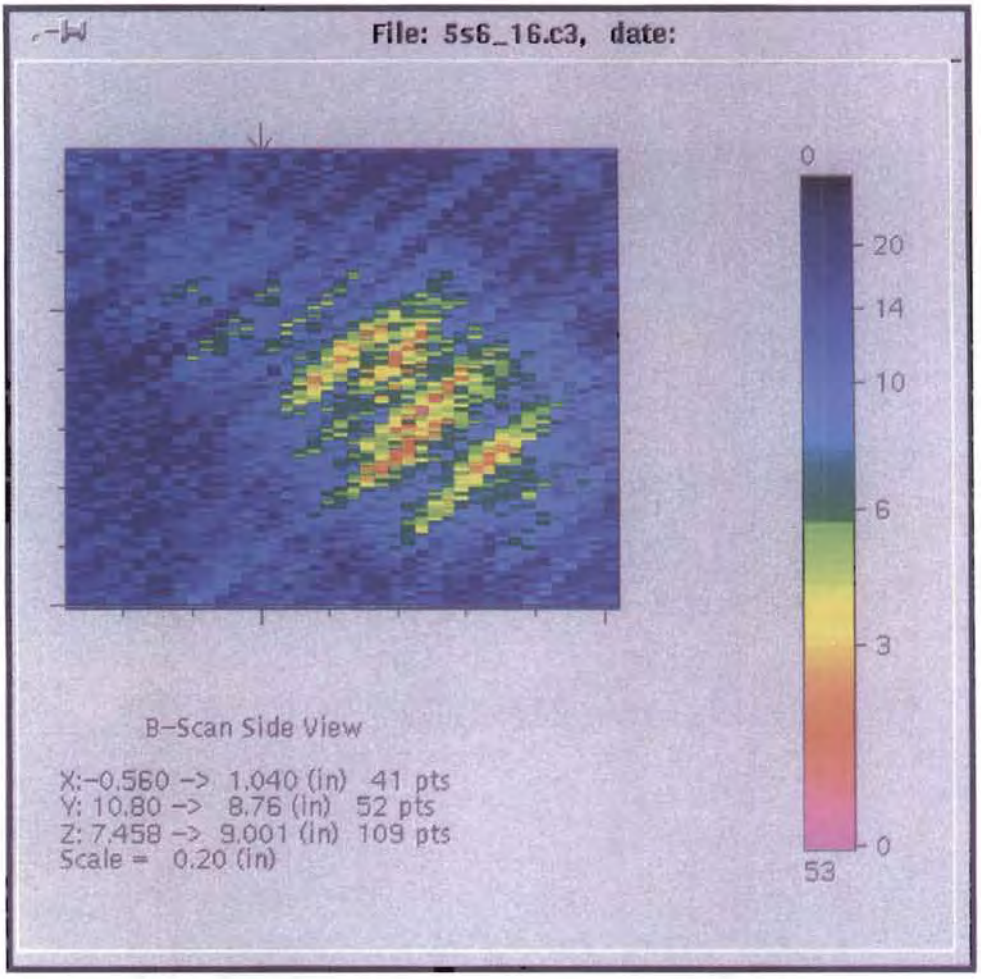

Figure 4.10 Detection of a cloud-like shape

	1	2	3	4	5	6	7	8	9	10	11	12	13	14
1	0.00	0.86	3.24	7.12	6.31	0.45	2.41	3.27	1.27	0.84	0.89	3.29	2.56	5.05
2	0.86	0.00	2.45	6.92	6.20	0.52	1.62	2.64	1.04	0.70	0.08	2.48	2.29	4.29
3	3.24	2.45	0.00	5.93	5.44	2.97	0.84	1.03	2.97	3.02	2.46	0.17	2.28	2.09
4	7.12	6.92	5.93	0.00	2.19	7.20	6.10	4.98	7.84	7.60	6.97	6.07	4.67	5.31
5	6.31	6.20	5.44	2.19	0.00	6.47	5.53	4.43	6.95	6.84	6.27	5.61	3.95	5.51
6	0.45	0.52	2.97	7.20	6.47	0.00	2.14	3.13	1.03	0.48	0.52	3.00	2.60	4.78
7	2.41	1.62	0.84	6.10	5.53	2.14	0.00	1.26	2.23	2.21	1.63	0.89	1.90	2.77
8	3.27	2.64	1.03	4.98	4.43	3.13	1.26	0.00	3.35	3.31	2.68	1.19	1.50	2.20
9	1.27	1.04	2.97	7.84	6.95	1.03	2.23	3.35	0.00	0.66	1.02	2.97	3.17	4.95
10	0.84	0.70	3.02	7.60	6.84	0.48	2.21	3.31	0.66	0.00	0.66	3.02	2.97	4.87
11	0.89	0.08	2.46	6.97	6.27	0.52	1.63	2.68	1.02	0.66	0.00	2.48	2.36	4.29
12	3.29	2.48	0.17	6.07	5.61	3.00	0.89	1.19	2.97	3.02	2.48	0.00	2.43	2.07
13	2.56	2.29	2.28	4.67	3.95	2.60	1.90	1.50	3.17	2.97	2.36	2.43	0.00	3.48
14	5.05	4.29	2.09	5.31	5.51	4.78	2.77	2.20	4.95	4.87	4.29	2.07	3.48	0.00

Figure 4.11 Distance matrix for the clustering of detections from different inspection modes. The table shows the distances between 14 distinct indication in inches. This matrix shows the indications 2 and 11 are close (distance = 0.08").

ZONE	X	X2	Y	Y2	Z	Z2	ECHOES																	
1	0.16		103.52		3.2		1																	
2	-0.34	-0.24	101.92		2.91	2.97		2									11							
3	-0.26	-0.08	96.96	97.04	3.06	3.2			3									12						
4	0.8		95.44		9.06					4														
5	4.48		96.96		8.14						5													
6	-0.32		102.96		2.94							6												
7	-0.16		98.72		3.2								7											
8	0.56		97.28		4.17									8										
9	0.62		102.48		2.06										9									
10	-0.34		102.88		2.46											10								
11	-0.26		96.96		3.06														12					
12	-2.18		93.84		4.03															14				
13	0		0		0																15	16	17	18	19	20
14	0		0		0																15	16	17	18	19	20
15	0		0		0																15	16	17	18	19	20
16	0		0		0																15	16	17	18	19	20
17	0		0		0																15	16	17	18	19	20
18	0		0		0																15	16	17	18	19	20
19	0		0		0																15	16	17	18	19	20
20	0		0		0																15	16	17	18	19	20

Figure 4.12 Multimodal detection sheet for one portion of the weldment. This sheet shows the indications reduced to account for multimodal detection. Zone 2 in this matrix shows that indications 2 and 11 are not considered to be two detections of the same indication. Coordinates of the indications in this table are given in inches.

#	Filename		X	DX	Y	DY	Z	DZ	S	N	METHOD	MATERIAL	V/P	COMMENTS:
				LOS		LOS		m6dB						
1	5s0	352.2	0.05	0.18	350.3	0.12	0.42		120	50	n/a	weld	v	Original detection
2	5s1	352.c12	0.18	0.2	350	0.14	0.39		131	16	n/a	weld	v	Original detection
3	5s2	352.c12												No confirmation
4	5s3	352.c12												No confirmation
5	5s4	352.c12	0.35		350.5	0.51	0.69	.3*	14	6	top-bottom	weld	v	Original detection
6	5s5	352.c12	0.3	0.5	350.1		0.59	0.09	14	7	packet	weld	v	Confirmation
7	5s6	352.2												No confirmation
8	5s7	352.2												No confirmation
9	5s8	352.2												No confirmation
10	5s9	352.2												No confirmation

Figure 4.13 Characterization work sheet for one indication. There were 3 detections of this indication in the final pass in modes 1, 2, and 5. A confirmation of this indication was found in mode 5. The position and size of the indication is given in inches. The signal and noise levels are given in digitizer units (0-255).

5 Results of the Analysis of SAFT-UT Inspections at PVRUF Vessel

In this chapter, the analysis of SAFT-UT images is discussed, and the important features of the most significant indications are described. The indications are detected and characterized by interpreting the images provided by the SAFT-UT system. The characteristics of the larger indications are provided in tabular form and references are given to the complete set of SAFT-UT images in Appendix A. Where sizing results are given, SAFT-UT rules were used to conservatively size indication zones to insure that all potentially larger flaws would be included in the validation plan.

5.1 Analysis of SAFT-UT Images

SAFT-UT images are presented in three engineering views: side view, end view, and C-scan view. The image in Figure 5.1 shows the echo from planar indication #1 in the weldment of the inner-surface zone in mode 1: near surface normal beam. The figure is made up of the three engineering views and a view of the file header information. The display at the top left of the figure is the B-scan end view. The display at the top right is the C-scan view. The display at the bottom right is the B-scan side view. Finally, the display at the bottom left is the header information from this data file: 5s1_352.c12.

The display of the B-scan end view is made up of three parts. The first is the image of the indication. Tick marks along the left side and bottom of the image can be used to estimate the material coordinates of the flaw. The gray scale bar at the right shows the amplitude scale of the data--in this view varying from 131 to 0, as indicated.

The final part of the end view is the axis label portion, containing five lines of information. The first line identifies the view as the B-Scan end view. By definition, the B-Scan end view in SAFT-UT is a view of Y vs. Z, where Y is the length axis as measured along the circumference of the vessel, and Z corresponds to the depth axis as measured from the vessel's inner surface toward the outer surface. The next three lines give the material coordinates of the data volume. Here, the Y-axis is the horizontal axis and starts at 350.11 inches at the left of the image and ends at 349.84 inches at the right of the image (metric units are not available on the SAFT-UT images at this time and the analysis described in this section will be inches to be consistent with the axis on the SAFT-UT images). The Z axis is the vertical axis and starts at 0.268 in. at the top of the view and ends at 0.564 in. at the bottom of the view. The fifth and last line gives the distance between tick marks on the left and bottom edges of the image, 0.05 in. in this case. The X-axis is perpendicular to the display plane in the B-Scan end view.

The indication shown in Figure 5.1 is detectable, based on its signal strength of 131/255. The signal amplitude of 131 can be found at the bottom of the gray scale. The location of the indication is X = 0.20" (from the B-Scan side view), Y = 348.95" (from the B-Scan end view), and Z = 0.40" (from the B-Scan side view).

5.2 Indications in the Near-Surface Zone

The near-surface zone of the vessel is defined to be the first 25-mm of vessel thickness starting at the clad surface. This zone includes the cladding itself, which are nominally 6 mm thick, and the first 19-mm of ferric steel immediately outside the cladding.

The near-surface zone is further sub-divided into four regions. The near-surface weldment is defined to be the ferritic steel weld metal below the cladding. The near surface heat-affected zone is defined to be the first 6-mm of ferritic steel outside the near-surface weldment. The near-surface base metal is all ferritic steel outside the heat-affected zone. The cladding and clad-to-base-metal interface is the fourth region.

5.2.1 Indications in the Near-Surface, Weldment

This section reports the characterization of the eleven indications that were equal to or greater than 2 mm in size in the near-surface weldment. Tables 5.1 and 5.2 list the characterization data for nine planar indications and two volumetric ones. Through-wall extents of up to 8 mm were estimated. The tables give the location, type, and size of the indications. Appendix A describes the characterization process and identifies the analysis rules that were applied. Also included in Appendix A are the images of the indications.

Table 5.1 Planar indications in the weldment of the near-surface

ID	Mode	Through-wall extent size (mm)	Basis	Length size (mm)	Width size (mm)	Location in depth Z (mm)	Location from weld X (mm)	Coin shape	SNR value	Figure
1	Det: 1, 4, 10 Conf: 5	8 3	different depths WP (mode 4)	13	13	10 18	8	good	131/16	A.1
2	Det: 5 Conf: 3	6 2.5	different depths WP (mode 5)	NA	7	12-18	8	none	75/15	A.2
3	Det: 4	3	WP(mode 4)	10	NA	21	-8	none	13/6	A.3
4	Det: 4 Conf: 8	3 2.3	different depths WP (mode 4)	14	NA	16-19	-4 to -8	some	25/12	A.4
5	Det: 2, 4	2.3	WP (modes 2, 4)	10	NA	11 12	-6 to -14	some	63/12	A.5
6	Det: 4	2	WP(mode 4)	9	NA	16	-3	none	18/6	A.6
7	Det: 2	2	WP(mode 2)	11	NA	15	-6	none	52/12	A.7
8	Det: 7	2	WP(mode 7)	NA	10	23	11	none	69/28	A.8
9	Det: 4	2	WP(mode 4)	11	NA	24	12	none	16/3	A.9

Det = detection mode; NA = not applicable; Pat = pattern; Conf = confirmation mode; Loc = location; Ind = Indication; WP = wave packet; SNR = signal-to-noise ratio; Length = along the weld; width = across the weld.

Table 5.2 Volumetric indications in the weldment of the near-surface

ID	Detection mode	Through-wall extent size (mm)	Basis	Length size (mm)	Width size (mm)	Location in depth Z (mm)	Location from seld X (mm)	Coin shape	SNR value	Figure
1	Det: 7, 8 Conf: 3,4,5,9	6 2	different depths WP (modes 7, 8)	10	10	18 to 24	-6	none	97/30	A.10
2	Det: 9 Conf:2, 5,6,7,8	6 3	different depths WP (mode 9)	13	14	20 to 26	9	good	117/35	A.11

5.2.2 Indications in the Near-Surface, Heat Affected Zone

Tables 5.3 and 5.4 list the characterizations of the three indications that were greater than 2 mm (0.08 in.) in size in the near-surface, heat affected zone. One of the indications was planar and two were volumetric. Through-wall extents of up to 7 mm (0.28 in.) were estimated.

5.2.3 Indications in the Near-Surface, Base Metal

Tables 5.5 and 5.6 report the characterizations of the 31 largest indications in the near surface base metal. Twenty-one of the indications were characterized as planar and ten as volumetric. Volumetric indication number nine is omitted because it was merged with another indication. Through-wall extents of up to 8 mm (0.16 in.) were estimated.

5.2.4 Clad and Clad-to-Base Metal Interface

Tables 5.7 and 5.8 report the characterizations in the clad and clad-to-base metal interface. Table 5.7 lists four indications characterized as planar with through-wall extents of 1.5 mm (0.06 in.), as examples of the smaller indications in the SAFT-UT inspection of the cladding. Six of the indications were characterized as volumetric with through-wall extent estimated up to 3 mm (0.12 in.).

Table 5.3 Planar indications in the heat-affected zone of the near-surface

ID	Mode	Through-wall extent size (mm)	Basis	Length size (mm)	Width size (mm)	Location in depth Z (mm)	Location from weld X (mm)	Coin shape	SNR value	Figure
1	Det: 2, 3, 5	3	WP (modes 2, 3, 5)	14	10	13-14	11-18	good	88/25	A.12

Table 5.4 Volumetric indications in the heat-affected zone of the near-surface

ID	Detection mode	Through-wall extent size (mm)	Basis	Length size (mm)	Width size (mm)	Location in depth Z (mm)	Location from weld X (mm)	Coin shape	SNR value	Figure
1	Det: 6	7	cloud-like shape	7	13	20	6 to 17	none	118/25	A.13
	Conf:5	5	WP (mode 6)							
2	Det: 2	3	different depths	13	8	11 to 14	-14 to -25	none	71/20	A.14
	Conf:1	2.5	WP (mode 2)							

Table 5.5 Planar indications in the base metal of the inner surface zone

ID	Detection mode	Through-wall extent size (mm)	Basis	Length size (mm)	Width size (mm)	Location in depth Z (mm)	Location from weld X (mm)	Coin shape	SNR value	Figure
1	Det: 8	8	cloud-like shape	7	NA	18	122	none	165/70	A.15
		2.5	WP (mode 8)							
2	Det: 8	7.4	cloud-like shape	13	NA	20	112	none	190/35	A.16
		3.5	WP (mode 8)							
3	Det: 2	4	WP (mode 2)	12	NA	15	122	none	22/9	A.17
4	Det: 2	4	WP (mode 2)	9	NA	11	-46	none	25/5	A.18
5	Det: 4	3.6	WP (mode 4)	15	NA	12	-49	good	19/9	A.19
6	Det: 3, 5	3.5	WP (modes 3, 5)	12	20	13 to 16	-29	good	29/10	A.20
	Conf: 1	3	different depths							
7	Det: 4	3	WP (mode 4)	9	NA	13	32	none	22/7	A.21
8	Det: 3	2.5	WP (mode 3)	NA	11	15	100	none	14/7	A.22
9	Det: 3	2.5	WP (mode 3)	NA	7	17	-102	none	27/7	A.23
10	Det: 2	2.5	WP (mode 2)	7	NA	13	-18	none	24/10	A.24
11	Det: 4	2.5	WP (mode 4)	15	NA	15	20	none	15/6	A.25
12	Det: 8	2.5	WP (mode 8)	11	NA	19	113	some	216/45	A.26
13	Det: 8	2.3	WP (mode 8)	10	NA	14	142	none	154/50	A.27
		1.6	ring pattern							
14	Det: 8	2.3	WP (mode 8)	10	NA	20	43	none	143/45	A.28
15	Det: 2	2.3	WP (mode 2)	14	NA	17	-30	none	16/7	A.29
16	Det: 3	2.3	WP (mode 3)	NA	7	18	-104	none	12/6	A.30
17	Det: 8	2.3	WP (mode 8)	8	NA	20	46	none	130/50	A.31
18	Det: 7	2	WP (mode 7)	NA	11	22	39	none	85/30	A.32
19	Det: 7	2	WP (mode 7)	NA	16	25	106	none	91/40	A.33
20	Det: 3	2	WP (mode 3)	NA	8	12	81	none	24/8	A.34
21	Det: 2, 4	1.5	WP (modes 2, 4)	8	NA	8	-24	good	143/25	A.35

Table 5.6 Volumetric indications in the base metal of the inner surface zone

ID	Mode	Through-wall extent size (mm)	Basis	Length size (mm)	Width size (mm)	Location in depth Z (mm)	Location from weld X (mm)	Coin shape	SNR value	Figure
1	Det: 9 Conf: 1	6	cloud-like pat.	6	7	19 to 20	28	none	88/40	A.36
2	Det: 2 Conf: 3	3 2	WP (mode 2) different depths	13	7	18 to 20	79	none	8/3	A.37
3	Det: 7	2.5	ring around pat.	NA	12	20	71	none	100/25	A.38
4	Det: 5 Conf: 2	2.3	WP (mode 5)	12	12	16	-64	none	16/4	A.39
5	Det: 4 Conf:10	2 1	WP (mode 4) different depths	9	5	11-12	26	none	99/20	A.40
6	Det: 1, 7	2 1	different depths WP (modes 1, 7)	5	10	17 to 19	34	none	119/30	A.41
7	Det: 8	1.6	ring around pat.	8	NA	19	123	none	195/45	A.42
8	Det: 8	1.6	ring around pat.	12	NA	14	145	some	148/40	A.43
10	Det: 1, 2 Conf: 3,4	1.5 1	WP (modes 1, 2) different depths	11	11	10 to 11	79	good	212/25	A.44
11	Det: 1, 2	1.5 1	ind. w/o TOF different depths	10	7	8-9	24	none	102/25	A.45

Table 5.7 Planar indications in the cladding and in the clad-to-base metal interface

ID	Mode	Through-wall extent size (mm)	Basis	Length size (mm)	Width size (mm)	Location in depth Z (mm)	Location from weld X (mm)	Coin shape	SNR value	Figure
1	Det: 2	1.5	ind. w/o TOF	14	NA	6	NA	none	130/30	A.46
2	Det: 3, 5	1.5 1	ind. w/o TOF different depths	NA	7	6-7	NA	none	170/30	A.47
3	Det: 2	1.5	ind. w/o TOF	8	NA	6	9	none	97/30	A.48
4	Det: 3	1.5	ind. w/o TOF	NA	16	6	14	good	83/15	A.49

5.3 Indications Outside the Near Surface Zone

The zone outside the near surface zone is defined to be that portion of the vessel wall thickness starting at 25 mm (1.0 in.) of depth from the clad surface and extending to the outside surface of the vessel. This outer zone is further subdivided into three regions: weldment, heat-affected zone, and base metal. The heat-affected zone is defined to be the first 6 mm (0.24 in.) of base metal adjacent to the weldment.

5.3.1 Indications in the Weldment

This section reports the characterization of the largest indications in the weldment below the near surface zone. There were 28 fully characterized indications greater than or equal to 4 mm (0.16 in.) in the zone. Of these 28 indications, 26 were characterized as planar and 2 as volumetric. Tables 5.9 and 5.10 list the 16 largest planar indications and the 2 volumetric ones, respectively.

Table 5.8 Volumetric indications in the cladding and in the clad-to-base metal interface

ID	Mode	Through-wall extent size (mm)	Basis	Length size (mm)	Width size (mm)	Location in depth Z (mm)	Location from weld X (mm)	Coin shape	SNR value	Figure
1	Det: 2 Conf:3	3	WP (mode 2)	12	10	7-8	-36	some	162/20	A.50
		1	different depths							
2	Det: 2, 5	3	different depths	11	12	5-8	15	none	92/30	A.51
	Conf: 1,5	2.3	WP (modes 2, 5)							
3	Det: 3	2	different depths	6	18	6-8	18	good	83/25	A.52
	Conf: 1,5	1.5	coin shape							
4	Det: 1, 4	2	different depths	16	8	7-9	98	none	210/20	A.53
	Conf:3	1.5	ind. w/o TOF							
5	Det: 2, 5	1.5	ind. w/o TOF	12	11	6	21	some	112/40	A.54
	Conf:3									
6	Det: 1, 2	1.5	ind. w/o TOF	NA	NA	7-8	94	none	255/20	A.55
	Conf:3	1	different depths							

Table 5.9 Planar indications in the weldment

ID	Mode	Through-wall extent size (mm)	Basis	Length size (mm)	Width size (mm)	Location in depth Z (mm)	Location from weld X (mm)	SNR value	Figure
1	Det: 6	14	tip signal pat.	18	NA	64	-8	36/5	A.56
2	Det: 10	13	tip signal pat.	25	9	115	-8	56/11	A.57a-b
	Conf: 6								
3	Det: 6	11	tip signal pat.	18	NA	75	-7	21/3	A.58a-b
	Conf: 8	1	different depths						
4	Det: 6	11	tip signal pat.	18	NA	73	-7	25/5	A.59
5	Det: 6	9	tip signal pat.	16	NA	81	-6	37/6	A.60
6	Det: 6	9	tip signal pat.	30	NA	211	23	27/11	A.61
7	Det: 6, 8	9	tip signal pat.	16	NA	63-68	-8	15/5	A.62a-b
8	Det: 6, 8	7	WP (modes 6, 8)	24	NA	213-218	6	31/13	A.63a-b
		5	different depths						
9	Det: 6	7	WP (mode 6)	30	NA	213	24	121/15	A.64
10	Det: 6	6	tip signal pat.	19	NA	117	-7	60/12	A.65
11	Det: 6	6	WP (mode 6)	17	NA	213	16	90/45	A.66
12	Det: 6	6	WP (mode 6)	25	NA	213-215	16	109/40	A.67a-b
	Conf: 8	2	different depths						
13	Det: 6	6	WP (mode 6)	15	NA	209	10	43/10	A.68
14	Det: 6	6	WP (mode 6)	27	NA	212	9	115/40	A.69
15	Det: 6	4	cloud-like pat.	42	NA	212	10	53/13	A.70
16	Det: 6	4	cloud-like pat.	25	NA	203	-8	44/10	A.71

5.3.2 Indications in the Heat Affected Zone

There were 14 characterized indications greater than or equal to 4 mm (0.16 in.) in the heat affected zone. All 14 were characterized as planar. Table 5.11 lists the characterizations.

5.3.3 Indications in the Base Metal

In the base metal below the near surface zone, there were 39 characterized indications greater than or equal to 4 mm. Of these, 31 were characterized as planar and 8 as volumetric. Tables 5.12 and 5.13 report the characterizations of the 16 largest planar indications and the 8 volumetric ones, respectively.

Table 5.10 Volumetric indications in the weldment

ID	Mode	Through-wall extent size (mm)	Basis	Length size (mm)	Width size (mm)	Location in depth Z (mm)	Location from weld X (mm)	SNR value	Figure
1	Det: 9 Conf: 8	5	ring around pat.	23	17	116-121	12	51/10	A.72a-b
2	Det: 6	4	ring around pat.	9	NA	213	6	43/13	A.73

Table 5.11 Planar indications in the heat-affected zone

ID	Mode	Through-wall extent size (mm)	Basis	Length size (mm)	Width size (mm)	Location in depth Z (mm)	Location from weld X (mm)	SNR value	Figure
1	Det: 6	34	tip signal pat.	15	NA	135	20	31/4	A.74
2	Det: 8	18	tip signal pat.	75	NA	48	17	38/3	A.75
3	Det: 6	10	tip signal pat.	18	NA	73	-17	22/4	A.76
4	Det: 6	9	cloud-like pat.	21	NA	213	26	43/15	A.77
5	Det: 6	9	tip signal pat.	27	NA	224	24	29/8	A.78
6	Det: 6	8	WP (mode 6)	22	NA	216	26	120/25	A.79
7	Det: 6	7	tip signal pat.	14	NA	76	16	17/5	A.80
8	Det: 6	7	WP (mode 6)	10	NA	214	30	92/25	A.81
9	Det: 6	5	WP (mode 6)	22	NA	216-218	24	88/35	A.82a-b
	Conf: 8	4	WP (mode 8)						
		2	different depths						
10	Det: 6	5	WP (mode 6)	19	NA	134	23	57/18	A.83
11	Det: 6	5	WP (mode 6)	26	NA	208	23	38/10	A.84
12	Det: 6	4	WP (mode 6)	20	NA	215	30	71/20	A.85
13	Det: 6	4	WP (mode 6)	33	NA	232	-28	26/10	A.86
14	Det: 8	4	Cloud-like pat.	18	NA	189-192	-14	32/12	A.87a-b
	Conf: 6	3	WP (mode 3)						

Table 5.12 Planar Indications in the base metal

ID	Mode	Through-wall extent size (mm)	Basis	Length size (mm)	Width size (mm)	Location in depth Z (mm)	Location from weld X (mm)	SNR value	Figure
1	Det: 6 Conf: 8	26 1 13	tip signal pat.WP (mode 8) different depths	23	NA	123-136	28	27/5	A.88a-b
2	Det: 6 Conf: 8	15 3 1	Tip signal pat. WP (mode 8) different depths	41	NA	121-122	24	30/8	A.89a-b
3	Det: 7	13	tip signal pat.	NA	15	145	58	51/14	A.90
4	Det: 6	11	WP (mode 6)	30	NA	214	43	45/12	A.91
5	Det: 6	8	WP (mode 6)	27	NA	211	31	59/12	A.92
6	Det: 8	7	WP (mode 8)	16	NA	113	46	65/15	A.93
7	Det: 6	7	WP (mode 6)	20	NA	220	45	40/14	A.94
8	Det: 8	7	WP (mode 8)	28	NA	238	31	84/20	A.95
9	Det: 8 Conf: 6	7 4 1	tip signal pat. WP (mode 6) different depths	16	NA	110	37	62/20	A.96a-b
10	Det: 8	6	tip signal pat.	20	NA	201	-159	53/20	A.97
11	Det: 8	6	tip signal pat.	23	NA	203	-70	68/25	A.98a-b
12	Det: 6 Conf: 8	6 1	tip signal pat. different depths	17	NA	118	25	10/3	A.99a-b
13	Det: 6	4	cloud-like pat.	30	NA	123	36	58/20	A.100
14	Det: 8 Conf: 6	4 3	cloud-like pat. different depths	25	NA	192-195	-49	38/10	A.101a-b
15	Det: 9	4	cloud-like pat.	NA	18	220	90	25/7	A.102
16	Det: 6	4	cloud-like pat.	15	NA	122	36	52/14	A.103

Table 5.13 Volumetric indications in the base metal

ID	Mode	Through-wall extent size (mm)	Basis	Length size (mm)	Width size (mm)	Location in depth Z (mm)	Location from weld X (mm)	SNR value	Figure
1	Det: 6, 8 Conf: 10	7 1	Cloud-like pat. WP (mode 6)	19	6	108-115	28	105/25	A.104 a-c
2	Det: 6, 7, 8	5	WP (mode 6)	19	11	113-118	58	77/17	A.105 a-c
3	Det: 8 Conf: 6, 7, 9, 10	5 3-4 10	WP (mode 8) WP (modes 6, 7, 9, 10) different depths	12	48	86-96	56	35/10	A.106 a-e
4	Det: 7	5	Ring around pat.	NA	9	106	108	35/8	A.107
5	Det: 6 Conf: 7, 8	5 1 4	WP (mode 6) WP (modes 7, 8) ring around pat.	28	14	81-85	29	63/13	A.108 a-b
6	Det: 6 Conf: 10	5 2	WP (mode 6) different depths	20	9	128-130	31	86/24	A.109 a-b
7	Det: 6 Conf: 8	5 2.5 1	Ring around pat. WP (mode 8) different depths	46	NA	103-104	48	13/6	A.110 a-b
8	Det: 6	4	Ring around pat.	41	NA	119	26	79/24	A.111

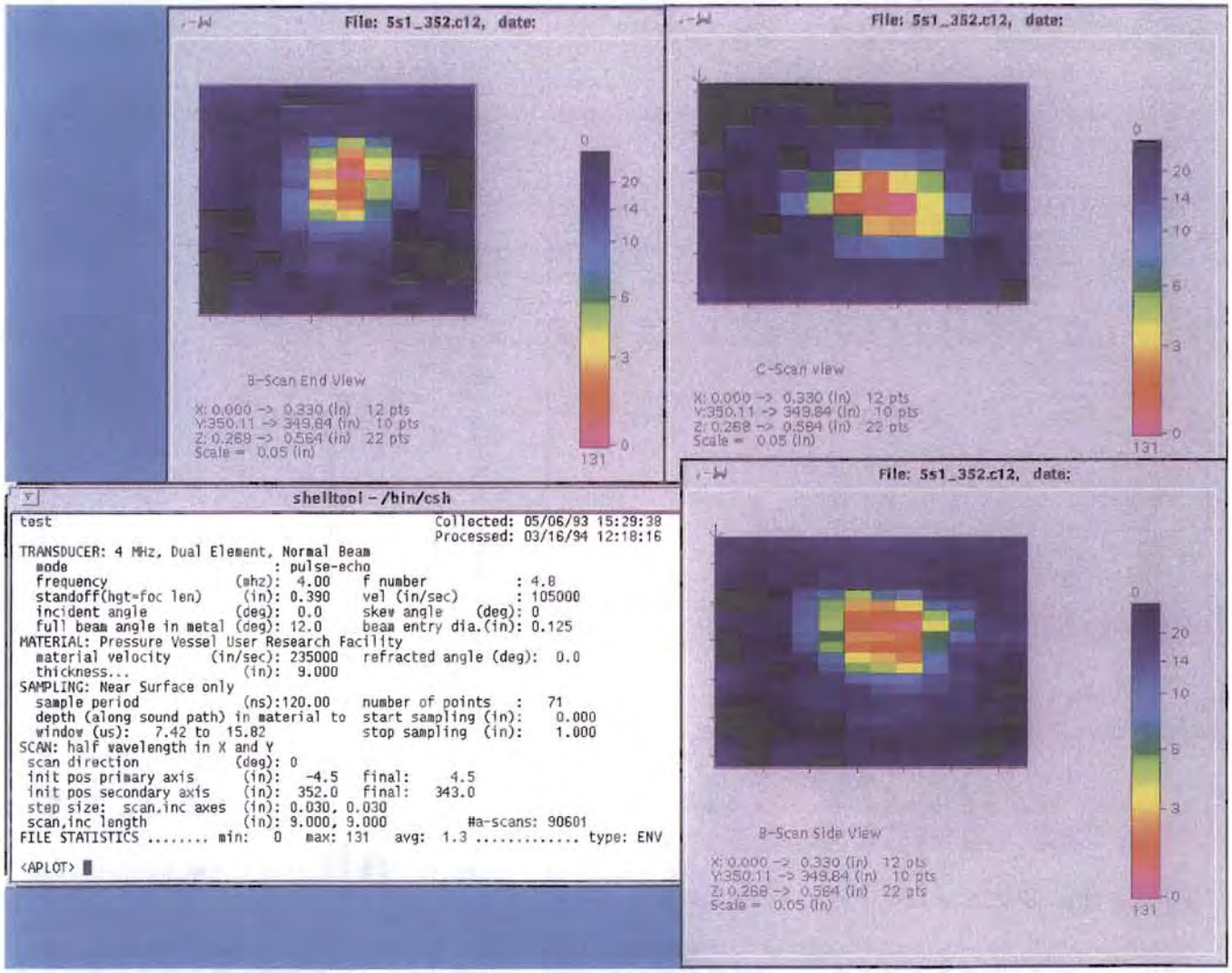

Figure 5.1 Mode 1 detection of planar indication #1 in the near surface zone

6 Distribution of Indications of Flaws in SAFT-UT Data

The characteristics and distribution of the fabrication flaws in reactor pressure vessels are necessary inputs to the fracture mechanics calculations for assessments of reactor pressure vessel integrity. Fracture mechanics calculations are based on flaws with specific characteristics. In order to provide the high quality detailed empirical data needed for fracture mechanics calculations, this program concentrated on estimating six different flaw rates in the PVRUF vessel. The six flaw rates proposed are all possible combinations of the two flaw types of interest (planar and volumetric) and three different locations (near surface, weldment with HAZ, and base metal). See Section 1.1 for further discussion.

The purpose of this section is to present the frequency distribution of all the indications found in the SAFT-UT inspections of the PVRUF vessel according to size, location, and type. The performance of the SAFT-UT system in terms of probability of detection, sizing error, and false call rate is discussed in Section 7. Flaw rate estimates are reported in Section 8, with a discussion of the estimation methodology.

6.1 Joint Frequency Distribution of Indications in the Near Surface Zone

Of particular interest are flaws near the inner surface of the vessel. For pressurized thermal shock (PTS) events, the calculations indicate that flaws situated outside the inner 30% of the vessel wall contribute little to RPV failure. Also, flaw depths greater than about 25% of the vessel thickness are not important, because the thermal stresses do not extend that far into the vessel. On the other hand, small flaws of depth less than 10% of the vessel wall make a substantial contribution to vessel failure under PTS conditions. It should be noted that these results concern the embrittled region of the vessel beltline.

Flaws as small as 6 mm (0.24 in.) can make a sizable contribution to the overall probability of vessel failure during PTS events. These flaws have been the focus of SAFT-UT measurements, since they have a large impact on vessel integrity. The flaw distributions used in fracture mechanics calculations tend to focus on welding flaws. In these calculations, the flaws are typically treated in a worst-case fashion, by assuming that the flaws are at the inner surface of the vessel and have a radial orientation. Welding flaws can occur either within the weld metal itself, or within the heat-affected zone of the base metal. These flaws can occur anywhere within the thickness of the welded cross-section.

Calculations indicate that cracks parallel to the vessel surface have no impact on vessel integrity. In fact, these results show negative stress intensity factors, meaning that such cracks will tend to close rather than open. Typical flaws of this type would be inclusions and laminations.

There are significant driving forces to propagate small cracks that are entirely within the cladding, or cracks that extend only slightly into the base metal. Vessel integrity is quite sensitive to such cracks, and estimates of both the number and sizes of cracks in the cladding are important. Therefore, detailed analysis of the cladding and of the base metal region adjacent to the cladding is reported. Underclad cracks can be produced by the heat input and stresses associated with the welding process used to apply the cladding to the inner surface of the vessel. These cracks will be in the base metal near the clad-to-base metal interface. Typical underclad cracks are shallow. Cracks in the cladding itself can be produced by mechanisms such as stress corrosion cracking. These cracks will also be shallow, but if conditions are right, they could occur in large numbers for a given vessel.

Table 6.1 shows the distribution for the near surface indications, characterized by the material zone in which the indication is located. Four zones were defined to classify the portion of the vessel where the indications are located: weldment, heat affected zone, base metal, and cladding. The latter category, cladding, includes the clad-to-base-metal interface. The characterized indications found in the PVRUF vessel have been assigned a type of either volumetric or planar. Planar flaws include those flaws that are most important to calculations of vessel integrity, such as vertically oriented cracks, lack of fusion in the weld, etc. Volumetric flaws include flaws such as slag inclusions, porosity, and laminations. The method used to determine the indication type is described in Section 4.

Table 6.1 PVRUF: Number of near surface indications by category

PVRUF: Number of indications in the near surface zone															
	through-wall extent of the indications (DZ)														
9/15/95	< 2 mm	2-3 mm		3-4 mm		4-5 mm		5-6 mm		6-7 mm		7-8 mm		Total >2 mm	
Location		V[a]	P[b]	V	P	V	P	V	P	V	P	V	P	V	P
Clad	978	2	0	2	0	0	0	0	0	0	0	0	0	4	0
Weld	87	0	5	0	2	0	0	0	0	2	1	0	1	2	9
Fusion (Haz)	47	0	0	1	1	0	0	0	0	0	0	1	0	2	1
Base	392	4	14	1	4	0	2	0	0	1	0	0	1	6	21
Total	1504	6	19	4	7	0	2	0	0	3	1	1	2	14	31
				Total number characterized > 2 mm = 45											
								Total number < 2 mm = 1504							
								Total number = 1549							

[a]Volumetric.
[b]Planar.

6.2 Joint Frequency Distribution of Indications Outside the Near Surface Zone

Flaws can occur anywhere in the zone outside the near surface. Welding flaws can occur at any location within the thickness of the welded cross-section. These flaws can occur either within the weld metal itself, or within the heat-affected zone of the base metal. Base metal flaws can be introduced into the original plate or forging prior to vessel assembly and welding. Typical flaws of this type would be inclusions and laminations, which are both most often encountered in the mid-thickness of the vessel cross-section.

As noted in Section 1.4, bounding calculations for low temperature overpressurization (LTOP) events show that there should be concern for flaws that are situated throughout the thickness of the vessel wall, in addition to flaws near the inner surface. Calculations also indicate that about half the calculated vessel failures are due not to surface flaws, but to flaws within the interior of the vessel wall.

For LTOP events, flaw depths less than 10% of the vessel wall thickness are relatively unimportant. Rather, it is the somewhat larger flaws in the range of 10% to 30% of wall thickness that contribute most toward vessel failure under LTOP conditions.

Table 6.2 shows the distribution for the deeper flaw indications, characterized by the material zone in which the indication is located. In contrast to the near surface, three zones were defined here to classify the portion of the vessel where the indications are located: weldment, heat-affected zone, and base metal.

Table 6.2 PVRUF: Number of indications outside the near-surface zones by category

PVRUF: number of indications outside the near surface zone															
	through-wall extent of indications (DZ)														
9/15/95	< 4 mm	4-6 mm		6-8 mm		8-10 mm		10-12 mm		12-14 mm		> 14 mm		Total >4 mm	
Location		V[a]	P[b]	V	P	V	P	V	P	V	P	V	P	V	P
Weld	352	2	11	0	7	0	4	0	2	0	1	0	1	2	26
Fusion (Haz)	174	0	6	0	2	0	3	0	1	0	0	0	2	0	14
Base	386	6	19	1	7	0	1	0	1	0	1	0	2	7	31
Total	912	8	36	1	16	0	8	0	4	0	2	0	5	9	71
				Total number characterized >4 mm = 80											
								total number < 4 mm = 912							
								total number = 992							

[a]Volumetric.
[b]Planar.

7 Estimates of SAFT-UT Performance

In this section, the performance of the SAFT-UT system is described in terms of probability of detection, sizing error, and false call rate. To properly utilize the SAFT-UT results shown in Section 6 in an estimation procedure for flaw rates, it is necessary to understand the detection and sizing capabilities of SAFT-UT. This section also presents some valuable detection and sizing information from other tests involving the SAFT-UT system and from the Programme for the Inspection of Steel Components, Phase II (PISC II).

7.1 Probability of Detecting a Flaw

Results from the PISC II program have shown that three distinct flaw types should be considered in quantifying the probability of detection (POD) of flaws in heavy section steel (Nichols, 1988). These three types are smooth planar flaws, rough planar flaws, and volumetric flaws. Smooth planar flaws (e.g., thermal fatigue cracks) were found to be the most difficult to detect; rough planar flaws are easier to detect; and volumetric flaws such as slag inclusions and porosity had significantly higher POD than the other two types.

In the PISC II exercises, advanced UT techniques were used to inspect extensive amounts of pressure vessel material. The POD estimates shown in Table 7.1 were obtained from a logistic curve fit to this inspection data (Heasler 1993). As one can see from the table, the advanced procedures do best with volumetric flaws.

Table 7.2 shows the estimated POD in the SAFT-UT inspections of the Midland blocks. The POD for volumetric flaws with through-wall extent in the range of 1 to 2 mm (0.04 to 0.08 in.) was estimated at 0.7 for both near-surface and sub-surface flaws. This estimate is based on the SAFT-UT detection results reported in Appendix B of this document: viz., three detections of four flaws in the near-surface zone and two indications of three flaws in the weld root.

7.2 Sizing Error

SAFT-UT was used in the PISC III program for a full scale vessel (FSV) test at the Materialprufungsanstalt (MPA) Laboratory in Stuttgart, Germany. This test involved the characterization of 12 indications in a full-scale reactor pressure vessel (PISC III report, 1993). The flaws in that FSV test had a range of 6 to 110 mm (0.24 to 4.33 in.) in through-wall extent (Doctor et al., 1994). SAFT-UT tended to undersize the flaws by an average of 3.7 mm (0.14 in.), and the standard deviation of the SAFT-UT results from the true state was 4.7 mm (0.18 in.).

In a destructive analysis of Midland Block 1-8, 13 indications reported by the EPRI Center UT were selected for examination. The true state for the through-wall extent of a flaw is taken to be the value reported by the destructive analysis, as shown in Table 7.3. The through-wall extent was not determined by the destructive analysis for flaws numbered 1, 4, 9, 12, and 13; and no comparison can be made to an SAFT-UT depth estimate. Two flaws (numbered 2 and 10) were not detected in the SAFT-UT data. One flaw (number 3) was not inspected by SAFT-UT because it was at the end of the block.

The two small flaws in the weld root (numbered 5 and 6) were undersized by SAFT-UT. The three small flaws at the clad-to-base-metal interface (numbered 7, 8, and 11) were oversized by SAFT-UT.

7.3 False Call Probability

The results of the advanced methods inspections of the PISC II program gave an upper limit for false call probability (FCP) of 0.12 for volumetric flaws in thick section material (0.8 for clad flaws). This value was reported in Heasler (1993) and was calculated from the number of detections in material without known flaws. But this number is only an upper limit because no destructive test was performed to confirm that the material was blank.

The Midland destructive test results do not directly apply to a calculation of false call probability for SAFT-UT. The Midland destructive tests were performed to examine selected indications in the EPRI NDE Center UT data (Foulds, 1993). The selection of the locations for destructive analysis was reportedly biased toward the more significant indications (the larger ones) in the UT data.

Table 7.1 POD for advanced procedures from fits to PISC-II data

Flaw type	Material	POD (2 mm[a])	POD (6 mm[a])	POD (12 mm[a])
Smooth planar	Base	b	0.19	0.23
	Clad	b	0.19	0.25
Rough planar	Base	b	0.35	0.60
	Clad	b	0.16	0.40
Volumetric	Base	0.30	0.84	0.99
	Clad	0.18	0.60	b

[a]Through-wall extent of flaw.
[b]No estimation.

Table 7.2 Estimated POD for SAFT-UT inspections of the Midland blocks

Through-wall extent	1-2 mm	6 mm	12 mm
POD for near-surface flaws	0.7	--	--
POD for weld and base metal flaws	0.7	0.84	0.99

Table 7.3 True-state table for through-wall extent

EPRI NDE center indication number	True state from destructive analysis	SAFT-UT estimate	Material
1	Not determined	Not applicable	Root
2	1 mm	Not detected	Root
3t	0.75 mm	Not inspected	Root
3b	3 mm		
4	Not determined	Not applicable	Root
5	2 mm	1.3 mm	Root
6t	2 mm[a]	1.3 mm	Root
6b	3.5 mm		
7	1 mm	< 2.2 mm	CBI[b]
8	2 mm	< 2.2 mm	CBI
9	Not determined	Not applicable	CBI
10a	1 mm	Not detected	CBI
10b	1 mm		
11	0.5 mm	< 2.2 mm	CBI
12	Not determined	Not applicable	CBI
13	Not determined	Not applicable	CBI

[a]Two flaws found and sized but no data provided on spatial relationship.
[b]Clad-to-Base-Metal interface zone.

8 Flaw Rate Estimates

This section reports the flaw rate estimates derived from the distributions of indications described in Section 6. The methodology for fitting a parametric model to the SAFT-UT data is fully described here. The statistical confidence intervals on the estimated flaw rates, as determined by the number of indications measured during the inspections of vessel material by SAFT-UT, are an important part of this analysis.

Tables 6.1 and 6.2 show the number of indications that were detected and characterized in the SAFT-UT measurements of the PVRUF vessel. These data are presented by categories of location, type, and size. We use the amount of material inspected, as given in Table 3.3, to calculate the indication densities, i.e., the number of indications per unit volume in each category. The estimates of flaw rates described in Section 7 also depend on the measured performance of the SAFT-UT inspection system. The methodology described in this section generates estimates of the cumulative flaw rate function, denoted $\Lambda(s)$, and defined in Equation 8.1

$$\Lambda(s) = \int_s^\infty \lambda(s)\, ds \tag{8.1}$$

where $\lambda(s)$ is the flaw rate function, defined as the expected number of flaws of size s per unit volume, and where the size s is the through-wall extent of the flaw.

8.1 Use of SAFT-UT Performance Data

The capabilities of an inspection procedure are quantified by the probability of detection curve, (POD(s)), and the root mean square sizing error, σ. The first statistic describes the detection capabilities of the procedure and the other summarizes its sizing accuracy.

The POD curve describes the capability of the inspection procedure to detect a flaw of a certain size. A typical POD curve is S-shaped; for a small flaw, POD is typically close to zero and rises to one for large flaws. An inspection procedure with a typical S-shaped POD, as illustrated in Figure 8.1, will produce a flaw rate function that underrepresents the small flaws. If $\lambda_o(s)$ represents the true flaw rate function, then an inspection procedure with detection capabilities of POD(s) will produce a data set of flaws distributed according to the flaw rate function:

$$\lambda_1(s) = \mathrm{POD}(s)\, \lambda_0(s) \tag{8.2}$$

where $\lambda_1(s)$ represents the expected number of detected flaws of size s per unit volume of material.

The fact that the inspection procedure does not furnish the true size of the flaw further modifies the observed flaw rate function. We make the assumption that the inspection procedure provides the user with a size estimate that is contaminated with Gaussian error having a mean of zero and standard deviation of σ, so that the observed size is

$$s_{obs} = s_{true} + e \tag{8.3}$$

These sizing errors tend to "smear out" the flaw rate function. More specifically, the resulting flaw rate function calculated from inaccurately sized flaws is given by:

$$\begin{aligned} \lambda_2(s) &= \int_0^\infty \phi(s - z; \sigma)\, \lambda_1(z) dz \\ &= \int_0^\infty \phi(s - z; \sigma)\, \mathrm{POD}(z)\, \lambda_0(z) dz \end{aligned} \tag{8.4}$$

where $\phi(z;\sigma)$ represents a Gaussian density function with standard deviation of σ and mean of zero.

In practice, s_{obs} is always positive, even though the model allows for the possibility of negative flaw sizes. In other words, the Gaussian model does not produce a completely accurate description of sizing errors on small flaws. This is typically not a problem, because small flaws are not found (POD = 0). Another assumption of this model that could potentially cause more significant problems concerns the false call ratio. This estimation procedure assumes that there are no false calls in the data. If the false call rate of the inspection procedure is significantly different from zero, the estimate produced by this procedure will be too large, and the shape of the cumulative flaw rate function will be incorrect.

Equation 8.4 summarizes the basic estimation problem that must be solved; we want to estimate $\lambda_o(s)$, but the inspection procedure gives data for $\lambda_2(s)$. For this particular problem, we have chosen to use the method of maximum likelihood. Maximum likelihood requires us to specify a parametric form for the flaw rate function before a solution can be obtained. We have chosen a Weibull, a fairly common distribution for reliability work, and one that has previously been used for flaw size distributions (see Kennedy, Foulds, and Basin 1991). The specific form of the flaw rate function is therefore:

$$\lambda_0(s) = \beta_0\omega(s;\beta_1,\beta_2) = \beta_0\beta_1\beta_2 s^{\beta_2-1}\exp\left(-\beta_1 s^{\beta_2}\right) \quad (8.5)$$

or

$$\Lambda_0(s) = \beta_0\Omega(s;\beta_1,\beta_2) = \beta_0\exp\left(-\beta_1 s^{\beta_2}\right) \quad (8.6)$$

where $\Lambda_o(s)$ = the number of flaws with through-wall extent greater than s, per unit of weld volume;

β_o = the total number of flaws per unit of weld volume;

s = the through-wall extent of a flaw; and

β_1 and β_2 = the two parameters of the Weibull function that are to be fit to the empirical data.

8.2 Method of Estimation: Maximum Likelihood

If the data obtained from an inspection of T units of material includes M flaw indications, and the associated flaw depths, s_i, i = 1, 2, ... M, then the probability "density" for this data is given by:

$$f(M, s_1, s_2, ..., s_M) = \frac{e^{-\Lambda(0)T}}{M!}\prod_{i=1}^{M} T\lambda(s_i) \quad (8.7)$$

Assuming that the flaw rate function $\lambda(s)$ is determined by a vector of unknown parameters $\beta = \beta_1, \beta_2, ... \beta_n$), then the -2 log likelihood of the density is defined as:

$$\gamma(\beta) = 2\left[\log(M!) + T\Lambda(0;\beta) - \sum_{i=1}^{M}\log\left(T\lambda(s_i:\beta)\right)\right] \quad (8.8)$$

The method of maximum likelihood produces a solution to the vector β by finding the minimum of the function $\gamma(\beta)$ and an α-level confidence bound for this estimate, $\hat{\beta}$, which is given by the expression:

$$R_\alpha = \left(\beta : \gamma(\beta) - \gamma(\hat{\beta}) < \chi^2_\alpha(n)\right) \quad (8.9)$$

This confidence region on β can be translated into a confidence region on $\Lambda(s:\beta)$ (or $\lambda(s:\beta)$), by using the formulae:

$$\Lambda_{upper}(s) = \max_{\beta\varepsilon R_\alpha}\Lambda(s;\beta) \quad (8.9)$$

and

$$\Lambda_{lower}(s) = \min_{\beta\varepsilon R_\alpha}\Lambda(s;\beta) \quad (8.10)$$

8.3 Maximum Likelihood Using the Weibull Distribution

Since the flaw rate function we intend to utilize has a "Weibull" form as illustrated in Equation 8.6, the specific log-likelihood formula to be employed is:

$$\gamma(\beta) = 2\left[\log(M!) + T\beta_0\int_0^\infty POD(z)\omega(z;\beta_1\beta_2)\,dz - \sum_{i=1}^{M}\log\left(T\beta_0\int_0^\infty \phi(s_i - z;\sigma)POD(z)\omega(z;\beta_1\beta_2)\,dz\right)\right] \quad (8.12)$$

Because only three unknown parameters exist in this likelihood, it is possible to find the minimum using a modified exhaustive search. To accomplish this, β_o is expressed in terms of the two other unknown parameters. In fact, given specific values for β_1 and β_2, the value for β_o that minimizes the log-likelihood is:

$$\beta_0 = \frac{M}{\left[T\int_0^\infty POD(z)\omega(z;\beta_1\beta_2)\,dz\right]} \quad (8.13)$$

Therefore, the minimum for the log-likelihood expressed by Equation 8.13 is found by evaluating the likelihood over a regular grid of β_1 and β_2 values.

8.4 Data Requirements for the Estimation Method

In order to accurately estimate the flaw rate function, one must inspect enough material so that a "reasonable" number of flaws are found. In this section, we determine how many flaws are required to produce a reasonable estimate of the flaw rate function.

To determine the number of flaws required, maximum likelihood fits were performed on differently sized simulated data sets. These fits assumed that the inspected material contained flaws distributed according to the Marshall distribution (i.e., $\beta_1 = 1.60$ cm^{-1} and $\beta_2 = 1.0$). It was also assumed that the inspection procedure had no sizing error and fairly good POD characteristics. The specific cases listed in Table 8.1 were used to determine the effects of sample size and sizing error on flaw rate estimation accuracy. In practice, the sample size is adjusted according to the number of flaws found.

The acceptability of the fit is summarized by the confidence bandwidths associated with the unknown model parameters. For example, Figure 8.2 displays the 95%, 90%, 80%, and 50% confidence bounds on the β parameters in the Weibull distribution for a sample size of 3. From this plot, one can see that the confidence bounds do not close and it is quite obvious that 3 flaws do not provide enough information to adequately determine the flaw rate function. These confidence bounds can be translated into bounds on the cumulative rate function, as displayed in Figure 8.3. Figure 8.3 presents the cumulative rate function surrounded by 95% confidence bounds. As one can see from this plot, the shape of the curve is quite uncertain.

Table 8.2 summarizes the critical details of the maximum likelihood fits. The widths of the 95% confidence bounds on the two model parameters (β_1, β_2) are shown for various sample sizes. The results are fairly clear; acceptably accurate confidence bounds occur for sample sizes above 15, so one can expect good results from a fit to empirical data with this number of flaws. The table also shows that 10 flaws may be reasonable, but 5 are not.

Confidence bound plots for a sample size of 15 are presented in Figures 8.4 and 8.5. These plots are directly comparable to the results displayed for the sample size of 3 (Figure 8.2). As one can see, the size of the confidence interval has been dramatically reduced.

8.5 Near Surface Zone Flaw Rate Estimates

In the near surface zone, the largest number of planar indications occurred in the base metal, which had 419 detectable indications. Table 6.1 shows that 21 of these were greater than 2 mm (0.08 in.) in size. The inspections of the weld metal revealed 9 planar indications greater than or equal to 2 mm in size and a total of 98 detectable indications. The other categories in Table 6.1 contained 6 or fewer indications greater than 2 mm in size.

In this section, we report the fit of the Weibull distribution to the inspection data in Table 6.1. The resulting estimate neglects any detection or sizing errors. This approach gives the most "optimistic" result that can be obtained from the data, because the introduction of detection and sizing error will increase the flaw rate function and widen the confidence interval.

Weibull fits to the empirical data were satisfactory for the planar indications in the weldment and for the planar indications in the base metal. These two subsets of the SAFT-UT data have different distributions, as shown by the parametric model. The Weibull fits were unsatisfactory when the smallest indications (less than 2 mm [0.08 in.] in size) were included in the data, as evidenced by the model's overprediction of the flaw rate in the size range of 3 to 5 mm (0.12 to 0.2 in.), and underprediction for flaws greater than 6 mm (0.24 in.) in size. This effect is still present in the model's performance without including the smallest indications, which tends to confirm some difficulty in fitting this parametric model to the distribution of the empirical data.

A formulation for the Weibull distribution equivalent to that used in Equations 8.5 and 8.6 is:

$$\Lambda(s) = \beta_0 e^{-\left(\frac{s}{\alpha}\right)^{\beta}} \qquad (8.14)$$

and this form is more commonly encountered in the literature. For this reason, the fits to the SAFT-UT data are reported in terms of Equation (8.14).

Table 8.1 Maximum likelihood fits run to determine sample size

Inspection characteristics	Flaw distribution	Sample sizes (no. of flaws)
Perfect POD, RMS=0	Marshall	3,5,10,15,50,100
Volumetric POD, RMS=0	Marshall	3,5,10,15,50,100

Volumetric POD = logit (-1.97 + 5.73s).
Marshall Distribution: $= \Gamma_o \exp^{-1.60s}$, where s is in cm.

Table 8.2 Parameter confidence bound widths for different sample sizes

Sample size	$\beta_1 = 1.60$ cm^{-1} CBW (β_1)	$\beta_2 = 1.0$ CBW (β_2)
	Perfect POD, sizing RMS = 0	
3	∞	3.31
5	∞	2.54
10	19.95	1.56
15	12.82	1.17
50	2.85	0.39
100	1.42	0.39
	Volumetric POD, sizing RMS = 0	
3	∞	2.92
5	∞	2.34
10	15.675	1.36
15	9.975	0.97
50	2.850	0.39
100	1.425	0.19

CBW = confidence bound width.

Figure 8.6 shows the 50, 80, 90, and 95% confidence bounds on the α and β parameters from Equation (8.14) in the Weibull fit to the distribution of the 9 largest indications in the near surface weldment.

Figure 8.7 presents the 95% confidence bounds on the cumulative flaw rate Weibull function fit to the 9 largest indications in the near surface weldment. The quality of the fit is good; that is, the tendency to underpredict the smaller indications and overpredict the larger ones is not great. The upper 95% confidence bound on the fit is more than 200% of the prediction, reflecting the small sample size of 9 indications. The significant feature of this figure is the large flaw density that becomes apparent when expressed in flaws per cubic meter, especially when compared to the base metal, as described below.

Figure 8.8 shows the confidence bounds on the α and β parameters of the Weibull function fit to the 21 largest indications in the near surface base metal. The confidence intervals are moderately reduced compared to Figure 8.6, because the sample size increased from 9 to 21. There is considerable overlap in the confidence regions presented in Figures 8.6 and 8.8, indicating that the near surface weldment and base-metal distributions do not differ significantly (except in terms of gross flaw density).

Figure 8.9 presents the 95% confidence bounds on the cumulative flaw rate Weibull function fit to the 21 largest indications in the near surface base metal. The quality of the fit is only fair; that is, the tendency to underpredict the smaller indications and overpredict the larger ones is apparent. The upper 95% confidence bound on the fit is reduced to about 150% of the prediction, reflecting the larger sample size compared to Figure 8.7. The significant feature of this figure is the significantly lower flaw density for near surface base metal, compared to near surface weldment as shown in Figure 8.7.

8.6 Outside the Near Surface Zone Flaw Rate Estimates

Approximately equal numbers of planar indications occurred in the weldment and base metal in the zone below the near surface. There were a total of 380 detectable indications in the weldment and 424 in the base metal, a difference of only 10%. Table 6.2 shows that there were 38 indications in the base metal that were greater than 4 mm in size and 28 in the weldment. The HAZ had 14 indications greater than 4 mm in size. The other categories in Table 6.2 contained 7 or fewer indications greater than 4 mm in size.

In this section, we report the fit of the Weibull distribution to the inspection data in Table 6.2. The resulting estimate neglects any detection or sizing errors.

Weibull fits to the empirical data were satisfactory for all 3 categories of planar indications--weldment, HAZ, and base metal--but only when the indications smaller than 4 mm in size were excluded from the fit. A Weibull fit is also reported for the 7 volumetric indications in the base metal. The Weibull fits were unsatisfactory when the smallest indications (less than 4 mm in size) were included in the data, as evidenced by the model's biased overprediction of the flaw rate in the size range of 5 to 12 mm, and underprediction for flaws greater than 15 mm in size.

Figure 8.10 shows the 50, 80, 90, and 95% confidence bounds on the α and β parameters in the Weibull fit to the distribution of the 26 largest planar indications in the weldment. Figure 8.11 presents the 95% confidence bounds on the cumulative flaw rate Weibull function fit to the 26 largest planar indications in the weldment. The quality of the fit is very good; that is, there is no tendency to underpredict the smaller indications or over-predict the larger ones. The upper 95% confidence bound on the fit is about 150% of the prediction, reflecting the larger sample size of 26 indications compared to 9 indications for Figure 8.7. The significant feature of this figure is the quality of the fit and the higher flaw rate values compared to the base metal, as described below.

Figure 8.12 shows the confidence bounds on the α and β parameters of the Weibull function fit to the 14 largest indications in the heat affected zone. The confidence intervals have increased by a considerable amount, compared to Figure 8.10. This is caused, in part, by one large indication, planar indication #1 in the heat affected zone.

Figure 8.13 presents the 95% confidence bounds on the cumulative flaw rate Weibull function fit to the 14 largest indications in the heat affected zone. The quality of the fit is only fair; that is, the tendency to underpredict the smaller indications and overpredict the larger ones is apparent. The upper 95% confidence bound on the fit is increased to more than 200% of the prediction. The significant feature of this figure is the significantly higher flaw density for the heat affected zone, compared to the weldment and the base metal.

Figure 8.14 shows the confidence bounds on the α and β parameters of the Weibull function fit to the 7 largest volumetric indications in the base metal. The confidence intervals have increased by a considerable amount compared to Figure 8.10. This is caused, in part, by the fact that the empirical distribution here is limited to only two sizes.

Figure 8.15 presents the 95% confidence bounds on the cumulative flaw rate Weibull function fit to the 7 largest volumetric indications in the base metal. The quality of the fit is poor because of the limited distribution of the empirical data.

Figure 8.16 shows the confidence bounds on the α and β parameters of the Weibull function fit to the 31 largest planar indications in the base metal. The confidence intervals are reduced as expected for the relatively large sample size of 31.

Figure 8.17 presents the 95% confidence bounds on the cumulative flaw rate Weibull function fit to the 31 largest planar indications in the base metal. The quality of the fit is only fair; that is, the tendency to underpredict the smaller indications and overpredict the larger ones is apparent. The upper 95% confidence bound on the fit is reduced to about 150% of the prediction, reflecting the larger sample size of 31 indications. The significant feature of this figure is the significantly lower flaw density for base metal, compared to the weldment and heat affected zone.

8.7 Comparison to Other Published Flaw Rate Estimates

Table 8.3 shows the flaw rate parameters for the Weibull model fits to the six different indication rates extracted from the SAFT-UT inspections of PVRUF. Table 8.4 shows the flaw rate parameters for Weibull fits that have been previously published (Foulds et al. 1993)--including the data from SAFT-UT inspections of the Midland vessel (Appendix B of this report).

Table 8.3 PVRUF flaw rate function parameters

Location	Data set	α (mm)	β_1	β_0 flaws/m^3
Near surface	Planar, weldment	4.11	2.19	1100
	Planar, base metal	3.5	2.68	280
Outside near surface	Planar, weldment	8	2.93	137
	Planar, heat affected zone	10.9	1.46	274
	Volumetric, base metal	5.6	6.5	25
	Planar, base metal	8	1.79	34

Table 8.4 Published flaw rate function parameters

Data set	α (mm)	β_1	β_0, flaws/m^3
Marshall distribution[a]	6.25	1	0.4-40
SAFT-UT, 31 flaws[b]	3.81	1.39	966
EPRI NDE center UT, Sandia report[c]	4.70	1.30	409

[a]Marshall (1982) without preservice inspection and repair.
[b]Data from Midland report. SAFT-UT inspections of four Midland blocks without adjustment of POD or sizing error.
[c]Data reported in Foulds (1993).

Table 8.5 shows the results for the cumulative flaw rate function for 3, 6, and 12 mm for the six parametric flaw rate functions fit to the PVRUF data. Table 8.6 shows the cumulative flaw rates from previously published reports.

In summary, the SAFT-UT data from the PVRUF vessel provides information on flaw density and distribution as a function of flaw type and location. The most significant difference between the flaw rates reported here and those reported in Marshall 1982 is that the total density of flaws found by SAFT-UT is higher than that reported in (Marshall, 1982).

Table 8.5 PVRUF estimates of cumulative indication rates from Weibull fits to the indication frequencies

Location	Data set	Λ (3mm) indications/m^3	Λ (6mm) indications/m^3	Λ (9mm) indications/m^3	Λ (12mm) indications/m^3	Λ (15mm) indications/m^3
Near surface	Planar, weldment	660	110	4.2	0.03	<.01
	Planar, base metal	140	4.0	<.01	<0.01	<.01
Outside near surface	Planar, weldment	130	89	33	5.2	0.25
	Planar, heat affected zone	235	180	128	87	55
	Volumetric, base metal	24	5.2	<.01	<0.01	<.01
	Planar, base metal	29	19	9.9	4.3	1.6

Table 8.6 Published estimates of cumulative flaw rates for weldment using Weibull fit

Data set	Λ (3mm) flaws/m^3	Λ (6mm) flaws/m^3	Λ (9mm) flaws/m^3	Λ (12mm) flaws/m^3	Λ (15mm) flaws/m^3
Marshall[a] (β_o = 40 flaws/m^3	25	15	9.4	6	3.6
Midland, SAFT-UT[b]	470	147	36	7	1.2
Midland, EPRI[c]	230	104	40	14	4.4

[a] Marshall (1982) without preservice inspection and repair.
[b] SAFT-UT inspections of four Midland blocks without adjustment for POD or sizing error.
[c] Data reported in Foulds (1993).

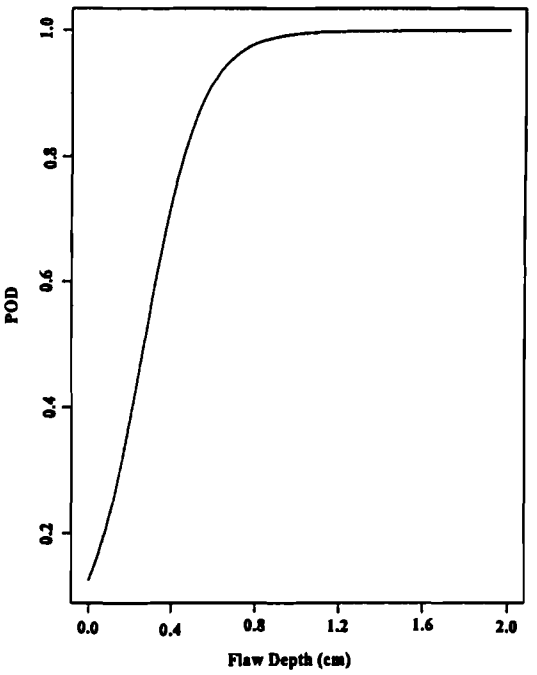

Figure 8.1 Typical probability of detection curve

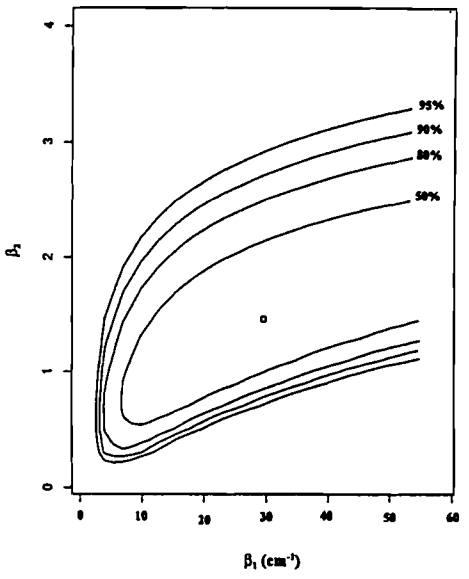

(Volumetric POD, No Sizing Error)
95% bound on β_0 = (0.80, 35.89)

Figure 8.2 Confidence bounds on model parameters for sample size of 3

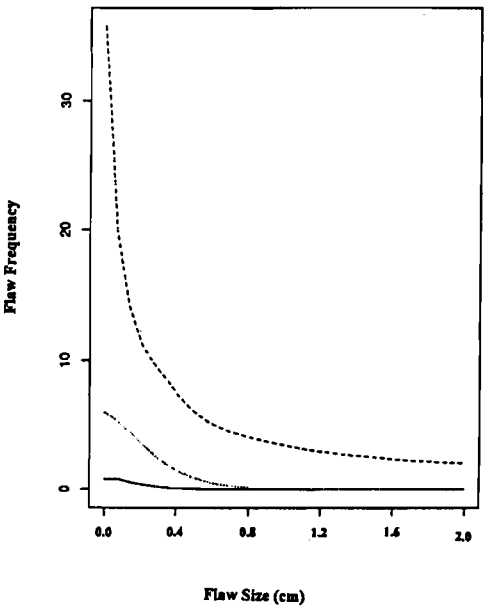

(Volumetric POD, No Sizing Error)

Figure 8.3 Cumulative flow rate function with 95% confidence bounds for a sample size of 3

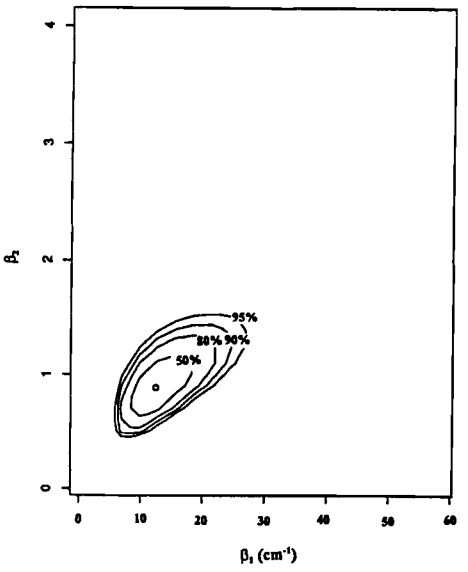

(Volumetric POD, No Sizing Error)
95% Confidence Bound on β_0 = (14.57, 80.27)

Figure 8.4 Confidence bounds on model parameters for sample size of 15

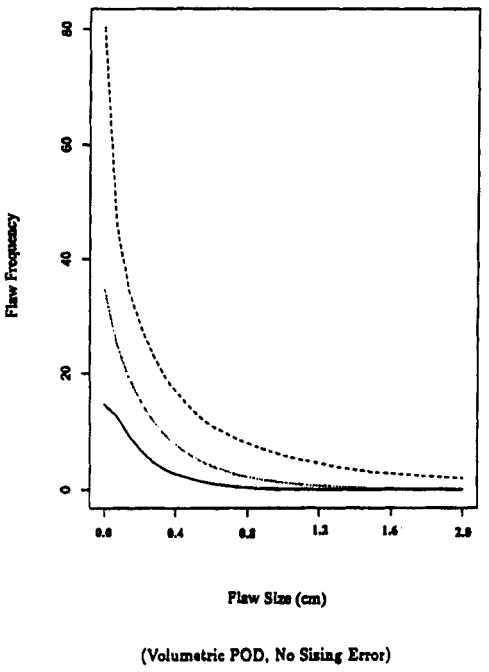

Figure 8.5 Cumulative flaw rate function with 95% confidence bounds for a sample size of 15

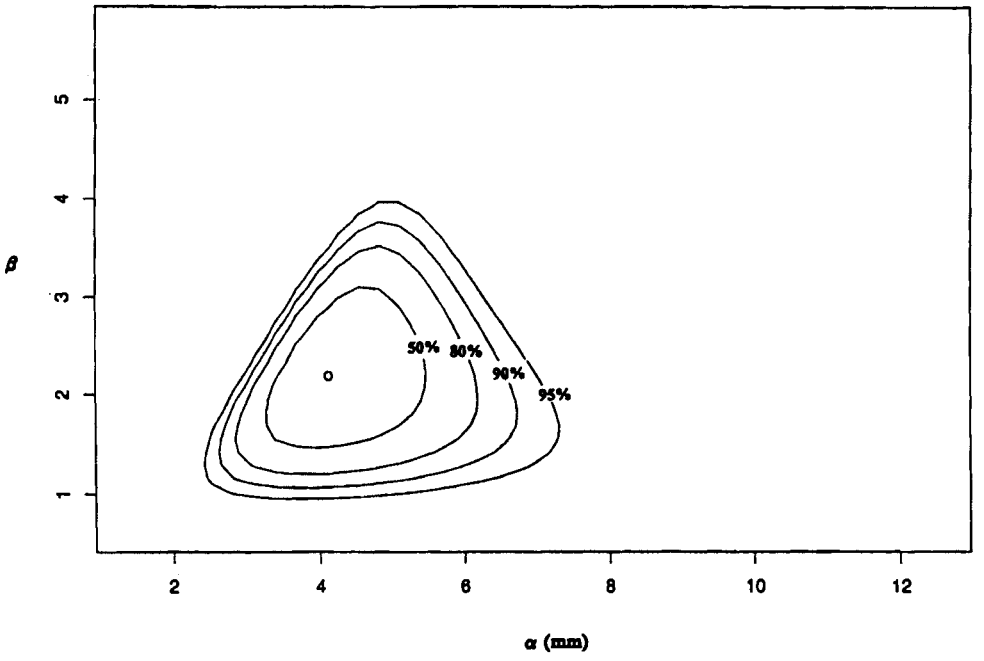

Figure 8.6 Parameter estimates with confidence bounds for simple Weibull fit to the SAFT-UT data of 9 planar indications in the near surface weldment

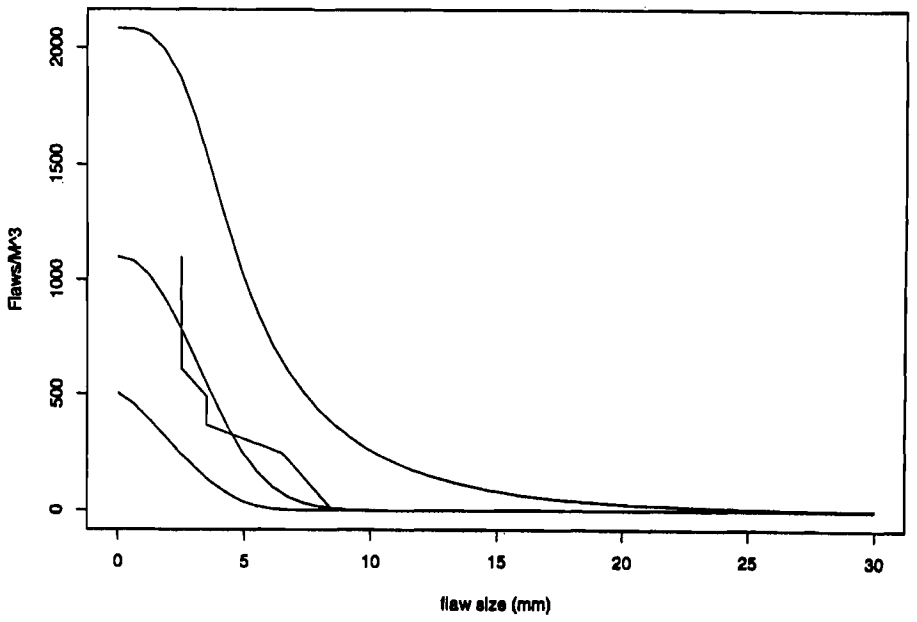

Figure 8.7 Estimate of cumulative flaw rate function with 95% confidence interval for simple Weibull fit to the SAFT-UT data of 9 planar indications in the near surface weldment

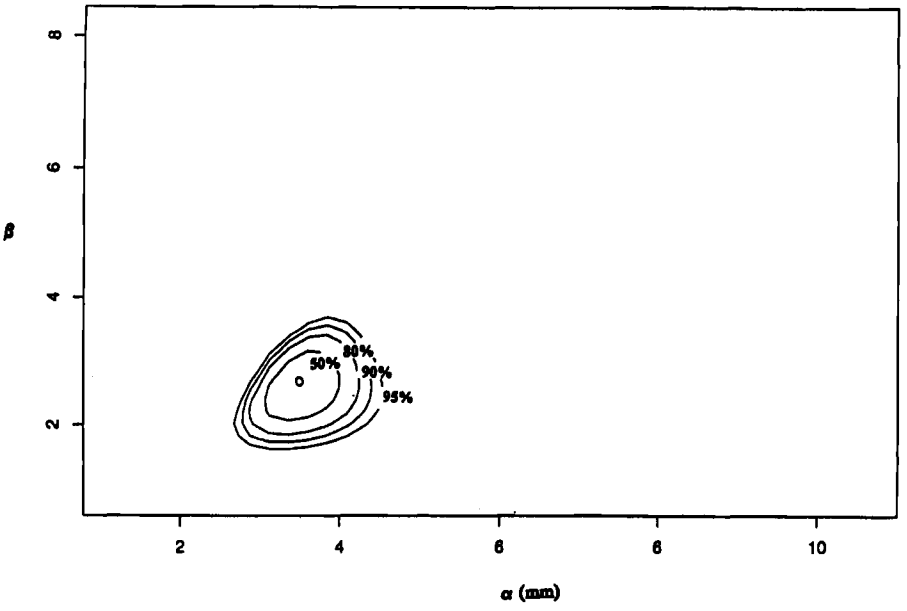

Figure 8.8 Parameter estimates with confidence bounds for simple Weibull fit to the SAFT-UT data of 21 planar indications in the near surface base metal

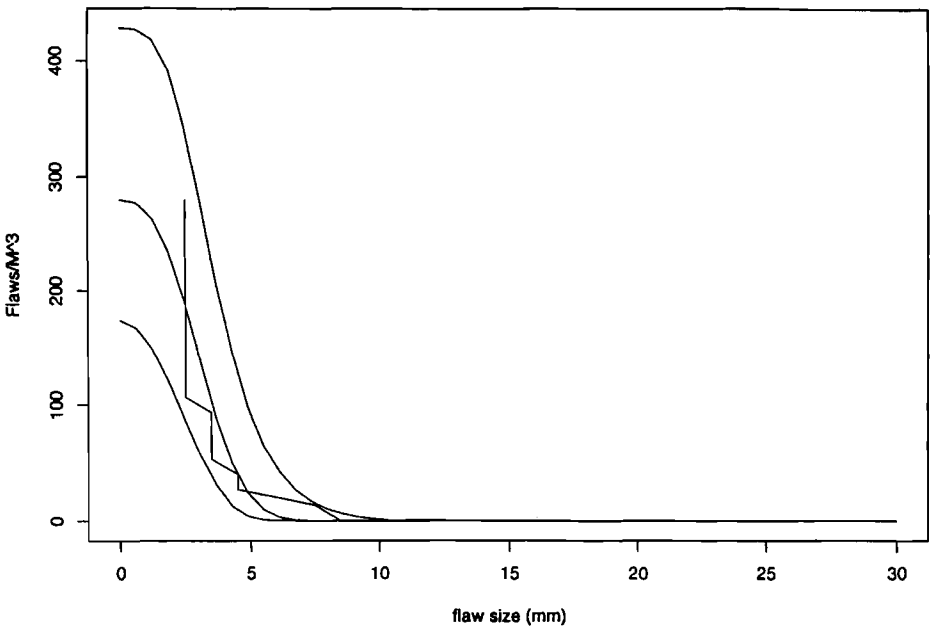

Figure 8.9 Estimate of cumulative flaw rate function with 95% confidence interval for simple Weibull fit to the SAFT-UT data of 21 planar indications in the near surface base metal

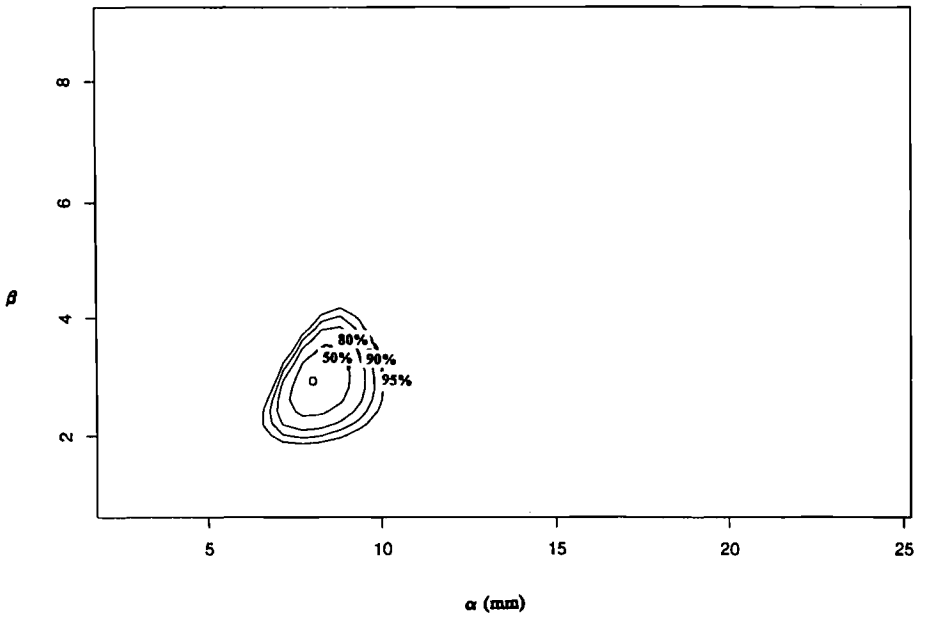

Figure 8.10 Parameter estimates with confidence bounds for simple Weibull fit to the SAFT-UT data of 26 planar indications in the weldment below the near surface

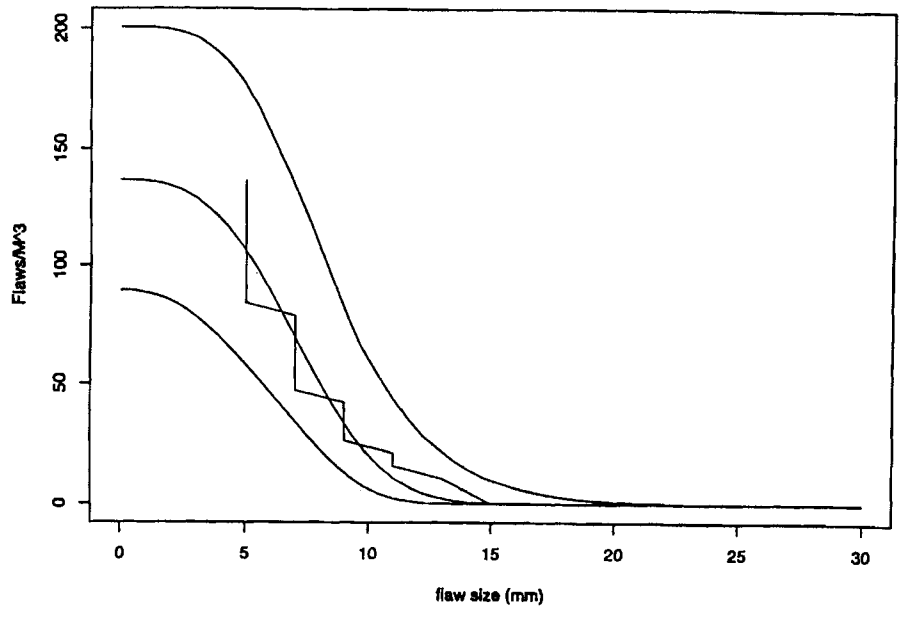

Figure 8.11 Estimate of cumulative flaw rate function with 95% confidence interval for simple Weibull fit to the SAFT-UT data of 26 planar indications in the weldment below the near surface

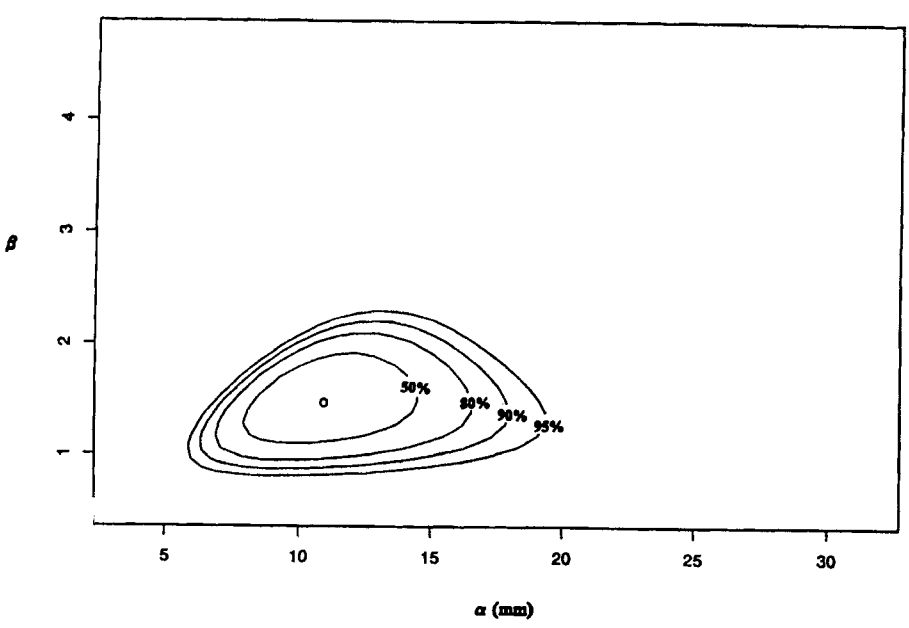

Figure 8.12 Parameter estimates with confidence bounds for simple Weibull fit to the SAFT-UT data of 14 planar indications in the heat affected zone below the near surface

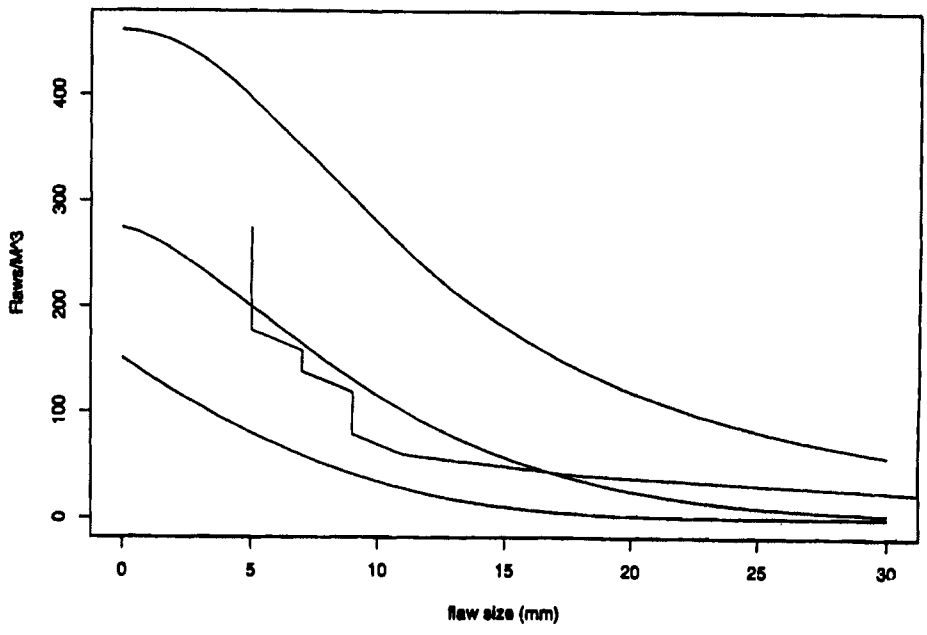

Figure 8.13 Estimate of cumulative flaw rate function with 95% confidence interval for simple Weibull fit to the SAFT-UT data of 14 planar indications in the heat affected zone below the near surface

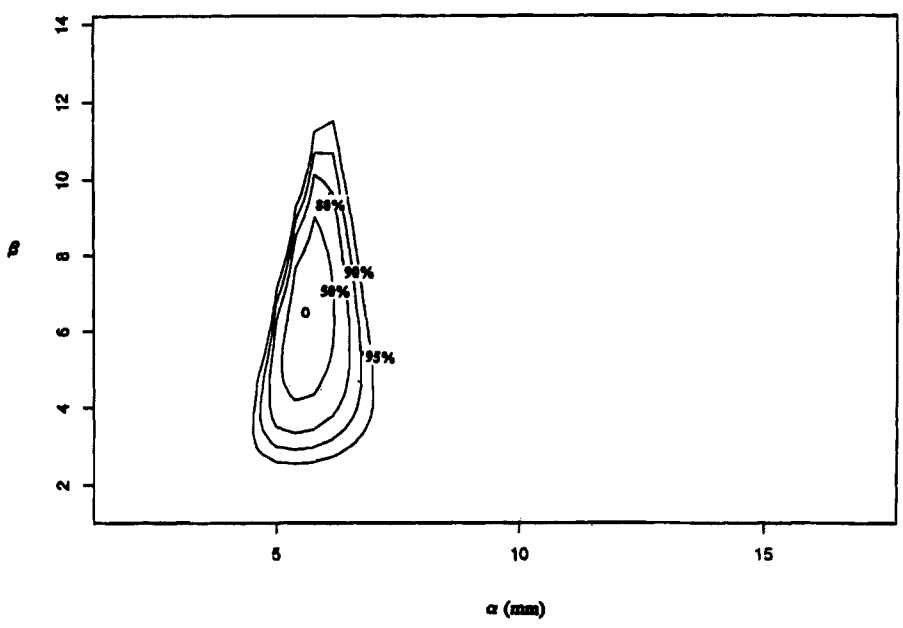

Figure 8.14 Parameter estimates with confidence bounds for simple Weibull fit to the SAFT-UT data of 7 volumetric indications in the base metal below the near surface

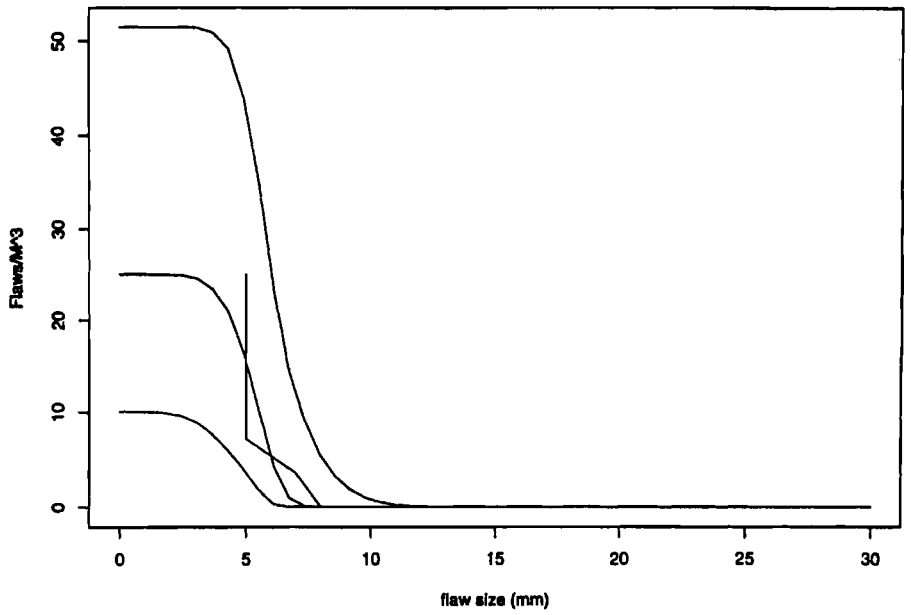

Figure 8.15 Estimate of cumulative flaw rate function with 95% confidence interval for simple Weibull fit to the SAFT-UT data of 7 volumetric indications in the base metal below the near surface

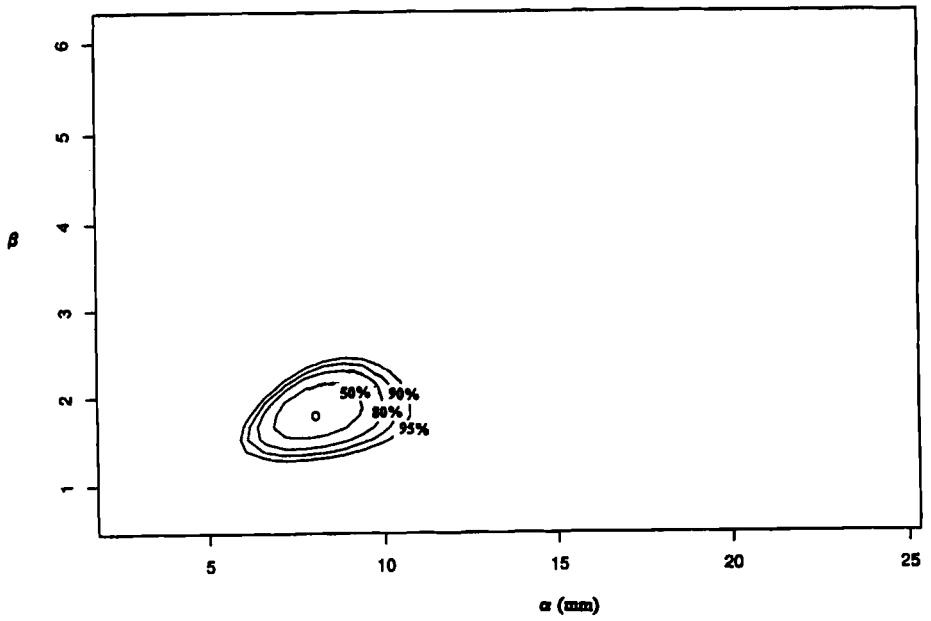

Figure 8.16 Parameter estimates with confidence bounds for simple Weibull fit to the SAFT-UT data of 31 planar indications in the base metal below the near surface

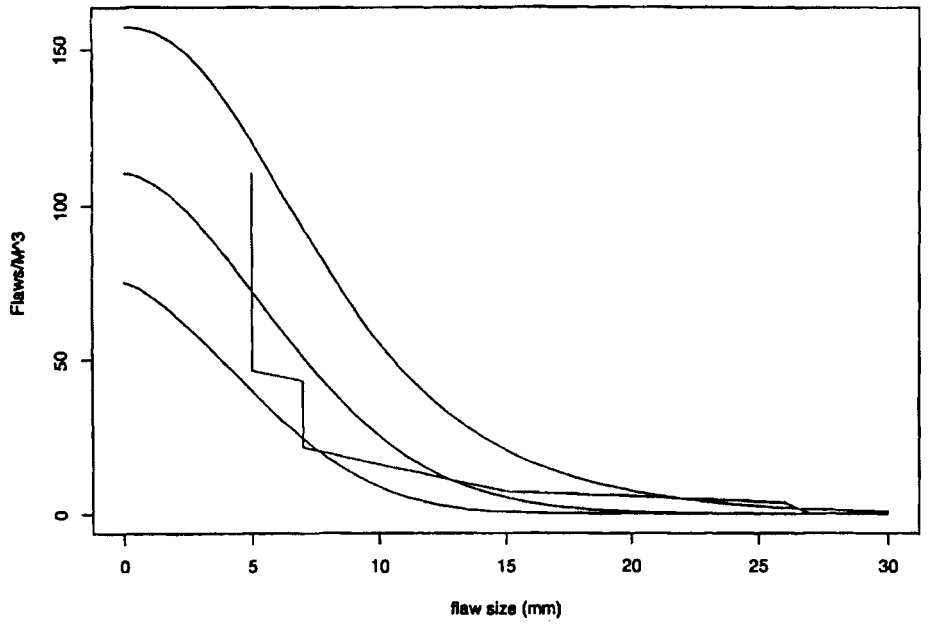

Figure 8.17 Estimate of cumulative flaw rate function with 95% confidence interval for simple Weibull fit to the SAFT-UT data of 31 planar indications in the base metal below the near surface

9 Discussion of Flaw Rate Estimates

This section discusses the flaw rate estimates given in Section 8. Two important questions arise from these new flaw rates. Why were so many flaw indications found in the vessel by SAFT-UT given the inspections that were performed on it by the fabricator? What is the origin of the difference between the number of indications found by SAFT-UT and the number predicted by the Marshal distribution?

9.1 SAFT-UT Flaw Indications and Inspections During Fabrication

The PVRUF vessel had been inspected by RT and several UT examinations from both the inside and the outside surfaces while it was being fabricated during the late 1970s and early 1980s. There were a number of repairs that were performed on the vessel based on the NDE results. One can assume that some large flaws were detected and that they were repaired. In order to understand why the SAFT-UT results detected so many flaws, the sensitivity of the inspections conducted must be under stood.

The SAFT-UT database that was obtained on PVRUF was created to develop information on the density and distribution of reactor pressure vessel (RPV) fabrication flaws. The data was not taken based on ASME Code requirements. It was expected that most of the flaws that would be detected would be small and thus, the inspection was conducted at very high sensitivity. The data can be related to ASME Code requirements by comparing the response from side drilled holes and end milled slots in the calibration block that was provided with the PVRUF vessel. The inspection sensitivity based on these ASME standard reflectors would be at a DAC of less than 5%.

For the inspections that were conducted by the fabricator, it is expected that these examinations were performed to the required ASME Code at that time. Prior to 1986, the code requirements included using procedures based on 50% DAC inspection sensitivity. For examinations conducted from the inside of the RPV it was common practice to gate out the first inch of RPV material as a result of inspection transducer ring down. Transducer ring down occurs in single-element transducers when exitation adversely affects reception during the first few microseconds. The use of dual element transducers essentially eliminates this problem and industry has adopted them for conducting effective examinations of the RPV near surface zone. Therefore, it is expected that none of the underclad near-surface flaws in the PVRUF database would have been detected from the inside. The use of 50% DAC would not have detected the flaws in the PVRUF database found in the remainder of the vessel wall because these flaws generally had a low ultrasonic response. The results from PISC II (Nichols and Crutzen 1988) show that for a flaw 50 mm deep the probability of detection would only be 10% for procedures based on 50% DAC.

In 1986 the ASME Section XI Code was changed based on PISC II results to require that an effective near surface examination be performed and that a 20% DAC sensitivity procedure be used. Whenever a utility up dates their ISI program to the 1986 or later editions of the ASME Code, the procedures would have met these requirements. The requirement of using an effective near surface technique would have meant that they used a transducer technique similar to that used by PNNL but without the SAFT processing of the data. Therefore, it would be expected that the larger (high signal-to-noise) flaws in the PVRUF database would have been detected in the near surface zone (first 25 mm). For the remainder of the vessel wall thickness, the use of 20% DAC sensitivity effectiveness must be related through the PISC II study. In the PISC II study it was found that for flaws 17 mm in depth (largest validated flaw in the PVRUF database) a procedure that used a 20% DAC level of sensitivity would have an average probability of detection of 45%.

Finally, inspections that would be performed today for those personnel, equipment and procedures that have successfully passed the performance demonstration test specified in ASME Section XI Code Appendix VIII, it is expected that they would detect all of the larger flaws in the PVRUF data base. This position is supported by the PISC II data, which shows for advanced techniques a probability of detection of 95% for a flaw 17-mm in depth.

9.2 PVRUF Flaw Rates and the Marshall Distribution

A question arises regarding the difference in numbers of flaws that were found in the PVRUF inspections versus

those predicted by the Marshall distribution. The PVRUF results are based on high sensitivity inspections. Work is in progress and this work will be fully documented in the Volume 2 of this report, supporting the fact that these 2500 indications are being confirmed to be flaws. Most of these flaws are very small, are probably not important to structural integrity, but they are flaws. The Marshall distribution was developed in the 1970s and was based on UT examination of 44 LWR vessels, augmented by information pertaining to defects in non-nuclear vessels. The detection efficiency for the UT inspections at that time was based on expert opinion and led the Marshall Study Group to recommend that "careful experiments be carried out to determine the efficiency of detection of cracks in vessels by ultrasonic methods (UKAEA, 1976)." Early UT examination procedures were not designed to detect many of the flaws that were found in the PVRUF inspections. These small flaws are important to developing distribution and density functions for the occurrence of flaws in reactor vessels, particularly in the process of extrapolating the data to describe the flaw occurrence in the full population of RPVs in the U.S. In the 1980s some new failure modes became very important such as pressurized thermal shock, in some of these cases the smaller flaws became more important. Although, they do not have as high a probability of causing a vessel failure the probability of their occurrence is higher. Based on these differences it is not surprising that there are differences between the 1990s PVRUF high sensitivity empirical results and those developed by expert opinion from the 1970s.

10 Validation Plan

This section describes the validation tests planned for the indications recorded by SAFT-UT. The performance of SAFT-UT has been measured previously, but additional confirmation by destructive testing is required to provide the necessary high quality flaw data for use in probabilistic fracture mechanics analysis, such as pressurized thermal shock (PTS) analysis.

The SAFT-UT system was used at PVRUF because of the need for high probability of detection and accurate sizing, especially for small flaws. Reasonable estimation of the density and distribution of fabrication flaws in unused material requires a system with these properties, and a large data set. More than 2500 indications were acquired with the SAFT-UT system.

This section describes the identification of material for removal from the PVRUF vessel and the location of the largest indications in the vessel. Indications were selected for destructive testing to validate the flaw rate estimates in Section 8.

10.1 Removal of Material from PVRUF for Destructive Testing

The plan for the removal of material from PVRUF proposes that large blocks be cut from the vessel and sent to PNNL. The size of the proposed blocks is 60 cm across the weld and 120 cm along the weld, with the weld centered in the width of the block. Approximately 60% of the beltline weld and 100% of the intermediate-to-upper-shell-course weld are to be available for validation of the SAFT-UT data.

Prior to the removal of any material, the vessel's inside surface will be marked to identify the material for validation. The locations for cuts will be designed to avoid the most significant indications (i.e., so that these indications are deep within the block rather than near a cut), and this will lead to blocks of different lengths. The lengths will vary from 60 to 120 cm. The material will be marked with fiducial points in such a way as to provide enough information to identify the PNNL material coordinates for each of the blocks.

Tables 10.1 and 10.2 show the locations along the welds for the 15 largest fully characterized indications in a number of categories for SAFT-UT indications from the PVRUF vessel.

10.2 Selection of Indications for Destructive Testing

The objective of the destructive test is to validate the flaw rates derived in Section 8 of this report. It was established in Chapter 8 that 15 flaws are a reasonable minimum number from which to determine a flaw-rate function. One approach to the validation task would be to perform destructive tests on the 15 largest indications for each of the flaw rates estimated in Section 8.

However, one or two of the analysis rules described in Section 4 determine the size of the largest flaws used to estimate each of the flaw rate functions. Therefore, verifying these sizing rules is a more efficient method of conducting the validation. The recommended validation steps include the following:

1. Select the most important indication type for each flaw rate. This may be the largest indication or it may be a typical indication from a large group.

2. Use construction radiographs to correlate with SAFT-UT images and as a basis for final selection of indications to be destructively tested. These records are available and their usefulness should be determined as part of the validation. These images may help distinguish planar vs. volumetric flaw types before the destructive test. Also, they may help in extrapolating the destructive test results over the entire SAFT-UT data set.

Table 10.1 Location of the largest indications along the weld, near surface zone

	Near surface													
	Weld				Haz		Base				Clad			
	P		V		V		P		V		P		V	
Rank	Weld	Y(in.)	Weld	Y(in.)	Weld	Y(in.)	Weld	Y(in.)	Weld	Y(in.)	Weld	Y(in.)	Weld	Y(in.)
1	5	58	5	350	5	479	4	129	4	27	5	473	5	479
2	4	29	5	479	4	52	4	156	5	317	5	473	5	479
3	5	52	5	75	5	247	4	37	5	311	5	483	5	473
4	5	109	4	196	n/a	n/a	4	142	4	200	5	478	5	484
5	4	33	n/a	n/a	n/a	n/a	4	127	5	420	n/a	n/a	4	539
6	4	59	n/a	n/a	n/a	n/a	4	71	4	209	n/a	n/a	4	20
7	4	197	n/a	n/a	n/a	n/a	4	123	5	353	n/a	n/a	n/a	n/a
8	5	371	n/a	n/a	n/a	n/a	4	125	4	49	n/a	n/a	n/a	n/a
9	5	175	n/a	n/a	n/a	n/a	4	167	n/a	n/a	n/a	n/a	n/a	n/a
10	4	184	n/a	n/a	n/a	n/a	5	200	n/a	n/a	n/a	n/a	n/a	n/a
11	n/a	n/a	n/a	n/a	n/a	n/a	5	238	n/a	n/a	n/a	n/a	n/a	n/a
12	n/a	n/a	n/a	n/a	n/a	n/a	5	205	n/a	n/a	n/a	n/a	n/a	n/a
13	n/a	n/a	n/a	n/a	n/a	n/a	4	33	n/a	n/a	n/a	n/a	n/a	n/a
14	n/a	n/a	n/a	n/a	n/a	n/a	4	109	n/a	n/a	n/a	n/a	n/a	n/a
15	n/a	n/a	n/a	n/a	n/a	n/a	4	165	n/a	n/a	n/a	n/a	n/a	n/a

Table 10.2 Location of the largest indication along the weld outside the near surface zone

	Full volume											
	Weld				Haz				Base			
	P		V		P		V		P		V	
Rank	Weld	Y(in.)	Weld	Y(in.)	Weld	Y(in.)	Weld	Y(in.)	Weld	Y(in.)	Weld	Y(in.)
1	5	11	4	539	4	220	5	80	5	60	5	181
2	4	215	5	10	5	23	n/a	n/a	4	530	5	238
3	5	102	5	29	5	2	n/a	n/a	5	312	5	348
4	4	193	5	8	5	152	n/a	n/a	5	9	5	214
5	4	194	4	69	4	162	n/a	n/a	5	3	5	11
6	5	10	n/a	n/a	5	24	n/a	n/a	5	261	5	229
7	5	513	n/a	n/a	5	3	n/a	n/a	5	311	5	343
8	5	103	n/a	n/a	4	138	n/a	n/a	5	495	5	344
9	5	467	n/a	n/a	5	3	n/a	n/a	5	515	5	214
10	5	519	n/a	n/a	5	4	n/a	n/a	5	315	5	180
11	4	113	n/a	n/a	4	87	n/a	n/a	5	489	5	460
12	5	3	n/a	n/a	5	317	n/a	n/a	4	47	4	38
13	5	4	n/a	n/a	5	6	n/a	n/a	5	173	5	114
14	5	29	n/a	n/a	4	36	n/a	n/a	5	15	5	197
15	5	4	n/a	n/a	5	10	n/a	n/a	4	86	5	10

3. Validate the location of each selected indication in the block. This will be done before the block is cut, using the same inspection mode that originally detected the indication. A lengthy scan need not be performed; rather, a simple manual measurement may be sufficient.

4. Cut the block for normal beam inspection. The first cut on a large indication will be made to expose a surface for a normal beam UT inspection of the indication. This will determine if the large indication is composed of a number of smaller ones, and will locate the indication more precisely in the material.

5. Prepare the indication for metallography if its size is validated by a normal beam test. After the normal beam test, a decision can be made as to whether or not this indication still contributes to the flaw-rate function. For example, if a large indication is re-characterized as two small ones in the normal beam test, then there may be no reason to perform metallography. The metallographic process will probably require that the material containing the indication be extracted and formed into a cube for grinding, polishing, and etching.
6. Perform metallographic analysis.

Another method recommended for validation is the use of the tandem SAFT-UT mode. This inspection can be performed on the blocks removed from the PVRUF vessel without any further cutting. Tandem mode inspections can also be used to extrapolate the destructive test results over the entire SAFT-UT data set.

11 Reliability Requirements for ISI Systems

Reactor pressure vessel inservice inspections (ISI) produce data that can be used to estimate the number and sizes of flaws in a vessel. This chapter discusses what characteristics ISI procedure/equipment/personnel should have to produce an acceptable flaw inventory for a vessel. The flaw estimation problem faced during ISI is a bit different than the problem dealt with in other portions of this report: an ISI is focused on determining the number and sizes of flaws in a specific reactor pressure vessel, while this report has focused on estimating a generic flaw frequency function for a population of vessels.

In order to perform a series of calculations on the utilization of ISI results, it is necessary to determine the amount of RPV weldment that is inspected during an outage. For PWRs the normal procedure is to perform ISI from the inside of the vessel and in order to do this, all of the reactor internals are removed. In addition, there are a number of fixed costs associated with setting up the RPV inspection system. Consequently, the normal practice is to only inspect the PWR RPV once during a ten-year interval and to inspect all the ASME-required locations that are accessible. In the case of BWRs, the ISI program is somewhat more complicated because of the inspection requirements that must be met and the six different models of BWRs. Some plants conduct some nozzle inspections every three years and perform inspections of the upper portion of the RPV at those times. They only inspect below the nozzles once during a ten-year interval.

Thus, during each three-year period, differing amounts of the vessel are examined. The amount of the BWR RPV that is inspected at any one time will range from about one third to about two thirds. For this chapter, we will assume that if ISI is performed that one third of the RPV weldments will be inspected. Since most of the time when ISI is performed more than this amount will be inspected, it is conservative in the analysis to assume the lower bound.

The flaws found by inspection typically represent only a portion of the total population of flaws present. After inspection, flaws in the vessel can be divided into three categories:

- Flaws found by inspection,
- Flaws missed by inspection,
- Flaws not inspected.

Furthermore, the reported flaw sizes will differ from the actual sizes because of sizing error. To evaluate the consequences of imperfect inspection, it is reasonable to concentrate on those flaws not found (i.e., missed + not inspected), because these are the ones that may potentially impact the structural integrity of the vessel; it is assumed the flaws that are found will be repaired or shown to be of no safety consequence.

Even though inspection provides direct information on only the first of these three categories of flaws, it is possible to use the inspection data to say something about the last two categories. In fact, if the inspection is properly calibrated[1] the flaws in the last two categories can be estimated.

In order to evaluate how adequate inspection is, our strategy is to measure how well inspection can estimate the number of flaws in the last two categories. An adequate inspection procedure will be one that gives results that do not differ substantially from perfect inspection, as measured by the mean square error of the estimate. We will attempt to bound the mean square error so that the challenge to structural integrity would be evaluated as essentially the same whether using imperfect inspection or perfect inspection results.

11.1 Quantitative Model of Inservice Inspection

The number of flaws of size s in T meters of weldment is assumed to have a Poisson distribution with mean $\lambda(s)T$, where $\lambda(s)$ is the flaw frequency function.

After inspection, the state of the pressure vessel can be described by two curves, $N_F(s)$ and $N_U(s)$. The curve $N_F(s)$ describes the number and sizes of flaws found by inspection, while $N_U(s)$ describes the flaws not found. The curves are defined as follows:

$N_F(s)$: The number of flaws of size greater than s found by inspection of T_1 meters of weldment.

[1] A calibrated inspection is one with well known POD curve and sizing error. This is not the typical NDE meaning for calibration.

$N_U(s)$: The number of flaws of size greater than s unfound. This includes flaws missed by inspection and flaws in the un-inspected T_2 meters of material.

Inspection directly produces $N_F(s)$, but to conduct a complete structural integrity assessment, one also requires $N_U(s)$, the flaws not found by inspection. It so happens that the unfound flaw curve can be estimated from inspection results, using the same estimation methods that have been used to estimate generic flaw frequency functions.

The closeness of the estimate $\hat{N}_U(s)$ to the desired curve $N_U(s)$ depends on the inspection's detection and sizing capabilities, so a reasonable way to evaluate the inspection capabilities is to evaluate the error between the estimate and the desired value, using an appropriate statistic.

Naturally, one wants to specify the inspection probability of detection (POD) and sizing capability so that this error is small. But it is difficult to specify absolute bounds on this error, without performing some sort of analysis that relates the error to structural integrity. Since a detailed analysis is beyond the scope of this evaluation, we will employ an approximate curve in the analysis. The curve, R(s) is plotted in Figure 11.1 and is meant to roughly represent the probability of failure for a single crack under a PTS event.

From this curve, one can see that the impact on structural integrity associated with flaws smaller than 3 mm is very small. Between 3 mm and 8 mm, the impact increases from 0 to 10^{-3}, a value that is not insignificant. Between 8 mm and 12 mm, the impact increases dramatically to one of certain failure (Simonen 1986a). The benchmark points on the curve (3, 8, and 12 mm) are connected with straight lines to produce a simple curve. Given this curve, it is possible to calculate the expected number of flaws that would fail during a PTS event, which is:

$$R_T = \left| \int R(s)\, d\, N_U(s) \right| \qquad (11.1)$$

and

$$\hat{R}_T = \left| \int R(s)\, d\, \hat{N}_U(s) \right|. \qquad (11.2)$$

This study will evaluate the acceptability of $\hat{N}_U(s)$ (and the corresponding inspection capabilities) by calculating the root mean square error of $\hat{R}_T$, which is defined as:

$$\mathrm{RMSE}(\hat{R}_T) = \sqrt{E\left(\left(\hat{R}_T - R_T\right)^2\right)}, \qquad (11.3)$$

where E(X) denotes the expected value of X. The root mean square error associated with an (imperfect) inspection will be considered acceptable if it is less than a certain proportion of the RMSE achieved for perfect inspection. In this study, we will use the proportion 150% to define acceptability.

11.2 Scenarios for Evaluating Different Aspects of Inspection Capability

Inspection capability can be divided into four components, which can be separately evaluated. These four components are the inspection procedure's 1) POD, 2) uncertainty associated with the POD, 3) sizing error, and 4) uncertainty associated with the sizing error. To evaluate inspection capability, the following five scenarios will be utilized, which will allow each of the four components of inspection to be compared to a base case. The scenarios are:

Perfect Inspection: (Base Case) POD(s) = 1 and sizing error is zero.

Imperfect Detection: POD(s) < 1, but the sizing error is zero, **and POD(s) is assumed to be known.**

Imperfectly Calibrated POD: POD(s) < 1, sizing error is zero, and POD(s) is imperfectly known.

Imperfect Sizing: The sizing error is not zero, but is assumed to be known; it is Gaussian with mean 0 and a standard deviation of σ_s. POD is assumed to be 1.

Imperfectly Calibrated Sizing: POD(s) = 1, but the standard deviation (σ_s) associated with sizing error is imperfectly known.

Each component of inspection capability will be evaluated by comparing the base case RMSE against the RMSE produced when that component is varied. Acceptable thresholds for that component will be chosen so that the RMSE is inflated no more than 150%. In the next sections, the mean square error for $\hat{R}_T$ will be calculated for each scenario.

The general estimator for $\hat{N}_U(s)$ that will be used in this evaluation is:

$$\hat{N}_U(s) = \left| \int_s^{\infty} \frac{Pnd(z)T_1 + T_2}{POD(z)T_1} d N_F(z) \right| \quad (11.4)$$

In this equation, POD(z) represents the probability of detection for a flaw of size z mm, while Pnd(z) = 1 - POD(z). It should be noted that this formula is not the only way $\hat{N}_U(s)$ could be estimated, but it is the simplest estimation formula. This formula accounts for missed flaws and is unbiased when POD is known. A formula very similar to this is used in the steam generator IPC (Improved Plugging Criteria) inspections to deal with unfound flaws.

11.2.1 Perfect Inspection Scenario (Base Case)

If inspection is perfect, then POD(s) = 1 and the estimator reduces to:

$$\hat{N}_U(s) \frac{T_2}{T_1} N_F(s) \quad (11.5)$$

and the MSE for $\hat{R}_T$ is:

$$MSE(\hat{R}_T) = \frac{T_2(T_1 + T_2)}{T_1} \int R^2(s) T(s) ds \quad (11.6)$$

11.2.2 Imperfect Detection Scenario

In this case, the estimator cannot be simplified. The MSE associated with the estimator is:

$$MSE(\hat{R}_T) = \frac{T_1 + T_2}{T_1} \int R^2(s) \lambda(s) \frac{Pnd(s)T_1 + T_2}{POD(s)} ds \quad (11.7)$$

The objective is to put a bound on MSE and solve for POD(s). This is an ill-determined problem, unless some constraint is placed on POD(s). To make the problem tractable, the POD curve will be assumed to have a shape similar to the curve R(s). Specifically, the POD curve will have the shape illustrated in Figure 11.2: from 3 mm to 8 mm, it will be assumed to be constant with value β_1; from 8 mm to 12 mm, it will rise linearly to β_2; and for sizes larger than 12 mm, the curve will remain constant.

In other words, the POD curve will have a form described by:

$$POD(s|\beta) = \beta_1 V(s) + \beta_2 (1 - V(s)) \quad (11.8)$$

where V(s) = 1 for any s < 8 mm, V(s) = 0 for any s > 12 mm, and V(s) is linear between 8 mm and 12 mm.

11.2.3 Imperfectly Calibrated POD Scenario

In this scenario, the POD curve originates from a calibration exercise which has fit a curve to detection data. It has some sort of parametric form, which can be represented by POD(s|β). For example, Equation 11.8 represents such a form.

The $\beta = (\beta_1, \beta_2)$ represents the parameter vector estimated by the regression. The regression determines β imperfectly, and this is expressed in terms of an uncertainty (i.e., Bayesian posterior) distribution $f(\beta|\hat{\beta})$. The uncertainty of the whole curve can be described by the covariance:

$$H(z,s) = Cov\left(POD(z|\beta), POD(s|\beta)\right) \quad (11.9)$$

The estimate for this scenario is actually produced by using the best estimate $\hat{\beta}$ for β in Equation 11.8:

$$MSE(\hat{R}_T) = \frac{T_1 + T_2}{T_1} \int R^2(s) \lambda(s) \frac{Pnd(s|\hat{\beta})T_1 + T_2}{POD(s|\beta)} ds + (T_1 + T_2)^2 \iint R(s)\lambda(s)R(z) \frac{H(x,z)}{POD(s|\beta)\,Pnd(z|\hat{\beta})} dsdz \quad (11.10)$$

For this scenario, the above formula is to be used to determine a bound on H(s,z). This again is an ill-determined

problem, and to make it tractable, we utilize the functional form for POD introduced previously. If POD has the form introduced there, then H(s,z) can be expressed as:

$$H(s,z) = \frac{2}{N}\hat{\beta}_1\left(1-\hat{\beta}_1\right)V(s)V(z) + \hat{\beta}_2\left(1-\hat{\beta}_2\right)\left(1-V(s)\right)\left(1-V(z)\right) \quad (11.11)$$

where N represents the sample size used in the regression experiment. This sample size effectively determines H(s,z), so the determination of appropriate bounds for uncertainty of the POD curve can be considered equivalent to the determination of N.

11.2.4 Imperfect Sizing Scenario

Let $\lambda_F(s)$ represent the expected value of $N_F(s)$, assuming that flaw sizes are contaminated with Gaussian error. In other words, the relationship between $\lambda_F(s)$ and the true $\lambda(s)$ is:

$$\lambda_F(s) = \int \lambda(z)\,\phi\left(\frac{z-s}{\sigma_s}\right)dz \quad (11.12)$$

where $\phi(x)$ is the Gaussian density function:

$$\phi(x) = \frac{1}{\sqrt{2\pi}}\exp\left(-\frac{x^2}{2}\right) \quad (11.13)$$

The MSE for this scenario is:

$$MSR(\hat{R}_T) = T_2\int R^2(s)\lambda(s)ds + \frac{T_2^2}{T_1} \int R^2(s)\lambda_F ds + \left(T_2\int R(s)\lambda(s) - \lambda_F(s)ds\right)^2 \quad (11.14)$$

For this scenario, the objective is to use the above equation to place bounds on σ_s, the sizing error standard deviation. Equations 11.12, 11.13, and 11.14 provide enough information to accomplish this.

11.2.5 Imperfectly Calibrated Sizing Scenario

Under this scenario, we assume that the sizing error standard deviation σ_s is not known, but has to be estimated by, say $\hat{\sigma}_s$, with ν degrees of freedom (i.e., $\nu + 2$ data points in the calibration experiment). This means that the true and the estimated σ_s can be related through a conditional distribution of the form:

$$f\left(\sigma_s \mid \hat{\sigma}_s, \nu\right) \quad (11.15)$$

and the MSE is now:

$$MSE\left(\hat{R}_T - \hat{\sigma}_s, \nu\right) = \int MSE\left(\hat{R}_T - \sigma_s\right) f\left(\sigma_s \mid \hat{\sigma}_s, \nu\right) d\sigma_s \quad (11.16)$$

This equation is used to determine an acceptable value for ν.

11.3 Flaw Distribution Function

As one can see from the formulas presented in the previous sections, $RMSE(\hat{R}_T)$ depends on the flaw distribution function $\lambda(s)$. In order to evaluate the desired RMSE, we must supply approximate values for $\lambda(s)$, and the natural approximations to use are the estimates for PVRUF, which have been produced in Chapter 8 of this report.

These flaw distribution functions are derived from the Weibull distribution so that $\lambda(s)$ has the form:

$$\lambda(s) = \beta_0(\beta/\alpha)(s/\alpha)^{\beta-1}\exp\left(-(s/\alpha)^{\beta}\right) \quad (11.17)$$

where the α, β, and β_0 are the parameters that determine the function. The PVRUF inspection has furnished sets of flaw distributions as presented in Table 11.1.

These flaw distribution functions are plotted in Figure 11.3. The objective is to use these eight estimates to represent flaw distributions that are typical of reactor

Table 11.1 Flaw distributions from PVRUF

$\lambda(s)$	Location/data set	α (*mm*)	β_1	β_0 (flaws/m^3)
$\lambda_1(s)$	Near surface/planar, weldment	4.11	2.19	1100
$\lambda_2(s)$	Near surface/planar, base metal	3.5	2.68	280
$\lambda_3(s)$	Outside near surface/planar, weldment	8	2.93	137
$\lambda_4(s)$	Outside near surface/planar, HAZ	10.9	1.46	274
$\lambda_5(s)$	Outside near surface/volumetric, base metal	5.6	6.5	25
$\lambda_6(s)$	Outside near surface/planar, base metal	8	1.79	34

vessels generally. We will calculate the RMSE associated with each different $\lambda(s)$, and choose requirements so that all or almost all of the associated RMSE are less than the 150% criteria. Ideally, one would like to see that the RMSE is not strongly influenced by $\lambda(s)$, or if it is, is influenced in only a simple way.[1] We therefore hope that all the different cases presented above will produce roughly the same inspection requirements.

It should be noted that a typical reactor contains about a cubic meter of weldment, so the unit, flaws per reactor could also be placed on the parameter β_0 in Table 11.1.

11.4 Results from Scenario Evaluations

In this section, the RMSE formulas are applied for each scenario to produce tables relating RMSE to each of the four components of inspection (i.e., POD, POD uncertainty, sizing error, sizing error uncertainty). The numbers were calculated by numerical integration with a computer code.

For these evaluations, it was assumed that only one third of the weldment in the reactor was inspected ($T_1 = 1/3$ and $T_2 = 2/3$).

11.4.1 Base Case Scenario Results

Evaluating Equation 11.6 for the six flaw distribution functions yields the results presented in Table 11.2. As one can see from this table, the RMSE varies considerably among the six distributions. One can also see that the RMSE is roughly proportional to average $E(R_T)$, so this table shows that there is considerable variability in this population of six flaw distributions: the population ranges from a distribution having a small impact on structural integrity ($\lambda_5(s)$) to one that has a large impact on structural integrity ($\lambda_4(s)$).

Table 11.2 RMSE for base case

$\lambda(s)$	RMSE $\left(\hat{R}_T\right)$	$E(R_T)$
$\lambda_1(s)$	1.417	2.055
$\lambda_2(s)$	0.026	0.022
$\lambda_3(s)$	5.508	15.173
$\lambda_4(s)$	14.460	76.215
$\lambda_5(s)$	0.004	0.007
$\lambda_6(s)$	3.618	5.280

It is useful to consider flaw distributions that display this sort of variability for this evaluation. If the evaluation produces consistent requirements for inspection using these disparate flaw distribution functions, we have good evidence that the requirements are generally valid.

It should also be noted that the units for R_T and its RMSE are "number of flaws important to structural integrity." If the curve were correct, flaws important to structural integrity would be important in a PTS accident scenario.

11.4.2 Imperfect Detection Scenario Results

In this scenario, we examine a set of 16 POD curves, whose lower POD parameter (β_1) has been set at 5%, 10%, 30%, and 50%, while the upper POD parameter (β_2) has been set at 50%, 70%, 90%, and 95%. The inflation in RMSE from the base case (i.e., RMSE (Imperfect Detection)/RMSE (Base Case)) is shown in Table 11.3.

[1] For example, RMSE might be proportional to $\lambda_5(s)$.

Table 11.3 RMSE (imperfect detection)/RMSE (base case)

POD(s)		Flaw distribution function $\lambda(s)$					
β_1	β_2	$\lambda_1(s)$	$\lambda_2(s)$	$\lambda_3(s)$	$\lambda_4(s)$	$\lambda_5(s)$	$\lambda_6(s)$
5%	50%	248	344	190	165	522	173
5%	70%	213	309	158	*134	517	*142
5%	90%	189	284	*137	*114	513	*121
5%	95%	184	279	*132	*110	512	*117
10%	50%	228	289	184	164	372	170
10%	70%	198	264	*154	*134	369	*140
10%	90%	177	246	*133	*113	366	*119
10%	95%	173	242	*129	*109	366	*115
30%	50%	183	198	168	160	211	163
30%	70%	163	187	*142	*131	210	*134
30%	90%	*148	178	*124	*111	209	*115
30%	95%	*145	176	*120	*107	209	*111
50%	50%	158	158	158	158	158	158
50%	70%	*143	*151	*134	*129	158	*131
50%	90%	*131	*145	*117	*110	*157	*112
50%	95%	*128	*144	*113	*106	*157	*108

Overall, proportions vary from a low of 106% to a high of 522%. The RMSE ratios in the above table that are close to or less than the 150% threshold are marked with an asterisk. It is useful to point out that even for a bad case like $\beta_1 = 30\%$ and $\beta_2 = 50\%$, the RMSE inflation of 211% for λ_5 indicates that it is still a useful inspection; one could very well argue an inspection with POD as low as 50% for large flaws would still yield useful results.

It can be seen that distributions $\lambda_5(s)$ and $\lambda_2(s)$ present the most difficult estimation tasks for inspection: for these distributions, the POD curve has to be at 50% for small flaws and at 90% for large flaws. If we ignore these two difficult distributions for a moment, one can see that a POD curve with $\beta = (30\%, 90\%)$ meets the RMSE criteria.

We will select POD thresholds of $\beta = (30\%, 90\%)$, although this does not meet the 150% target for the two most difficult distributions. In other words, POD is acceptable if it is above 30% for flaws in the 3-8 mm range, and above 90% for flaws larger than 12 mm.

11.4.3 Imperfectly Calibrated POD Scenario Results

In this scenario, we examine how much RMSE is inflated because the POD curve is imperfectly known. The case chosen for comparison is not the perfect inspection scenario, but the case chosen in the last section ($\beta = (30\%, 90\%)$). The uncertainty in the POD curve is represented with a sample number, N, which describes the number of calibration measurements that need to be taken to obtain the stated RMSE. The results are shown in Table 11.4.

All the values in Table 11.4 are below the target value of 150%, indicating a calibration experiment with as little as 10 measurements would be acceptable. These results indicate that the typical performance demonstration test, with from 10-30 flaws, is acceptable.

Table 11.4 RMSE (imperfectly calibrated POD)/RMSE (imperfect detection)

σ(POD)	Flaw distribution function $\lambda(s)$					
N	$\lambda_1(s)$	$\lambda_2(s)$	$\lambda_3(s)$	$\lambda_4(s)$	$\lambda_5(s)$	$\lambda_6(s)$
10	111	111	116	144	138	104
20	106	106	108	124	121	102
30	104	104	106	116	114	101

11.4.4 Imperfect Sizing Scenario Results

In this scenario, sizing errors of 0.5, 1, 2, and 3 mm were examined. Table 11.5 presents the relative RMSEs.

Three distributions listed in the table seem to be relatively sensitive to sizing error ($\lambda_1(s)$, $\lambda_2(s)$, and $\lambda_5(s)$); while the other three are more insensitive to sizing error. For the three insensitive distributions, one could tolerate a 3-mm sizing error; for the sensitive distributions, a sizing error less than half a mm is required.

Figure 11.4 shows how sizing error smears the flaw distributions. The plot is for a sizing error of 1 mm. In this case, there are large differences between the different distributions. The sizing error can distort a distribution with a sharp peak, but will not cause problems in a more diffuse distribution.

Table 11.5 RMSE (imperfect sizing)/RMSE (base case)

	Flaw distribution function $\lambda(s)$					
σ_s	$\lambda_1(s)$	$\lambda_2(s)$	$\lambda_3(s)$	$\lambda_4(s)$	$\lambda_5(s)$	$\lambda_6(s)$
0.5mm	111	160	101	100	453	100
1mm	184	507	106	100	3,165	101
2mm	766	4,475	134	101	20,128	104
3mm	2,071	17,777	179	103	46,517	110

11.4.5 Imperfectly Calibrated Sizing Scenario Results

In this scenario, we assess how much RMSE is inflated due to the uncertainty in the sizing error standard deviation σ_s, by comparing the RMSE with that of the imperfect sizing (with σ_s perfectly known) case. The sizing error standard deviation σ_s has to be estimated in a calibration experiment by $\hat{\sigma}_s$ with ν degrees of freedom. We examine how large a value of ν is required for the inflation of RMSE to be within the target value of 150%. The RMSE is calculated for six situations, using a $\hat{\sigma}_s$ of 0.5 mm or 1 mm, and using a ν of 5, 10, and 15.

From Table 11.6, it can be seen that for the three flaw distributions insensitive to sizing errors (i.e., $\lambda_3(s)$,$\lambda_4(s)$, and $\lambda_6(s)$), the desired uncertainty is achieved with as little as 7 (i.e., 5 + 2) data points in the calibration experiment, with $\hat{\sigma}_s$ = 0.5 or 1 mm. However, in order for all the flaw distribution functions considered to achieve the desired accuracy, at least 17 data points are required in the calibration experiment, with $\hat{\sigma}_s$ = 0.5 mm.

Table 11.6 RMSE (imperfect calibrated sizing)/RMSE (imperfect sizing)

		Flaw distribution function $\lambda(s)$					
$\hat{\sigma}_s$	ν	$\lambda_1(s)$	$\lambda_2(s)$	$\lambda_3(s)$	$\lambda_4(s)$	$\lambda_5(s)$	$\lambda_6(s)$
0.5mm	5	138	426	101	100	557	100
0.5mm	10	106	130	100	100	201	100
0.5mm	15	103	113	100	100	151	100
1mm	5	242	622	106	100	326	101
1mm	10	144	240	102	100	188	100
1mm	15	122	161	101	100	150	100

11.5 Recommended Requirements for ISI

From the scenarios presented in previous sections, it is clear that the detection and sizing properties must be known, if some estimate for the flaws not-found is to be made. Since an estimate for the unfound flaws is important in a pressure vessel safety analysis, one can argue that a fundamental requirement is: for the inspection procedure to be considered acceptable, the probability of detection curve (POD(s)) and sizing error (σ_s) should be known.

This means that estimates (with a known uncertainty) can be supplied for these two quantities. Ideally, the estimates should be empirically determined through a performance demonstration, but it may also be acceptable to use generic estimates, if the inspection procedure is particularly well behaved.

It is important to note that one needs to know detection and sizing information for all sizes of flaws; a test that estimates detection and sizing for one particular size is not necessarily adequate. On the other hand, it is always possible to identify a smallest flaw size of interest; flaws smaller than this size are of no importance and we need not worry about the ability of ISI to find these flaws. The scenarios evaluated in the previous sections allow requirements about the four components of inspection to be generated. These are:

POD Curve: POD should be above 30% for flaws in the 3-8 mm range and above 90% for flaws larger than 12 mm.

POD Uncertainty: A POD curve determined from approximately 20 well-placed measurements will exhibit acceptable uncertainty.

Sizing Error: A sizing error standard deviation of 0.5 mm is required.

Sizing Error Uncertainty: A sizing error standard deviation determined from approximately 20 data points in a calibration experiment will produce an acceptable uncertainty.

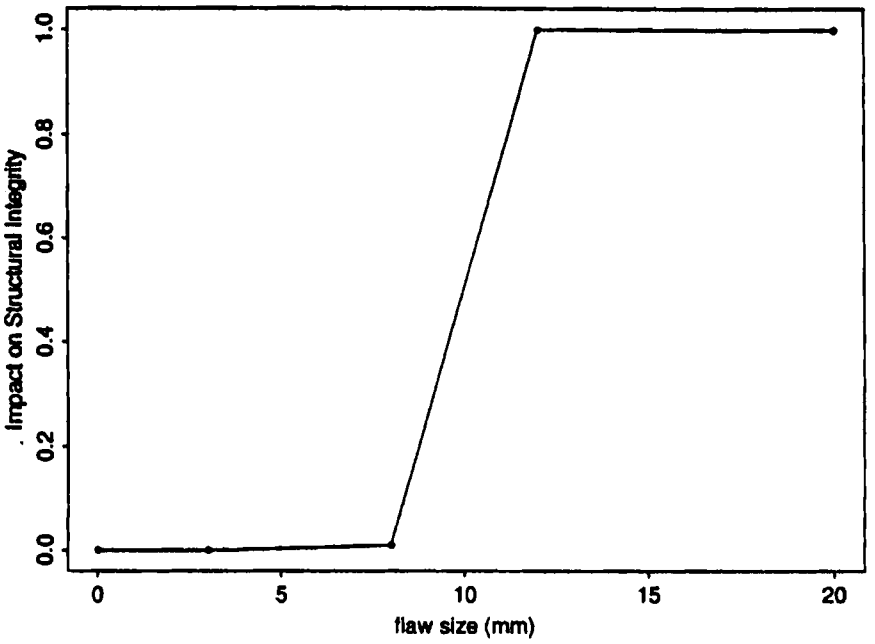

Figure 11.1 Impact of pressure vessel flaws on structural integrity

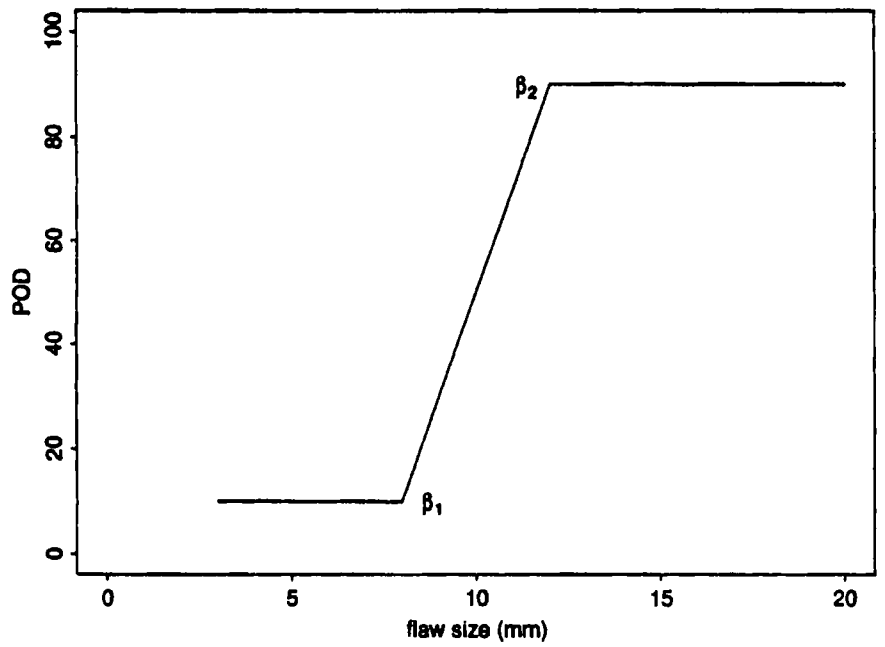

Figure 11.2 Imperfectly calibrated POD scenario

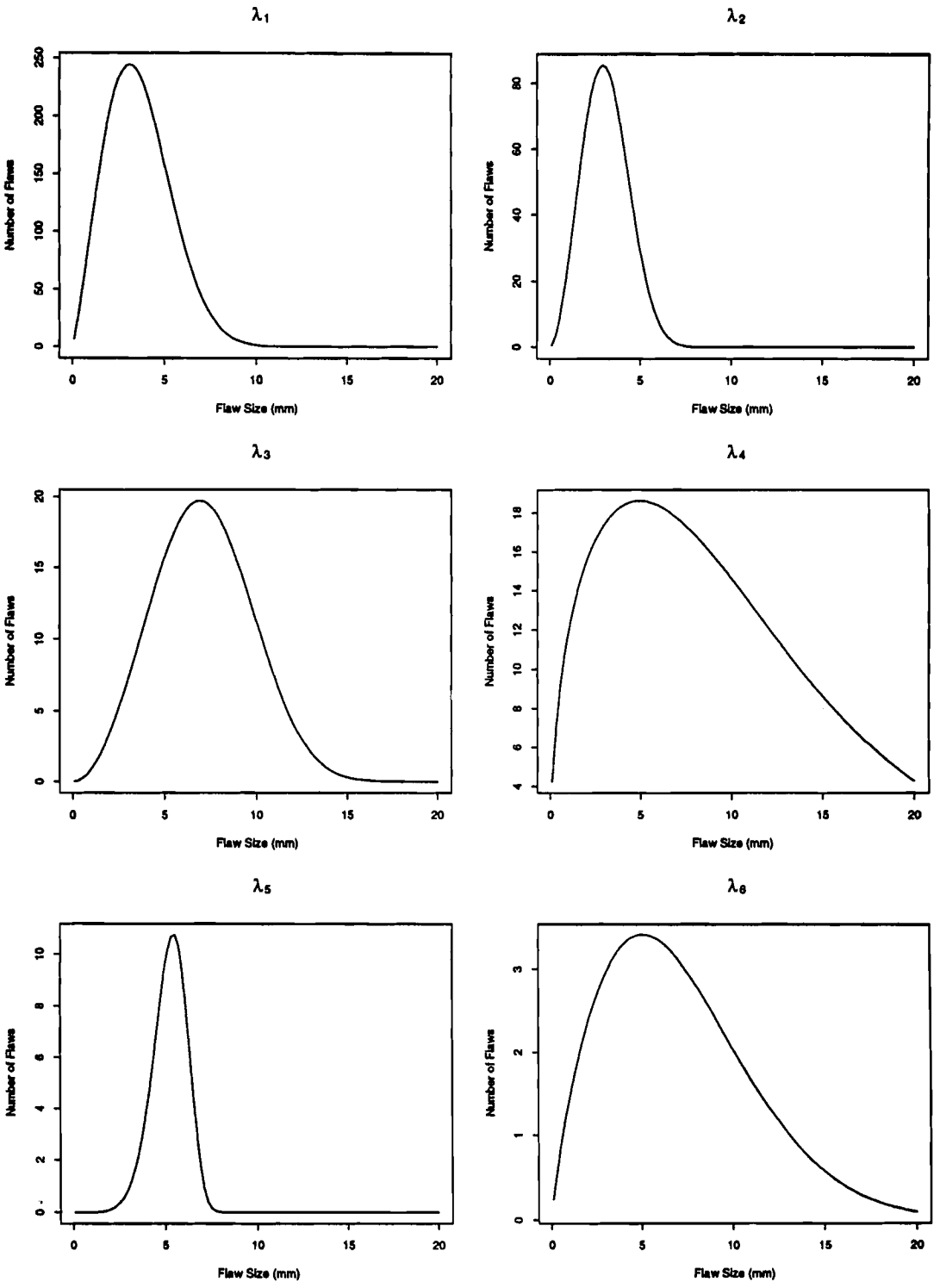

Figure 11.3 Flaw distribution functions λ_1, λ_2, λ_3, λ_4, λ_5, and λ_6 from PVRUF

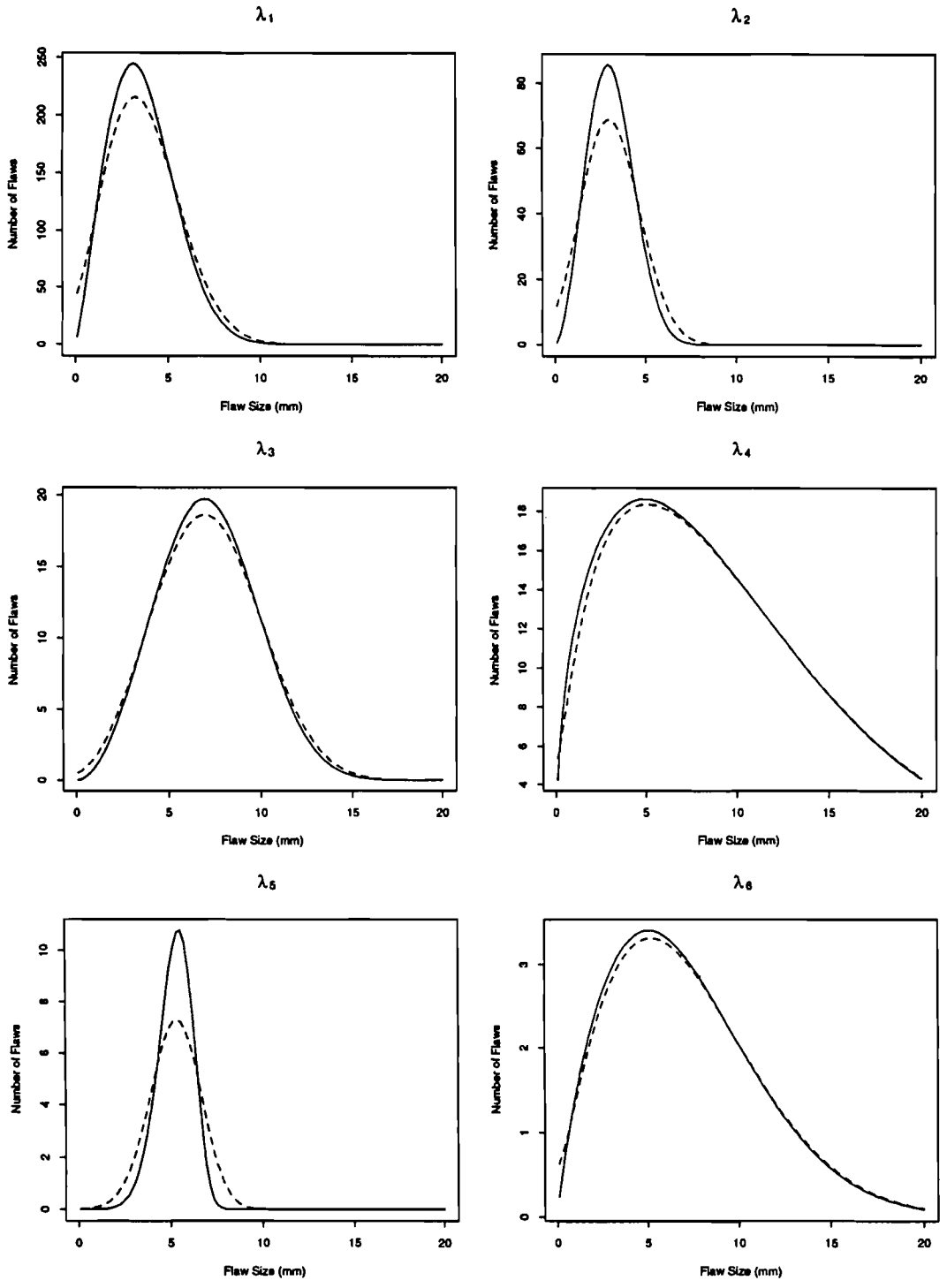

Figure 11.4 Flaw distribution functions: solid curves represent true functions, dashed curves represent found functions for λ_1, λ_2, λ_3, λ_4, λ_5, and λ_6. $\sigma s = 1$ mm is used

12 Conclusions

The SAFT-UT inspection of the PVRUF vessel recorded a large number of flaw indications and PNNL staff carefully analyzed the entire data set for flaws of interest in fracture mechanics calculations. The principal conclusions obtained in this project are as follows:

1) The data set provided enough information for the estimation of six different flaw rate functions that contain significant information on the size, location, type, and density of fabrication flaws in reactor pressure vessels.

2) The density of flaws in the PVRUF vessel is significantly greater than predicted by a Marshall distribution.

3) The performance of SAFT-UT was consistent with our expectations and the system produced a high quality data set.

There were 2500 detectable indications in the SAFT-UT inspections of the PVRUF vessel, using consistently applied detection rules. At the start of the inspections, PNNL expected that 80% of the indications would be small, that is, on the order of 2 mm in through-wall size. This was based on experience gained from the inspections of the Midland vessel. The data presented in this report show that 97% of the indications were less than 2 mm in through-wall size in the near surface zone, that is, within 25 mm of the inner surface of the PVRUF vessel. For the portion of the vessel wall beyond 25 mm in depth, 80% were smaller than 4 mm in through-wall size. The rate of false detections in this analysis is expected to be low because the detection rules were developed from the high correlation of SAFT-UT indications with flaws, as validated by destructive tests of material removed from the Midland vessel. The SAFT-UT sizing rules were created to conservatively size indication zones to ensure that all potentially large flaws would be included in the validation plan.

The distribution of the empirical data, reported in Section 6, provided enough information to apply a parametric model of the cumulative flaw rate to six different subsets of the data with reasonable confidence bounds on the results. It was possible to extract distinct distributions for the weldment and the base metal in the near surface zone. The comparison of these two distributions shows significantly higher indication rates in the weldment compared with the base metal in the near surface zone. It was also possible to extract different distributions for the weldment, heat-affected zone, and base metal in the portion of the vessel wall beyond 25 mm from the inner surface. These distributions also show a significantly higher indication rate in the heat affected zone and weldment as compared to the base metal.

For the near surface zone, the weldment has a greater measured density of flaws than the base metal. The flaw density ratio of the near surface weldment and the near surface base metal can be extracted from the analysis presented in Section 8. For all planar flaws, the $\beta_o(s)$ values from Table 8.3 yield an indications ratio of 4 to 1 for the weldment compared to the base metal in the near surface zone. Table 8.5 shows that this ratio increases when only the larger flaws are considered: 5 to 1 for Λ(3mm) and 28 to 1 for Λ(6mm). This is a reasonable result, because planar flaws include cracks and lack of fusion in the weld, and the base metal is thought to contain mostly volumetric flaws with little through-wall extent. The validation of the SAFT-UT indications by metallographic analysis is expected to confirm the relative densities of the two distinct populations.

For the portion of the vessel outside the near surface zone, the flaw distribution functions for the weldment and the heat-affected zone show a greater estimated density of flaws compared to the base metal. Table 8.3 shows a ratio of 4 to 1 for the weldment compared to the base metal. Table 8.5 shows how this ratio changes when only the larger flaws are considered: 5 to 1 for Λ(3mm), 5 to 1 for Λ(6mm) and 1 to 1 for Λ (12mm). For all planar flaws, Table 8.3 shows a ratio of 8 to 1 for the heat affected zone compared to the base metal. Table 8.5 shows how this ratio changes when only the larger flaws are considered: 8 to 1 for Λ(3mm), 10 to 1 for Λ(6mm) and 20 to 1 for Λ(12mm). It can be concluded that the interface between the weldment and the base metal (i.e., the heat-affected zone) contains the greatest density of large planar flaws. Since it was expected that the mid-wall portion of the base metal contains a population of volumetric flaws with little through-wall extent, it is clear that a determination of the nature of the larger SAFT-UT indications in the outside the near surface portion of the

vessel can add significantly to our understanding of fabrication flaws in reactor pressure vessels.

This report contains in Tables 8.3 and 8.5 estimated flaw rate functions for six different subsets of the SAFT-UT indications, with confidence bounds. The densities of flaws predicted by the SAFT-UT inspections are significantly greater in all six cases than those predicted by a Marshall distribution of flaws.

Finally, the SAFT-UT system and the measurement plan for PVRUF worked very well. The 10 inspection modes produced complementary information on the size, type, location, and density of flaws that is important in fracture mechanics calculations. The added value of each modality was demonstrated in detection and characterization of the indications, as described in Sections 4 and 5.

The calibration and vessel scanning procedures were routinely and successfully applied during the 18 months of data collection at PVRUF. The image quality of the SAFT-UT inspections was very high because of the fine sample spacing specified in the measurement plan, and the careful execution of the calibration and scanning procedures.

13 Recommendations

Three recommendations are appropriate at the completion of this program. First, and most important, validate the flaw rate estimates derived from the SAFT-UT inspections. Second, develop a methodology to produce generalized flaw densities and distributions for the entire population of vessels or classes of vessels. Third, improve the SAFT-UT system to make it more efficient for use in the inspection of reactor pressure vessels.

The indication rates reported in Section 8 should be validated to verify the necessary high quality of flaw statistics for use in fracture mechanics calculations, such as for pressurized thermal shock (PTS) analysis. The inspection data provided enough indications to estimate the six different indication rates in the RPV, as reported in Section 8. Relatively few of the larger indications are determining factors in these distributions. An area of uncertainty in the empirical data, however, is the accuracy with which the larger indications have been sized. The destructive analysis of material removed from the Midland vessel provided detection and sizing confirmation for small flaws in the depth size range of 0.5 to 2.0 mm (0.02 to 0.08 in.). This program provides a data set of fully documented indications of real preservice fabrication flaws that cover a much wider size range. The flaw rates estimated from this data set should be the principal focus of the destructive validation discussed in Section 9 of this report.

To produce generalized flaw density and distribution functions for the entire population of vessels or classes of vessels, existing statistical models, such as the U.K. model (Chapman 1993) investigated under NRC JCN L2606, should be evaluated for their ability to predict vessel-specific flaw densities and distributions for use with and comparison to inservice inspection results from operating reactors. Future work, in NRC JCN W6275, will use the data from the SAFT-UT measurements of the PVRUF vessel to benchmark and calibrate Chapman's predictive model. A calibrated predictive model, such as the one developed by Chapman, should provide, when used with ISI data, a means of extrapolating the flaw rates from this project to the entire population of vessels in the U.S.

In future applications of SAFT-UT to the inspection of nuclear reactor components, effort should be directed toward reducing the time and cost of data acquisition, data processing, flaw detection, and flaw characterization. The speed of data acquisition could be significantly improved by designing and building an eight-channel data system for use on RPVs. The speed of data processing should be increased to keep up with the data acquisition rate. The speed of flaw detection should be improved using pattern matching and on-line analysis rules to provide a near real-time flaw detection and reporting capability. Some of the significant indications should be characterized using tandem SAFT-UT and other sizing methods.

14 References

ABB-CE Report CEN-622-A. 1996. "Generic Upper Shelf Values for Linde 1092, 124 and 0091 Weld.

Booth, D. L. 1989. "Material Documentation Report for the Weld Material Removed from the Consumers Power (Midland) Reactor Vessel (620-0012-51)." The Babcock and Wilcox Company, Nuclear Power Division, Lynchburg, Virginia.

Chapman, V. 1993. "Simulation of Defects in Weld Construction," *Pressure Vessel and Piping Conference,* Reliability and Risk in Pressure Vessels and Piping, PVP-Vol. 251, PP 81-89. American Society of Mechanical Engineers, New York.

Doctor, S. R., et al. 1991. "Progress in Evaluation and Improvement in Nondestructive Examination Reliability for Inservice Inspection of Light Water Reactors (LWRs) and Characterizing Fabrication Flaws in Reactor Pressure Vessels," *Proc. US NRC 19th Water Reactor Safety Information Meeting,* Vol. 1, NUREG/CP-0119. U.S. Nuclear Regulatory Commission, Washington, D.C.

Doctor, S. R., G. J. Schuster, L. D. Reid, T. E. Hall. 1995. Development and Validation of a Real-Time SAFT-UT System for the Inspection of Light Water Reactor Components, NUREG/CR-4583, PNL-5822.

Doctor, S. R., L. J. Angel, A. A. Diaz, R. V. Harris, Jr., F. A. Simonen, and G. J. Schuster. 1994. "Reliability of NDE - Cast Stainless Steel, SAFT-UT Performance, PISC III Program Status, and Evaluation of Computer-Based UT/ISI Systems," *Proc. of 21st Water Reactor Safety Information Meeting,* Vol. 1, NUREG/CP-0133. U.S. Nuclear Regulatory Commission, Washington, D.C.

Electric Power Research Institute. 1995. "BWR Vessel and Internals Project, BWR Reactor Pressure Vessel Shell Weld Inspection Recommendations (BWRVIP-05)." EPRI TR-105697.

Foulds, J. R. and E. L. Kennedy. 1993. *Midland Reactor Pressure Vessel Flaw Distribution,* SAND93-7064. Failure Analysis Associates, Inc., Menlo Park, California.

Hall, T. E., L. D. Reid, and S. R. Doctor. 1988. *The SAFT-UT Real-Time Inspection System - Operational Principles and Implementation,* NUREG/CR-5075. Prepared for the U.S. Nuclear Regulatory Commission, Washington, D.C.

Heasler, P. G., T. T. Taylor, and S. R. Doctor. 1993. *Statistically Based Reevaluation of PISC-II Round Robin Test Data,* NUREG/CR-5410. Pacific Northwest Laboratory, Richland, Washington.

Kennedy, E. L., J. R. Foulds, and S. L. Basin. 1991. Nuclear Reactor Pressure Vessel Flaw Distribution Development, Phase II - Methodology and Application, SAND91-7073.

K.H. Luk. 1993. *Pressurized-Water Reactor Internals Aging Degradation Study – A Phase 1 Report,* NUREG/CR-6048.

Marshall, W. 1982. "An Assessment of the Integrity of PWR Pressure Vessels, Summary Report," first report of a study group under the Chairmanship of Sir Walter Marshall, CBE FRS, UDAEA, London.

Nichols, R. W., and S. Crutzen. 1988. *Ultrasonic Inspection of Heavy Section Steel Components, The PISC-II Final Report,* Elsevier Applied Science, New York, New York.

Pennell, W. E., and C. E. Pugh. 1989. "Mission Survey for the Pressure Vessel Research Users' Facility (PVRUF), NUREG/CR-5350, Oak Ridge National Laboratory, Oak Ridge, Tennessee.

PISC III Report No. 26 - Action 2, Phase 1. *Evaluation of the Sizing Results of 12 Flaws of the Full Scale Vessel Installation.* 1993. EUR 15371 EN. Prepared for Programme for the Inspection of Steel Components. Commission of the European Communities, Brussels, Luxembourg.

Rosinski S. T., E. L. Kennedy, J. R. Foulds, and K. M. Kinsman. 1990. *PWR Vessel Flaw Distribution Development: An Overview of Feasibility.* American Society for Mechanical Engineers. PVP - Vol. 193.

Silk, M. G. 1991. "Flaw Size Distributions in Pressure Vessels and Flaw Detection Probabilities in NDT," British Jrn NDT, Vol. 33, No. 10.

Simonen, E. P., K. I. Johnson, and F. A. Simonen. 1985. *Vessel Integrity Simulation Analyses (VISA) Code Sensitivity Study,* NUREG/CR-4267, PNL-5469.

Simonen, F. A., K. I. Johnson, A. M. Liebetrau, D. W. Engel, and E. P. Simonen. 1986a. *VISA-II - A Computer Code for Predicting the Probability of Reactor Pressure Vessel Failure.* NUREG/CR-4486. Prepared for the Nuclear Regulatory Commission, Washington, D.C., Pacific Northwest Laboratory, Richland, Washington.

Simonen, F. A., M. R. Garnich, E. P. Simonen, S. H. Bian, K. K. Nomura, W. E. Anderson, L. T. Pedersen. 1986b. *Reactor Pressure Vessel Failure Probability Following Through-Wall Cracks Due to Pressurized Thermal Shock Events,* NUREG/CR-4483, PNL-5727.

Simonen, F.A. 1984. "The Impact of Nondestructive Examination Unreliability on Pressure Vessel Fracture Predictions", NUREG/CR-3743, PNL-5062.

Simonen, F. A., M. A. Khaleel. 1995. "A Model for Predicting Vessel Failure Probabilities Due to Fatigue Crack Growth", *Pressure Vessel and Piping Conference.* Fatigue and Fracture Mechanics, PVP-Vol. 304, PP 401-416. American Society of Mechanical Engineers, New York.

UKAEA. 1976. "An Assessment of the Integrity of PWR Vessels."

Ultrasonic Inspection of Heavy Section Steel Components, The PISC II Final Report, 1988. Ed. by R. W. Nichols and S. Crutzen. Elsevier Science Publishing Co., Inc., New York.

U.S. Nuclear Regulatory Commission. 1979. "Effects of Residual Elements on Predicted Radiation Damage to Reactor Vessel Materials". Regulatory Guide 1.99, Revision 1. US NRC, Washington, D.C.

U.S. Nuclear Regulatory Commission. 1988. "Radiation Embrittlement of Reactor Vessel Materials". Regulatory Guide 1.99, Revision 2. US NRC, Washington, D.C.

Vesely, W. E., E. K. Lynn, and F. F. Goldberg. 1978. "The OCTAVIA Computer Code: PWR Reactor Pressure Vessel Failure Probabilities Due to Operationally Caused Pressure Transients." NUREG-0258, U.S. Nuclear Regulatory Commission, Washington, D.C.

Appendix A

SAFT-UT Images of the Most Significant Flaws

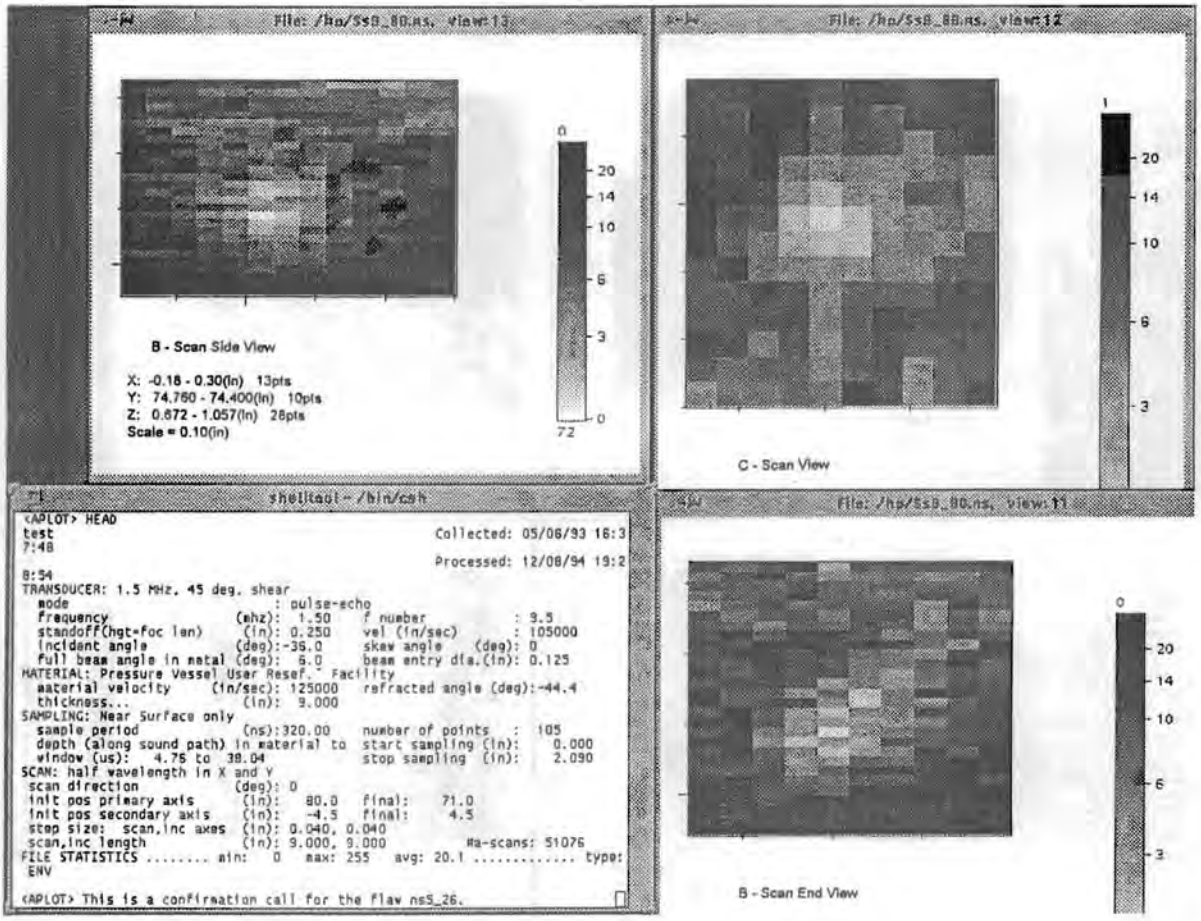

Figure A.10f Volumetric indication #1 in the near surface weldment: mode 9

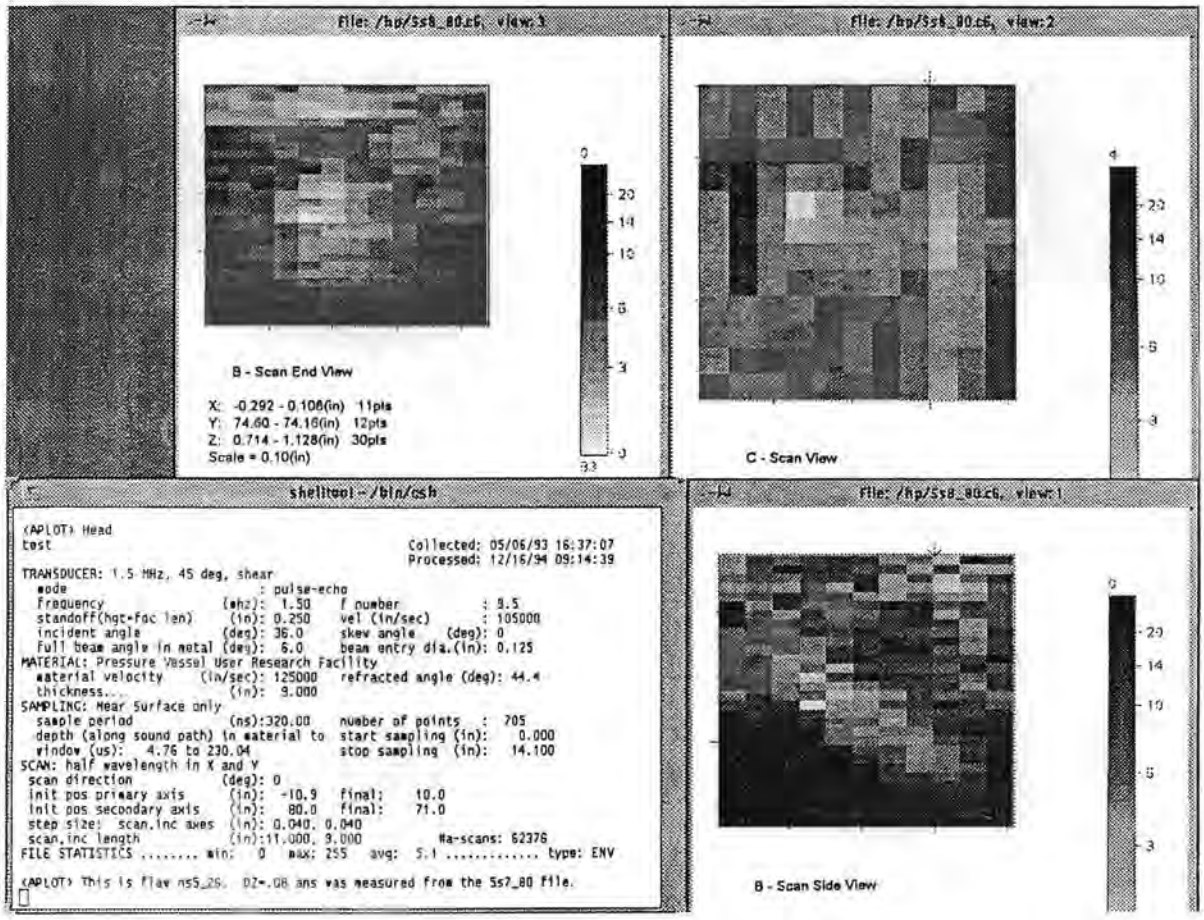

Figure A.10e Volumetric indication #1 in the near surface weldment: mode 8

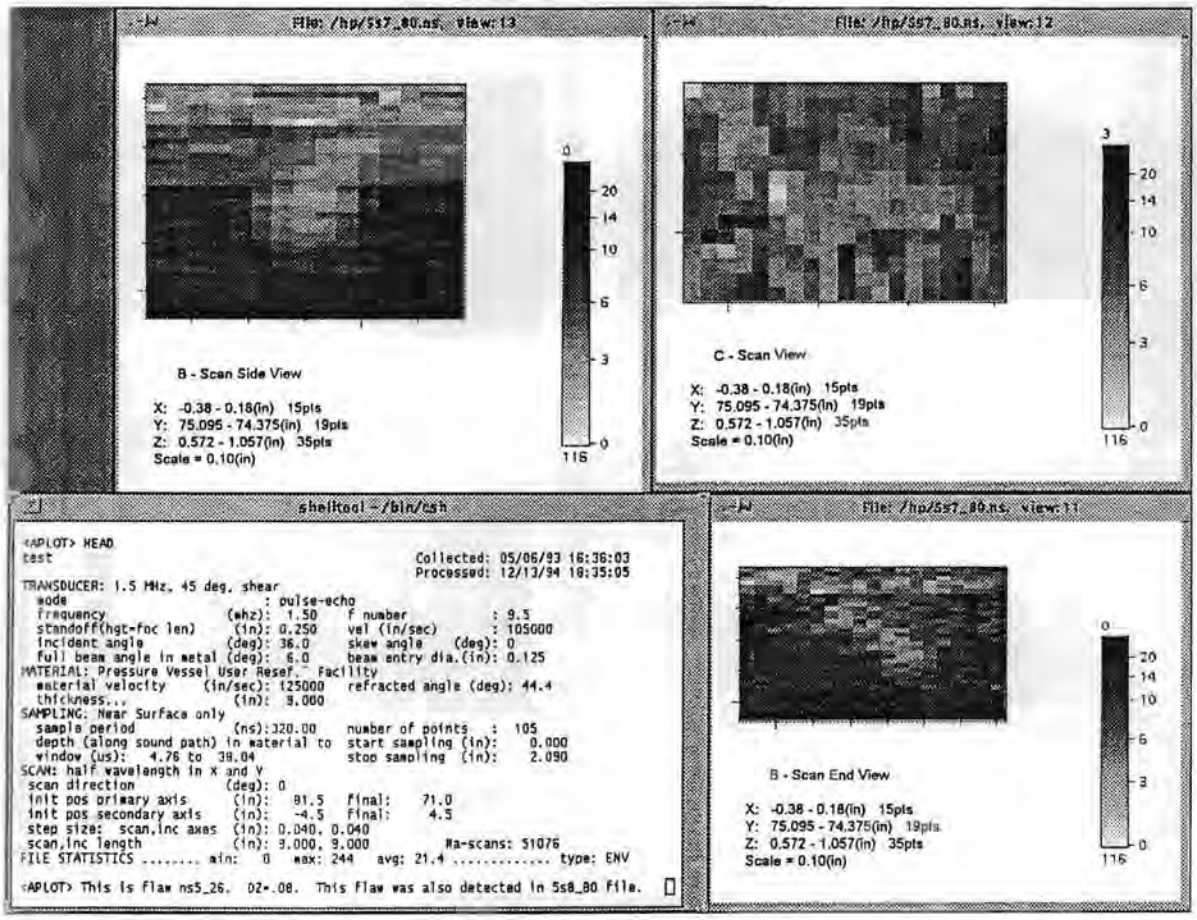

Figure A.10d Volumetric indication #1 in the near surface weldment: mode 7

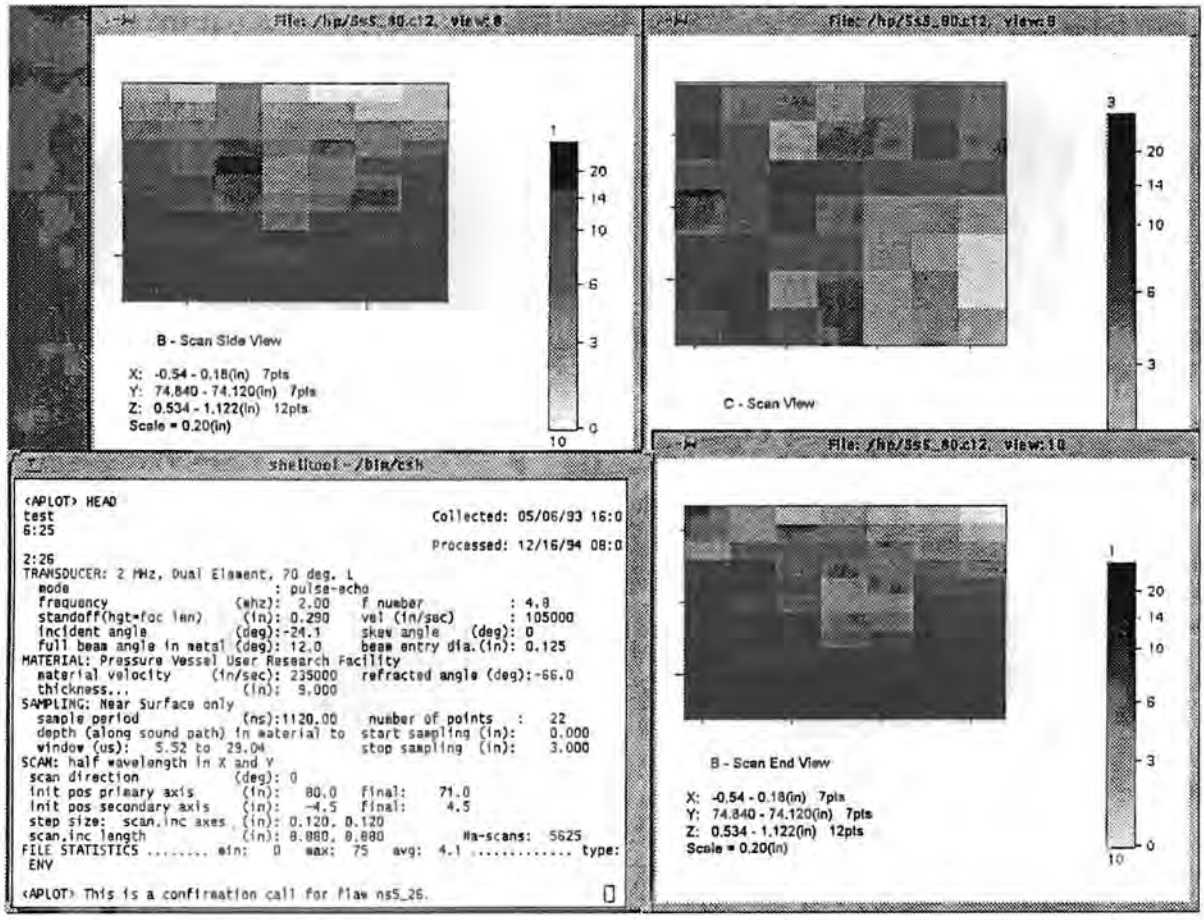

Figure A.10c Volumetric indication #1 in the near surface weldment: mode 5

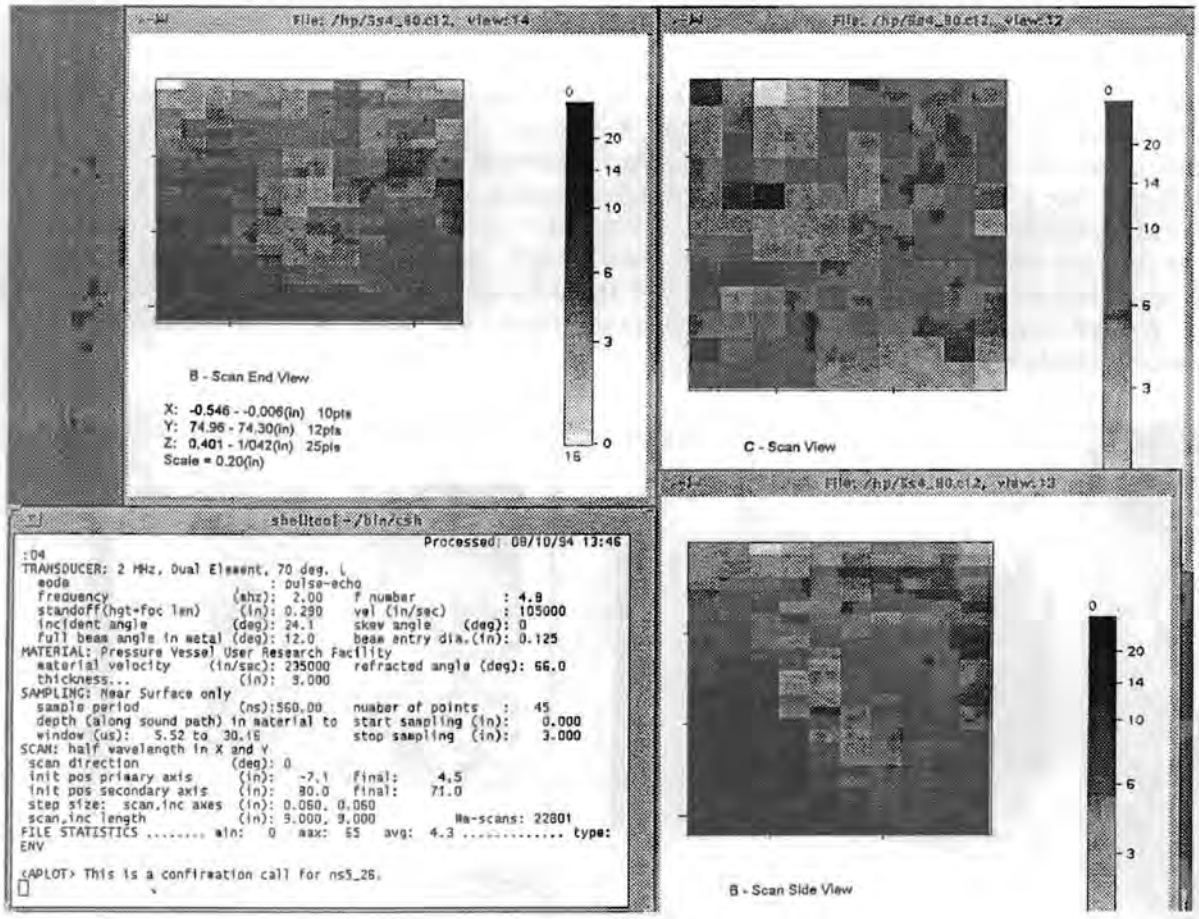

Figure A.10b Volumetric indication #1 in the near surface weldment: mode 4

Volumetric Indications in the Near Surface Weldment

Figures A.10a-f shows volumetric indication #1 in the near surface weldment. This volumetric indication has a through-wall extent of 6 mm based on different depth estimates of 18 to 24 mm. The detections were made in modes 7 and 8 where they had isolated TOF shape at depths of 20 to 24 mm. There were confirmations in modes 3, 4, 5, and 9 at depths of 18 to 23 mm. The wave packet width in modes 7 and 8 gives an alternate depth size of 2 mm. The indication is characterized as volumetric based on detection in orgothonal modes. There is no evidence of coin shape in the end views. The length is 10 mm and was made to LOS in mode 4. The width is 10 mm and was made to LOS in mode 5. The range of aspect ratios (length/depth) of this indication is 1.7 to 5. The maximum amplitude-to-noise ratio is of medium range at 97 to 30. With an X coordinate of -6 mm, the indication is clearly in the weld metal. With Z coordinates of 18 to 24 mm, the indication is clearly below the cladding.

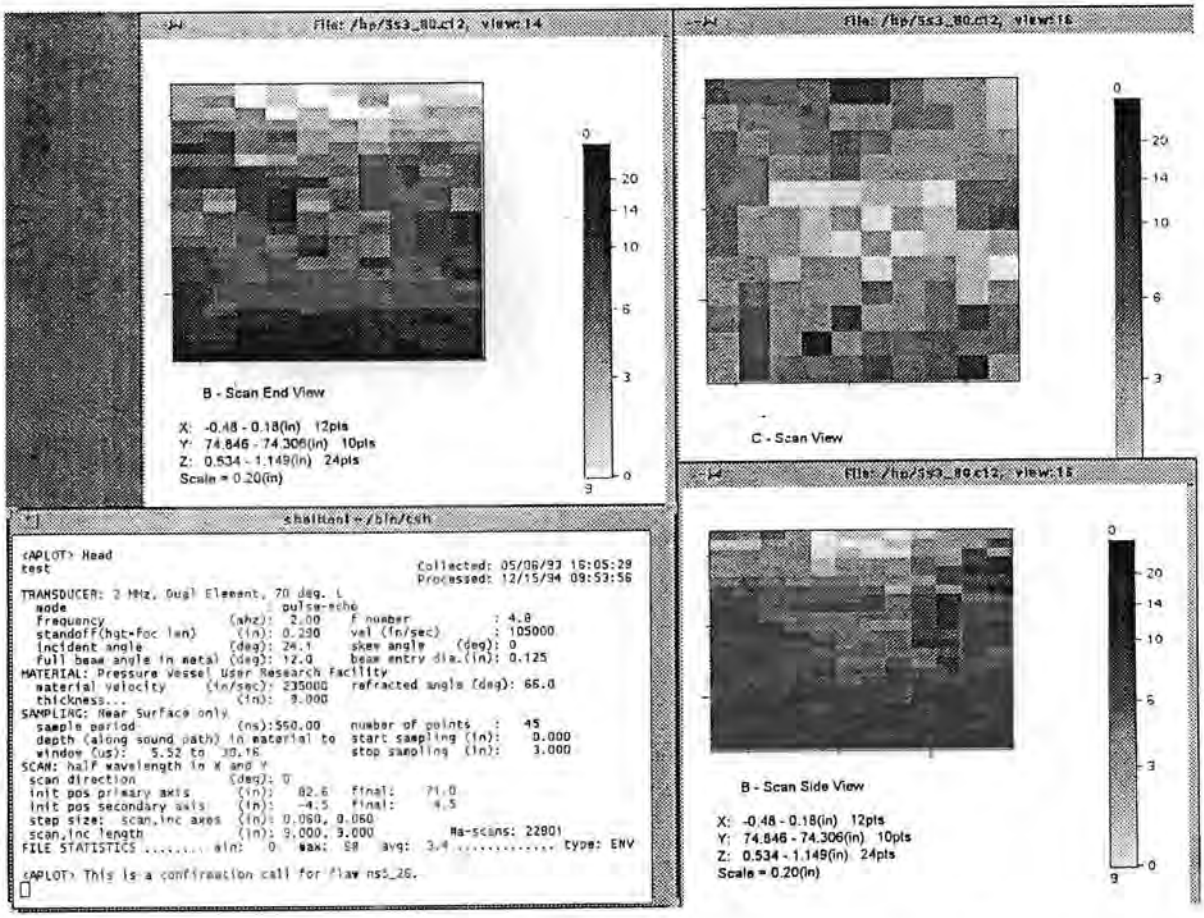

Figure A.10a Volumetric indication #1 in the near surface weldment: mode 3

Figure A.9 shows planar indication #9 in the near surface weldment. This planar indication has a through-wall extent of 2 mm based on wave packet width. The detection was made in mode 4 where it had isolated TOF shape at a depth of 24 mm. There were no confirmations in other modes. The indication is characterized as planar based on lack of normal beam detection. There is no evidence of coin shape in the end view of mode 4. The length is 11 mm and was made to LOS. The aspect ratio (length/depth) of this indication is 6 giving an orientation along the weld. The maximum amplitude-to-noise ratio is high at 16 to 3. With an X coordinate of 12 mm, the indication is in the weld metal, possibly in the HAZ. With a Z coordinate of 24 mm, the indication is clearly below the cladding.

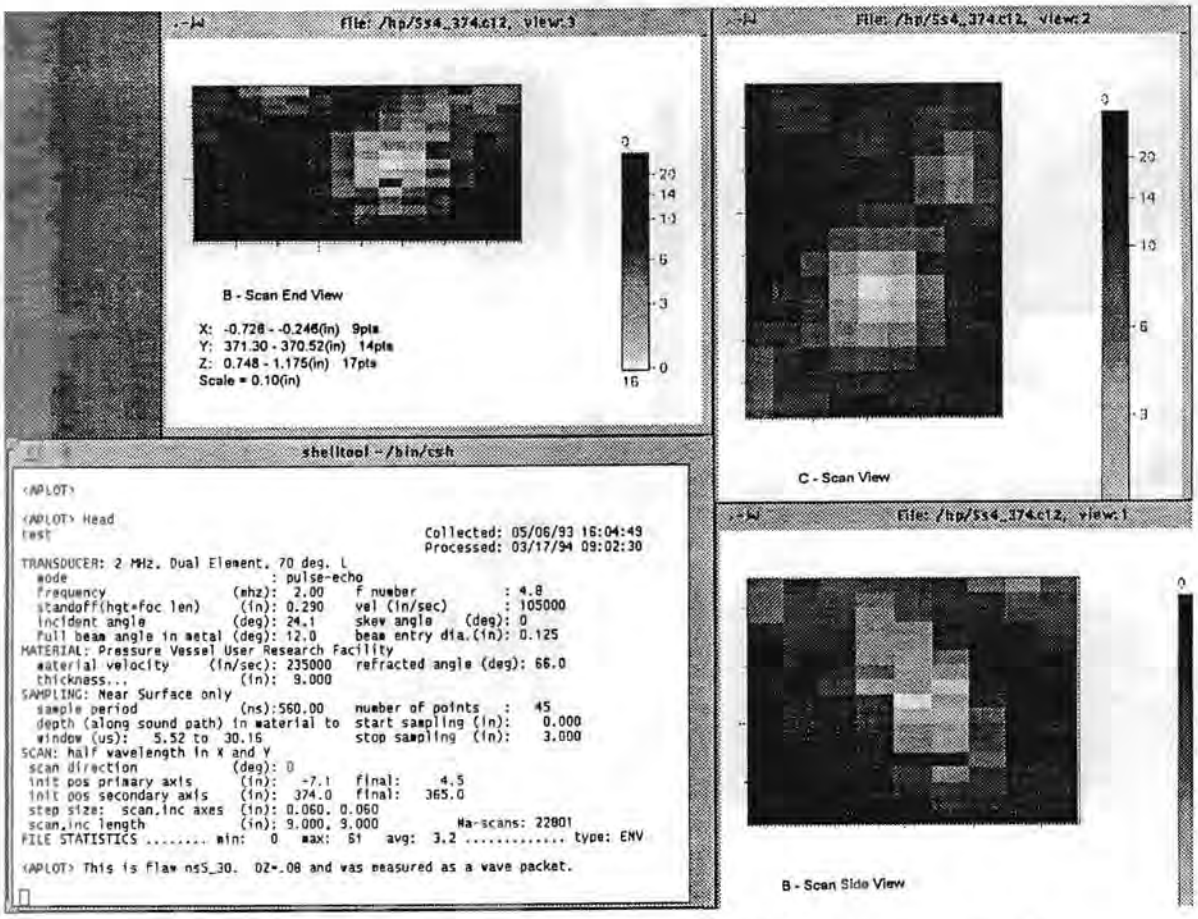

Figure A.9 Planar indication #9 in the near surface weldment: mode 4

Figure A.8 shows planar indication #8 in the near surface weldment. This planar indication has a through-wall extent of 2 mm based on wave packet width. The detection was made in mode 7 where it had isolated TOF shape at a depth of 23 mm. There were no confirmations in other modes. The indication is characterized as planar based on lack of normal beam detection. There is no evidence of coin shape in the side view of mode 7. The width is 10 mm and was made to LOS in mode 7. The aspect ratio (width/depth) of this indication is 5 giving an orientation across the weld. The maximum amplitude-to-noise ratio is of medium range at 69 to 28. With an X coordinate of 11 mm, the indication is in the weld, possibly in the HAZ. With a Z coordinate of 23 mm, the indication is clearly below the cladding.

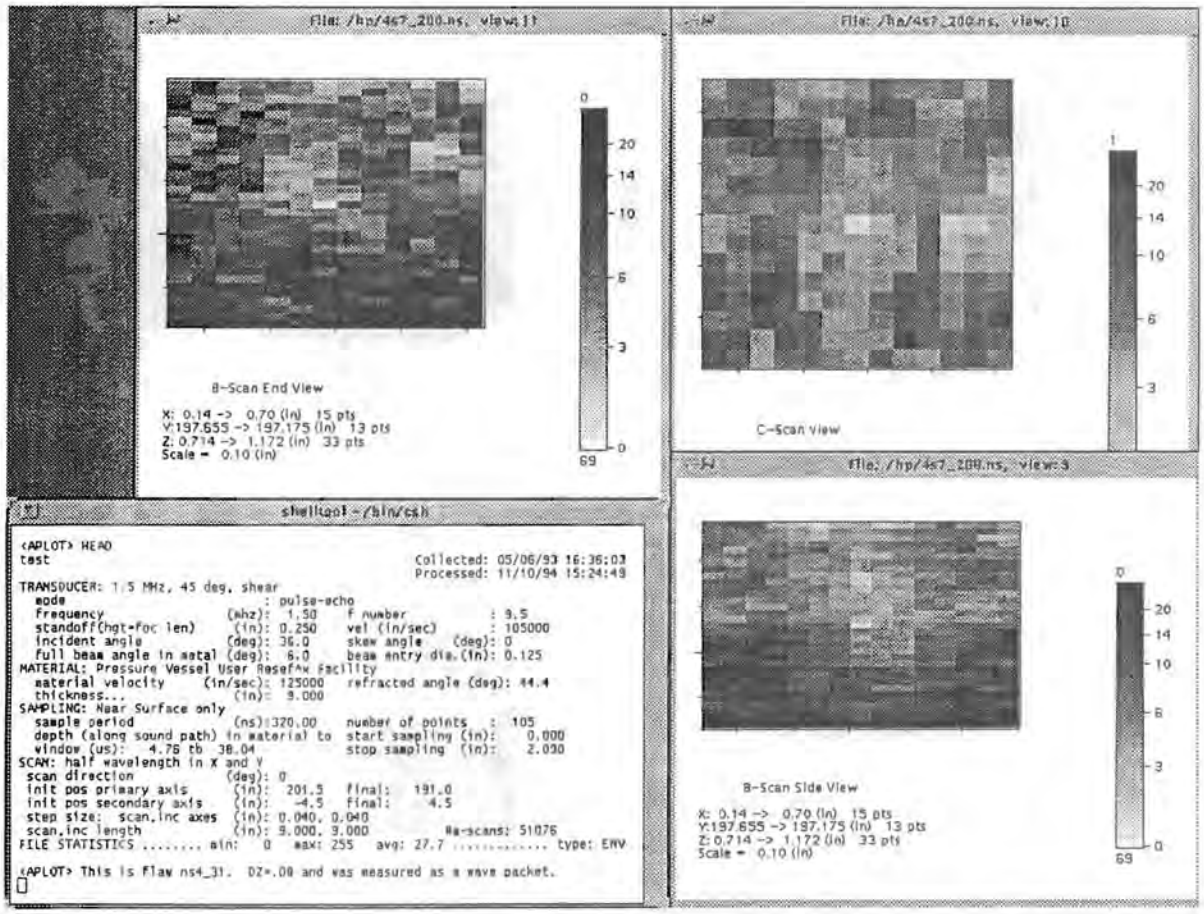

Figure A.8 Planar indication #8 in the near surface weldment: mode 7

Figure A.7 shows planar indication #7 in the near surface weldment. This planar indication has a through-wall extent of 2 mm based on wave packet width. The detection was made in mode 2 where it had isolated TOF shape at a depth of 15 mm. There were no confirmations in other modes. The indication is characterized as planar based on lack of normal beam detection. There is no evidence of coin shape in the end view of mode 2. The length is 11 mm and was made to LOS in mode 2. The aspect ratio (length/depth) of this indication is 5 giving an orientation along the weld. The maximum amplitude-to-noise ratio is high at 52 to 12. With an X coordinate of -6 mm, the indication is clearly in the weld metal. With a Z coordinate of 15 mm, the indication is clearly below the cladding.

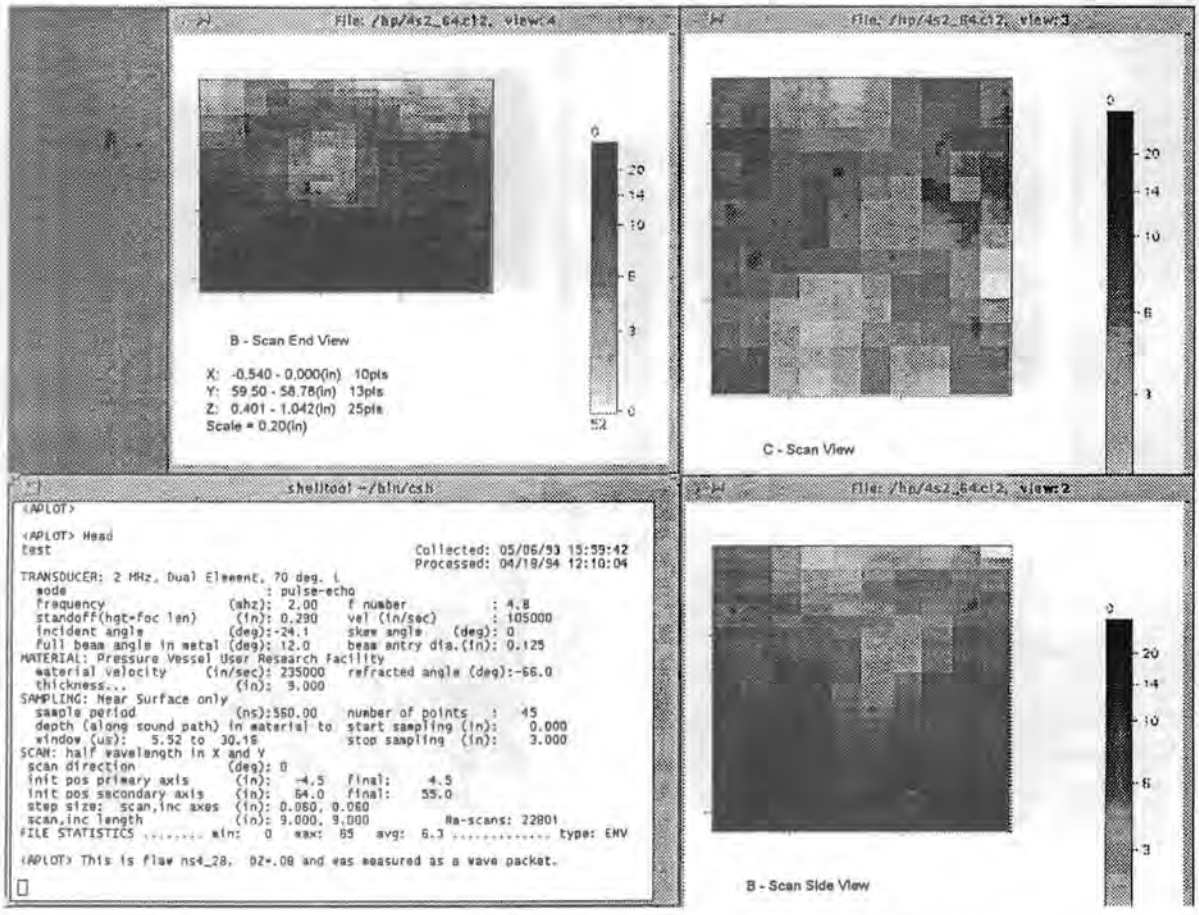

Figure A.7 Planar indication #7 in the near surface weldment: mode 2

Figure A.6 shows planar indication #6 in the near surface weldment. This planar indication has a through-wall extent of 2 mm based on wave packet width. The detection was made in mode 4 where it had isolated TOF shape at a depth of 16 mm. There were no confirmations in other modes. The indication is characterized as planar based on lack of normal beam detection. There is no evidence of coin shape in the end view of mode 4. The length is 9 mm and was made to LOS in mode 4. The aspect ratio (length/depth) of this indication is 4 giving an orientation along the weld. The maximum amplitude-to-noise ratio is of medium range at 18 to 6. With an X coordinate of -3 mm, the indication is clearly in the weld metal. With a Z coordinate of 16 mm, the indication is clearly below the cladding.

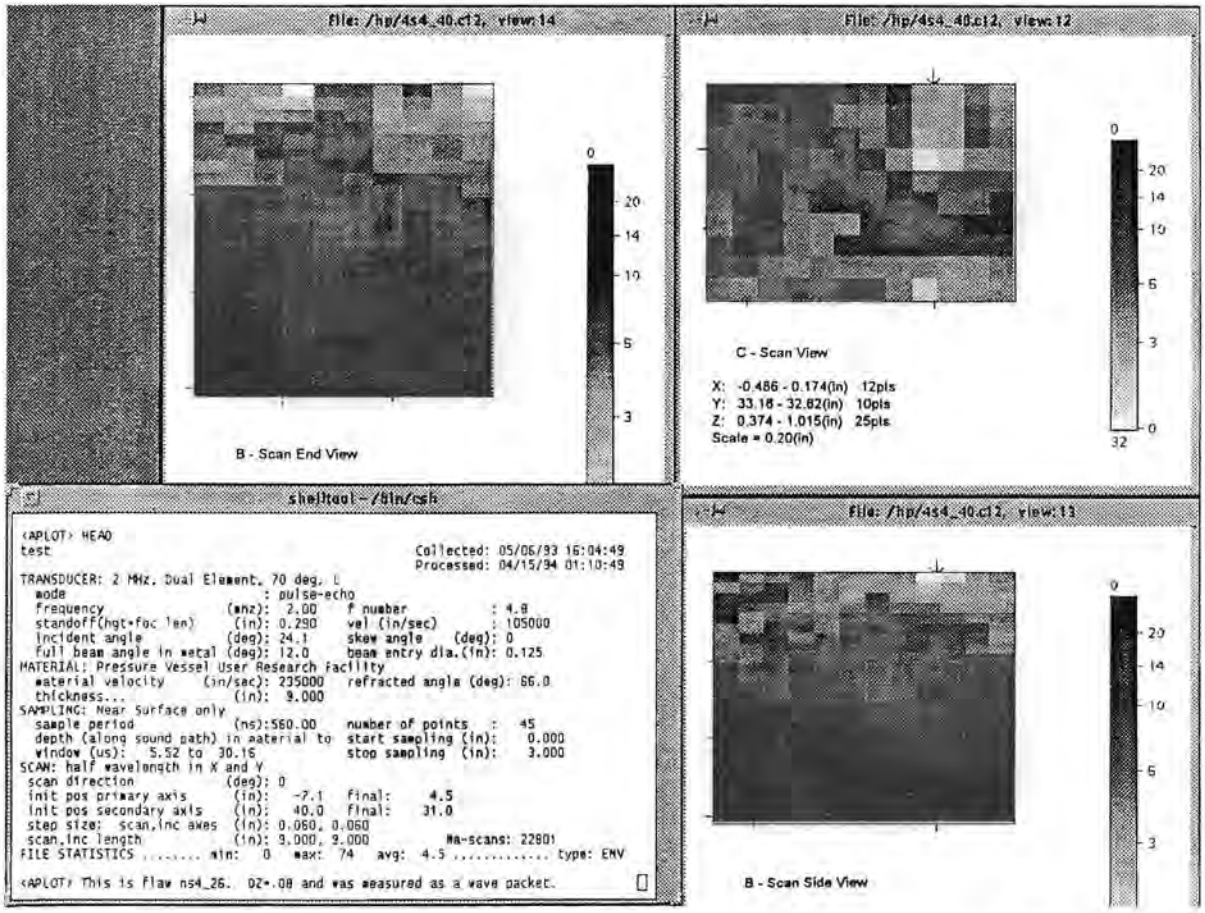

Figure A.6 Planar indication #6 in the near surface weldment: mode 4

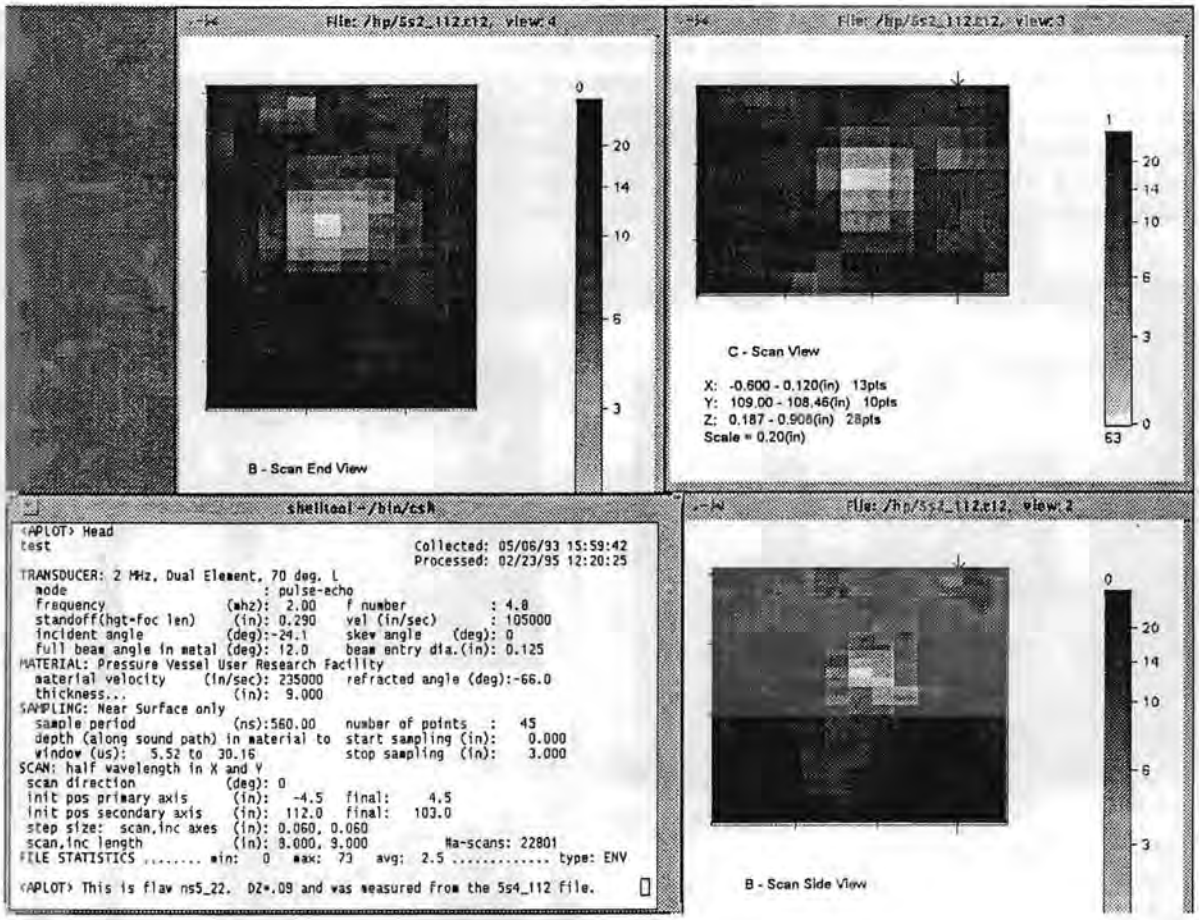

Figure A.5b Planar indication #5 in the near surface weldment: mode 2

Figures A.5a-b show planar indication #5 in the near surface weldment. This planar indication has a through-wall extent of 2.3 mm based on wave packet width. Detections were made in modes 2 and 4 where the indication had isolated TOF shapes at depths of 11 and 12 mm. The indication is characterized as planar based on lack of normal beam detection. There is some evidence of coin shape in the end view of mode 2. The length is 10 mm and was made to LOS in mode 2. The aspect ratio (length/depth) of this indication is 4 giving an orientation along the weld. The maximum amplitude-to-noise ratio is high at 63 to 12. With X coordinates of -6 and -14 mm, the indication is in the weld, possibly in the HAZ. With Z coordinates of 11 and 12 mm, the indication is clearly below the cladding.

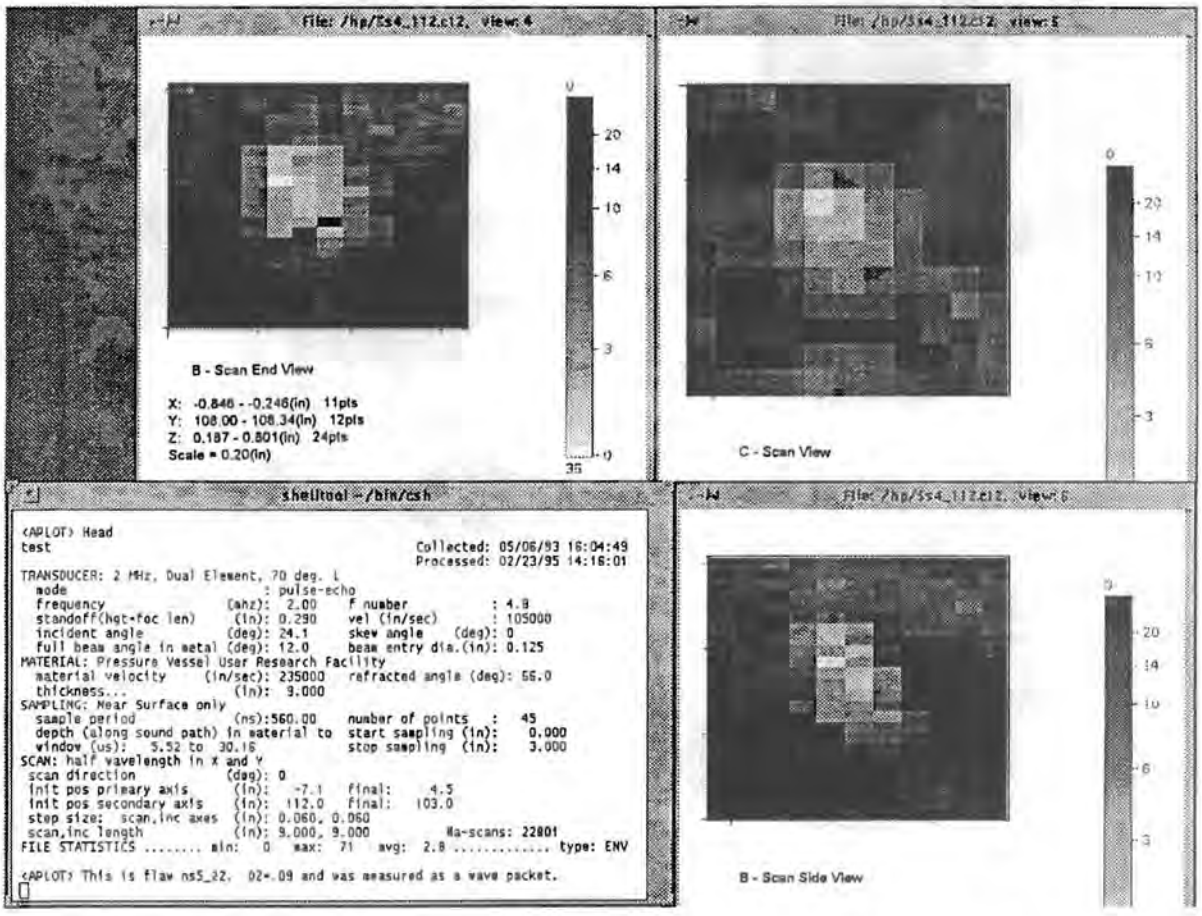

Figure A.5a Planar indication #5 in the near surface weldment: mode 4

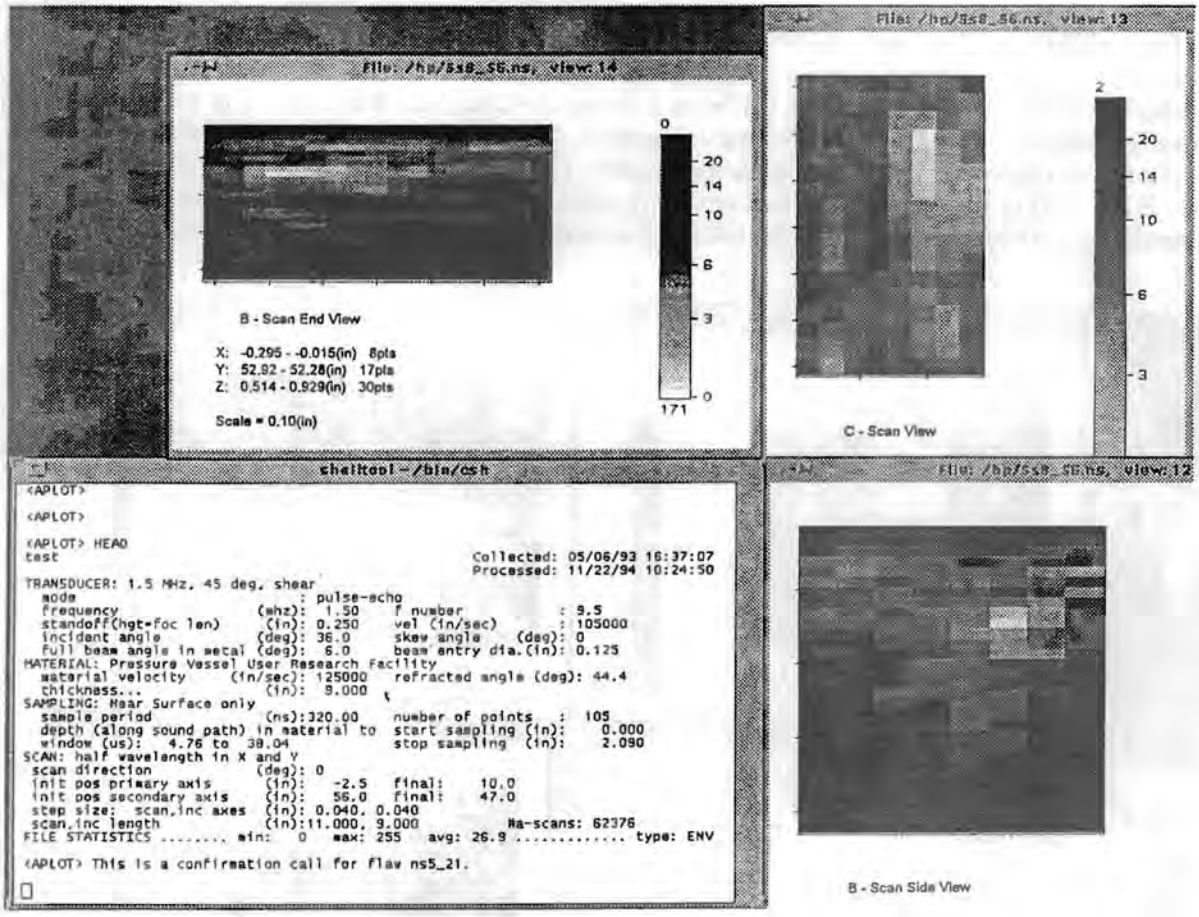

Figure A.4b Planar indication #4 in the near surface weldment: mode 8

Figures A.4a-b show planar indication #4 in the near surface weldment. This planar indication has a through-wall extent of 3 mm based on different depth estimates of 16 to 19 mm. The detection was made in mode 4 where it had isolated TOF shape at a depth of 16 mm. There was a confirmation in mode 8 at a depth of 19 mm. The wave packet width in mode 4 gives an alternate depth size of 2.3 mm. The indication is characterized as planar based on lack of normal beam detection. There is some evidence of coin shape in the end view of mode 4. The length is 14 mm and was made to LOS in mode 8. The aspect ratio (length/depth) of this indication is 5 giving an orientation along the weld. The maximum amplitude-to-noise ratio is low at 25 to 12. The X coordinates of -4 to -8 mm show that the indication is 2 to 4 mm from the HAZ. The Z coordinates of 16 to 19 mm show that the indication is clearly below the cladding.

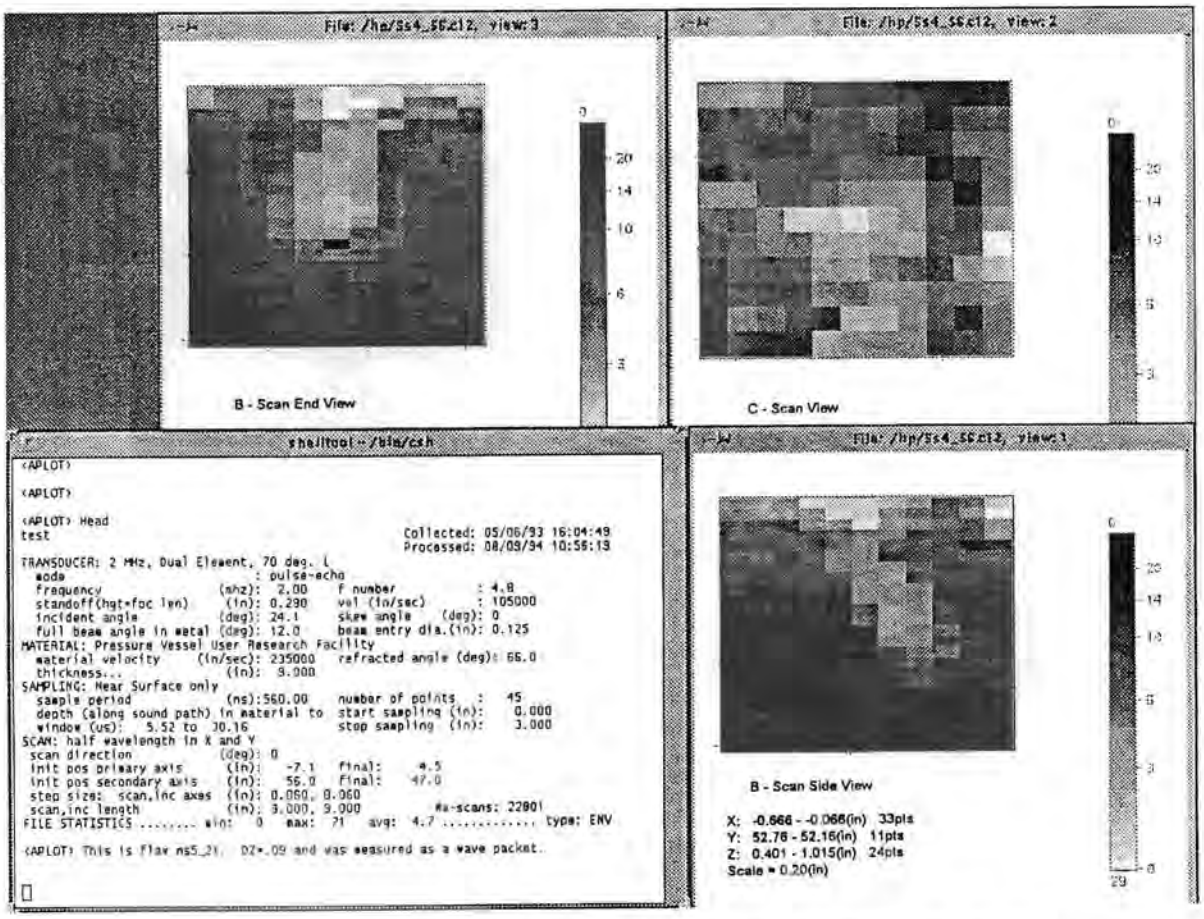

Figure A.4a Planar indication #4 in the near surface weldment: mode 4

Figure A.3 shows planar indication #3 in the near surface weldment. This planar indication has a through-wall extent of 3 mm based on wave packet width. The detection was made in mode 4 where it had isolated TOF shape at a depth of 21 mm. There was no confirmation in other modes and the indication is characterized as planar based on lack of normal beam detection. There is no evidence of coin shape in the end view. The length is 10 mm and was made to LOS in mode 4. The aspect ratio (length/depth) of this indication is 3 implying that it is probably oriented along the weld. The maximum amplitude-to-noise ratio is low at 13 to 6. With an X coordinate of -8 mm, the indication is 2 mm from the HAZ. With a Z coordinate of 21 mm, the indication is clearly below the cladding.

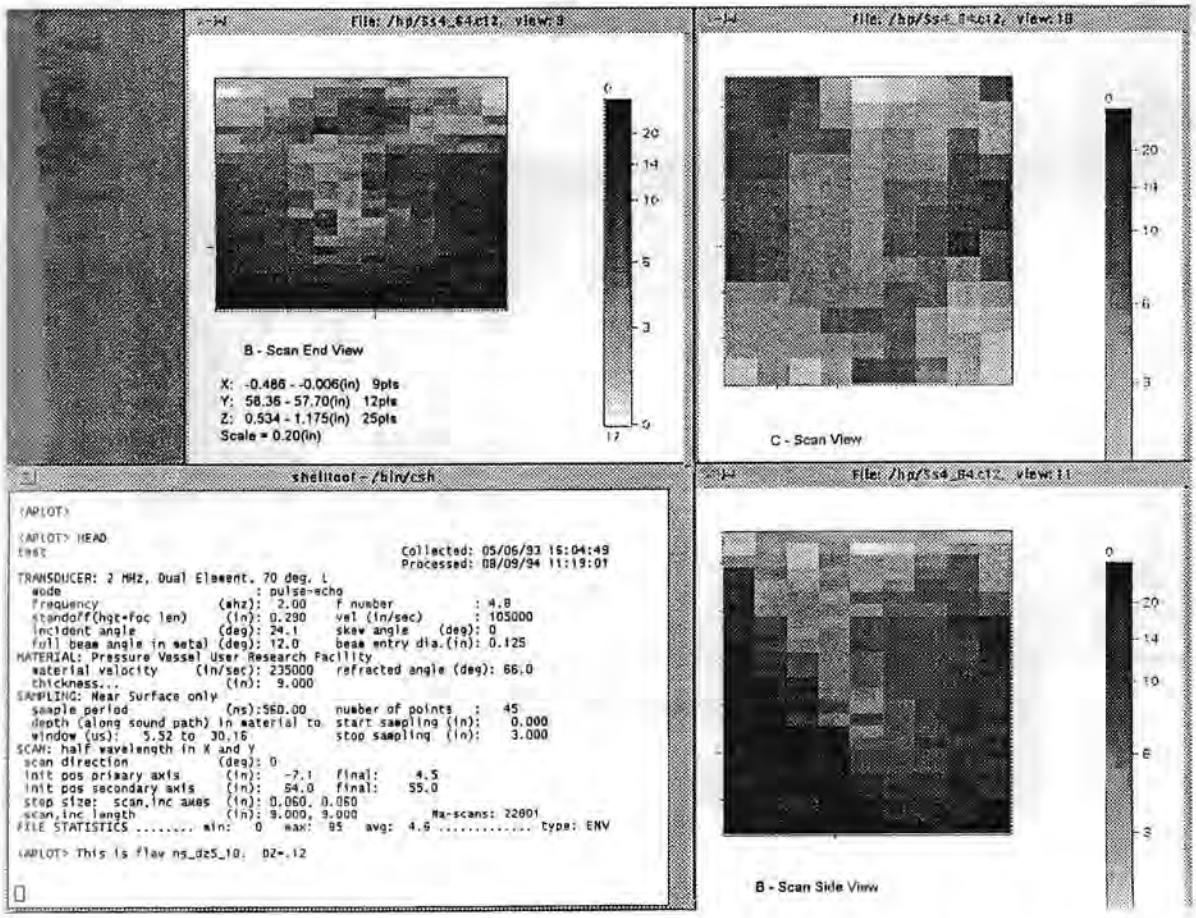

Figure A.3 Planar Indication #3 in the near surface weldment: mode 4

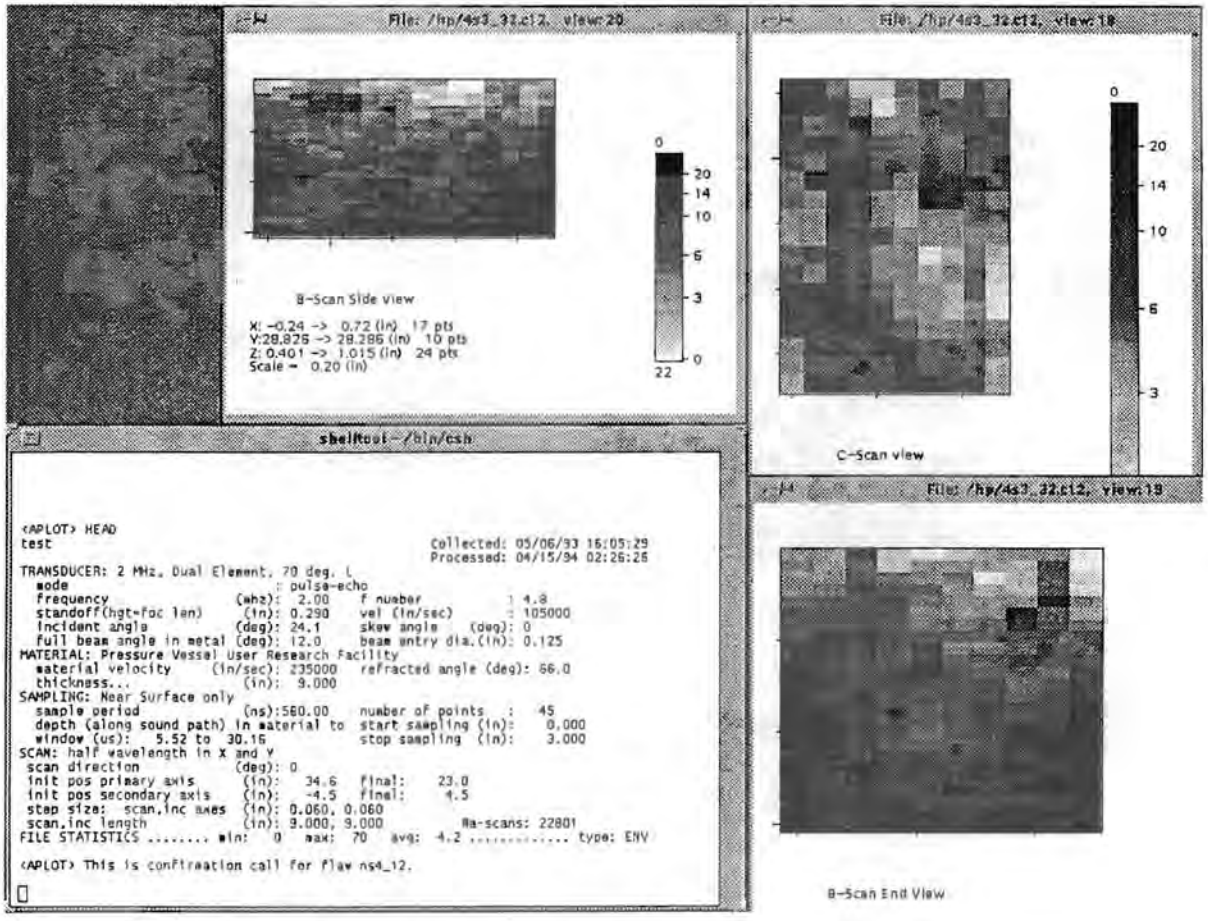

Figure A.2b Planar indication #2 in the near surface weldment: mode 3

Figures A.2a-b show planar indication #2 in the near surface weldment. This planar indication has a through-wall extent of 6 mm based on different depth estimates of 12 to 18 mm. The detection was made in mode 5 where it had isolated TOF shape at a depth of 18 mm. There was a confirmation in mode 3 at a depth of 12 mm. The wave packet width in mode 5 gives an alternate size of 2.5 mm. The indication is characterized as planar based on lack of normal beam detection. There is no evidence of coin shape in the side view of modes 3 or 5. The width is 7 mm and was made to LOS in mode 5. The range of aspect ratios (width/depth) of this indication is 1 to 3. The maximum amplitude-to-noise ratio is high at 75 to 15. With an X coordinate of 8 mm, the indication is 2 mm from the HAZ. With Z coordinates of 12-18 mm, the indication is clearly below the claddding.

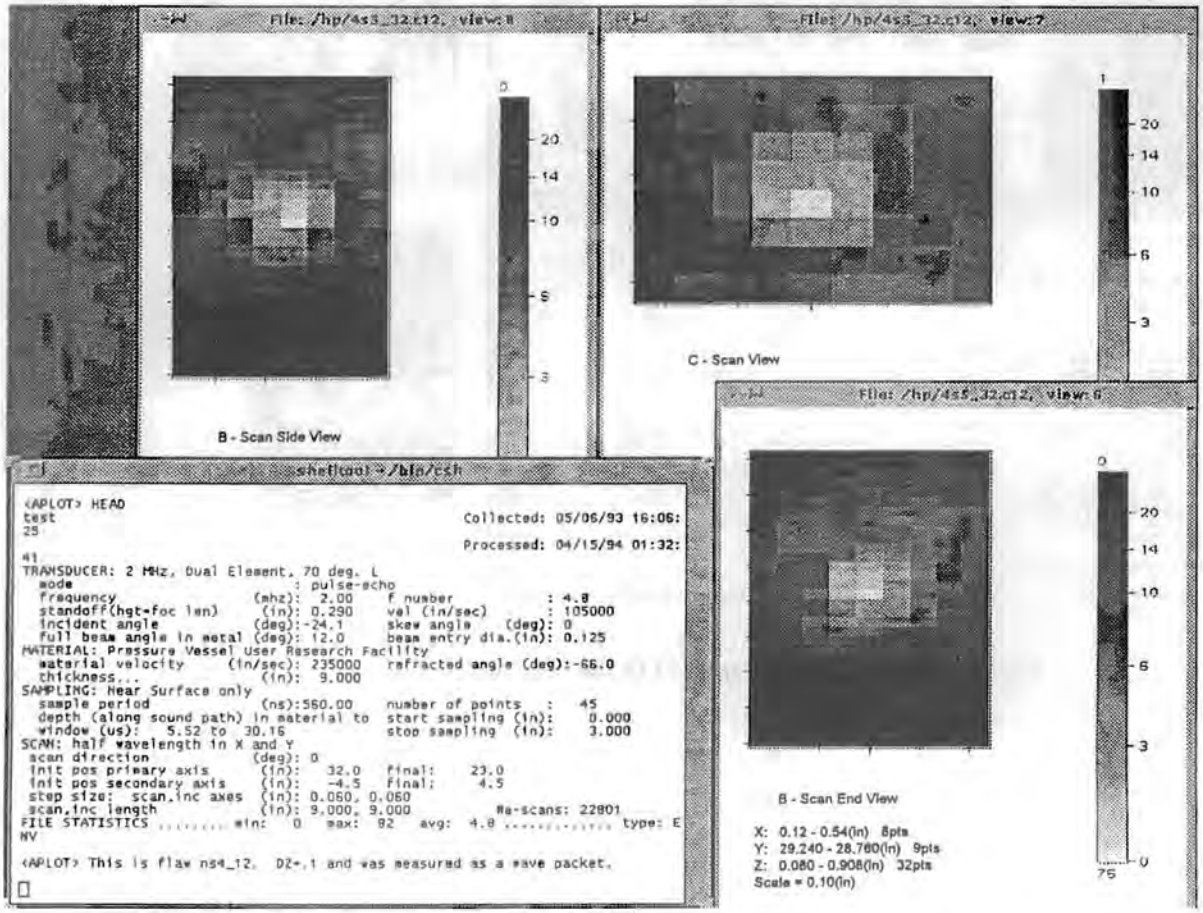

Figure A.2a Planar indication #2 in the near surface weldment: mode 5

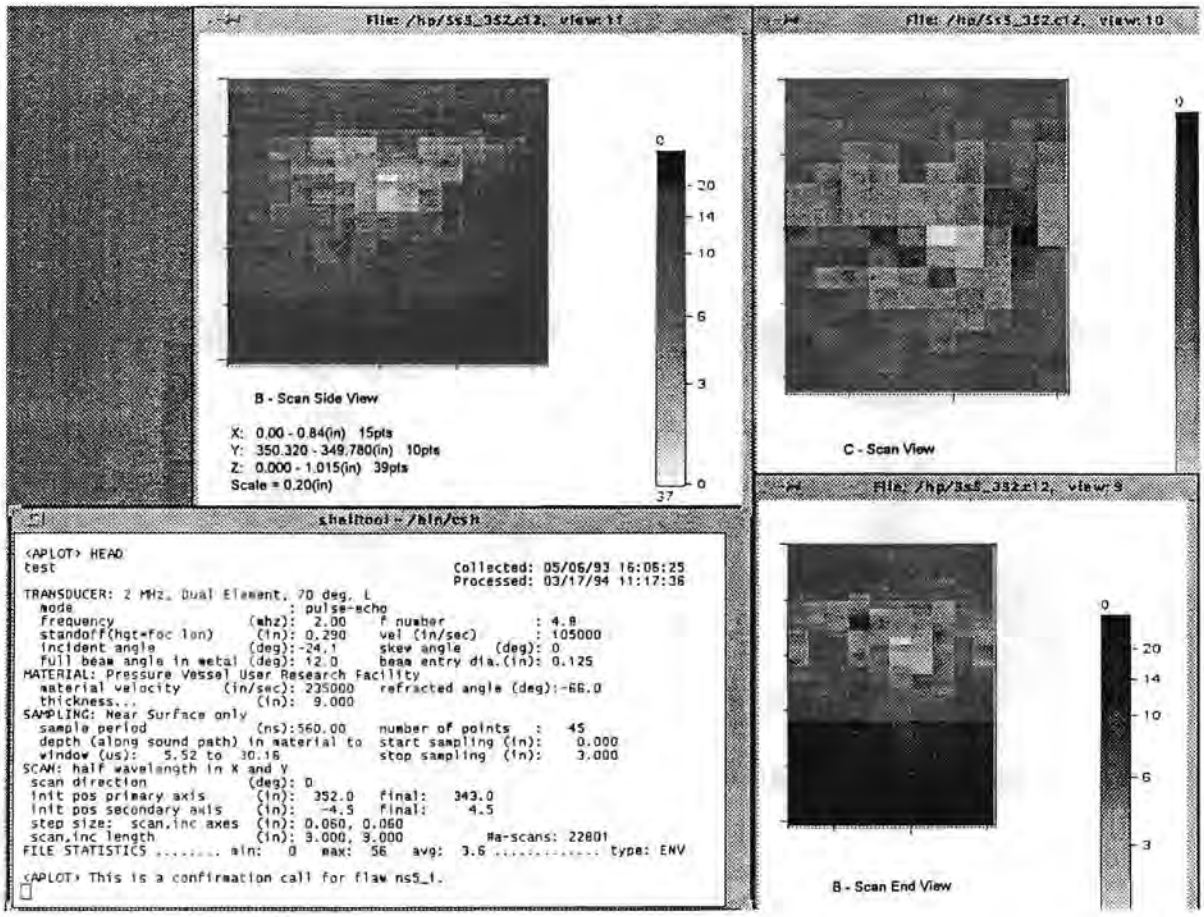

Figure A.1d Planar Indication #1 in the near surface weldment: mode 5

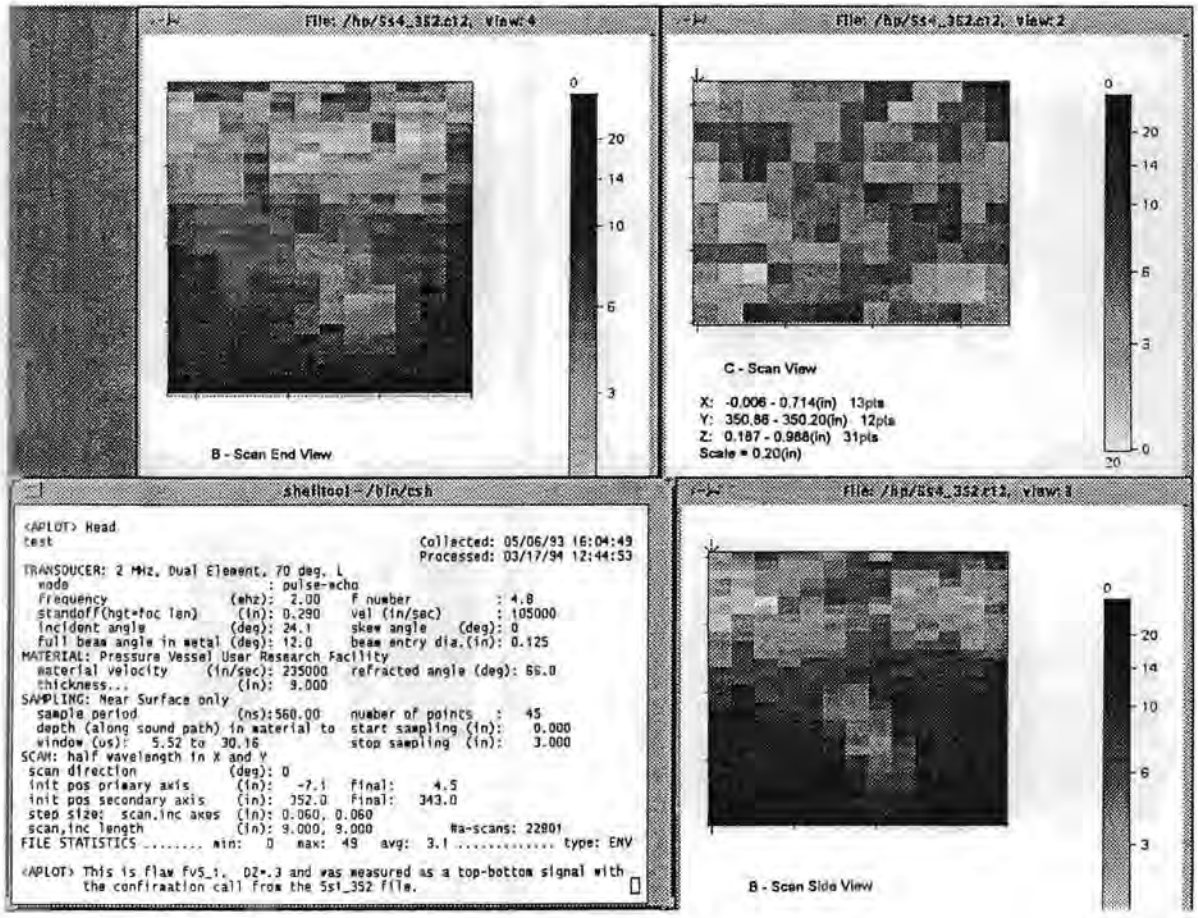

Figure A.1c Planar indication #1 in the near surface weldment: mode 4

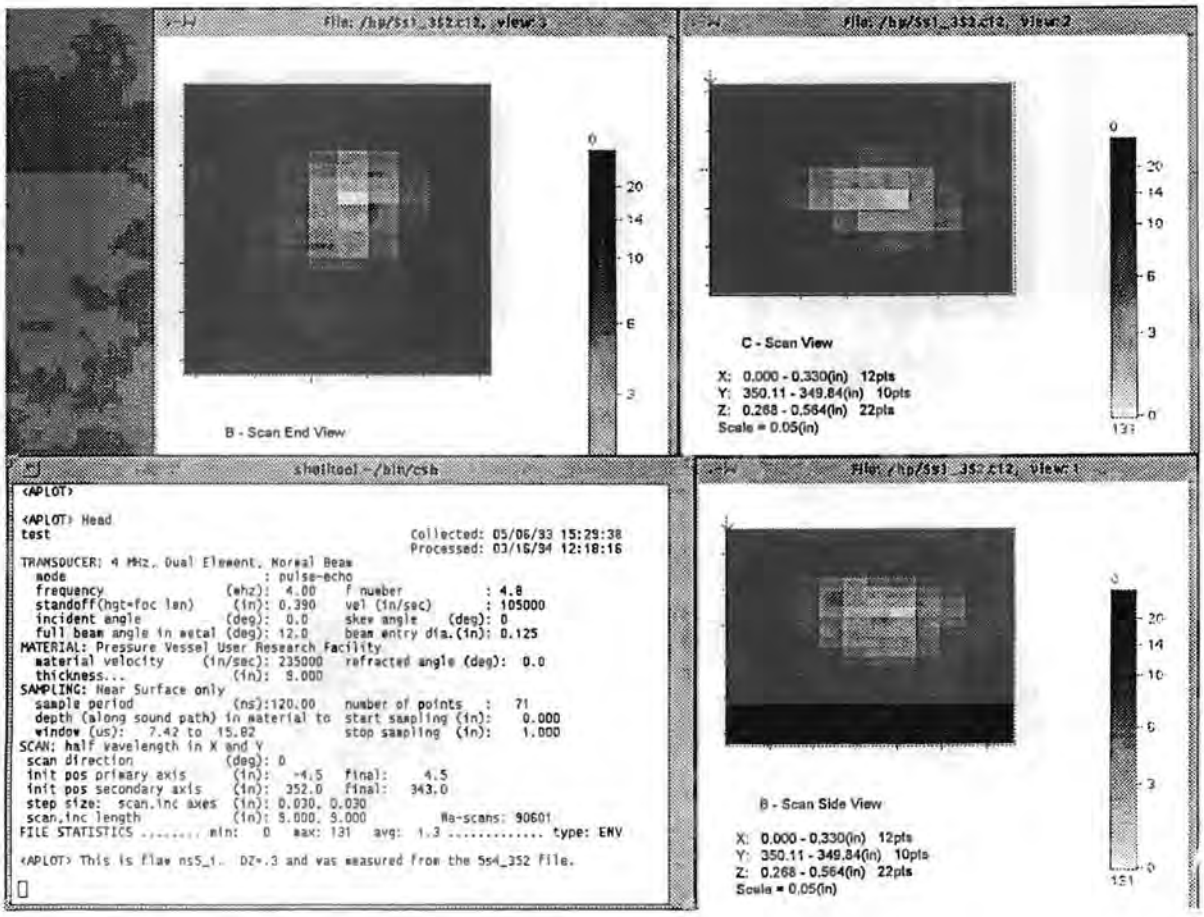

Figure A.1b Planar indication #1 in the near surface weldment: mode 1

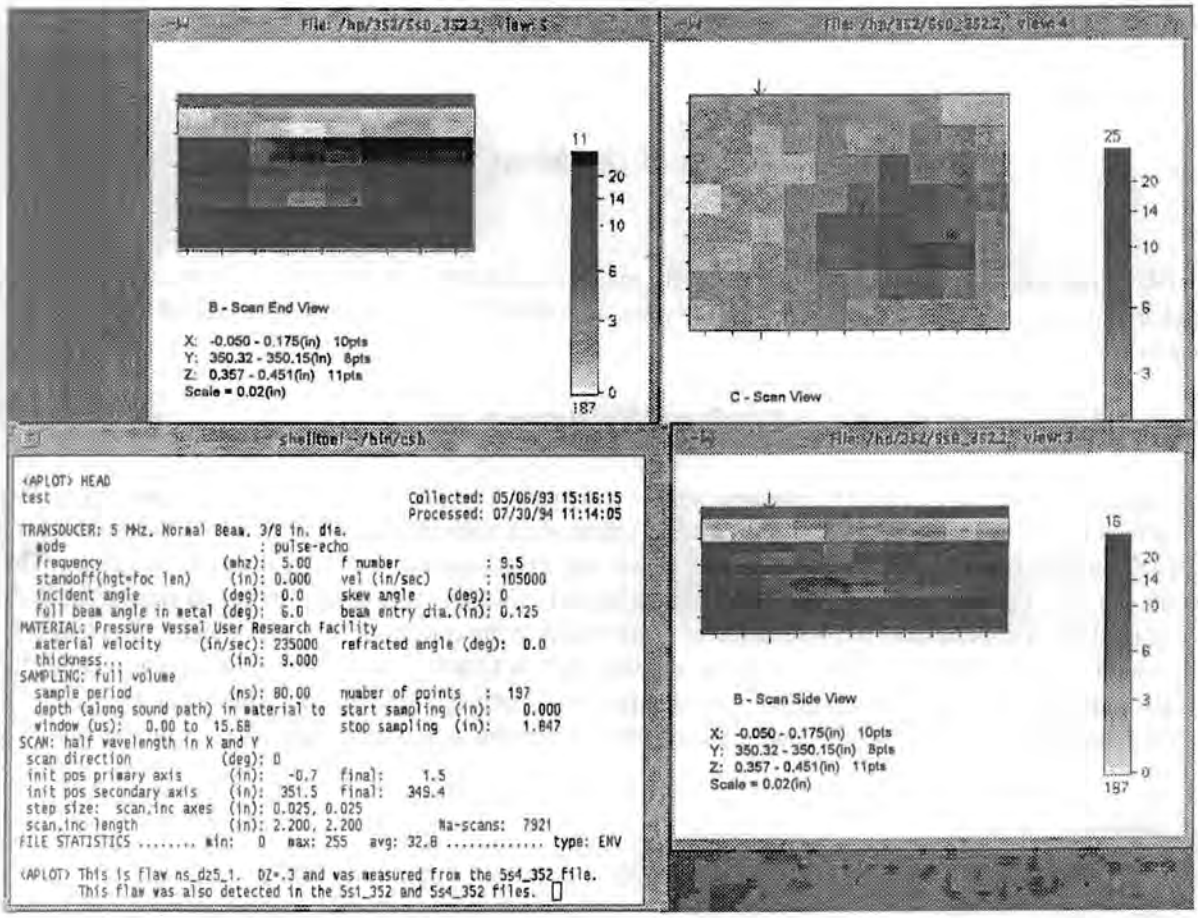

Figure A.1a Planar indication #1 in the near surface weldment: mode 10

Appendix A

SAFT-UT Images of the Most Significant Flaws

The SAFT-UT images display the vessel's axes and list the material coordinates rather than the scanner coordinates. The units in the images are given in inches, as determined by the software, and displays in metric units are not available at this time. Metric units are given in the text whenever possible.

Planar Indications in the Near Surface Weldment

Figures A.1a-d show planer indication #1 in the near surface weldment. This plan indication has a through-wall extent of 8 mm based on different depth estimates of 10 to 18 mm. The detections were made in modes 0, 1, and 4. In the mode 4 inspection, the indication had isolated TOF shape at a depth of 18 mm. There was a confirmation in mode 5 at a depth of 15 mm. The wave packet width in mode 4 gives a smaller size of 3 mm. There is good evidence of coin shape in the end view of mode 4 and in the side view of mode 5. The indication is characterized as planar based on the coin shape in modes 4 and 5. The length is 13 mm and was made to LOS in mode 4. The width is 13 mm and was made to LOS in mode 5. The range of aspect radios (length/ depth) of this indication is 1.6 to 3. The maximum amplitude-to-noise ratio is 8 (131 to 16). With an X coordinate of 8 mm, the indication is 2 mm from the HAZ. With Z coordinates of 10 to 18 mm, the indication is clearly below the cladding.

Figures A.11a-f show volumetric indication #2 in the near surface weldment. This volumetric indication has a through-wall extent of 6 mm based on different depth estimates of 20 to 26 mm. The detection was made in mode 9 where it had isolated TOF shape at a depth of 23 mm. There were confirmations in modes 2, 5, 6, 7, and 8 at depths of 20 to 26 mm. The wave packet width in mode 9 gave an alternate depth size of 3 mm. The indication is characterized as volumetric based on detection in orgothonal modes. There is good evidence of coin shape in the end view of mode 2 but the depth of the indication implies that it is not connected to the cladding. The length is 13 mm and was made to LOS in mode 2. The width is 14 mm and was made to LOS in mode 5. The range of aspect ratios (length/depth) of this indication is of medium range at 117 to 35. With an X coordinate of 9 mm, the indication is in the weld metal and 2 mm from the HAZ. With a Z coordinate of 25 mm the indication is clearly below the cladding.

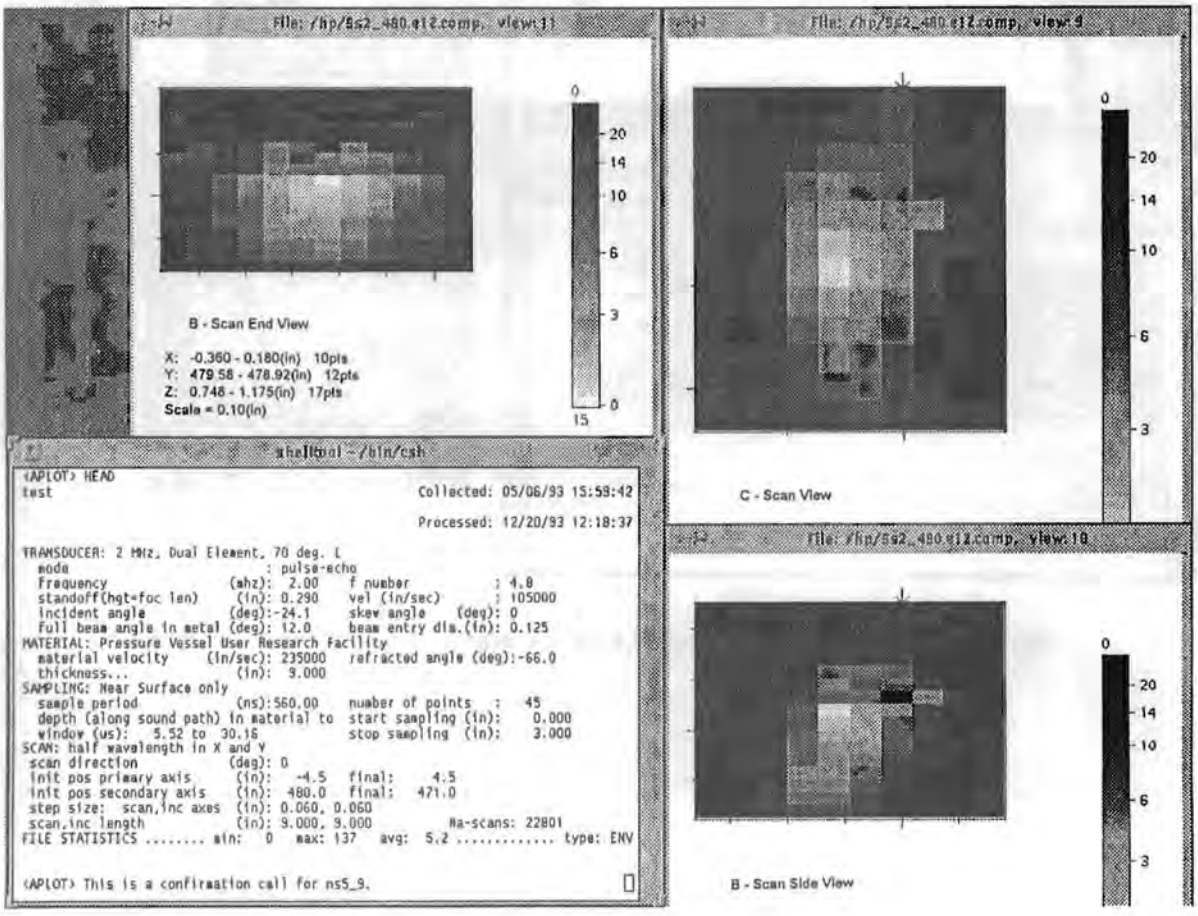

Figure A.11a Volumetric indication #2 in the near surface weldment: mode 2

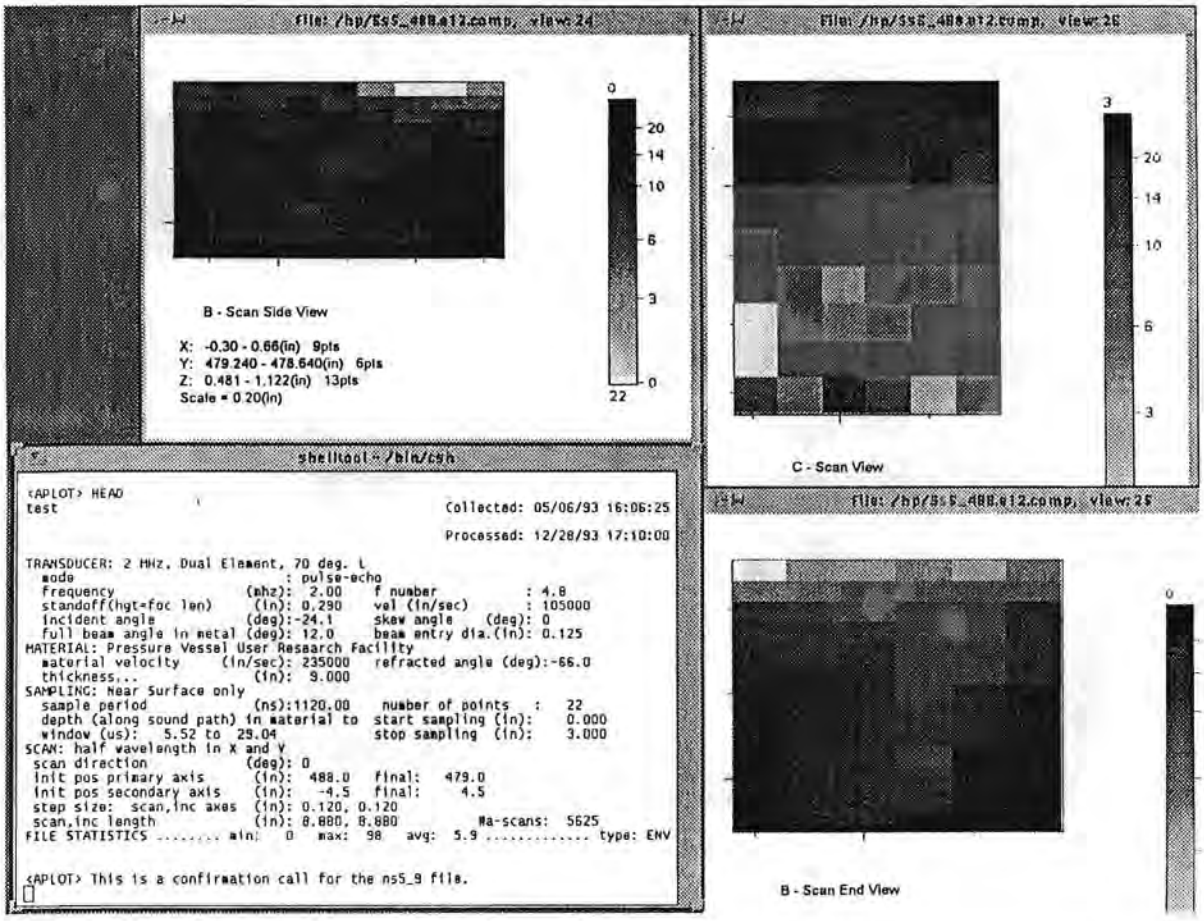

Figure A.11b - Volumetric indication #2 in the near surface weldment: mode 5

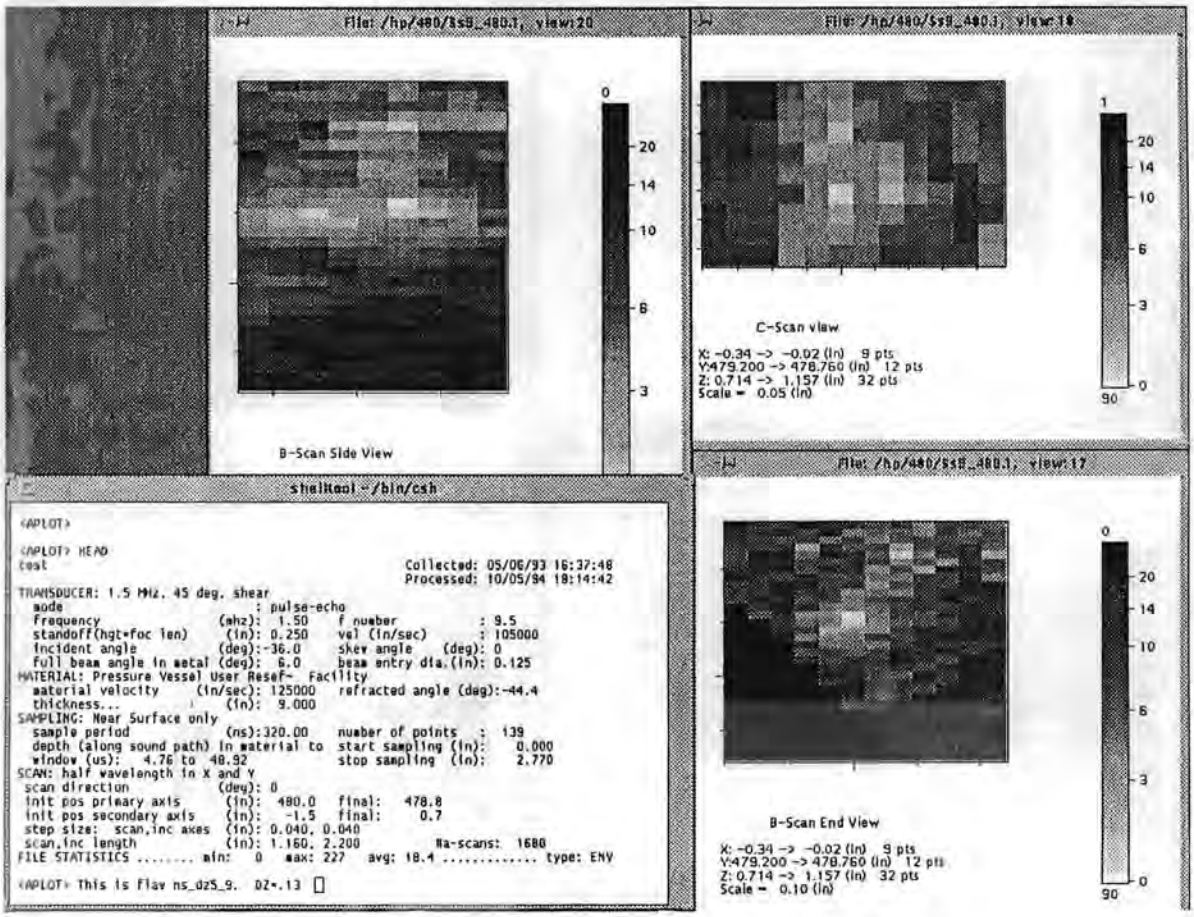

Figure A.11c - Volumetric indication #2 in the near surface weldment: mode 9

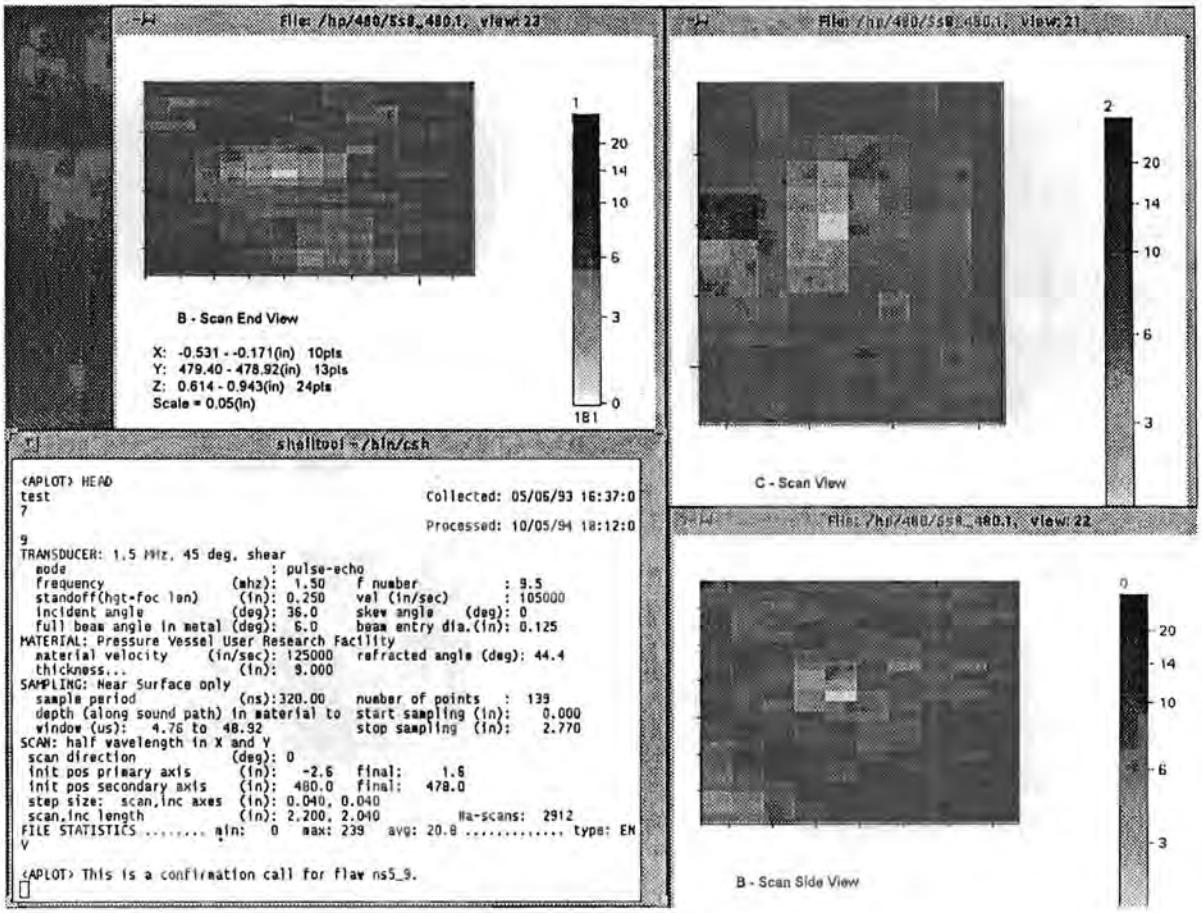

Figure A.11d - Volumetric indication #2 in the near surface weldment: mode 8

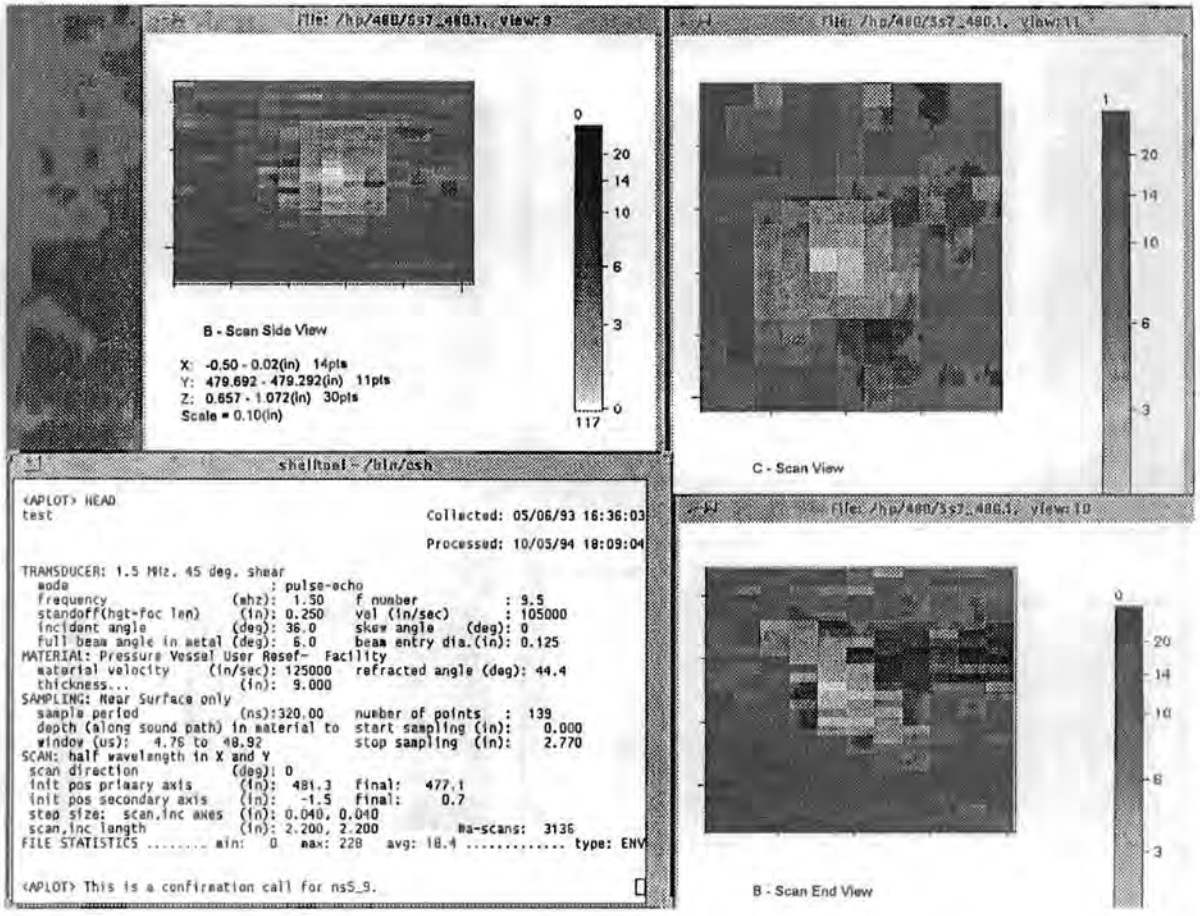

Figure A.11e - Volumetric indication #2 in the near surface weldment: mode 7

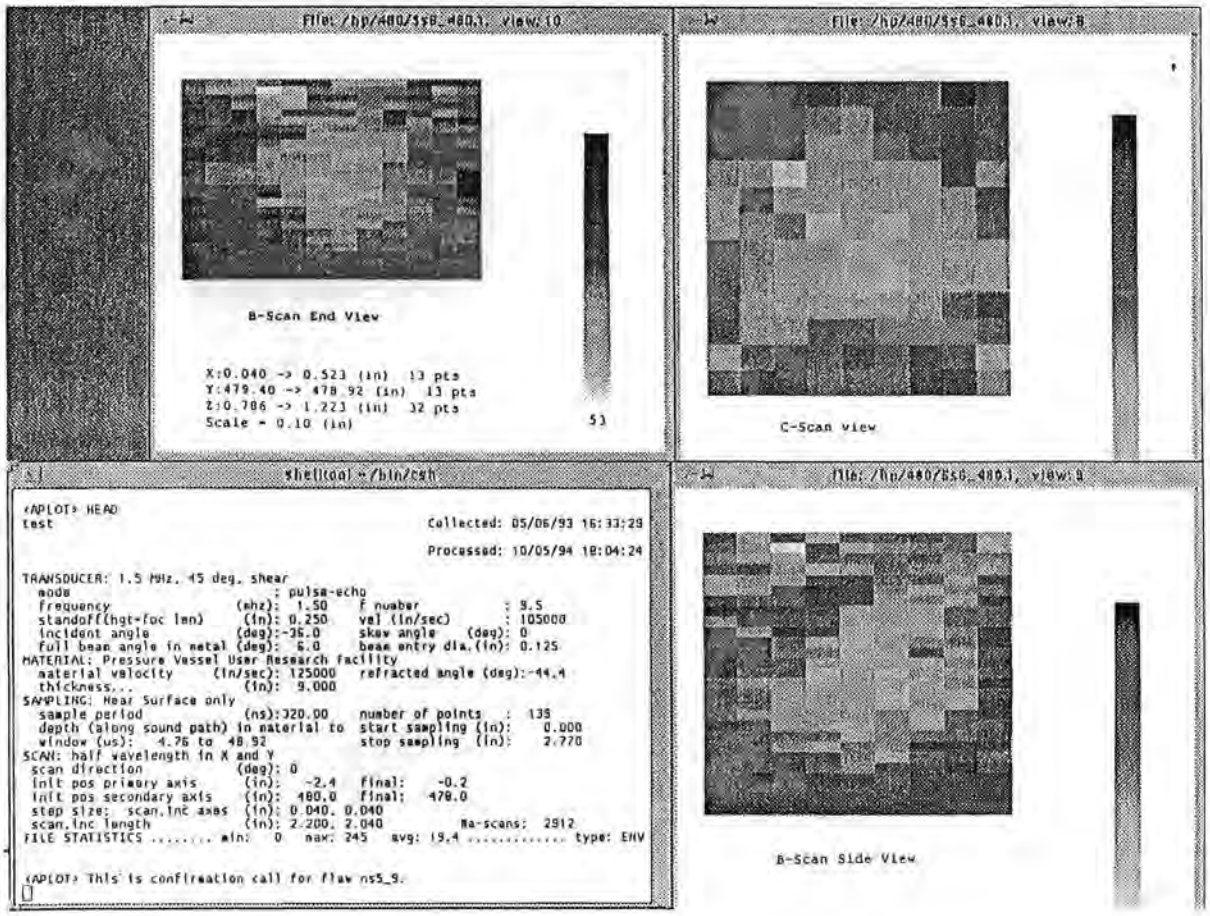

Figure A.11f - Volumetric indication #2 in the near surface weldment: mode 6

Planar Indications in the Near Surface HAZ

Figures A.12a-c show planar indication #1 in the near surface HAZ. This planar indication has a through-wall extent of 3 mm based on wave packet width. Detections were made in modes 2, 3, and 5 where it had isolated TOF shape at depths of 13 to 14 mm. There is good evidence of coin shape in the end view of mode 2. The indication is characterized as planar based on the coin shape in mode 2. The length is 2 mm and was made to LOS in mode 2. The width is 10 mm and was made to LOS in mode 3. The aspect ratio (length/depth) of this indication is 5 giving an orientation along the weld. The maximum amplitude-to-noise ratio is of medium range at 88 to 25. With X coordinates of 11 to 18 mm, the indication is probably in the HAZ. The Z coordinate of 13 to 14 mm shows that the indication is below the cladding by at least 4 to 5 mm.

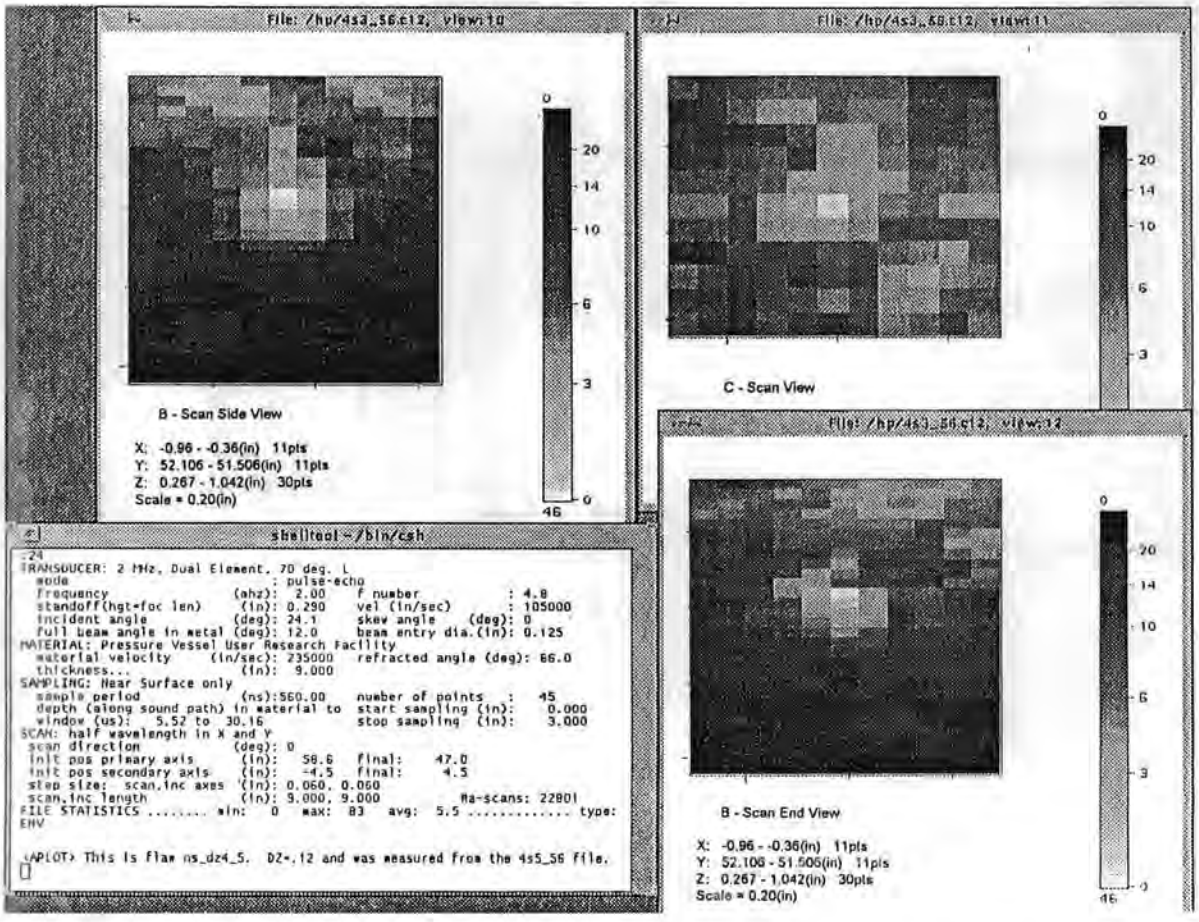

Figure A.12a - Planar indication #1 in the near surface HAZ: mode 3

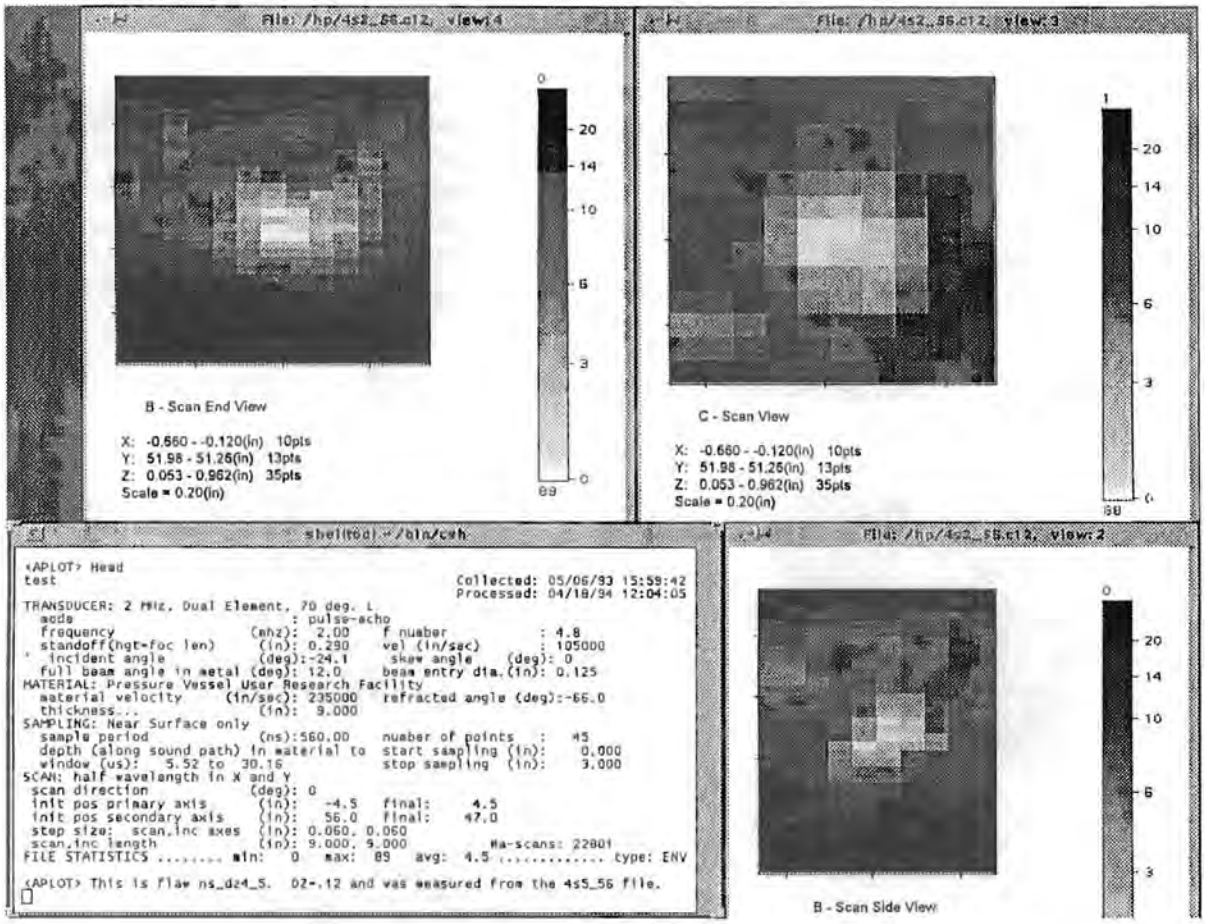

Figure A.12b - Planar indication #1 in the near surface HAZ: mode 2

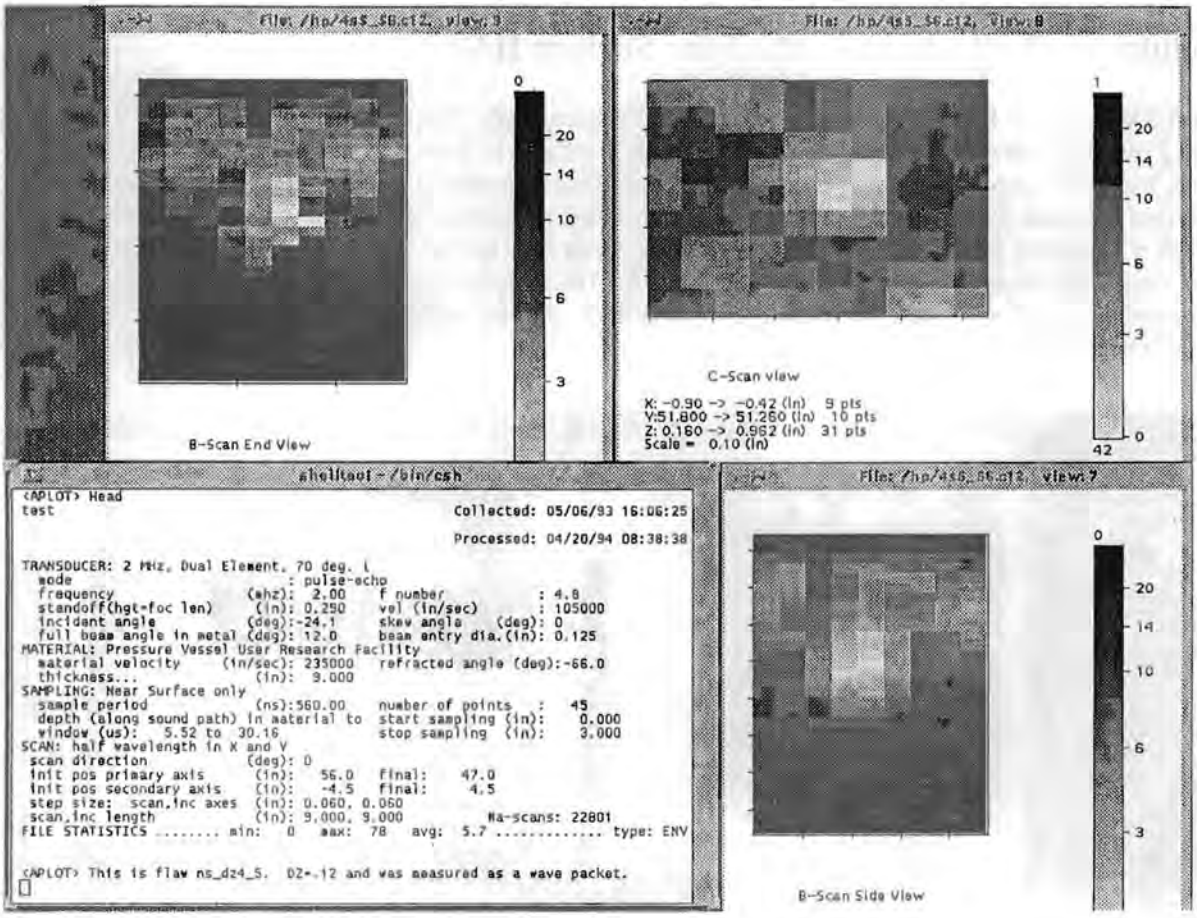

Figure A.12c - Planar indication #1 in the near surface HAZ: mode 5

Volumetric Indications in the Near Surface HAZ

Figures A.13a-b show volumetric indication #1 in the near surface HAZ. This volumetric indication has a through-wall extent of 7 mm based on wave packet width. The detection was made in mode 6 where it had isolated TOF and possibly cloud-like shapes at a depth of 20 mm. There was a confirmation in mode 5 at a depth of 20 mm. The indication is characterized as volumetric based on detection in orgothonal modes. There is no evidence of coin shape in the end views. The length is 7 mm and was made to LOS in mode 6. The width is 13 mm and was made to LOS in mode 5. The range of aspect ratios (width/depth) of this indication is 1.8 to 2.6. The maximum amplitude-to-noise ratio is high at 118 to 25. With X coordinates of 6 to 17 mm, the indication is in the HAZ, possibly in the weld. With a Z coordinate of 20 mm, the indication is clearly below the cladding.

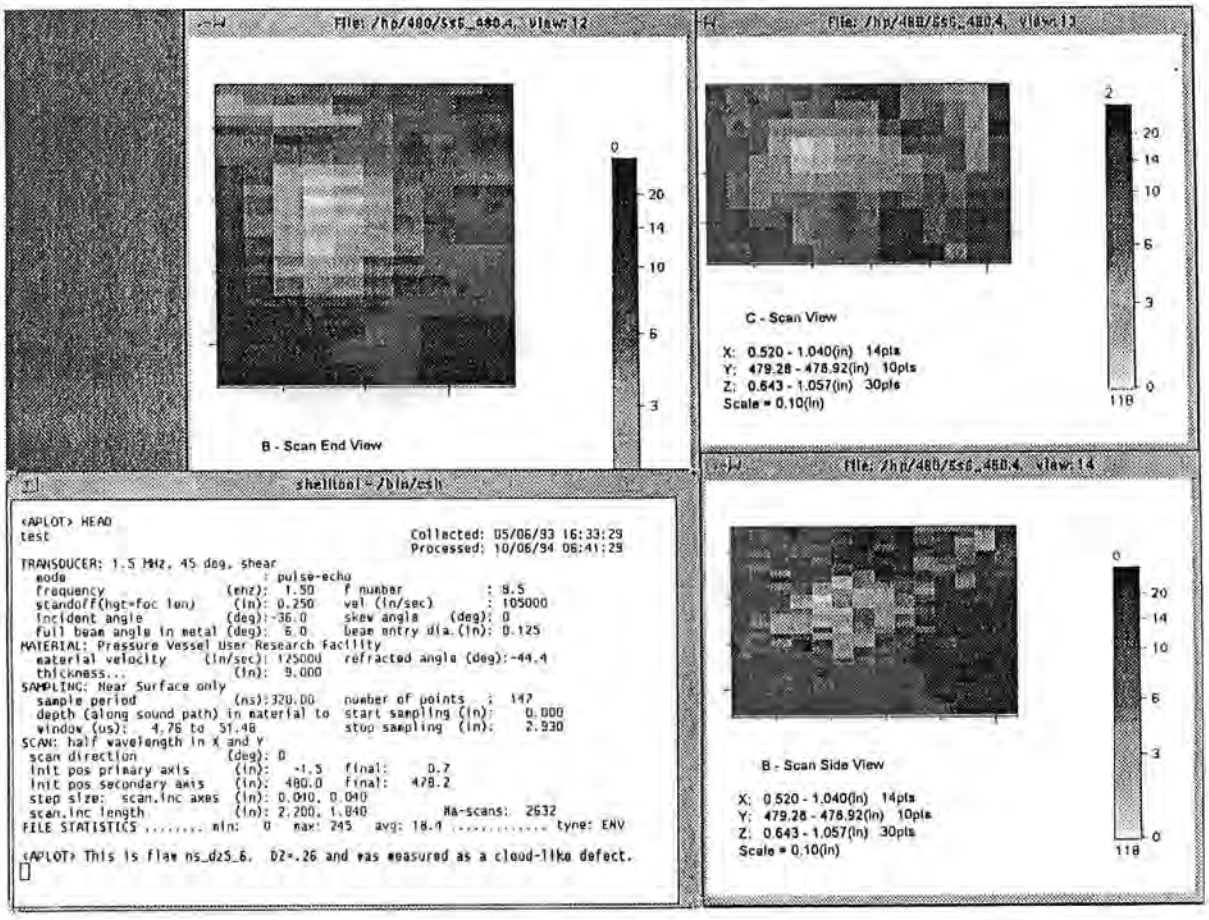

Figure A.13a - Volumetric indication #1 in the near surface HAZ: mode 6

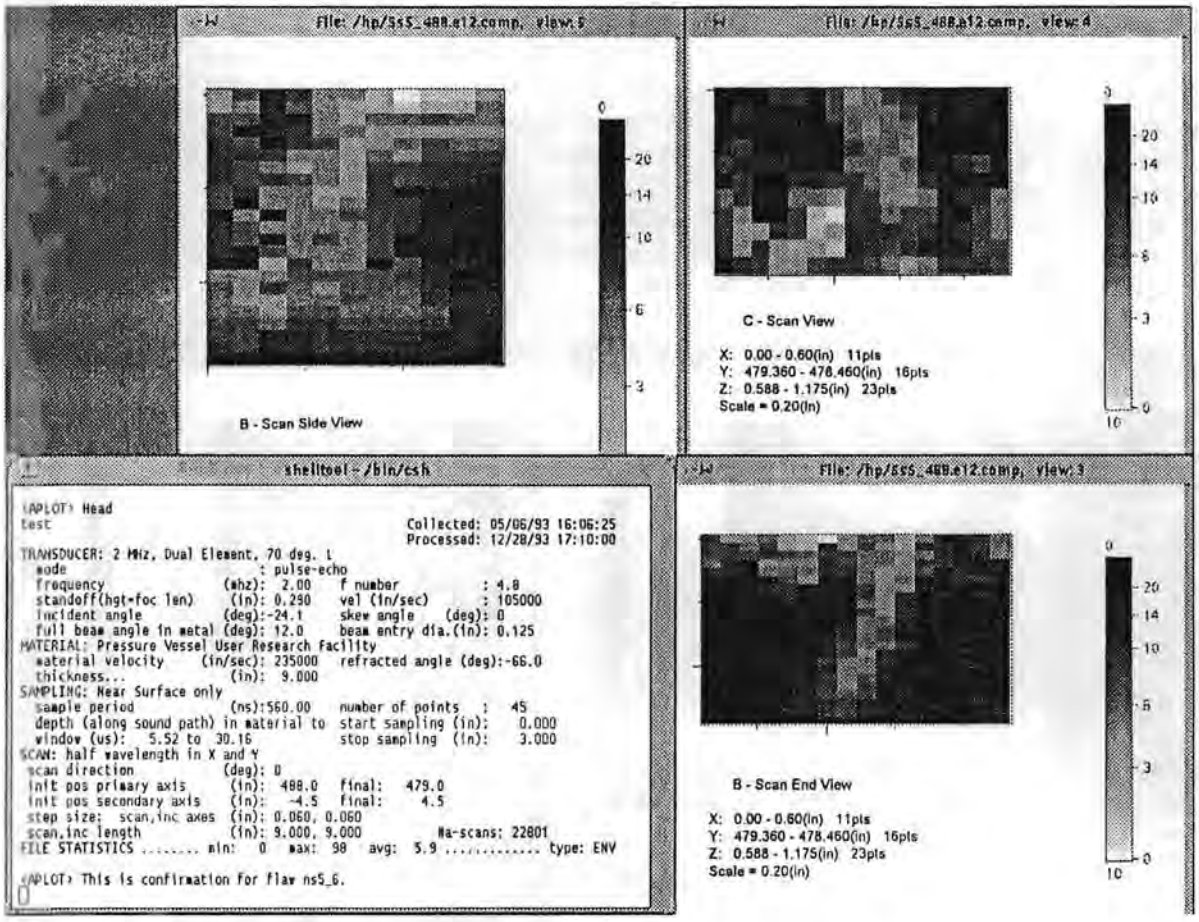

Figure A.13b - Volumetric indication #1 in the near surface HAZ: mode 5

Figures A.14a-b show volumetric indication #2 in the near surface HAZ. This volumetric indication has a through-wall extent of 3 mm based on different depth estimates of 11 to 14 mm. The detection was made in mode 2 where it had isolated TOF shape at a depth of 11 mm. There was a confirmation in mode 1 at a depth of 14 mm. The wave packet width in mode 2 gave an alternate depth size of 2.5 mm. The indication is characterized as volumetric based on normal beam detection. There is no evidence of coin shape in the end views. The length is 13 mm and was made to LOS in mode 2. The width is 8 mm and was made to LOS in mode 1. The range of aspect ratios (length/depth) of this indication is 4 to 6 giving an orientation along the weld. The maximum amplitude-to-noise ratio is of medium range at 71 to 20. With X coordinates of -14 to -25 mm, the indication is in the HAZ, possibly in the base metal. With Z coordinates of 11 to 14 mm, the indication is below the cladding by at least 2 mm.

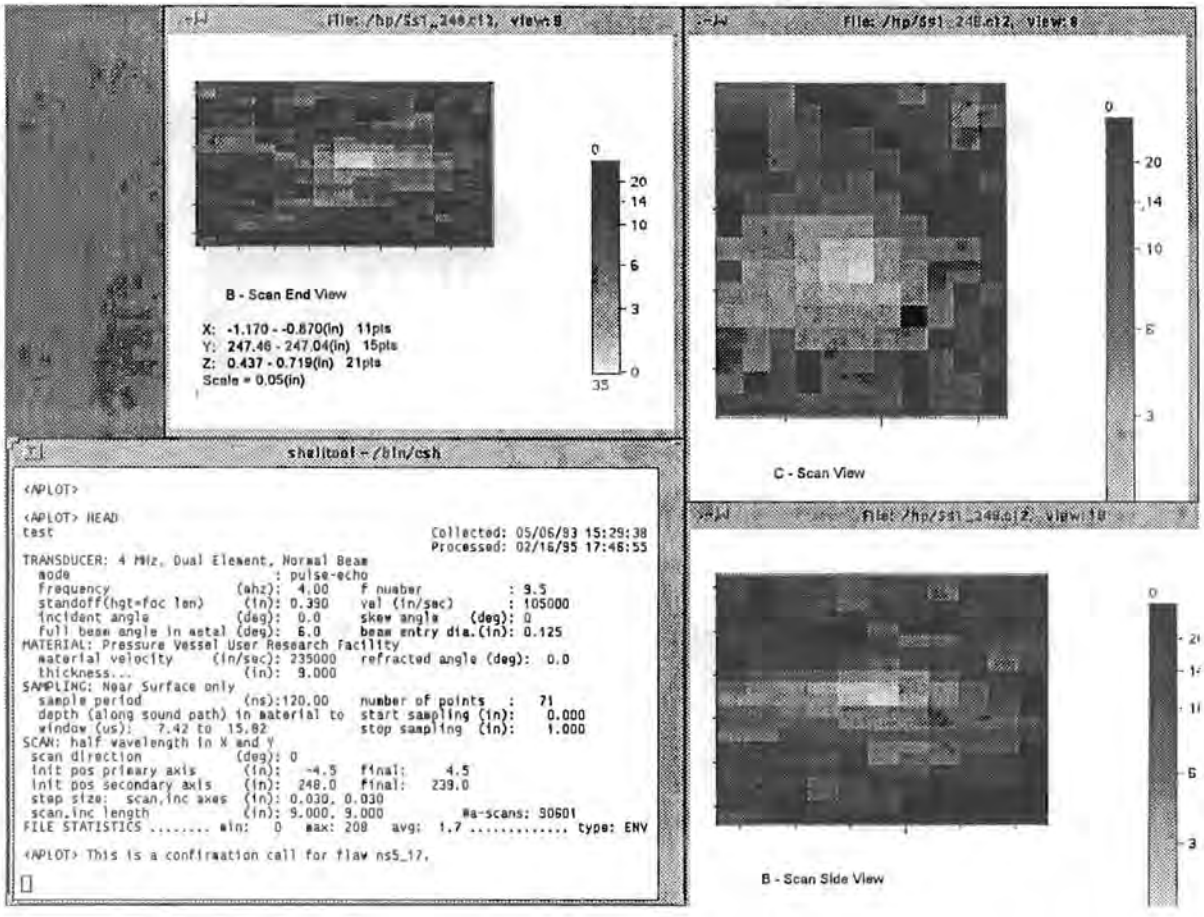

Figure A.14a - Volumetric indication #2 in the near surface HAZ: mode 1

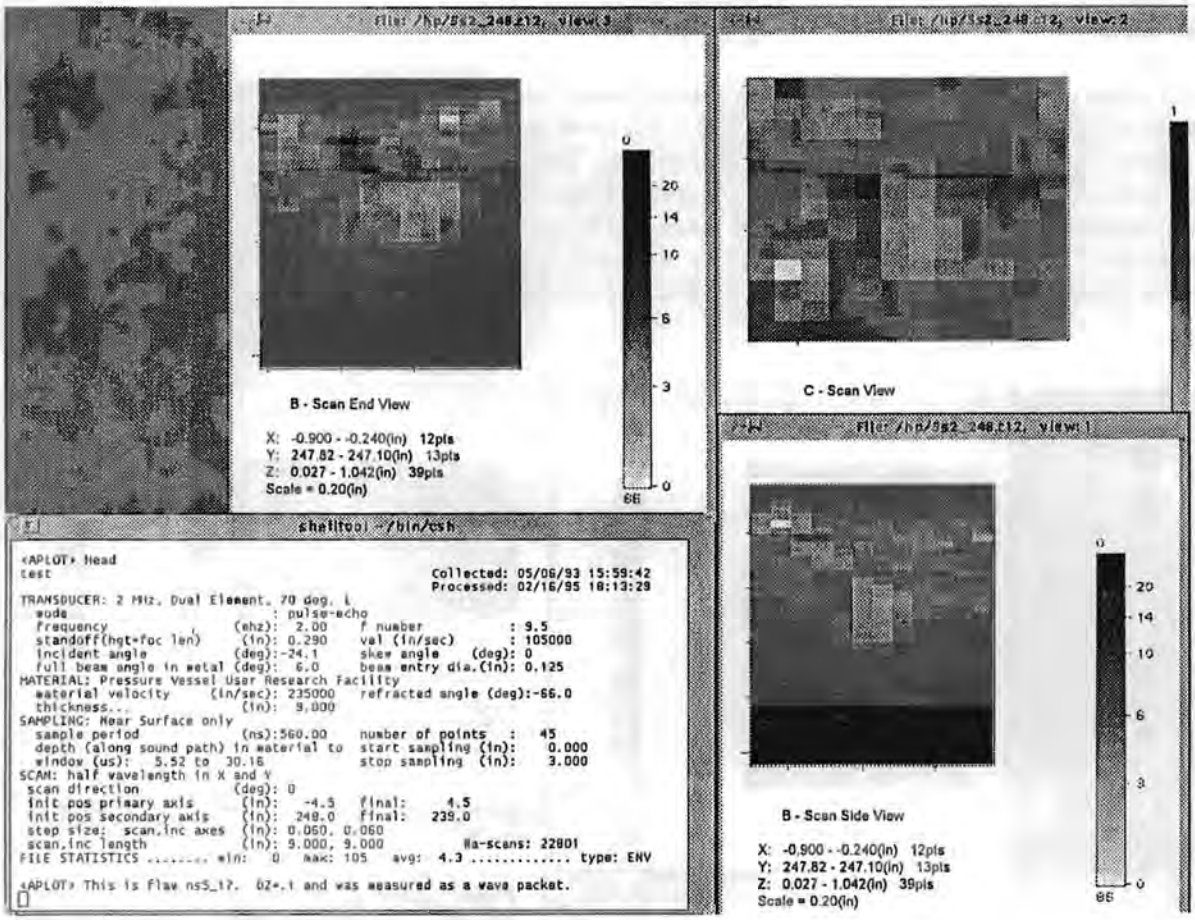

Figure A.14b - Volumetric indication #2 in the near surface HAZ: mode 2

Planar Indications in the Near Surface Base Metal

Figure A.15 shows planar indication #1 in the near surface base metal. This planar indication has a through-wall extent of 8 mm based on LOS in a cloud like shape, possibly 2.5 mm based on wave packet width. The detection was made in mode 8 where it had isolated TOF shape at a depth of 18 mm. There were no confirmations in other modes. The indication is characterized as planar based on lack of normal beam detection. There is no evidence of coin shape in the end view of mode 8. The length is 7 mm and was made to LOS in mode 8. The range of aspect ratios (length/depth) of this indication is 0.7 to 2.8. The maximum amplitude-to-noise ratio is low at 165 to 70. With an X coordinate of 122 mm, the indication is clearly in the base metal. With a Z coordinate of 18 mm, the indication is clearly below the cladding.

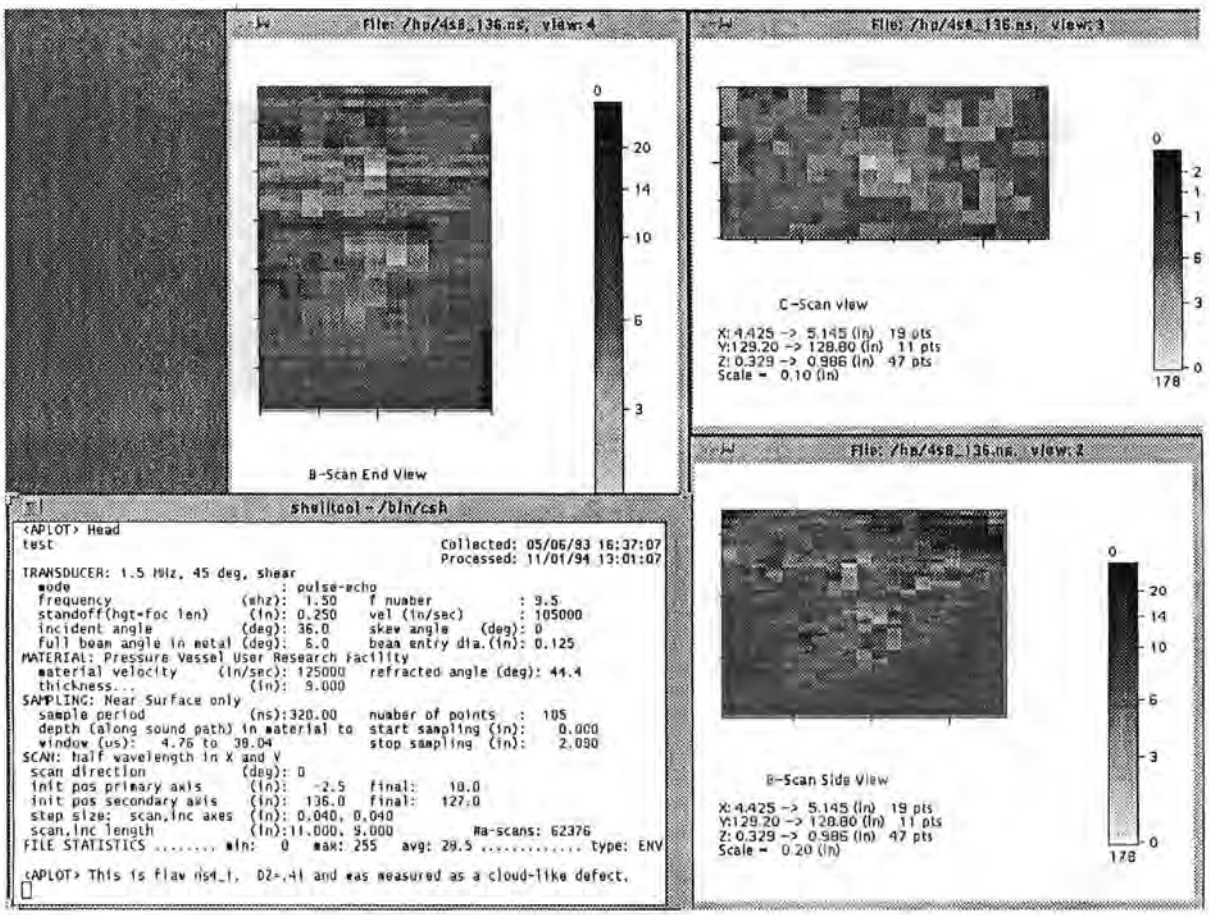

Figure A.15 - Planar indication #1 in the near surface base metal: mode 8

Figure A.16 shows planar indication #2 in the near surface base metal. This planar indication has a through-wall extent of 7.4 mm based on LOS in a cloud like shape, possibly 3.5 mm based on wave packet width. The detection was made in mode 8 where it had isolated TOF shape at a depth of 20 mm. There were no confirmations in other modes. The indication is characterized as planar based on lack of normal beam detection. There is no evidence of coin shape in the end view of mode 8. The length is 13 mm and was made to LOS in mode 8. The range of aspect ratios (length/depth) of this indication is 1.8 to 4. The maximum amplitude-to-noise ratio is high at 190 to 35. With an X coordinate of 112 mm, the indication is clearly in the base metal. With a Z coordinate of 20 mm, the indication is clearly below the cladding.

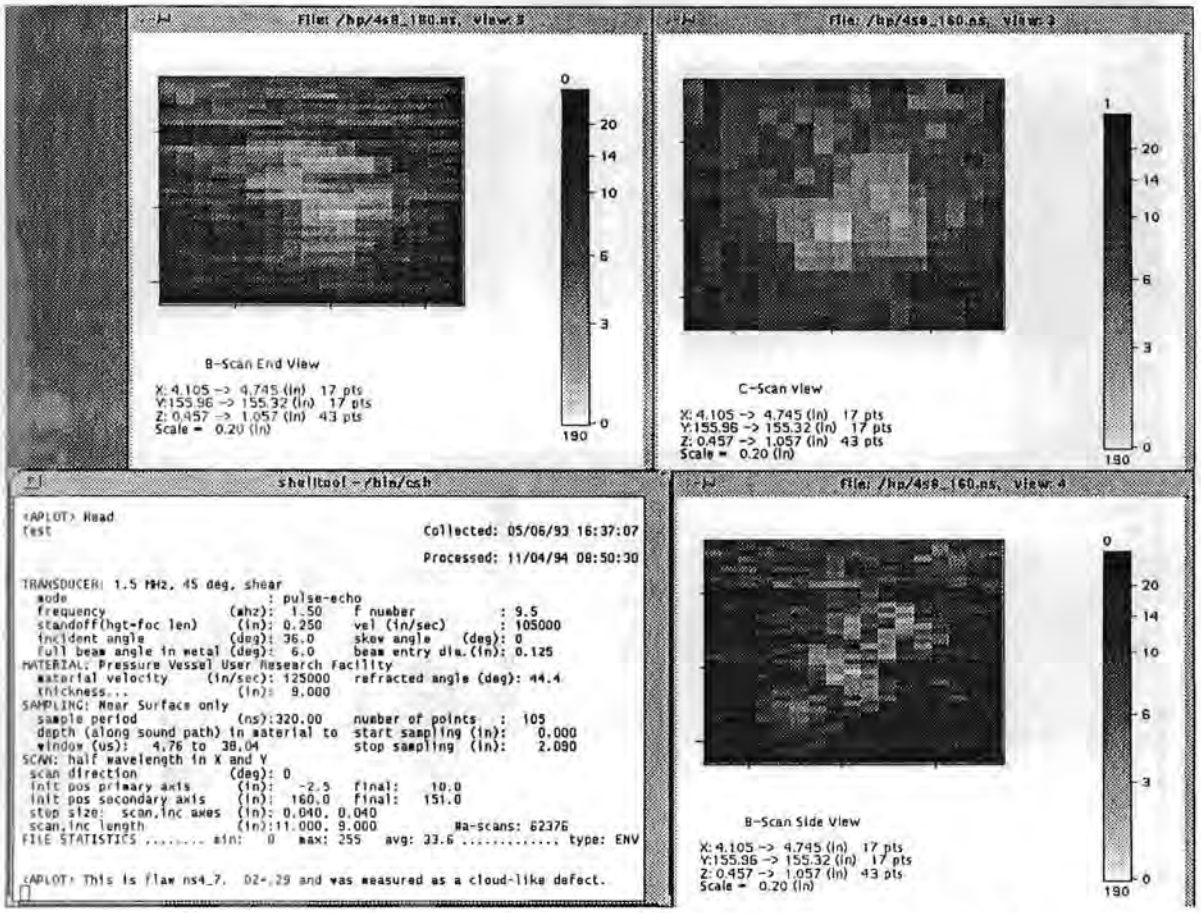

Figure A.16 - Planar indication #2 in the near surface base metal: mode 8

Figure A.17 shows planar indication #3 in the near surface base metal. This planar indication has a through-wall extent of 4 mm based on wave packet width. The detection was made in mode 2 where it had isolated TOF shape at a depth of 15 mm. There were no confirmations in other modes. The indication is characterized as planar based on lack of normal beam detection. There is no evidence of coin shape in the end view of mode 2. The length is 12 mm and was made to LOS in mode 2. The aspect ratio (length/depth) of this indication is 3 giving an orientation along the weld. The maximum amplitude-to-noise ratio is of medium range at 22 to 9. With an X coordinate of 122 mm, the indication is clearly in the base metal. With a Z coordinate of 15 mm, the indication is clearly below the cladding.

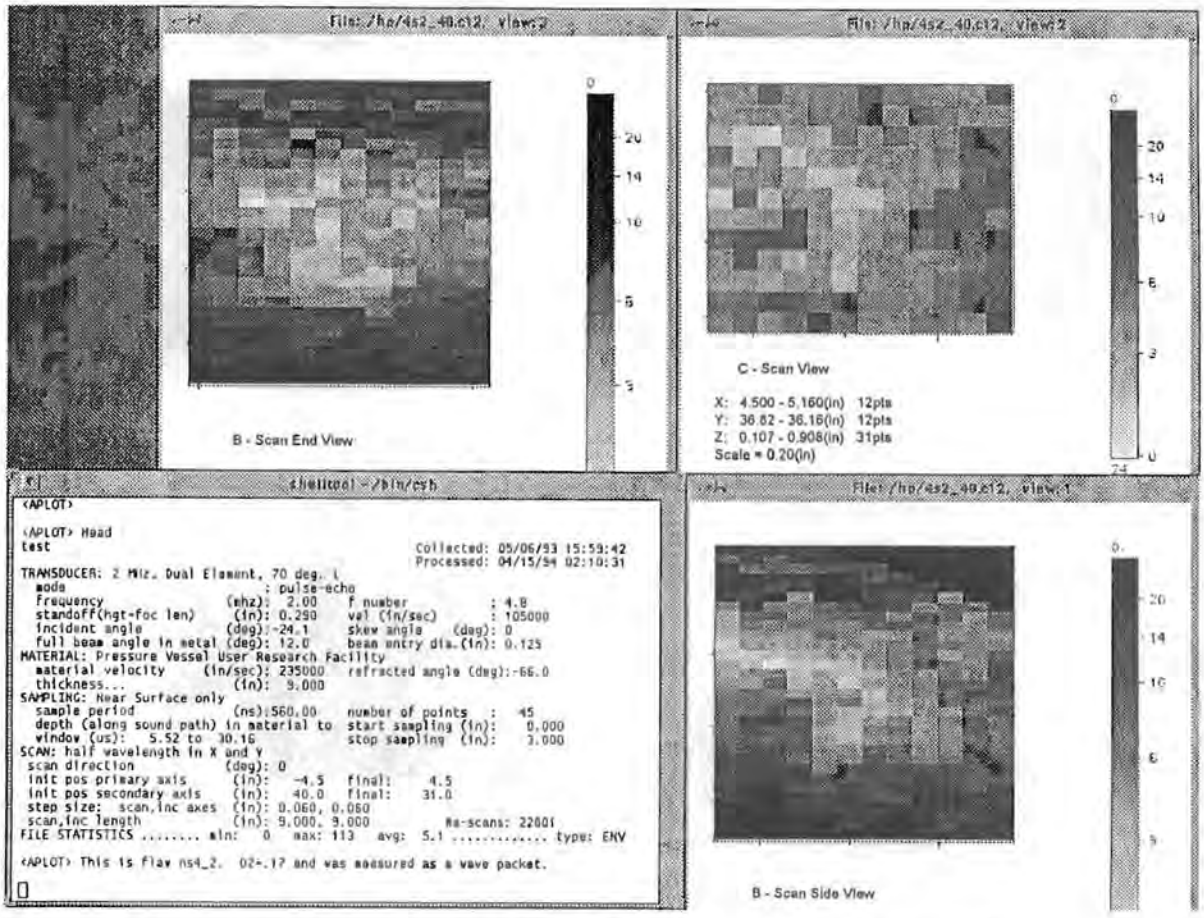

Figure A.17 - Planar indication #3 in the near surface base metal: mode 2

Figure A.18 shows planar indication #4 in the near surface base metal. This planar indication has a through-wall extent of 4 mm based on wave packet width. The detection was made in mode 2 where it had isolated TOF shape at a depth of 11 mm. There were no confirmations in other modes. The indication is characterized as planar based on lack of normal beam detection. There is no evidence of coin shape in the end view of mode 2. The length is 9 mm and was made to LOS in mode 2. The aspect ratio (length/depth) of this indication is 2 which is unusually low compared to the other indications detected in this data set. The maximum amplitude-to-noise ratio is high at 25 to 5. With an X coordinate of -46 mm, the indication is clearly in the base metal. With a Z coordinate of 11 mm, the indication is below the cladding by 2 mm.

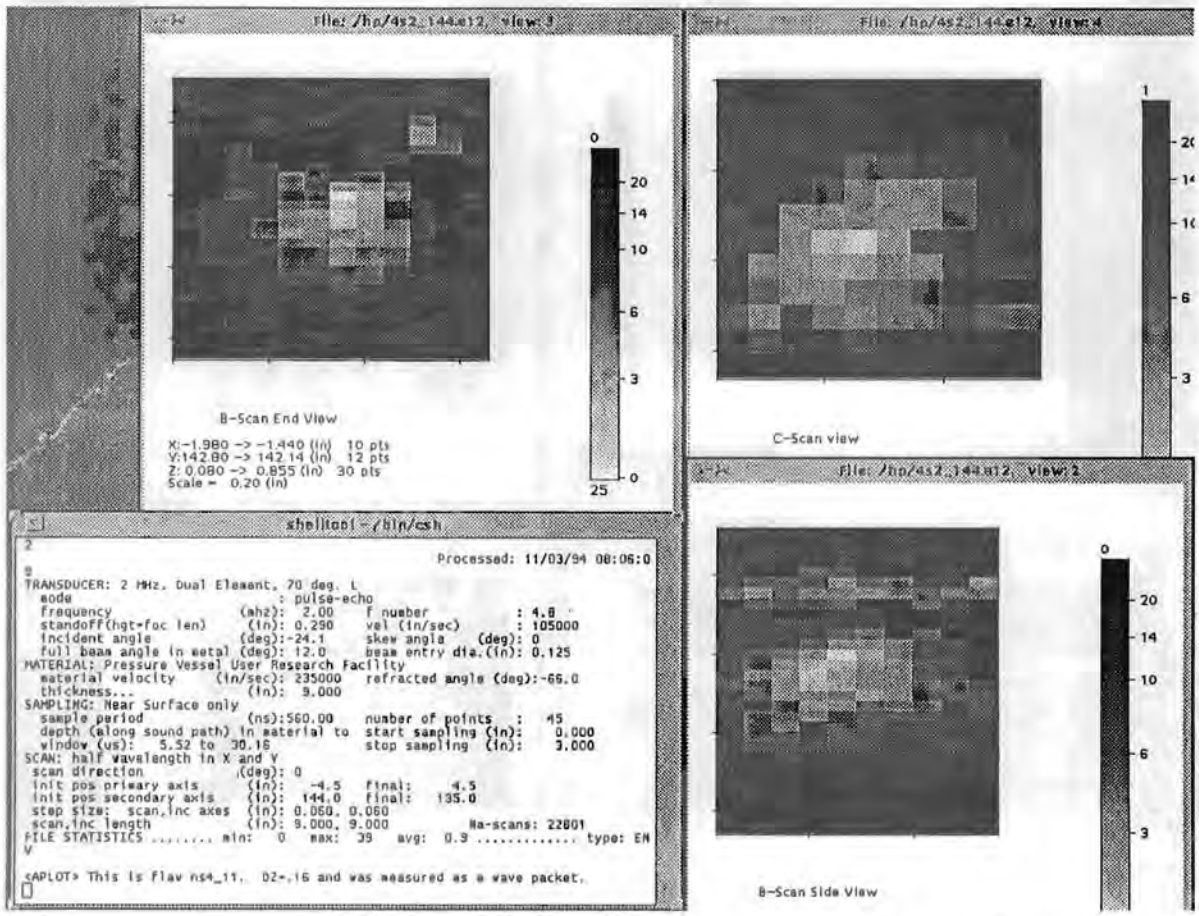

Figure A.18 - Planar indication #4 in the near surface base metal: mode 2

Figure A.19 shows planar indication #5 in the near surface base metal. This planar indication has a through-wall extent of 3.6 mm based on wave packet width. The detection was made in mode 4 where it had isolated TOF shape at a depth of 12 mm. There were no confirmations in other modes. The indication is characterized as planar based on lack of normal beam detection. There is good evidence of coin shape in the end view of modes 4. The length is 15 mm and was made to LOS in mode 4. The aspect ratio (length/depth) of this indication is 4 giving an orientation along the weld. The maximum amplitude-to-noise ratio is low at 19 to 9. With an X coordinate of -49 mm, the indication is clearly in the base metal. With a Z coordinate of 12 mm, the indication is below the cladding by 3 mm.

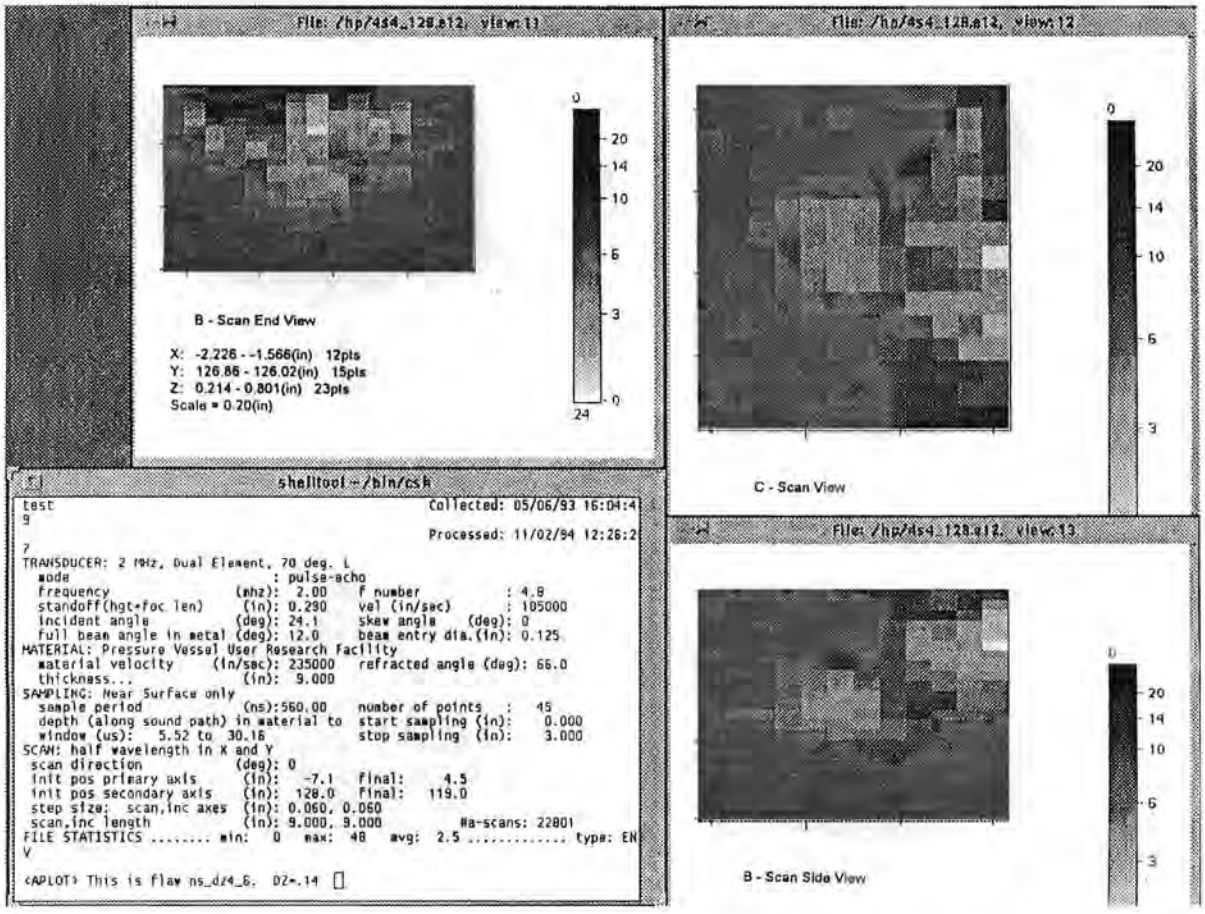

Figure A.19 - Planar indication #5 in the near surface base metal: mode 4

Figures A.20a-c show planar indication #6 in the near surface base metal. This planar indication has a through-wall extent of 3.5 mm based on wave packet width. The detections were made in modes 3 and 5 where it had isolated TOF shape at depths of 13 and 16 mm. The shape quality is good for this indication. There was a confirmation in mode 1 at a depth of 14 mm. The different Z values 13 to 16 mm give an alternate depth size of 3 mm. There is good evidence of coin shape in the end view of mode 3. The indication is characterized as planar based on the coin shape in mode 3. The length is 12 mm and was made to LOS in mode 1. The width is 20 mm and was made to LOS in mode 3. The aspect ratio (width/depth) of this indication is 6 which tends to confirm planar orientation. The maximum amplitude-to-noise ratio is of medium range at 29 to 10. With an X coordinate of -29 mm, the indication is clearly in the base metal. With a Z coordinate of 13 mm, the indication is below the cladding by 4 mm.

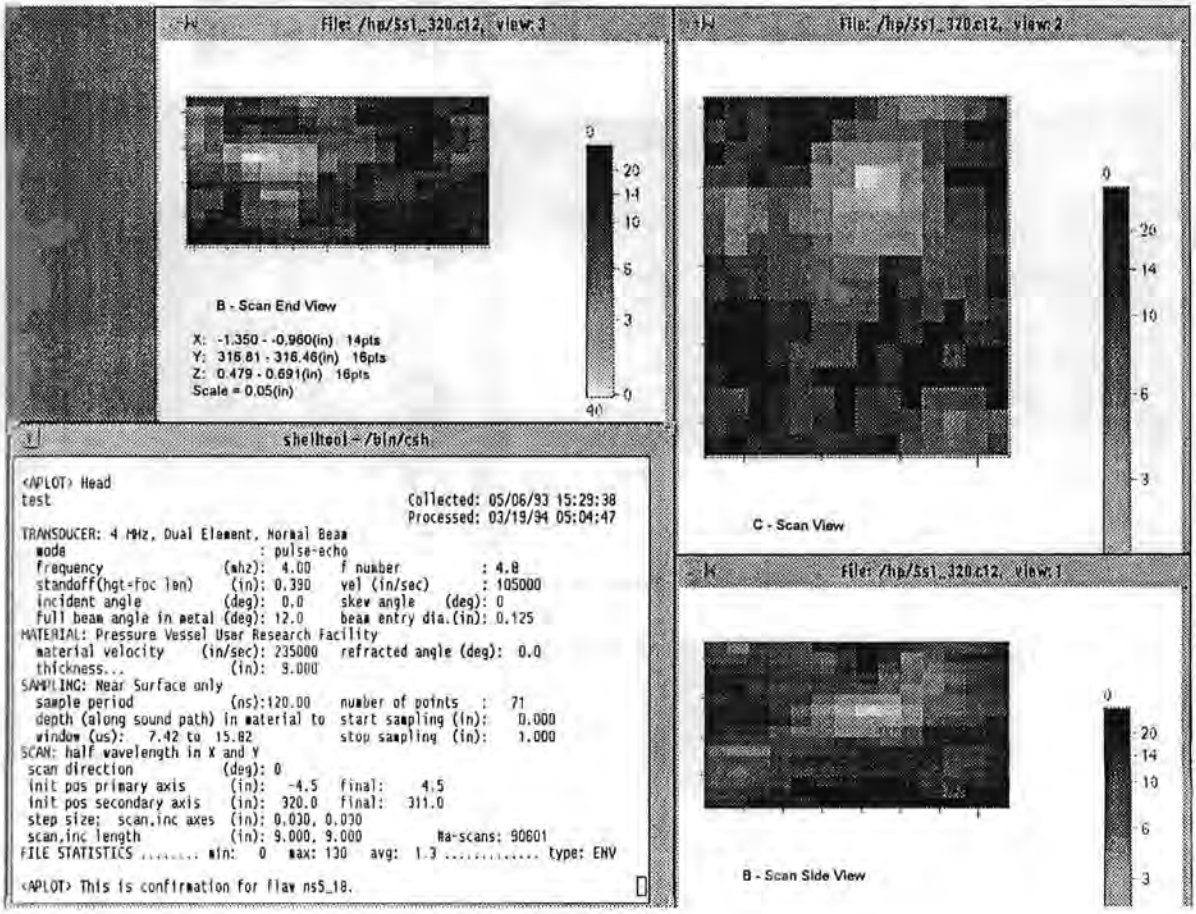

Figure A.20a - Planar indication #6 in the near surface base metal: mode 1

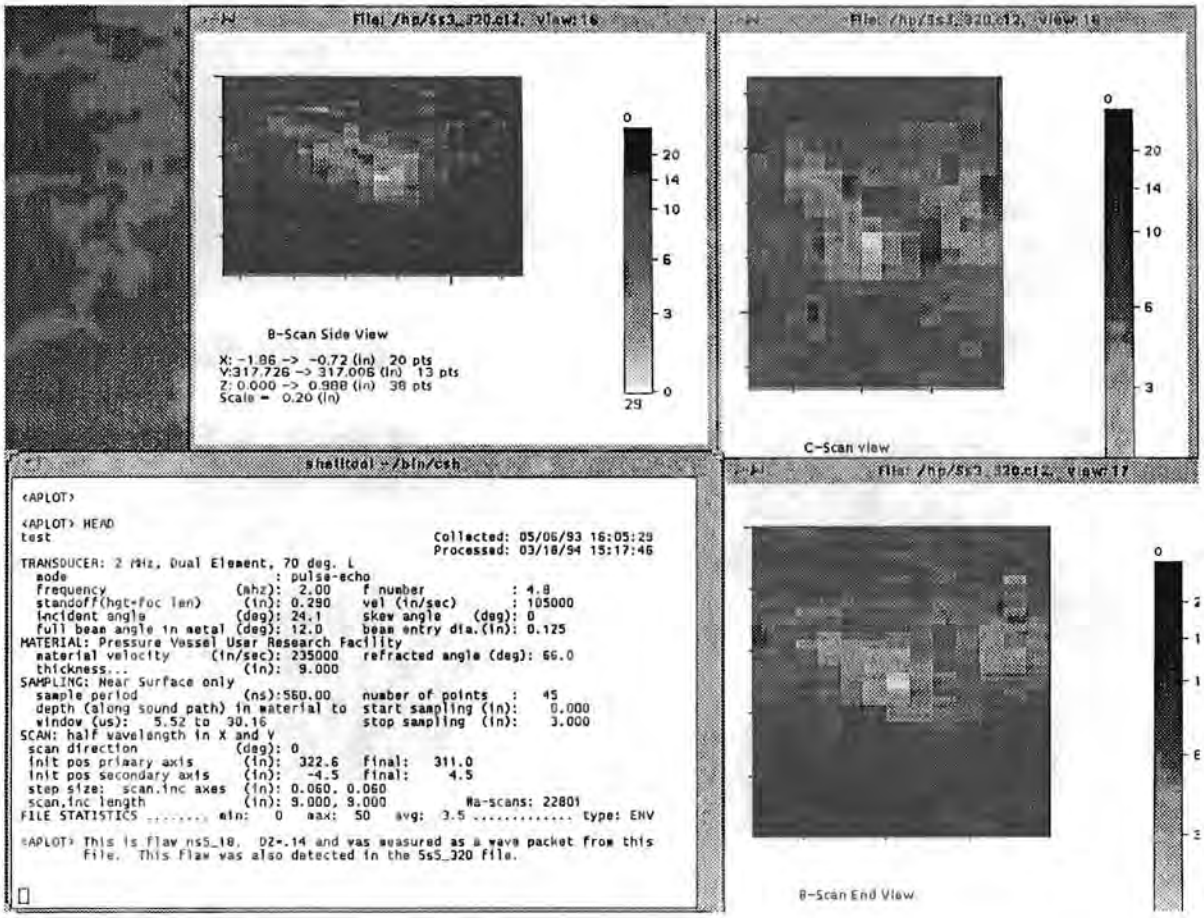

Figure A.20b - Planar indication #6 in the near surface base metal: mode 3

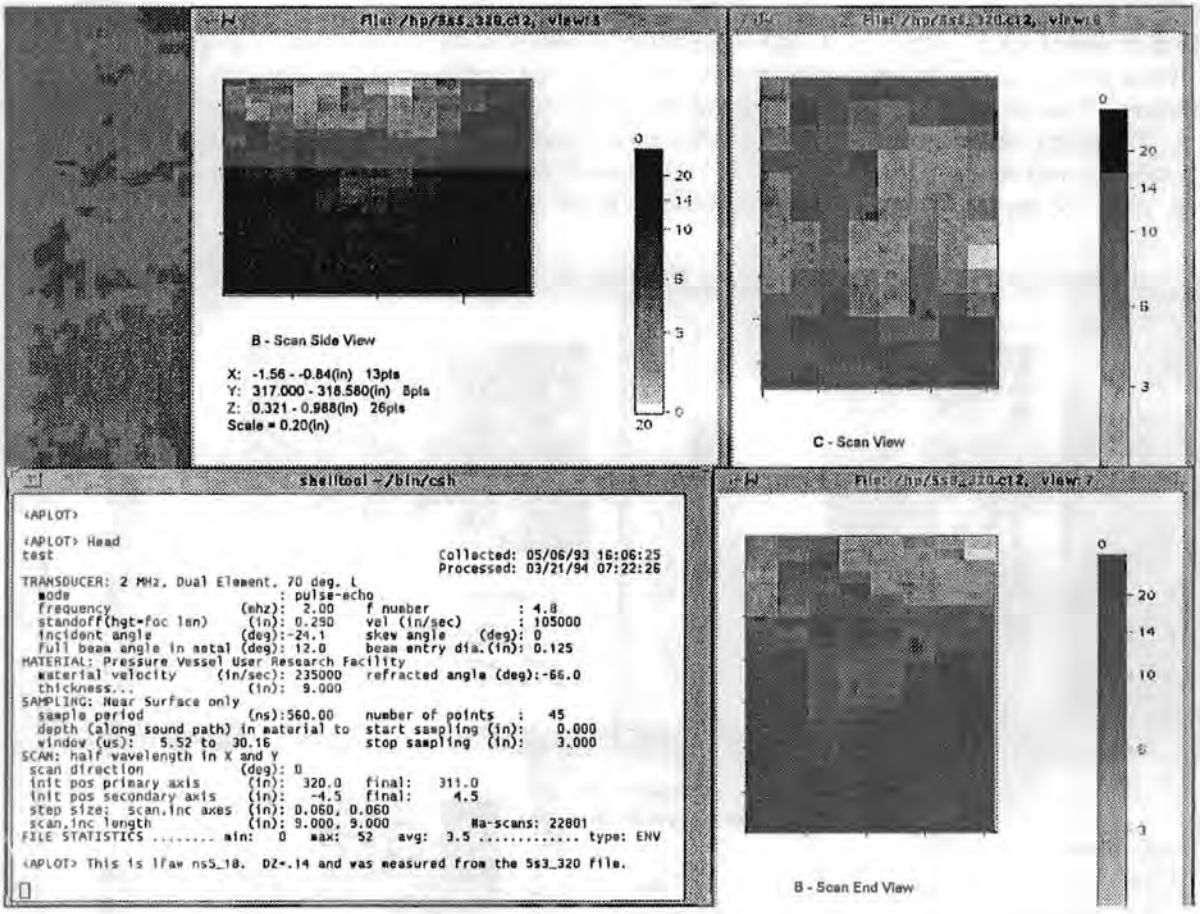

Figure A.20c - Planar indication #6 in the near surface base metal: mode 5

Figure A.21 shows planar indication #7 in the near surface base metal. This planar indication has a through-wall extent of 3 mm based on wave packet width. The detection was made in mode 4 where it had isolated TOF shape at a depth of 13 mm. There were no confirmations in other modes. The indication is characterized as planar based on lack of normal beam detection. There is no evidence of coin shape in the end view of mode 4. The length is 9 mm and was made to LOS in mode 4. The aspect ratio (length/depth) of this indication is 3 giving an orientation along the weld. The maximum amplitude-to-noise ratio is of medium range at 22 to 7. With an X coordinate of 32 mm, the indication is clearly in the base metal. With a Z coordinate of 13 mm, the indication is below the cladding by 4 mm.

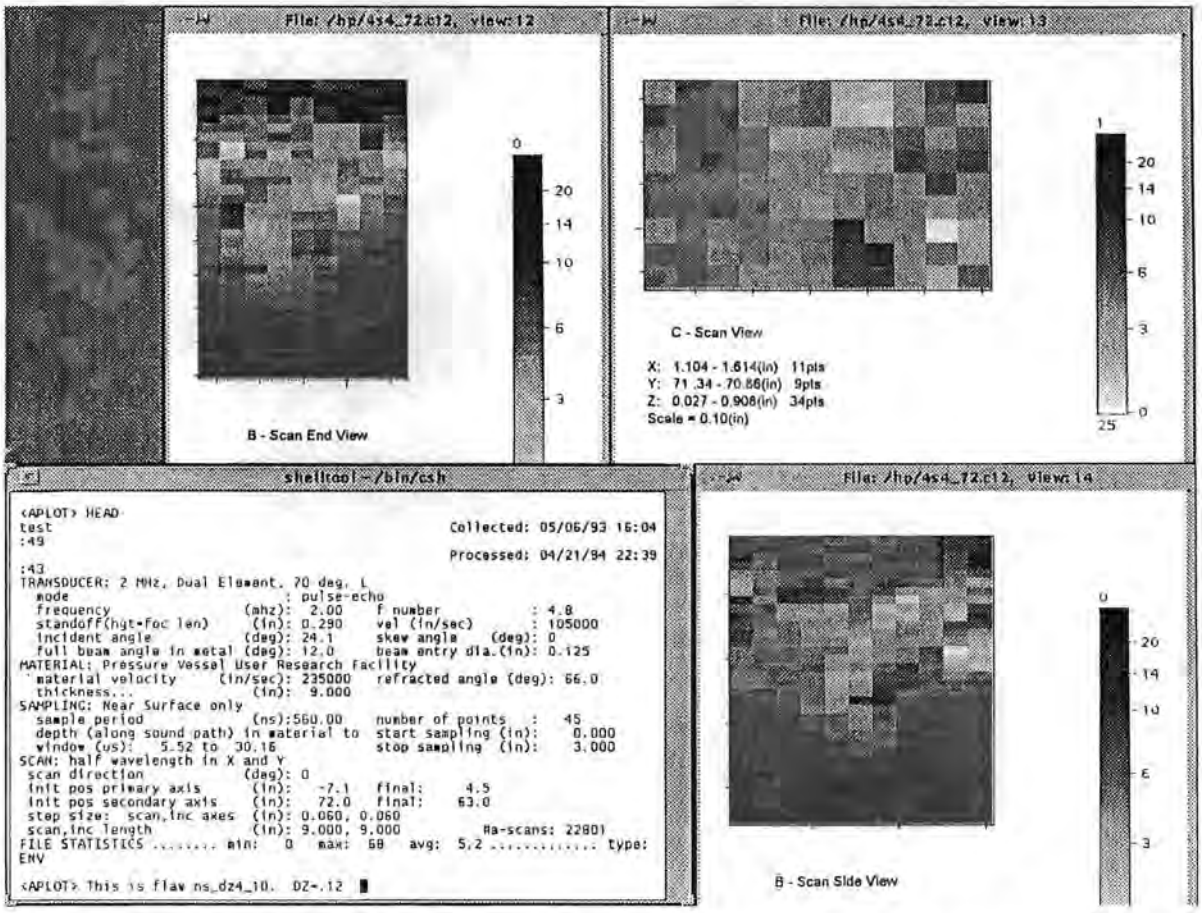

Figure A.21 - Planar indication #7 in the near surface base metal: mode 4

Figure A.22 shows planar indication #8 in the near surface base metal. This planar indication has a through-wall extent of 2.5 mm based on wave packet width. The detection was made in mode 3 where it had isolated TOF shape at a depth of 15 mm. There were no confirmations in other modes. The indication is characterized as planar based on lack of normal beam detection. There is no evidence of coin shape in the side view of mode 3. The width is 11 mm and was made to LOS in mode 3. The aspect ratio (width/depth) of this indication is 4 giving an orientation across the weld. The maximum amplitude-to-noise ratio is low at 14 to 7. With an X coordinate of -100 mm, the indication is clearly in the base metal. With a Z coordinate of 15 mm, the indication is clearly below the cladding.

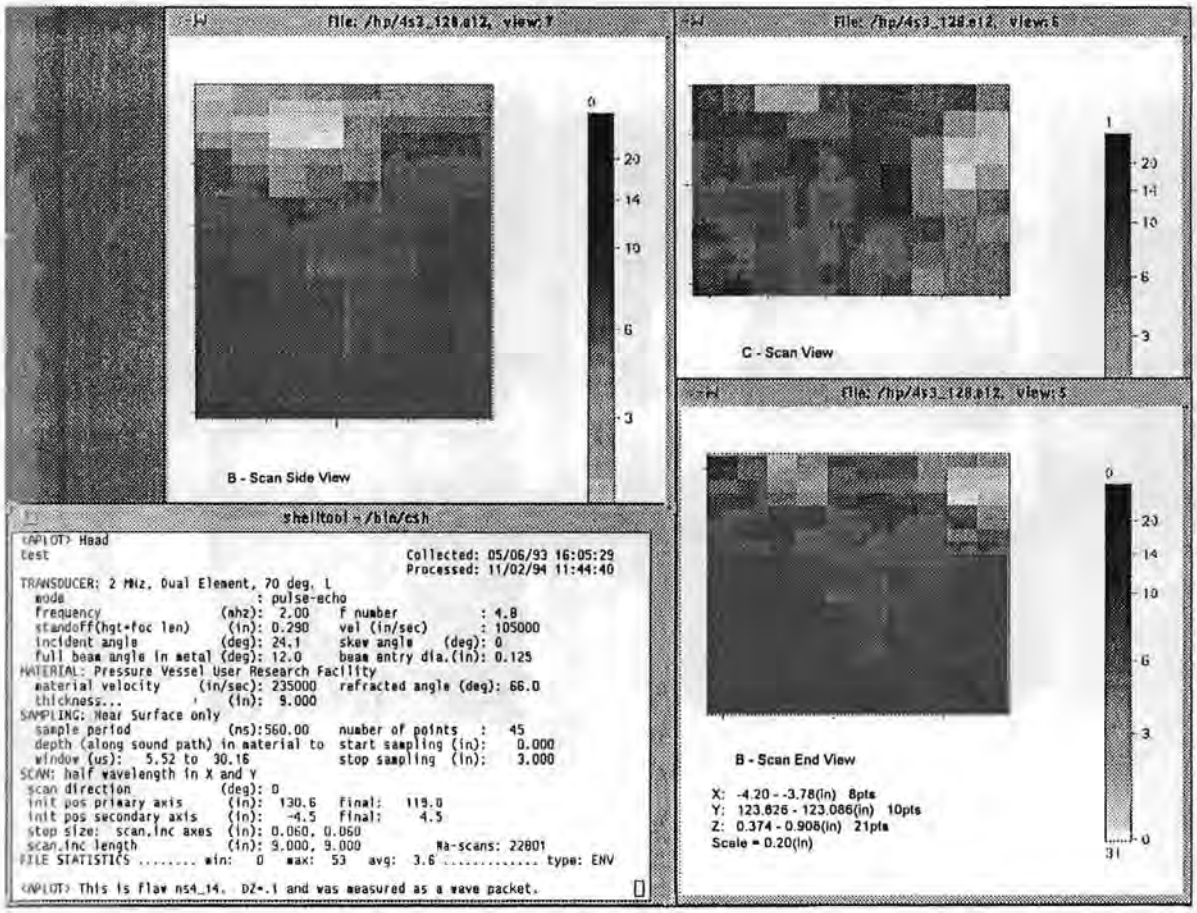

Figure A.22 - Planar indication #8 in the near surface base metal: mode 3

Figure A.23 shows planar indication #9 in the near surface base metal. This planar indication has a through-wall extent of 2.5 mm based on wave packet width. The detection was made in mode 3 where it had isolated TOF shape at a depth of 17 mm. There were no confirmations in other modes. The indication is characterized as planar based on lack of normal beam detection. There is no evidence of coin shape in the side view of mode 3. The width is 7 mm and was made to LOS in mode 3. The aspect ratio (width/depth) of this indication is 2.8 giving an orientation across the weld. The maximum amplitude-to-noise ratio is of medium range at 27 to 7. With an X coordinate of -102 mm, the indication is clearly in the base metal. With a Z coordinate of 17 mm, the indication is clearly below the cladding.

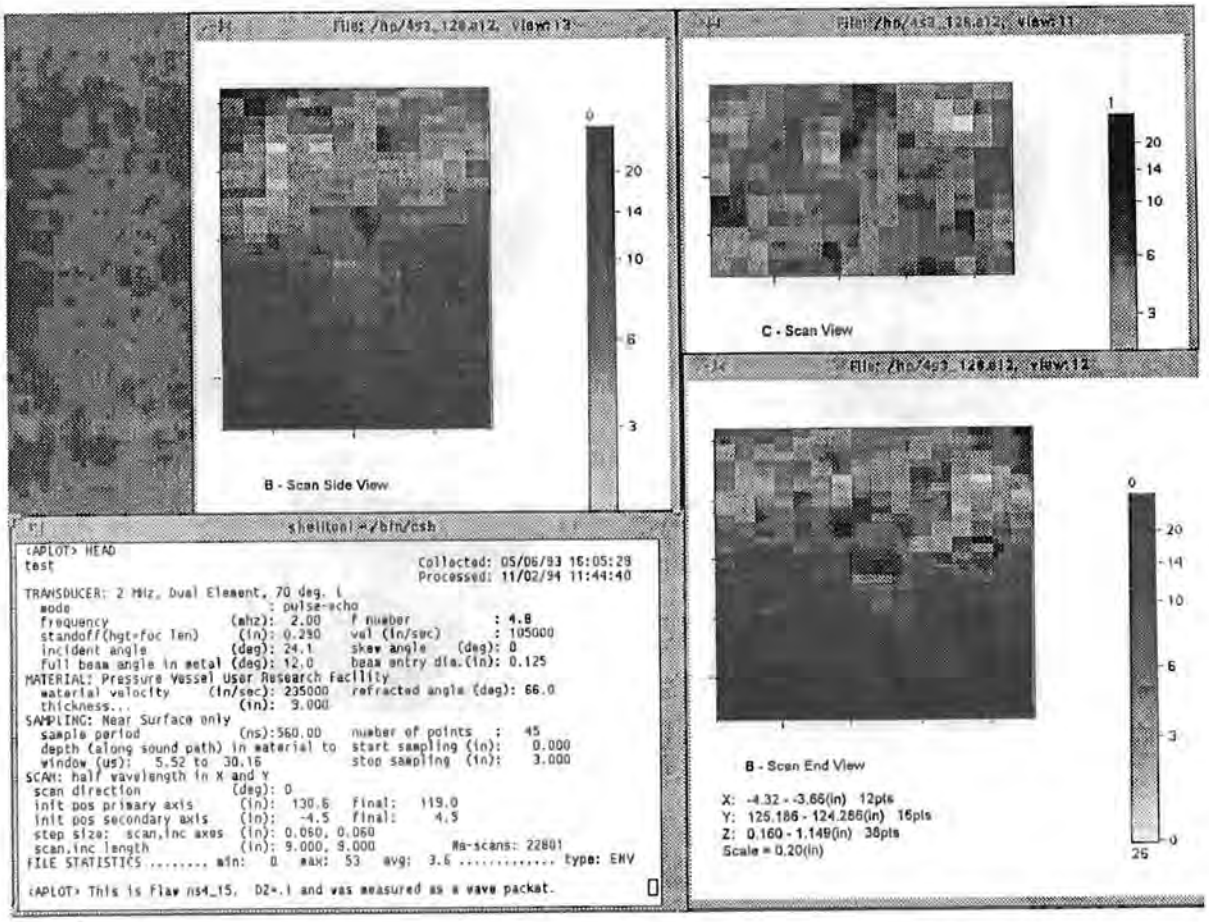

Figure A.23 - Planar indication #9 in the near surface base metal: mode 3

Figure A.24 shows planar indication #10 in the near surface base metal. This planar indication has a through-wall extent of 2.5 mm based on wave packet width. The detection was made in mode 2 where it had isolated TOF shape at a depth of 13 mm. There were no confirmations in other modes. The indication is characterized as planar based on lack of normal beam detection. There is no evidence of coin shape in the end view of modes 2. The length is 7 mm and was made to LOS in mode 2. The aspect ratio (length/depth) of this indication is 2.8 giving an orientation along the weld. The maximum amplitude-to-noise ratio is of medium range at 24 to 10. With an X coordinate of -18 mm, the indication is in the base metal, possibly in the HAZ. With a Z coordinate of 13 mm, the indication is below the cladding by 4 mm.

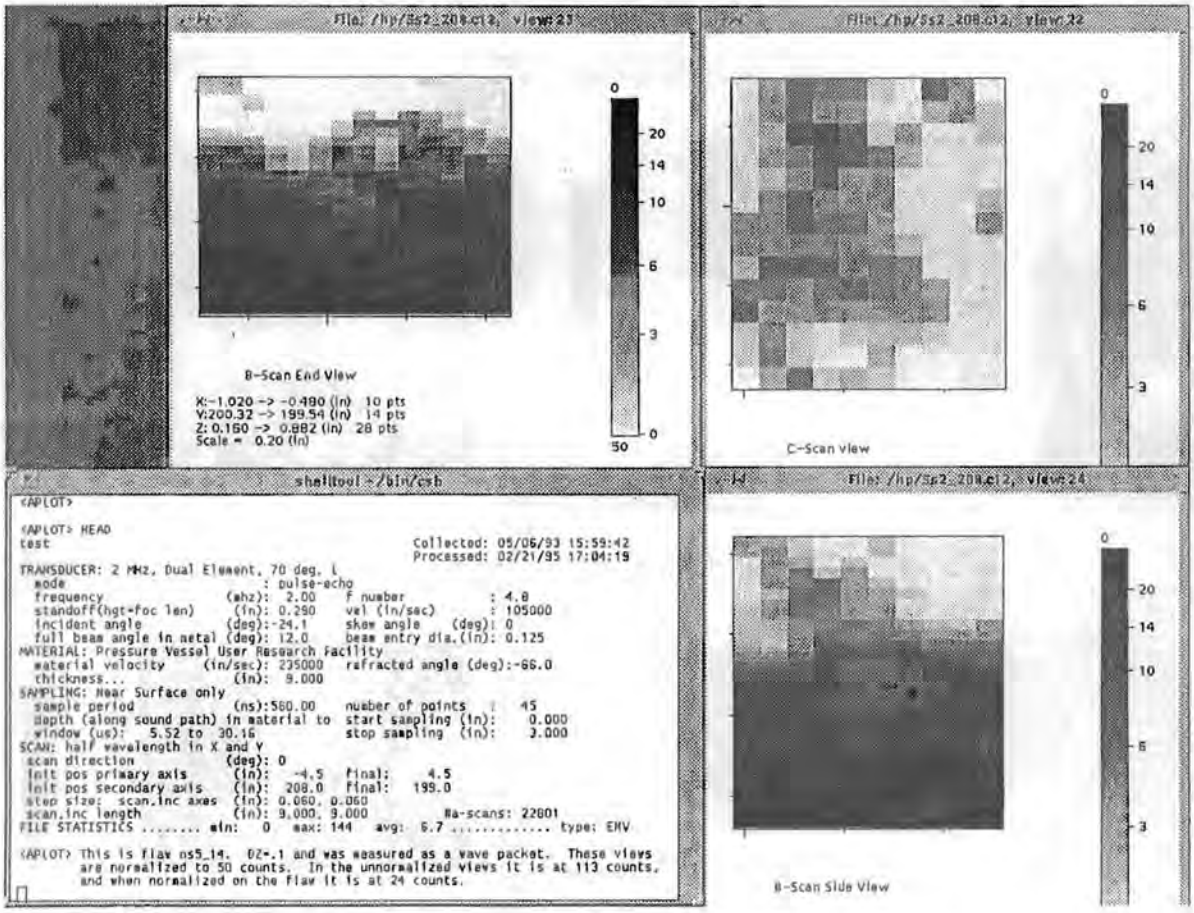

Figure A.24 - Planar indication #10 in the near surface base metal: mode 2

Figure A.25 shows planar indication #11 in the near surface base metal. This planar indication has a through-wall extent of 2.5 mm based on wave packet width. The detection was made in mode 4 where it had isolated TOF shape at a depth of 15 mm. The TOF shape may be artificial do to the limits of the scanning aperture; the shape quality is poor for this indication. There were no confirmations in other modes. The indication is characterized as planar based on lack of normal beam detection. There is no evidence of coin shape in the end view of mode 4. The length is 15 mm and was made to LOS in mode 4. The aspect ratio (length/depth) of this indication is 6 giving an orientation along the weld. The maximum amplitude-to-noise ratio is of medium range at 15 to 6. With an X coordinate of 20 mm, the indication is in the base metal. With a Z coordinate of 15 mm, the indication is clearly below the cladding.

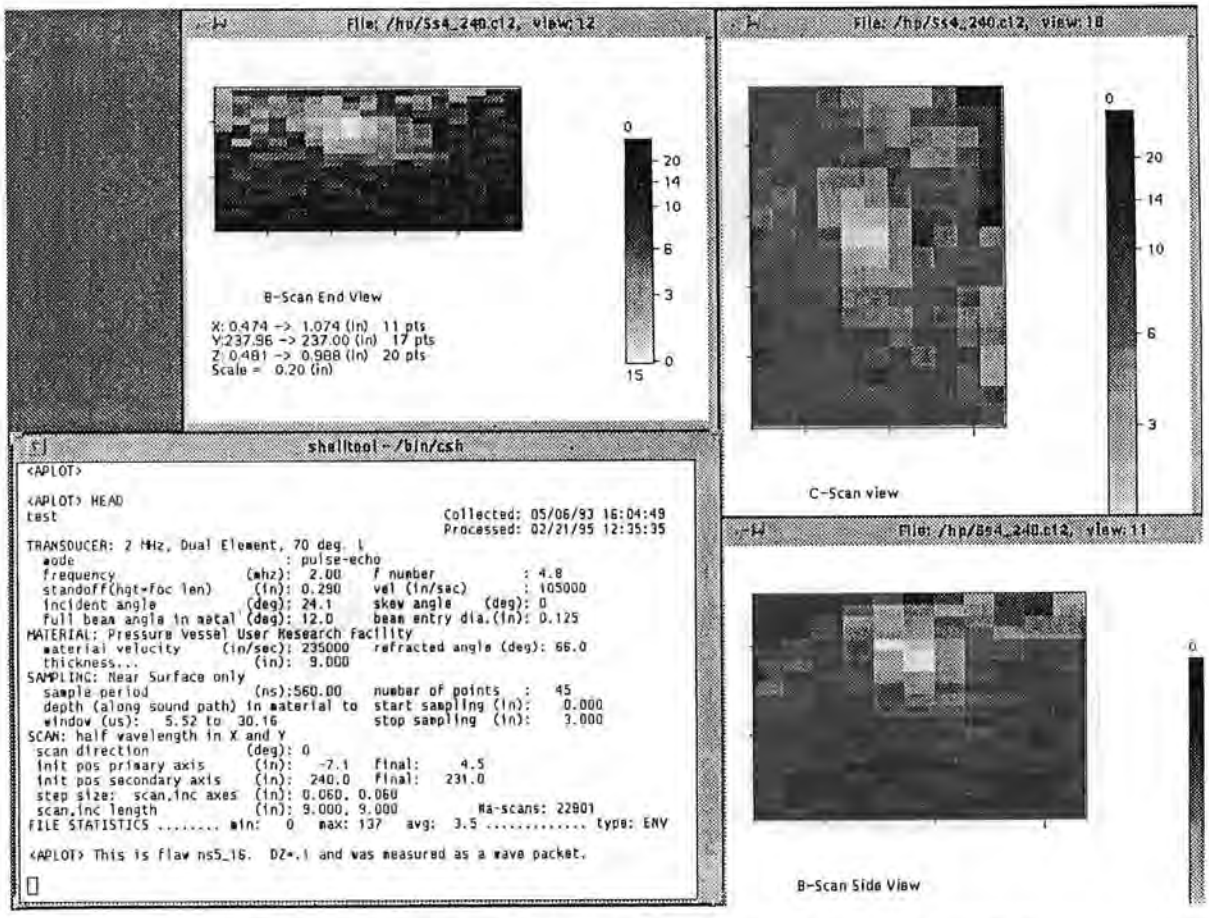

Figure A.25 - Planar indication #11 in the near surface base metal: mode 4

Figure A.26 shows planar indication #12 in the near surface base metal. This planar indication has a through-wall extent of 2.5 mm based on wave packet width. The detection was made in mode 8 where it had isolated TOF shape at a depth of 19 mm. There were no confirmations in other modes. The indication is characterized as planar based on lack of normal beam detection. There is some evidence of coin shape in the end view of mode 8. The length is 11 mm and was made to LOS in mode 8. The aspect ratio (length/depth) of this indication is 4 giving an orientation along the weld. The maximum amplitude-to-noise ratio is high at 216 to 45. With an X coordinate of 113 mm, the indication is clearly in the base metal. With a Z coordinate of 19 mm, the indication is clearly below the cladding.

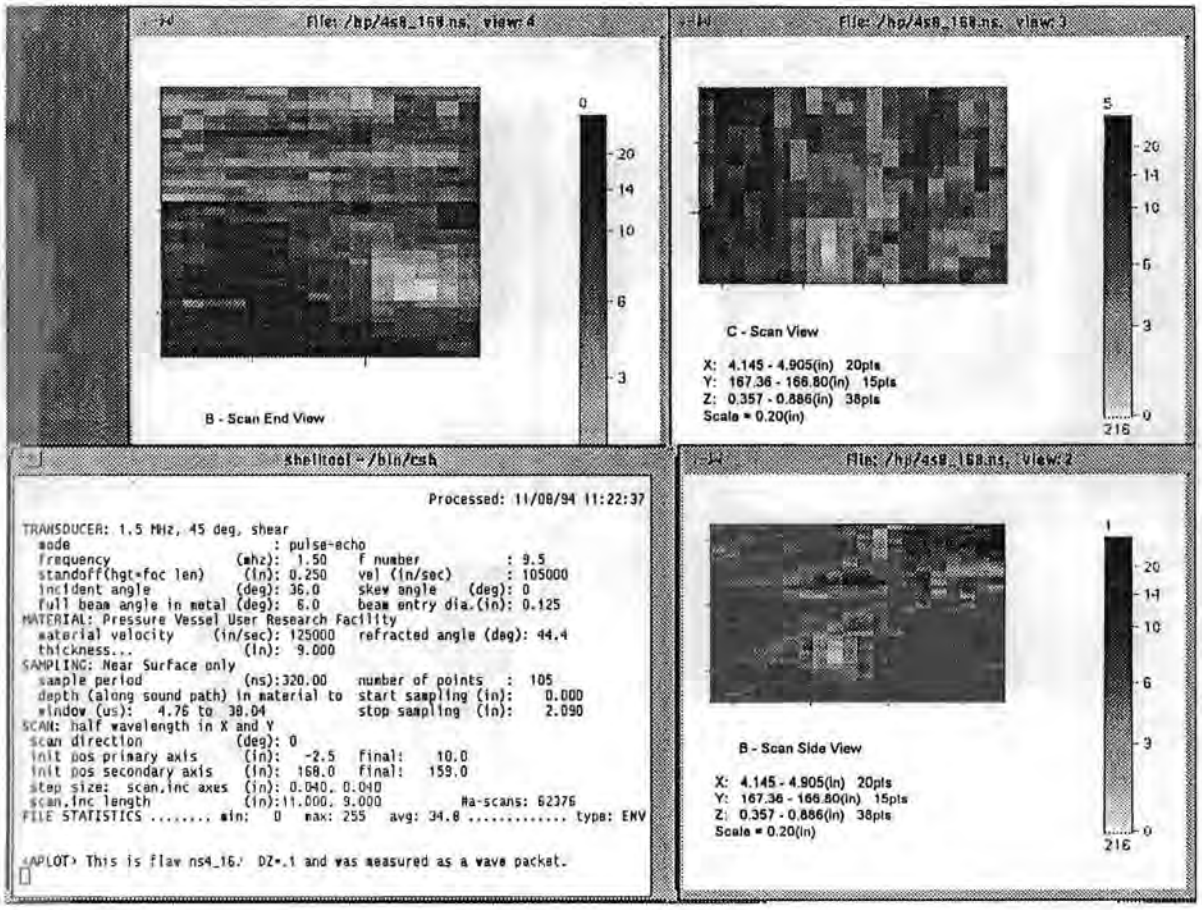

Figure A.26 - Planar indication #12 in the near surface base metal: mode 8

Figure A.27 shows planar indication #13 in the near surface base metal. This planar indication has a through-wall extent of 2.3 mm based on wave packet width, possibly 1.6 mm based on ring around pattern. The detection was made in mode 8 where it displayed TOF shape at a depth of 14 mm. The shape quality is good for this indication. There were no confirmations in other modes. The indication is characterized as planar based on lack of normal beam detection. There is no evidence of coin shape in the end view of mode 8. The length is 10 mm and was made to LOS in mode 8. The aspect ratio (length/depth) of this indication is 6 giving an orientation along the weld. The maximum amplitude-to-noise ratio is of medium range at 154 to 50. With an X coordinate of 142 mm, the indication is clearly in the base metal. With a Z coordinate of 14 mm, the indication is clearly below the cladding.

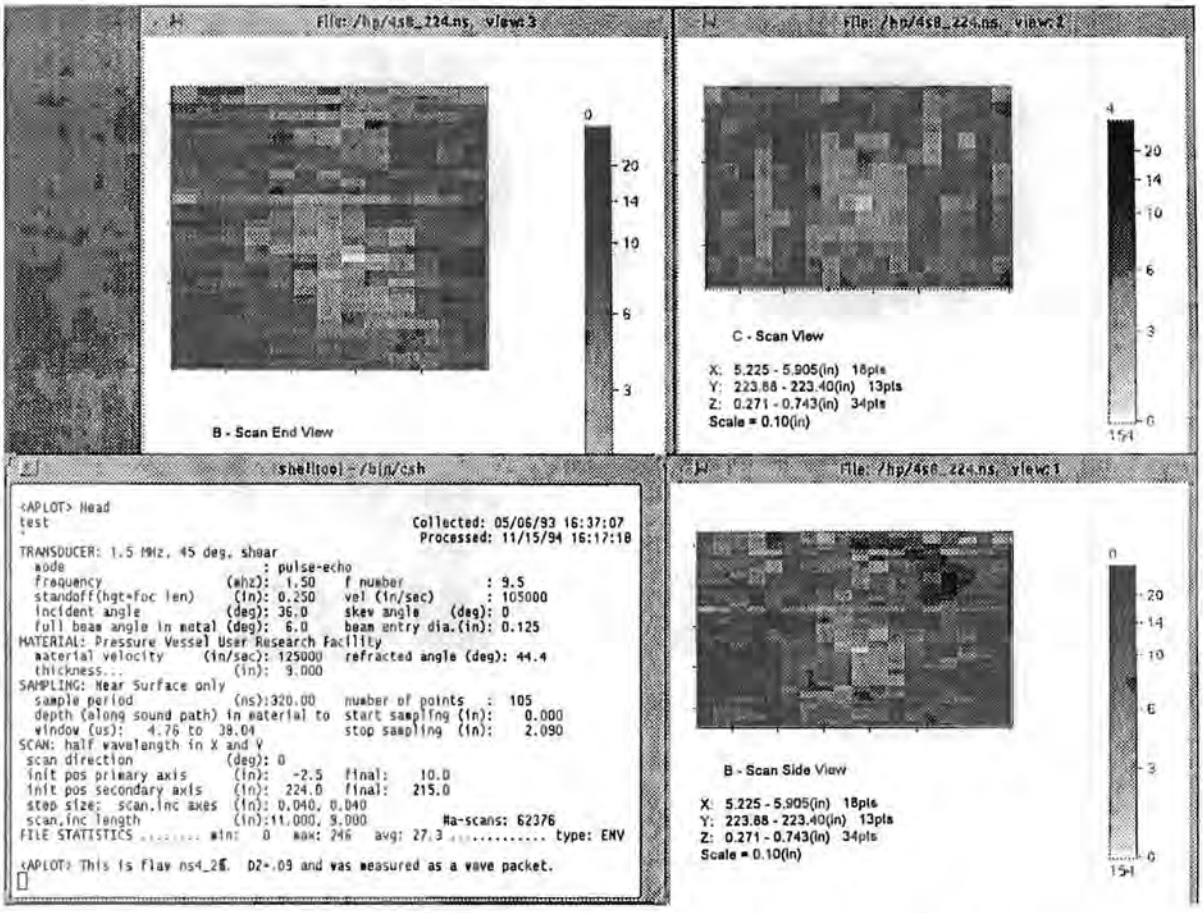

Figure A.27 - Planar indication #13 in the near surface base metal: mode 8

Figure A.28 shows planar indication #14 in the near surface base metal. This planar indication has a through-wall extent of 2.3 mm based on wave packet width. The detection was made in mode 8 where it had isolated TOF shape at a depth of 20 mm. The shape quality is good for this indication. There were no confirmations in other modes. The indication is characterized as planar based on lack of normal beam detection. There is some evidence of coin shape in the end view of mode 8. The length is 10 mm and was made to LOS in mode 8. The aspect ratio (length/depth) of this indication is 4 giving an orientation along the weld. The maximum amplitude-to-noise ratio is of medium range at 143 to 45. With an X coordinate of 43 mm, the indication is clearly in the base metal. With a Z coordinate of 20 mm, the indication is clearly below the cladding.

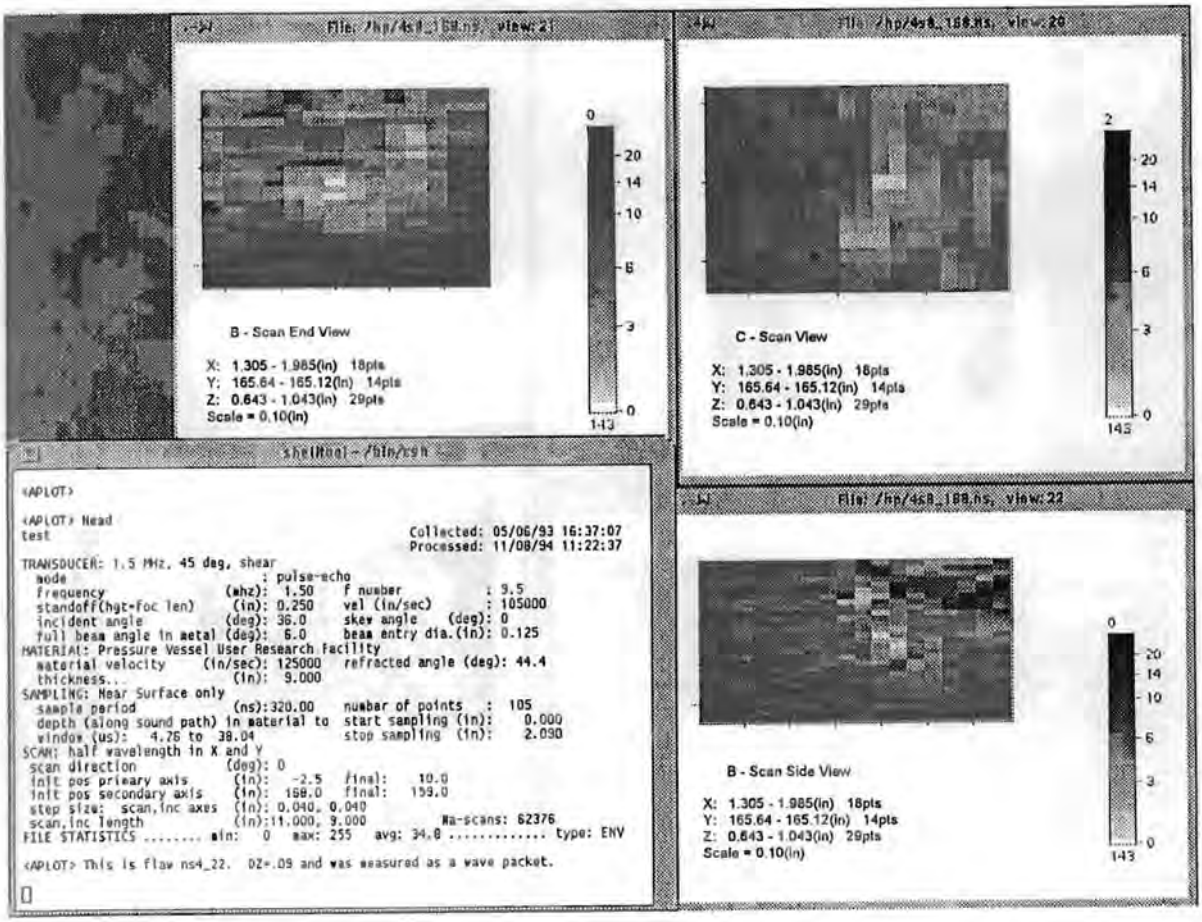

Figure A.28 - Planar indication #14 in the near surface base metal: mode 8

Figure A.29 shows planar indication #15 in the near surface base metal. This planar indication has a through-wall extent of 2.3 mm based on wave packet width. The detection was made in mode 2 where it had isolated TOF shape at a depth of 17 mm. The shape quality is good for this indication. There were no confirmations in other modes. The indication is characterized as planar based on lack of normal beam detection. There is no evidence of coin shape in the end view of mode 2. The length is 14 mm and was made to LOS in mode 2. The aspect ratio (length/depth) of this indication is 6 giving an orientation along the weld. The maximum amplitude-to-noise ratio is of medium range at 16 to 7. With an X coordinate of -30 mm, the indication is clearly in the base metal. With a Z coordinate of 17 mm, the indication is clearly below the cladding.

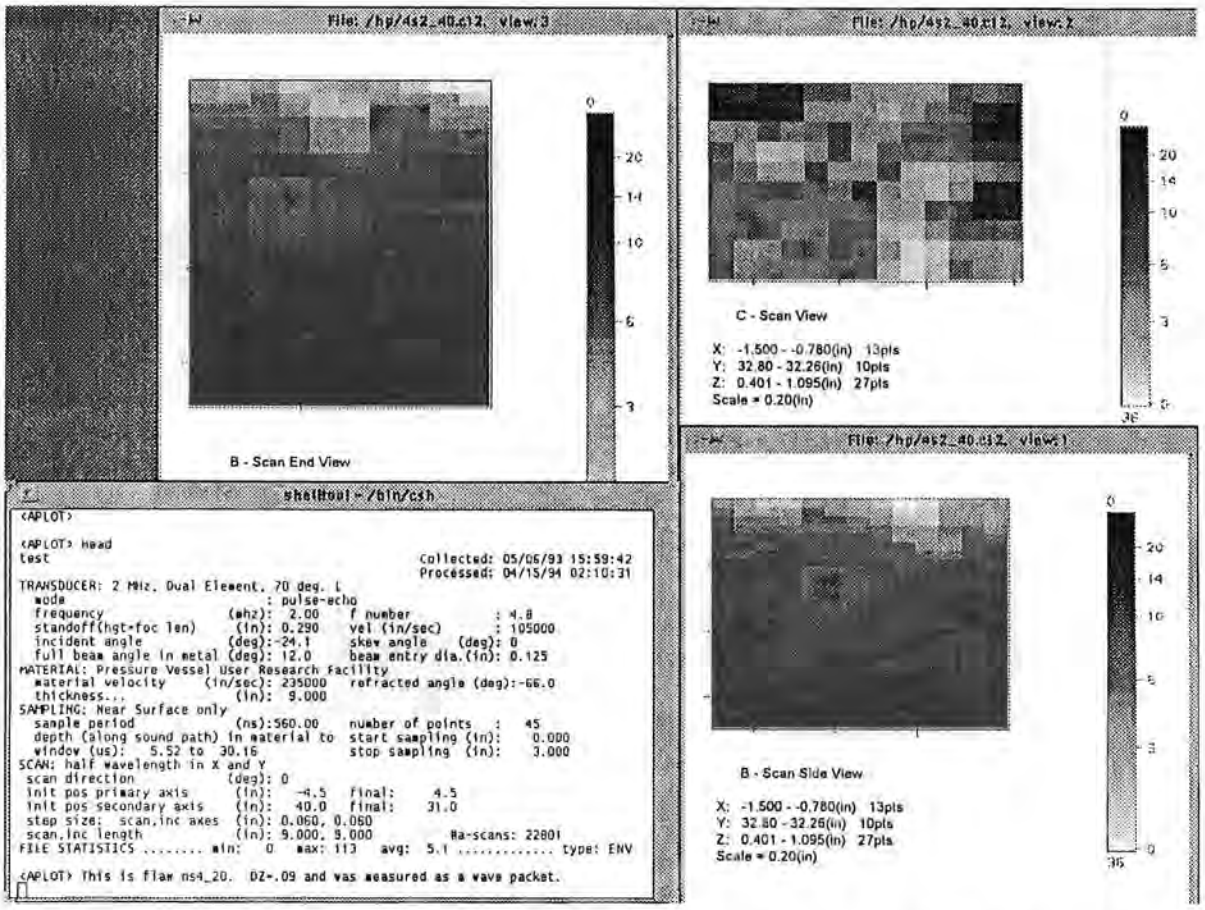

Figure A.29 - Planar indication #15 in the near surface base metal: mode 2

Figure A.30 shows planar indication #16 in the near surface base metal. This planar indication has a through-wall extent of 2.3 mm based on wave packet width. The detection was made in mode 3 where it had isolated TOF shape at a depth of 18 mm. The TOF shape may be artificial because of the limits of the scanning aperture; the shape quality is fair for this indication. There were no confirmations in other modes. The indication is characterized as planar based on lack of normal beam detection. There is no evidence of coin shape in the end view of mode 3. The width is 7 mm and was made to LOS in mode 3. The aspect ratio (width/depth) of this indication is 3 giving an orientation across the weld. The maximum amplitude-to-noise ratio is low at 12 to 6. With an X coordinate of -104 mm, the indication is clearly in the base metal. With a Z coordinate of 18 mm, the indication is clearly below the cladding.

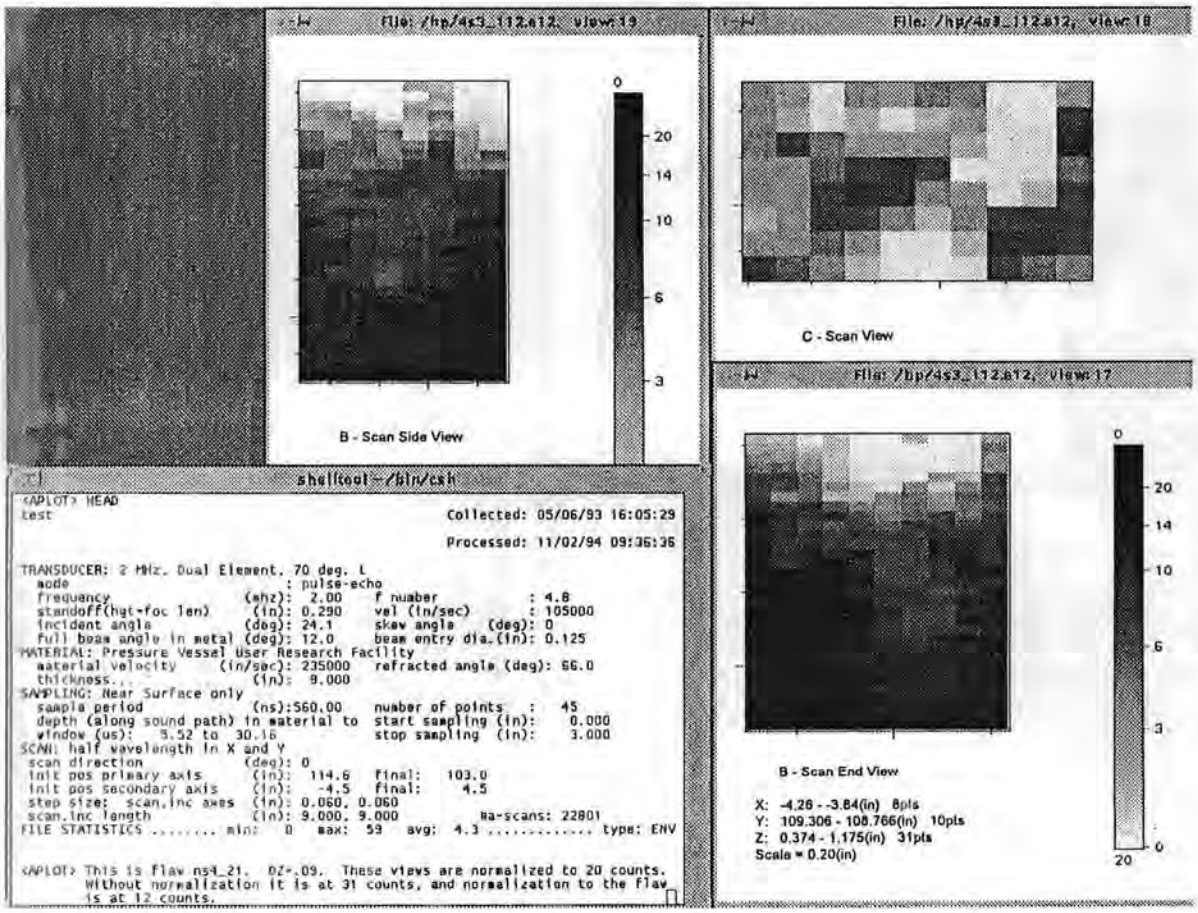

Figure A.30 - Planar indication #16 in the near surface base metal: mode 3

Figure A.31 shows planar indication #17 in the near surface base metal. This planar indication has a through-wall extent of 2.3 mm based on wave packet width. The detection was made in mode 8 where it had isolated TOF shape at a depth of 20 mm. The shape quality is poor for this indication. There were no confirmations in other modes. The indication is characterized as planar based on lack of normal beam detection. There is no evidence of coin shape in the end view of mode 8. The length is 8 mm and was made to LOS in mode 8. The aspect ratio (length/depth) of this indication is 3 giving an orientation along the weld. The maximum amplitude-to-noise ratio is of medium range at 130 to 50. With an X coordinate of 46 mm, the indication is clearly in the base metal. With a Z coordinate of 20 mm the indication is clearly below the cladding.

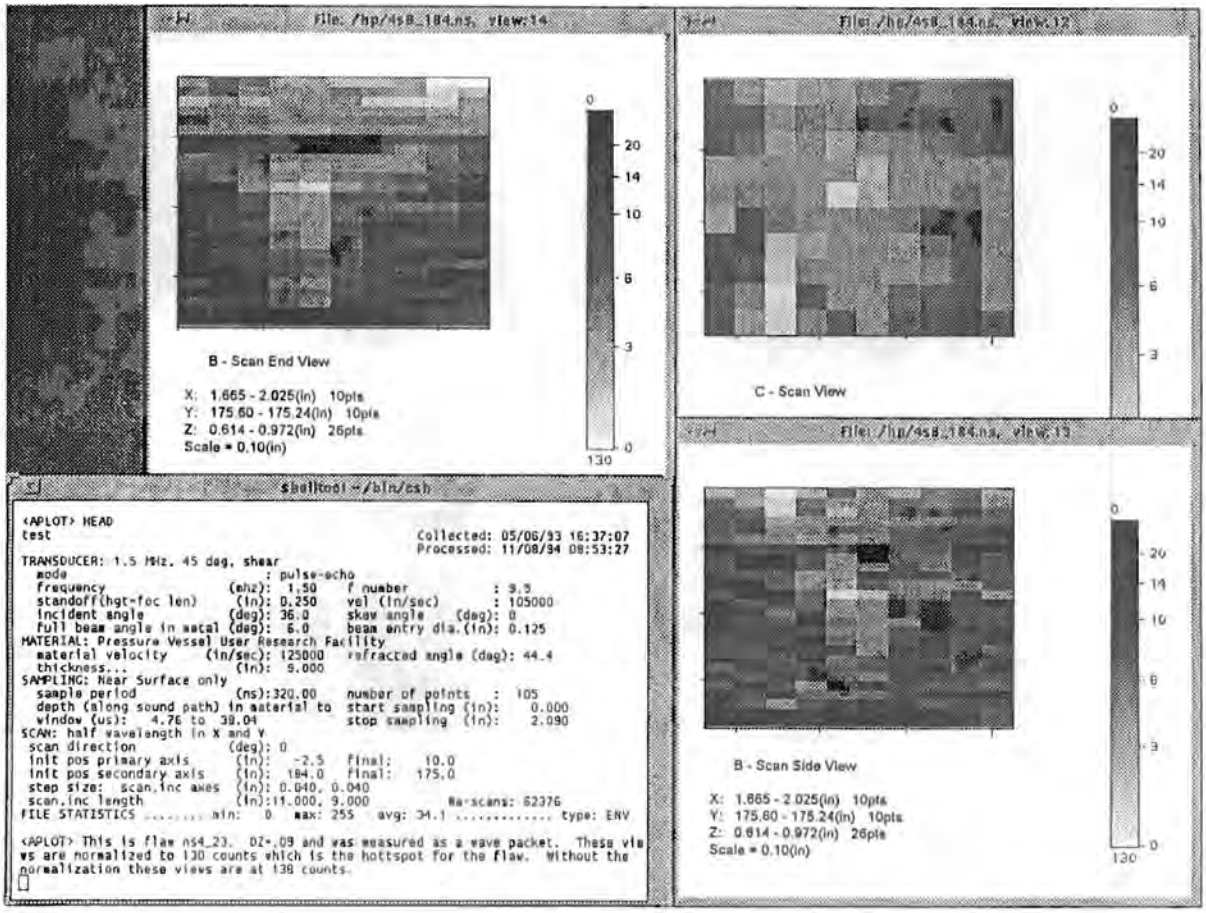

Figure A.31 - Planar indication #17 in the near surface base metal: mode 8

Figure A.32 shows planar indication #18 in the near surface base metal. This planar indication has a through-wall extent of 2 mm based on wave packet width. The detection was made in mode 7 where it had isolated TOF shape at a depth of 22 mm. The shape quality is fair for this indication. There were no confirmations in other modes. The indication is characterized as planar based on lack of normal beam detection. There is no evidence of coin shape in the side view of mode 7. The width is 11 mm and was made to LOS in mode 7. The aspect ratio (width/depth) of this indication is 6 giving an orientation across the weld. The maximum amplitude-to-noise ratio is of medium range at 85 to 30. With an X coordinate of 39 mm, the indication is clearly in the base metal. The Z coordinate of 22 mm shows that the indication is below the cladding.

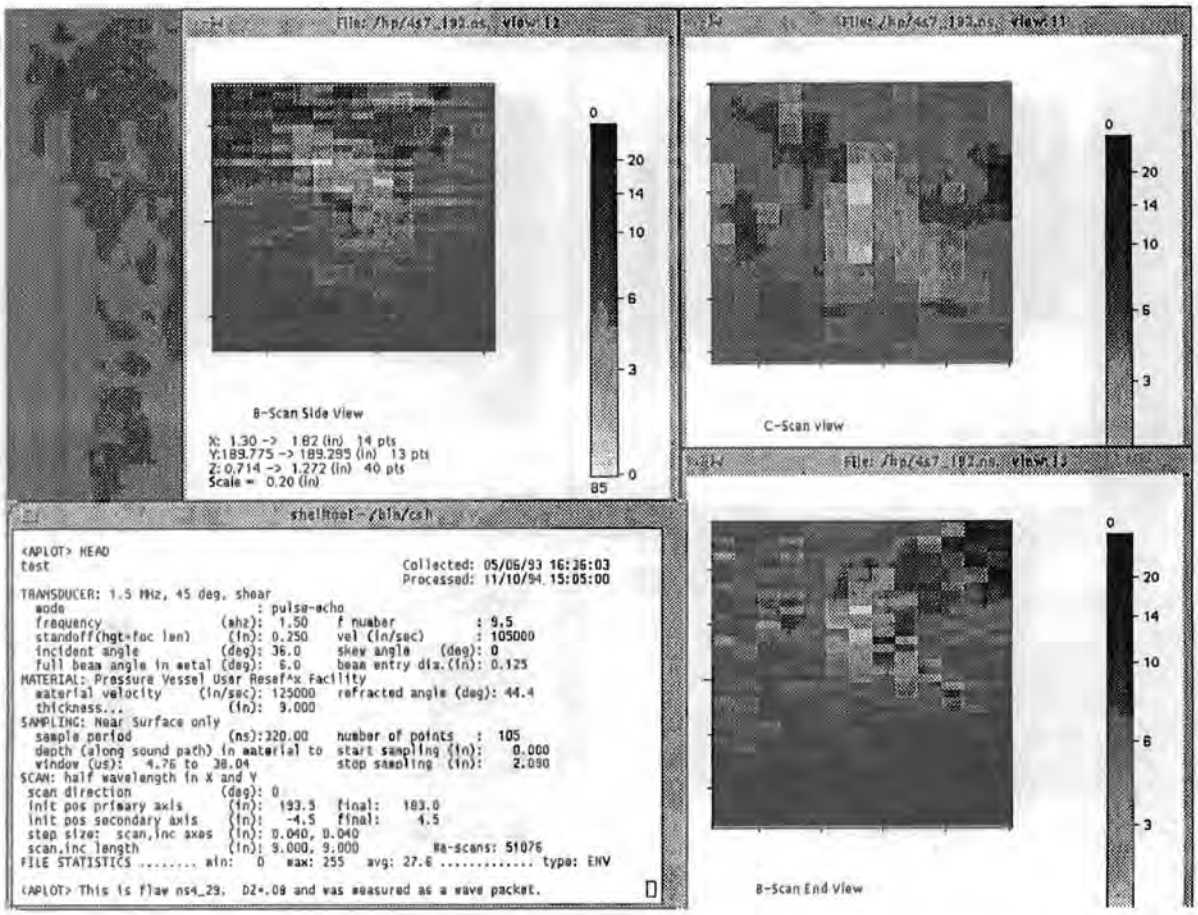

Figure A.32 - Planar indication #18 in the near surface base metal: mode 7

Figure A.33 shows planar indication #19 in the near surface base metal. This planar indication has a through-wall extent of 2 mm based on wave packet width. The detection was made in mode 7 where it had isolated TOF shape at a depth of 25 mm. The shape quality for this indication is poor and broken up, implying that more than one small flaw may be present There were no confirmations in other modes. The indication is characterized as planar based on lack of normal beam detection or detection of orthogonal modes. There is no evidence of coin shape in the side view of mode 7. The width is 16 mm and was made to LOS in mode 7. The aspect ratio (width/depth) of this indication is 8 which tends to confirm more than one small flaw. The maximum amplitude-to-noise ratio is of medium range at 91 to 40. With an X coordinate of 106 mm, the indication is clearly in the base metal. With a Z coordinate of 25 mm, the indication is clearly below the cladding.

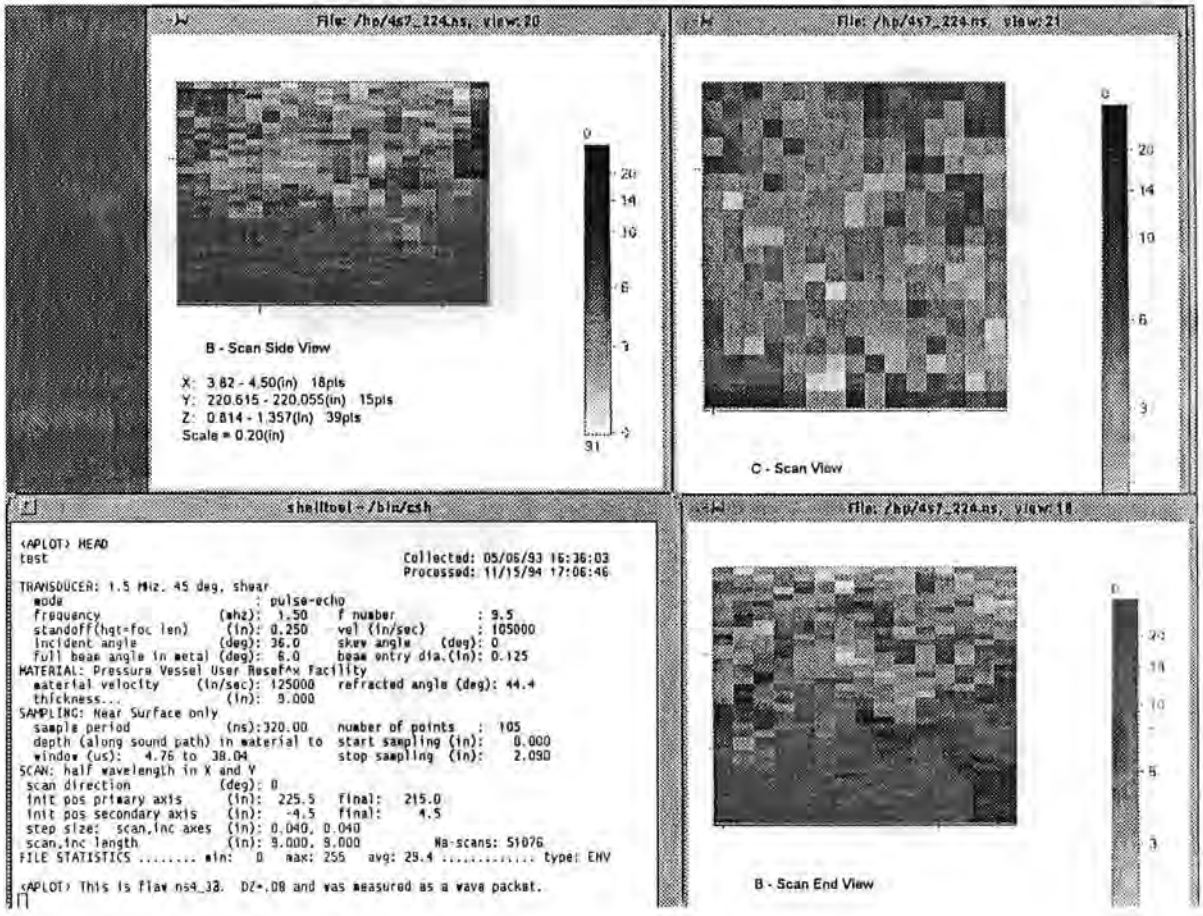

Figure A.33 - Planar indication #19 in the near surface base metal: mode 7

Figure A.34 shows planar indication #20 in the near surface base metal. This planar indication has a through-wall extent of 2 mm based on wave packet width. The detection was made in mode 3 where it had isolated TOF shape at a depth of 12 mm. The shape quality is fair for this indication. There were no confirmations in other modes. The indication is characterized as planar based on lack of detection in normal beam or orthogonal modes. There is no evidence of coin shape in the side view of mode 3. The width is 8 mm and was made to LOS in mode 3. The aspect ratio (width/depth) of this indication is 4 giving an orientation across the weld. The maximum amplitude-to-noise ratio is of medium range at 24 to 8. With an X coordinate of 81 mm, the indication is clearly in the base metal. With a Z coordinate of 12 mm, the indication is below the cladding by 3 mm.

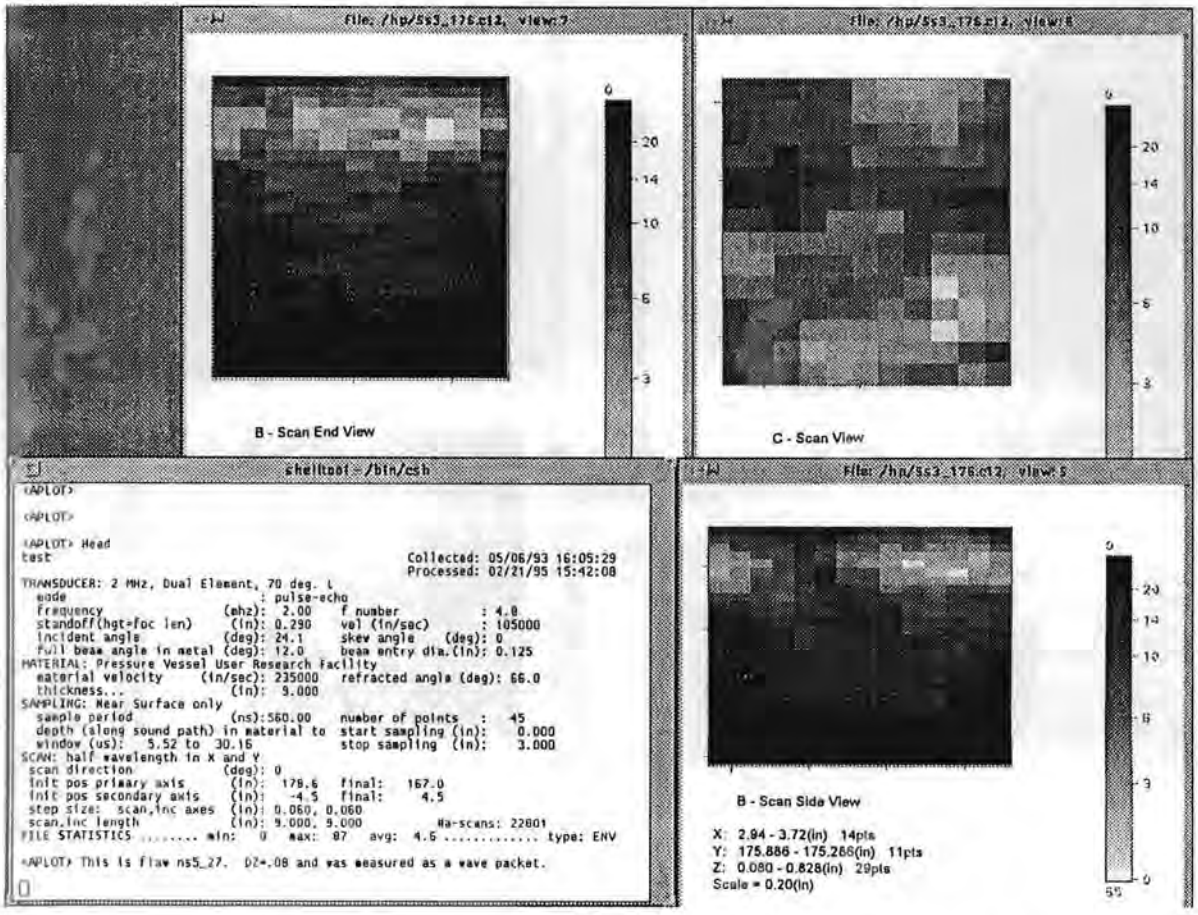

Figure A.34 - Planar indication #20 in the near surface base metal: mode 3

Figures A.35a-b show planar indication #21 in the near surface base metal. This planar indication has a through-wall extent of 1.5 mm based on wave packet width. The detections were made in modes 2 and 4 where they had isolated TOF shape at a depth of 8 mm. The TOF shape quality for this indication is fair. The indication is characterized as planar based on lack of normal beam detection. There is good evidence of coin shape in the end view of mode 4. The length is 8 mm and was made to LOS in mode 4. The aspect ratio (length/depth) of this indication is 5 giving an orientation along the weld. The maximum amplitude-to-noise ratio is high at 143 to 25. With an X coordinate of -24 mm, the indication is clearly in the base metal. The Z coordinate of 8 mm shows that the indication is in the base metal, possibly in the cladding.

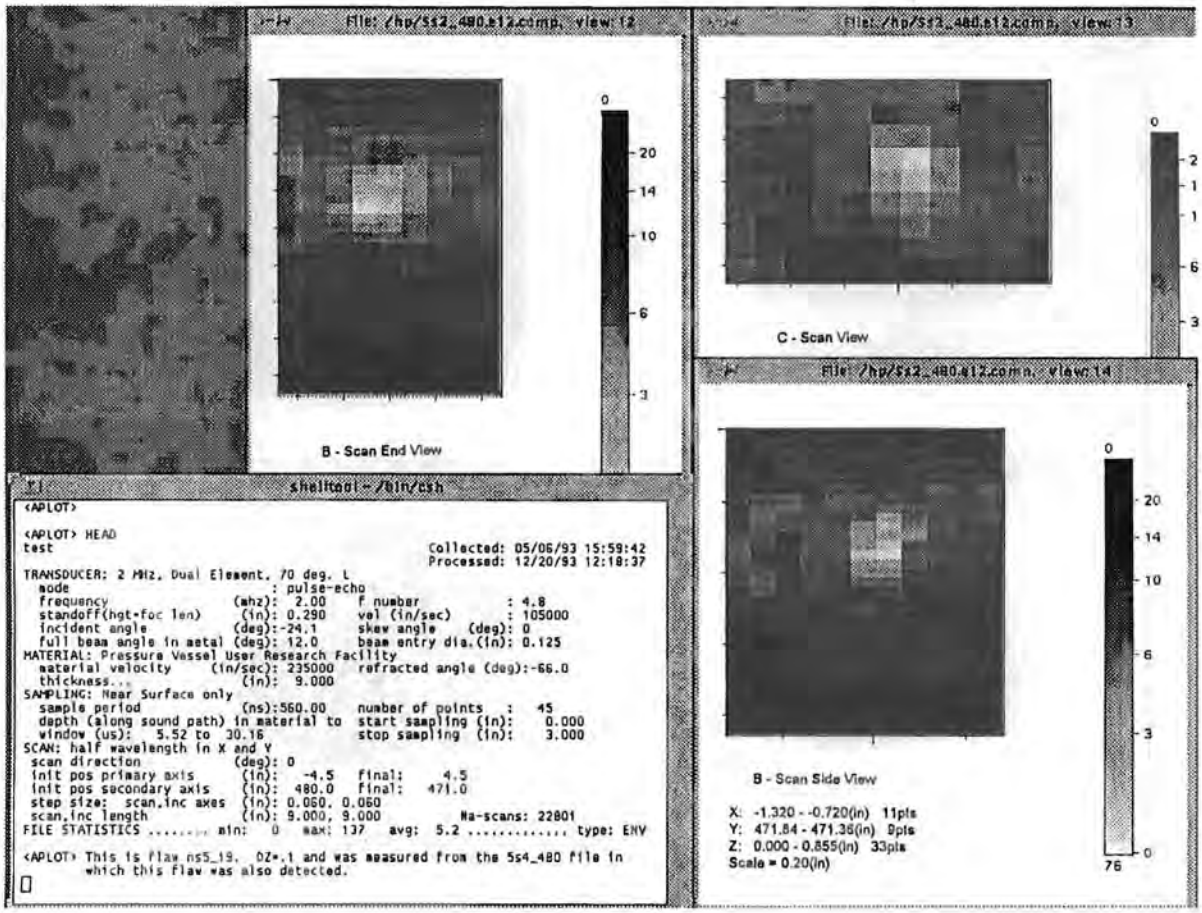

Figure A.35a - Planar indication #21 in the near surface base metal: mode 2

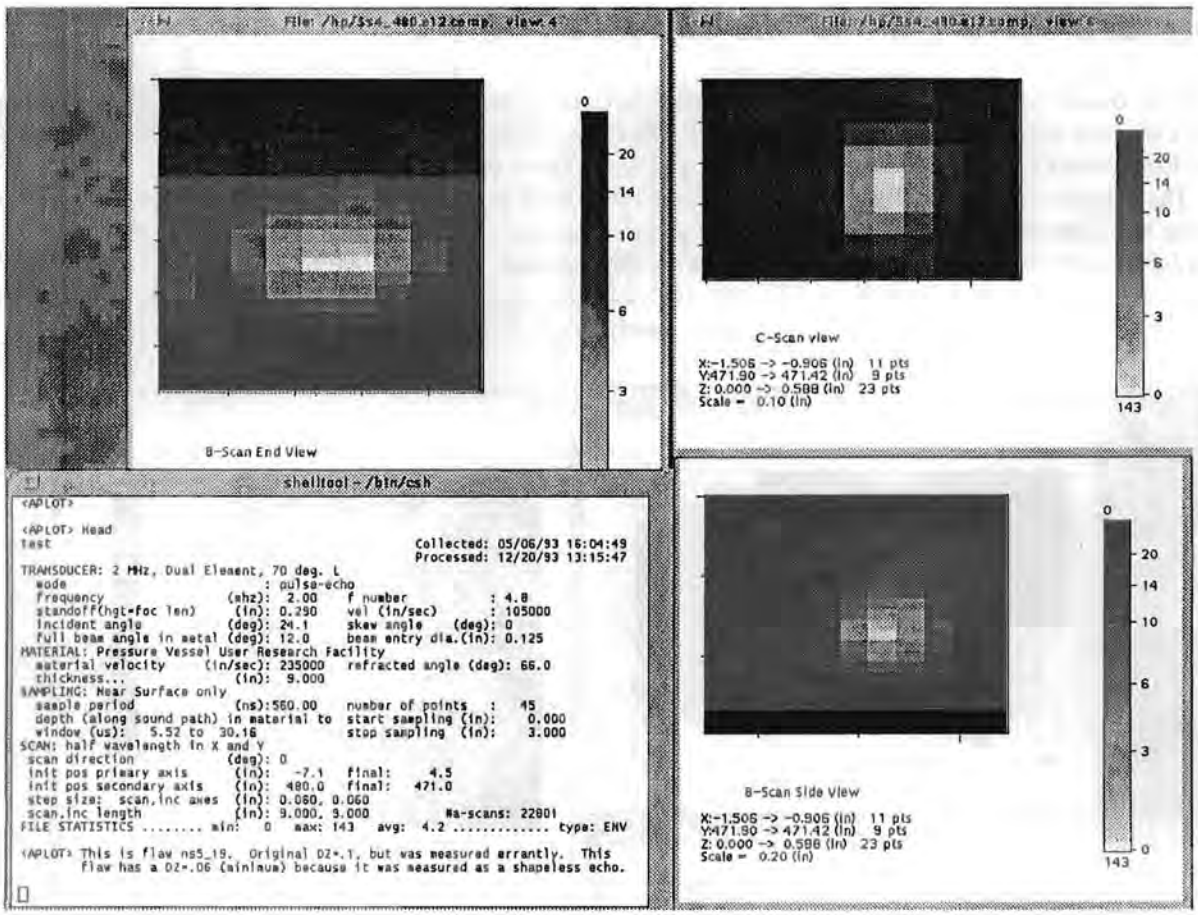

Figure A.35b - Planar indication #21 in the near surface base metal: mode 4

Volumetric Indications in the Near Surface Base Metal

Figures A.36a-b show volumetric indication #1 in the near surface base metal. This volumetric indication has a through-wall extent of 6 mm based LOS in a cloud like pattern. The detection was made in mode 9 where it failed to display TOF shape but looked more cloud like in nature at a depth of 20 mm. There was a confirmation in mode 1 at a depth of 19 mm. The indication is characterized as volumetric based on normal beam detection. There is no evidence of coin shape in the side view of mode 9. The length is 6 mm and was made to LOS in mode 1. The width is 7 mm and was made to LOS in mode 9. The aspect ratio (width/depth) of this indication is 1.2, and the length-to-depth ratio is 1.0. The maximum amplitude-to-noise ratio is low at 88 to 40. With an X coordinate of 28 mm, the indication is clearly in the base metal. With a Z coordinate of 20 mm, the indication is clearly below the cladding.

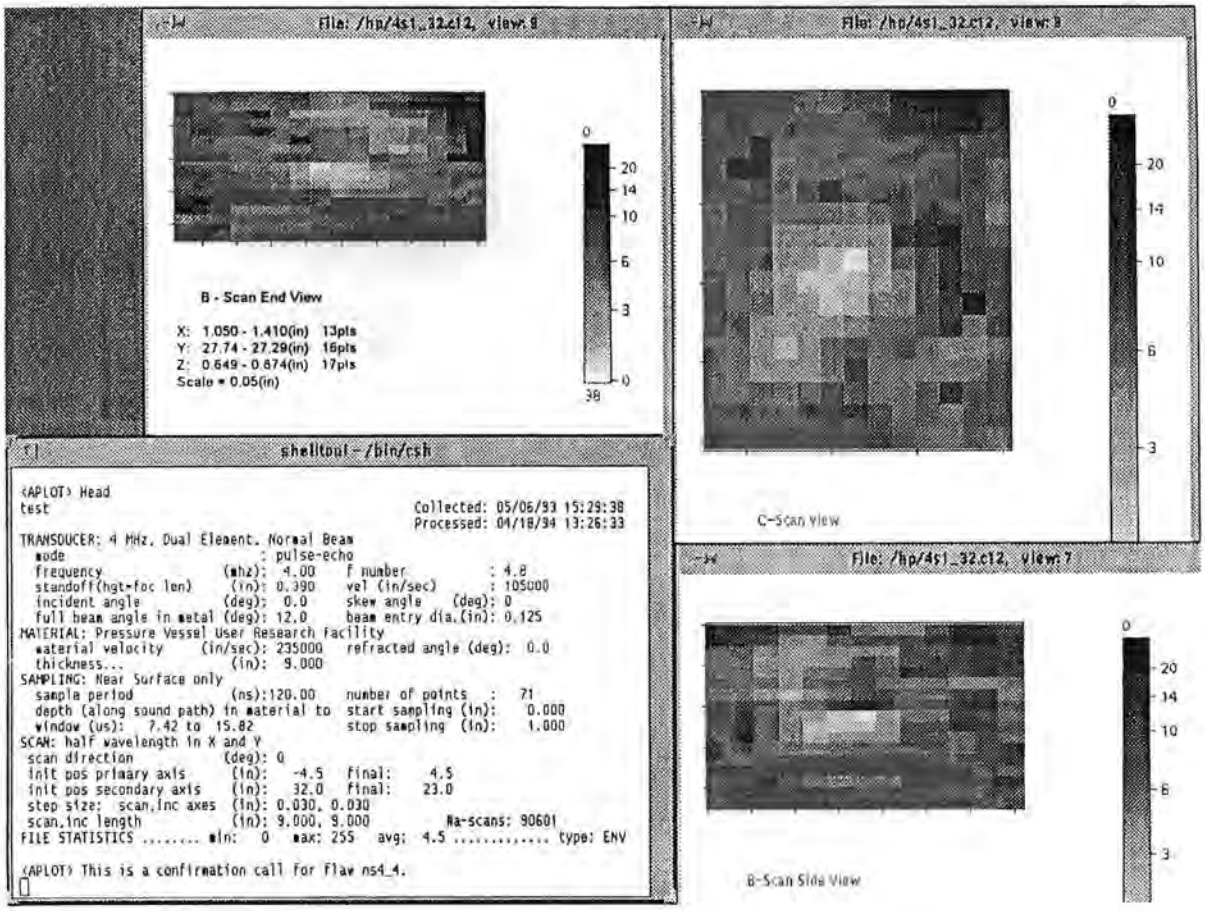

Figure A.36a - Volumetric indication #1 in the near surface base metal: mode 1

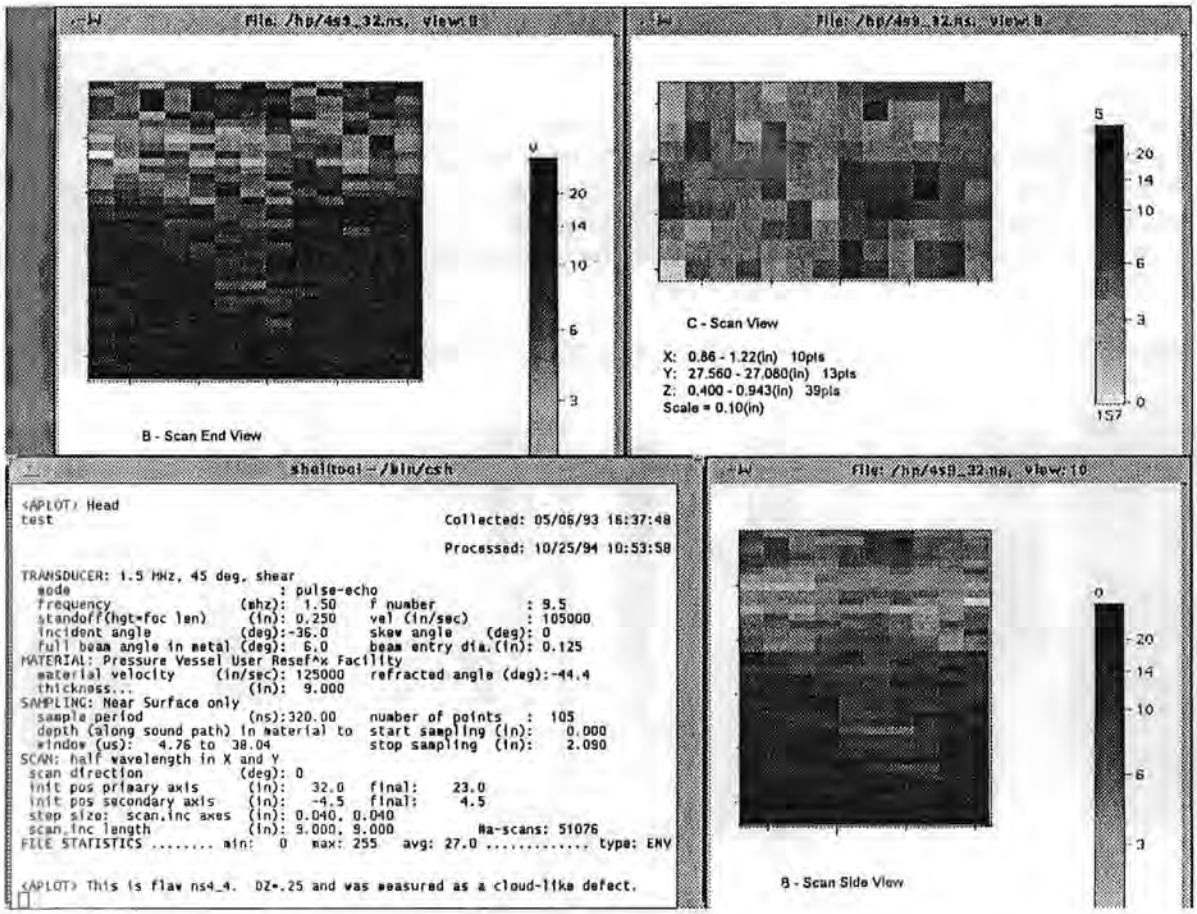

Figure A.36b - Volumetric indication #1 in the near surface base metal: mode 9

Figures A.37a-b show volumetric indication #2 in the near surface base metal. This volumetric indication has a through-wall extent of 3 mm based on wave packet width. The detection was made in mode 2 where it had isolated TOF shape at a depth of 20 mm. The shape quality is poor for this indication. There was a confirmation in mode 3 at a depth of 18 mm. The different Z values 18 to 20 give an alternate depth size of 2 mm. The indication is characterized as volumetric based on detection in orthogonal modes. There is no evidence of coin shape in the end view of mode 2 and side view of mode 3. The length is 13 mm and was made to LOS mode 2. The width is 7 mm and was made to LOS in mode 3. The aspect ratio (length/depth) of this indication is 4 giving an orientation along the weld. The maximum amplitude-to-noise ratio is of medium range at 8 to 3. With an X coordinate of 79 mm, the indication is clearly in the base metal. With a Z coordinate of 18 mm, the indication is clearly below the cladding.

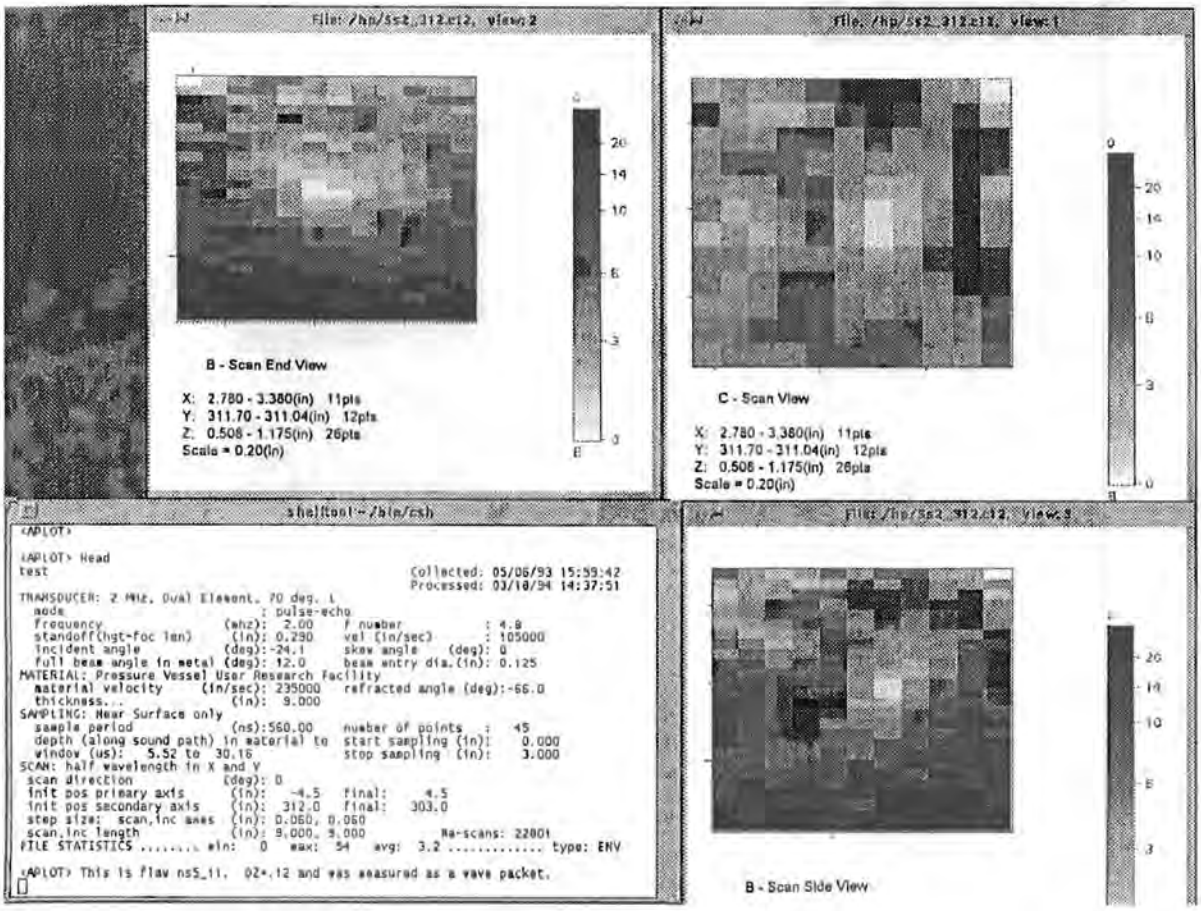

Figure A.37a - Volumetric indication #2 in the near surface base metal: mode 2

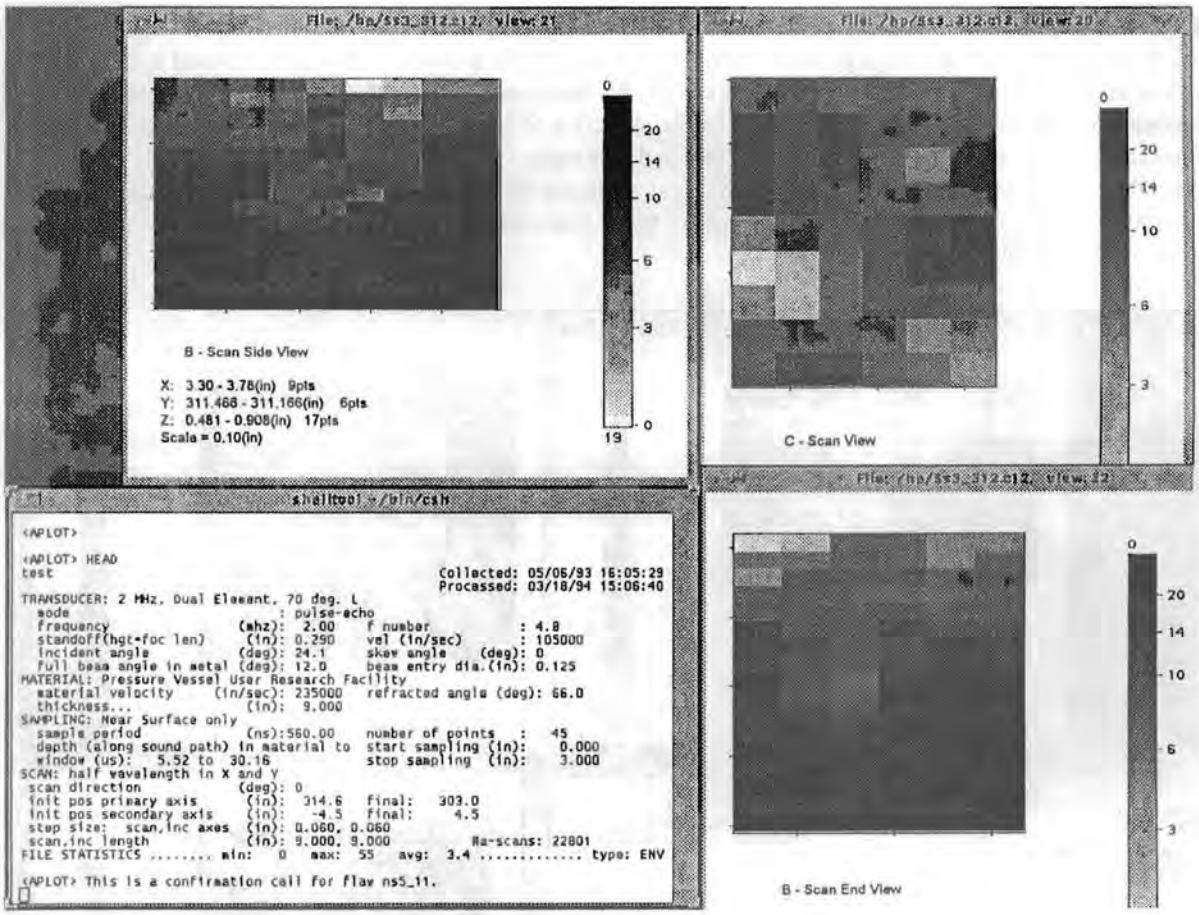

Figure A.37b - Volumetric indication #2 in the near surface base metal: mode 3

Figure A.38 shows volumetric indication #3 in the near surface base metal. This volumetric indication has a through-wall extent of 2.5 mm based on ring around pattern. The detection was made in mode 7 where it displayed a pair of TOF shapes at a depth of 20 mm. The shape quality is good for this indication. There were no confirmations in other modes. The indication is characterized as volumetric based on the detection of ring around shape. There is no evidence of coin shape in the side view of mode 7. The width is 12 mm and was made to LOS in mode 7. The aspect ratio (width/depth) of this indication is 5 giving an orientation across the weld. The maximum amplitude-to-noise ratio is high at 100 to 25. With an X coordinate of 71 mm, the indication is clearly in the base metal. With a Z coordinate of 20 mm, the indication is clearly below the cladding.

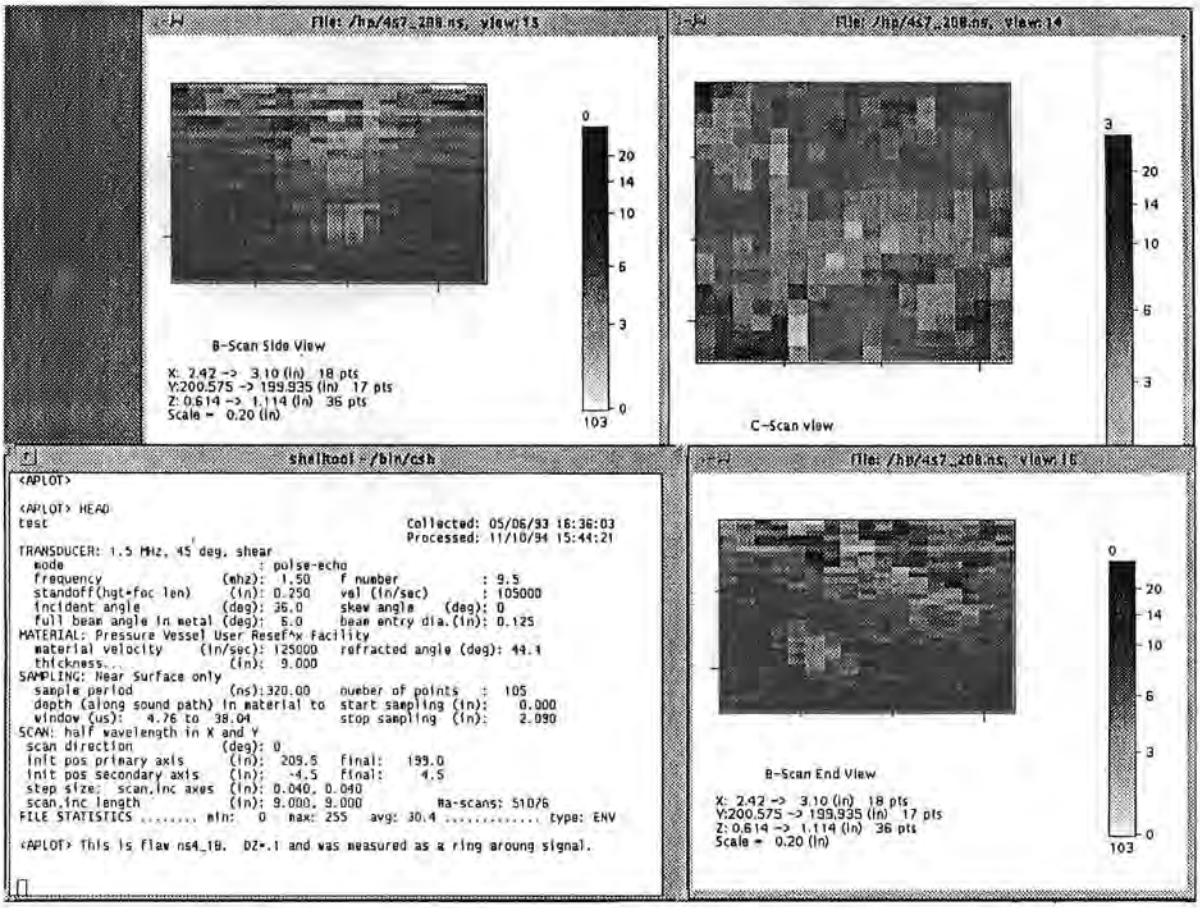

Figure A.38 - Volumetric indication #3 in the near surface base metal: mode 7

Figures A.39a-b show volumetric indication #4 in the near surface base metal. This volumetric indication has a through-wall extent of 2.3 mm based on wave packet width. The detection was made in mode 5 where it had isolated TOF shape at a depth of 16 mm. The shape quality is good for this indication. There was a confirmation in mode 2 at a depth of 16 mm. The two Z values of 16 mm give an alternate depth size of less than 1.5 mm. The indication is characterized as volumetric based on detection in orthogonal modes. There is no evidence of coin shape in the end view of mode 2 and side view of mode 5. The length is 12 mm and was made to LOS in mode 2. The width is 12 mm and was made to LOS in mode 5. The range of aspect ratios (length/depth) of this indication is 5 to 8. With an X coordinate of -64 mm, the indication is clearly in the base metal. With a Z coordinate of 16 mm, the indication is clearly below the cladding.

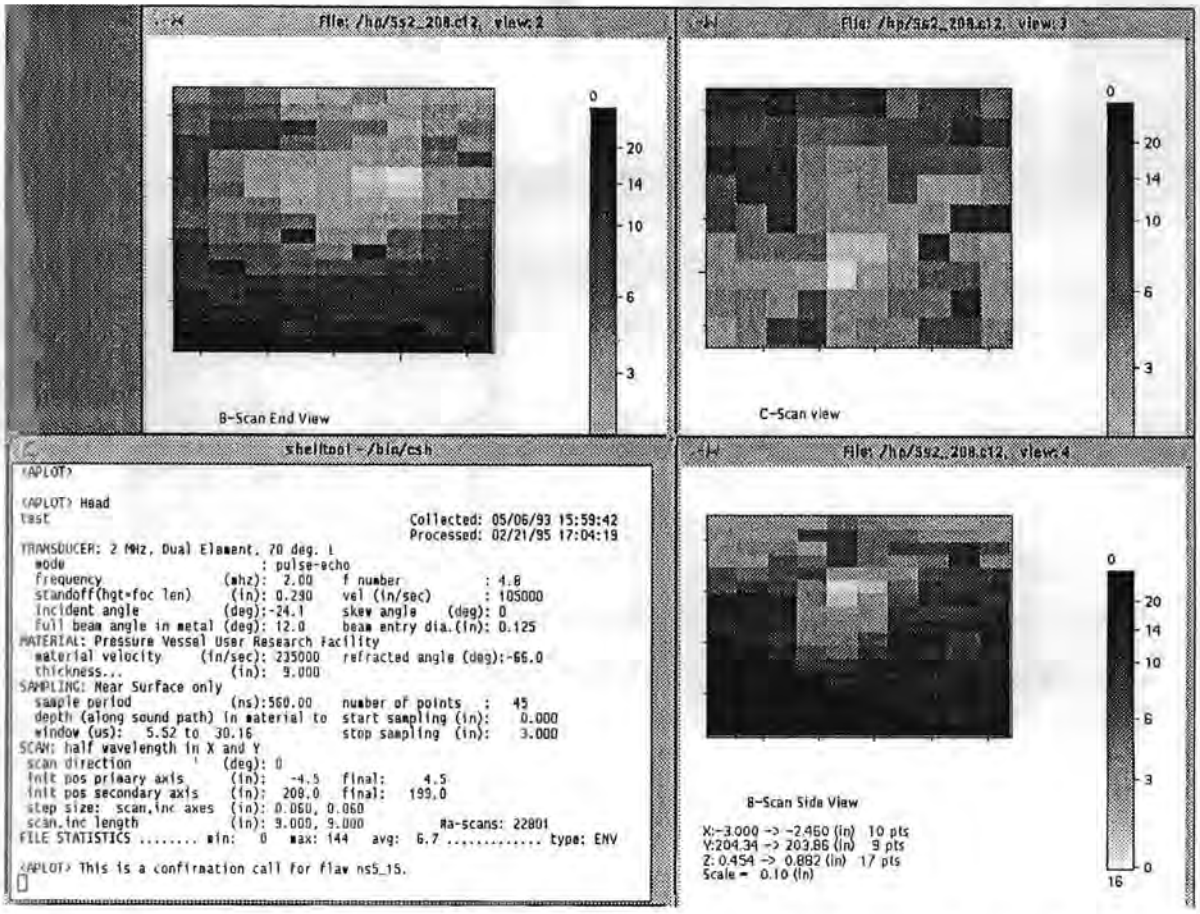

Figure A.39a - Volumetric indication #4 in the near surface base metal: mode 2

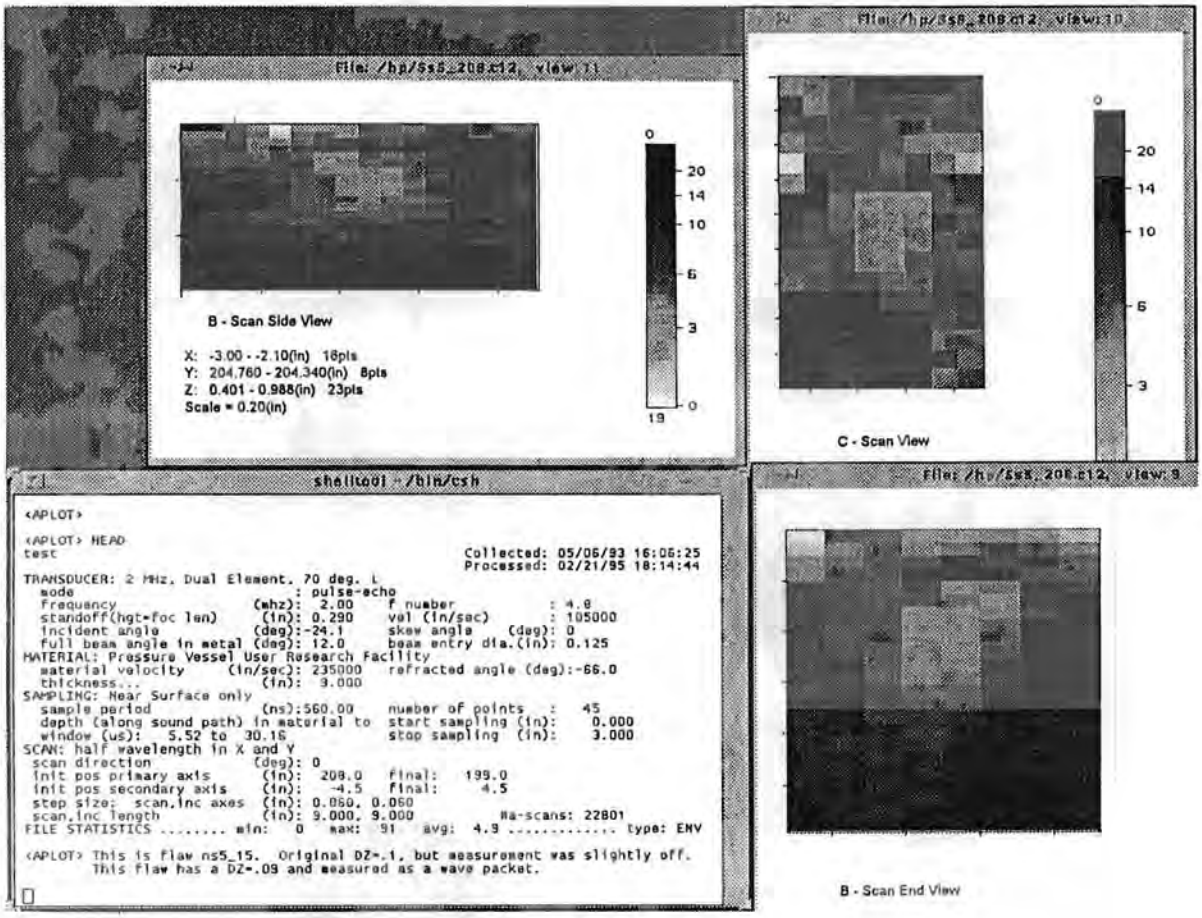

Figure A.39b - Volumetric indication #4 in the near surface base metal: mode 5

Figures A.40a-b show volumetric indication #5 in the near surface base metal. This volumetric indication has a through-wall extent of 2 mm based on wave packet width. The detection was made in mode 4 where it had isolated TOF shape at a depth of 11 mm. The shape quality is poor but not unusual for a shallow indication. There was a confirmation in mode 10 at a depth of 12 mm. The different Z values 10 to 11 mm give an alternate depth size of 1 mm. The indication is characterized as volumetric based on normal beam detection. There is no evidence of coin shape in the end view of mode 4. The length is 9 mm and was made to LOS in mode 4. The width is 5 mm and was made to LOS in mode 10. The aspect ratio (length/depth) of this indication is 4 giving an orientation along the weld. The maximum amplitude-to-noise ratio is high at 99 to 20. With an X coordinate of 26 mm, the indication is clearly in the base metal. With a Z coordinate of 10 to 11 mm, the indication is below the cladding by 1 to 2 mm.

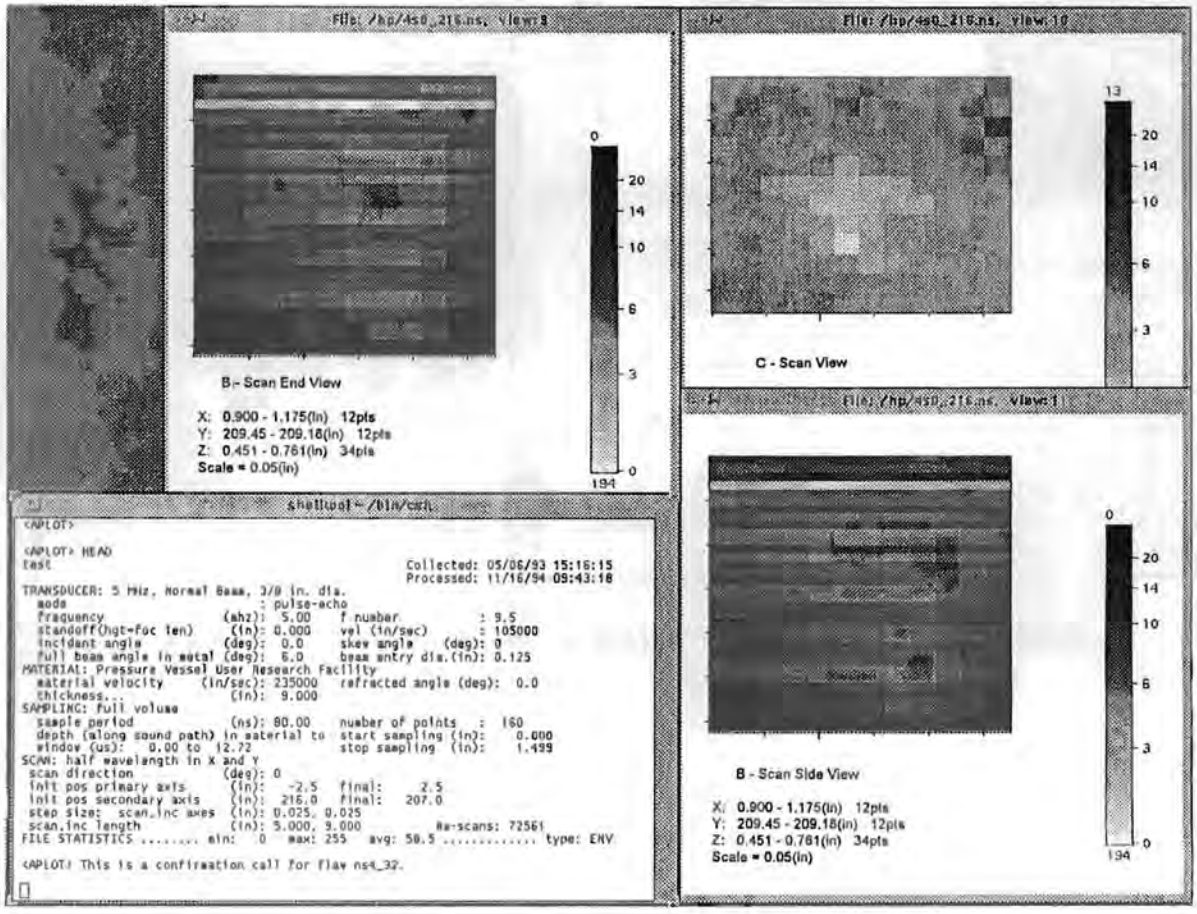

Figure A.40-a - Volumetric indication #5 in the near surface base metal: mode 10

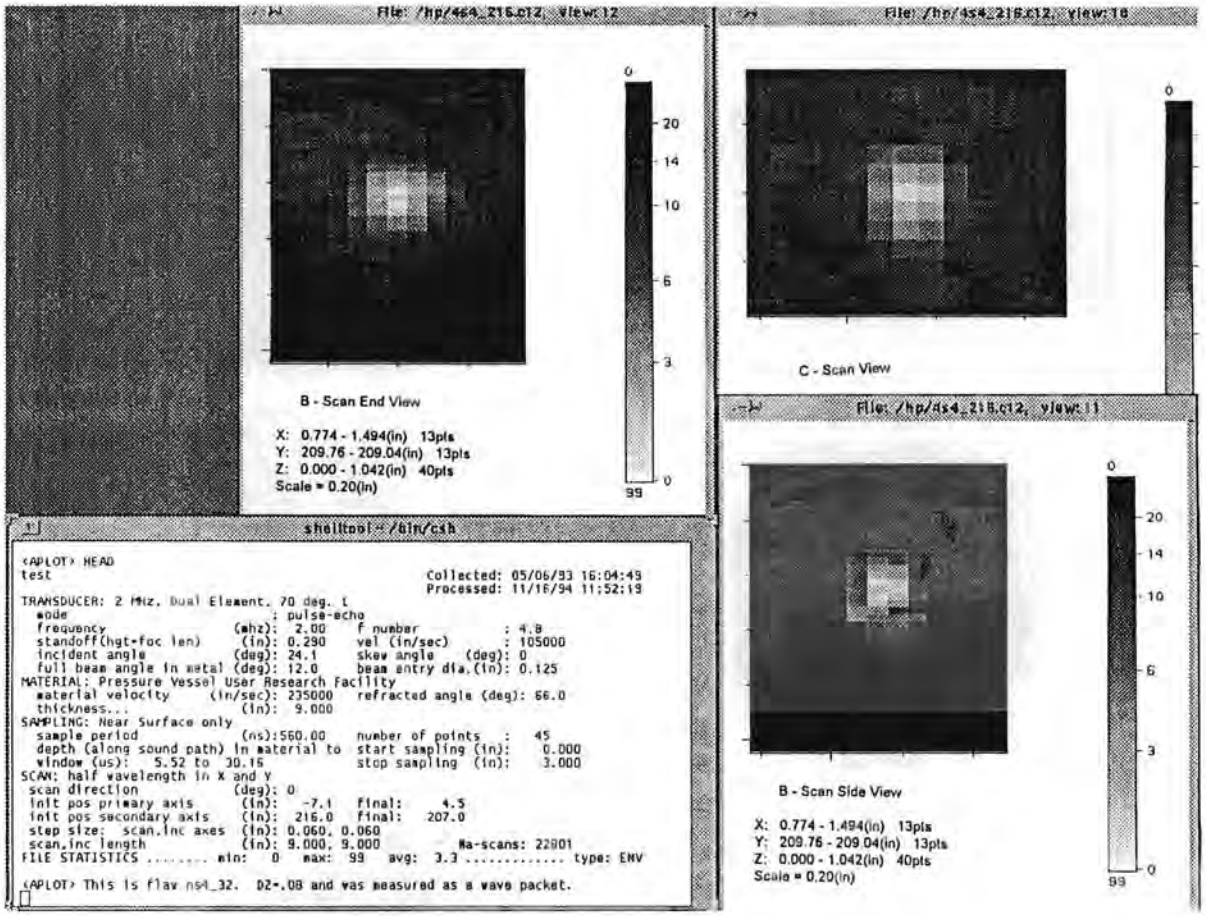

Figure A.40b - Volumetric indication #5 in the near surface base metal: mode 4

Figures A.4a-b show volumetric indication #6 in the near surface base metal. This volumetric indication has a through-wall extent of 2 mm based on different depth estimates, and an alternate size of 1 mm based on wave packet width. The detection was made in modes 1 and 7 where it had isolated TOF shape at depths of 17 and 19 mm. The shape quality is poor for this indication. There were no confirmations in other modes. The indication is characterized as volumetric based on normal beam detection. There is no evidence of coin shape in the side view of mode 7. The length is 5 mm and was made to LOS in mode 1. The width is 10 mm and was made to LOS in mode 7. The range of aspect ratios (width/depth) of this indication is 3 to 10. the maximum amplitude-to-noise ratio is of medium range at 119 to 30. With an X coordinate of 34 mm, the indication is clearly in the base metal. With a Z coordinate of 17 mm, the indication is clearly below the cladding.

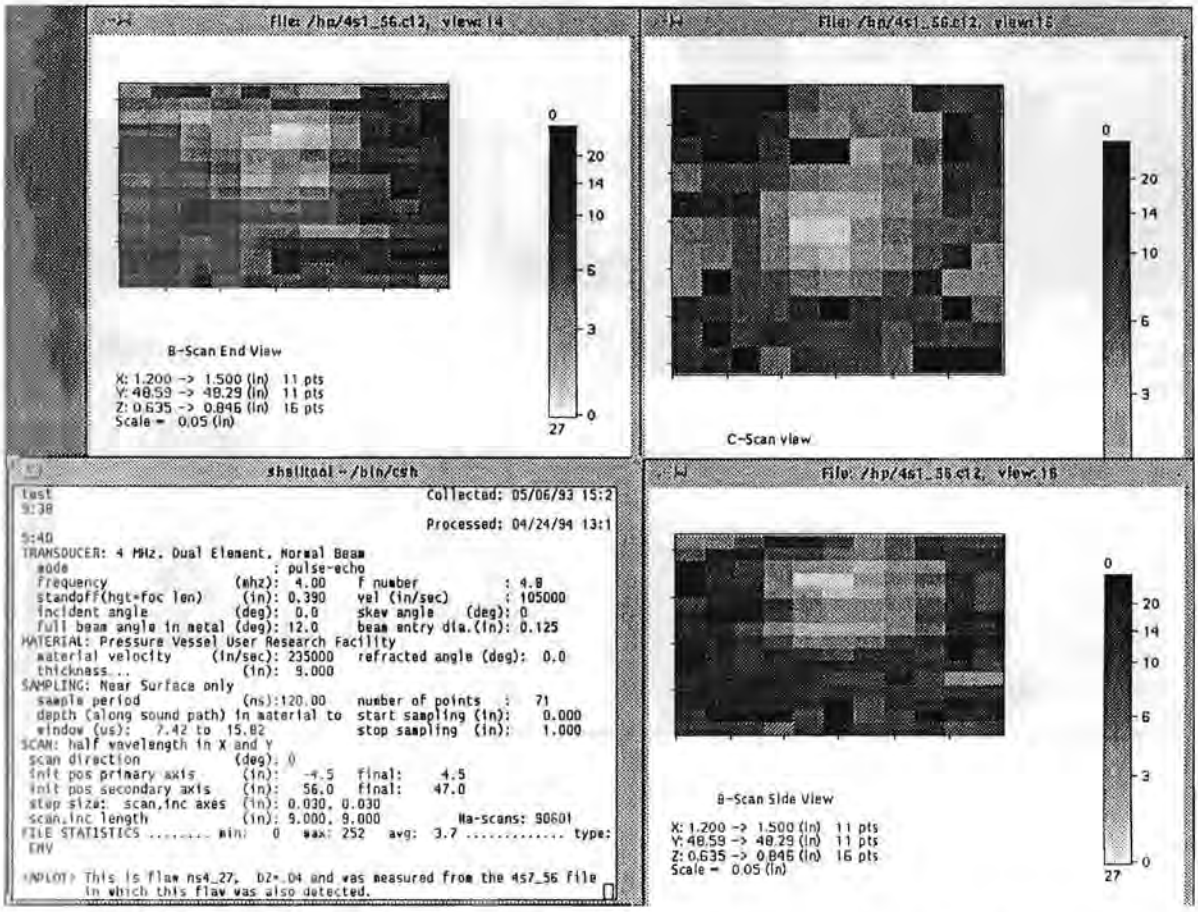

Figure A.41a – Volumetric indication #6 in the near surface base metal: model 1

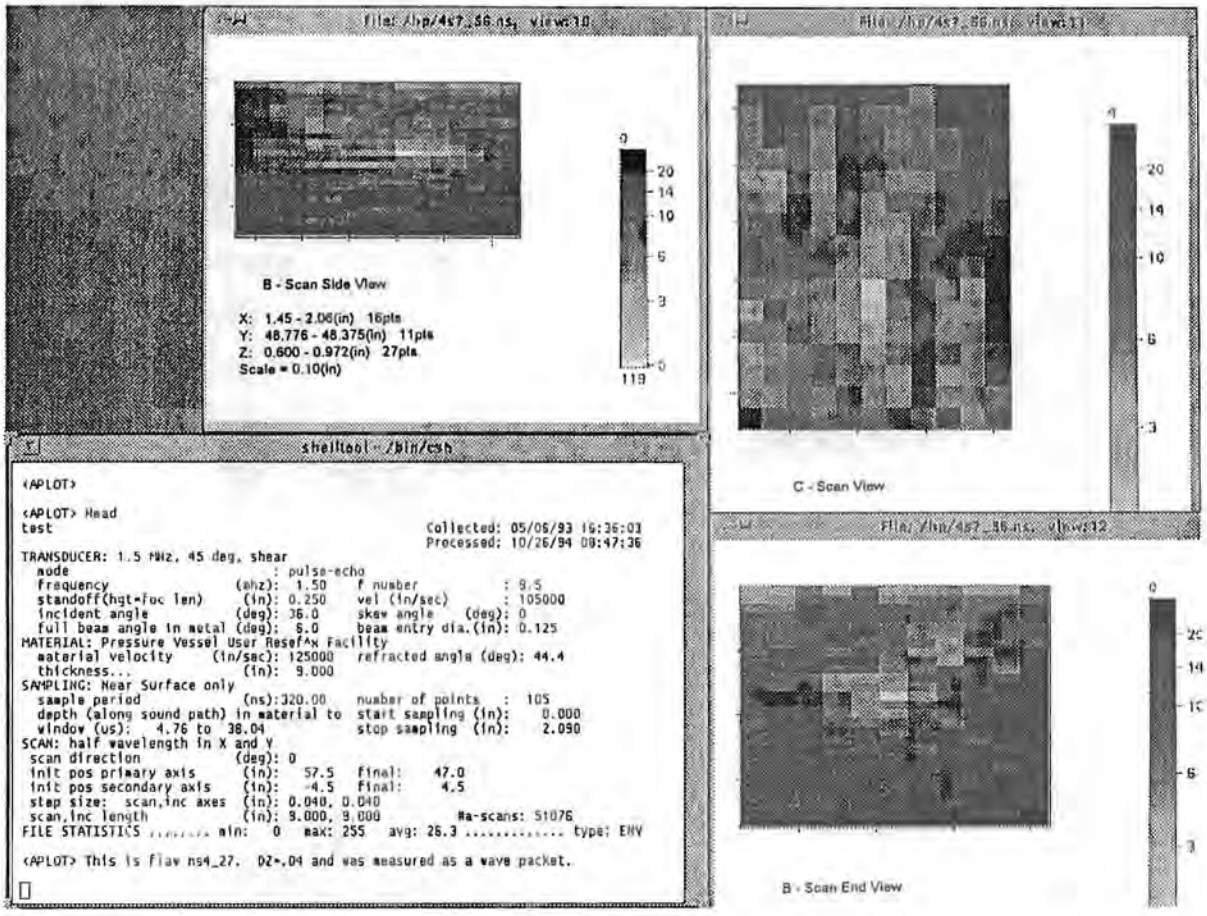

Figure A.41b - Volumetric indication #6 in the near surface base metal: mode 7

Figure A.42 shows volumetric indication #7 in the near surface base metal. This volumetric indication has a through-wall extent of 1.6 mm based on ring around pattern. The detection was made in mode 8 where it displayed a pair of TOF shapes at a depth of 19 mm. The shape quality is good for this indication. There were no confirmations in other modes. The indication is characterized as volumetric based on the detection of ring around shape. There is no evidence of coin shape in the end view of mode 8. The length is 8 mm and was made to LOS in mode 8. The aspect ratio (width/depth) of this indication is 5 giving an orientation along the weld. The maximum amplitude-to-noise ratio is high at 195 to 45. With an X coordinate of 123 mm, the indication is clearly in the base metal. With a Z coordinate of 19 mm, the indication is clearly below the cladding.

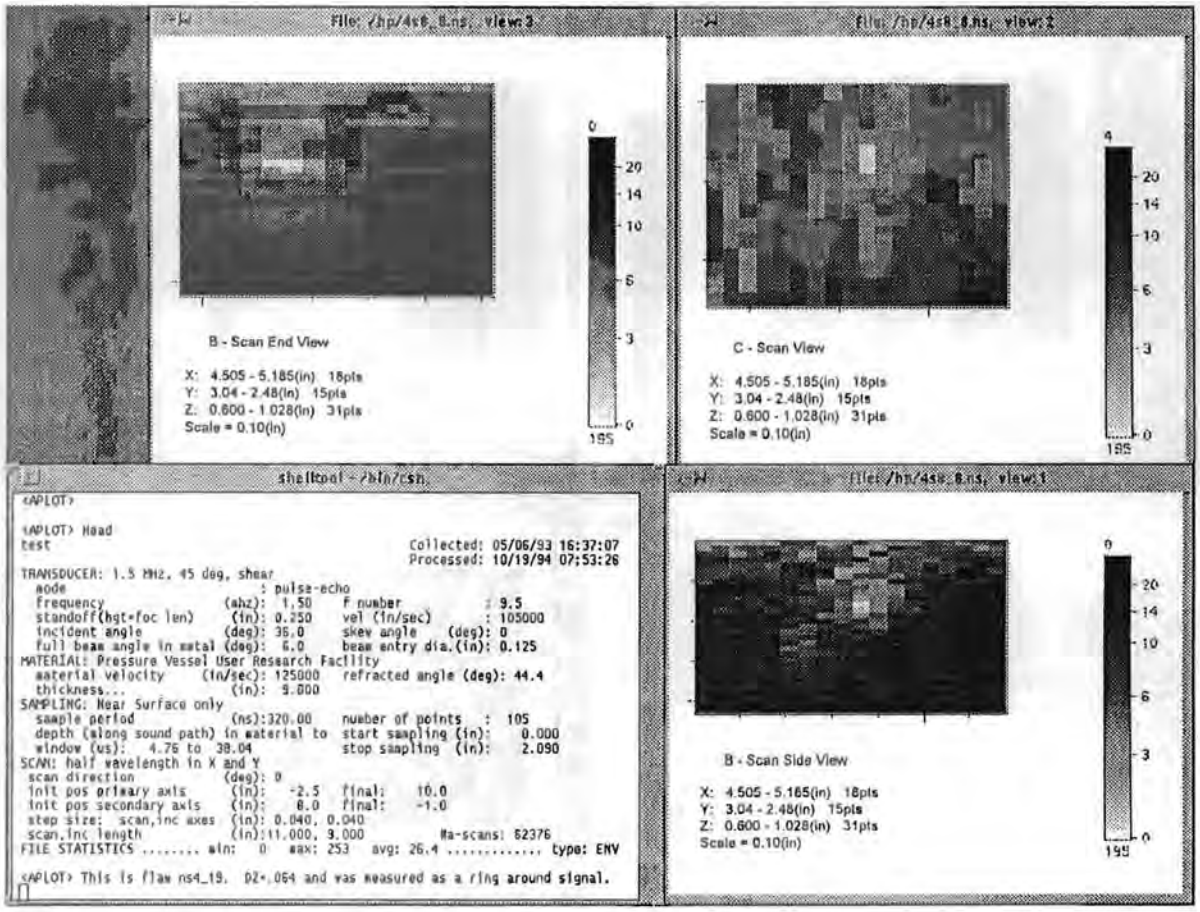

Figure A.42 - Volumetric indication #7 in the near surface base metal: mode 8

Figure A.43 shows volumetric indication #8 in the near surface base metal. This volumetric indication has a through-wall extent of 1.6 mm based on ring around pattern. The detection was made in mode 8 where it displayed a pair of TOF shapes at a depth of 14 mm. There were no confirmations in other modes. The indication is characterized as volumetric based on the detection of ring around shape. There is some evidence of coin shape in the end view of mode 8. The length is 12 mm and was made to LOS in mode 8. The aspect ratio (length/depth) of this indication is 3 giving an orientation along the weld. The maximum amplitude-to-noise ratio is of medium range at 148 to 40. With an X coordinate of 145 mm, the indication is clearly in the base metal. With a Z coordinate of 14 mm, the indication is clearly below the cladding.

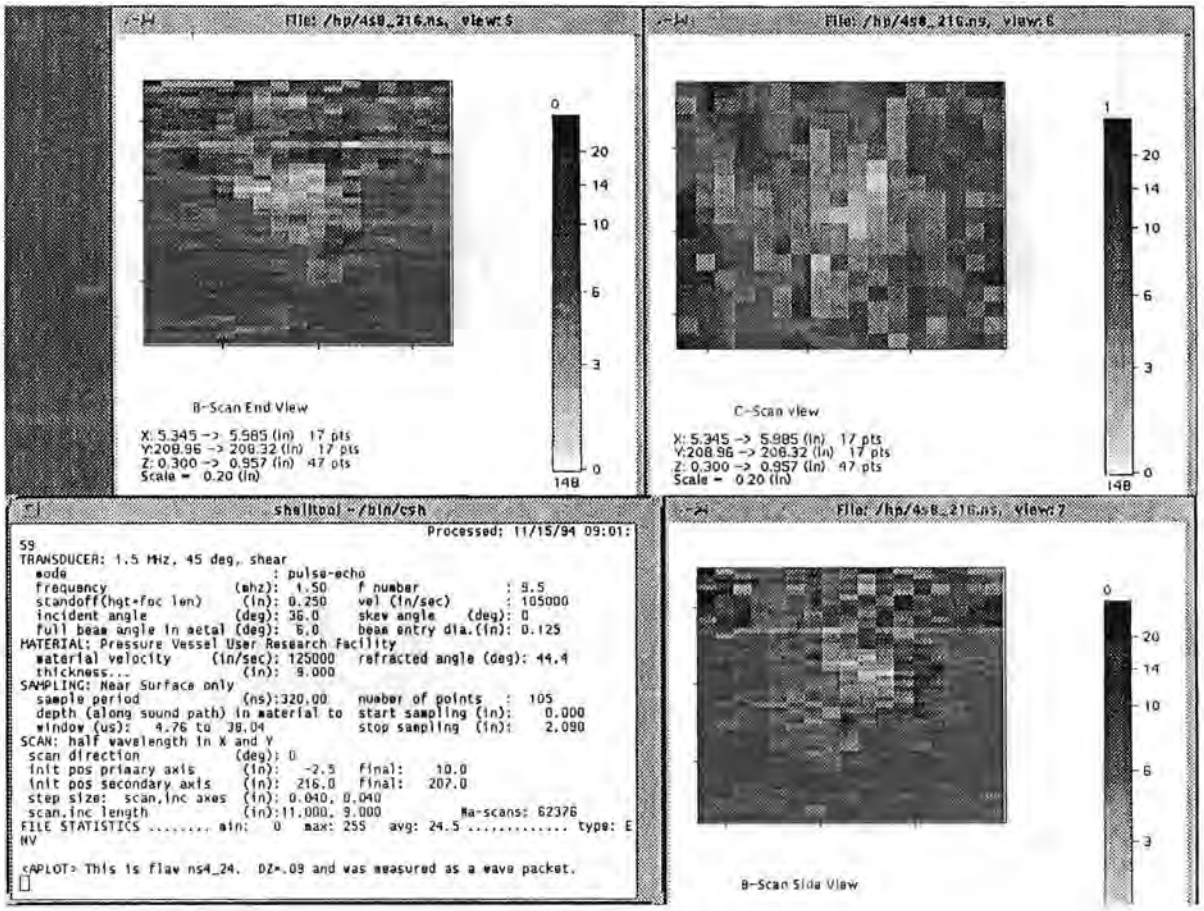

Figure A.43 - Volumetric indication #8 in the near surface base metal: mode 8

Figures A.44a-c show volumetric indication #10 in the near surface base metal. (Note: volumetric indication #9 in the near surface base metal was merged with volumetric indication #7). This volumetric indication has a through-wall extent of 1.5 mm based on wave packet width. Detections were made in modes 1 and 2. It had isolated TOF shape in mode 2 at a depth of 11 mm and normal beam shape in mode 1 at 10 mm. The shape quality is poor but not unusual for a shallow indication. There were confirmations in modes 3 and 4 at a depth of 11 mm. The different Z values 10 to 11 mm give an alternate depth size of 1 mm. The indication is characterized as volumetric based on normal beam detection. There is good evidence of coin shape in the end view of mode 2 which tends to characterize the indication as volumetric. The length is 11 mm and was made to LOS in mode 2. The width is 11 mm and was made to LOS in mode 3. The aspect ratio (length/depth) of this indication is 7 and the width-to-depth ratio is also 7 which tends to confirm volumetric orientation. The maximum amplitude-to-noise ratio is high at 212 to 25. With an X coordinate of 79 mm, the indication is clearly in the base metal. With a Z coordinate of 10 mm, the indication is below the cladding, and possibly connected to it.

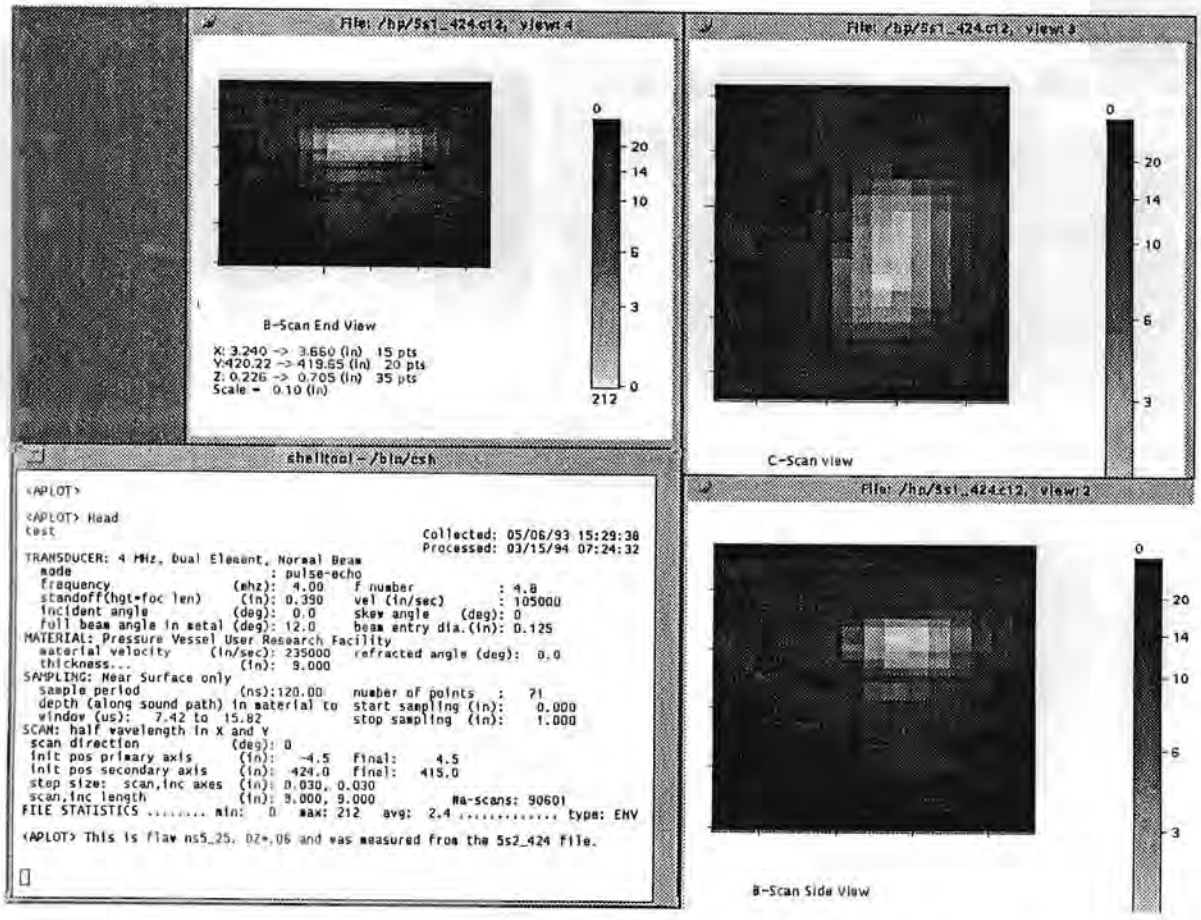

Figure A.44a - Volumetric indication #10 in the near surface base metal: mode 1

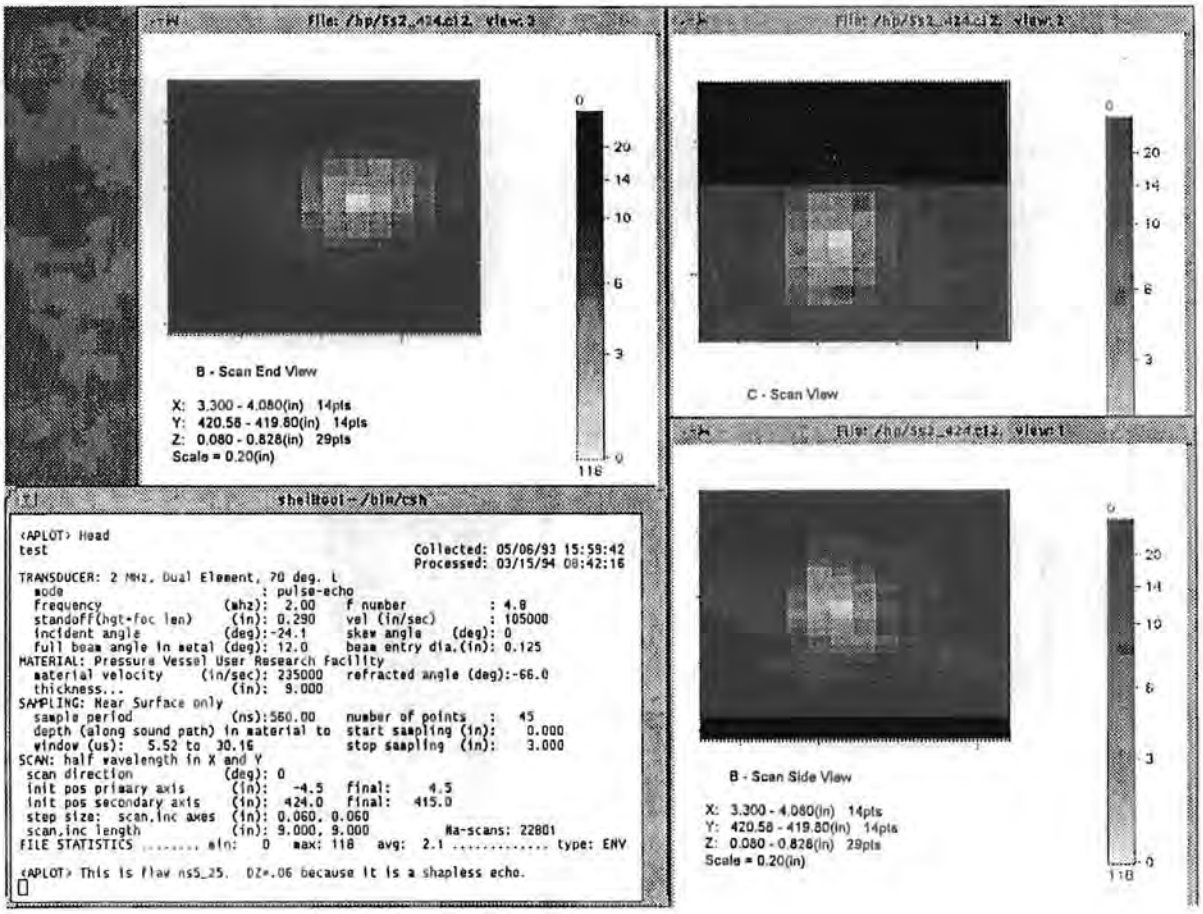

Figure A.44b - Volumetric indication #10 in the near surface base metal: mode 2

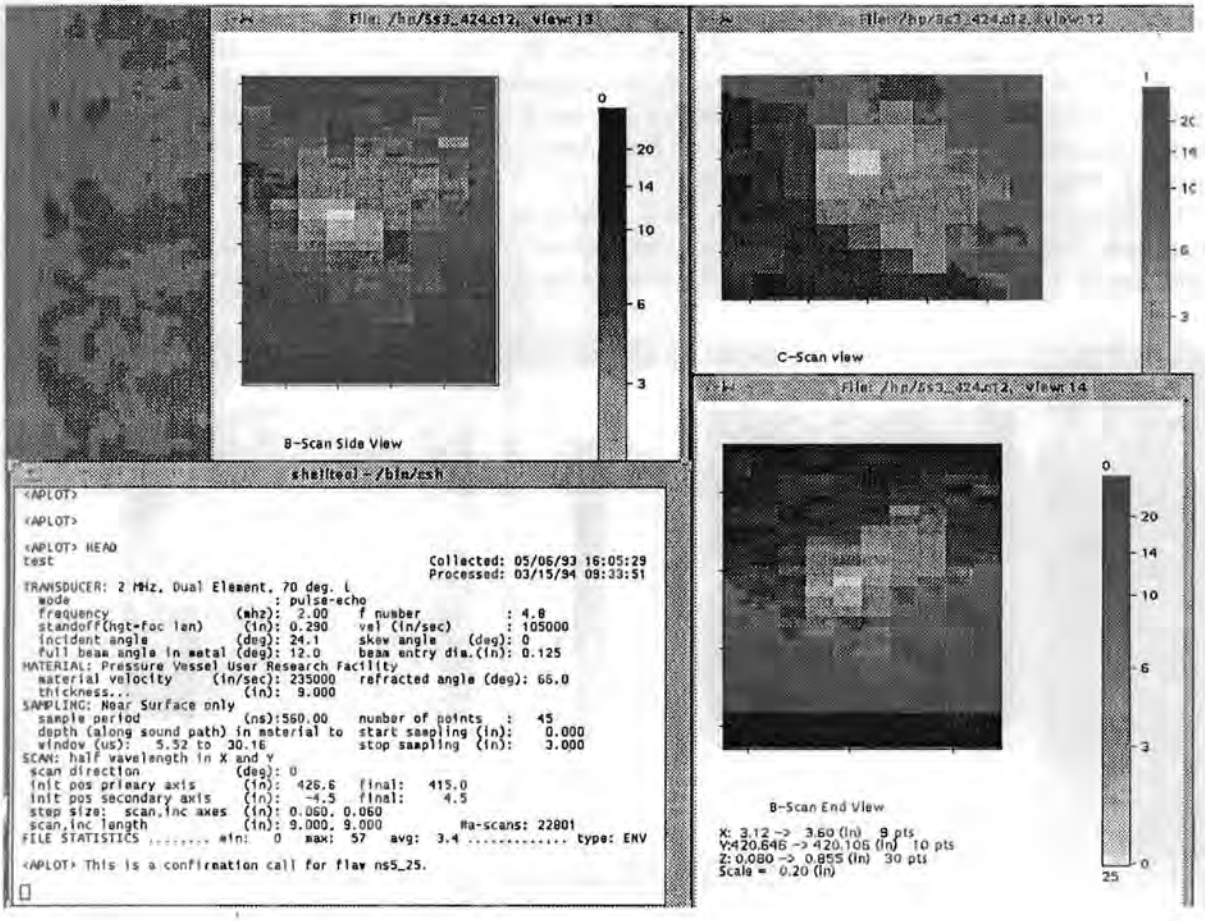

Figure A.44c - Volumetric indication #10 in the near surface base metal: mode 3

Figures A.45a-b show volumetric indication #11 in the near surface base metal. This volumetric indication has a through-wall extent of less than 1.5 mm based on a bright indication without TOF shape at depth of less than 10 mm. The detection was made in modes 1 and 2 where the bright, shallow indication failed to take shape at depths of 8 and 9 mm. There were no confirmations in other modes. The different Z values 8 to 9 give an alternate depth size of 1 mm. The indication is characterized as volumetric based on normal beam detection. There is no evidence of coin shape in the end view of mode 2. The length is 10 mm and was made to LOS in mode 2. The width is 7 mm and was made to LOS in mode 1. The aspect ratio (length/depth) of this indication is 7 giving an orientation along the weld. The maximum amplitude-to-noise ratio is high at 102 to 25. With an X coordinate of 24 mm, the indication is clearly in the base metal. The Z coordinate of 8 to 9 mm shows that the indication is below the cladding, and possibly connected to it.

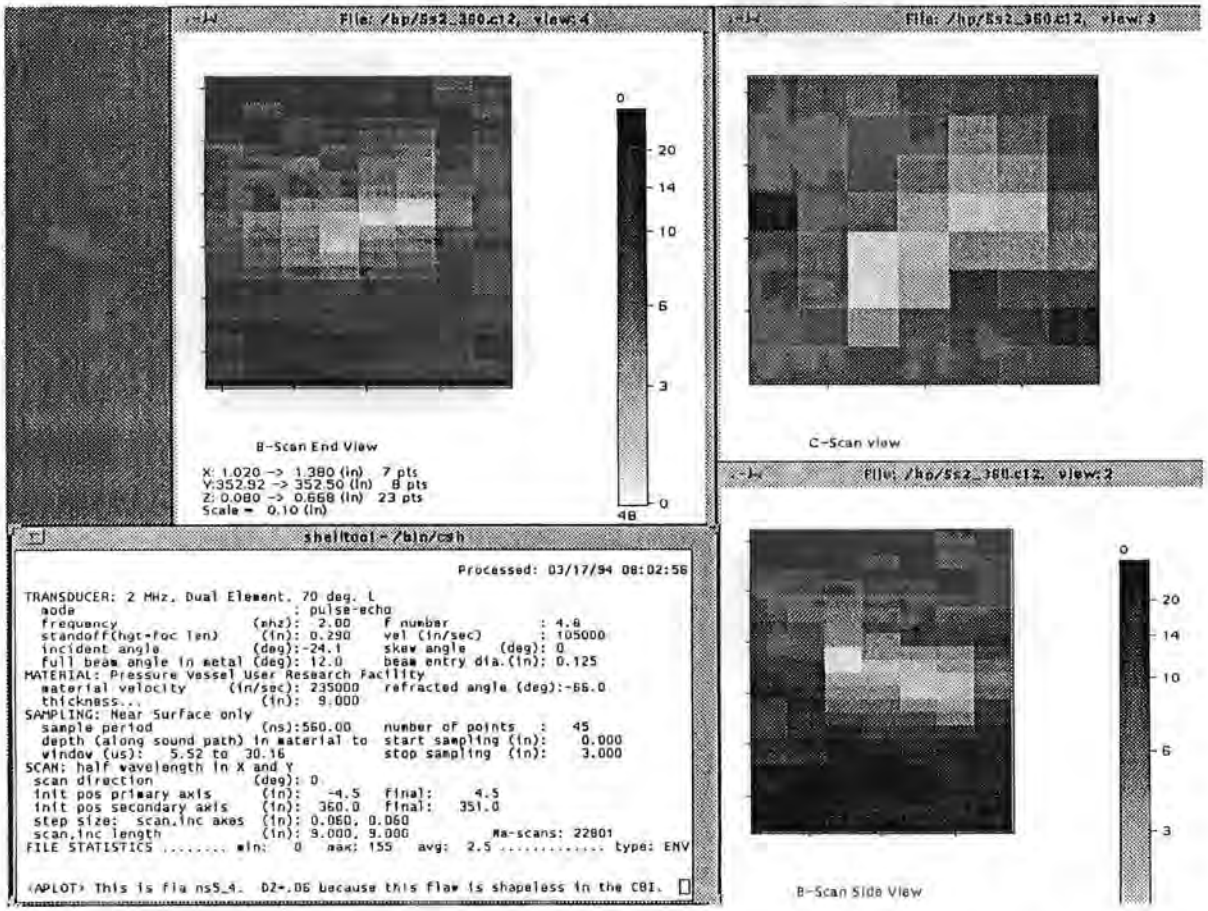

Figure A.45a - Volumetric indication #11 in the near surface base metal: mode 2

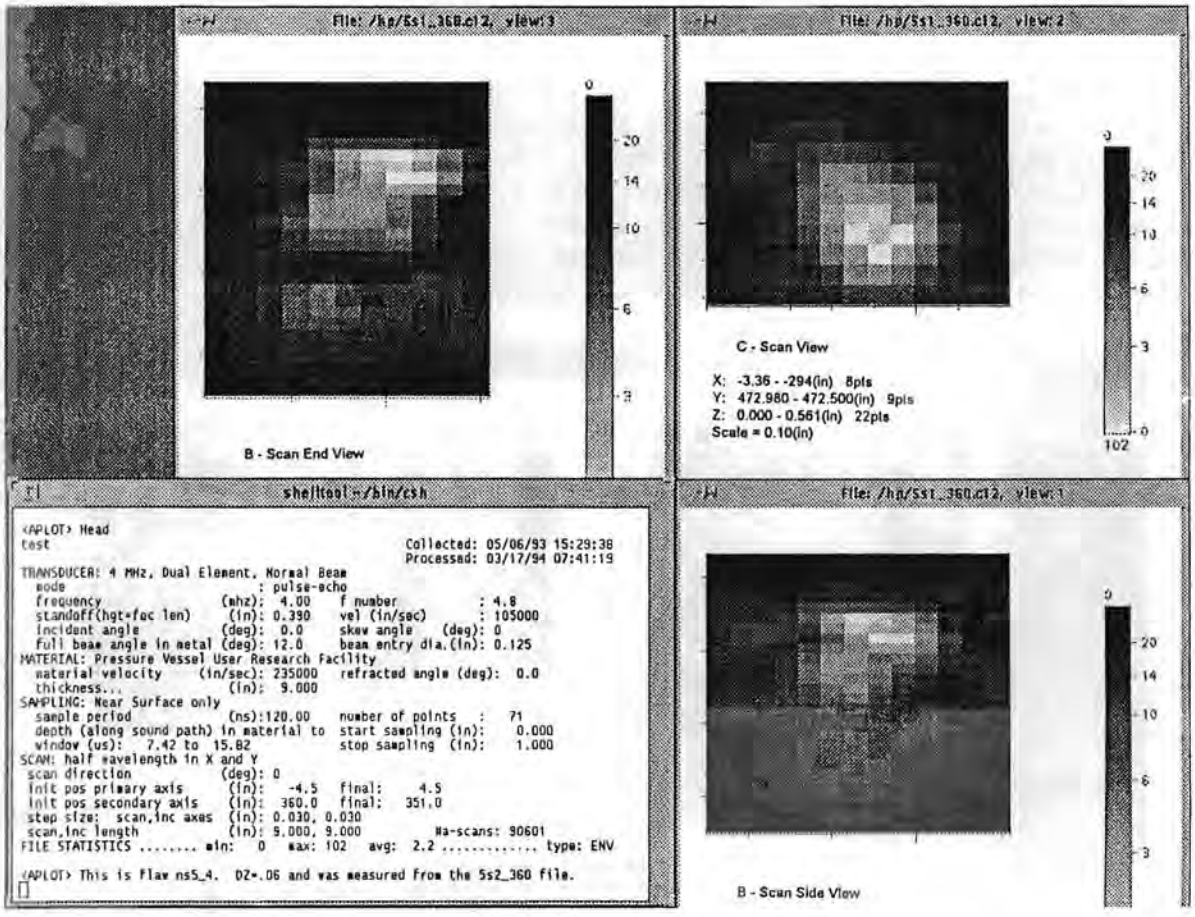

Figure A.45b - Volumetric indication #11 in the near surface base metal: mode 1

Planar Indications in the Cladding

Figure A.46 shows planar indication #1 in the cladding. This planar indication has a through-wall extent of less than 1.5 mm based on an indication without TOF shape at the clad to base metal interface. The detection was made in mode 2 where it lost TOF shape but remained brighter than 95 counts at a depth of 6 mm. There were no confirmations in other modes. The indication is characterized as planar based on lack of detection in normal beam or orthogonal modes. There is no evidence of coin shape in the end view of mode 2. The length is 14 mm and was made to LOS in mode 2. The aspect ratio (length/depth) of this indication is 9. The maximum amplitude-to-noise ratio is high at 130 to 30. The Z coordinate of 6 mm shows that the indication is in the clad-to-base metal interface.

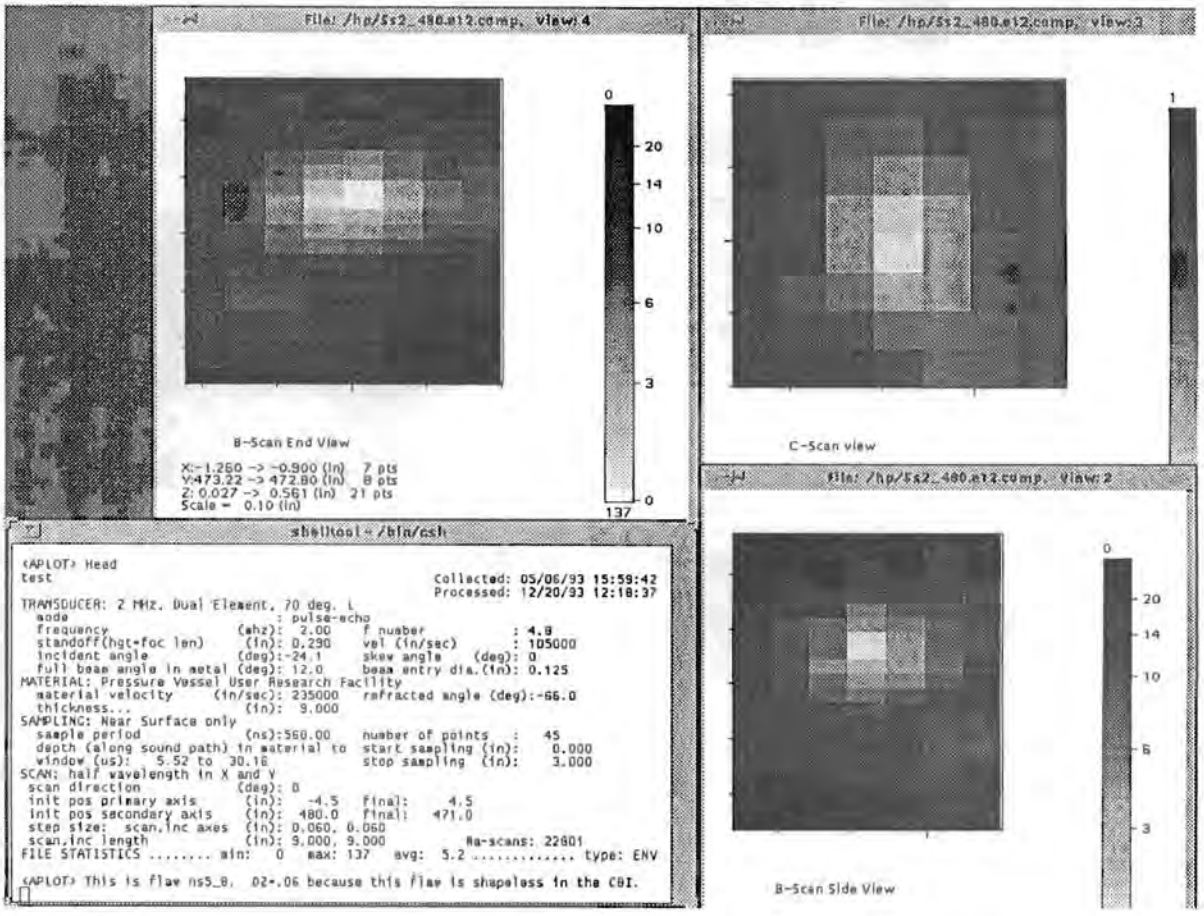

Figure A.46 - Planar indication #1 in the cladding: mode 2

Figures A.47a-b show planar indication #2 in the cladding. This planar indication has a through-wall extent of less than 1.5 mm based on an indication without TOF shape at the clad to base metal interface. The detection was made in modes 3 and 5 where it lost TOF shape but remained brighter than 95 counts at depths of 6 and 7 mm. There were no confirmations in other modes. The two Z values of 6 to 7 mm give an alternate depth size of 1 mm. The indication is characterized as planar based on lack of detection in normal beam or orthogonal modes. There is no evidence of coin shape in the side view of modes 3 and 5. The width is 7 mm and was made to LOS in modes 3 and 5. The aspect ratio (width/depth) of this indication is 5. The maximum amplitude-to-noise ratio is high at 170 to 30. The Z coordinate of 6 to 7 mm shows that the indication is in the clad-to-base metal interface.

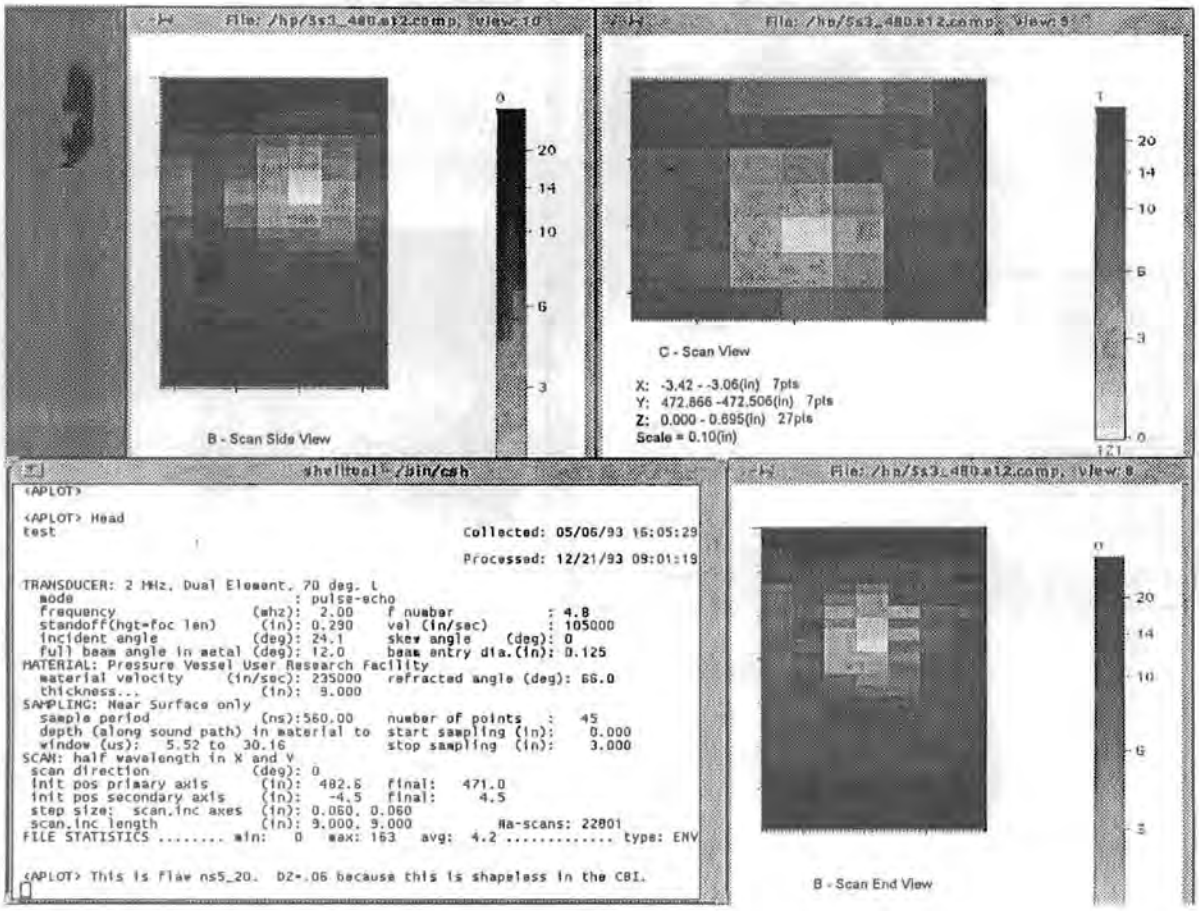

Figure A.47a - Planar indication #2 in the cladding: mode 3

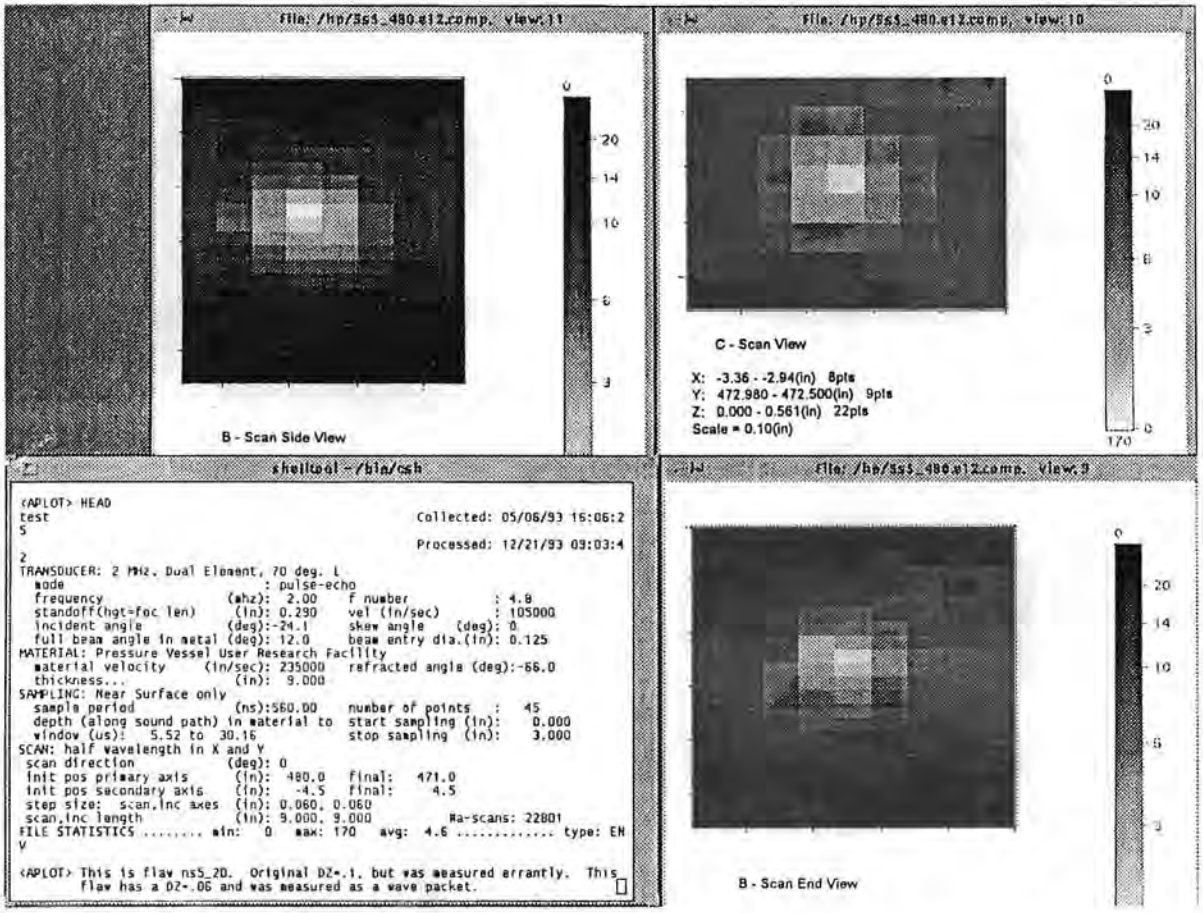

Figure A.47b - Planar indication #2 in the cladding: mode 5

Figure A.48 shows planar indication #3 in the cladding. This planar indication has a through-wall extent of less than 1.5 mm based on an indication without TOF shape at the clad to base metal interface. The detection was made in mode 2 where it failed to display TOF shape but remained brighter than 95 counts at a depth of 6 mm. There were no confirmations in other modes. The indication is characterized as planar based on lack of detection in normal beam or orthogonal modes. There is no evidence of coin shape in the end view of mode 2. The length is 8 mm and was made to LOS in mode 2. The aspect ratio (length/depth) of this indication is 5 giving an orientation along the weld. The maximum amplitude-to-noise ratio is of medium range at 97 to 30. The Z coordinate of 6 mm shows that the indication is in the clad-to-base metal interface. The X coordinate of 9 mm shows that the indication is over the weld.

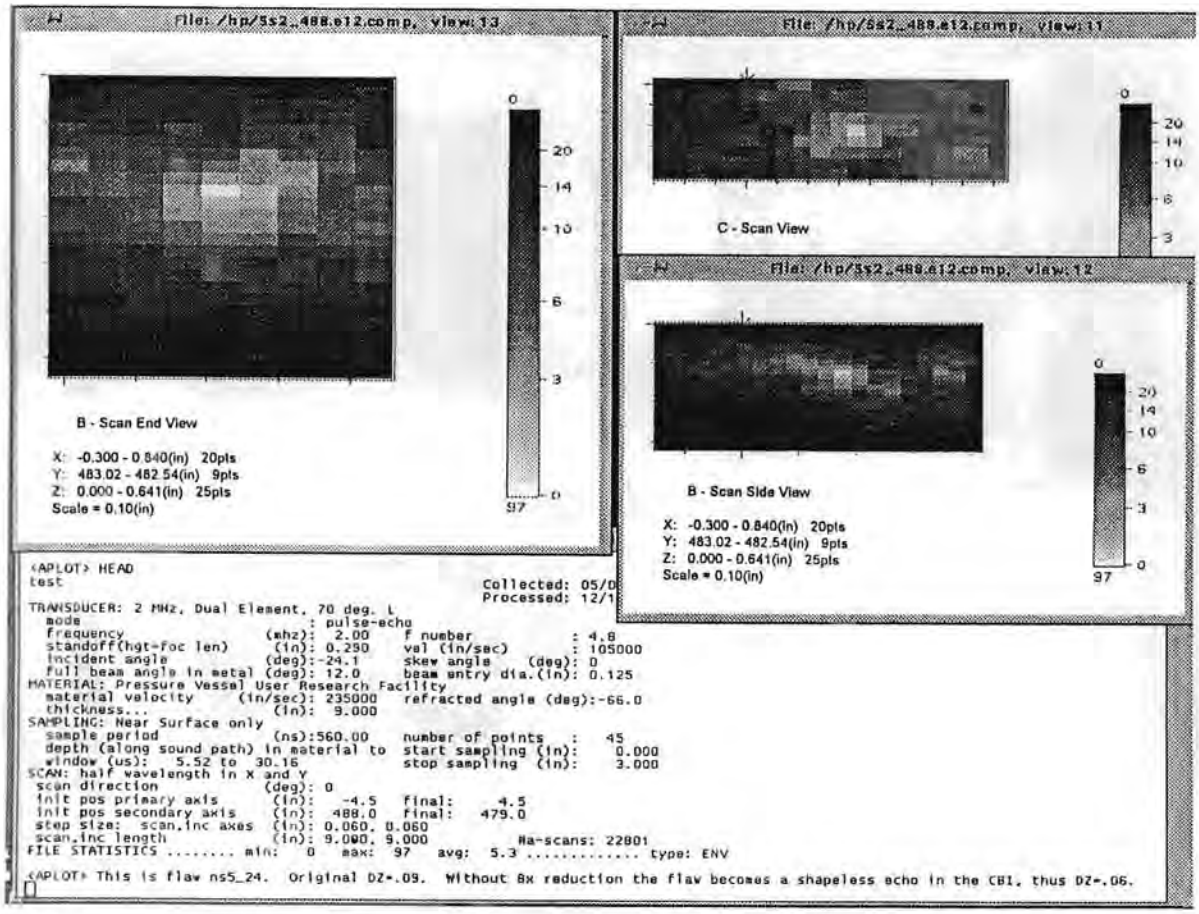

Figure A-48. Planar indication #3 in the cladding: mode 2

Figure A.49 shows planar indication #4 in the cladding. This planar indication has a through-wall extent of less than 1.5 mm based on an indication without TOF shape at the clad to base metal interface. The detection was made in mode 3 where it displayed evidence of coin shape at a depth of 6 mm. There were no confirmations in other modes. The indication is characterized as planar based on lack of detection in normal beam or orthogonal modes. There is good evidence of coin shape in the side view of mode 3 which tends to confirm the indication as planar. The width is 16 mm and was made to LOS in mode 3. The aspect ratio (width/depth) of this indication is 11 which tends to indicate a larger through-wall extent than 1.5 mm. The maximum amplitude-to-noise ratio is high at 83 to 15. The Z coordinate of 6 mm shows that the indication is in the clad-to-base metal interface. The X coordinate of 14 mm shows that the indication is over the HAZ.

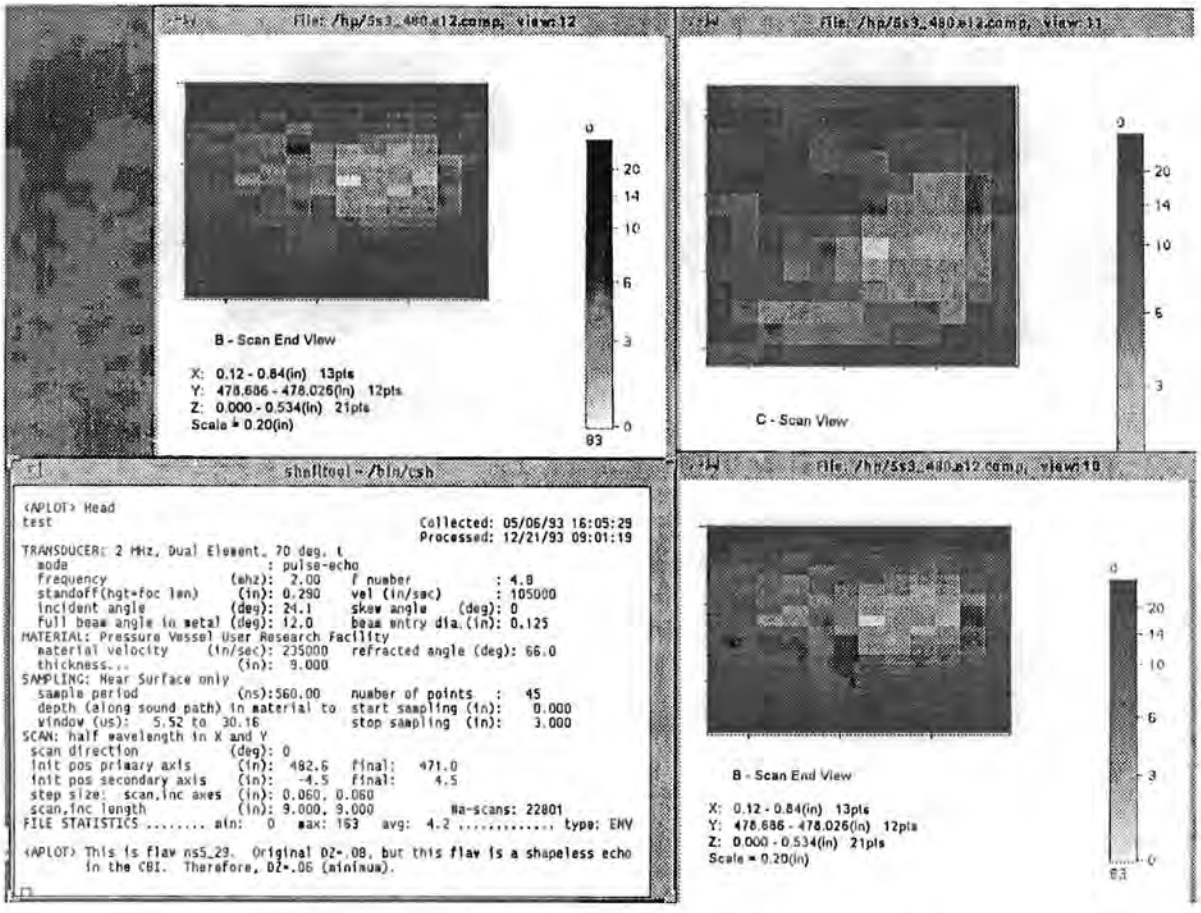

Figure A.49 - Planar indication #4 in the cladding: mode 3

Volumetric Indications in the Cladding

Figures A.50a-b show volumetric indication #1 in the cladding. This volumetric indication has a through-wall extent of 3 mm based on wave packet width. The detection was made in mode 2 where it had isolated TOF shape at a depth of 7 mm. The shape quality is good for this indication. There was a confirmation in mode 3 at a depth of 8 mm. The different Z values of 7 to 8 mm give an alternate depth size of 1 mm. The indication is characterized as volumetric based on detection in orthogonal modes. There is some evidence of coin shape in the end view of mode 2. The length is 12 mm and was made to LOS in mode 2. The width is 10 mm and was made to LOS in mode 3. The range of aspect ratios (length/depth) of this indication is 4 to 12 which tends to confirm the larger through-wall extent. The maximum amplitude-to-noise ratio is high at 162 to 20. The Z coordinate of 7 to 8 mm shows that the indication is in the clad-to-base metal interface. The X coordinate of -36 mm shows that the indication is over the base metal.

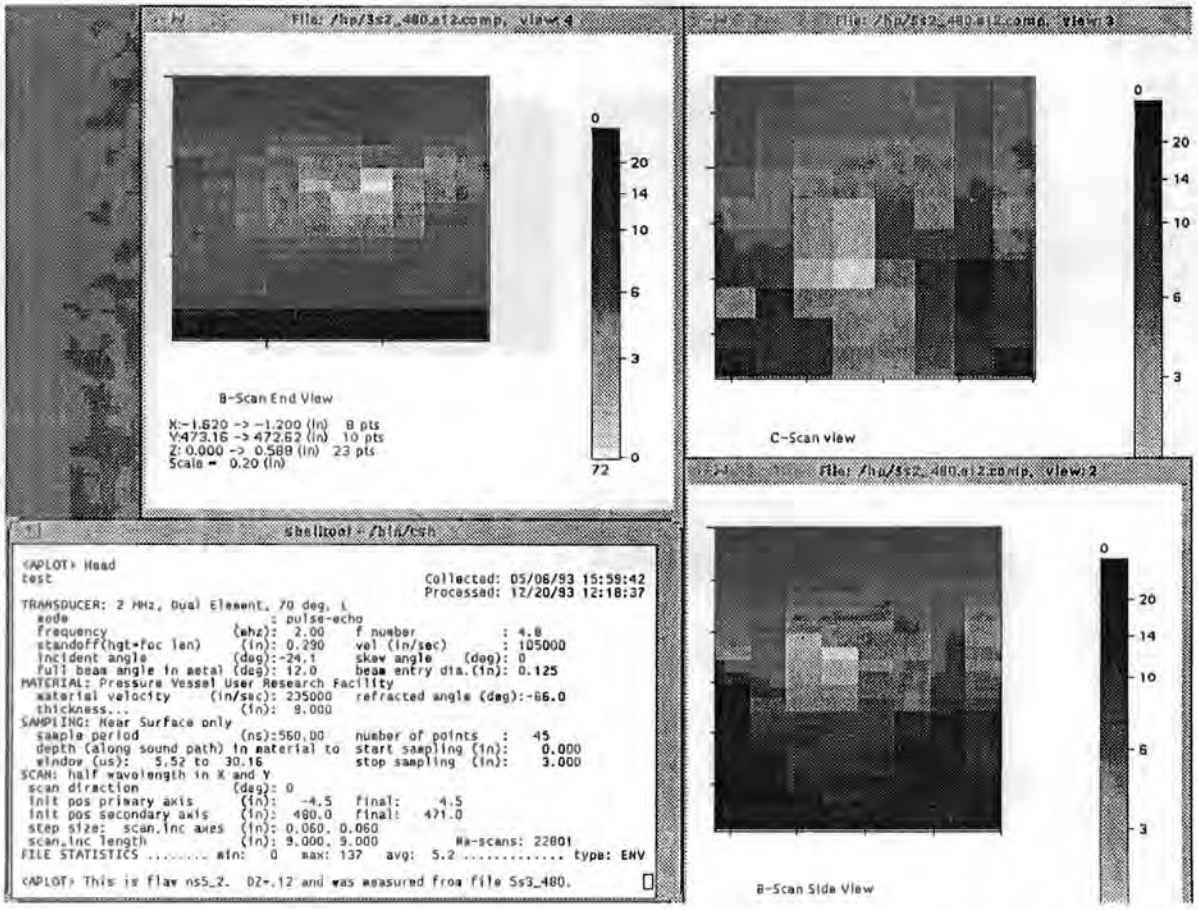

Figure A.50a - Volumetric indication #1 in the cladding: mode 2

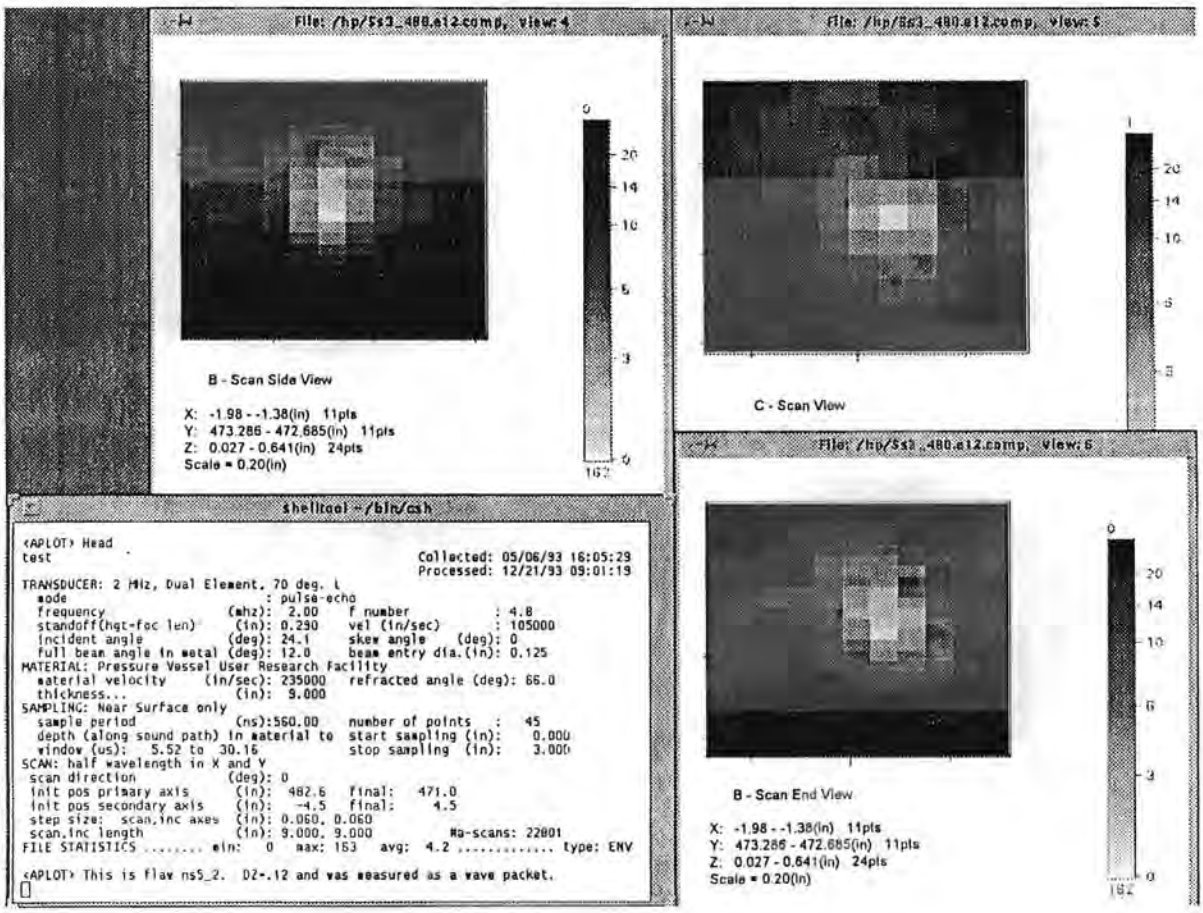

Figure A.50b - Volumetric indication #1 in the cladding: mode 3

Figures A.51a-d show volumetric indication #2 in the cladding. This volumetric indication has a through-wall extent of 3 mm based on different depth estimates of 5 to 8 mm and a smaller size of 2.3 mm based on wave packet width. The detection was made in modes 2 and 5 where it had isolated TOF shape at depths of 5 and 6 mm. The shape quality is poor but not unusual for a shallow indication and is broken up indicating that more than one small flaw is present. There were confirmations in modes 1 and 3 at depths of 6 and 8 mm. The indication is characterized as volumetric based on normal beam detection. There is no evidence of coin shape in the end view of modes 2, the side view of mode 3, and the side view of mode 5. The length is 11 mm and was made to LOS in mode 2. The width is 12 mm and was made to LOS in mode 5. The aspect ratio (width/depth) of this indication is 5 and the length-to-depth ratio is 5 which tends to confirm volumetric orientation. The maximum amplitude-to-noise ratio is of medium range at 92 to 30. The Z coordinates of 5 to 8 mm show that the indication is in the clad-to-base metal interface. The X coordinate of 15 mm shows that the indication is over the HAZ.

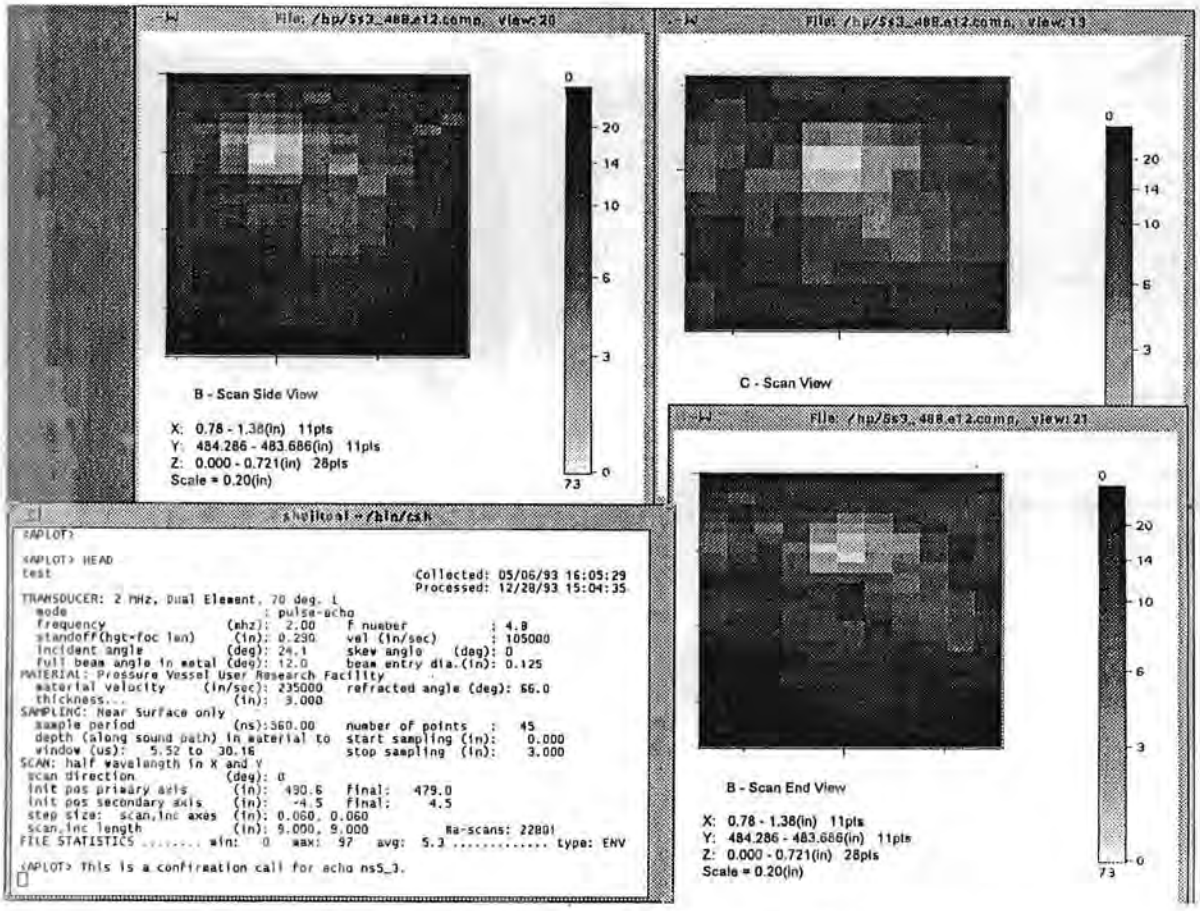

Figure A.51a - Volumetric indication #2 in the cladding: mode 3

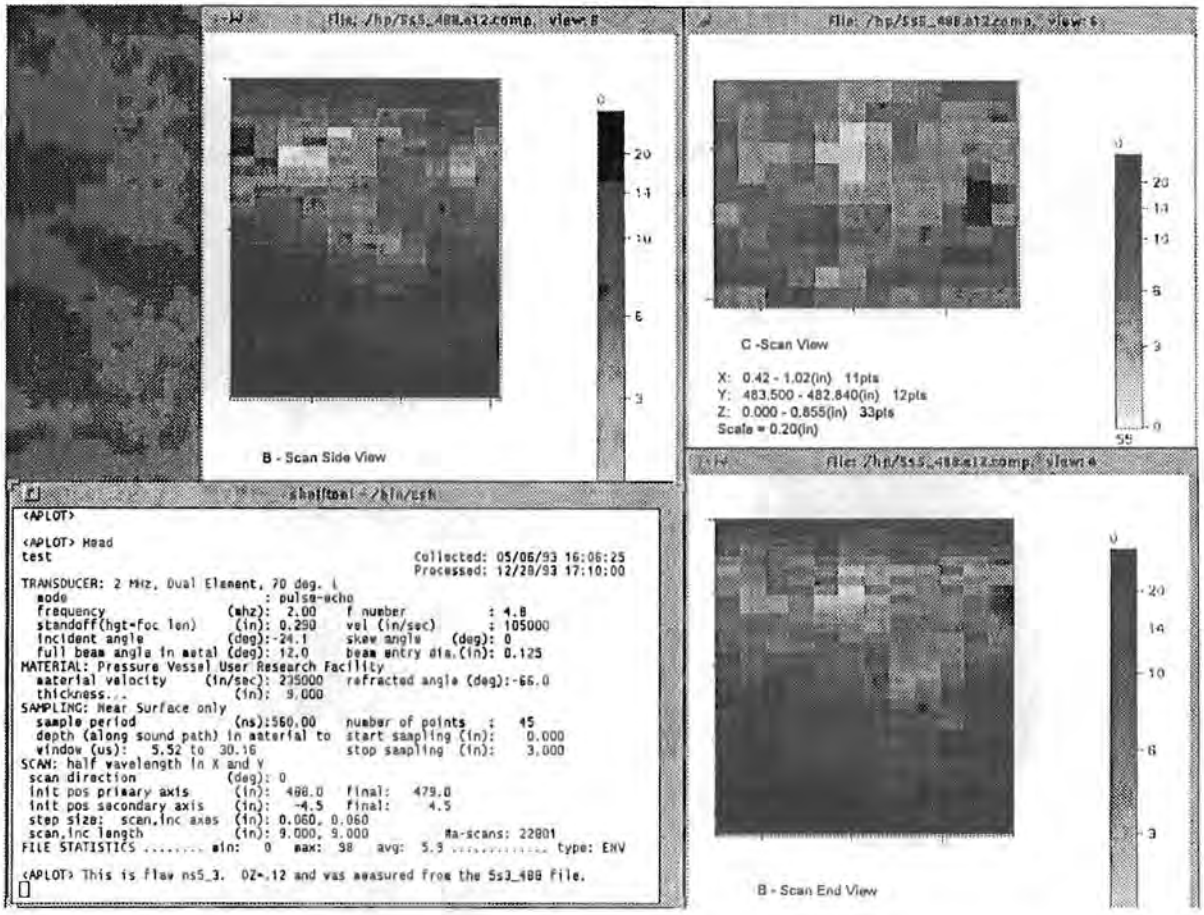

Figure A.51b - Volumetric indication #2 in the cladding: mode 5

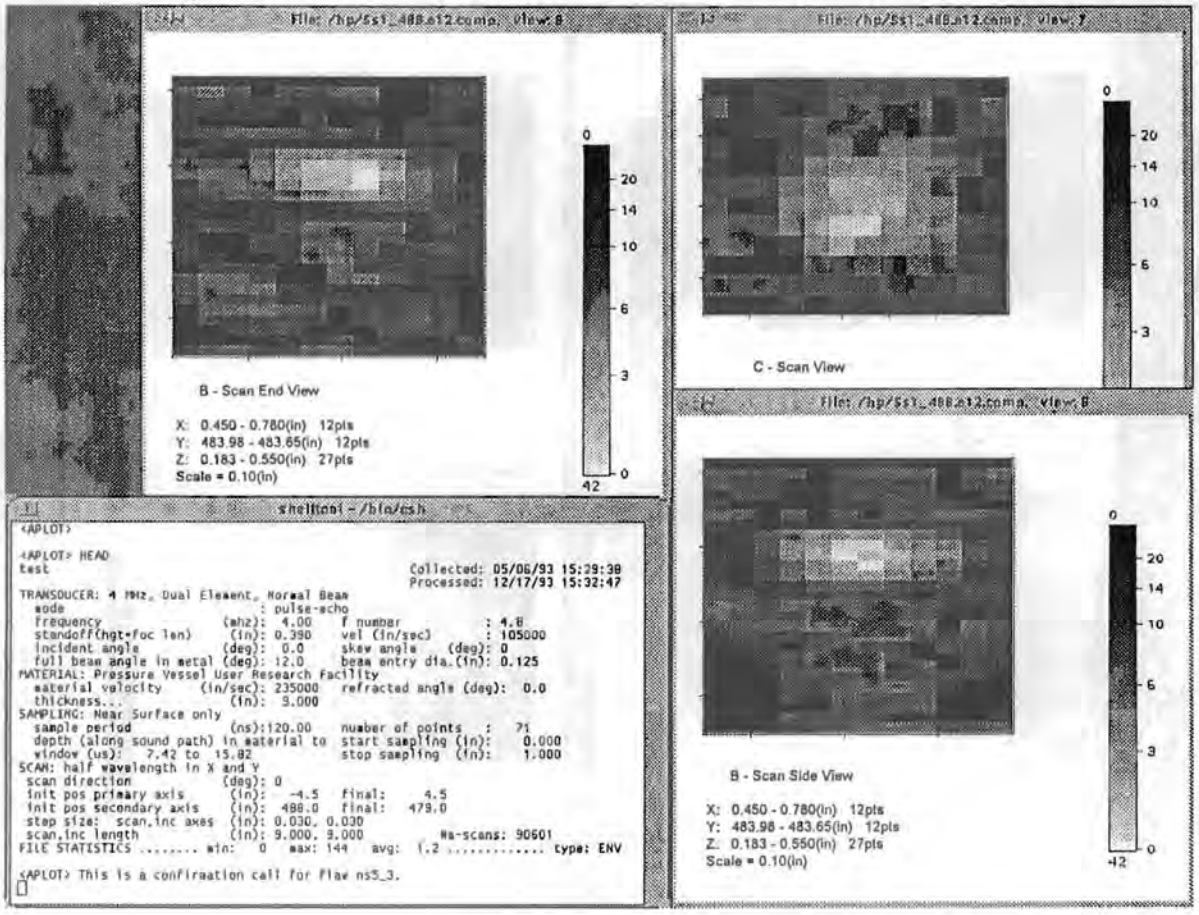

Figure A.51c - Volumetric indication #2 in the cladding: mode 1

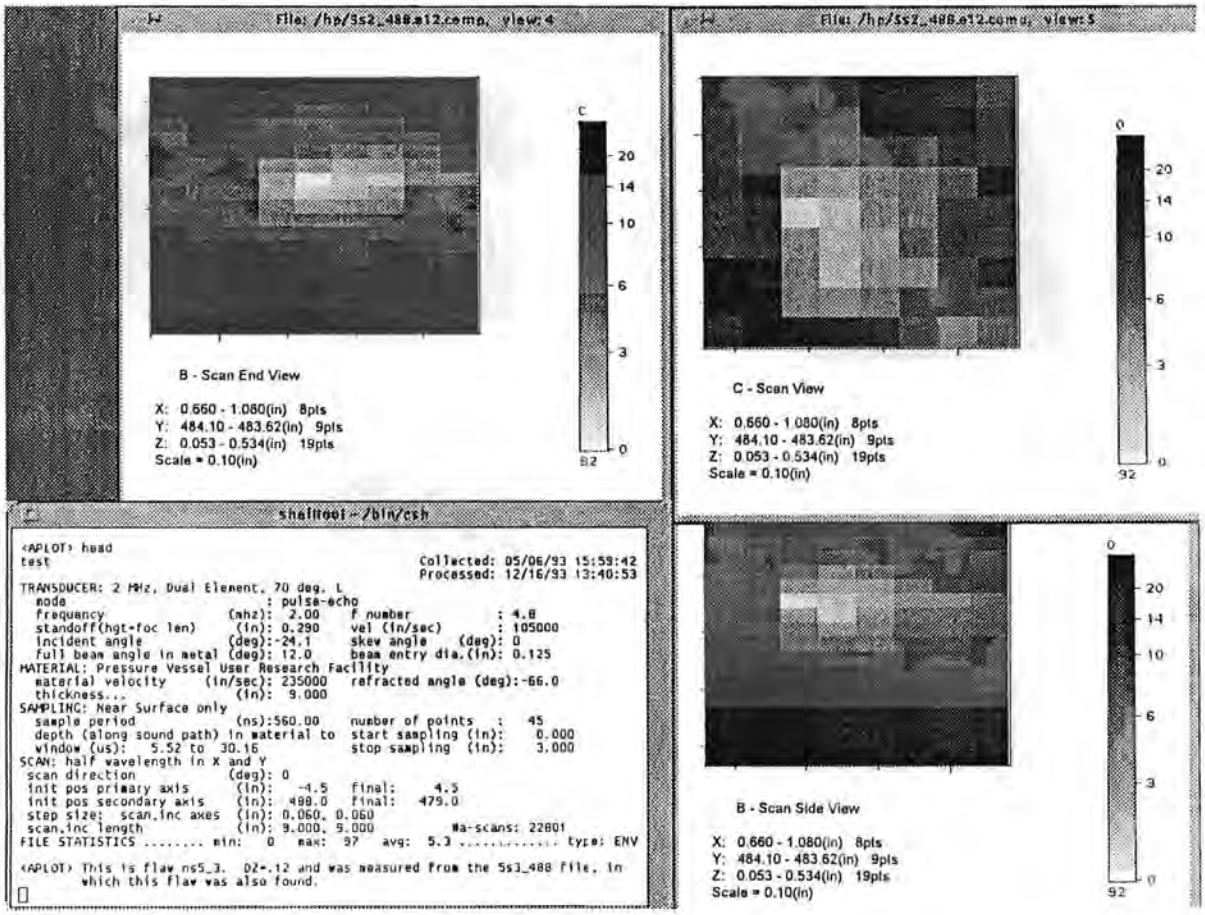

Figure A.51d - Volumetric indication #2 in the cladding: mode 2

Figures A.52a-c show volumetric indication #3 in the cladding. This planar indication has a through-wall extent of 2 mm based on different depth estimates and less than 1.5 mm based on a coin shaped indication at the clad to base metal interface. The detection was made in mode 3 where it displayed coin shape at a depth of 6 mm. There were confirmations in modes 1 and 5 at depths of 6 and 8 mm. The different Z values of 6 to 8 mm give an alternate depth size of 2 mm. The indication is characterized as volumetric based on normal beam detection. There is good evidence of coin shape in the side view of mode 3. The length is 6 mm and was made to LOS in mode 1. The width is 18 mm and was made to LOS in mode 1. The range of aspect ratios (width/depth) of this indication is 9 to 12. The maximum amplitude-to-noise ratio is of medium range at 83 to 25. The Z coordinate of 6 to 8 mm shows that the indication is in the clad-to-base metal interface. The X coordinate of 18 mm shows that the indication is over the base metal.

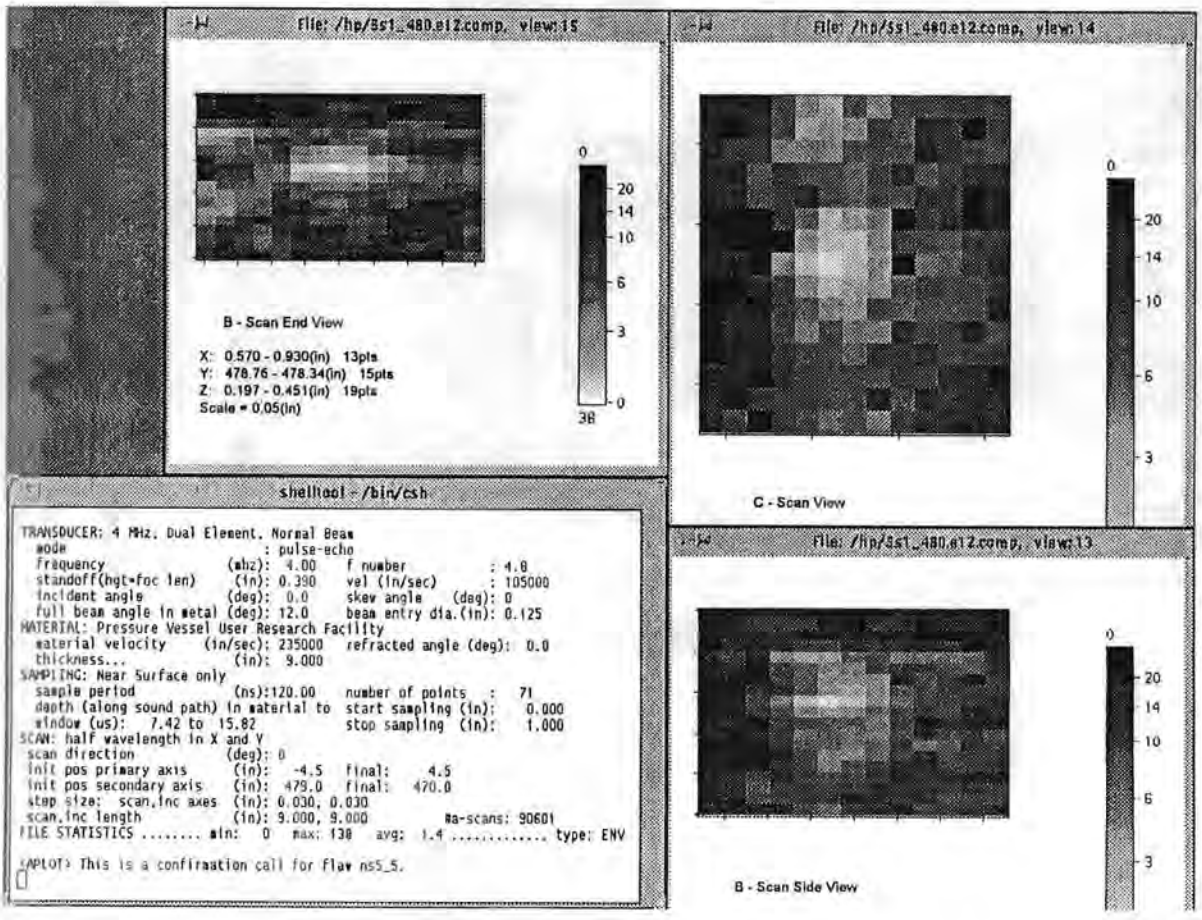

Figure A.52a - Volumetric indication #3 in the cladding: mode 1

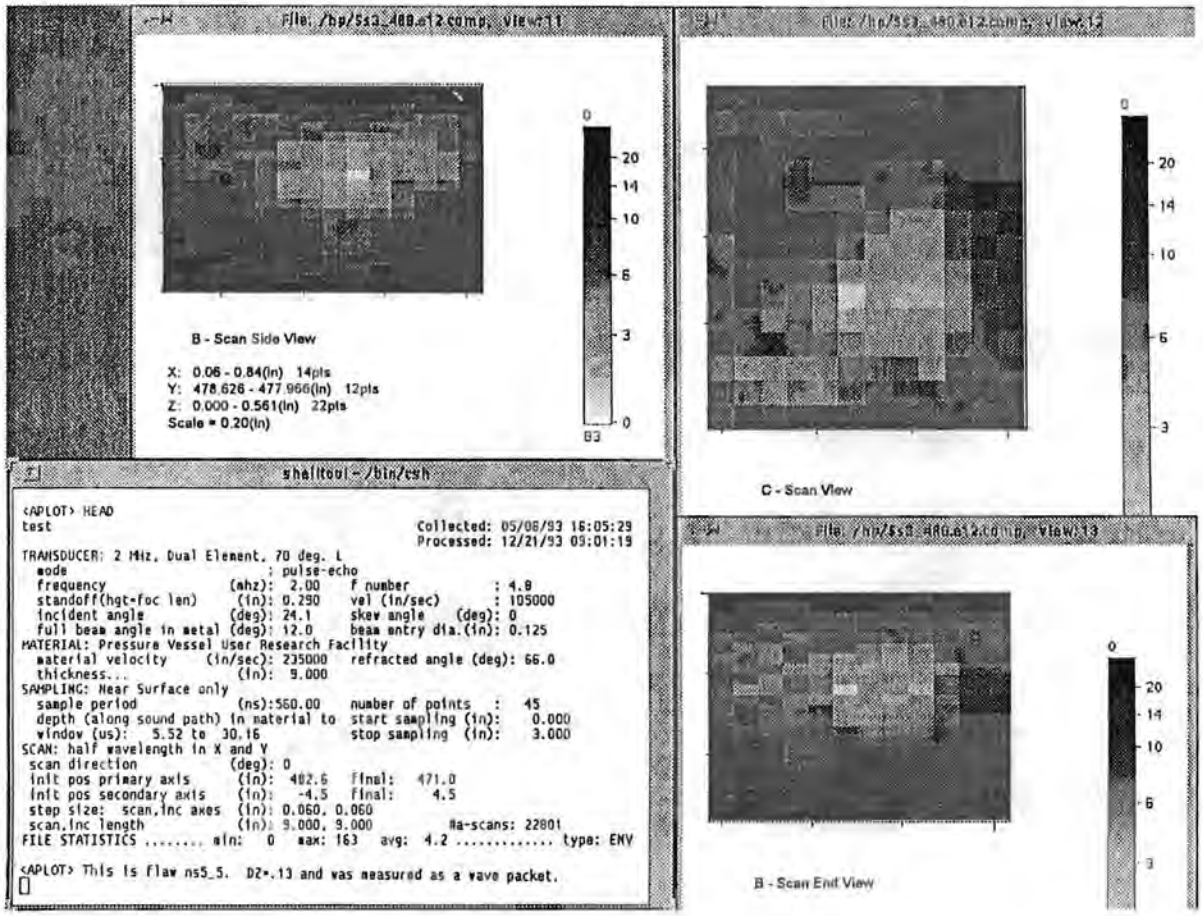

Figure A.52b - Volumetric indication #3 in the cladding: mode 3

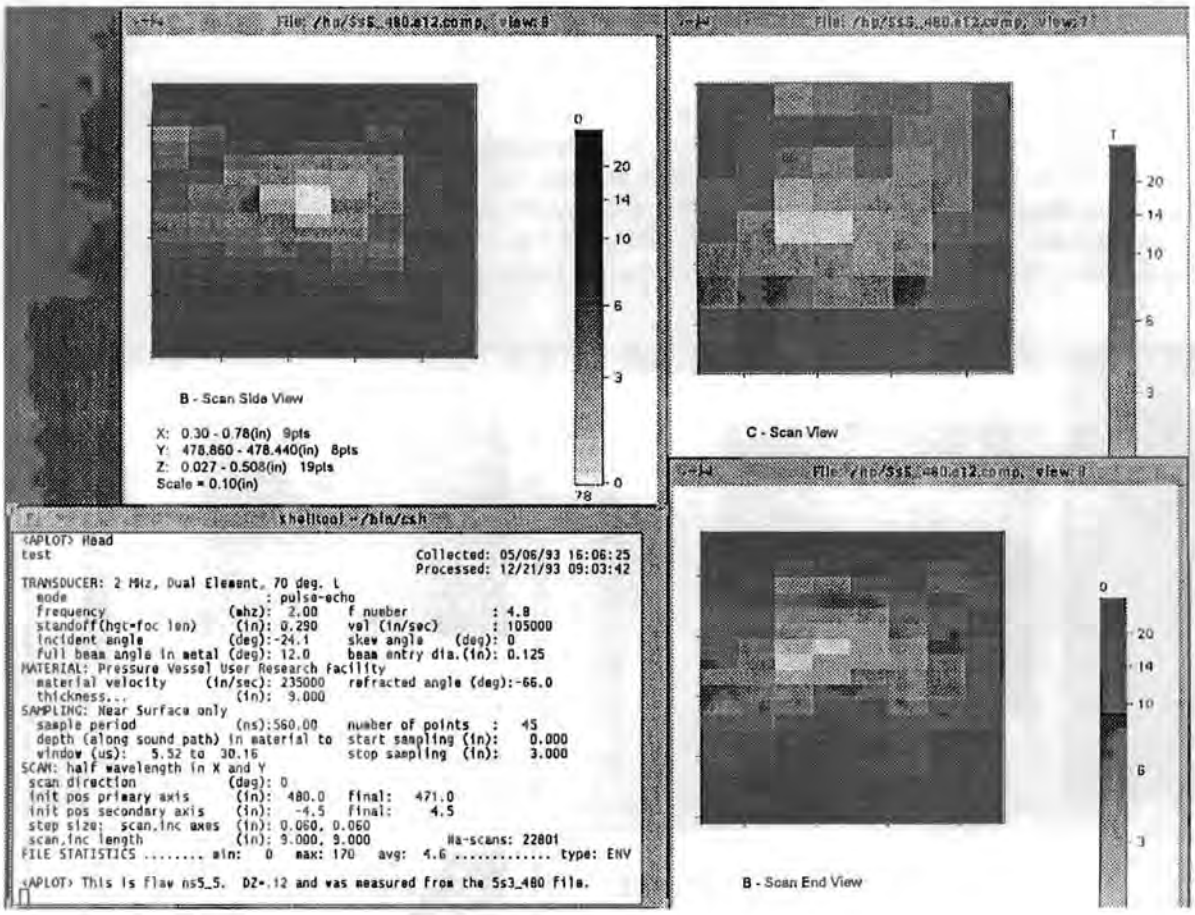

Figure A.52c - Volumetric indication #3 in the cladding: mode 5

Figures A.53a-d show volumetric indication #4 in the cladding. This volumetric indication has a through-wall extent of 2 mm based on different depth estimates of 7 to 9 mm and less than 1.5 mm based on an indication without TOF shape at the clad to base metal interface. The detection was made in modes 1 and 4 where it failed to display TOF shape but remained brighter than 95 counts at depths of 7 and 8 mm. There was a confirmation in mode 3 at a depth of 9 mm. The indication is characterized as volumetric based on normal beam detection. There is no evidence of coin shape in the side view of mode 3 and end view of mode 4. The length is 16 mm and was made to LOS in mode 4. The width is 8 mm and was made to LOS in mode 3. The range of aspect ratios (width/depth) of this indication is 9 to 11. The maximum amplitude-to-noise ratio is high at 210 to 20. The Z coordinate of 7 to 9 mm shows that this indication is in the clad-to-base metal interface. The X coordinate of 98 mm shows that the indication is over the base metal.

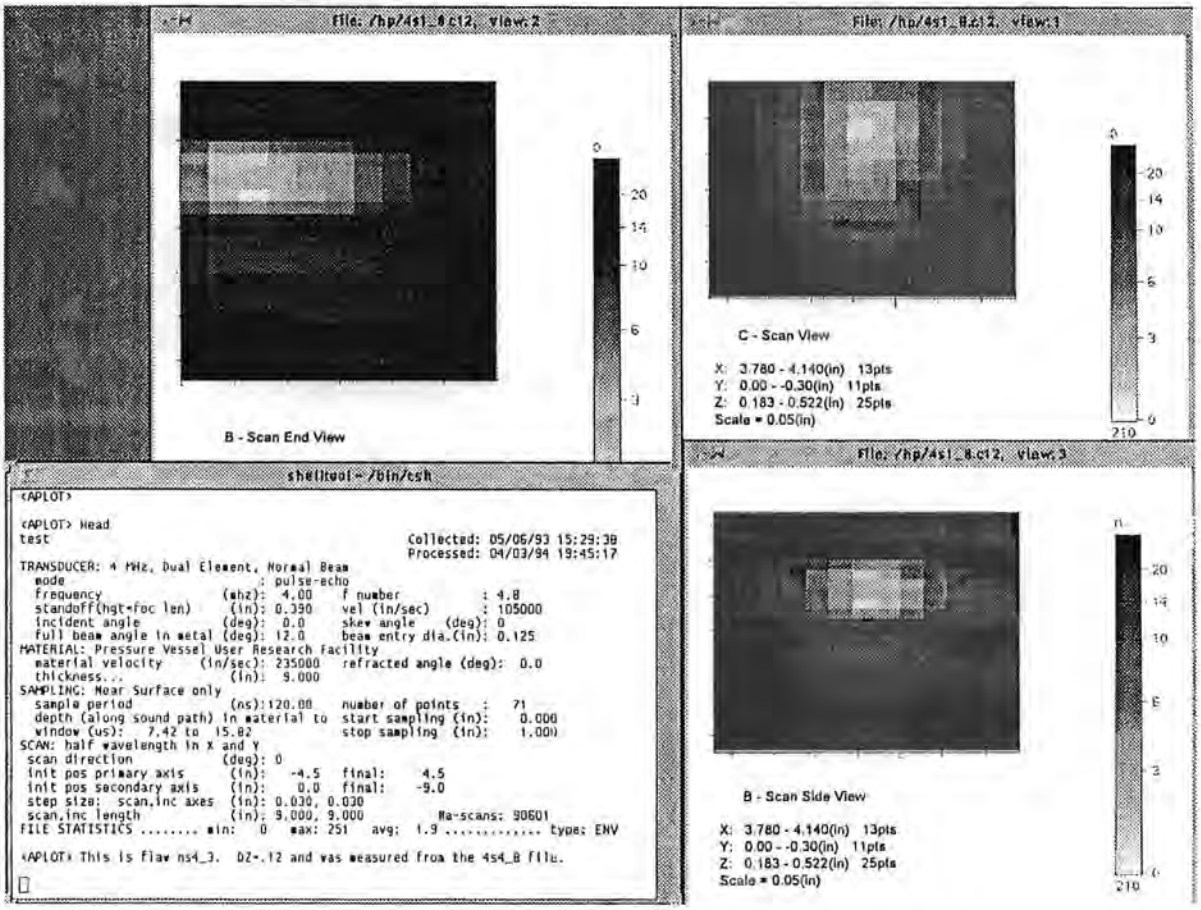

Figure A.53a - Volumetric indication #5 in the cladding: mode 1

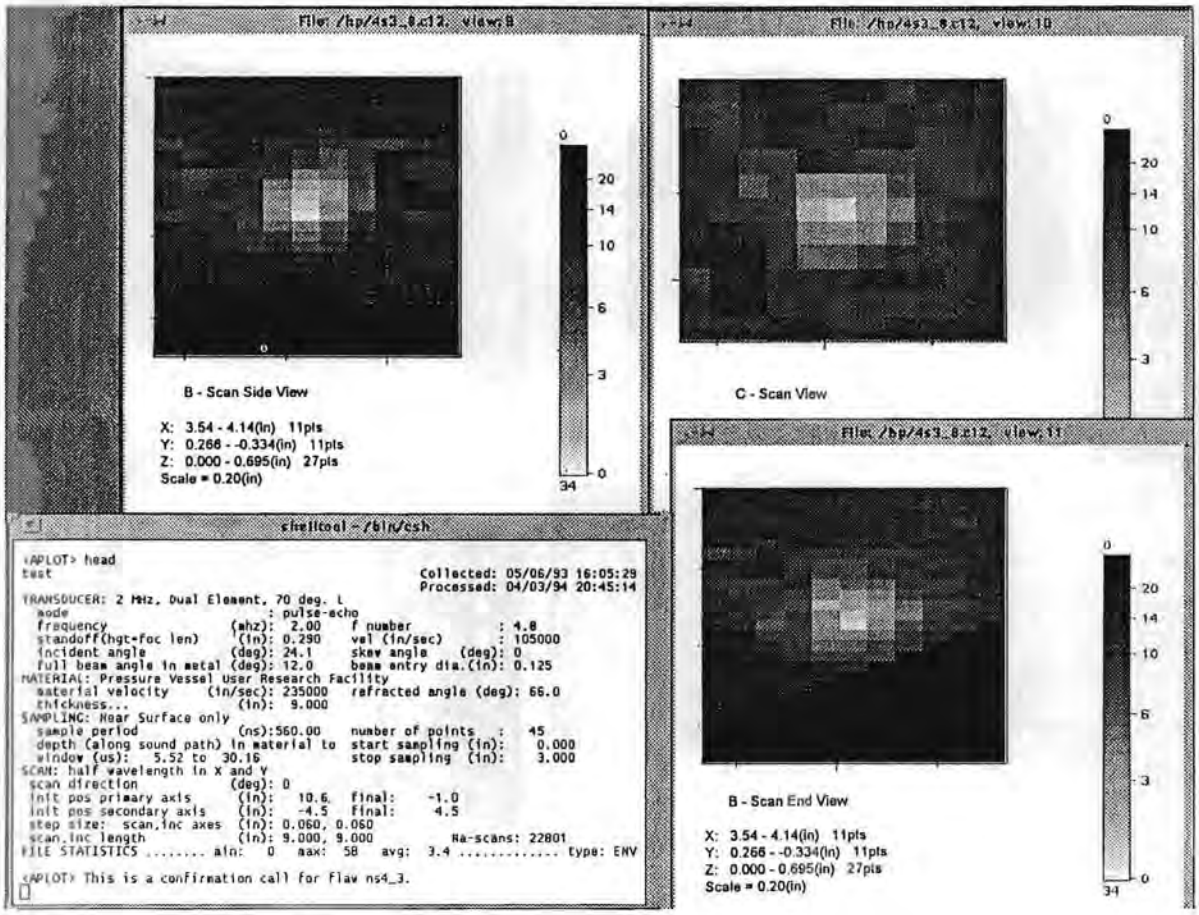

Figure A.53b - Volumetric indication #4 in the cladding: mode 3

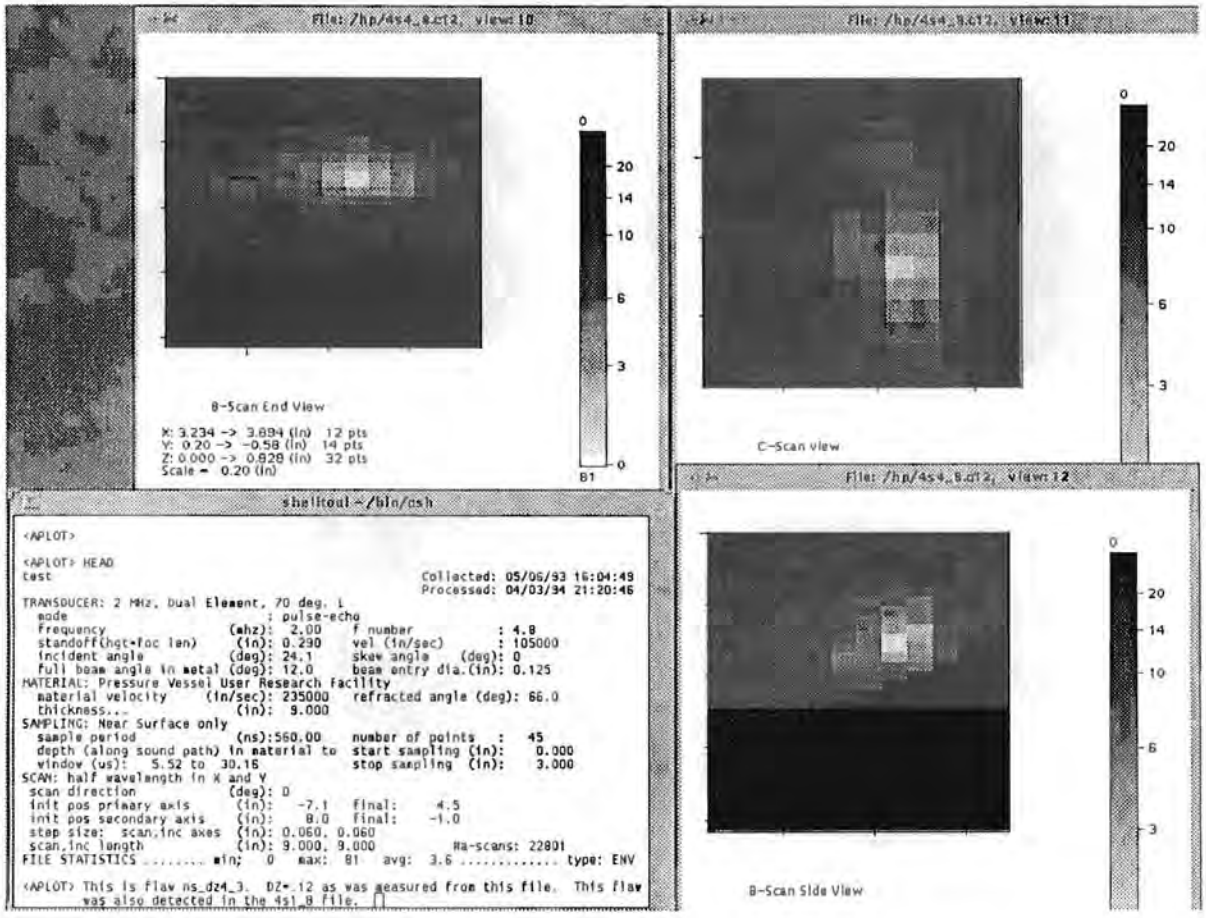

Figure A.53c - Volumetric indication #4 in the cladding: mode 4

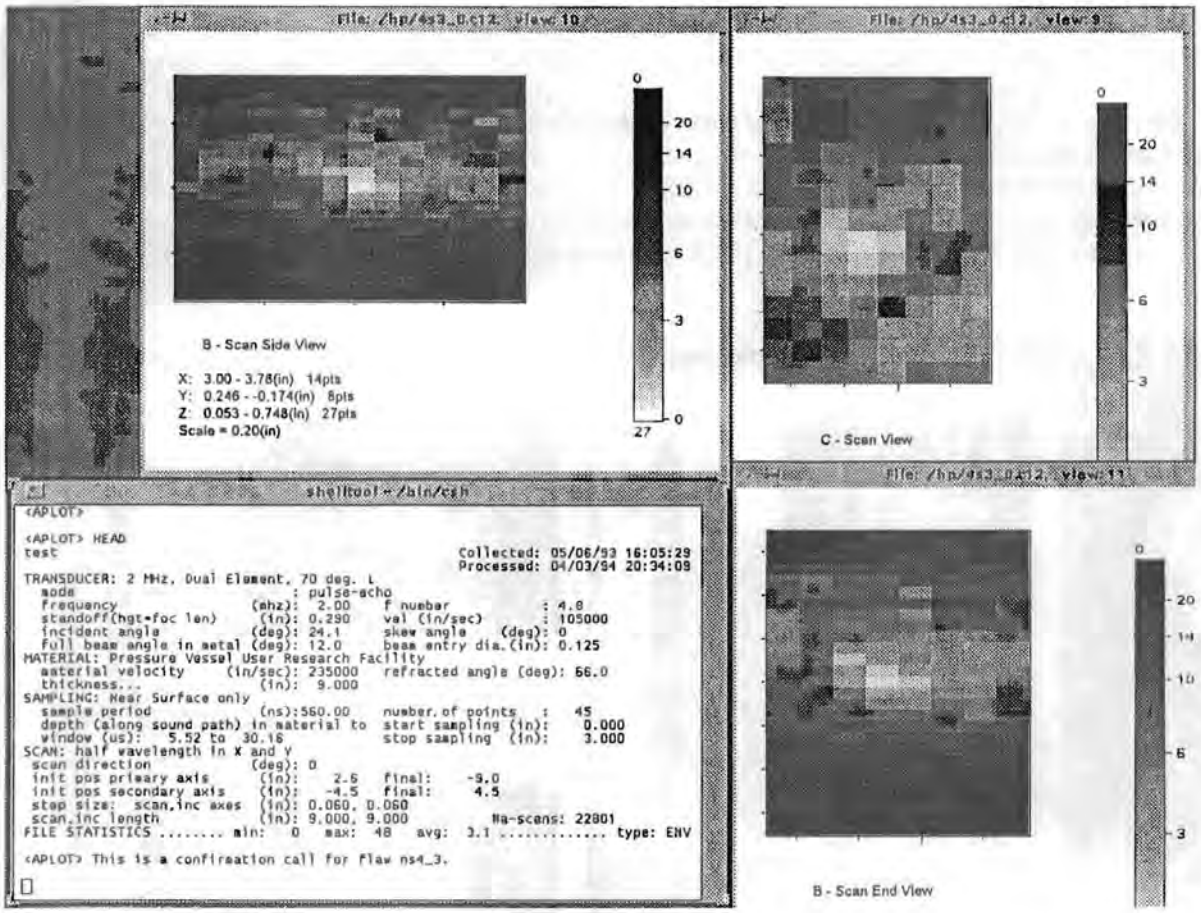

Figure A.53d - Volumetric indication #4 in the cladding: mode 3

Figures A.54a-c show volumetric indication #5 in the cladding. This volumetric indication has a through-wall extent of less than 1.5 mm based a bright indication without TOF shape in the clad to base metal interface. The detection was made in modes 2 and 5 where the bright, shallow indication failed to take shape at a depth of 6 mm. There was a confirmation in mode 3 at a depth of 6 mm. The three Z values of 6 mm give an alternate depth size of less than 1 mm. The indication is characterized as volumetric based on detection in orthogonal modes. There is some evidence of coin shape in the side view of mode 3. The length is 12 mm and was made to LOS in mode 2. The width is 11 mm and was made to LOS in mode 3. The maximum amplitude-to-noise ratio is of medium range at 112 to 40. The Z coordinate of 6 mm shows that the indication is in the clad-to-base metal interface. The X coordinate of 21 mm shows that the indication is over the base metal.

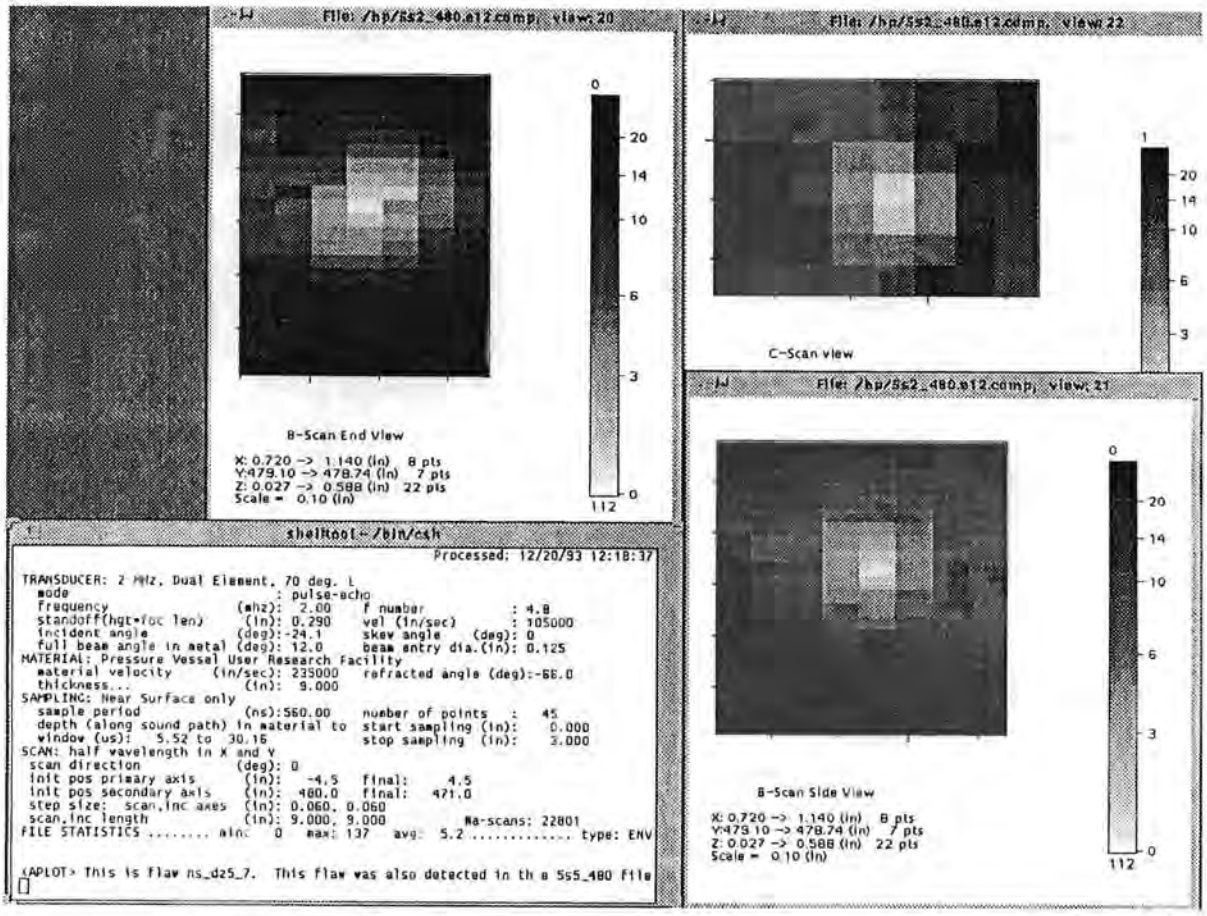

Figure A.54a - Volumetric indication #4 in the cladding: mode 2

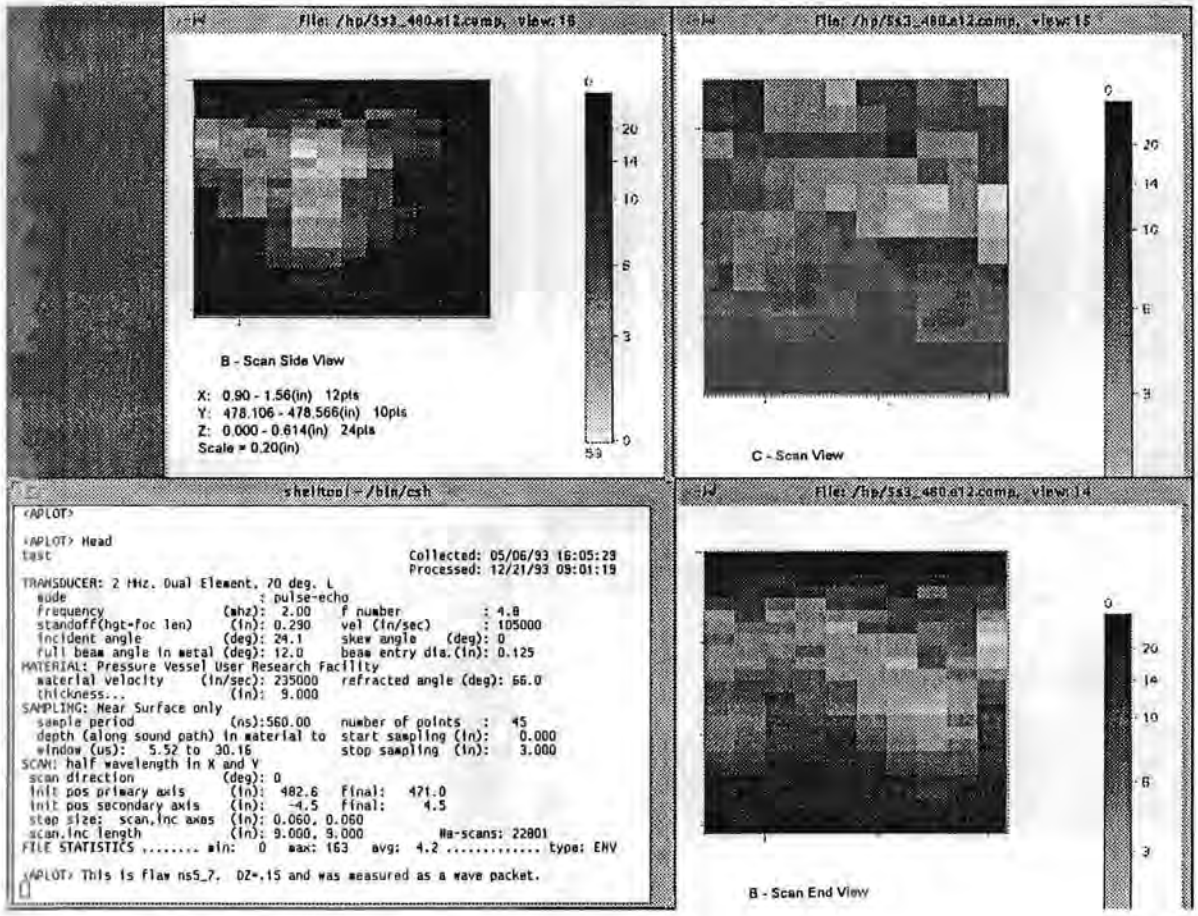

Figure A.54b - Volumetric indication #5 in the cladding: mode 3

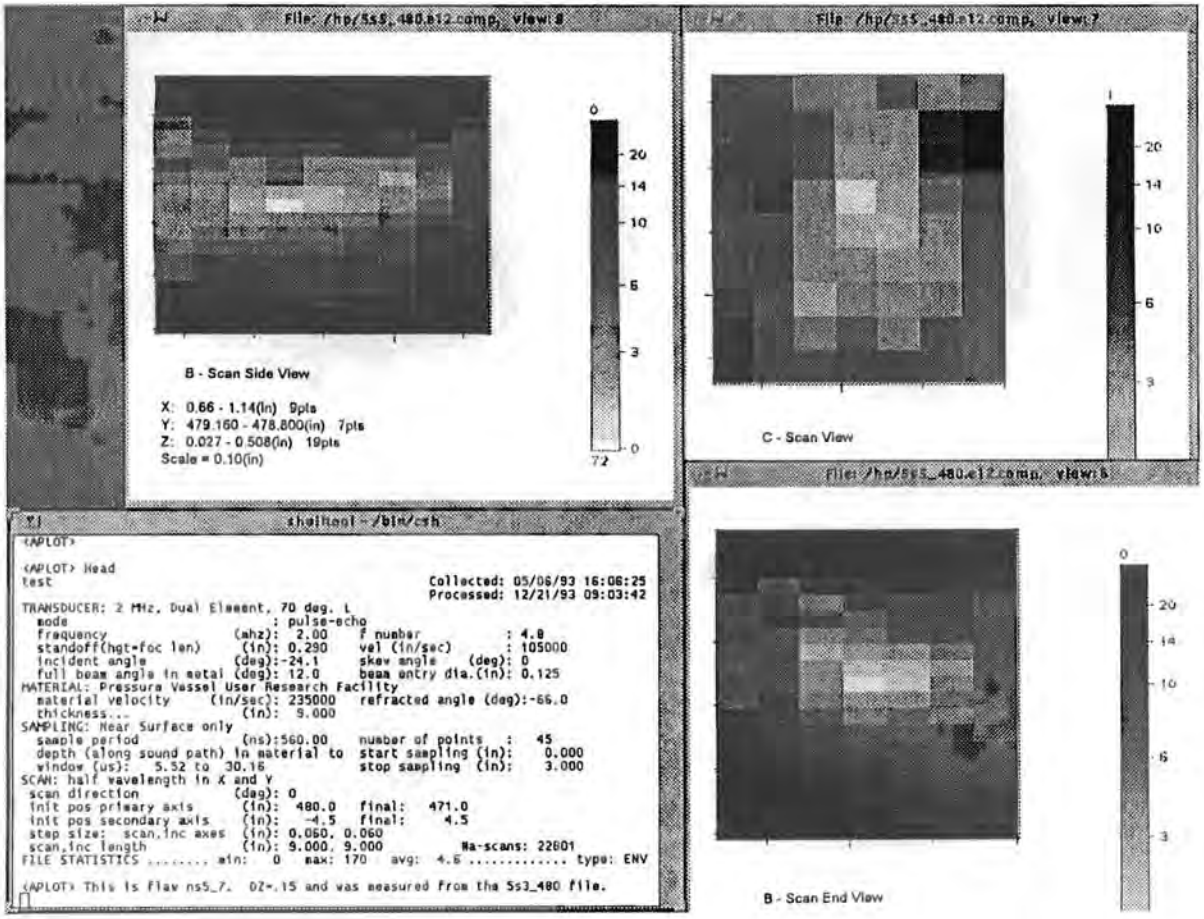

Figure A.54c - Volumetric indication #5 in the cladding: mode 5

Figures A.55a-c show volumetric indication #6 in the cladding. This volumetric indication has a through-wall extent of less than 1.5 mm based on an indication without TOF shape at the clad to base metal interface. The detection was made in modes 1 and 2 where the bright, shallow indication failed to take shape at a depth of 7 mm. There was a confirmation in mode 3 at a depth of 9 mm. The different Z values of 7 to 9 mm give an alternate depth size of 2 mm. The indication is characterized as volumetric based on normal beam detection. There is no evidence of coin shape in the end view of modes 2 and the side view of mode 3. The maximum amplitude-to-noise ratio is high at 255 to 20. The Z coordinate of 7 to 9 mm shows that the indication is in the clad-to-base metal interface. The X coordinate of 94 mm shows that the indication is over the base metal.

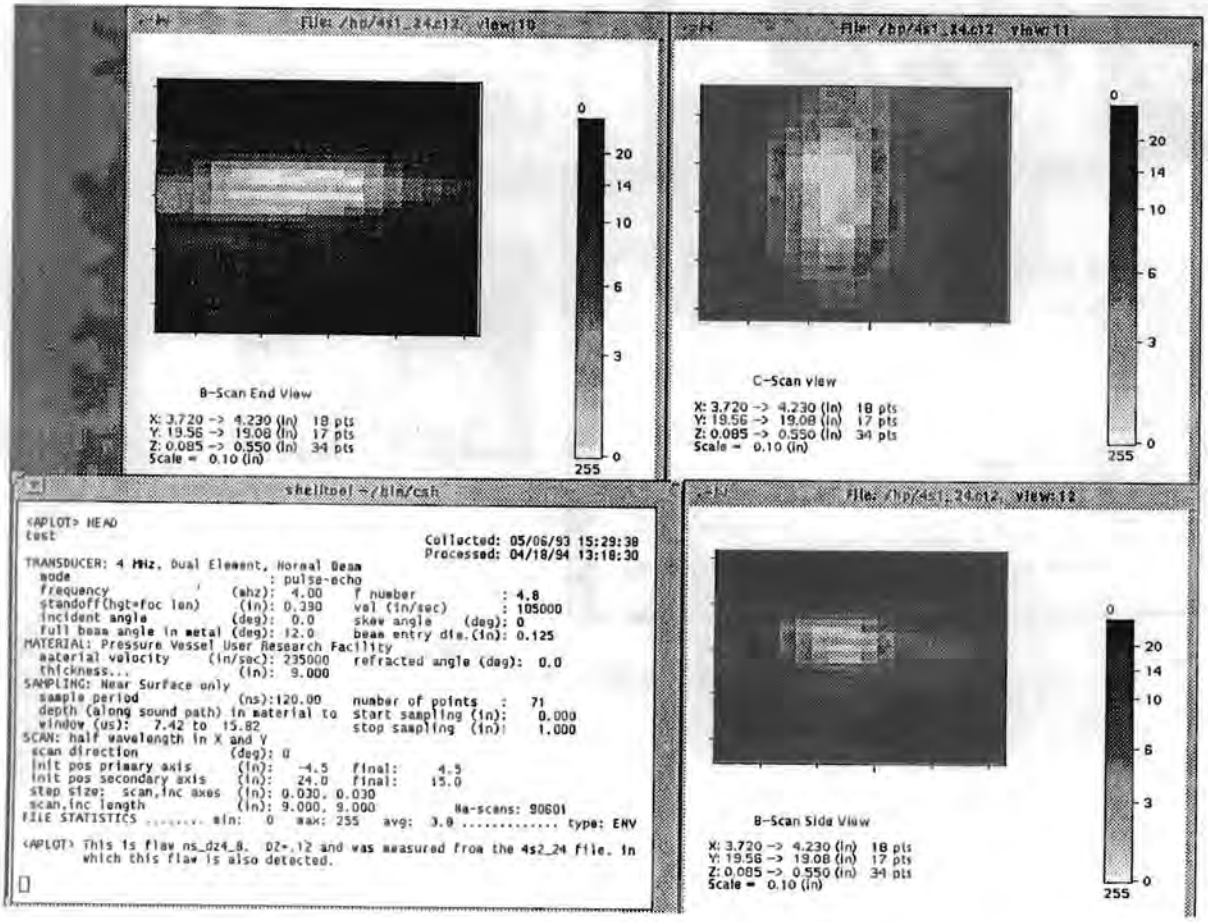

Figure A.55a - Volumetric indication #6 in the cladding: mode 1

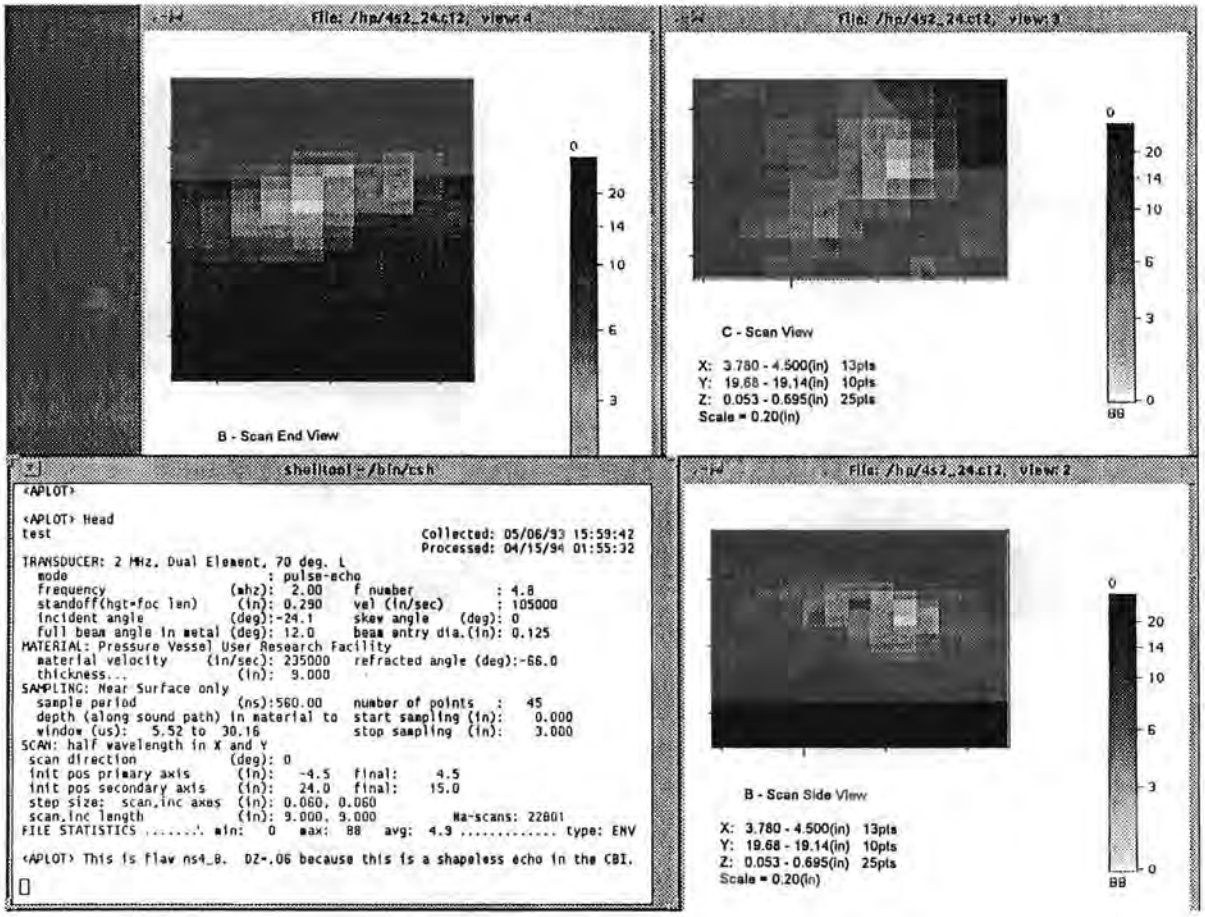

Figure A.55b - Volumetric indication #6 in the cladding: mode 2

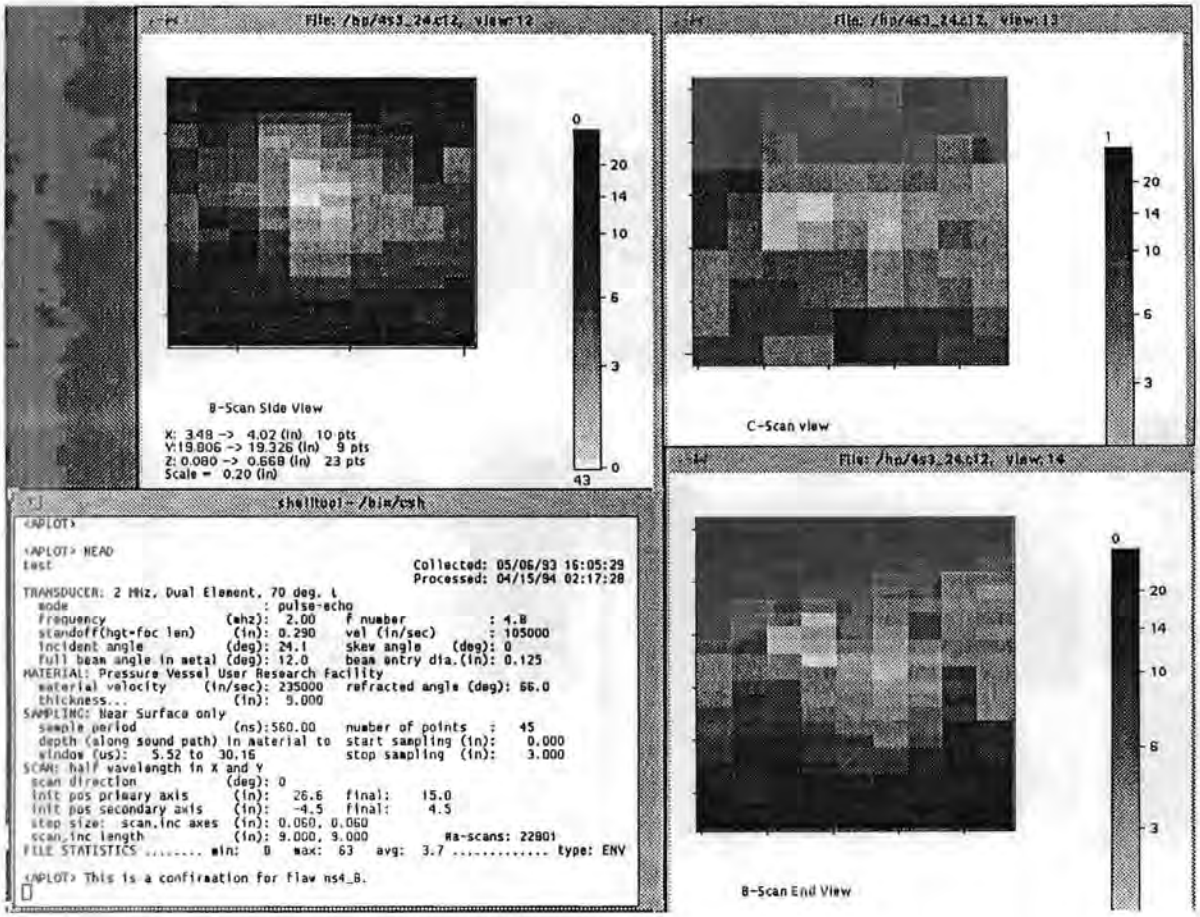

Figure A.55c - Volumetric indication #6 in the cladding: mode 3

Planar Indications in the Weldment Below 25 mm

Figure A.56 shows planar indication #1 in the weldment below 25 mm. This planar indication has a through-wall extent of 14 mm based on tip signal pattern. The detection was made in mode 6 where it displayed a pair of TOF shapes at a depth of 64 mm. The shape quality is good for this indication. There were no confirmations in other modes. The indication is characterized as planar based on the tip signal pattern. The length is 18 mm and was made to LOS in mode 6. The aspect ratio (length/depth) of this indication is 1.3. The maximum amplitude-to-noise ratio is high at 36 to 5. With an X coordinate of -8 mm, the indication is in the weld. With a Z coordinate of 64 mm, the indication is in the middle third of the vessel.

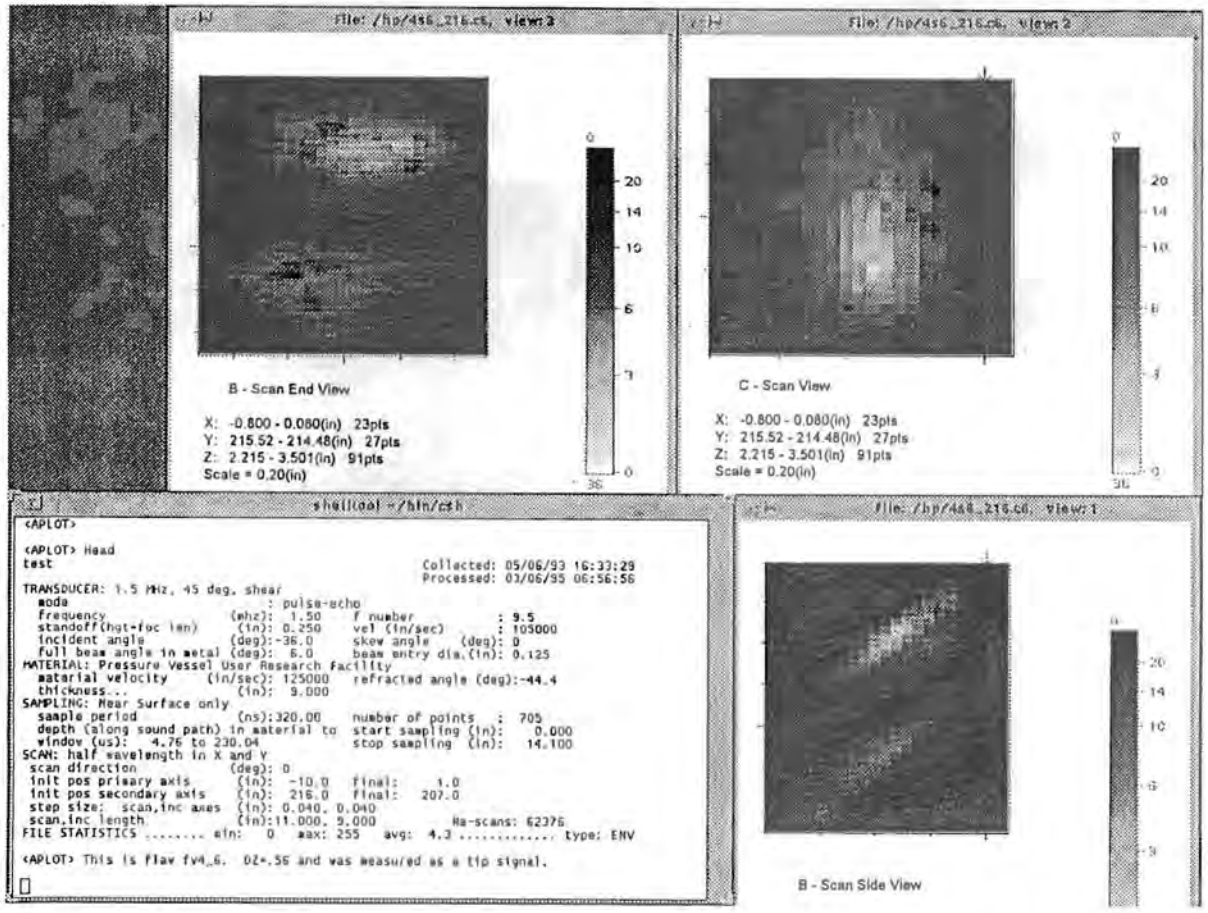

Figure A.56 - Planar indication #1 in the weldment below 25 mm: mode 6

Figures A.57a-b show planar indication #2 in the weldment below 25 mm. This planar indication has a through-wall extent of 13 mm based on tip signal pattern. The detection was made in mode 10 where it displayed normal beam shape at a depth of 115 mm. There was a confirmation in mode 6 at a depth of 112 mm. The confirmation mode detected the tip signal pattern. The indication is characterized as planar based on the tip pattern. The length is 25 mm and was made to LOS in mode 6. The width is 9 mm and was made to LOS in mode 10. The aspect ratio (length/depth) of this indication is 2. The maximum amplitude-to-noise ratio is high at 56 to 11. With an X coordinate of -8 mm, the indication is in the weld. With a Z coordinate of 115 mm, the indication is in the middle third of the vessel.

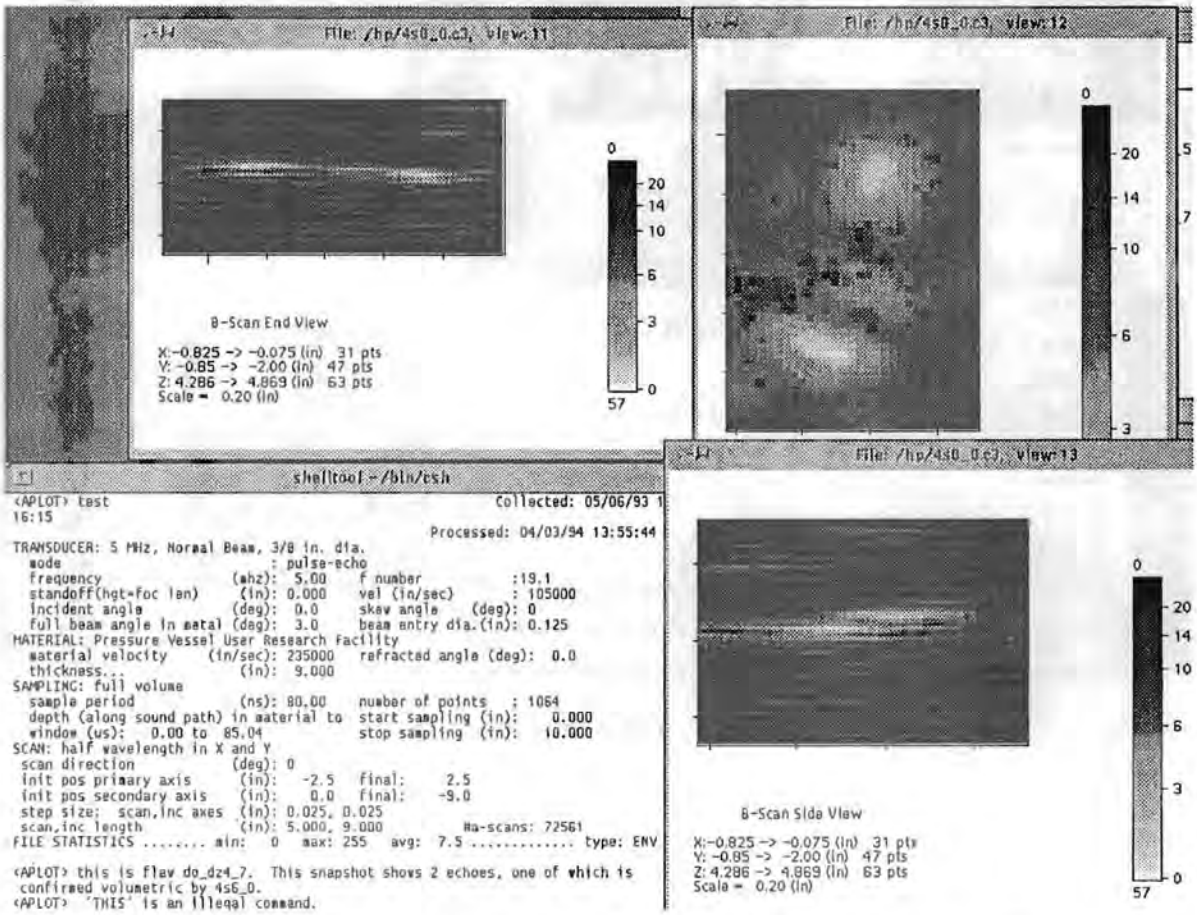

Figure A.57a - Planar indication #2 in the weldment below 25 mm: mode 10

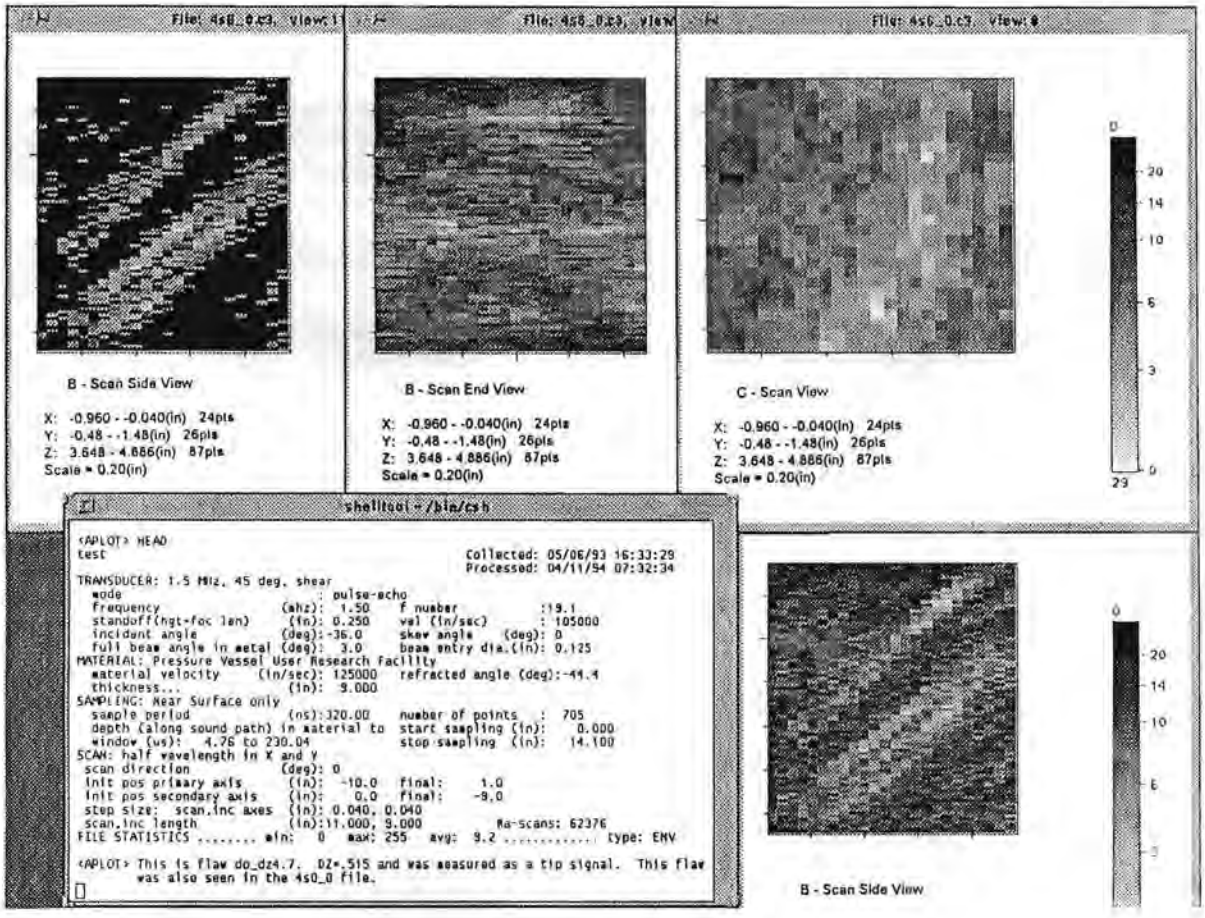

Figure A.57b - Planar indication #2 in the weldment below 25 mm: mode 6

Figures A.58a-b show planar indication #3 in the weldment below 25 mm. This planar indication has a through-wall extent of 11 mm based on tip signal pattern. The detection was made in mode 6 where it displayed a pair of TOF shapes at a depth of 75 mm. The shape quality is good for this indication. There was a confirmation in mode 8 at a depth of 74 mm. The different Z values of 74 to 75 mm give an alternate depth size of 1 mm. The indication is characterized as planar based on the tip signal pattern. The length is 18 mm and was made to LOS in mode 6. The range of aspect ratios (length/depth) of this indication is 1.6 to 18 which tends to confirm the larger through-wall extent. The maximum amplitude-to-noise ratio is high at 21 to 3. With an X coordinate of -7 mm, the indication is clearly in the weld. The Z coordinate of 75 mm shows that the indication is in the middle third of the vessel.

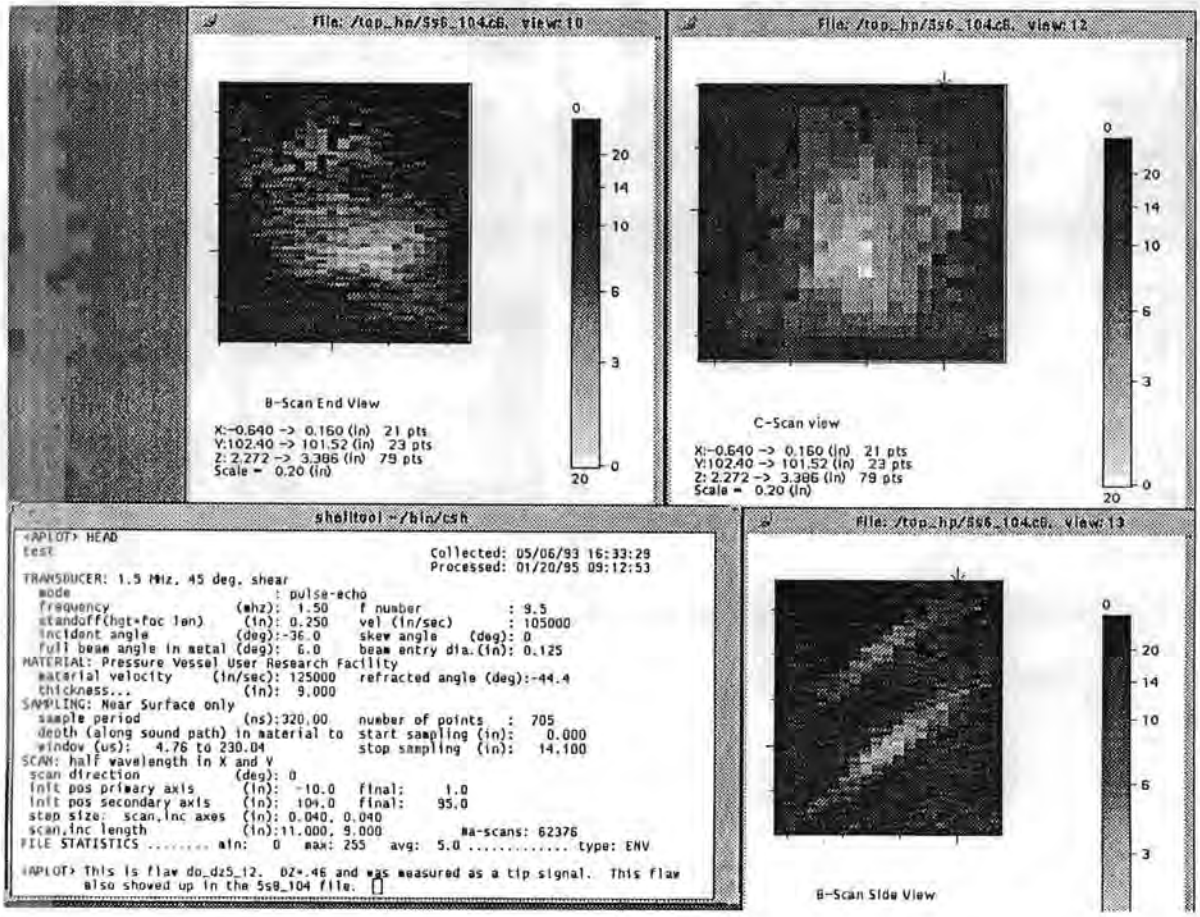

Figure A.58a - Planar indication #3 in the weldment below 25 mm: mode 6

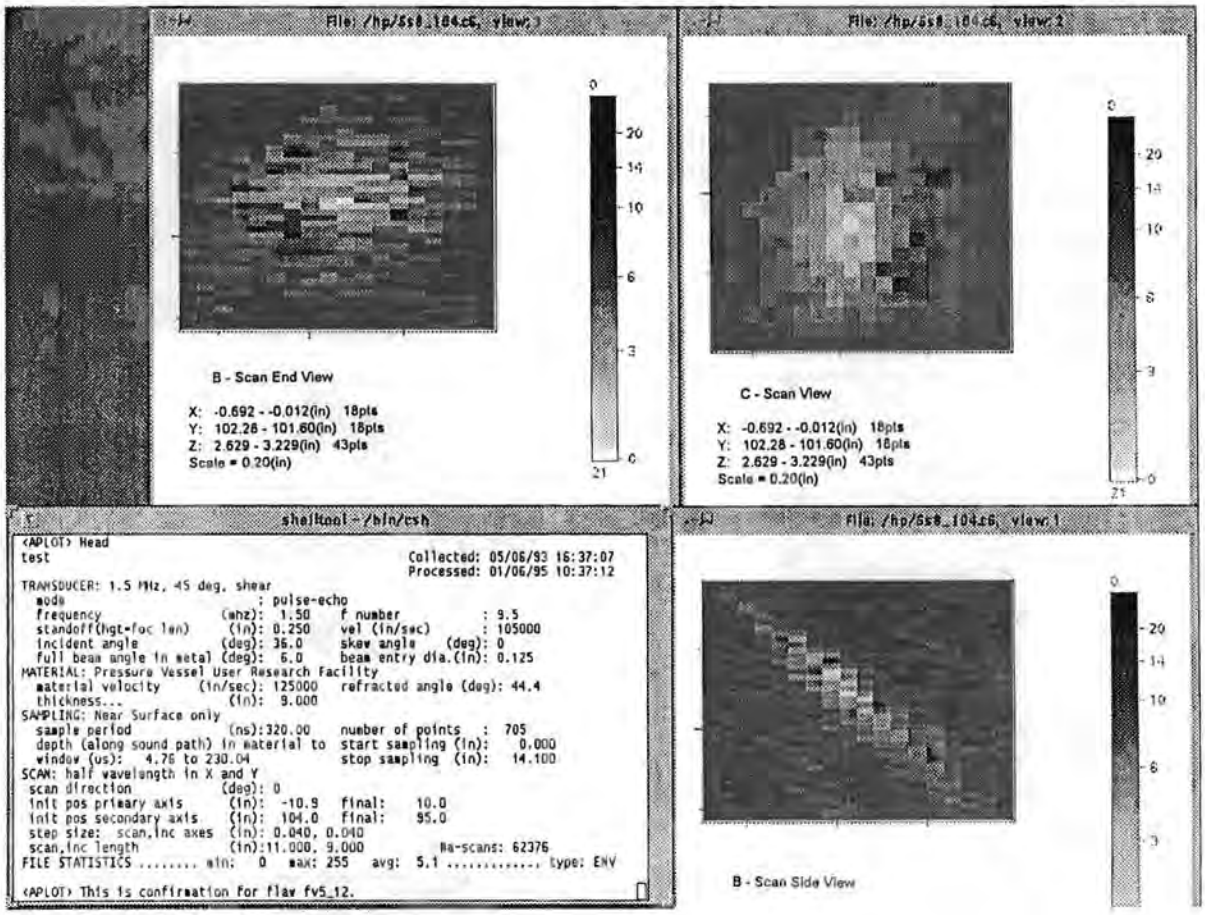

Figure A.58b - Planar indication #3 in the weldment below 25 mm: mode 8

Figure A.59 shows planar indication #4 in the weldment below 25 mm. This planar indication has a through-wall extent of 11 mm based on tip signal pattern. The detection was made in mode 6 where it displayed a pair of TOF shapes at a depth of 73 mm. The shape quality is good for this indication. There were no confirmations in other modes. The indication is characterized as planar based on the tip signal pattern. The length is 18 mm and was made to LOS in mode 6. The aspect ratio (length/depth) of this indication is 1.6. The maximum amplitude-to-noise ratio is high at 25 to 5. The X coordinate of -7 mm shows that the indication is in the weld. The Z coordinate of 73 mm shows that the indication is in the middle third of the vessel.

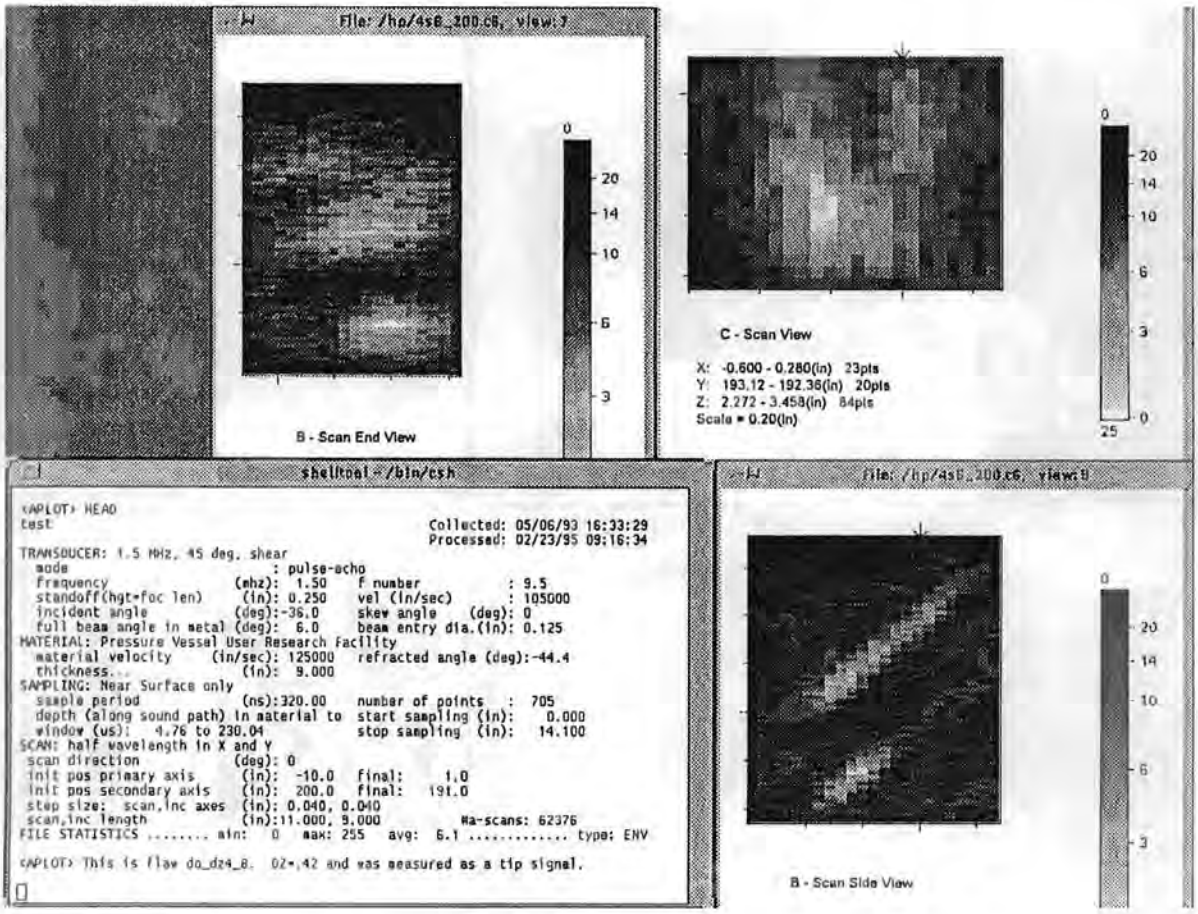

Figure A.59 - Planar indication #4 in the weldment below 25 mm: mode 6

Figure A.60 shows planar indication #5 in the weldment below 25 mm. This planar indication has a through-wall extent of 9 mm based on tip signal pattern. The detection was made in mode 6 where it displayed a pair of TOF shapes at a depth of 81 mm. The shape quality for this indication is good but broken up, implying that more than one small flaw may be present. There were no confirmations in other modes. The indication is characterized as planar based on the tip signal pattern. The length is 16 mm and was made to LOS in mode 6. The aspect ratio (length/depth) of this indication is 1.8. The maximum amplitude-to-noise ratio is high at 37 to 6. The X coordinate of -6 mm shows that the indication is in the weld. The Z coordinate of 81 mm shows that the indication is in the middle third of the vessel.

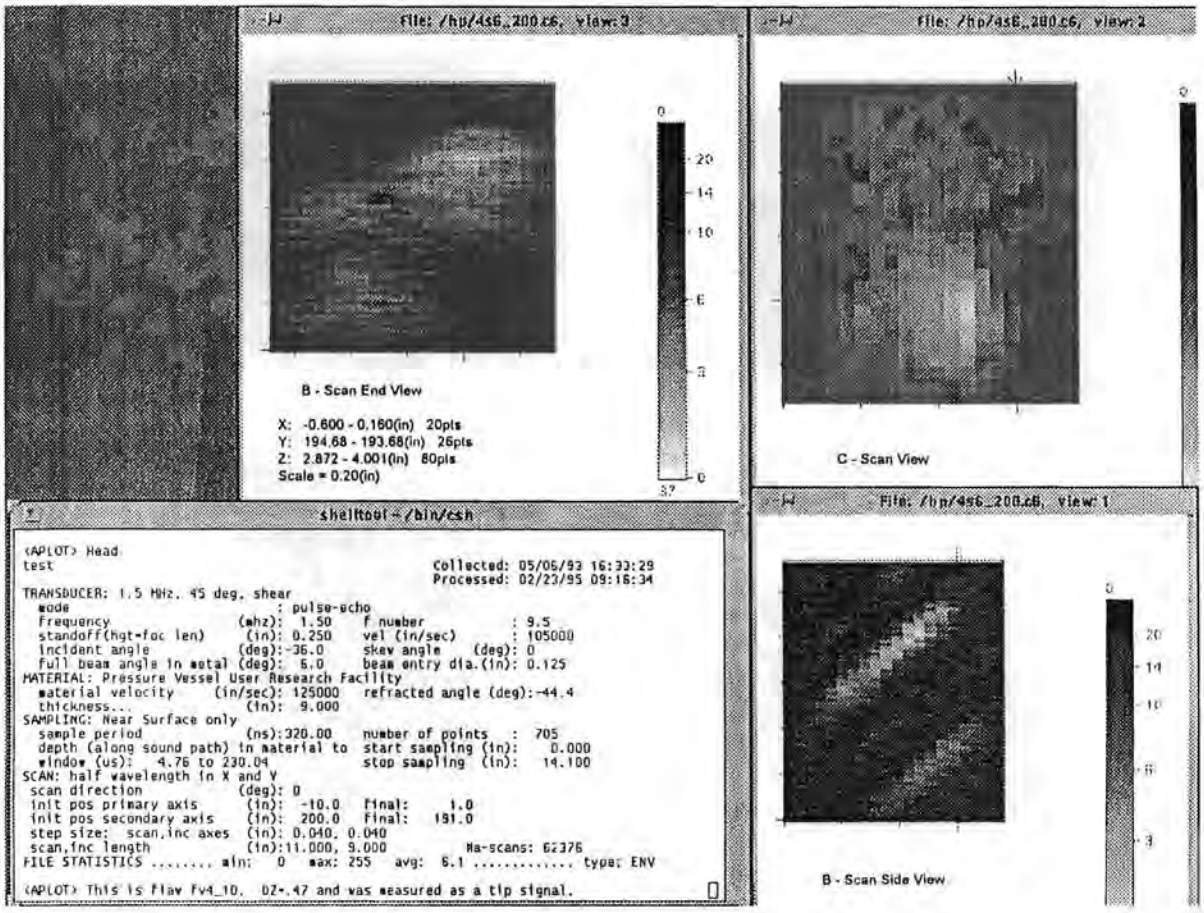

Figure A.60 - Planar indication #5 in the weldment below 25 mm: mode 6

Figure A.61 shows planar indication #6 in the weldment below 25 mm. This planar indication has a through-wall extent of 9 mm based on tip signal pattern. The detection was made in mode 6 where it displayed a pair of TOF shapes at a depth of 211 mm. The shape quality is good for this indication. There were no confirmations in other modes. The indication is characterized as planar based on the tip signal pattern. The length is 30 mm and was made to LOS in mode 6. The aspect ratio (length/depth) of this indication is 3. The maximum amplitude-to-noise ratio is of medium range at 27 to 11. The X coordinate of 23 mm shows that the indication is in the weld. The Z coordinate of 211 mm shows that the indication is near the outer wall of the vessel.

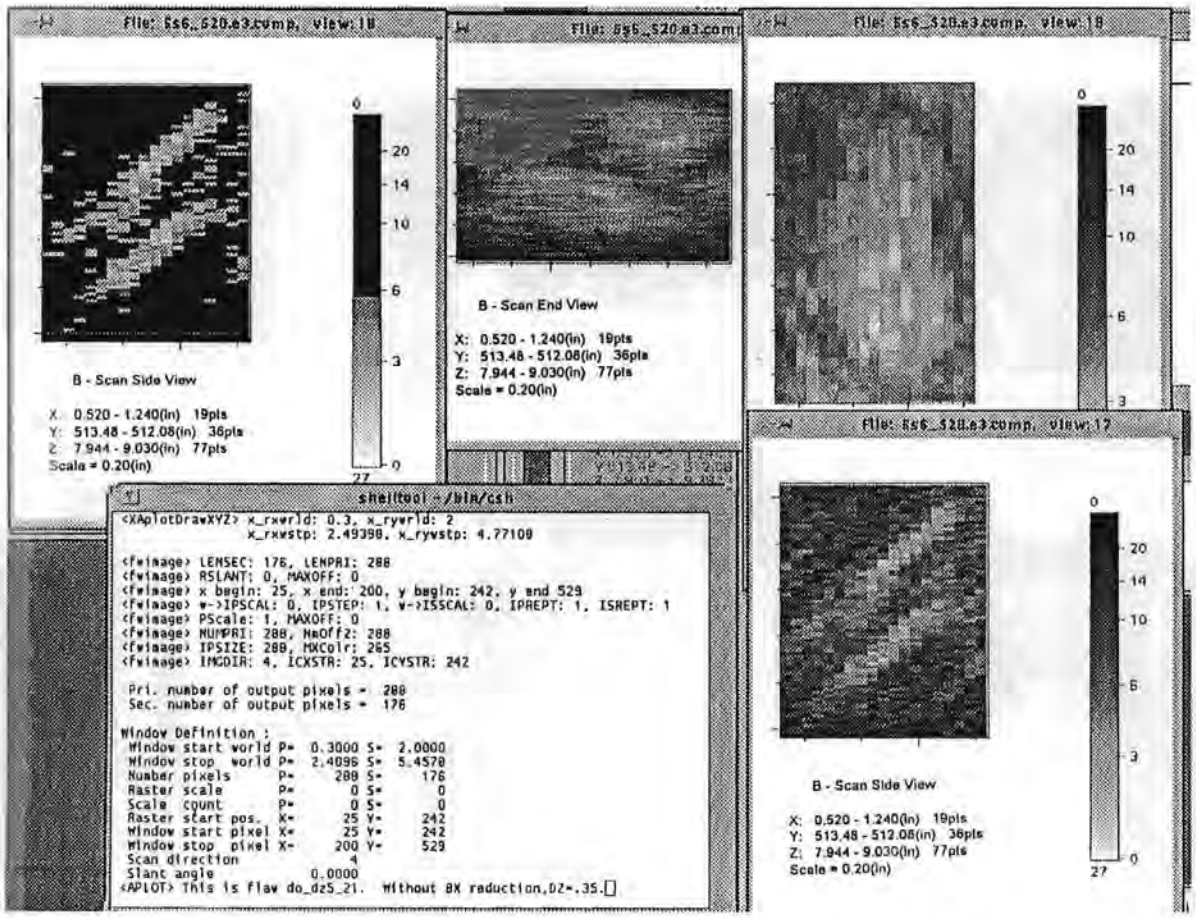

Figure A.61 - Planar indication #6 in the weldment below 25 mm: mode 6

Figures A.62a-b show planar indication #7 in the weldment below 25 mm. This planar indication has a through-wall extent of 9 mm based on tip signal pattern. The detection was made in modes 6 and 8 where it displayed a pair of TOF shapes at depths of 68 and 63 mm. The shape quality is good for this indication. There were no confirmations in other modes. The indication is characterized as planar based on the tip signal pattern. The length is 16 mm and was made to LOS in mode 8. The aspect ratio (length/depth) of this indication is 1.8. The maximum amplitude-to-noise ratio is high at 15 to 5. The X coordinate of -8 mm shows that the indication is in the weld. The Z coordinate of 63 to 68 mm shows that the indication is in the middle third of the vessel.

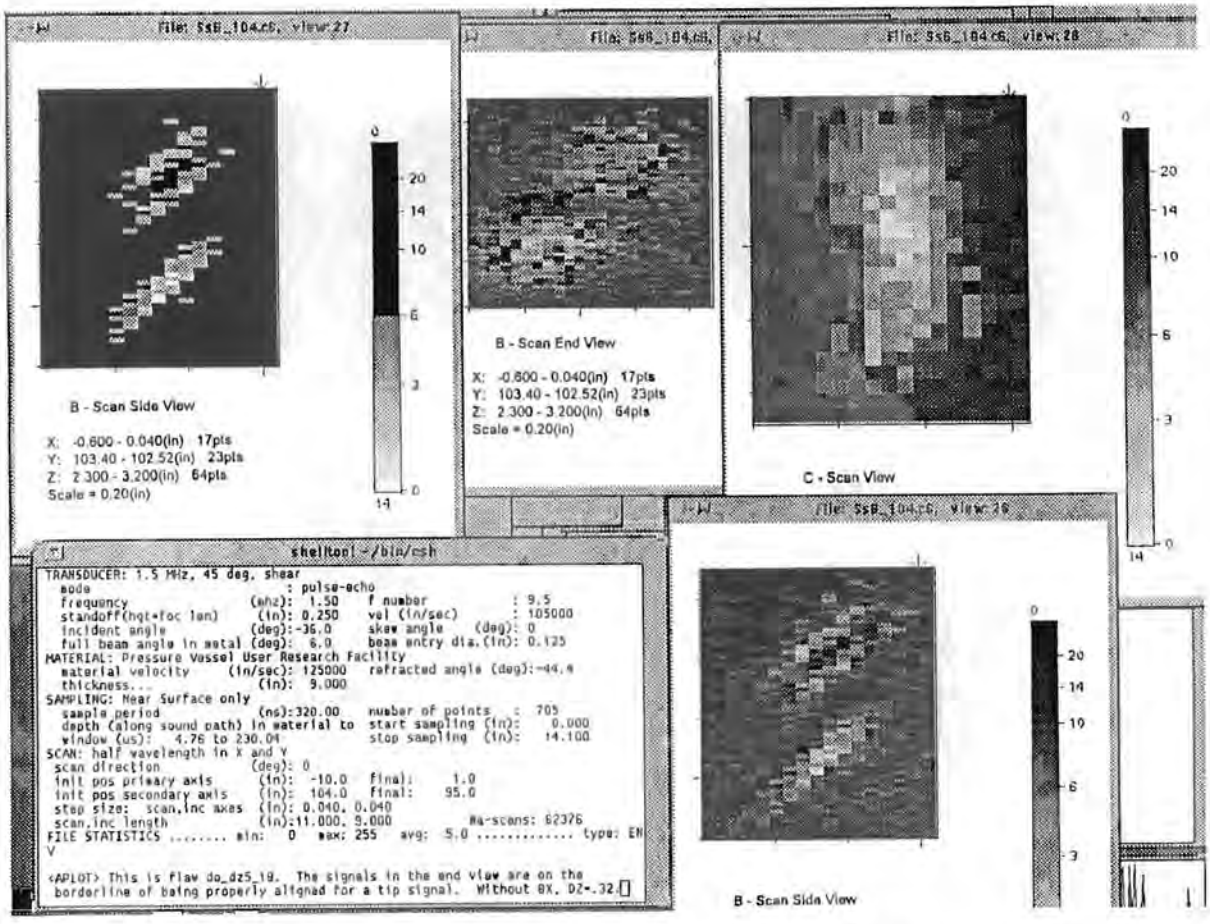

Figure A.62a - Planar indication #7 in the weldment below 25 mm: mode 6

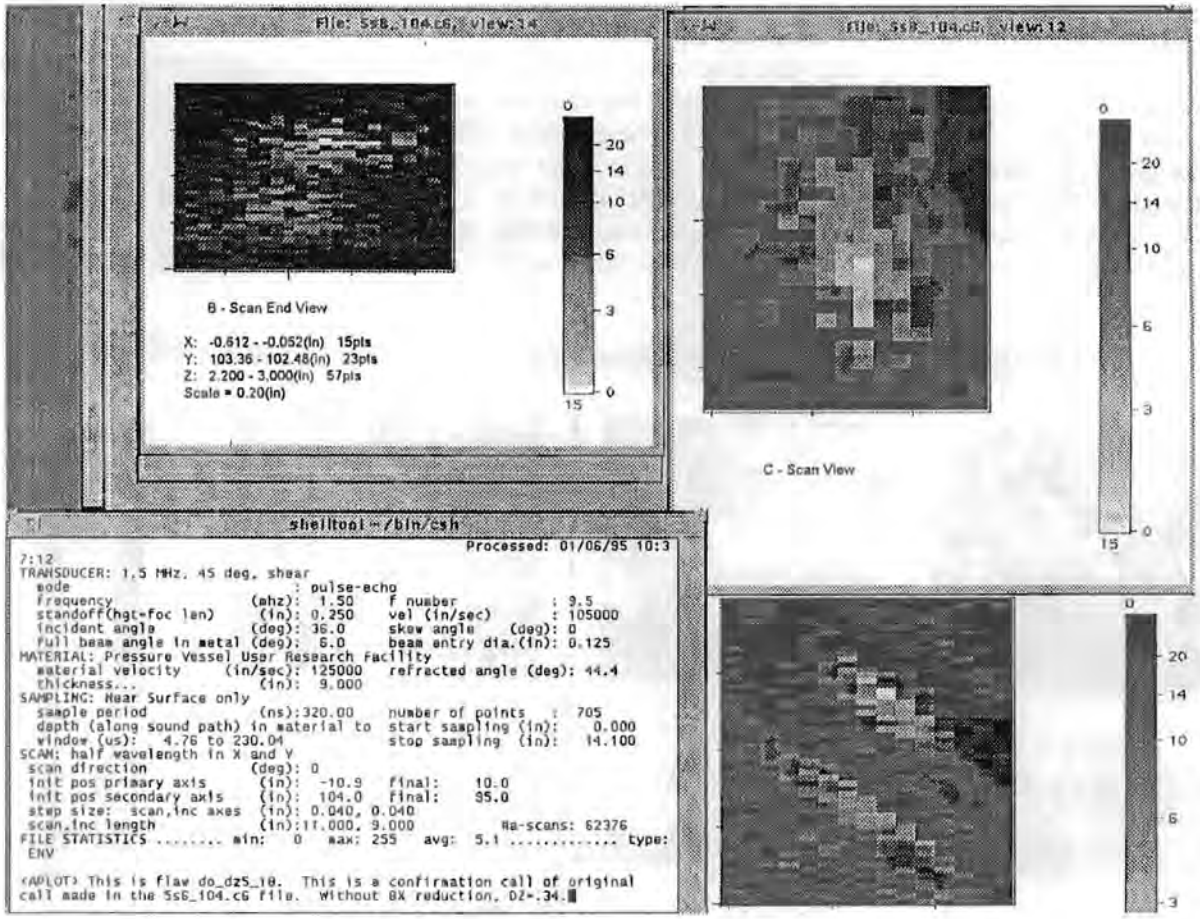

Figure A.62b - Planar indication #7 in the weldment below 25 mm: mode 8

Figures A.63a-b show planar indication #8 in the weldment below 25 mm. This planar indication has a through-wall extent of 7 mm based on wave packet width. The detection was made in modes 6 and 8 where it had isolated TOF shapes at depths of 213 and 218 mm. The shape quality is good for this indication and is broken up indicating that more than one small flaw may be present. There were no confirmations in other modes. The two Z values of 213 to 218 mm give an alternate depth size of 5 mm. The indication is characterized as planar based on lack of detection in normal beam or orthogonal modes. The length is 24 mm and was made to LOS in mode 6. The aspect ratio (length/depth) of this indication is 3. The maximum amplitude-to-noise ratio is of medium range at 31 to 13. The X coordinate of 6 mm shows that the indication is in the weld. The Z coordinate of 213 to 218 mm shows that the indication is near the outer wall of the vessel.

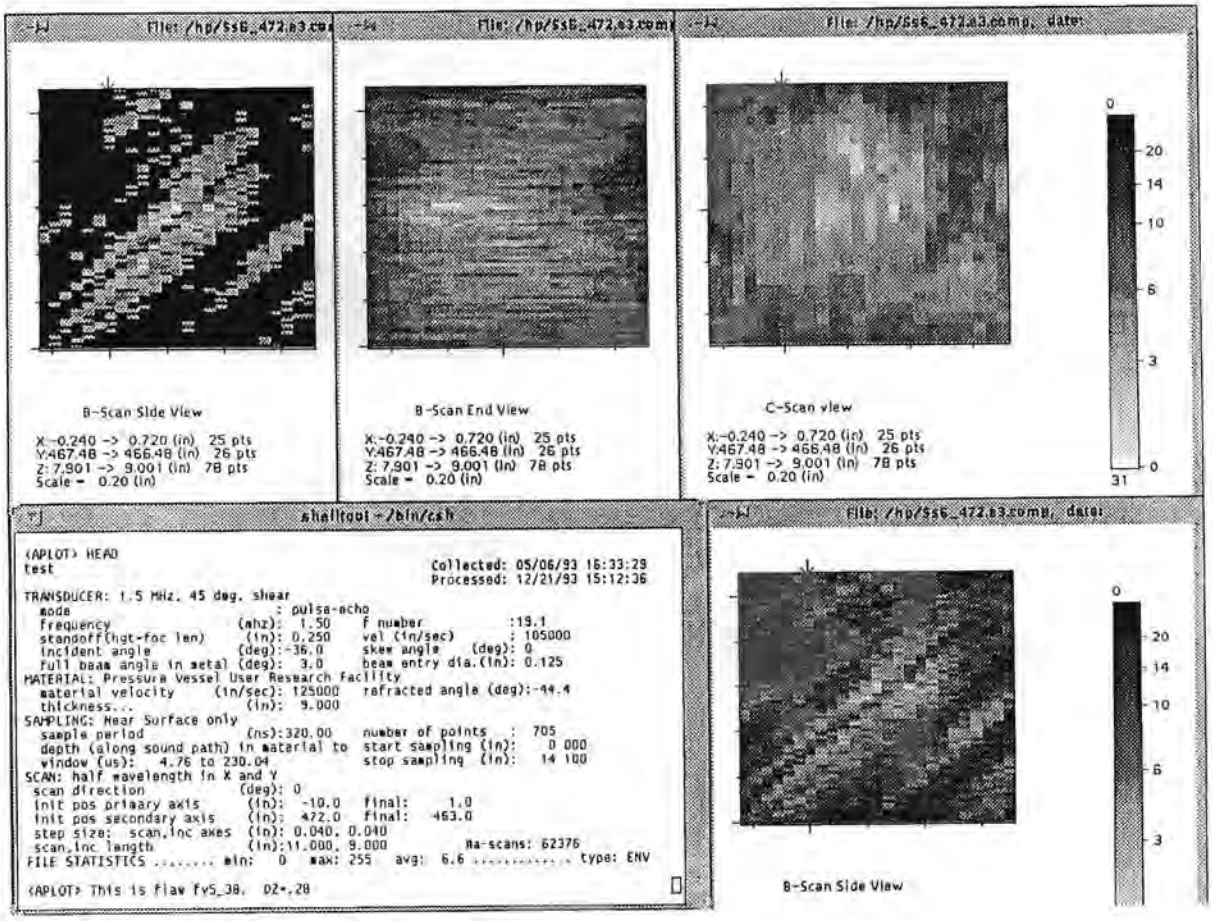

Figure A.63a - Planar indication #8 in the weldment below 25 mm: mode 6

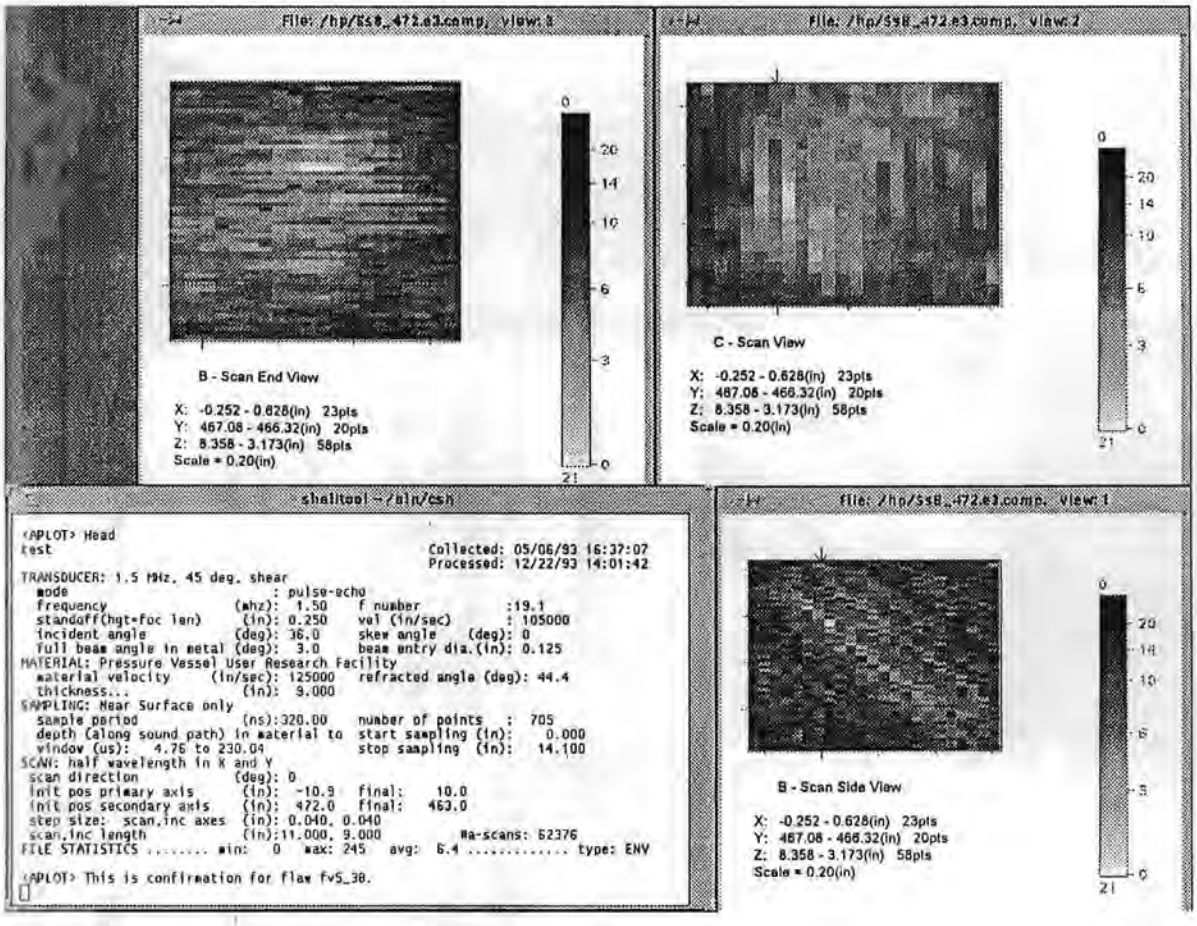

Figure A.63b - Planar indication #8 in the weldment below 25 mm: mode 8

Figure A.64 shows planar indication #9 in the weldment below 25 mm. This planar indication has a through-wall extent of 7 mm based on wave packet width. The detection was made in mode 6 where it had isolated TOF shape at a depth of 213 mm. The shape quality for this indication is good but broken up, implying that more than one small flaw may be present. There were no confirmations in other modes. The indication is characterized as planar based on lack of detection in normal beam or orthogonal modes. The length is 30 mm and was made to LOS in mode 6. The aspect ratio (length/depth) of this indication is 4 which tends to confirm the large through-wall extent. The maximum amplitude-to-noise ratio is high at 121 to 15. The X coordinate of 24 mm shows that the indication is in the weld. The Z coordinate of 213 mm shows that the indication is near the outer wall of the vessel.

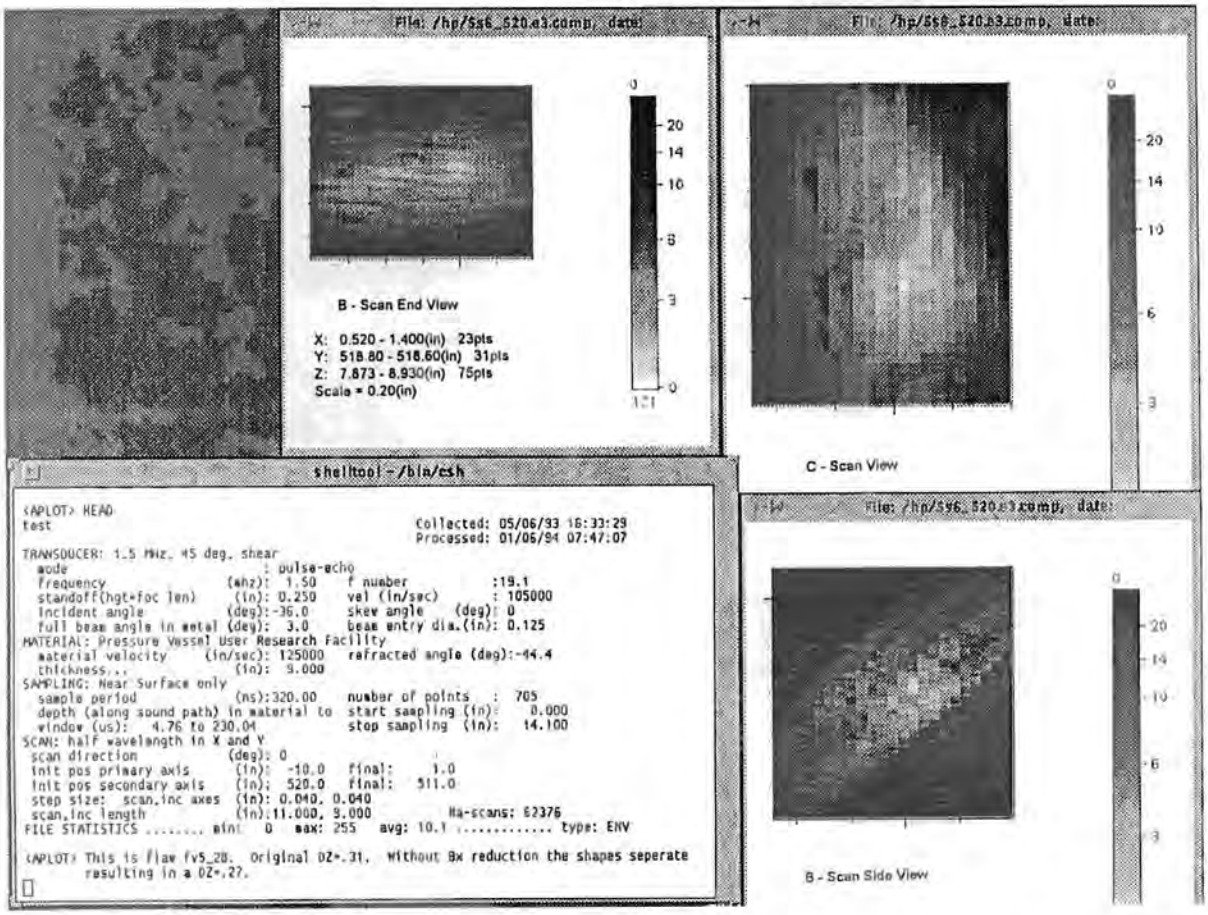

Figure A.64 - Planar indication #9 in the weldment below 25 mm: mode 6

Figure A.65 shows planar indication #10 in the weldment below 25 mm. This planar indication has a through-wall extent of 6 mm based on tip signal pattern. The detection was made in mode 6 where it displayed a pair of TOF shapes at a depth of 117 mm. The shape quality is good for this indication. There were no confirmations in other modes. The indication is characterized as planar based on lack of detection in normal beam or orthogonal modes. The length is 19 mm and was made to LOS in mode 6. The aspect ratio (length/depth) of this indication is 3. The maximum amplitude-to-noise ratio is high at 60 to 12. The X coordinate of -7 mm shows that the indication is in the weld. The Z coordinate of 117 mm shows that the indication is in the middle third of the vessel.

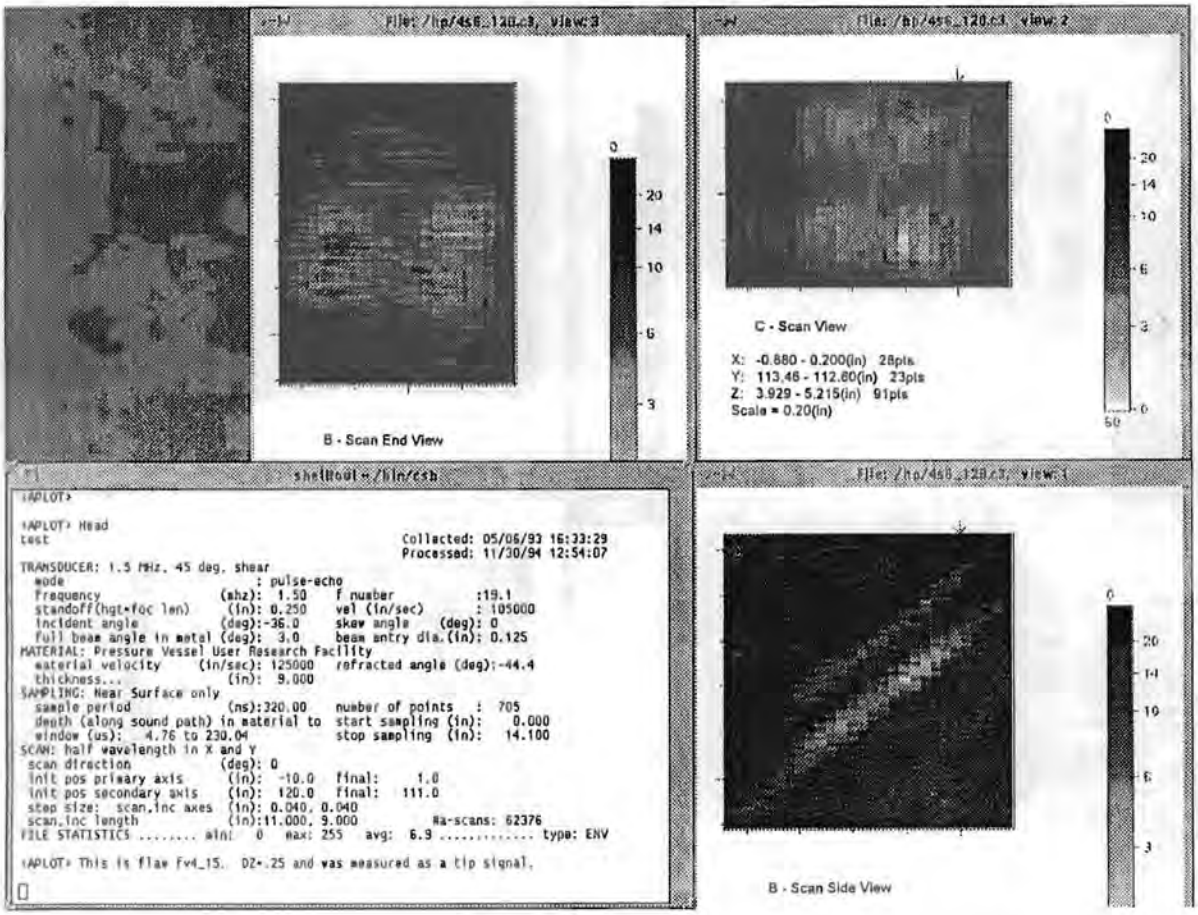

Figure A.65 - Planar indication #10 in the weldment below 25 mm: mode 6

Figure A.66 shows planar indication #11 in the weldment below 25 mm. This planar indication has a through-wall extent of 6 mm based on wave packet width. The detection was made in mode 6 where it had isolated TOF shape at a depth of 213 mm. The shape quality is good for this indication. There were no confirmations in other modes. The indication is characterized as planar based on lack of detection in normal beam or orthogonal modes. The length is 17 mm and was made to LOS in mode 6. The aspect ratio (length/depth) of this indication is 3. The maximum amplitude-to-noise ratio is low at 90 to 45. The X coordinate of 16 mm shows that the indication is in the weld. The Z coordinate of 213 mm shows that the indication is near the outer wall of the vessel.

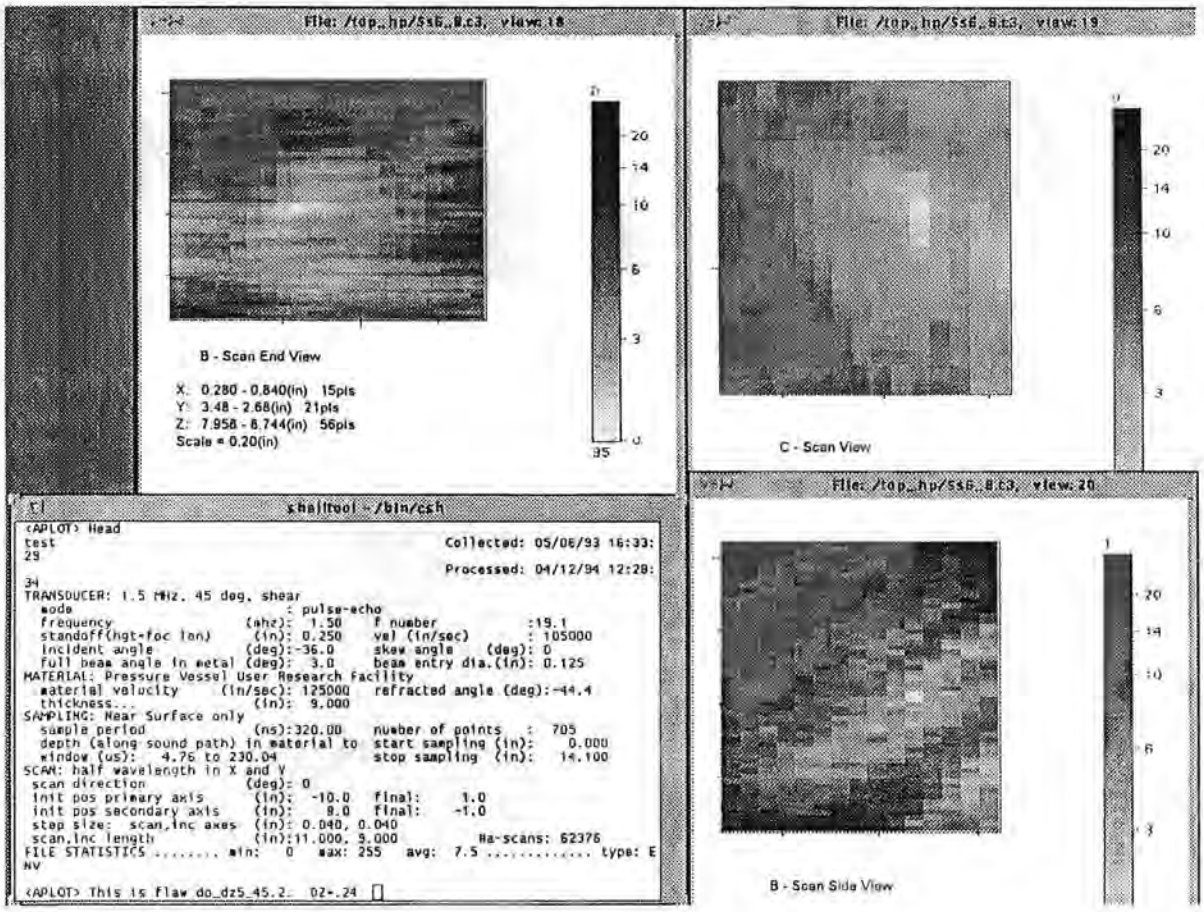

Figure A.66 - Planar indication #11 in the weldment below 25 mm: mode 6

Figures A.67a-b show planar indication #12 in the weldment below 25 mm. This planar indication has a through-wall extent of 6 mm based on wave packet width. The detection was made in mode 6 where it had isolated TOF shape at a depth of 215 mm. The shape quality is good for this indication. There was a confirmation in mode 8 at a depth of 213 mm. The two Z values of 213 to 215 mm give an alternate depth size of 2 mm. The indication is characterized as planar based on lack of normal beam detection or detection in orthogonal modes. The length is 25 mm and was made to LOS in mode 6. The aspect ratio (length/depth) of this indication is 4 which tends to confirm the large through-wall extent. The maximum amplitude-to-noise ratio is of medium range at 109 to 40. The X coordinate of 16 mm shows that the indication is in the weld. The Z coordinate of 213 to 215 mm shows that the indication is near the outer wall of the vessel.

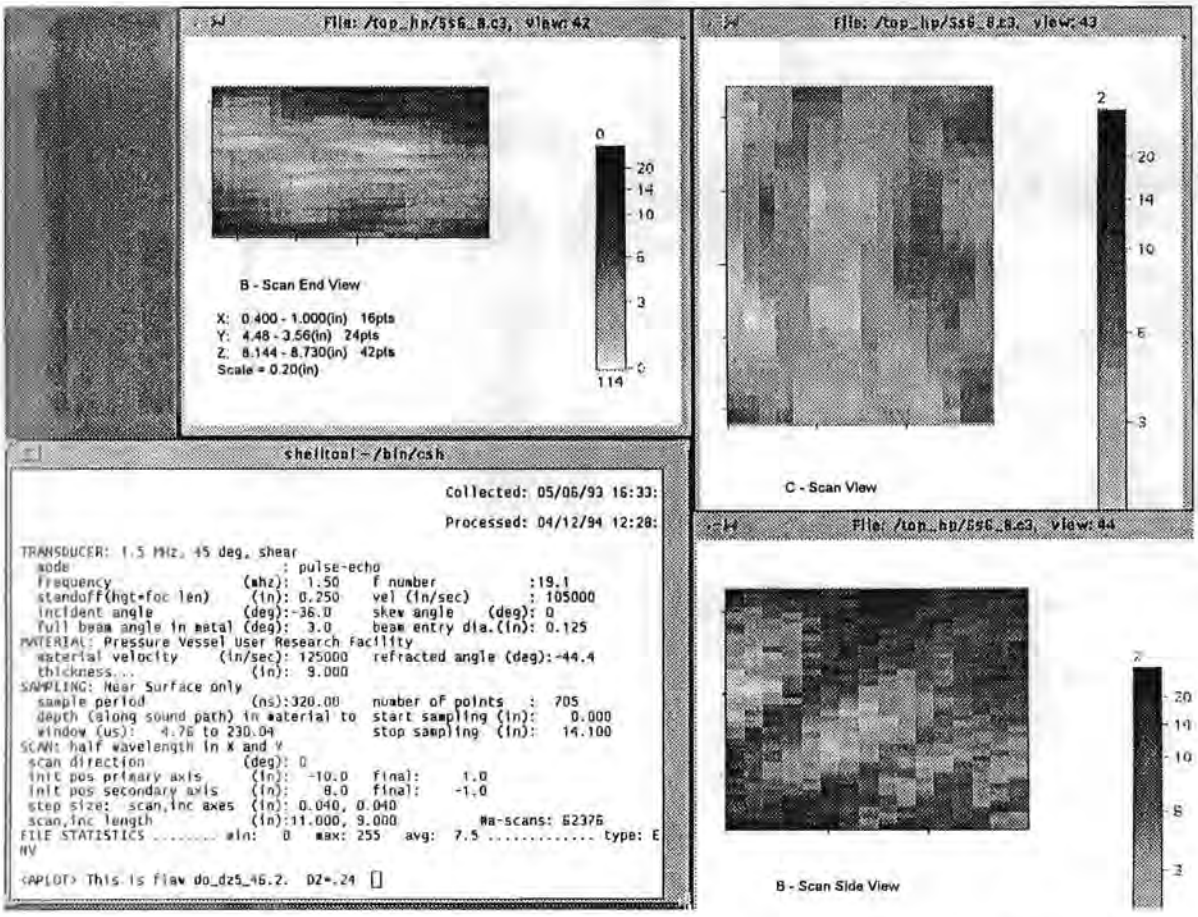

Figure A.67 - Planar indication #12 in the weldment below 25 mm: mode 6

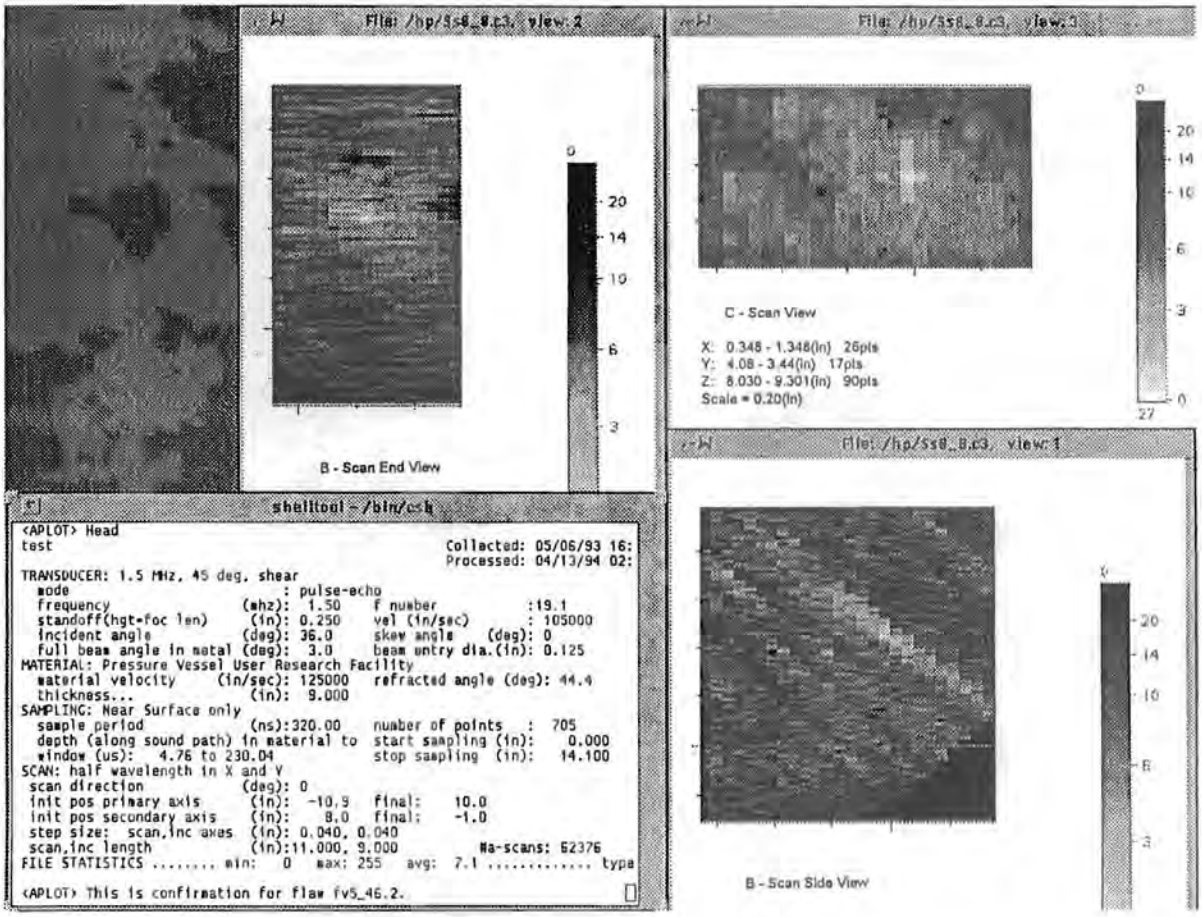

Figure A.67b - Planar indication #12 in the weldment below 25 mm: mode 8

Figure A.68 shows planar indication #13 in the weldment below 25 mm. This planar indication has a through-wall extent of 6 mm based on wave packet width. The detection was made in mode 6 where it had isolated TOF shape at a depth of 209 mm. The shape quality is good for this indication. There were no confirmations in other modes. The indication is characterized as planar based on lack of detection in normal beam or orthogonal modes. The length is 15 mm and was made to LOS in mode 6. The aspect ratio (length/depth) of this indication is 2.5. The maximum amplitude-to-noise ratio is high at 43 to 10. The X coordinate of 10 mm shows that the indication is in the weld. The Z coordinate of 209 mm shows that the indication is near the outer wall of the vessel.

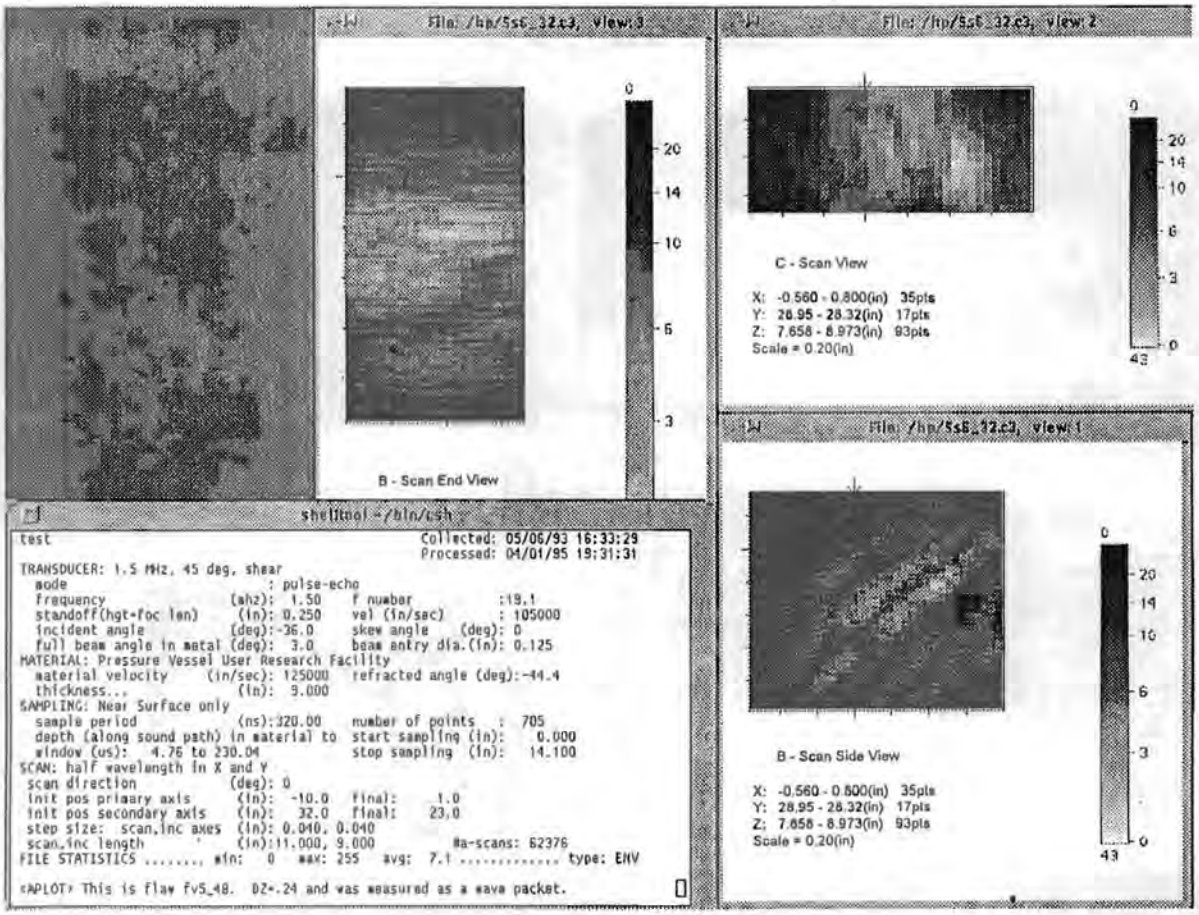

Figure A.68 - Planar indication #13 in the weldment below 25 mm: mode 6

Figure A.69 shows planar indication #14 in the weldment below 25 mm. This planar indication has a through-wall extent of 6 mm based on wave packet width. The detection was made in mode 6 where it had isolated TOF shape at a depth of 212 mm. The shape quality is good for this indication. There were no confirmations in modes. The indication is characterized as planar based on lack of detection in normal beam or orthogonal modes. The length is 27 mm and was made to LOS in mode 6. The aspect ratio (length/depth) of this indication is 4.5 which tends to confirm the large through-wall extent. The maximum amplitude-to-noise ratio is of medium range at 115 to 40. The X coordinate of 9 mm shows that the indication is in the weld. The Z coordinate of 212 mm shows that the indication is near the outer wall of the vessel.

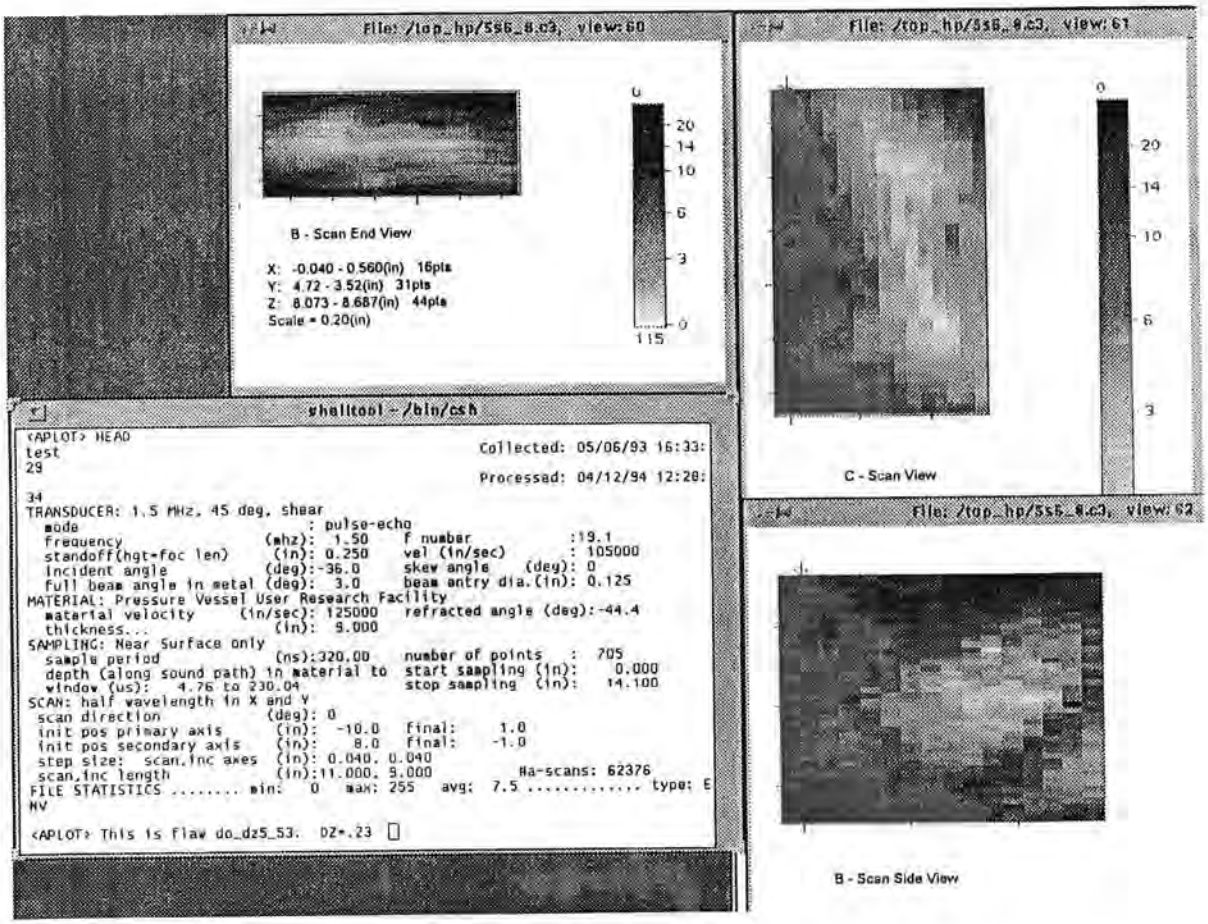

Figure A.69 - Planar indication #14 in the weldment below 25 mm: mode 6

Figure A.70 shows planar indication #15 in the weldment below 25 mm. This planar indication has a through-wall extent of 4 mm based on LOS in a cloud like pattern. The detection was made in mode 6 where the shape appeared cloud like in nature at a depth of 212 mm. The shape quality for this indication is fair but broken up, indicating that more than one small flaw may be present. There were no confirmations in other modes. The indication is characterized as planar based on lack of detection in normal beam or orthogonal modes. The length is 42 mm and was made to LOS in mode 6. The aspect ratio (length/depth) of this indication is 10. The maximum amplitude-to-noise ratio is high at 53 to 13. The X coordinate of 10 mm shows that the indication is in the weld. The Z coordinate of 212 mm shows that the indication is near the outer wall of the vessel.

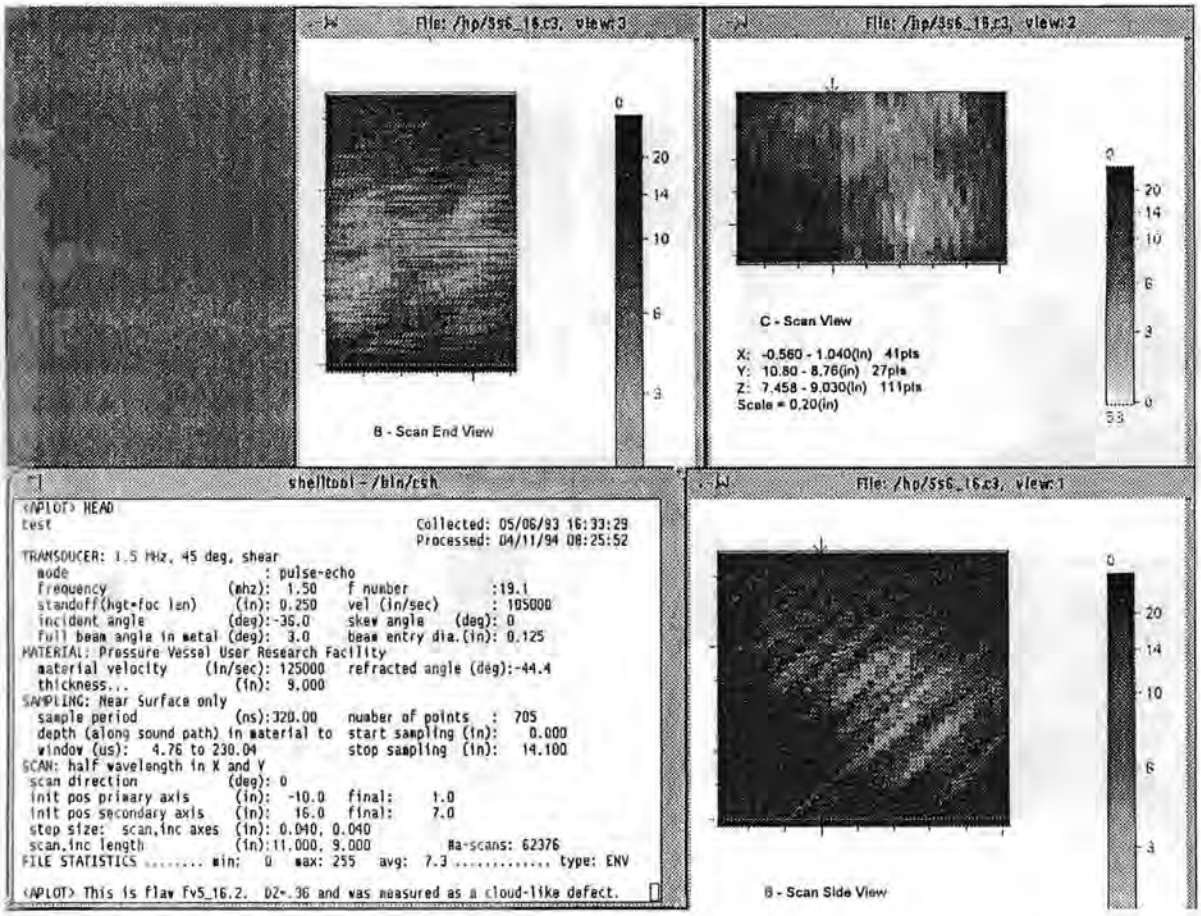

Figure A.70 - Planar indication #15 in the weldment below 25 mm: mode 6

Figure A.71 shows planar indication #16 in the weldment below 25 mm. This planar indication has a through-wall extent of 4 mm based on LOS in a cloud like pattern. The detection was made in mode 6 where the shape appeared cloud like in nature at a depth of 203 mm. The shape quality is poor and broken up indicating that more than one small flaw is present. There were no confirmations in other modes. The indication is characterized as planar based on lack of detection in normal beam or orthogonal modes. The length is 25 mm and was made to LOS in mode 6. The aspect ratio (length/depth) is 6 which tends to confirm the large through-wall extent. The maximum amplitude-to-noise ratio is high at 44 to 10. The X coordinate of -8 mm shows that the indication is clearly in the weld. The Z coordinate of 203 mm shows that the indication is near the vessel outer wall.

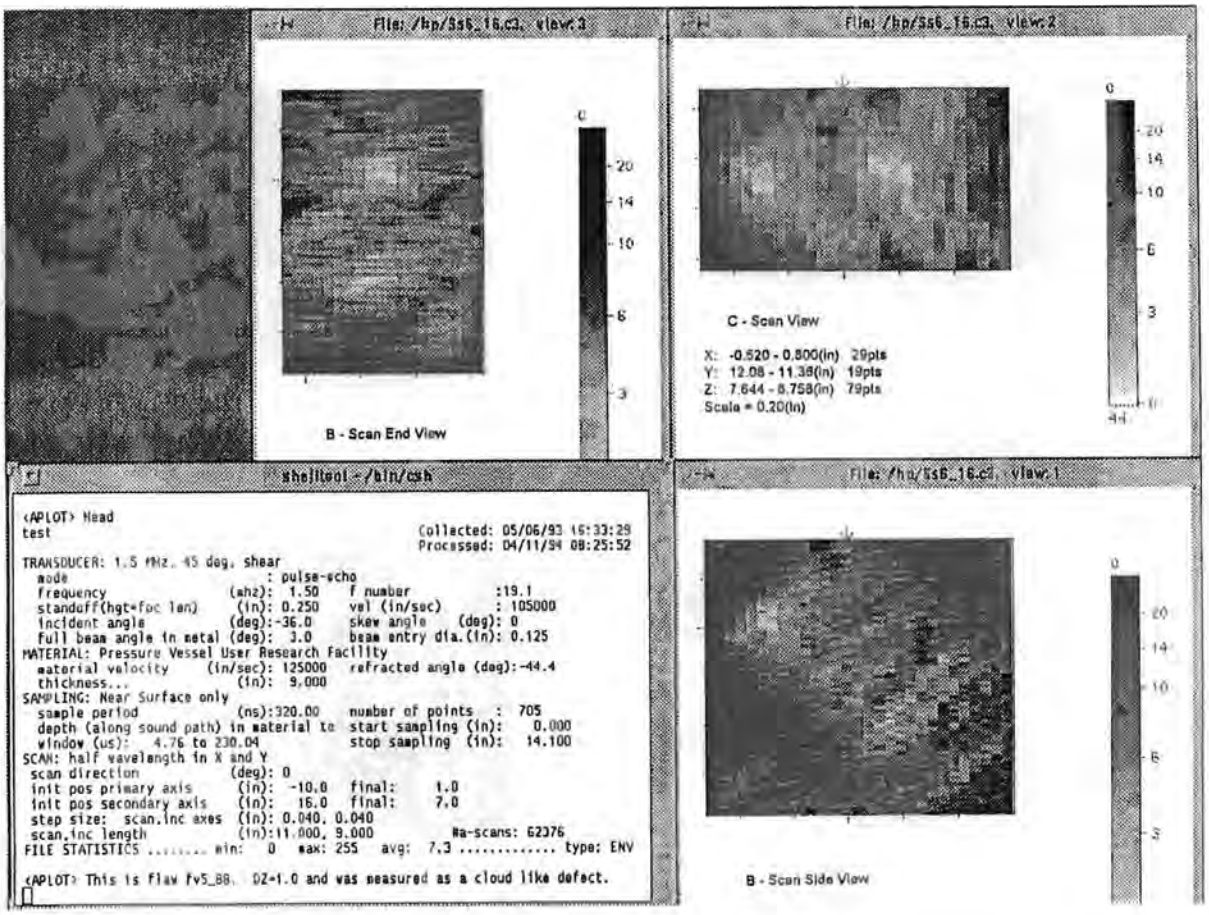

Figure A.71 - Planar indication #16 in the weldment below 25 mm: mode 6

Volumetric Indications in the Weldment Below 25 mm

Figures A.72a-b show volumetric indication #1 in the weldment below 25 mm. This volumetric indication has a through-wall extent of 5 mm based on ring around pattern. The detection was made in mode 9 where it displayed a pair of TOF shapes at a depth of 116 mm. The shape quality is good for this indication. There was a confirmation in mode 8 at a depth of 121 mm. The confirmation mode gave a through-wall extent of 5 mm based on wave packet width. The two Z values of 116 to 121 mm give an alternate depth size of 5 mm. The indication is characterized as volumetric based on the detection of ring around shape. The length is 23 mm and was made to LOS in mode 8. The width is 17 mm and was made to LOS in mode 9. The aspect ratio (length/depth) of this indication is 5 and the width-to-depth ratio is 3 which tends to confirm volumetric orientation. The maximum amplitude-to-noise ratio is high at 51 to 10. The X coordinate of 12 mm shows that the indication is in the weld. The Z coordinate of 116 to 121 mm shows that the indication is in the middle third of the vessel.

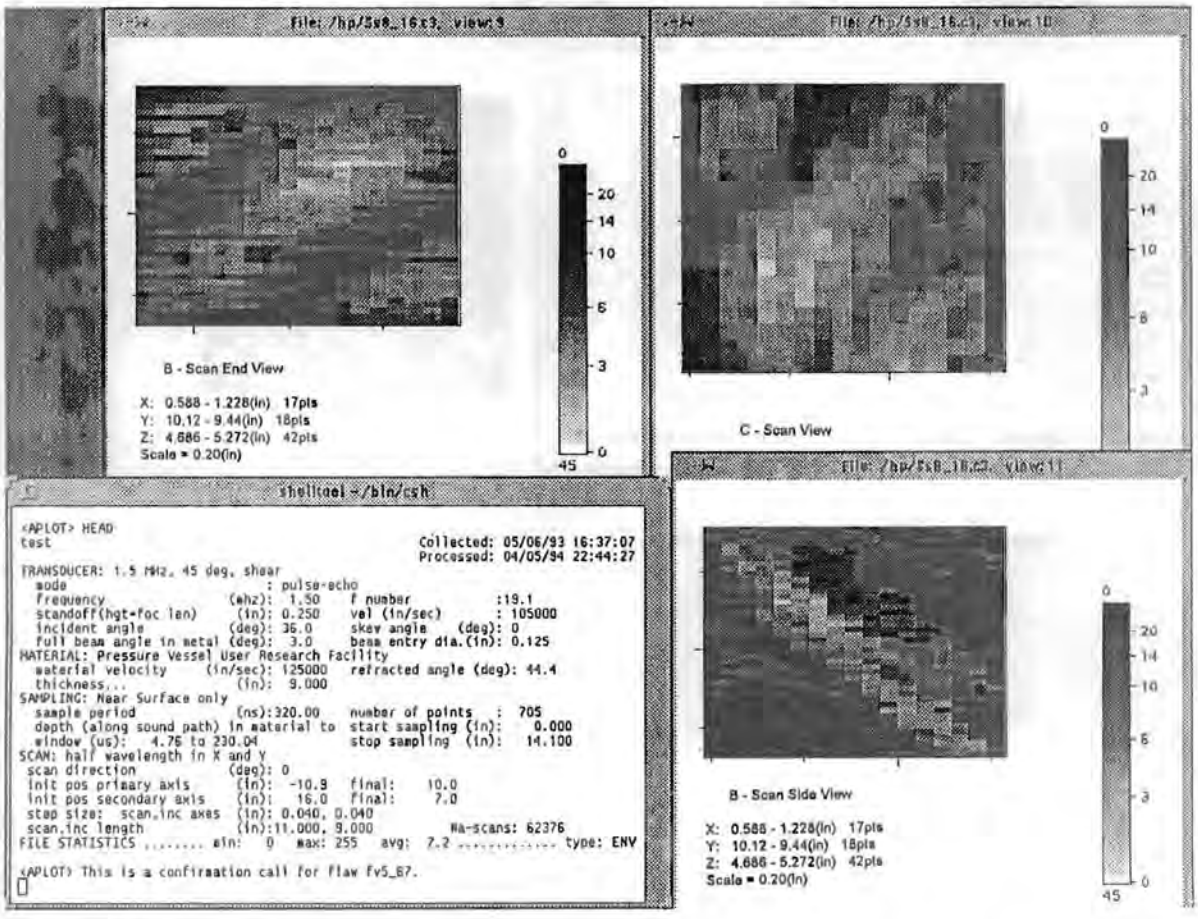

Figure A.72a - Volumetric indication #1 in the weldment below 25 mm: mode 8

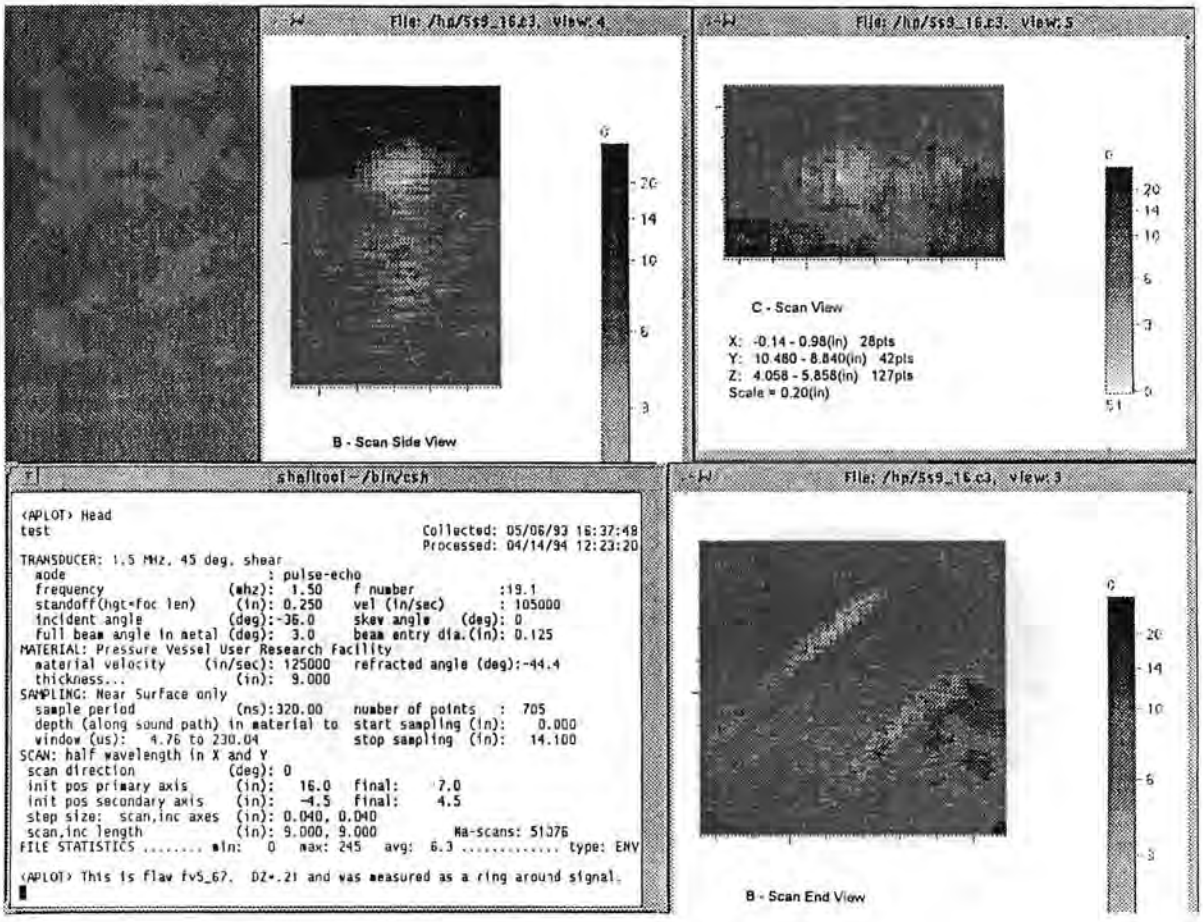

Figure A.72b - Volumetric indication #1 in the weldment below 25 mm: mode 9

Figure A.73 shows volumetric indication #2 in the weldment below 25 mm. This volumetric indication has a through-wall extent of 4 mm based on ring around pattern. The detection was made in mode 6 where it displayed a pair of TOF shapes at a depth of 213 mm. The shape quality is good for this indication. There were no confirmations in other modes. The indication is characterized as volumetric based on the detection of ring around shape. The length is 9 mm and was made to LOS in mode 6. The aspect ratio (length/depth) of this indication is 2. The maximum amplitude-to-noise ratio is of medium range at 43 to 13. The X coordinate of 6 mm shows that the indication is in the weld. The Z coordinate of 213 mm shows that the indication is near the outer wall of the vessel.

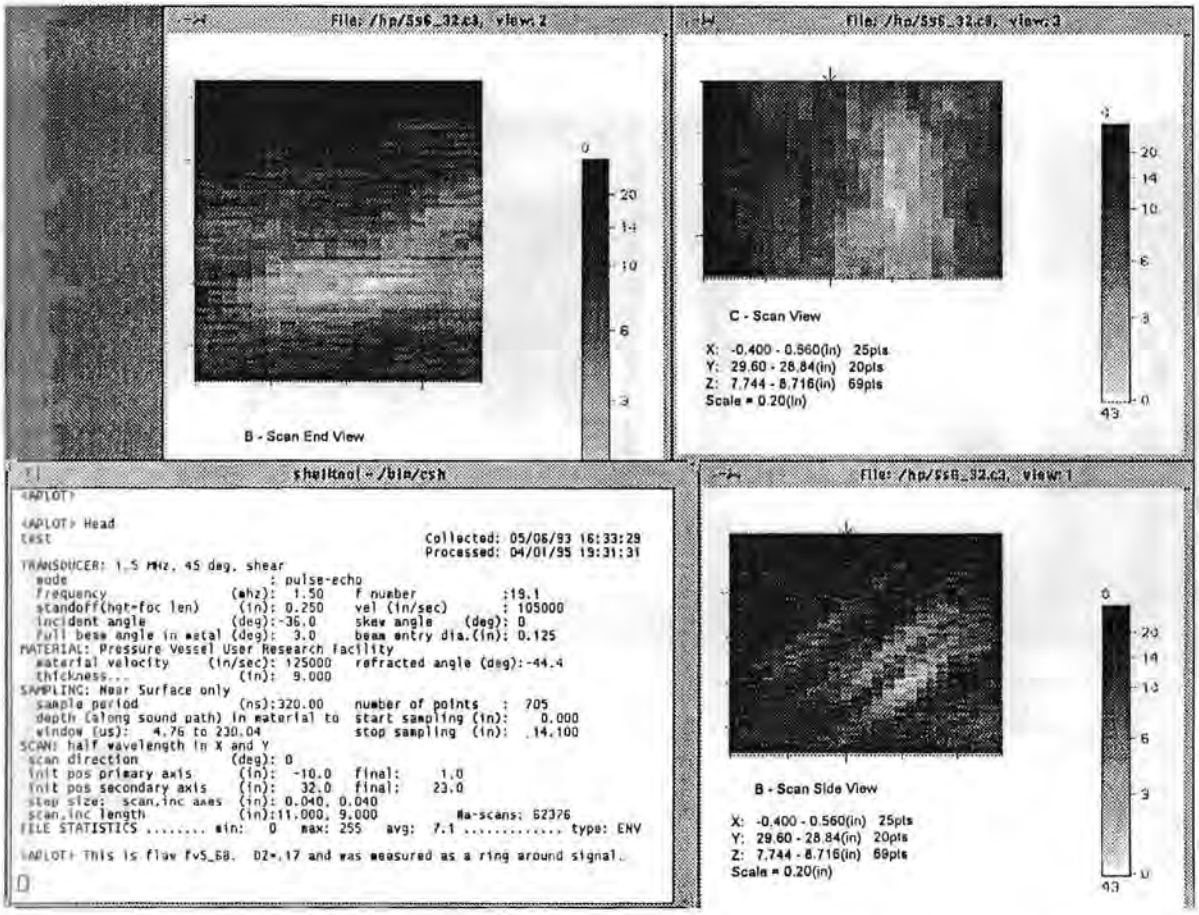

Figure A.73 - Volumetric indication #2 in the weldment below 25 mm: mode 6

Planar Indications in the HAZ Below 25 mm

Figure A.74 shows planar indication #1 in the heat affected zone below 25 mm. This planar indication has a through-wall extent of 34 mm based on tip signal pattern. The detection was made in mode 6 where it displayed a pair of TOF shapes at a depth of 135 mm. The shape quality is good for this indication. There were no confirmations in other modes. The indication is characterized as planar based on the tip signal pattern. Using LOS in mode 6, the length was measured as greater than 15 mm but was limited by the edge of the available aperture (data). The aspect ratio (length/depth) of this indication is greater than 0.4; the loss of data probably limits the length measurement. The maximum amplitude-to-noise ratio is high at 31 to 4. The X coordinate of 20 mm shows that the indication is probably in the HAZ. The Z coordinate of 135 mm shows that the indication is in the middle third of the vessel.

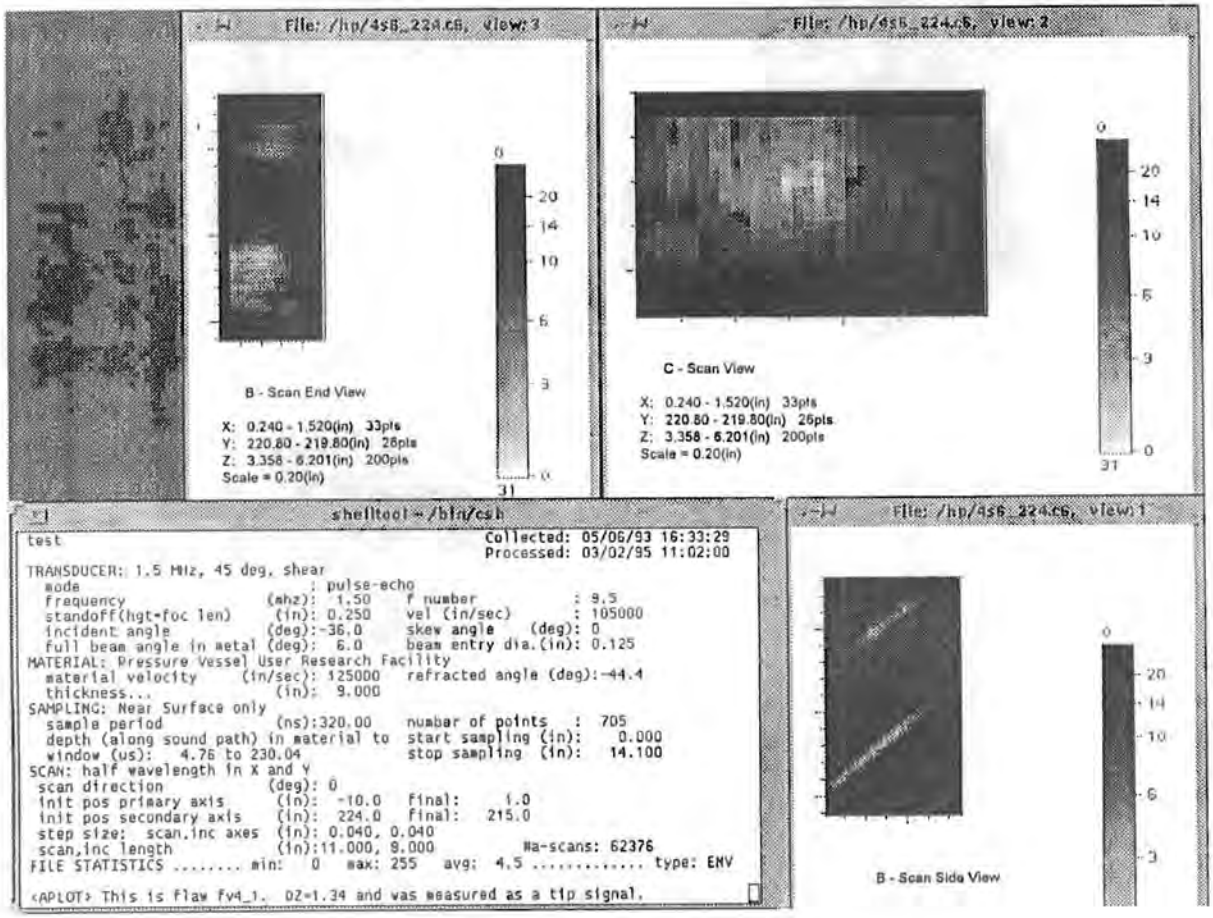

Figure A.74 - Planar indication #1 in the HAZ below 25 mm: mode 6

Figure A.75 shows planar indication #2 in the heat affected zone below 25 mm. This planar indication has a through-wall extent of 18 mm based on tip signal pattern. The detection was made in mode 8 where it displayed a pair of TOF shapes at a depth of 48 mm. The shape quality for this indication is good but broken up, implying that more than one small flaw may be present. There were no confirmations in other modes. The indication is characterized as planar based on the tip signal pattern. The length is 75 mm and was made to LOS in mode 6. The aspect ratio (length/depth) of this indication is 4 which tends to confirm the large through-wall extent. The maximum amplitude-to-noise ratio is high at 38 to 3. The X coordinate of 17 mm shows that the indication is probably in the HAZ. The Z coordinate of 48 mm shows that the indication is in the inner third of the vessel.

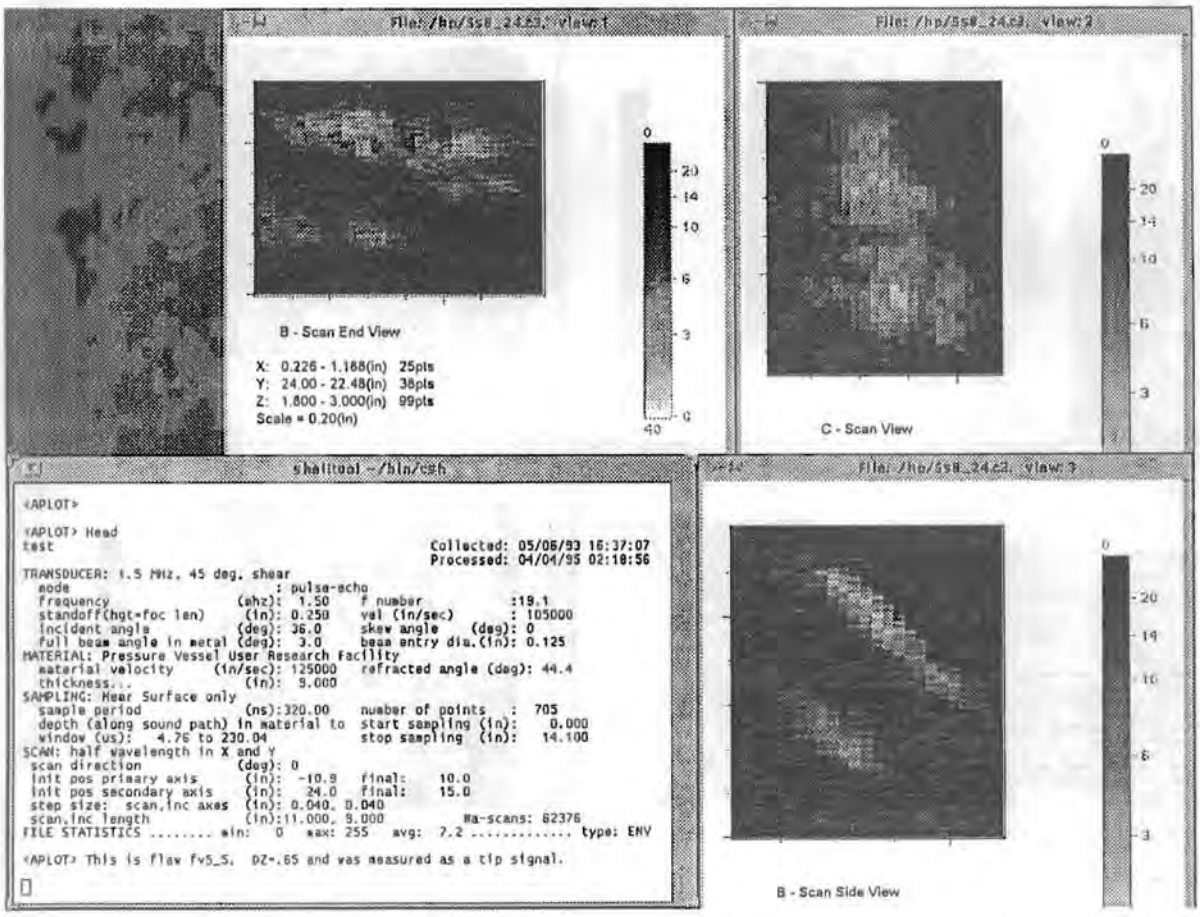

Figure A.75 - Planar indication #2 in the HAZ below 25 mm: mode 8

Figure A.76 shows planar indication #3 in the heat affected zone below 25 mm. This planar indication has a through-wall extent of 10 mm based on tip signal pattern. The detection was made in mode 6 where it displayed a pair of TOF shapes at a depth of 73 mm. The shape quality is good for this indication. There were no confirmations in other modes. The indication is characterized as planar based on the tip signal pattern. The length is 18 mm and was made to LOS in mode 6. The aspect ratio (length/depth) of this indication is 1.8. The maximum amplitude-to-noise ratio is high at 22 to 4. The X coordinate of -17 mm shows that the indication is probably in the HAZ. The Z coordinate of 73 mm shows that the indication is in the middle third of the vessel.

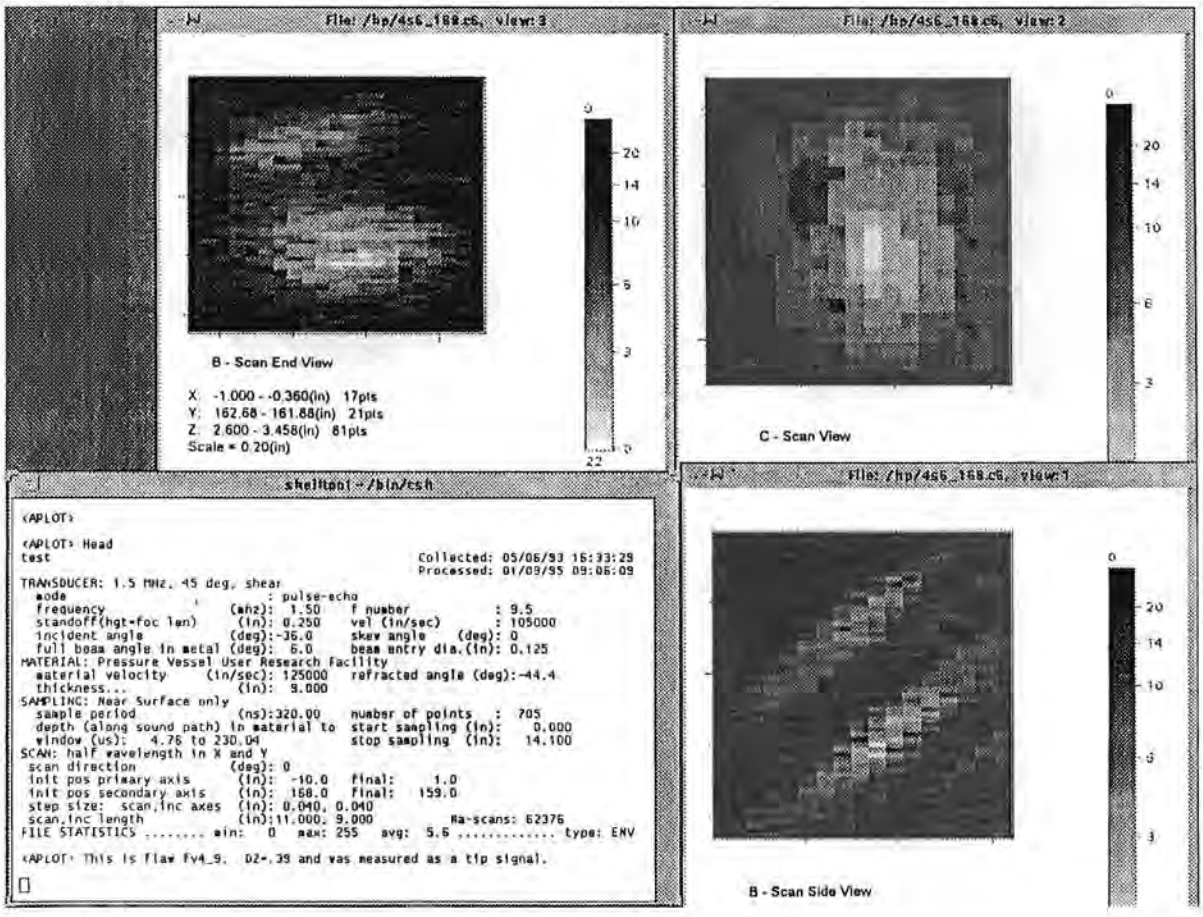

Figure A.76 - Planar indication #3 in the HAZ below 25 mm: mode 6

Figure A.77 shows planar indication #4 in the heat affected zone below 25 mm. This planar indication has a through-wall extent of 9 mm based on LOS in a cloud like pattern. The detection was made in mode 6 where the shape appeared cloud like in nature at a depth of 213 mm. The shape quality is good for this indication. There were no confirmations in other modes. The indication is characterized as planar based on lack of detection in normal beam or orthogonal modes. The length is 21 mm and was made to LOS in mode 6. The aspect ratio (length/depth) of this indication is 2. The maximum amplitude-to-noise ratio is of medium range at 43 to 15. The X coordinate of 26 mm shows that the indication is probably in the HAZ. The Z coordinate of 213 mm shows that the indication is near the outer wall of the vessel.

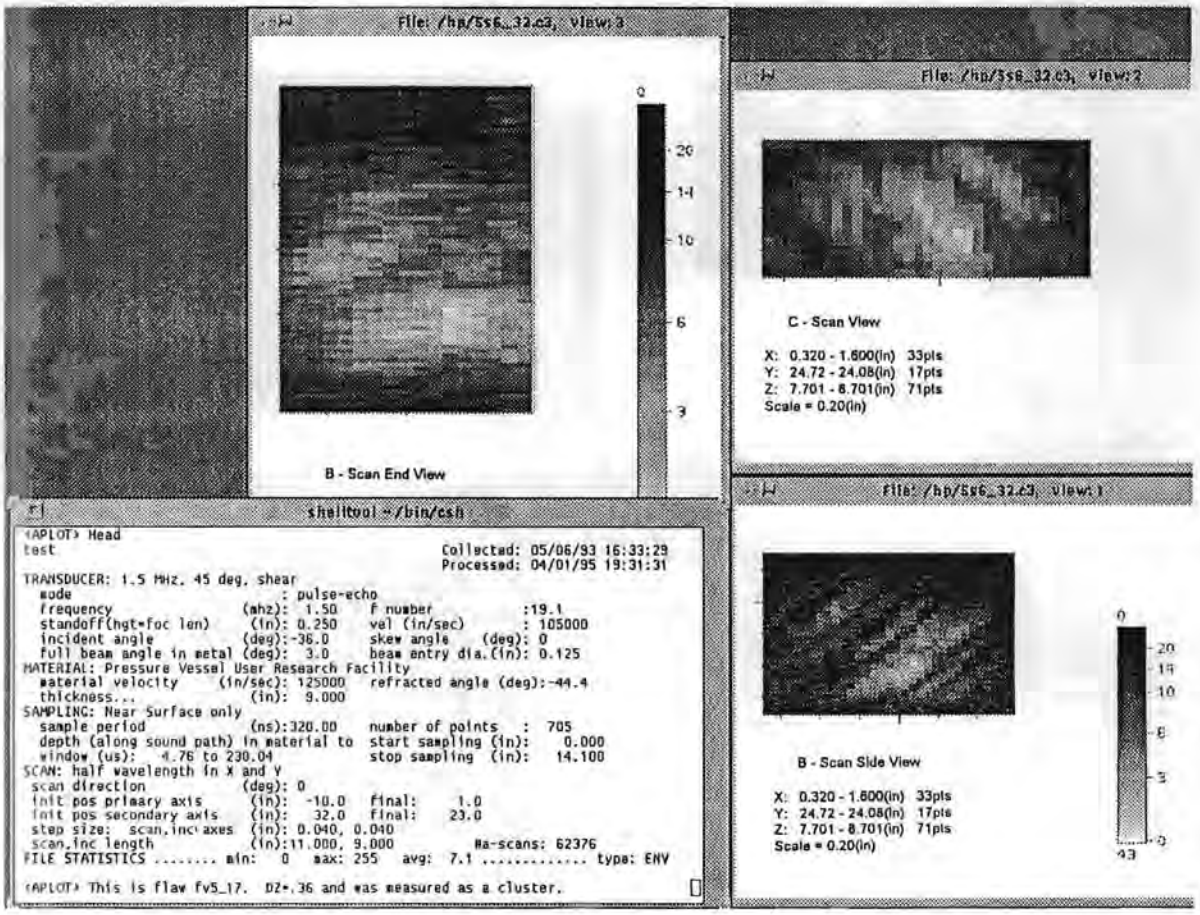

Figure A.77 - Planar indication #4 in the HAZ below 25 mm: mode 6

Figure A.78 shows planar indication #5 in the heat affected zone below 25 mm. This planar indication has a through-wall extent of 9 mm based on tip signal pattern. The detection was made in mode 6 where it displayed a pair of TOF shapes at a depth of 224 mm. The shape quality is good for this indication. There were no confirmations in other modes. The indication is characterized as planar based on the tip signal pattern. The length is 27 mm and was made to LOS in mode 6. The aspect ratio (length/depth) of this indication is 3. The maximum amplitude-to-noise ratio is of medium range at 29 to 8. The X coordinate of 24 mm shows that the indication is probably in the HAZ. The Z coordinate of 224 mm shows that the indication is near the outer wall.

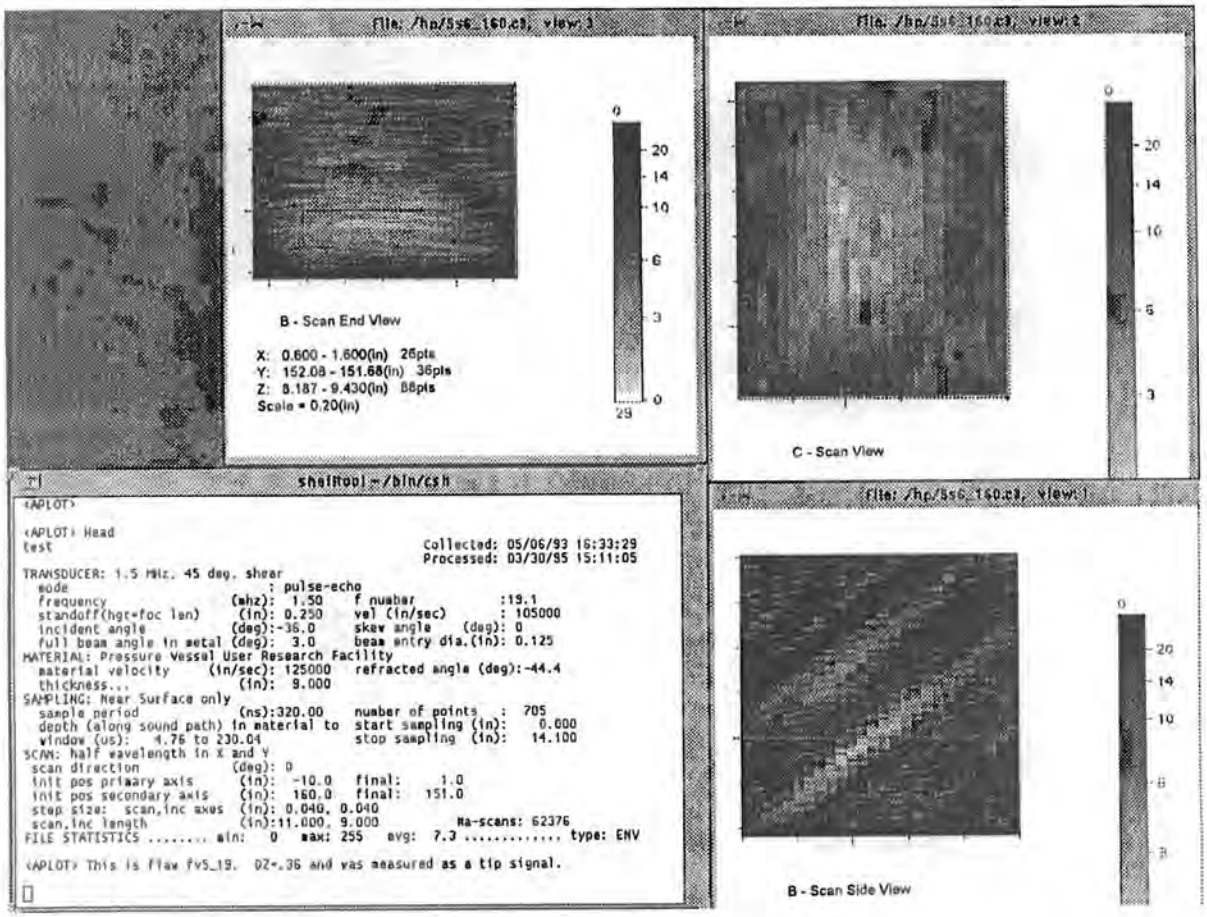

Figure A.78 - Planar indication #5 in the HAZ below 25 mm: mode 6

Figure A.79 shows planar indication #6 in the heat affected zone below 25 mm. This planar indication has a through-wall extent of 8 mm based on wave packet width. The detection was made in mode 6 at a depth of 216 mm. The shape has the appearance of a cluster or cloud. There were no confirmations in other modes. The indication is characterized as planar based on lack of detection in normal beam or orthogonal modes. The length is 22 mm and was made to LOS in mode 6. The aspect ratio (length/depth) of this indication is 3. The maximum amplitude-to-noise ratio is high at 120 to 25. The X coordinate of 26 mm shows that the indication is probably in the HAZ. The Z coordinate of 216 mm shows that the indication is near the outer wall of the vessel.

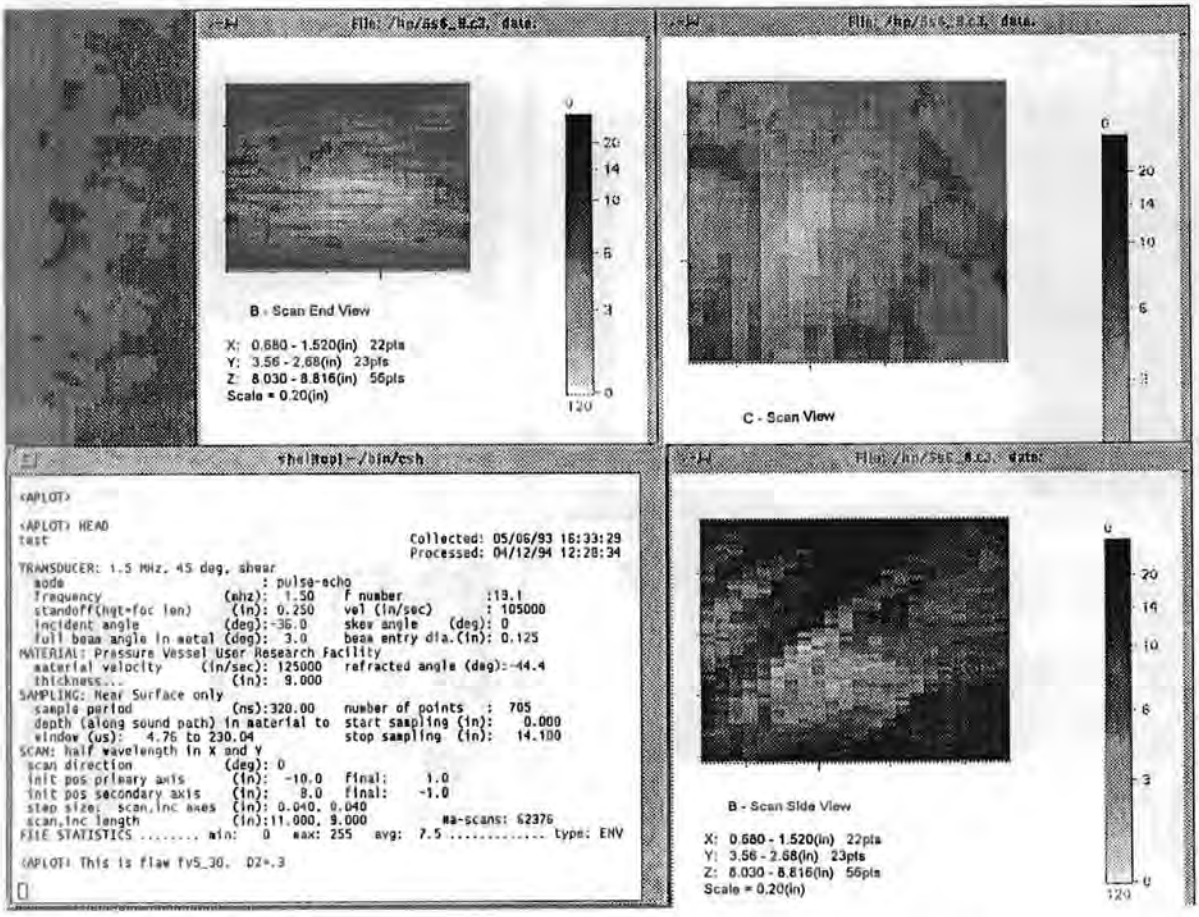

Figure A.79 - Planar indication #6 in the HAZ below 25 mm: mode 6

Figure A.80 shows planar indication #7 in the heat affected zone below 25 mm. This planar indication has a through-wall extent of 7 mm based on tip signal pattern. The detection was made in mode 6 where it displayed a pair of TOF shapes at a depth of 76 mm. The shape quality is good for this indication. There were no confirmations in modes. The indication is characterized as planar based on the tip signal pattern. The length is 14 mm and was made to LOS in mode 6. The aspect ratio (length/depth) of this indication is 2. The maximum amplitude-to-noise ratio is of medium range at 17 to 5. The X coordinate of 16 mm shows that the indication is probably in the HAZ. The Z coordinate of 76 mm shows that the indication is in the middle third of the vessel.

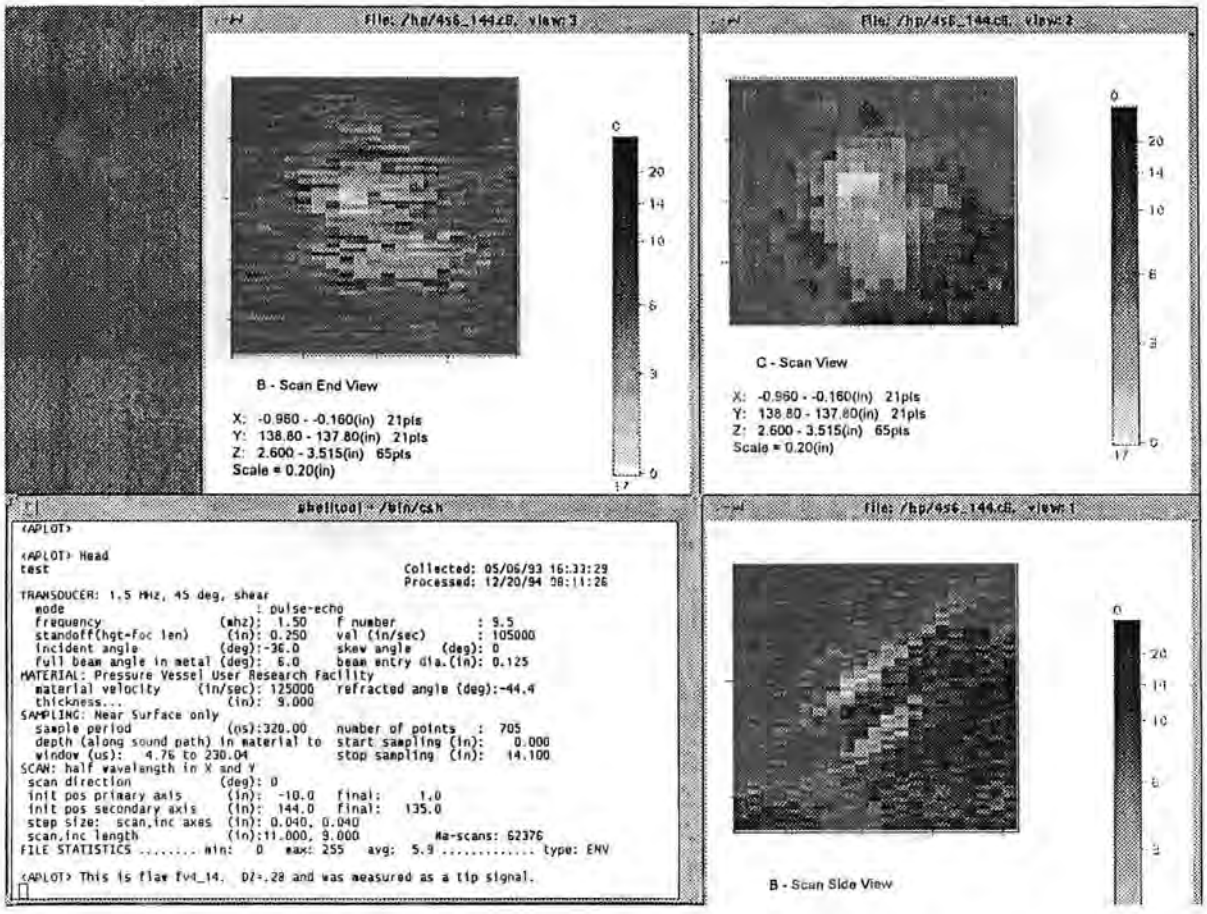

Figure A.80 - Planar indication #7 in the HAZ below 25 mm: mode 6

Figure A.81 shows planar indication #8 in the heat affected zone below 25 mm. This planar indication has a through-wall extent of 7 mm based on wave packet width. The detection was made in mode 6 where it had isolated TOF shape at a depth of 214 mm. The shape quality is good for this indication. There were no confirmations in other modes. The indication is characterized as planar based on lack of detection in normal beam or orthogonal modes. The length is 10 mm and was made to LOS in mode 6. The aspect ratio (length/depth) of this indication is 1.4. The maximum amplitude-to-noise ratio is of medium range at 92 to 25. The X coordinate of 30 mm shows that the indication is probably in the HAZ. The Z coordinate of 214 mm shows that the indication is near the outer wall of the vessel.

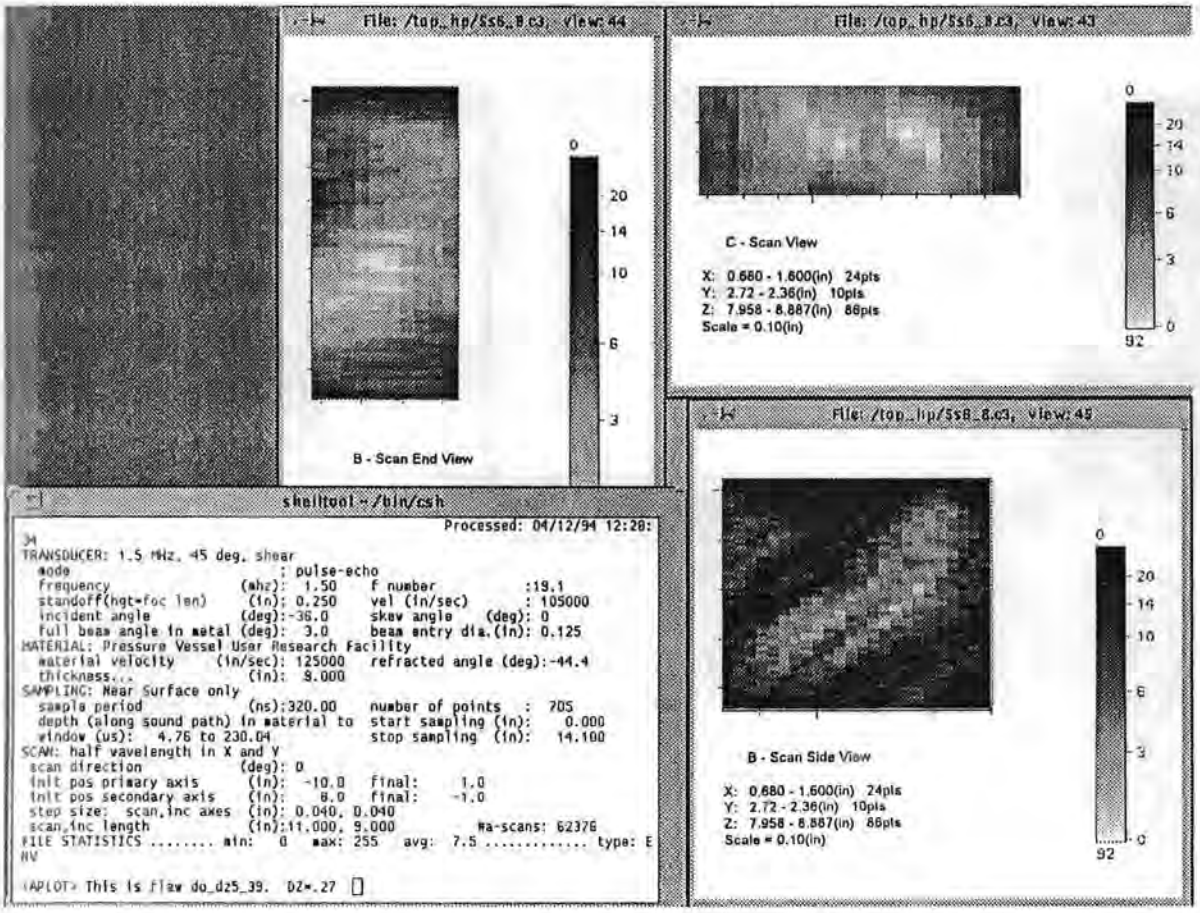

Figure A.81 - Planar indication #8 in the HAZ below 25 mm: mode 6

Figures A.82a-b show planar indication #9 in the heat affected zone below 25 mm. This planar indication has a through-wall extent of 5 mm based on wave packet width. The detection was made in mode 6 where it had isolated TOF shape at a depth of 218 mm. The shape quality is good but more than one TOF shape was present for this indication. There was a confirmation in mode 8 at depth of 216 mm. The confirmation mode gave a through-wall extent estimate of 4 mm based on wave packet width. The two Z values of 216 to 218 mm give an alternate depth size of 2 mm. The indication is characterized as planar based on lack of detection in normal beam or orthogonal modes. The length is 22 mm and was made to LOS in mode 6. The aspect ratio (length/depth) of this indication is 4 which tends to confirm the large through-wall extent. The maximum amplitude-to-noise ratio is of medium range at 88 to 35. The X coordinate of 24 mm shows that the indication is probably in the HAZ. The Z coordinate of 216 to 218 mm shows that the indication is near the outer wall of the vessel.

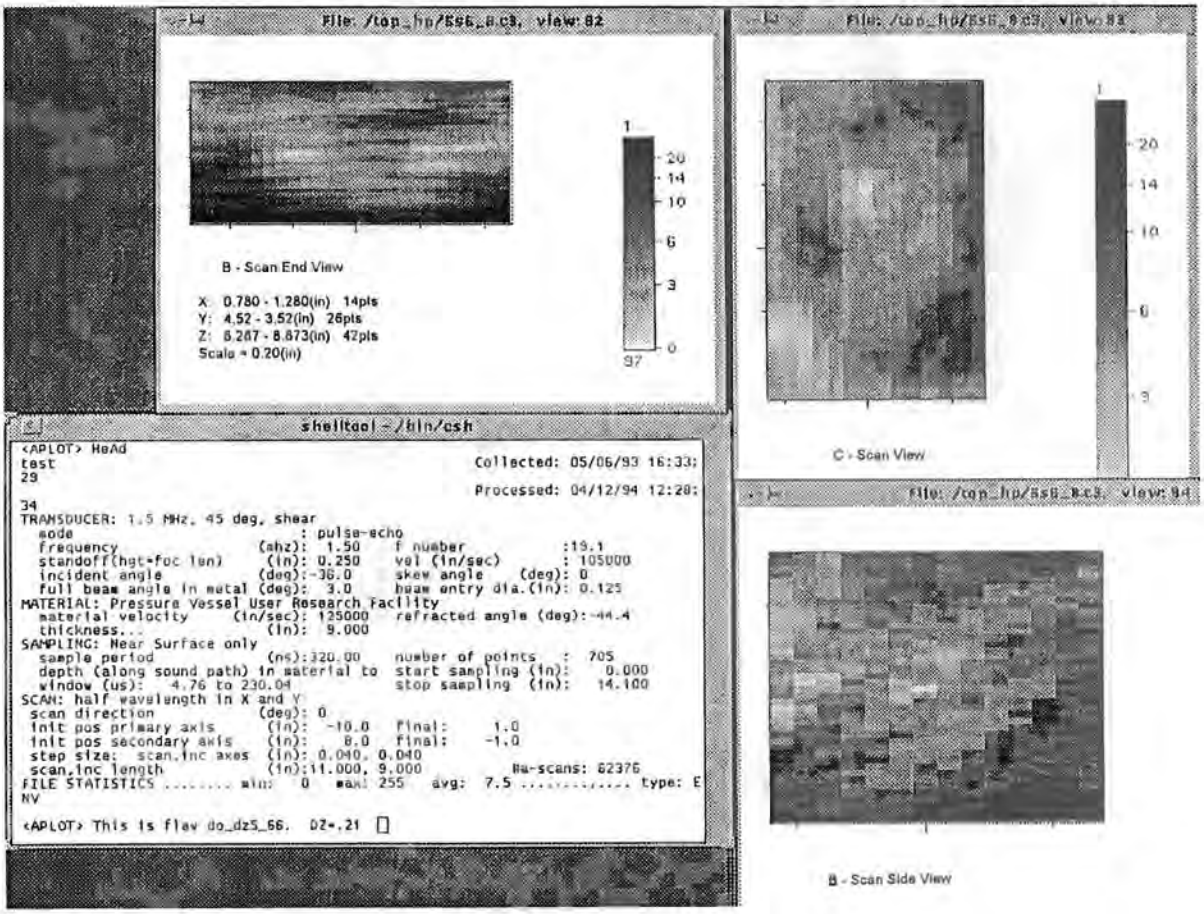

Figure A.82a - Planar indication #9 in the HAZ below 25 mm: mode 6

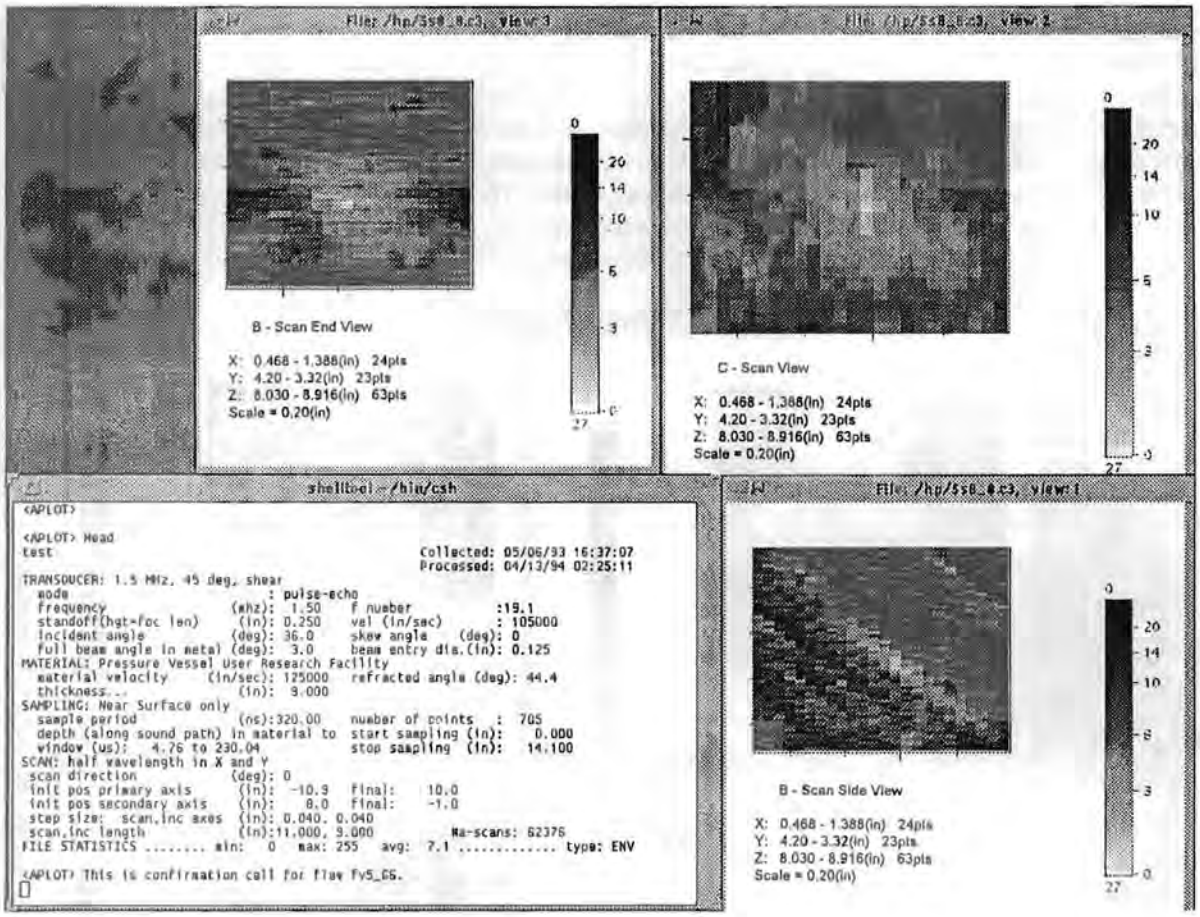

Figure A.82b - Planar indication #9 in the HAZ below 25 mm: mode 8

Figure A.83 shows planar indication #10 in the heat affected zone below 25 mm. This planar indication has a through-wall extent of 5 mm based on wave packet width. The detection was made in mode 6 where it had isolated TOF shape at a depth of 134 mm. The shape quality is good and more than one TOF shape was present for this indication. There were no confirmations in other modes. The indication is characterized as planar based on lack of detection in normal beam or orthogonal modes. The length is 19 mm and was made to LOS in mode 6. The aspect ratio (length/depth) of this indication is 4 which tends to confirm the large through-wall extent. The maximum amplitude-to-noise ratio is of medium range at 57 to 18. The X coordinate of 23 mm shows that the indication is probably in the HAZ. The Z coordinate of 134 mm shows that the indication is in the middle third of the vessel.

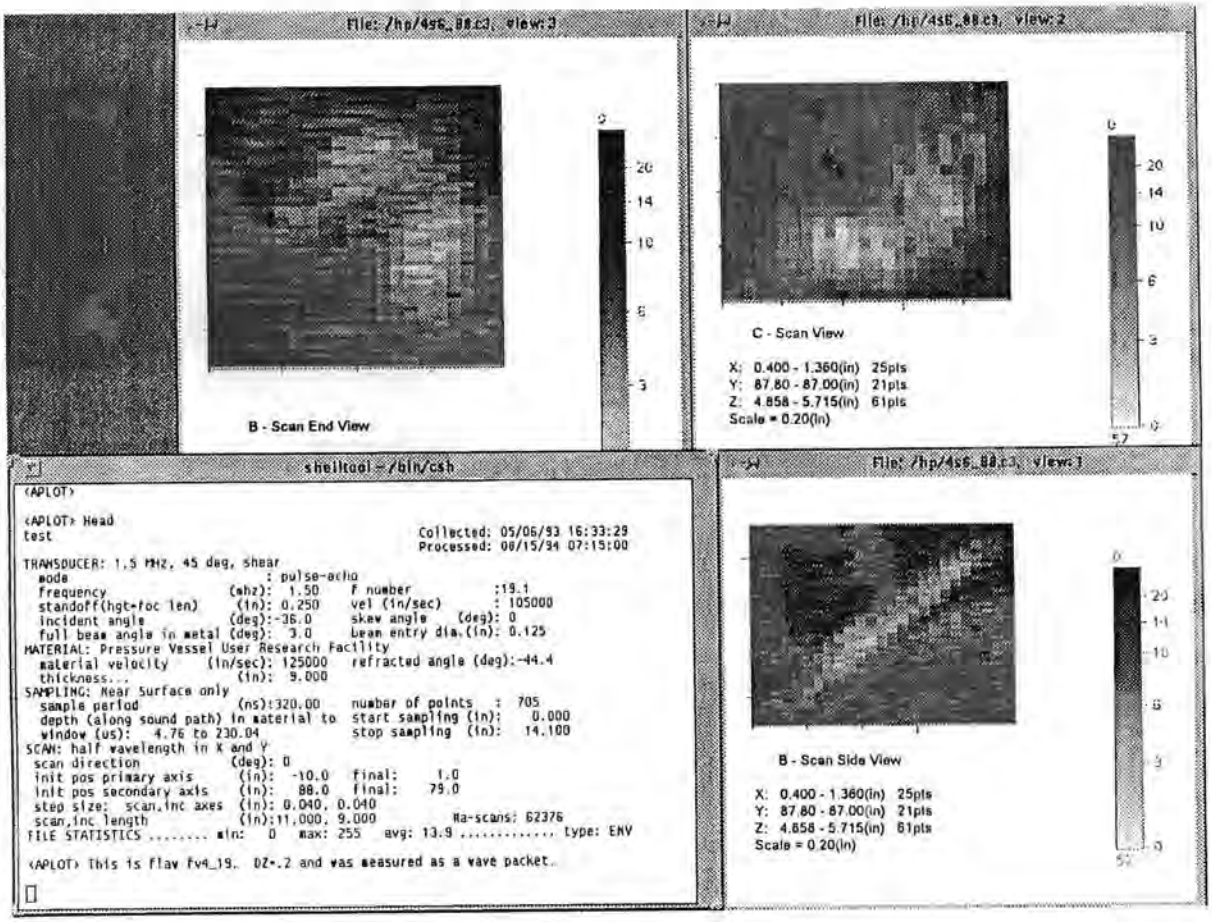

Figure A.83 - Planar indication #10 in the HAZ below 25 mm: mode 6

Figure A.84 shows planar indication #11 in the heat affected zone below 25 mm. This planar indication has a through-wall extent of 5 mm based on wave packet width. The detection was made in mode 6 where it had isolated TOF shape at a depth of 208 mm. The shape quality is good but more than one TOF shape was present for this indication. There were no confirmations in other modes. The indication is characterized as planar based on lack of detection in normal beam or orthogonal modes. The length is 26 mm and was made to LOS in mode 6. The aspect ratio (length/depth) of this indication is 5 which tends to confirm the large through-wall extent. The maximum amplitude-to-noise ratio is of medium range at 38 to 10. The X coordinate of 23 mm shows that the indication is probably in the HAZ. The Z coordinate of 21 mm shows that the indication is near the outer wall of the vessel.

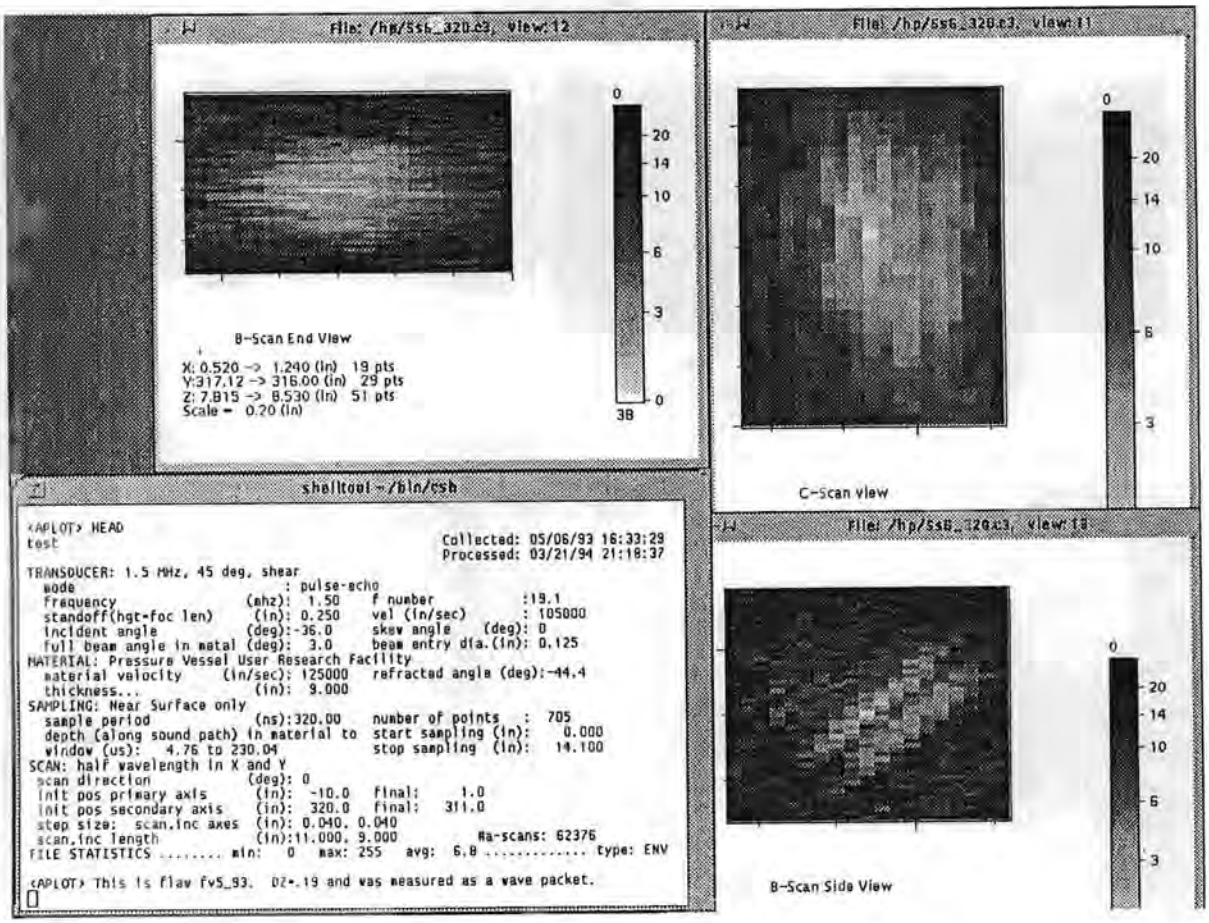

Figure A.84 - Planar indication #11 in the HAZ below 25 mm: mode 6

Figure A.85 shows planar indication #12 in the heat affected zone below 25 mm. This planar indication has a through-wall extent of 4 mm based on wave packet width. The detection was made in mode 6 where it had isolated TOF shape at a depth of 215 mm. The shape quality is good but more than one TOF shape was present for this indication. There were no confirmations in other modes. The indication is characterized as planar based on lack of detection in normal beam or orthogonal modes. The length is 20 mm and was made to LOS in mode 6. The aspect ratio (length/depth) of this indication is 5 which tends to confirm the large through-wall extent. The maximum amplitude-to-noise ratio is of medium range at 71 to 20. The X coordinate of 30 mm shows that the indication is probably in the HAZ. The Z coordinate of 215 mm shows that the indication near the outer wall of the vessel.

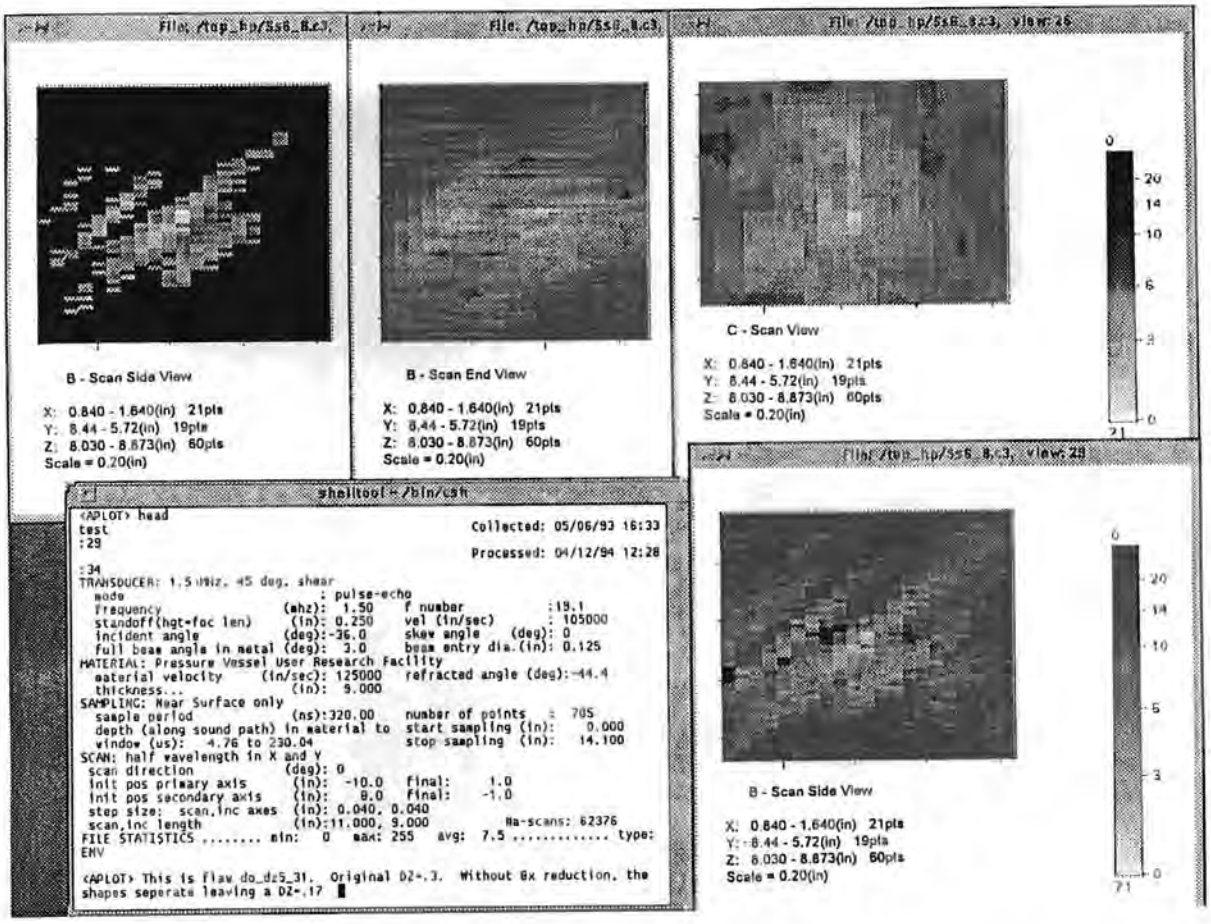

Figure A.85 - Planar indication #12 in the HAZ below 25 mm: mode 6

Figure A.86 shows planar indication #13 in the heat affected zone below 25 mm. This planar indication has a through-wall extent of 4 mm based on wave packet width. The detection was made in mode 6 where it had isolated TOF shape at a depth of 232 mm. The shape quality is good but more than one TOF shape was present for this indication. There were no confirmations in other modes. The indication is characterized as planar based on lack of detection in normal beam or orthogonal modes. The length is 33 mm and was made to LOS in mode 6. The aspect ratio (length/depth) of this indication is 8 which tends to confirm the large through-wall extent. The maximum amplitude-to-noise ratio is of medium range at 26 to 10. The X coordinate of -28 mm shows that the indication is probably in the HAZ. The Z coordinate of 232 mm shows that the indication is near the outer wall, possibly connected to the outer wall of the vessel.

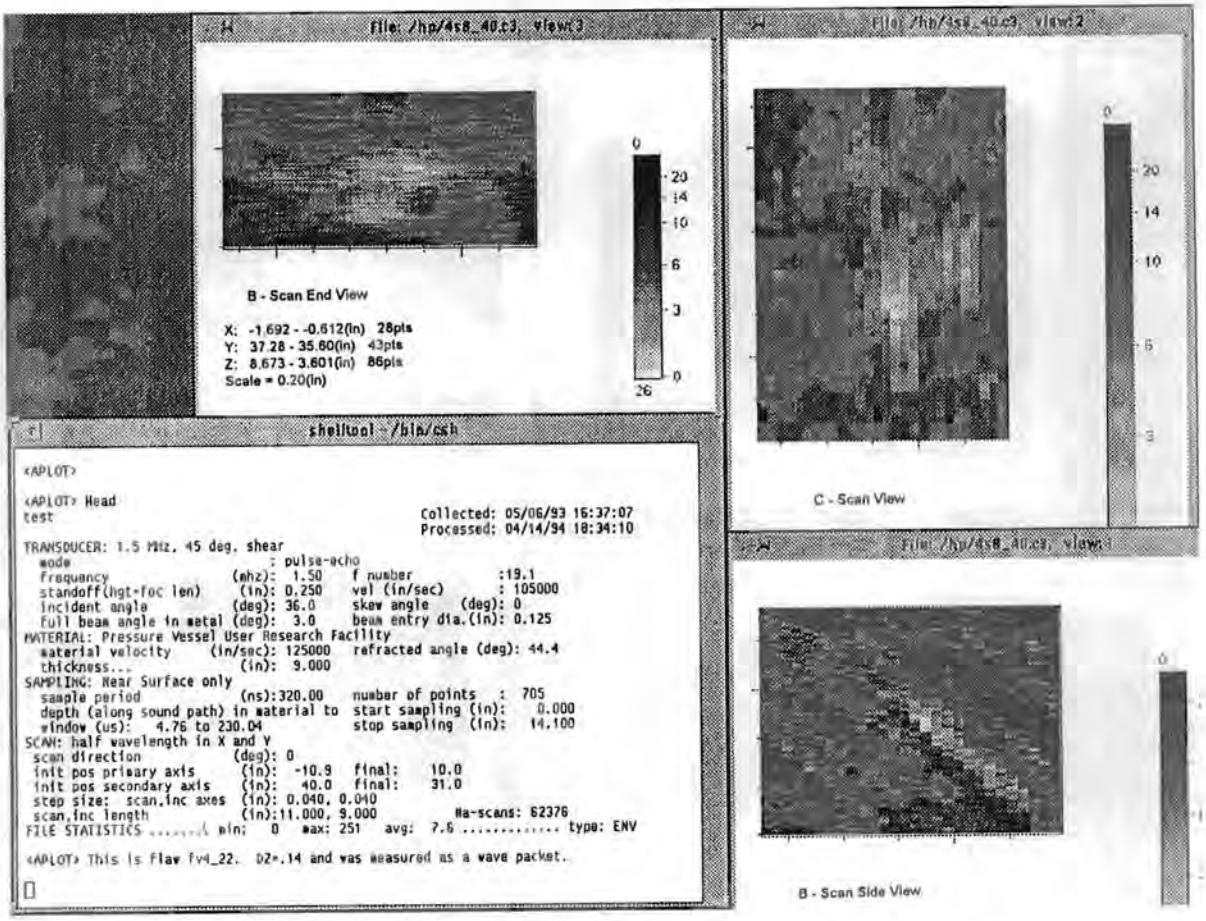

Figure A.86 - Planar indication #13 in the HAZ below 25 mm: mode 8

Figures A.87a-b show planar indication #14 in the heat affect zone below 25 mm. This planar indication has a through-wall extent of 4 mm based on LOS in a cloud like pattern. The detection was made in mode 8 where the shape appeared cloud like in nature at a depth of 189 mm. There was a confirmation in mode 6 at depth of 192 mm. The confirmation mode gave a through-wall extent estimate of 3 mm based on wave packet width. The two Z values of 189 to 192 mm give an alternate depth size of 3 mm. The indication is characterized as planar based on lack of detection in normal beam or orthogonal modes. The length is 18 mm and was made to LOS in mode 8. The aspect ratio (length/depth) of this indication is 4.5 which tends to confirm the large through-wall extent. The maximum amplitude-to-noise ratio is of medium range at 32 to 12. The X coordinate of -14 mm shows that the indication is probably in the HAZ. The Z coordinate of 189 to 192 mm shows that the indication is in the outer third of the vessel.

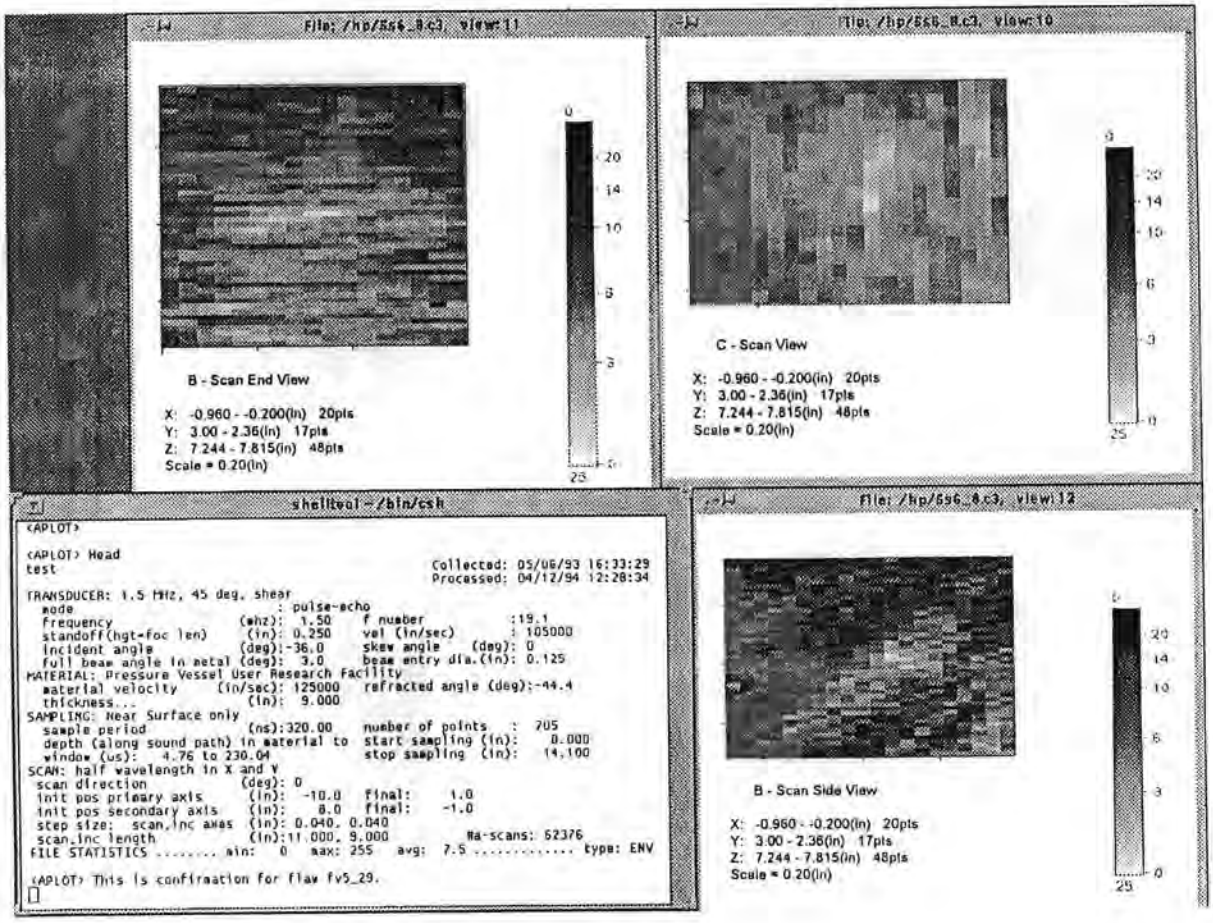

Figure A.87a - Planar indication #14 in the HAZ below 25 mm: mode 6

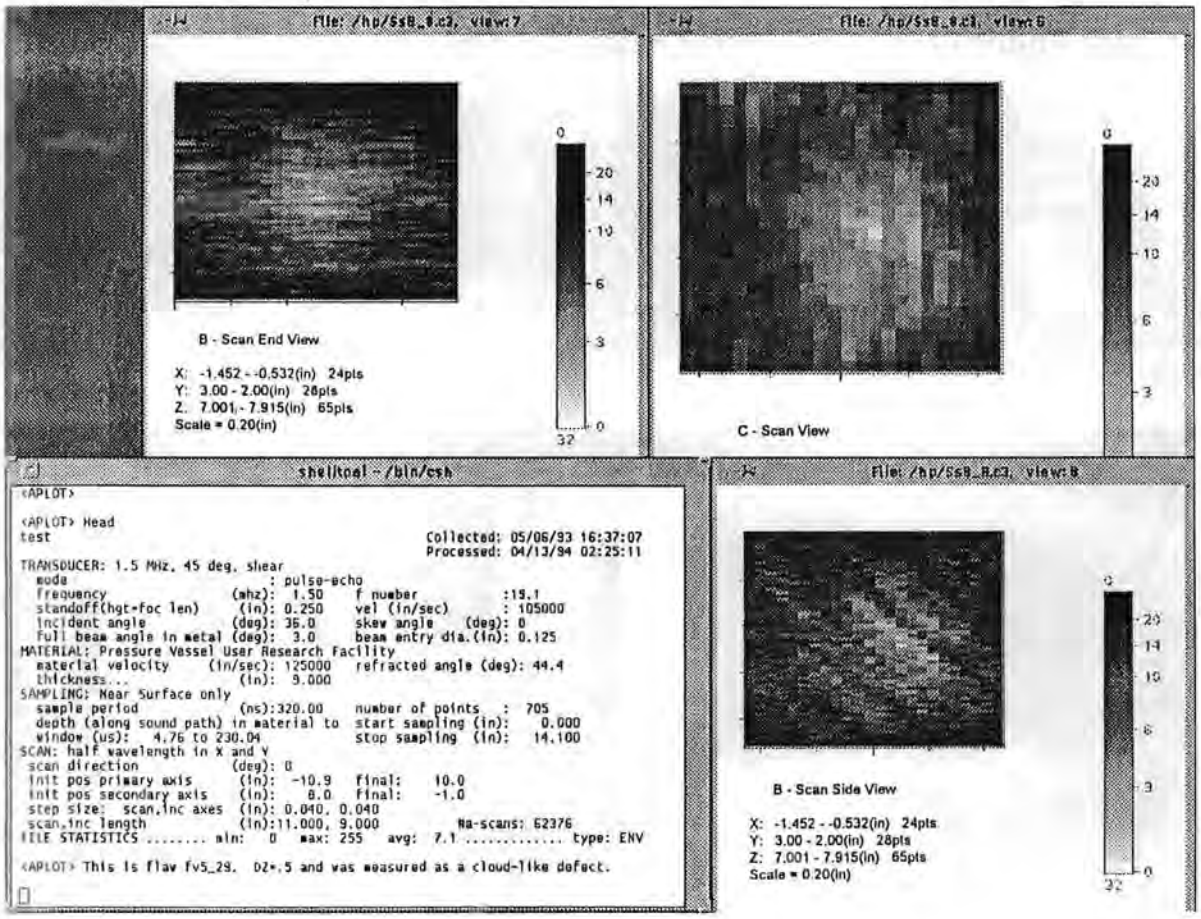

Figure A.87b - Planar indication #14 in the HAZ below 25 mm: mode 8

Planar Indications in the Base Metal Below 25 mm

Figures A.88a-b show planar indication #1 in the base metal below 25 mm. This planar indication has a through-wall extent of 26 mm based on tip signal pattern. The detection was made in mode 6 where it displayed a pair of TOF shapes at a depth of 136 mm. The shape quality is good for this indication. There was a confirmation in mode 8 at depth of 123 mm. The confirmation mode gave a through-wall extent estimate of 1 mm based on wave packet width. The two Z values of 123 to 136 mm give an alternate depth size of 13 mm. The indication is characterized as planar based on the tip signal pattern. The length is 23 mm and was made to LOS in mode 6. The range of aspect ratios (length/depth) of this indication is 0.9 to 1.8. The maximum amplitude-to-noise ratio is high at 27 to 5. The X coordinate of 28 mm shows that the indication is in the base metal, possibly HAZ. The Z coordinate of 123 to 136 mm shows that the indication is in the middle third of the vessel.

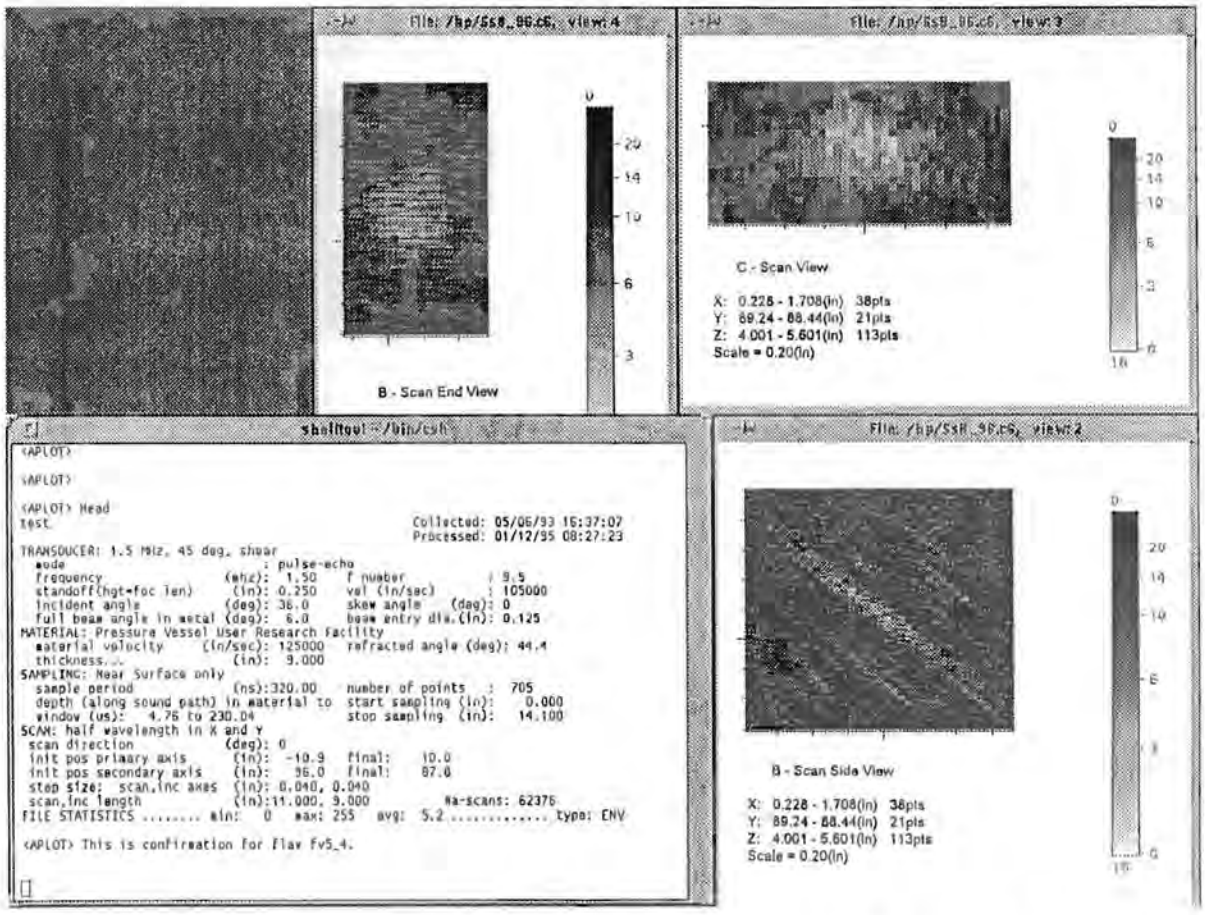

Figure A.88a - Planar indication #1 in the base metal below 25 mm: mode 8

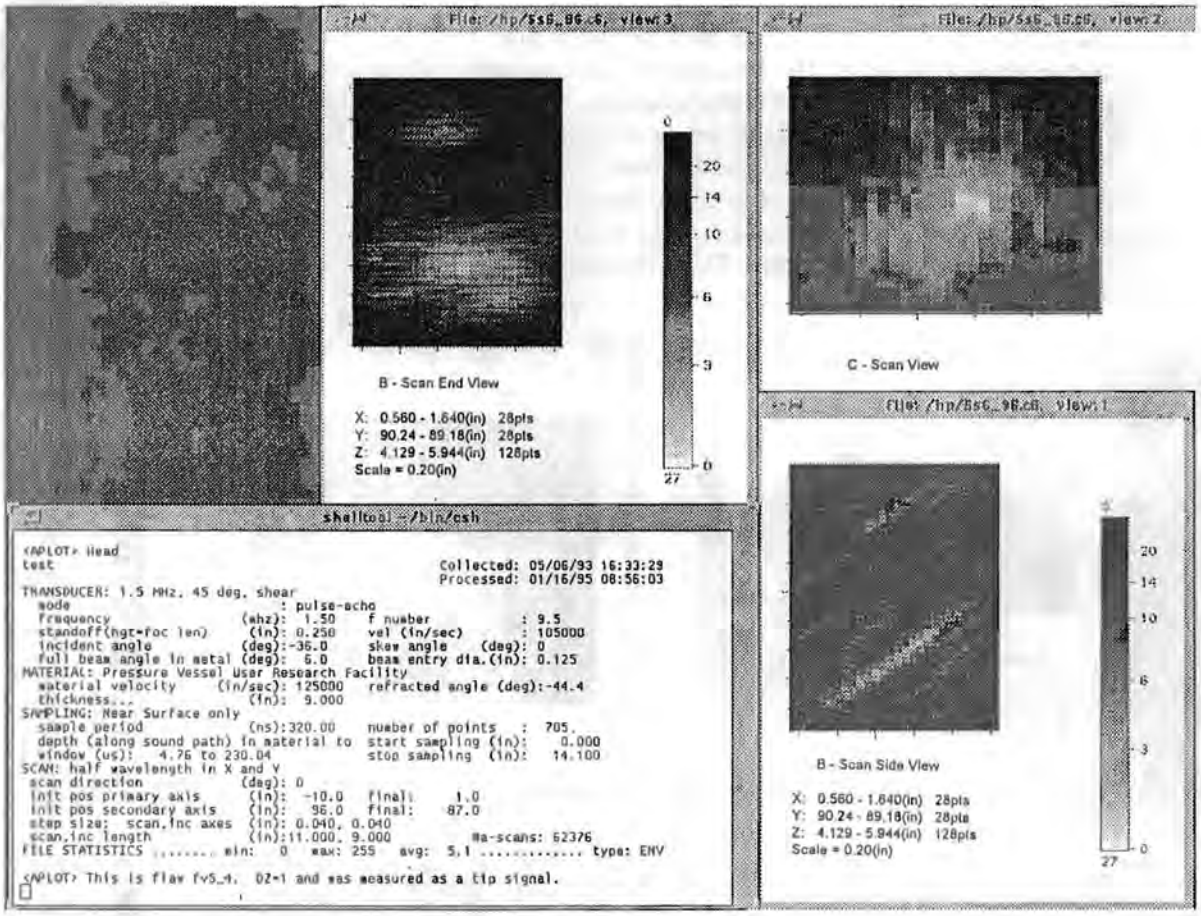

Figure A.88b - Planar indication #1 in the base metal below 25 mm: mode 6

Figures A.89a-b show planar indication #2 in the base metal below 25 mm. This planar indication has a through-wall extent of 15 mm based on tip signal pattern. The detection was made in mode 6 where it displayed a pair of TOF shapes at a depth of 121 mm. The shape quality is good for this indication. There was a confirmation in mode 8 at a depth of 122 mm. The confirmation mode gave a through-wall extent estimate of 3 mm based on ring around pattern. The two Z values of 121 to 122 mm give an alternate depth size of 1 mm. The indication is characterized as planar based on the tip signal pattern. The length is 41 mm and was made to LOS in mode 6. The aspect ratio (length/depth) of this indication is 3. The maximum amplitude-to-noise ratio is of medium range at 30 to 8. The X coordinate of 24 mm shows that the indication is in the base metal, possibly in the HAZ. The Z coordinate of 121 to 122 mm shows that the indication is in the middle third of the vessel.

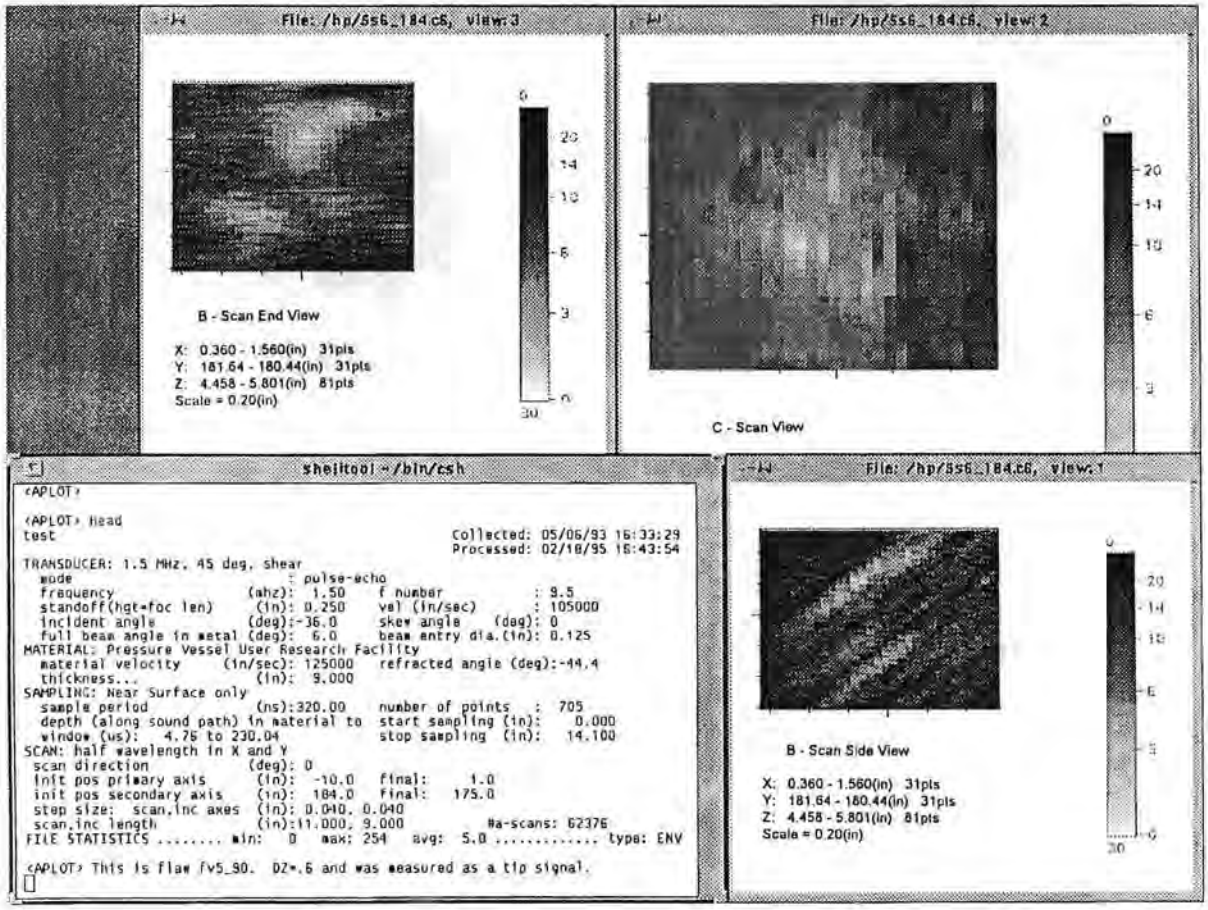

Figure A.89a - Planar indication #2 in the base metal below 25 mm: mode 6

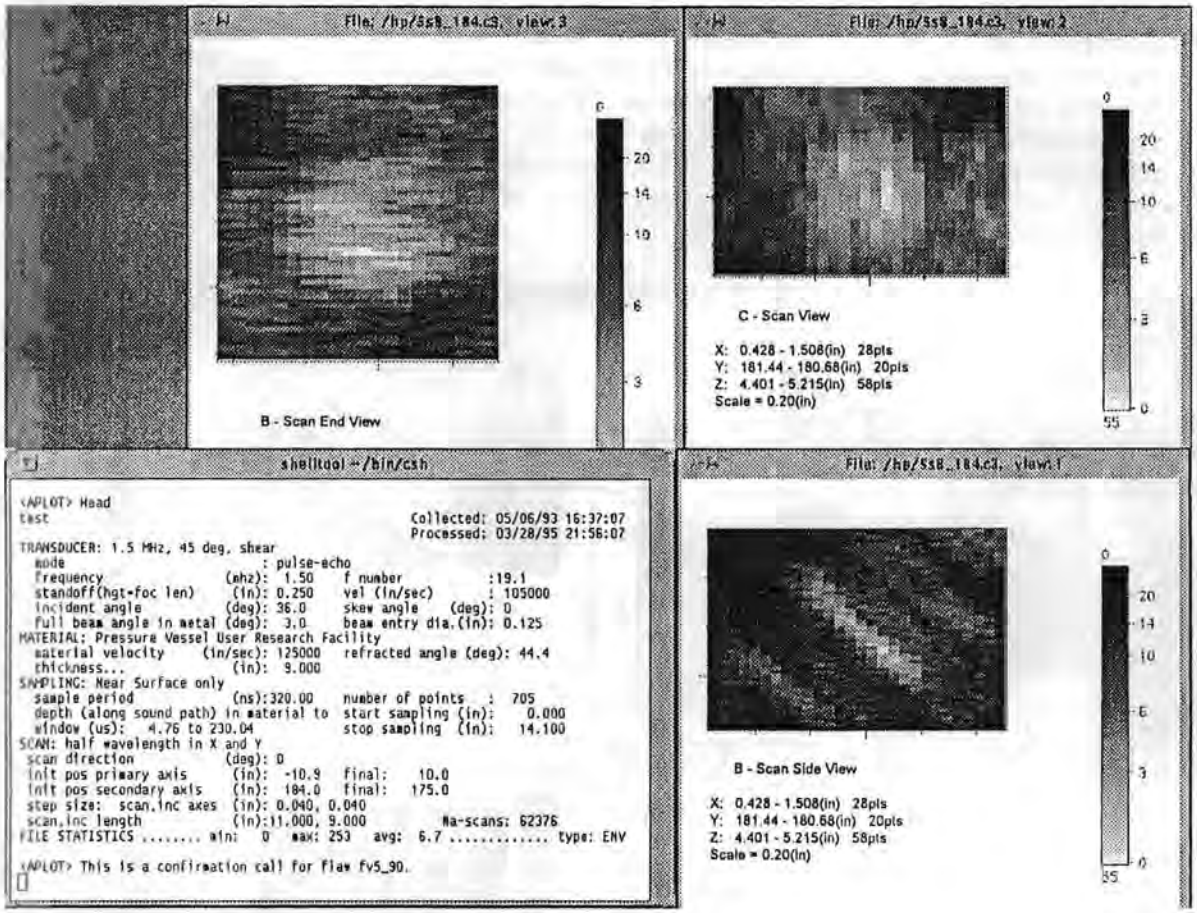

Figure A.89b - Planar indication #2 in the base metal below 25 mm: mode 8

Figure A.90 shows planar indication #3 in the base metal below 25 mm. This planar indication has a through-wall extent of 13 mm based on tip signal pattern. The detection was made in mode 7 where it displayed a pair of TOF shapes at a depth of 145 mm. The shape quality is good for this indication. There were no confirmations in other modes. The indication is characterized as planar based on the tip signal pattern. The width is 15 mm and was made to LOS in mode 7. The aspect ratio (width/depth) of this indication is 1.2. The maximum amplitude-to-noise ratio is of medium range at 51 to 14. The X coordinate of 58 mm shows that the indication is clearly in the base metal. The Z coordinate of 145 mm shows that the indication is in the middle third of the vessel.

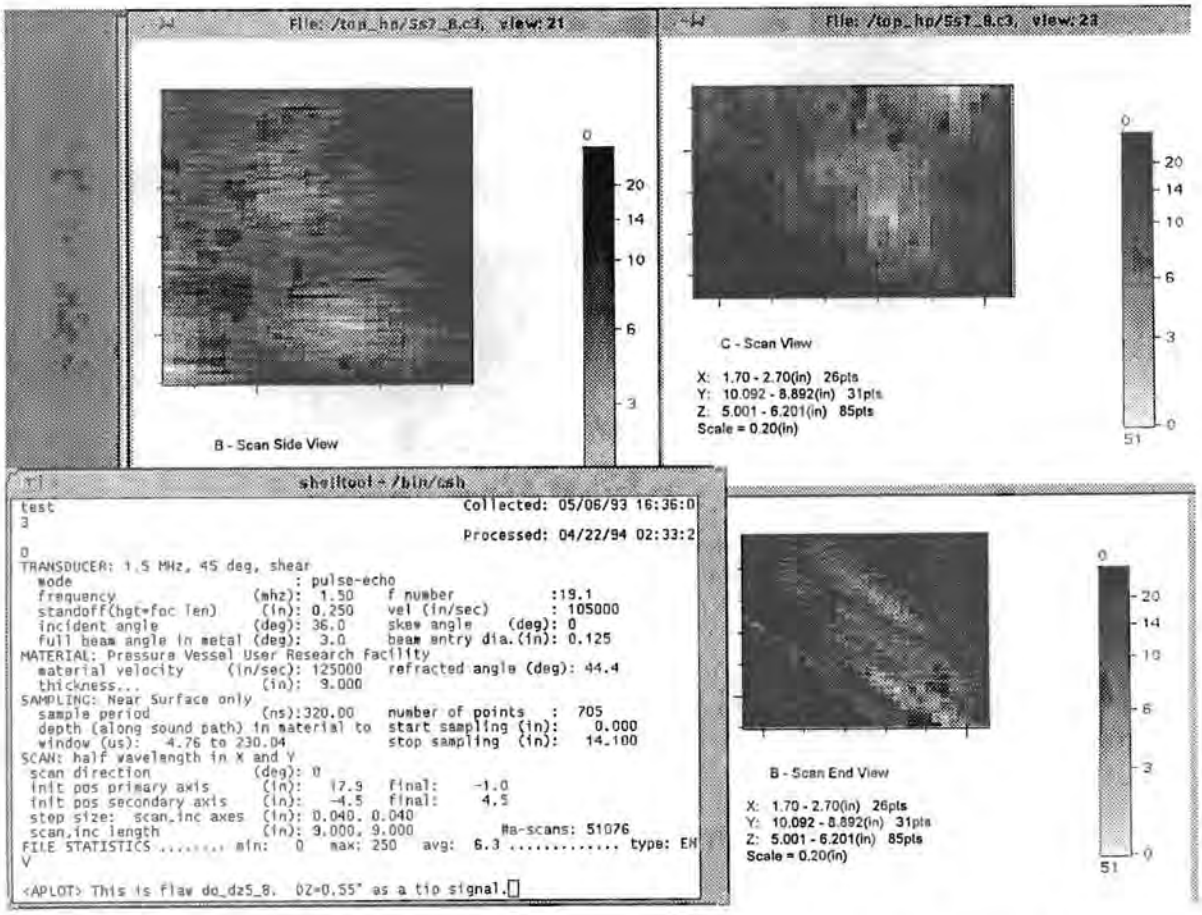

Figure A.90 - Planar indication #3 in the base metal below 25 mm: mode 7

Figure A.91 shows planar indication #4 in the base metal below 25 mm. This planar indication has a through-wall extent of 11 mm based on wave packet width. The detection was made in mode 6 where it had isolated TOF shape at a depth of 214 mm. The shape quality for this indication is good. Because more than one TOF shape was present the indication is broken up, implying that more than one small flaw may be present. There were no confirmations in other modes. The indication is characterized as planar based on lack of detection in normal beam or orthogonal modes. The length is 30 mm and was made to LOS in mode 6. The aspect ratio (length/depth) of this indication is 3. The maximum amplitude-to-noise ratio is of medium range at 45 to 12. The X coordinate of 43 mm shows that the indication is clearly in the base metal. The Z coordinate of 214 mm shows that the indication is near the outer wall of the vessel.

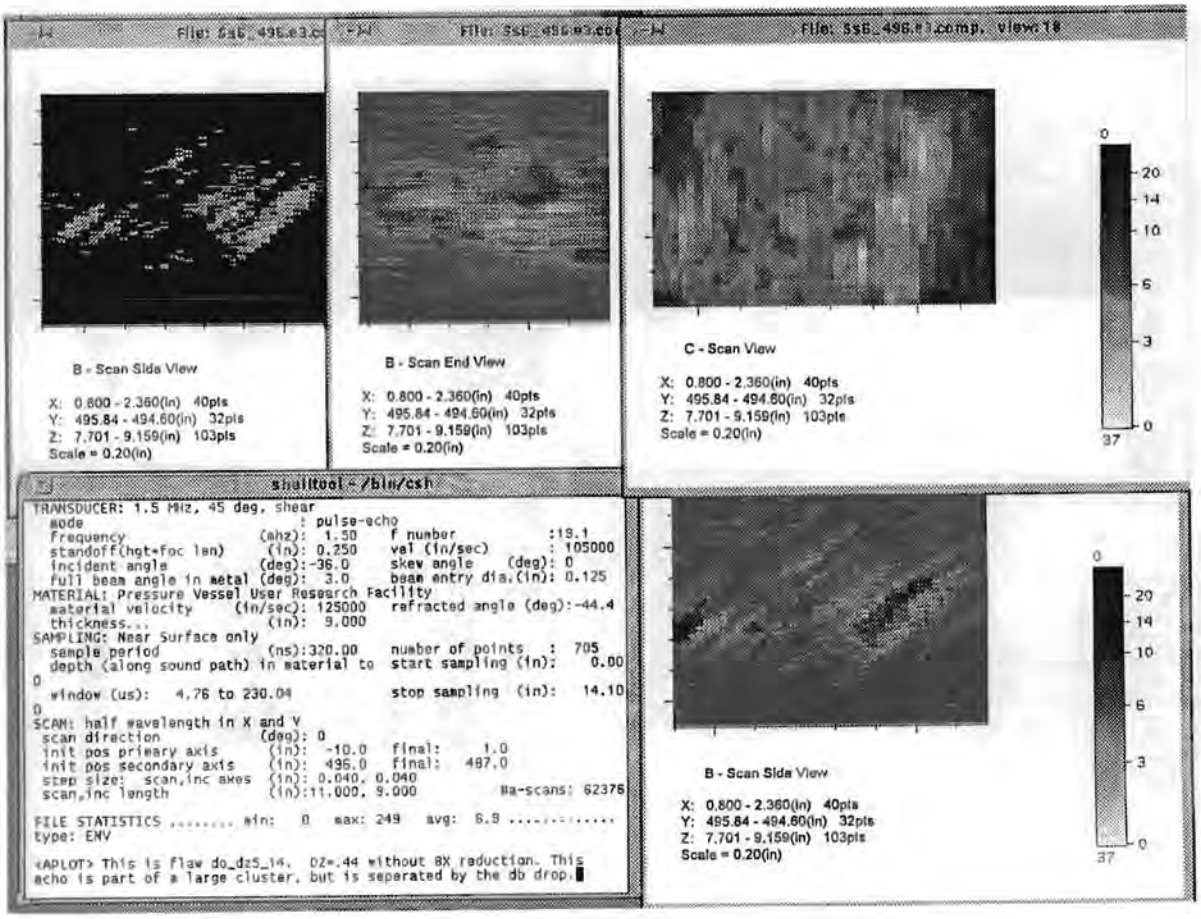

Figure A.91 - Planar indication #4 in the base metal below 25 mm: mode 6

Figure A.92 shows planar indication #5 in the base metal below 25 mm. This planar indication has a through-wall extent of 8 mm based on wave packet width. The detection was made in mode 6 where it had isolated TOF shape at a depth of 211 mm. The shape quality is good. More than one TOF shape was present for this indication, implying that more than one small flaw may be present. There were no confirmations in other modes. The indication is characterized as planar based on lack of detection in normal beam or orthogonal modes. The length is 27 mm and was made to LOS in mode 6. The aspect ratio (length/depth) of this indication is 3. The maximum amplitude-to-noise ratio is high at 59 to 12. The X coordinate of 31 mm shows that the indication is in the base metal, possibly HAZ. The Z coordinate of 211 mm shows that the indication is near the outer wall of the vessel.

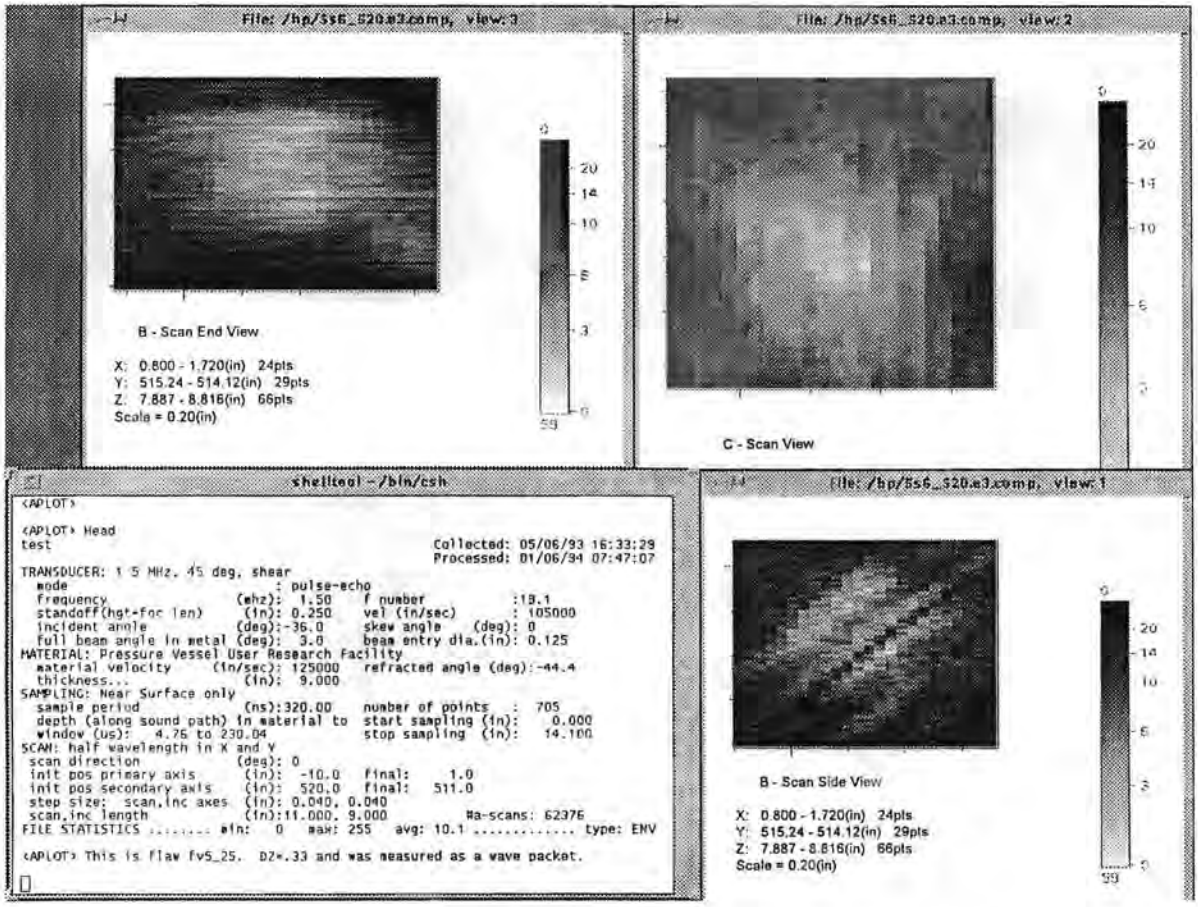

Figure A.92 - Planar indication #5 in the base metal below 25 mm: mode 6

Figure A.93 shows planar indication #6 in the base metal below 25 mm. This planar indication has a through-wall extent of 7 mm based on wave packet width. The detection was made in mode 8 where it had isolated TOF shape at a depth of 113 mm. More than one TOF shape was present. The shape quality for this indication is good but broken up, implying that more than one small flaw may be present. There were no confirmations in other modes. The indication is characterized as planar based on lack of detection in normal beam or orthogonal modes. The length is 16 mm and was made to LOS in mode 6. The aspect ratio (length/depth) of this indication is 2. The maximum amplitude-to-noise ratio is high at 65 to 15. The X coordinate of 46 mm shows that the indication is clearly in the base metal. The Z coordinate of 113 mm shows that the indication is in the middle third of the vessel.

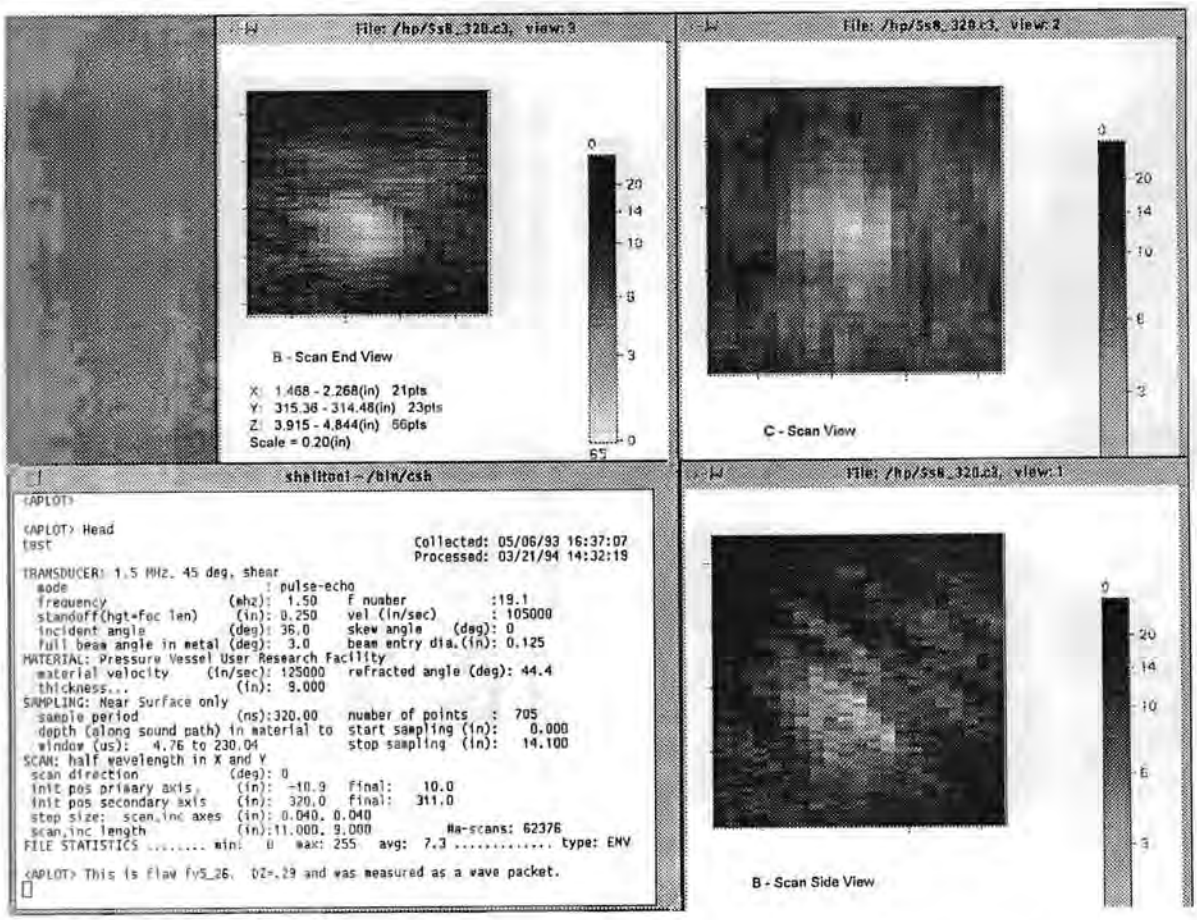

Figure A.93 - Planar indication #6 in the base metal below 25 mm: mode 8

Figure A.94 shows planar indication #7 in the base metal below 25 mm. This planar indication has a through-wall extent of 7 mm based on wave packet width. The detection was made in mode 8 where it had isolated TOF shape at a depth of 113 mm. More than one TOF shape was present. The shape quality for this indication is good but broken up, implying that more than one small flaw may be present. There were no confirmations in other modes. The indication is characterized as planar based on lack of detection in normal beam or orthogonal modes. The length is 16 mm and was made to LOS in mode 6. The aspect ratio (length/depth) of this indication is 2. The maximum amplitude-to-noise ratio is high at 65 to 15. The X coordinate of 46 mm shows that the indication is clearly in the base metal. The Z coordinate of 113 mm shows that the indication is in the middle third of the vessel.

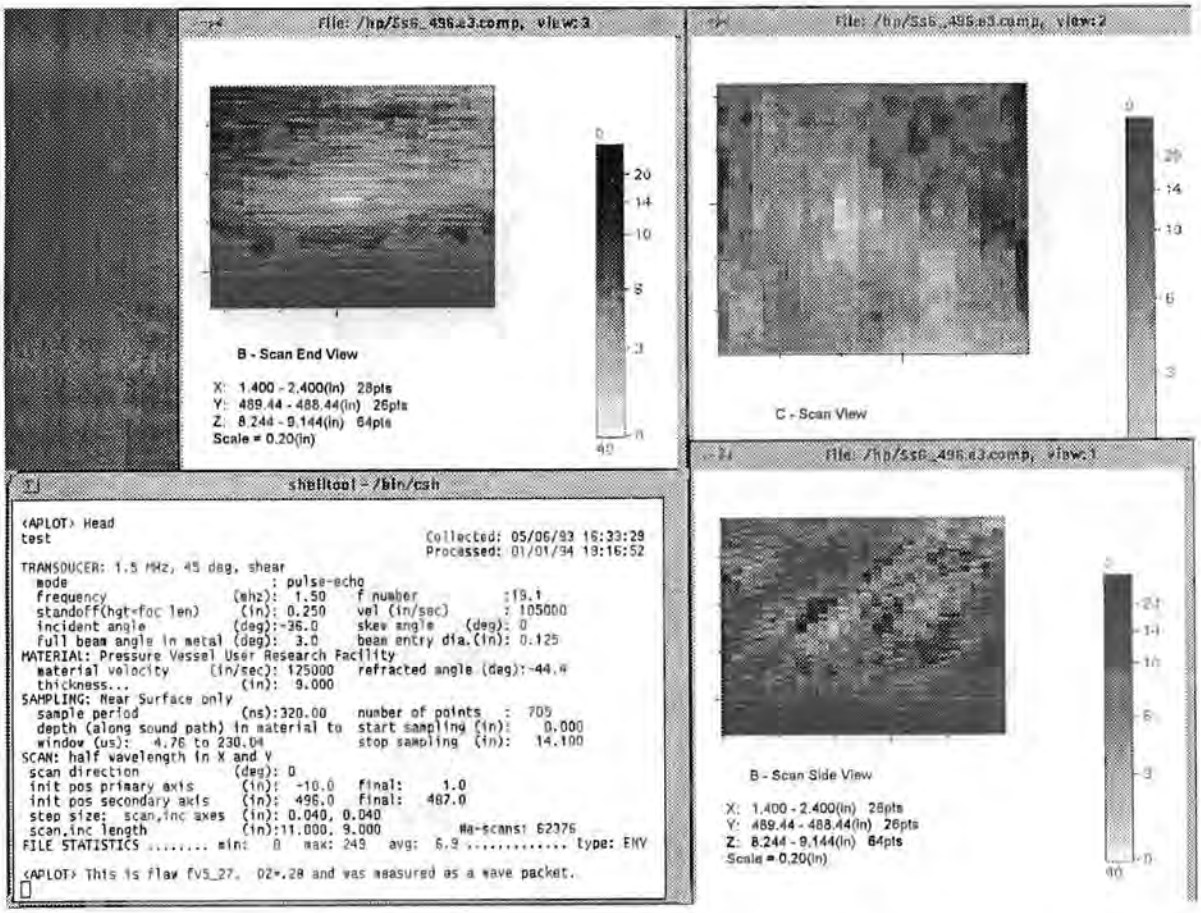

Figure A.94 - Planar indication #7 in the base metal below 25 mm: mode 6

Figure A.95 shows planar indication #8 in the base metal below 25 mm. This planar indication has a through-wall extent of 7 mm based on wave packet width. The detection was made in mode 8 where it had isolated TOF shape at a depth of 238 mm. More than one TOF shape was present. The shape quality for this indication is good but broken up, implying that more than one small flaw may be present. There were no confirmations in other modes. The indication is characterized as planar based on lack of detection in normal beam or orthogonal modes. The length is 28 mm and was made to LOS in mode 8. The aspect ratio (length/depth) of this indication is 4 which tends to confirm the large through-wall extent. The maximum amplitude-to-noise ratio is high at 84 to 20. The X coordinate of 31 mm shows that the indication is in the base metal, possibly HAZ. The Z coordinate of 238 mm shows that the indication is near the outer wall, possibly connected to the outer wall of the vessel.

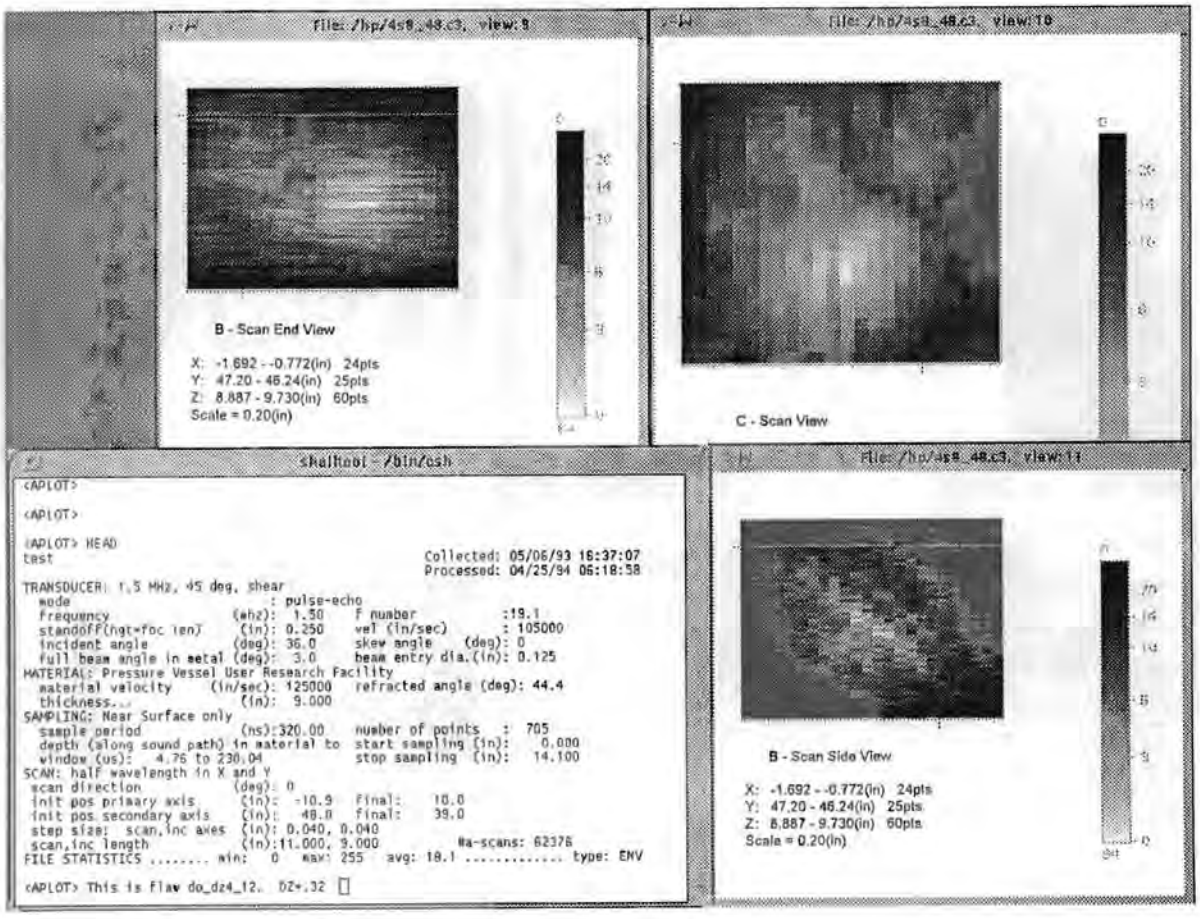

Figure A.95 - Planar indication #8 in the base metal below 25 mm: mode 8

Figures A.96a-b show planar indication #9 in the base metal below 25 mm. This planar indication has a through-wall extent of 7 mm based on tip signal pattern. The detection was made in mode 8 where it displayed a pair of TOF shapes at a depth of 110 mm. The shape quality is good for this indication. There was a confirmation in mode 6 at a depth of 111 mm. The confirmation mode gave a through-wall extent estimate of 4 mm based on wave packet width. The two Z values of 110 to 111 mm give an alternate depth size of 1 mm. The indication is characterized as planar based on the tip signal pattern. The length is 16 mm and was made to LOS in mode 6. The aspect ratio (length/depth) of this indication is 2. The maximum amplitude-to-noise ratio is of medium range at 62 to 20. The X coordinate of 37 mm shows that the indication is clearly in the base metal. The Z coordinate of 110 mm shows that the indication is in the middle third of the vessel.

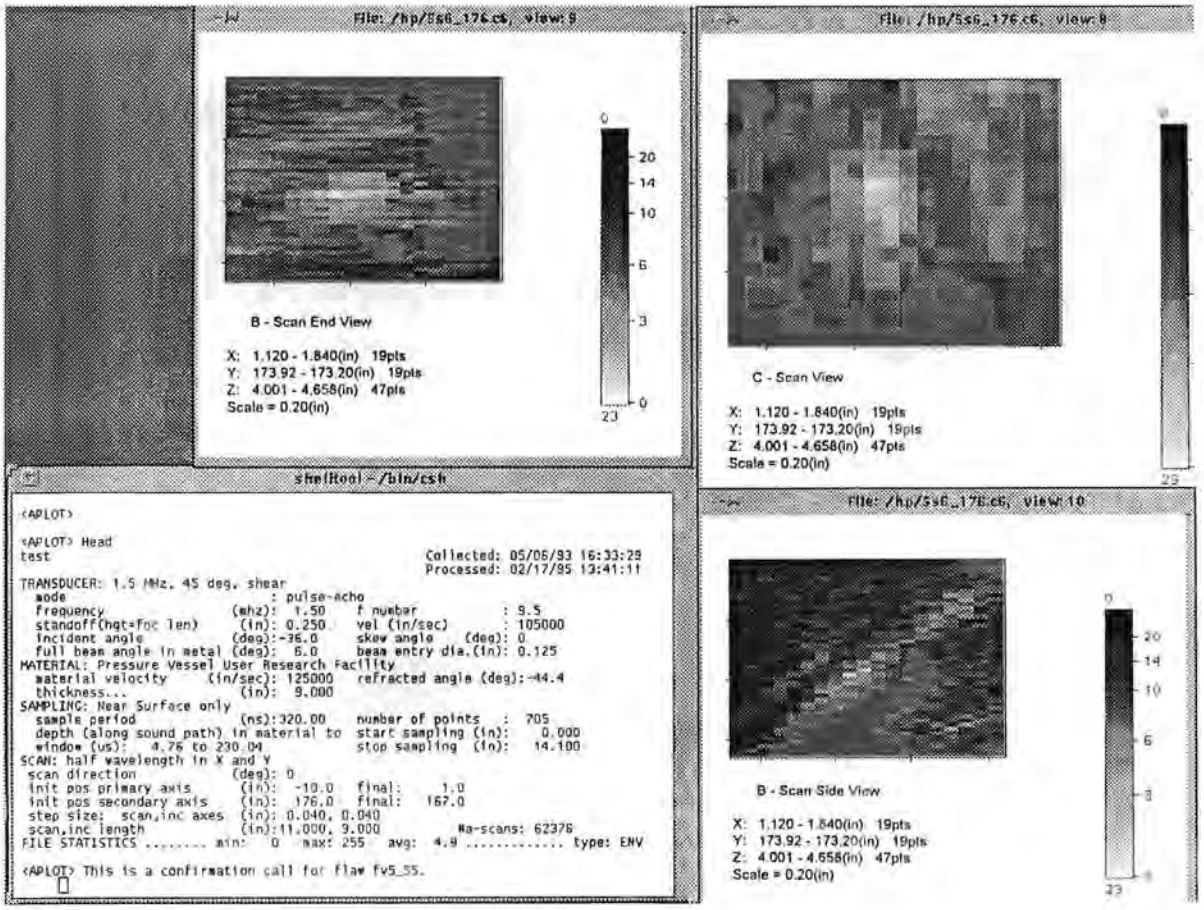

Figure A.96a - Planar indication #9 in the base metal below 25 mm: mode 6

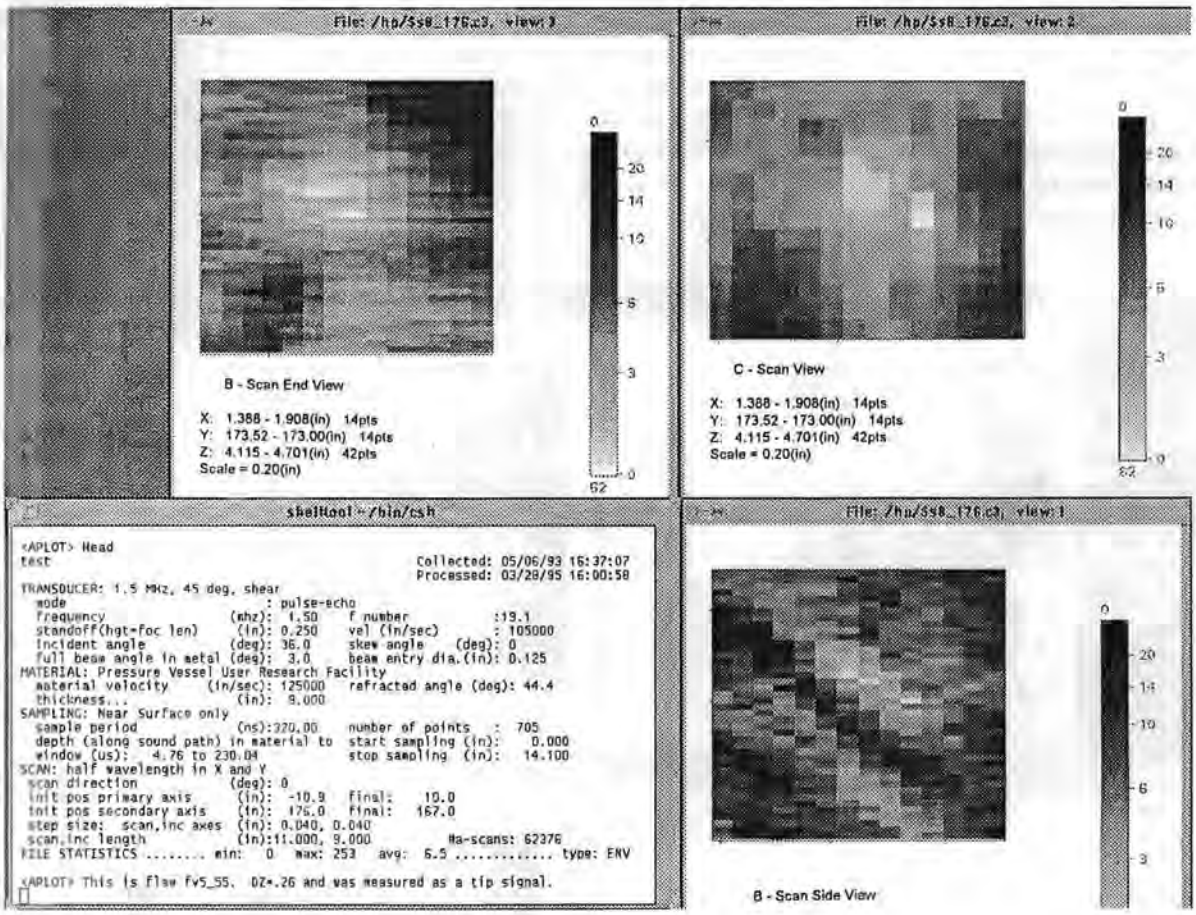

Figure A.96b - Planar indication #9 in the base metal below 25 mm: mode 8

Figure A.97 shows planar indication #10 in the base metal below 25 mm. This planar indication has a through-wall extent of 6 mm based on tip signal pattern. The detection was made in mode 8 where it displayed a pair of TOF shapes at a depth of 201 mm. The shape quality is good for this indication. There were no confirmations in other modes. The indication is characterized as planar based on the tip signal pattern. The length is 20 mm and was made to LOS in mode 8. The aspect ratio (length/depth) of this indication is 3. The maximum amplitude-to-noise ratio is of medium range at 53 to 20. The X coordinate of -159 mm shows that the indication is clearly in the base metal. The Z coordinate of 201 mm shows that the indication is in the outer third of the vessel.

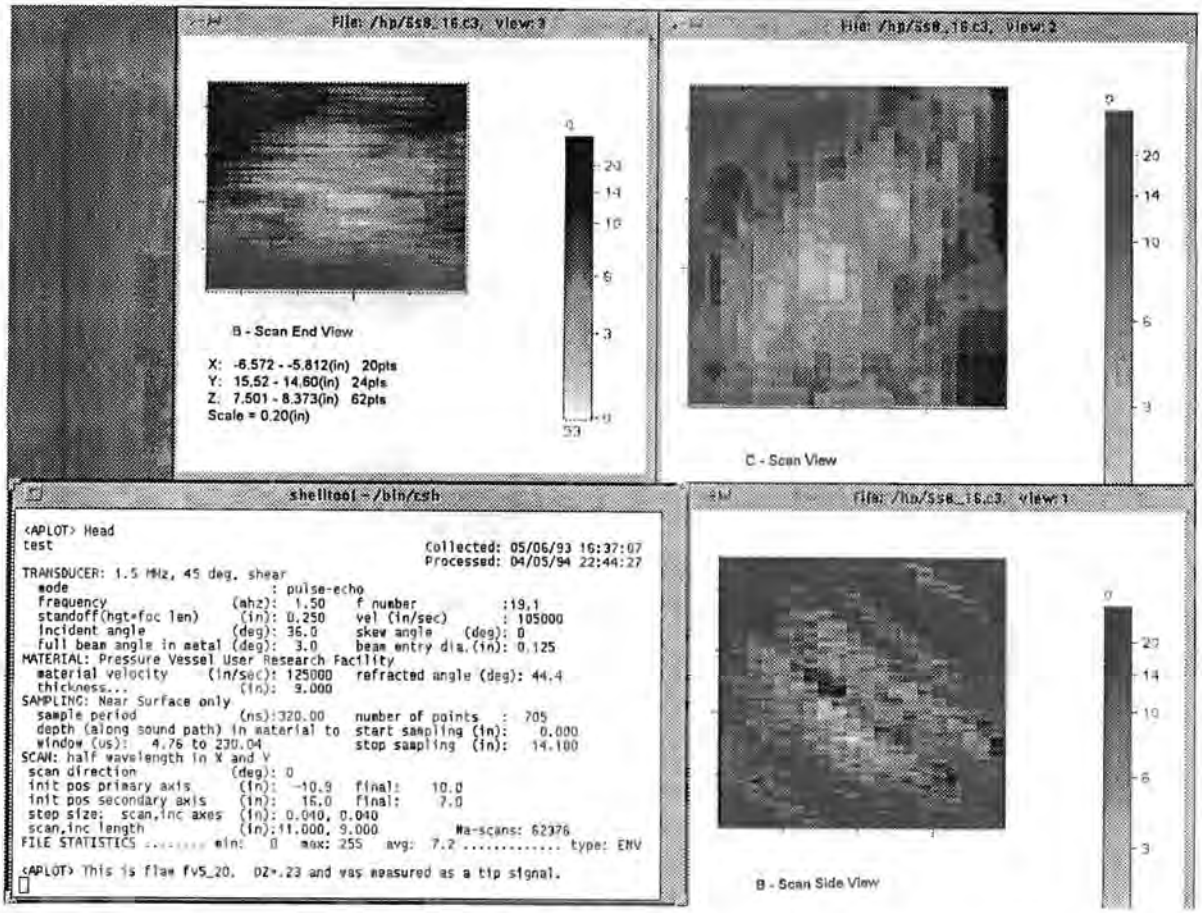

Figure A.97 - Planar indication #10 in the base metal below 25 mm: mode 8

Figures A.98a-b show planar indication #11 in the base metal below 25 mm. This planar indication has a through-wall extent of 6 mm based on tip signal pattern. The detection was made in mode 8 where it displayed a pair of TOF shapes. The shape quality is good for this indication. There were no confirmations in other modes. The indication is characterized as planar based on the tip signal pattern. The length is 23 mm and was made to LOS in mode 8. The aspect ratio (length/depth) of this indication is 4 which tends to confirm the large through-wall extent. The maximum amplitude-to-noise ratio is of medium range at 68 to 25. The X coordinate of -70 mm shows that the indication is in the base metal. The Z coordinate of 203 mm shows that the indication is in the outer third of the vessel.

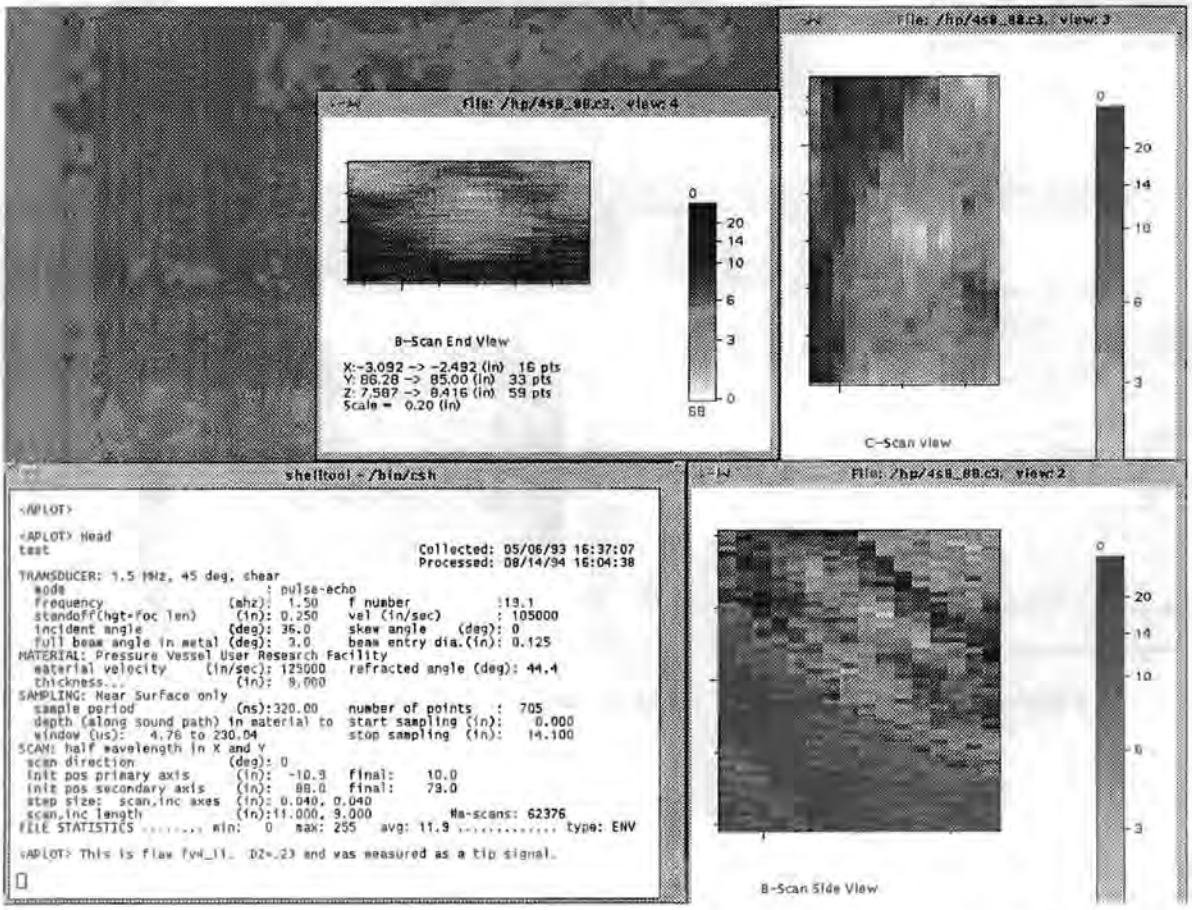

Figure A.98a - Planar indication #11 in the base metal below 25 mm: mode 8

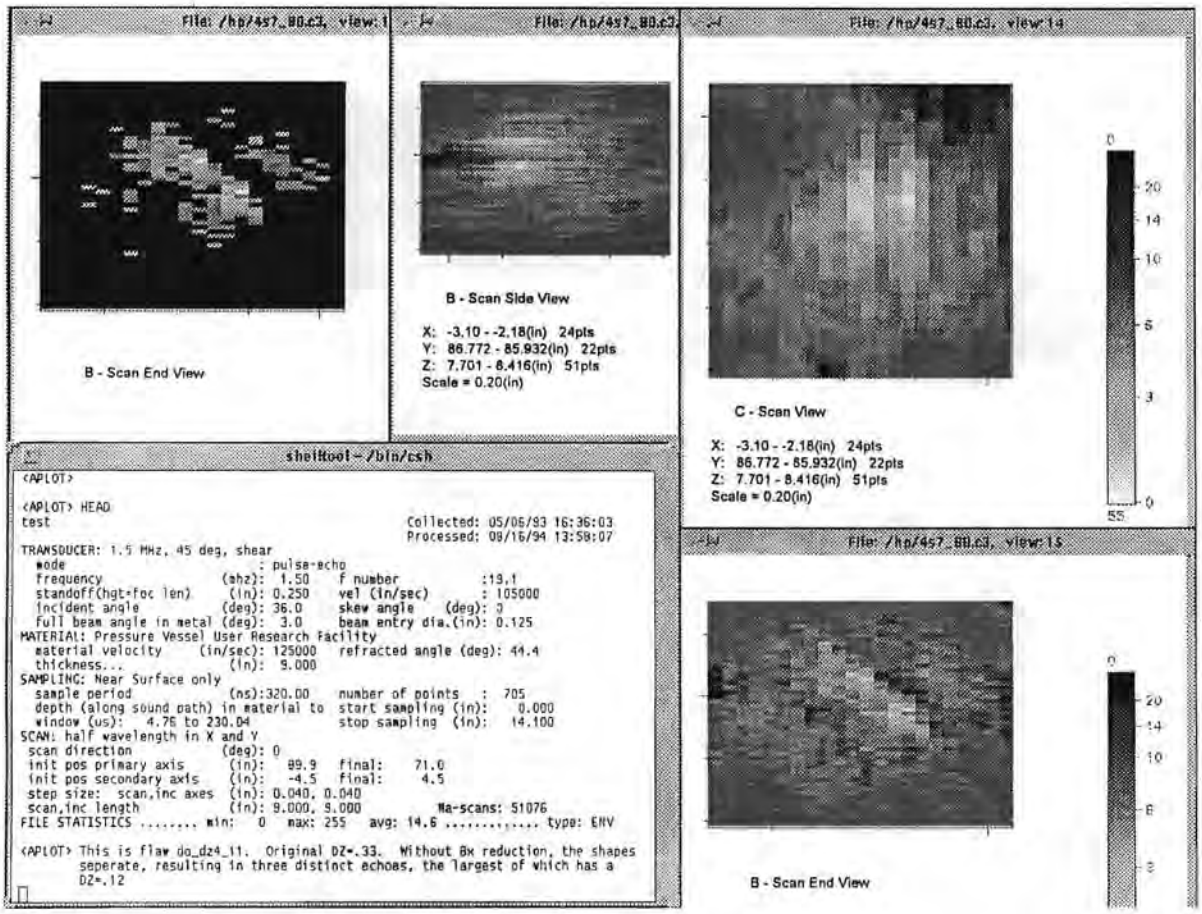

Figure A.98b - Planar indication #11 in the base metal below 25 mm: mode 7

Figures A.99a-b show planar indication #12 in the base metal below 25 mm. This planar indication has a through-wall extent of 6 mm based on tip signal pattern. The detection was made in mode 6 where it displayed a pair of TOF shapes at a depth of 118 mm. The shape quality is good for this indication. There was a confirmation in mode 8 at a depth of 119 mm. Based on LOS in a cloud like shape, the confirmation mode gave a through-wall extent estimate of 13 mm. The two Z values of 118 to 119 mm give an alternate depth size of 1 mm. The indication is characterized as planar based on the tip signal pattern. The length is 17 mm and was made to LOS in mode 6. The range of aspect ratios (length/depth) of this indication is 1.3 to 2.8. The maximum amplitude-to-noise ratio is of medium range at 50 to 15. The X coordinate of 25 mm shows that the indication is in the base metal, possibly in the HAZ. The Z coordinate of 118 mm shows that the indication is in the middle third of the vessel.

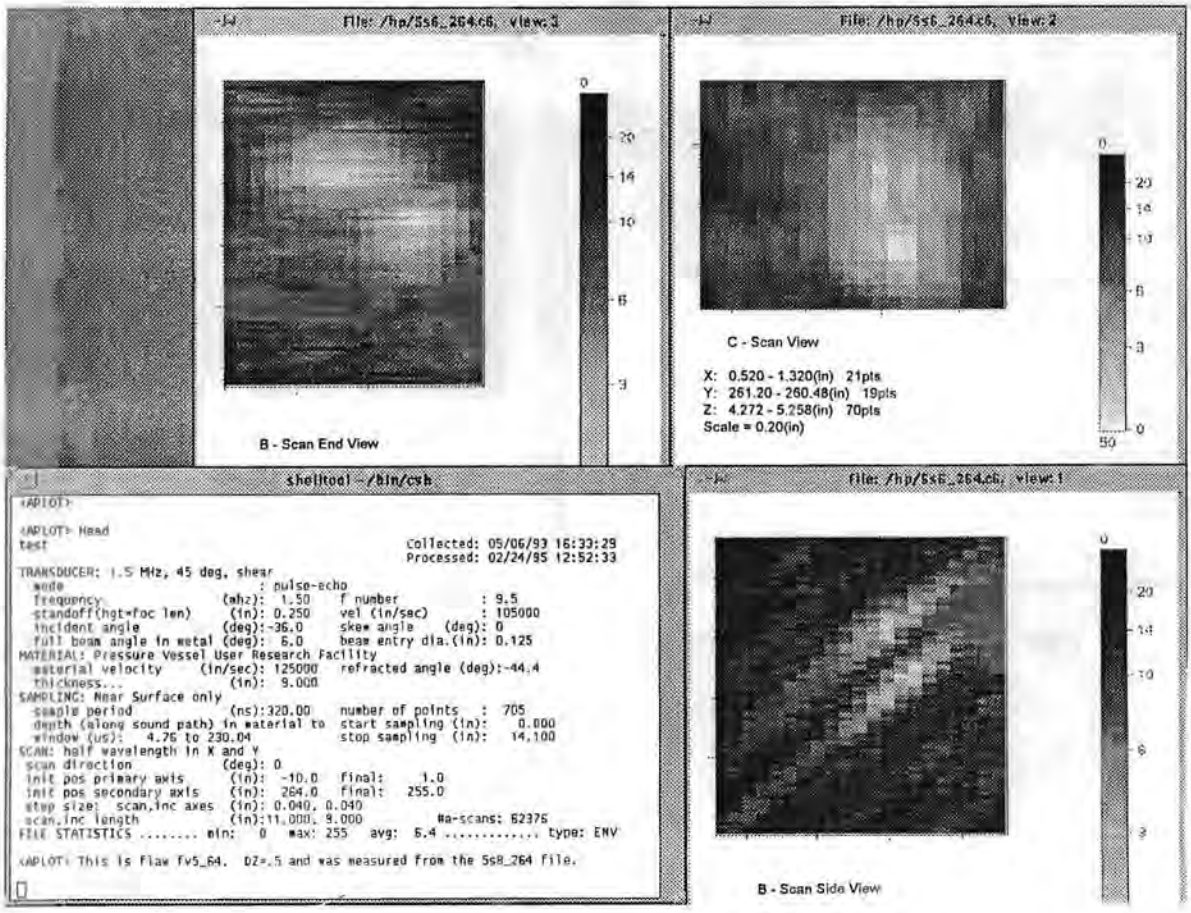

Figure A.99a - Planar indication #12 in the base metal below 24 mm: mode 6

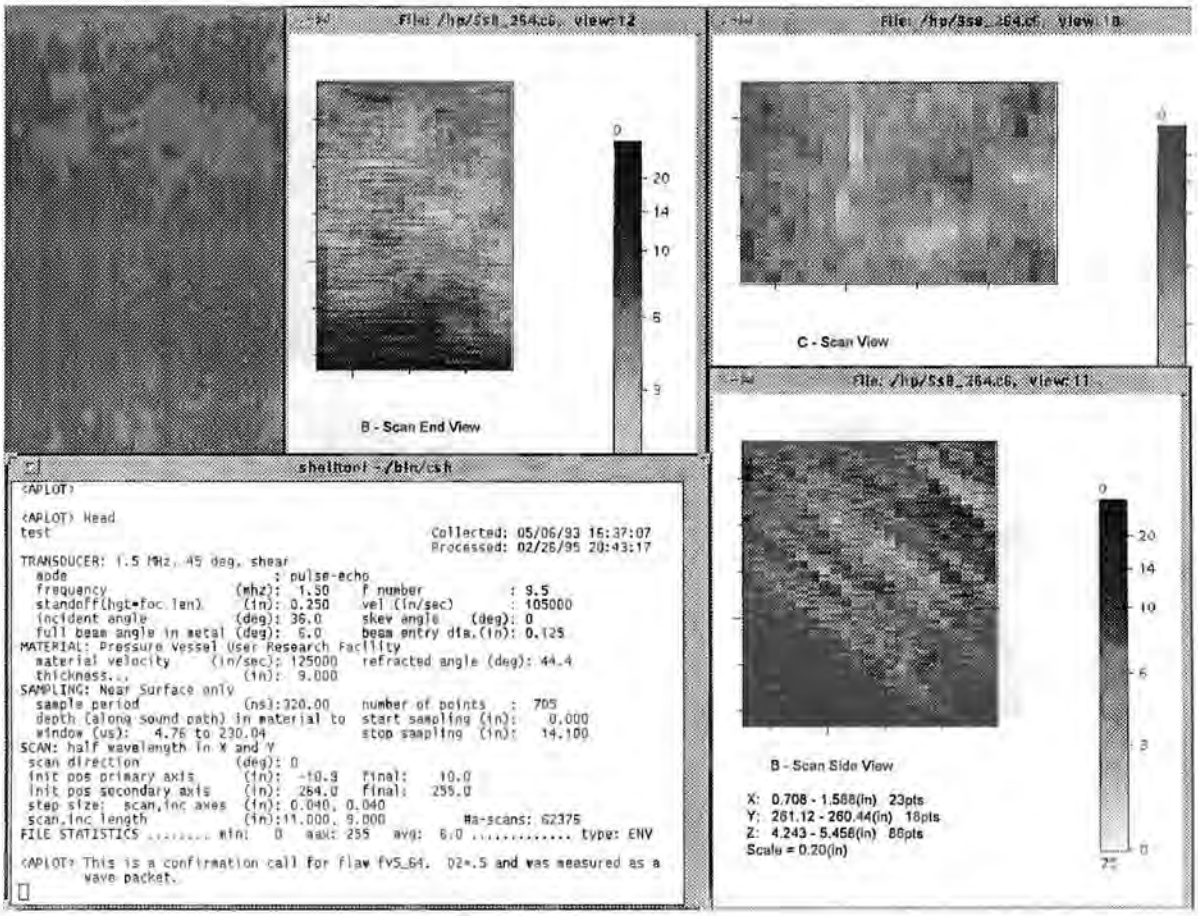

Figure A.99b - Planar indication #12 in the base metal below 25 mm: mode 8

Figure A.100 shows planar indication #13 in the base metal below 25 mm. Based on LOS in a cloud like pattern, this planar indication has a through-wall extent of 4 mm. The detection was made in mode 6 where the shape was cloud like in nature at a depth of 123 mm. The shape quality for this indication is good but broken up, implying that more than one small flaw may be present. There were no confirmations in other modes. The indication is characterized as planar based on lack of detection in normal beam or orthogonal modes. The length is 30 mm and was made to LOS in mode 6. The aspect ratio (length/depth) of this indication is 8 which tends to confirm the large through-wall extent. The maximum amplitude-to-noise ratio is of medium range at 58 to 20. The X coordinate of 36 mm shows that the indication is clearly in the base metal. The Z coordinate of 123 mm shows that the indication is in the middle third of the vessel.

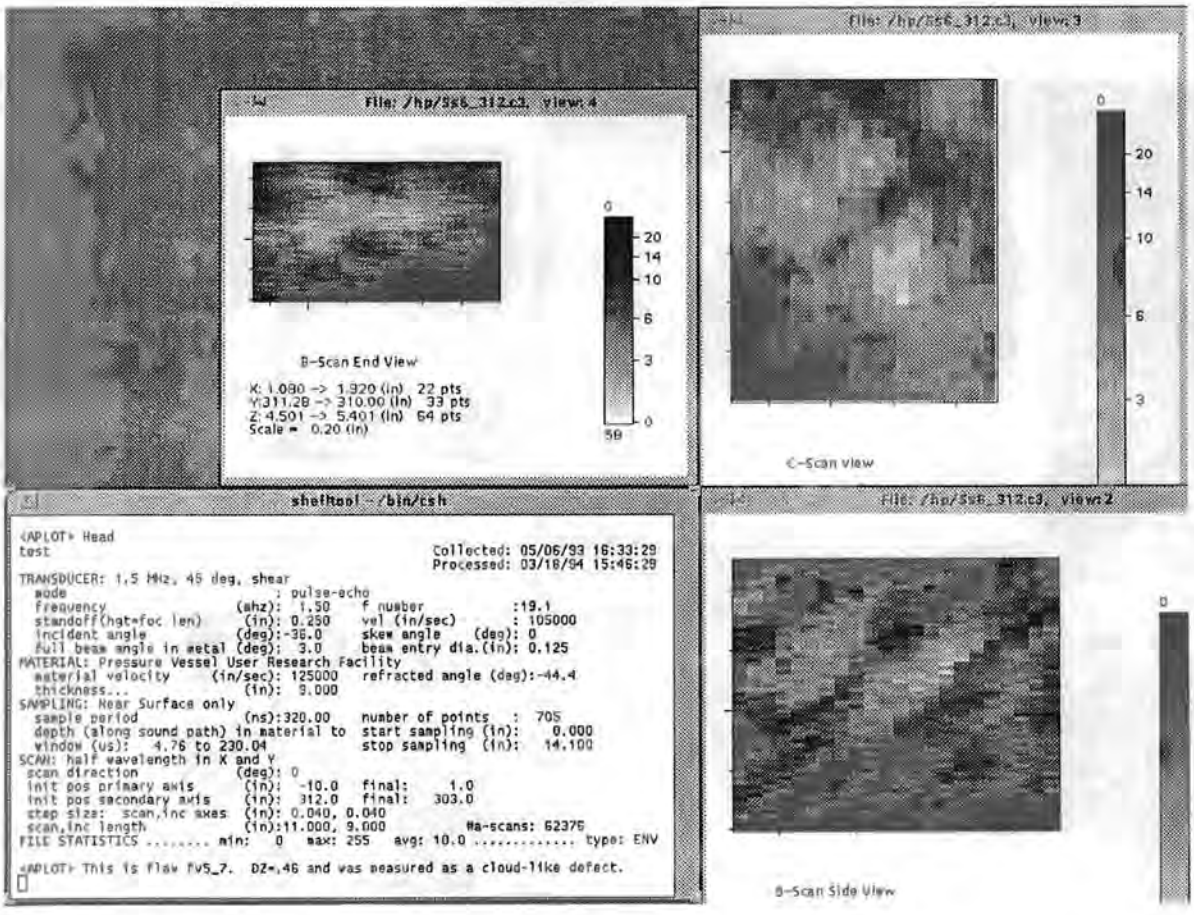

Figure A.100 - Planar indication #13 in the base metal below 25 mm: mode 6

Figures A.101a-b show planar indication #14 in the base metal below 25 mm. Based on LOS in a cloud like pattern, this planar indication has a through-wall extent of 4 mm. The detection was made in mode 8 where the shape was cloud like in nature at a depth of 192 mm. The shape quality for this indication is good but broken up, implying that more than one small flaw may be present. There was a confirmation in mode 6 at a depth of 195 mm which gave a through-wall extent estimate of 4 mm based on wave packet width. The two Z values of 192 to 195 mm give an alternate depth size of 3 mm. The indication is characterized as planar based on lack of detection in normal beam or orthogonal modes. The length is 25 mm and was made to LOS in mode 8. The aspect ratio (length/depth) of this indication is 6 which tends to confirm the large through-wall extent. The maximum amplitude-to-noise ratio is of medium range at 38 to 10. The X coordinate of -49 mm shows that the indication is clearly in the base metal. The Z coordinate of 192 to 195 mm shows that the indication is in the outer third of the vessel.

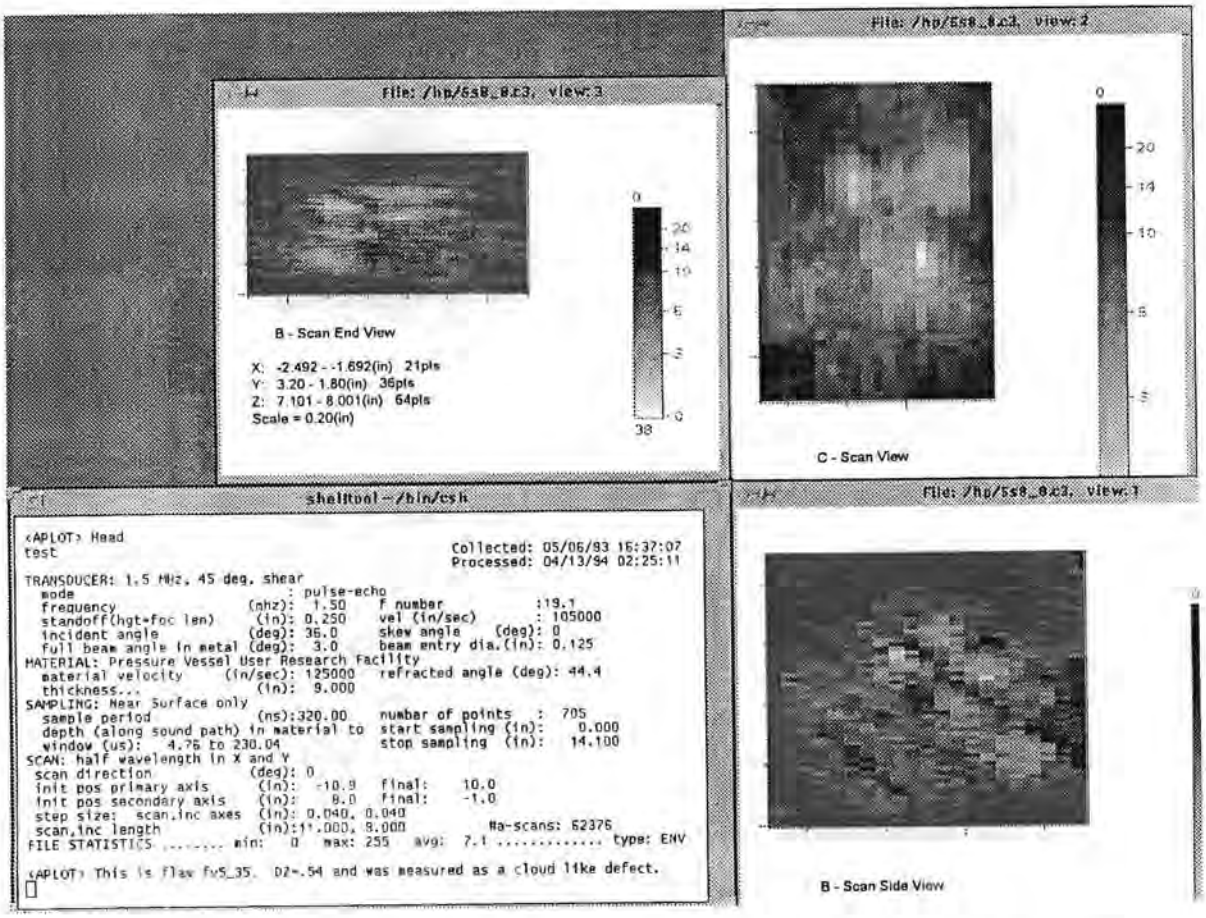

Figure A.101a - Planar indication #14 in the base metal below 25 mm: mode 8

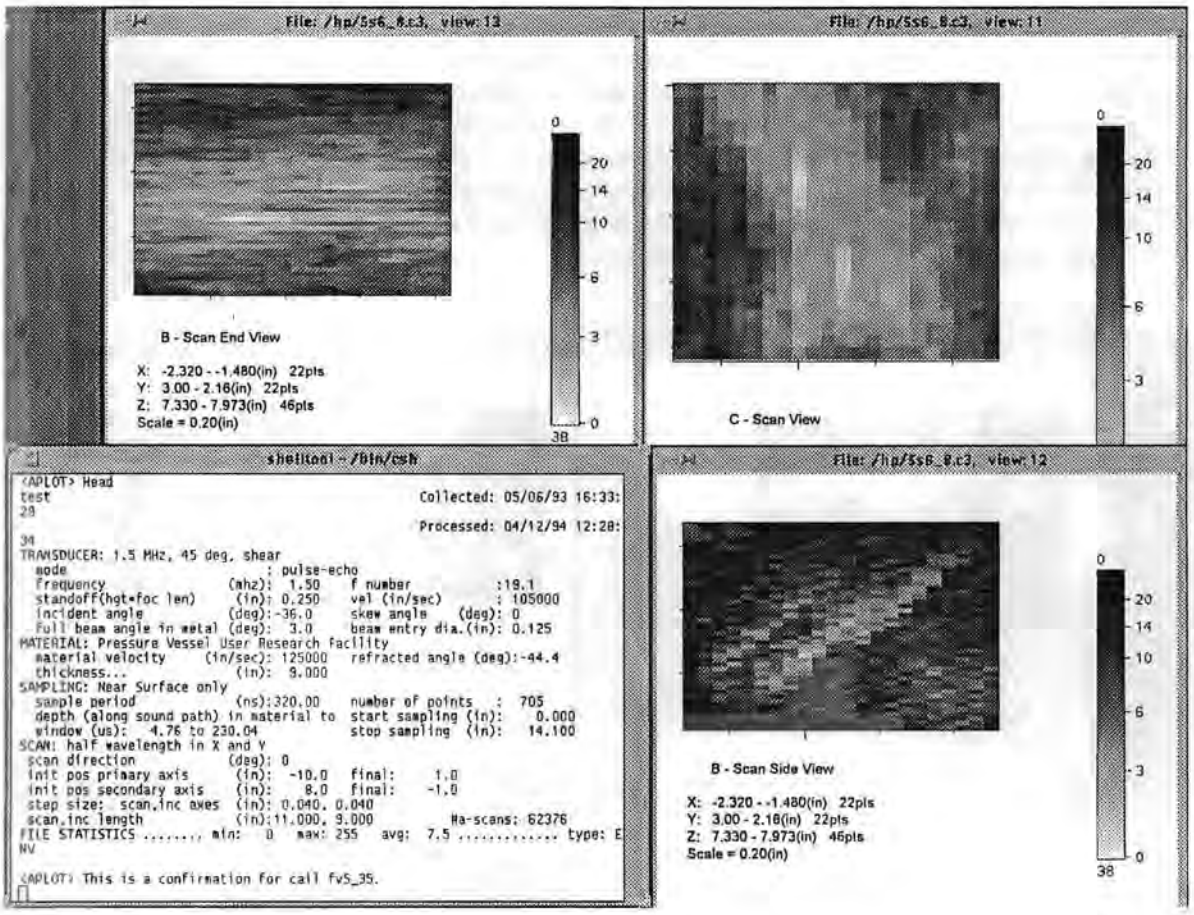

Figure A.101b - Planar indication #14 in the base metal below 25 mm: mode 6

Figure A.102 shows planar indication #15 in the base metal below 25 mm. Based on LOS in a cloud like pattern, this planar indication has a through-wall extent of 4 mm. The detection was made in mode 9 where the shape was cloud like in nature at a depth of 220 mm. The shape quality for this indication is good but broken up, implying that more than one small flaw may be present. There were no confirmations in other modes. The indication is characterized as planar based on lack of detection in normal beam or orthogonal modes. The width is 18 mm and was made to LOS in mode 9. The aspect ratio (width/depth) of this indication is 4. The maximum amplitude-to-noise ratio is of medium range at 25 to 7. The X coordinate of 90 mm shows that the indication is clearly in the base metal. The Z coordinate of 220 mm shows that the indication is in the near the outer wall of the of the vessel.

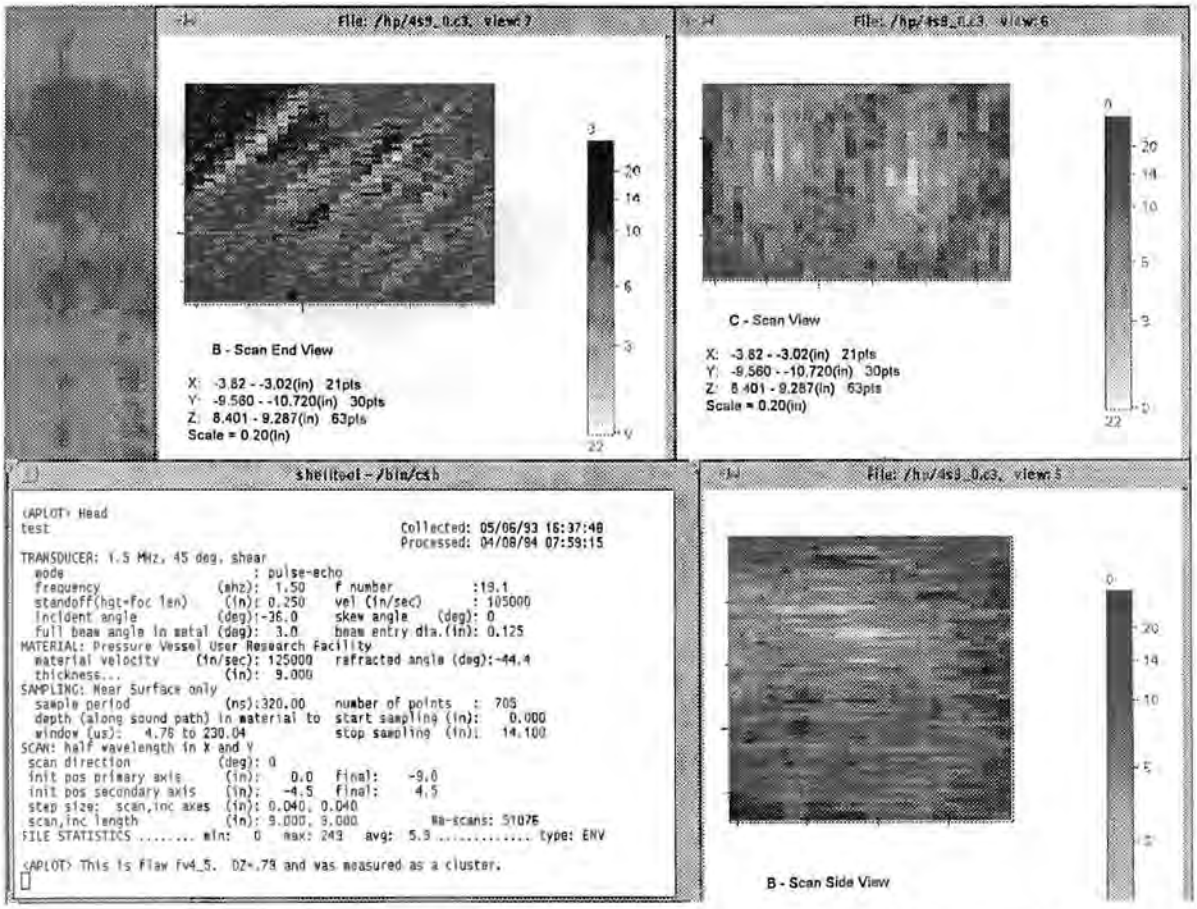

Figure A.102 - Planar indication #15 in the base metal below 25 mm: mode 9

Figure A.103 shows planar indication #16 in the base metal below 25 mm. Based on LOS in a cloud like pattern, this planar indication has a through-wall extent of 4 mm. The detection was made in mode 6 where the shape was cloud like in nature at a depth of 122 mm. The shape quality for this indication is good but broken up, implying that more than one small flaw may be present. There were no confirmations in other modes. The indication is characterized as planar based on lack of detection in normal beam or orthogonal modes. The length is 15 mm and was made to LOS in mode 6. The aspect ratio (length/depth) of this indication is 4. The maximum amplitude-to-noise ratio is of medium range at 52 to 14. The X coordinate of 36 mm shows that the indication is clearly in the base metal. The Z coordinate of 122 mm shows that the indication is in the middle third of the vessel.

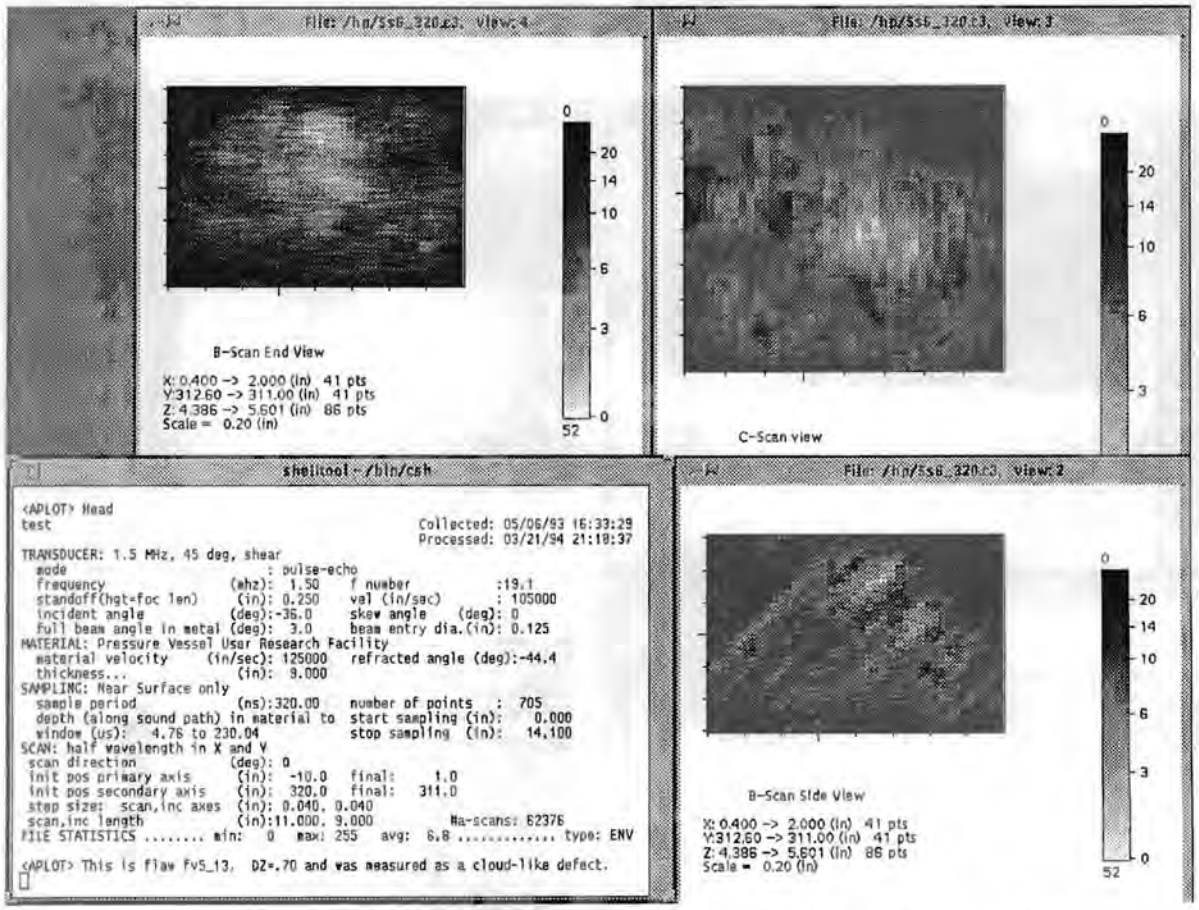

Figure A.103 - Planar indication #16 in the base metal below 25 mm: mode 6

Volumetric Indications in the Base Metal Below 25 mm

Figures A.104a-c show volumetric indication #1 in the base metal below 25 mm. Based on LOS in a cloud like pattern, this volumetric indication has a through-wall extent of 7 mm. The detection was made in modes 6 and 8. In mode 8 the shape was cloud like in nature at a depth of 108 mm. In mode 6 a through-wall extent estimate of 1 mm was obtained from a wave packet width. The shape quality is good for this indication. There was a confirmation in mode 10 at a depth of 115 mm. The two Z values of 108 to 115 mm give an alternate depth size of 7 mm. The indication is characterized as volumetric based on normal beam detection. The length is 19 mm and was made to LOS in mode 6. The width is 6 mm and was made to LOS in mode 10. The aspect ratio (length/depth) of this indication is 3. The maximum amplitude-to-noise ratio is high at 105 to 25. The X coordinate of 28 mm shows that the indication is in the base metal. The Z coordinate of 107 to 115 mm shows that the indication is in the middle third of the vessel.

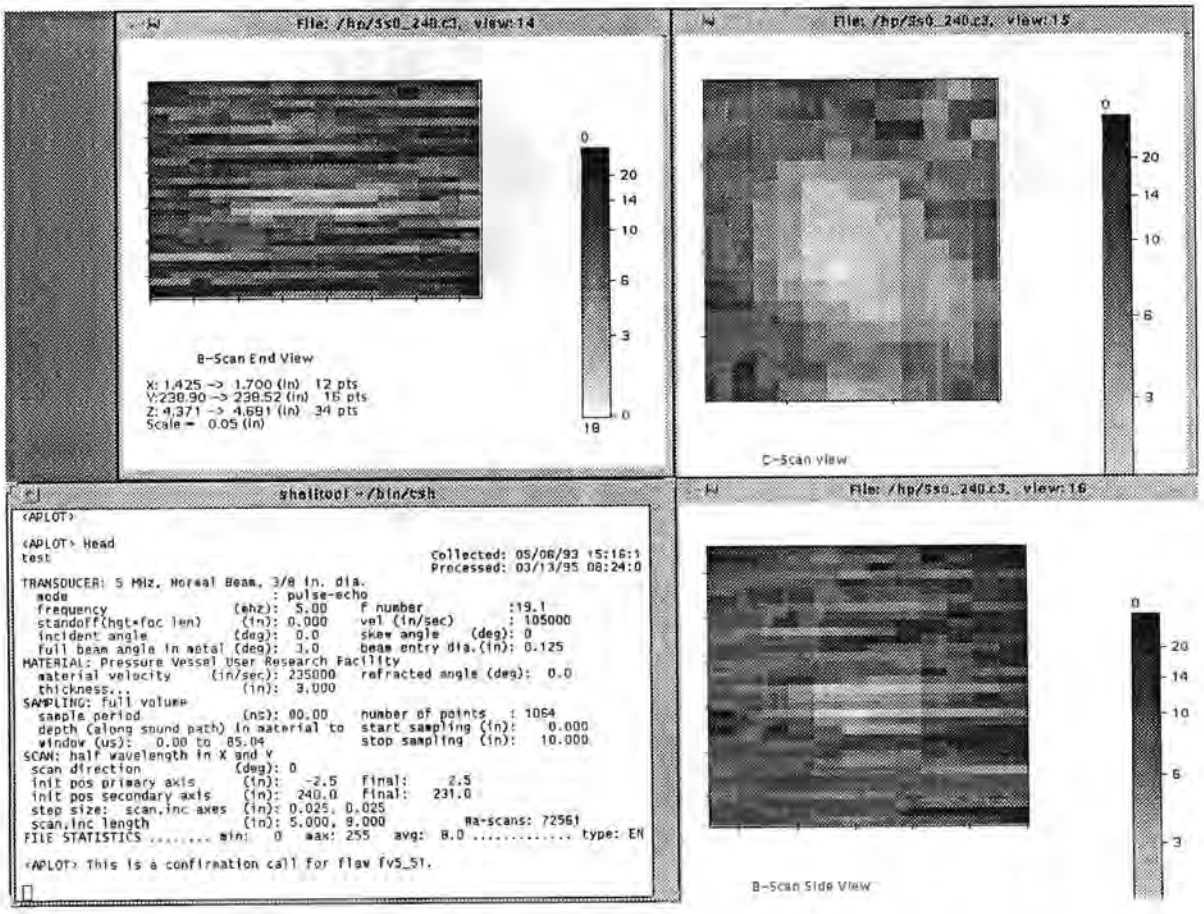

Figure A.104a - Volumetric indication #1 in the base metal below 25 mm: mode 10

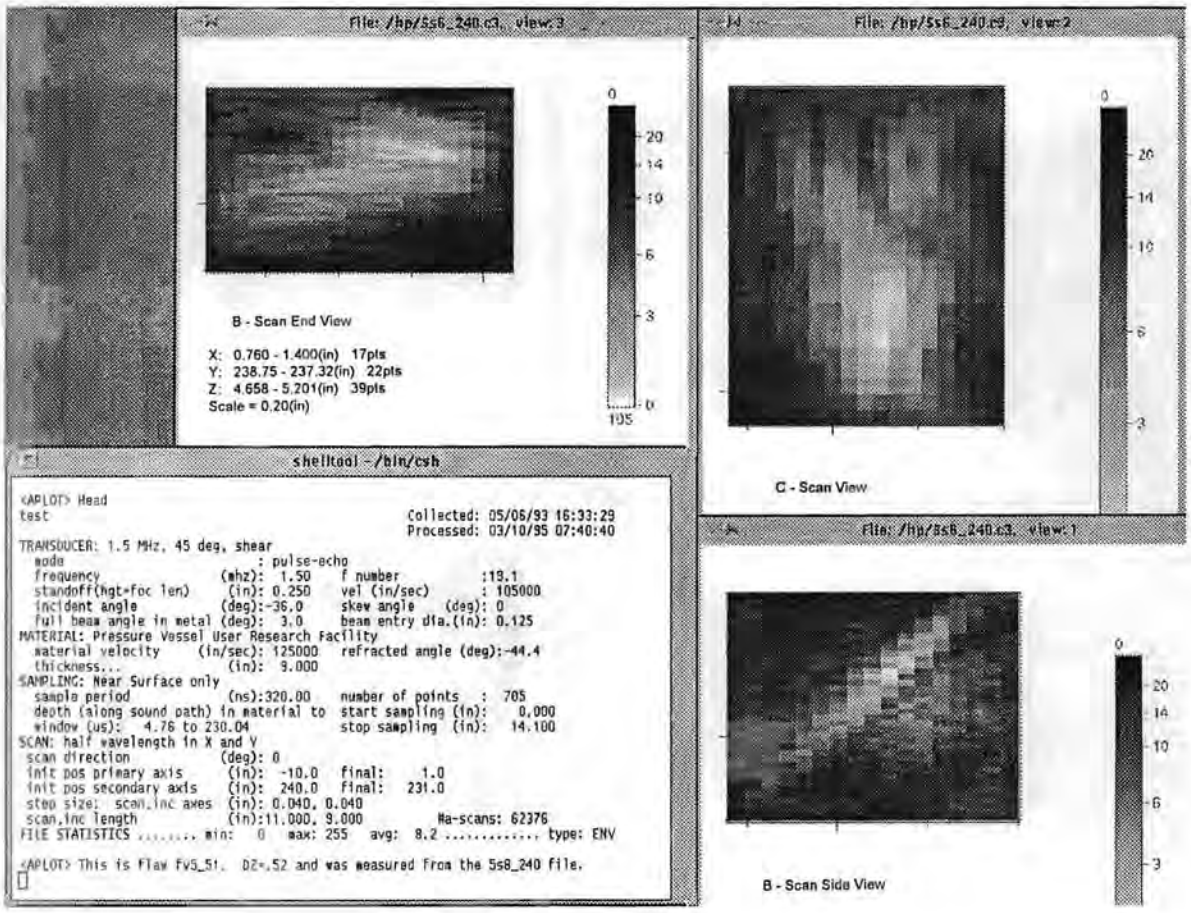

Figure A.104b - Volumetric indication #1 in the base metal below 25 mm: mode 6

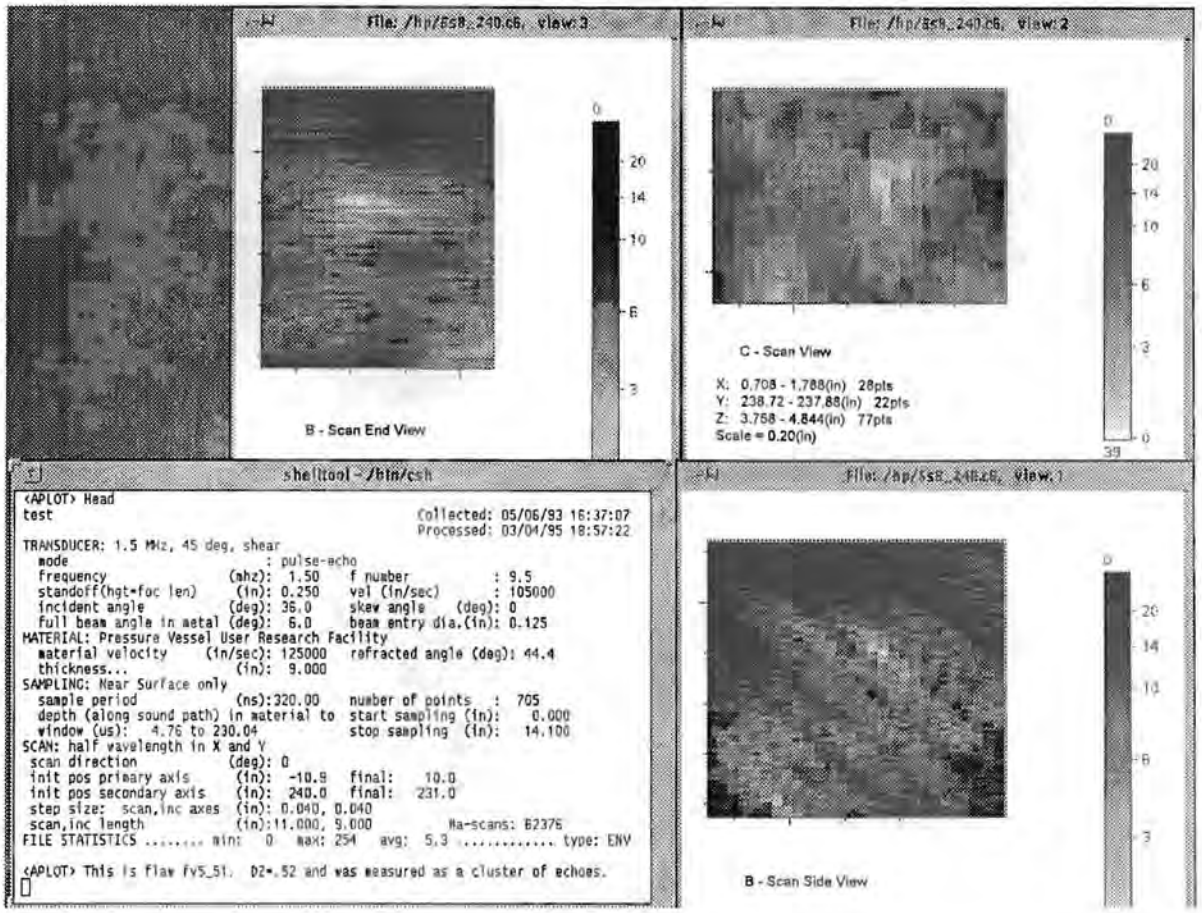

Figure A.104c - Volumetric indication #1 in the base metal below 25 mm: mode 8

Figures A.105a-c show volumetric indication #2 in the base metal below 25 mm. Based on wave packet width in mode 6, this volumetric indication has a through-wall extent of 5 mm. The detection was made in modes 6,7, and 10. In mode 6 it displayed TOF shape at a depth of 118 mm, while in mode 7 it displayed TOF shape at a depth of 113 mm and gave a through-wall extent of 3 mm based on wave packet width. The detection in mode found the indication at a depth of 117 mm. The different Z values of 113 to 118 mm give an alternate depth size of 5 mm. The indication is characterized as volumetric based on normal beam detection. The length is 19 mm and was made to LOS in mode 10. The width is 11 mm and was made to LOS in mode 10. The aspect ratio (length/depth) of this indication is 4 which tends to confirm the large through-wall extent. The maximum amplitude-to-noise ratio is high at 77 to 17. The X coordinate of 58 mm shows that the indication is clearly in the base metal. The Z coordinate of 113 to 118 mm shows that the indication is in the middle third of the vessel.

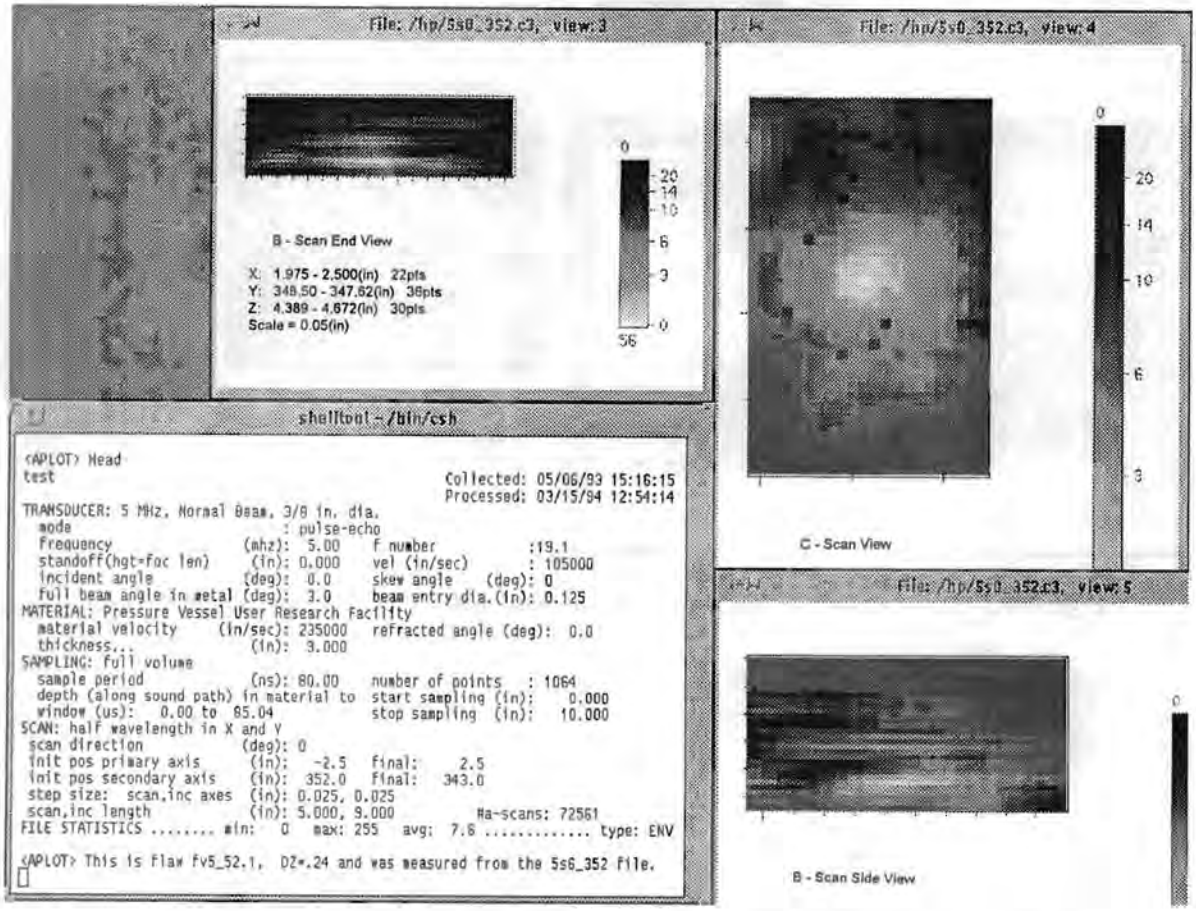

Figure A.105a - Volumetric indication #2 in the base metal below 25 mm: mode 10

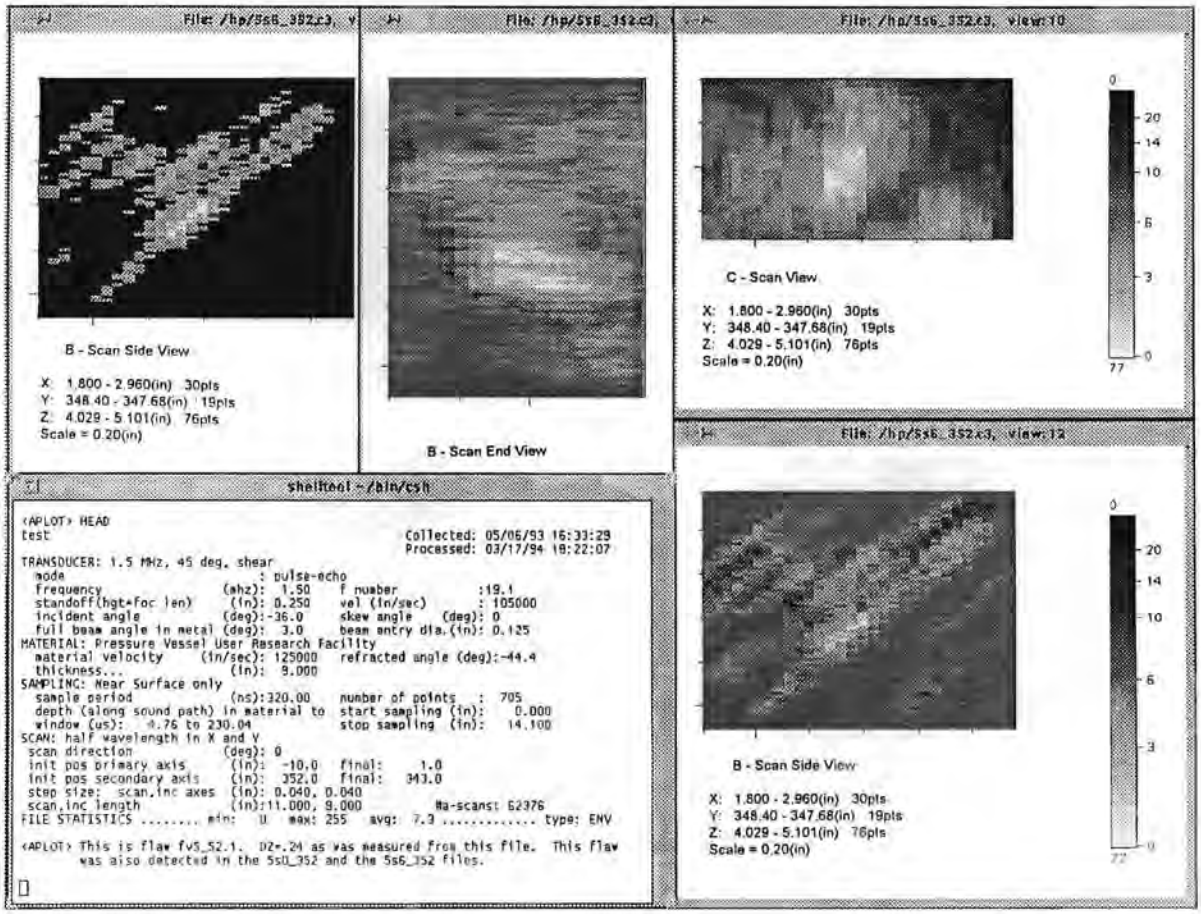

Figure A.105b - Volumetric indication #2 in the base metal below 25 mm: mode 6

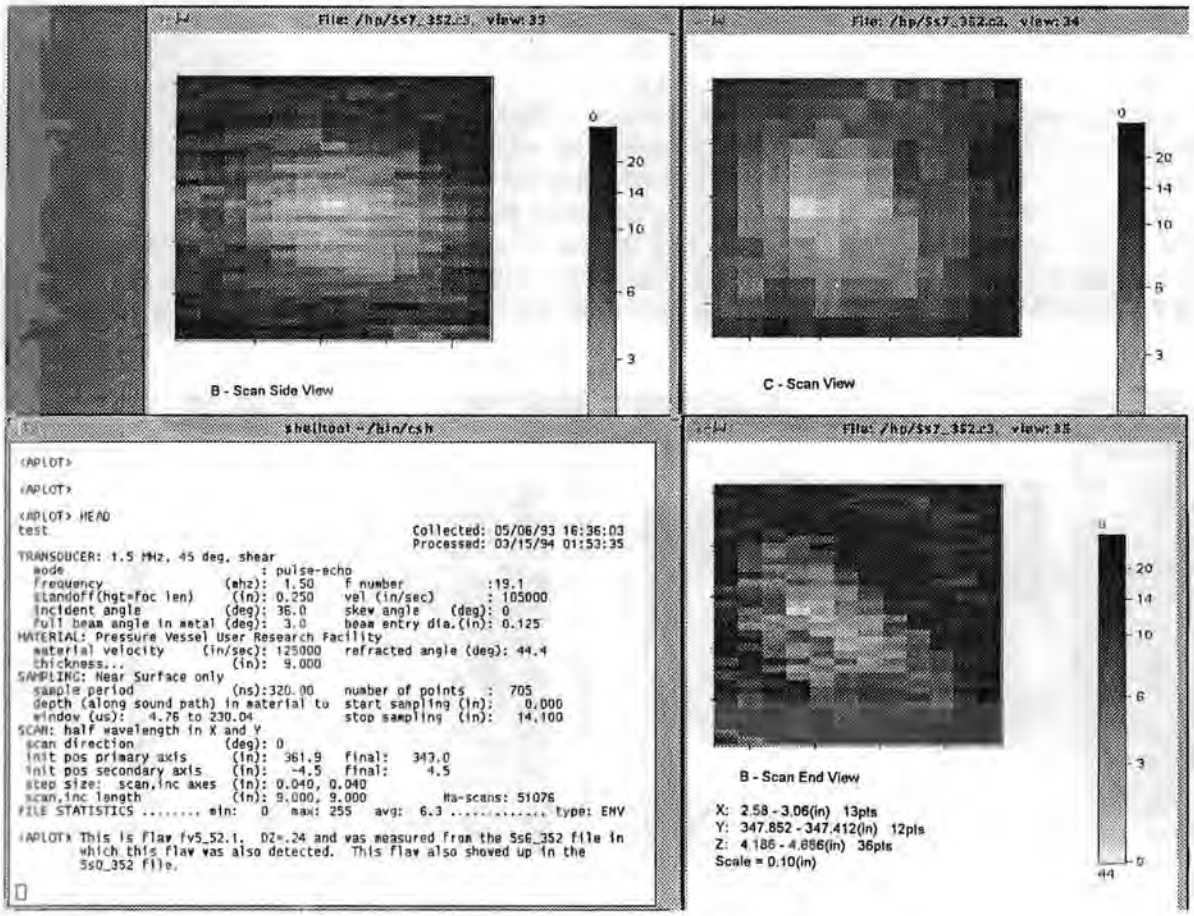


```
<APLOT>

<APLOT>

<APLOT> HEAD
test                                          Collected: 05/06/93 16:36:03
                                              Processed: 03/15/94 01:53:35
TRANSDUCER: 1.5 MHz, 45 deg, shear
  mode                    : pulse-echo
  frequency            (mhz):  1.50    f number          :19.1
  standoff(hgt=foc len)  (in): 0.250    vel (in/sec)      : 105000
  incident angle       (deg): 36.0      skew angle    (deg): 0
  full beam angle in metal (deg):  3.0  beam entry dia.(in): 0.125
MATERIAL: Pressure Vessel User Research Facility
  material velocity     (in/sec): 125000   refracted angle (deg): 44.4
  thickness...             (in):  9.000
SAMPLING: Near Surface only
  sample period          (ns):320.00    number of points   :  705
  depth (along sound path) in material to  start sampling (in):    0.000
  window (us):   4.76 to 230.04          stop sampling  (in):   14.100
SCAN: half wavelength in X and Y
 scan direction          (deg): 0
 init pos primary axis    (in):  361.9   final:   343.0
 init pos secondary axis  (in):   -4.5   final:     4.5
 step size:  scan,inc axes  (in): 0.040, 0.040
 scan,inc length          (in): 9.000, 9.000          #a-scans: 51076
FILE STATISTICS ..... min:   0   max: 255   avg:  6.3 ..... type: ENV

<APLOT> This is flaw fv5_52.1.  D2=.24 and was measured from the 5s6_352 file in
        which this flaw was also detected.  This flaw also showed up in the
        5s0_352 file.
```

Figure A.105c - Volumetric indication #2 in the base metal below 25 mm: mode 7

Figures A.106a-e show volumetric indication #3 in the base metal below 25 mm. This volumetric indication has a through-wall extent of 5 mm based on wave packet width. The detection was made in mode 8 where it had isolated TOF shape at a depth of 91 mm. More than one TOF shape was present. The shape quality for this indication is good but broken up, implying that more than one small flaw may be present. There were confirmations in modes 6,7,9, and 10 at depths of 86 to 96 mm. The confirmation modes gave a through-wall extent estimate of 3 to 4 mm based on wave packet width. The different Z values of 86 to 96 mm give an alternate depth size of 10 mm. The indication is characterized as volumetric based on normal beam detection and detection in orthogonal modes. The length is 12 mm and was made to LOS in mode 6. The width is 48 mm and was made to LOS in mode 9. The aspect ratio (width/depth) of this indication is 10. The maximum amplitude-to-noise ratio is of medium range at 35 to 10. The X coordinate of 56 mm shows that the indication is clearly in the base metal. The Z coordinate of 86 to 96 mm shows that the indication is in the middle third of the vessel.

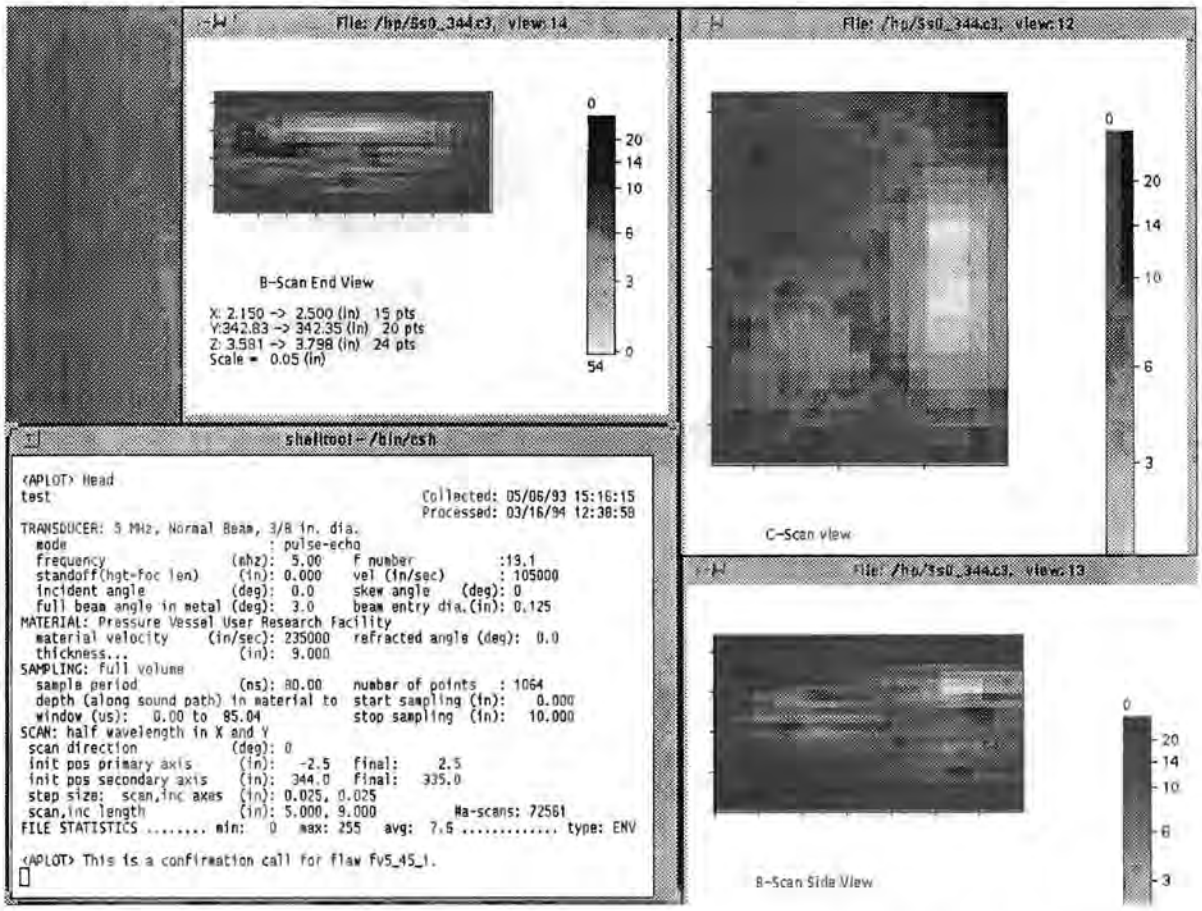

Figure A.106a - Volumetric indication #3 in the base metal below 25 mm: mode 10

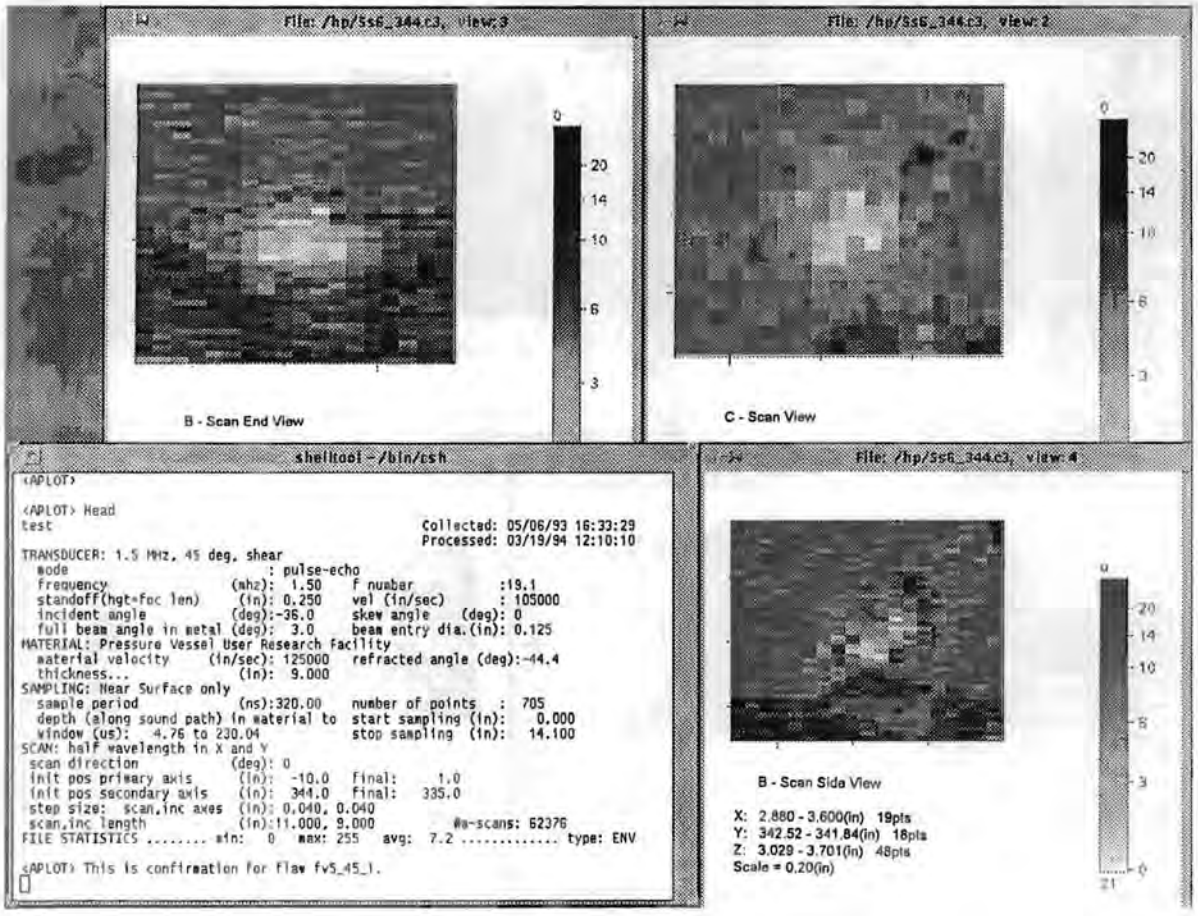

Figure A.106b - Volumetric indication #3 in the base metal below 25 mm: mode 6

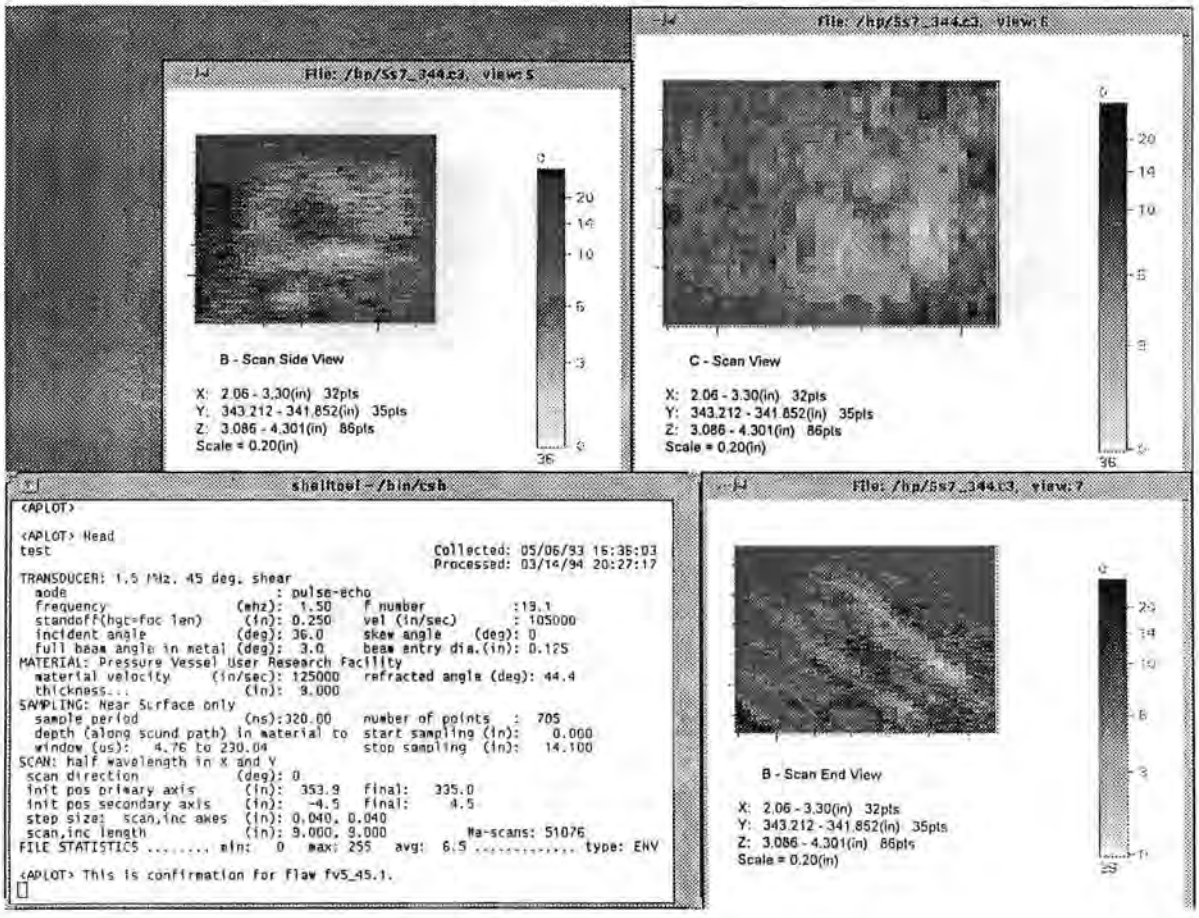

Figure A.106c - Volumetric indication #3 in the base metal below 25 mm: mode 7

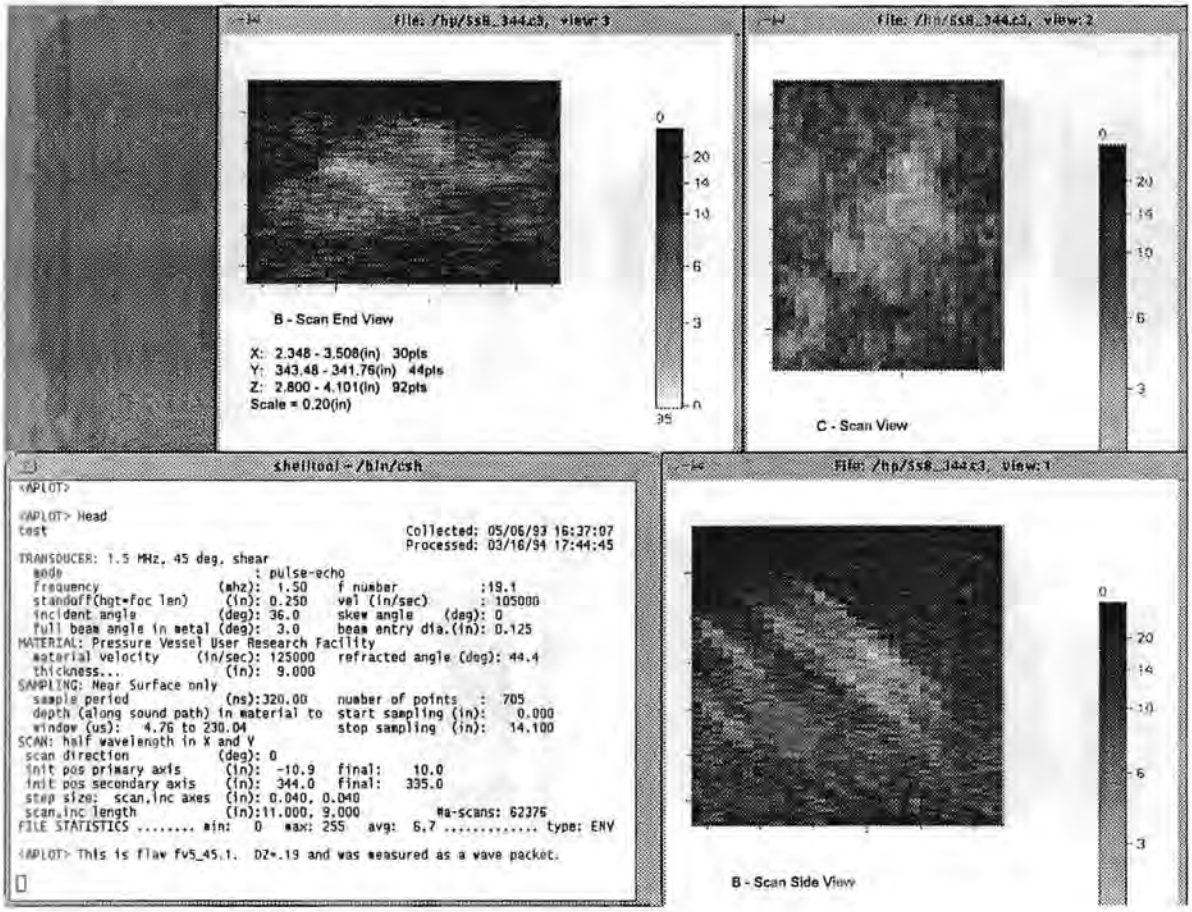

Figure A.106d - Volumetric indication #3 in the base metal below 25 mm: mode 8

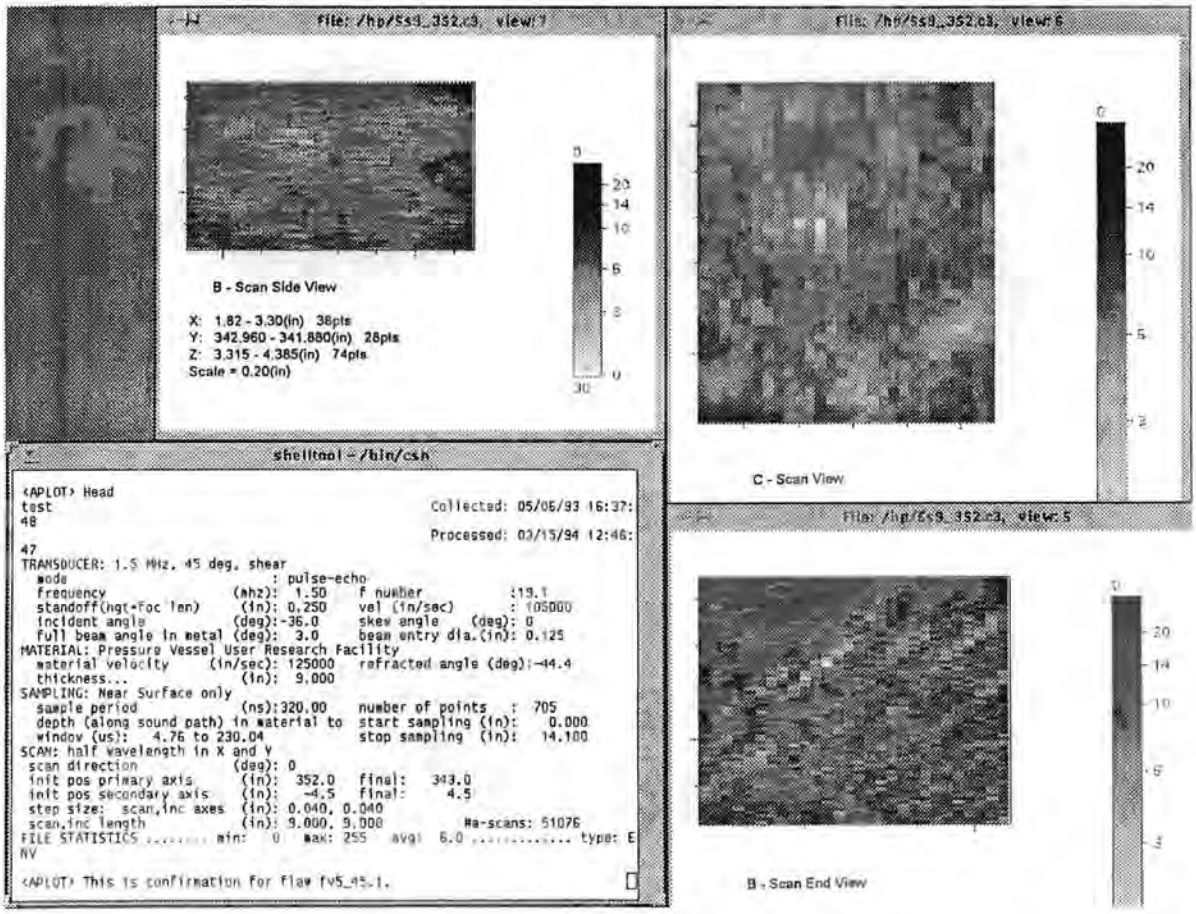

Figure A.106e - Volumetric indication #3 in the base metal below 25 mm: mode 9

Figure A.107 shows volumetric indication #4 in the base metal below 25 mm. This volumetric indication has a through-wall extent of 5 mm based on ring around pattern. The detection was made in mode 7 where it displayed a pair of TOF shapes at a depth of 106 mm. The shape quality is good for this indication. There were no confirmations in other modes. The indication is characterized as volumetric based on the detection of ring around shape. The width is 9 mm and was made to LOS in mode 7. The aspect ratio (width/depth) of this indication is 1.8. The maximum amplitude-to-noise ratio is high at 35 to 8. The X coordinate of 108 mm shows that the indication is clearly in the base metal. The Z coordinate of 106 mm shows that the indication is in the middle third of the vessel.

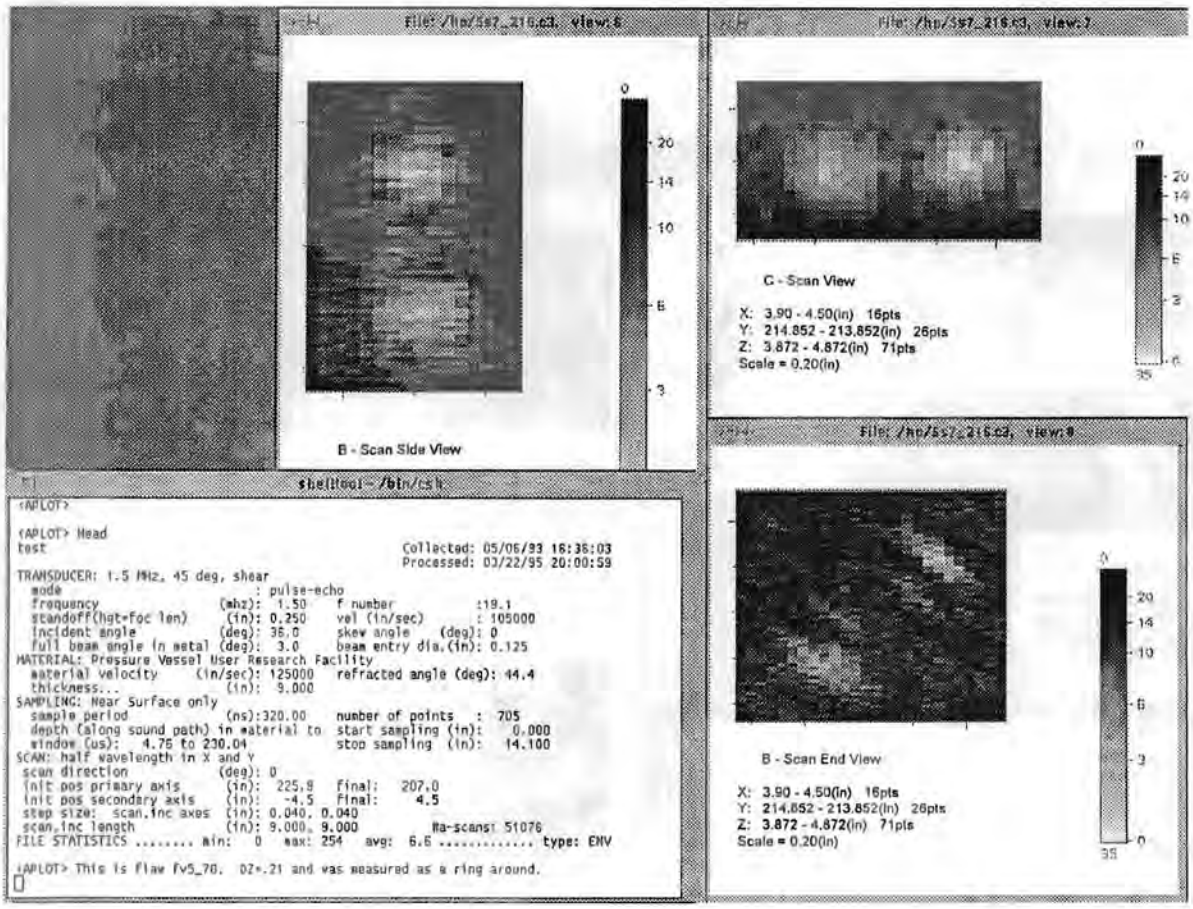

Figure A.107 - Volumetric indication #4 in the base metal below 25 mm: mode 7

Figures A.108a-b show volumetric indication #5 in the base metal below 25 mm. This volumetric indication has a through-wall extent of 5 mm based on wave packet width. The detection was made in mode 6 where it had isolated TOF shape at a depth of 85 mm. The shape quality is good for this indication. There were confirmations in modes 7 and 8 at depths of 81 and 82 mm. The confirmation mode gave a through-wall extent estimate of 1 mm based on wave packet width and 4 mm based on ring around pattern. The different Z values of 81 to 85 mm give an alternate depth size of 4 mm. The indication is characterized as volumetric based on detection in orthogonal modes and the detection of ring around shape. The length is 28 mm and was made to LOS in mode 6. The width is 14 mm and was made to LOS in mode 7. The range of aspect ratios (length/depth) of this indication is 6 to 7 which tends to confirm the large through-wall extent. The maximum amplitude-to-noise ratio is high at 63 to 13. The X coordinate of 29 mm shows that the indication is in the base metal, possibly in the HAZ. The Z coordinate of 81 to 85 mm shows that the indication is in the middle third of the vessel.

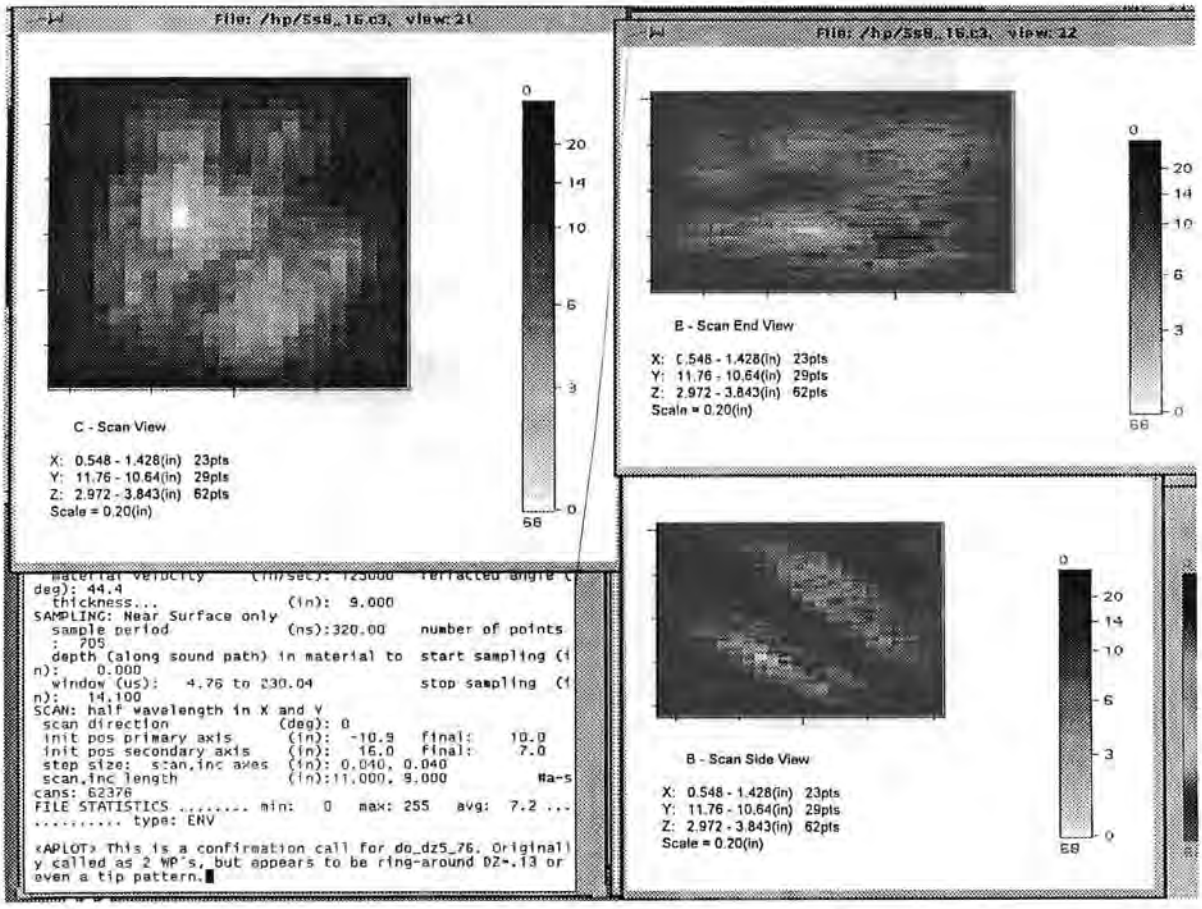

Figure A.108a - Volumetric indication #5 in the base metal below 25 mm: mode 8

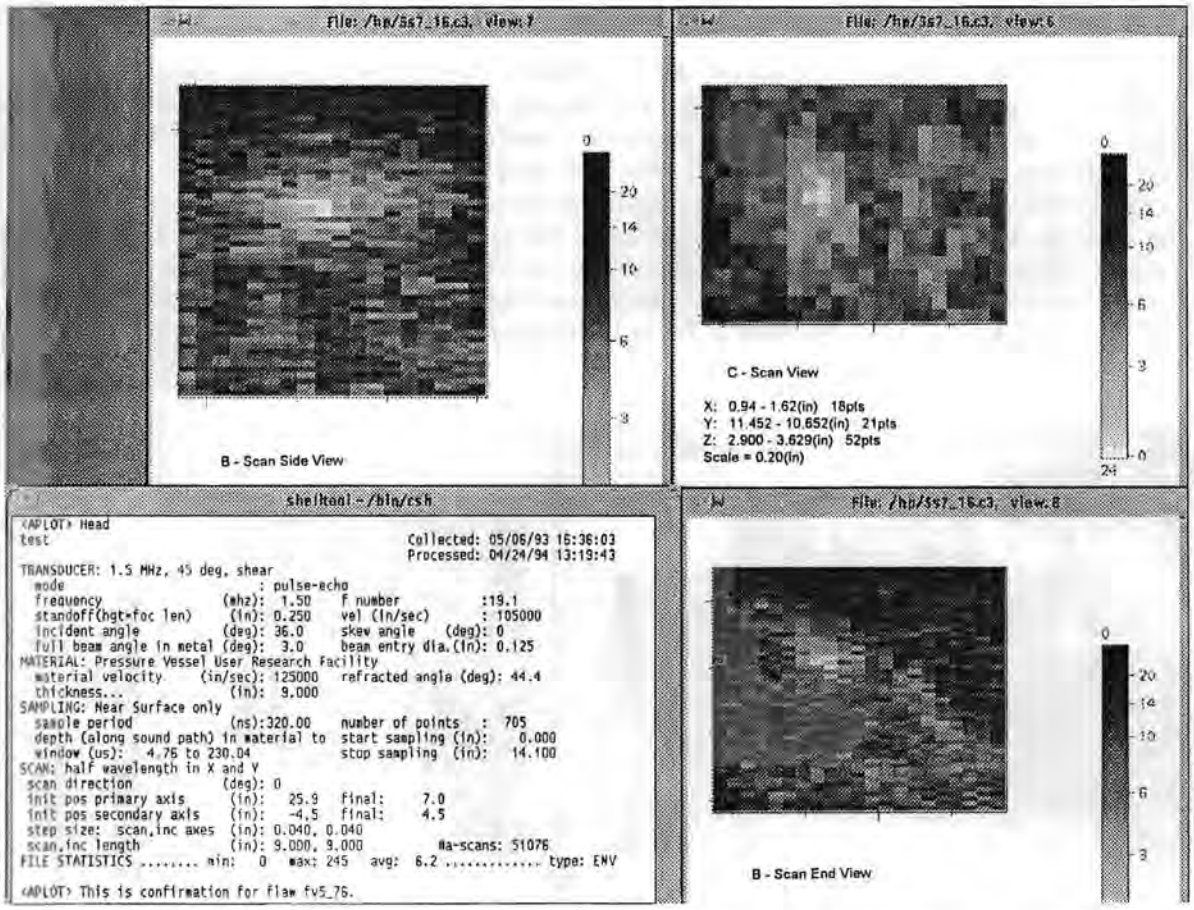

-Figure A.108b - Volumetric indication #5 in the base metal below 25 mm: mode 7

Figures A.109a-b show volumetric indication #6 in the base metal below 25 mm. This volumetric indication has a through-wall extent of 5 mm based on wave packet width. The detection was made in mode 6 where it had isolated TOF shape at a depth of 130 mm. The shape quality for this indication is good but broken up, implying that more than one small flaw may be present. There was a confirmation in mode 10 at a depth of 128 mm. The two Z values of 128 to 130 mm give an alternate depth size of 2 mm. The indication is characterized as volumetric based on normal beam detection. The length is 20 mm and was made to LOS in mode 6. The width is 9 mm and was made to LOS in mode 10. The aspect ratio (length/depth) of this indication is 4 which tends to confirm the large through-wall extent. The maximum amplitude-to-noise ratio is of medium range at 86 to 24. The X coordinate of 31 mm shows that the indication is in the base metal, possibly in the HAZ. The Z coordinate of 128 to 130 mm shows that the indication is in the middle third of the vessel.

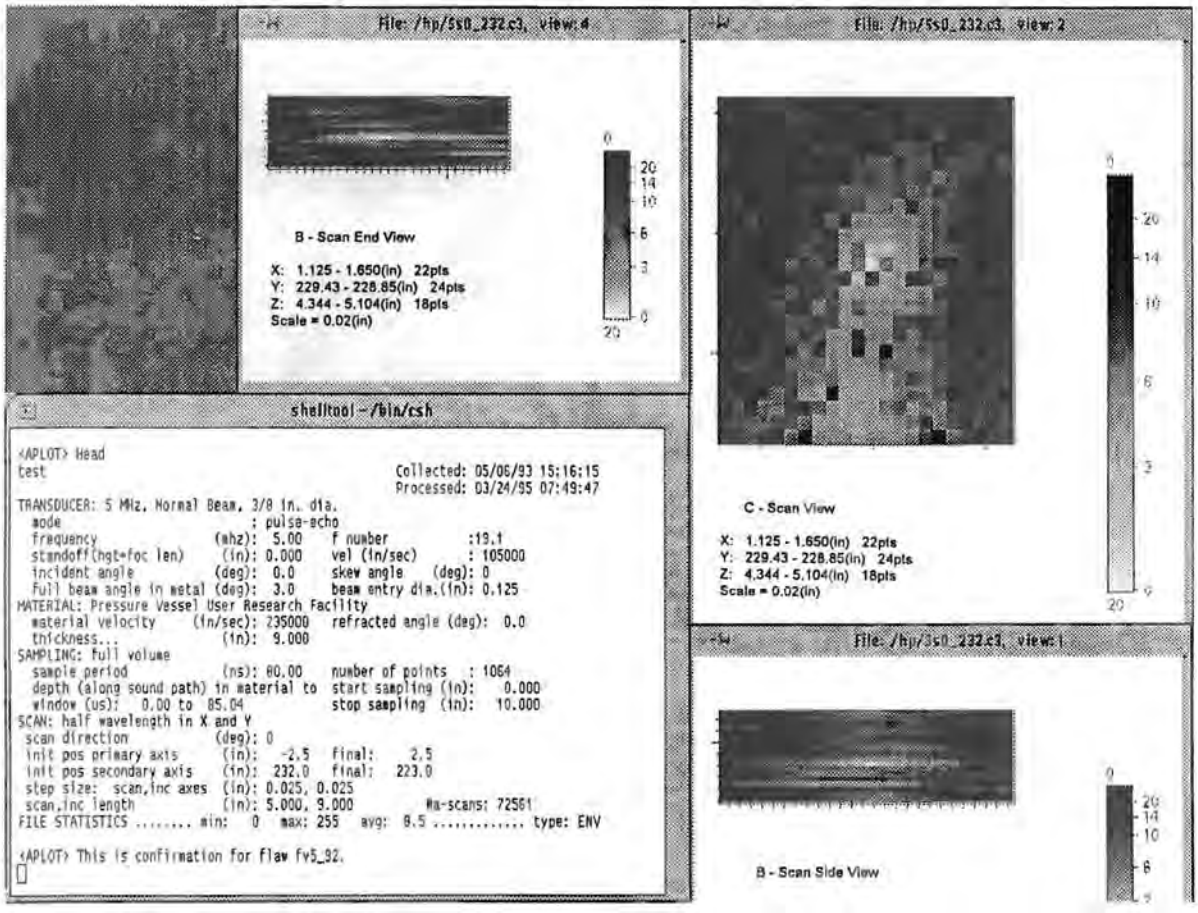

Figure A.109a - Volumetric indication #6 in the base metal below 25 mm: mode 10

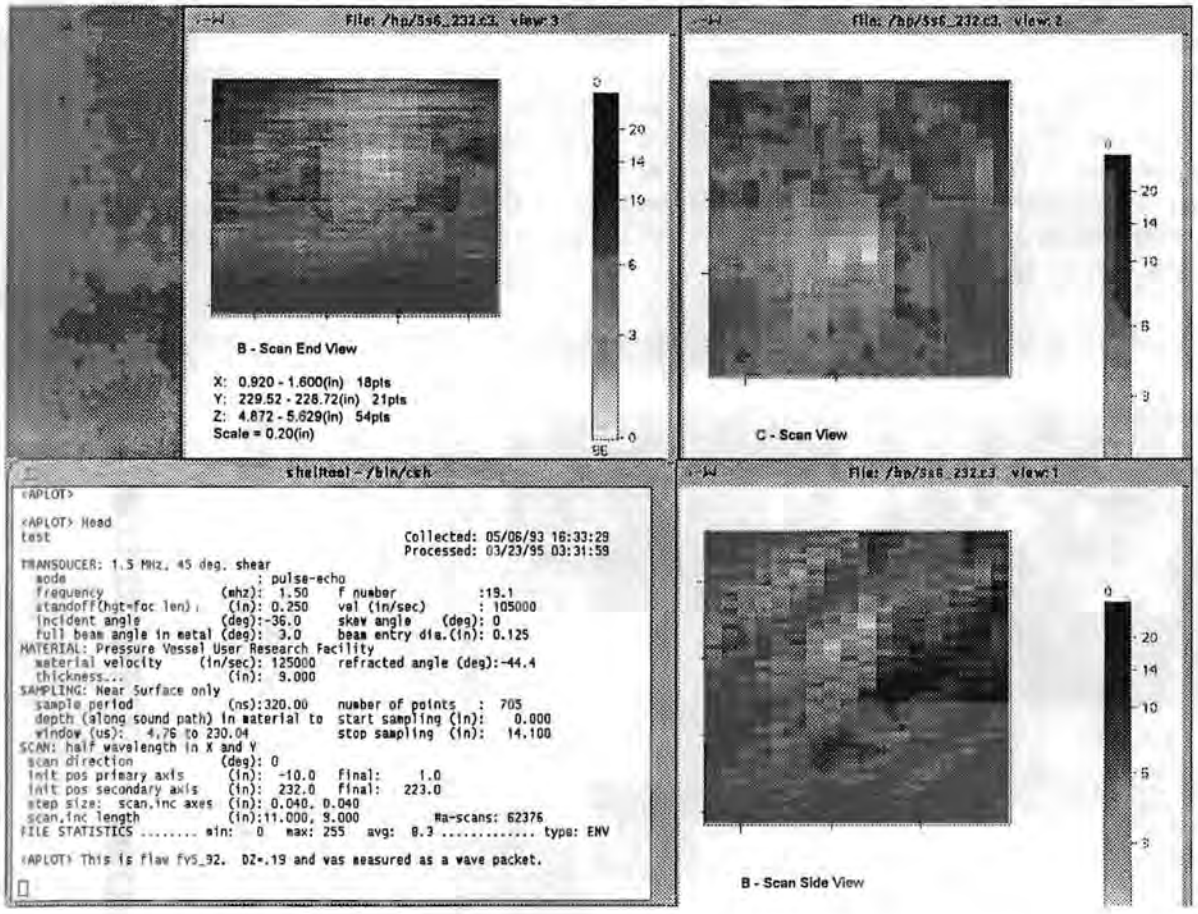

Figure A.109b - Volumetric indication #6 in the base metal below 25 mm: mode 6

Figures A.110a-b show volumetric indication #7 in the base metal below 25 mm. This volumetric indication has a through-wall extent of 5 mm based on ring around pattern. The detection was made in mode 6 where it displayed a pair of TOF shapes at a depth of 103 mm. The shape quality is good for this indication. There was a confirmation in mode 8 at depth of 104 mm. The confirmation mode gave a through-wall extent estimate of 2.5 mm based on wave packet width. The two Z values of 103 to 104 mm give an alternate depth size of 1 mm. The indication is characterized as volumetric based on the detection of ring around shape. The length is 46 mm and was made to LOS in mode 6. The aspect ratio (length/depth) of this indication is 9. The maximum amplitude-to-noise ratio is low at 13 to 6. The X coordinate of 48 mm shows that the indication is clearly in the base metal. The Z coordinate of 103 to 104 mm shows that the indication is in the middle third of the vessel.

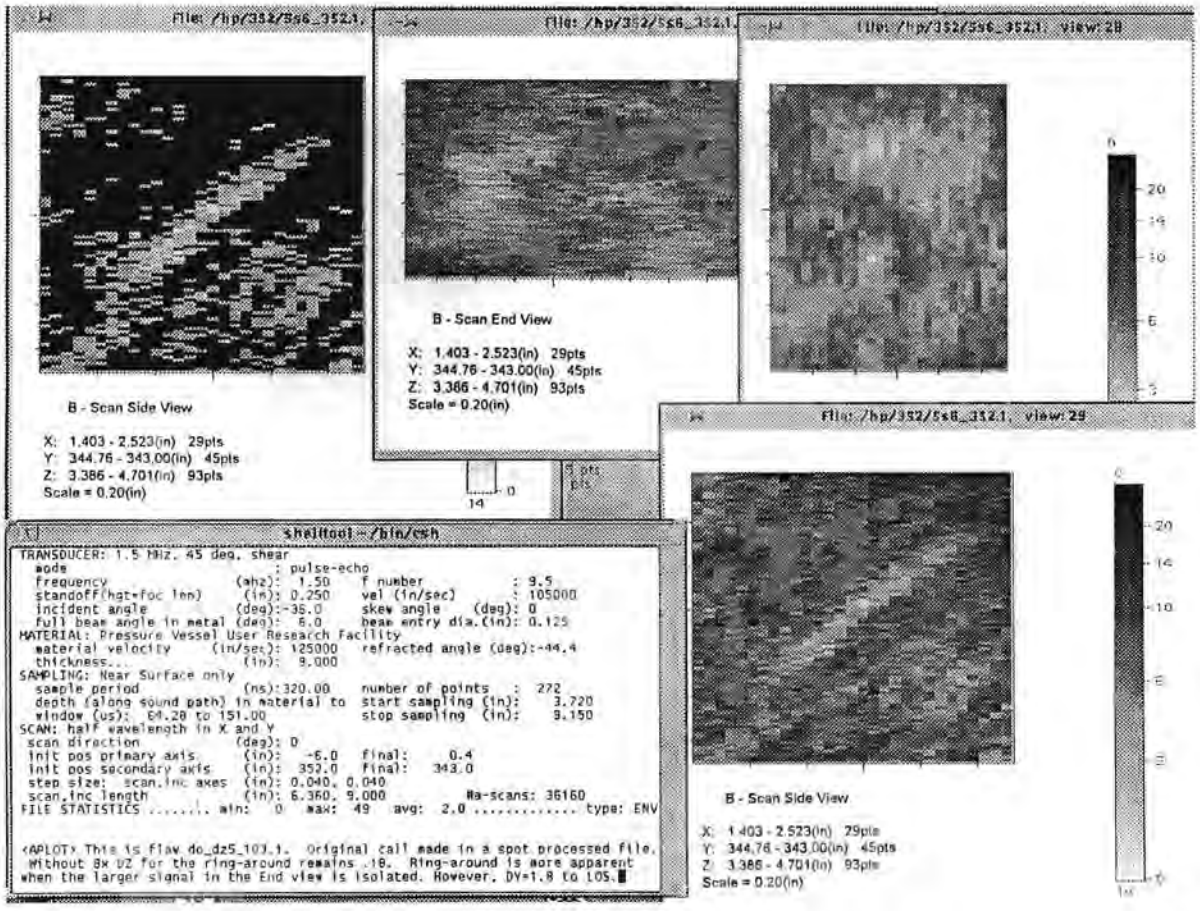

Figure A.110a - Volumetric indication #7 in the base metal below 25 mm: mode 6

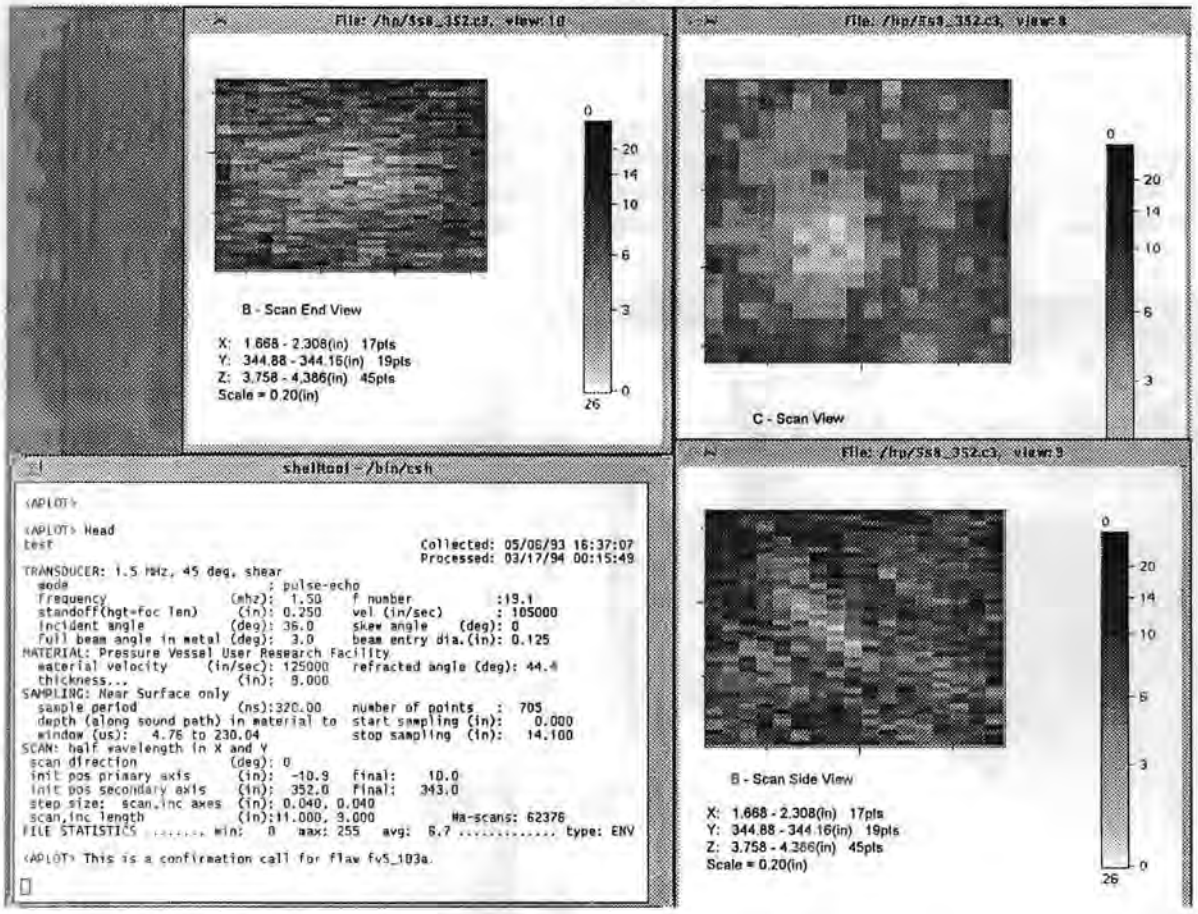

Figure A.110b - Volumetric indication #7 in the base metal below 25 mm: mode 8

Figure A.111 shows volumetric indication #8 in the base metal below 25 mm. This volumetric indication has a through-wall extent of 4 mm based on ring around pattern. The detection was made in mode 6 where it displayed a pair of TOF shapes at a depth of 119 mm. The shape quality for this indication is good but broken up, implying that more than one small flaw may be present. There were no confirmations in other modes. The indication is characterized as volumetric based on the detection of ring around shape. The length is 41 mm and was made to LOS in mode 6. The aspect ratio (length/depth) of this indication is 10 which tends to confirm the large through-wall extent. The maximum amplitude-to-noise ratio is of medium range at 79 to 24. The X coordinate of 26 mm shows that the indication is in the base metal, possibly in the HAZ. The Z coordinate of 119 mm shows that the indication is in the middle third of the vessel.

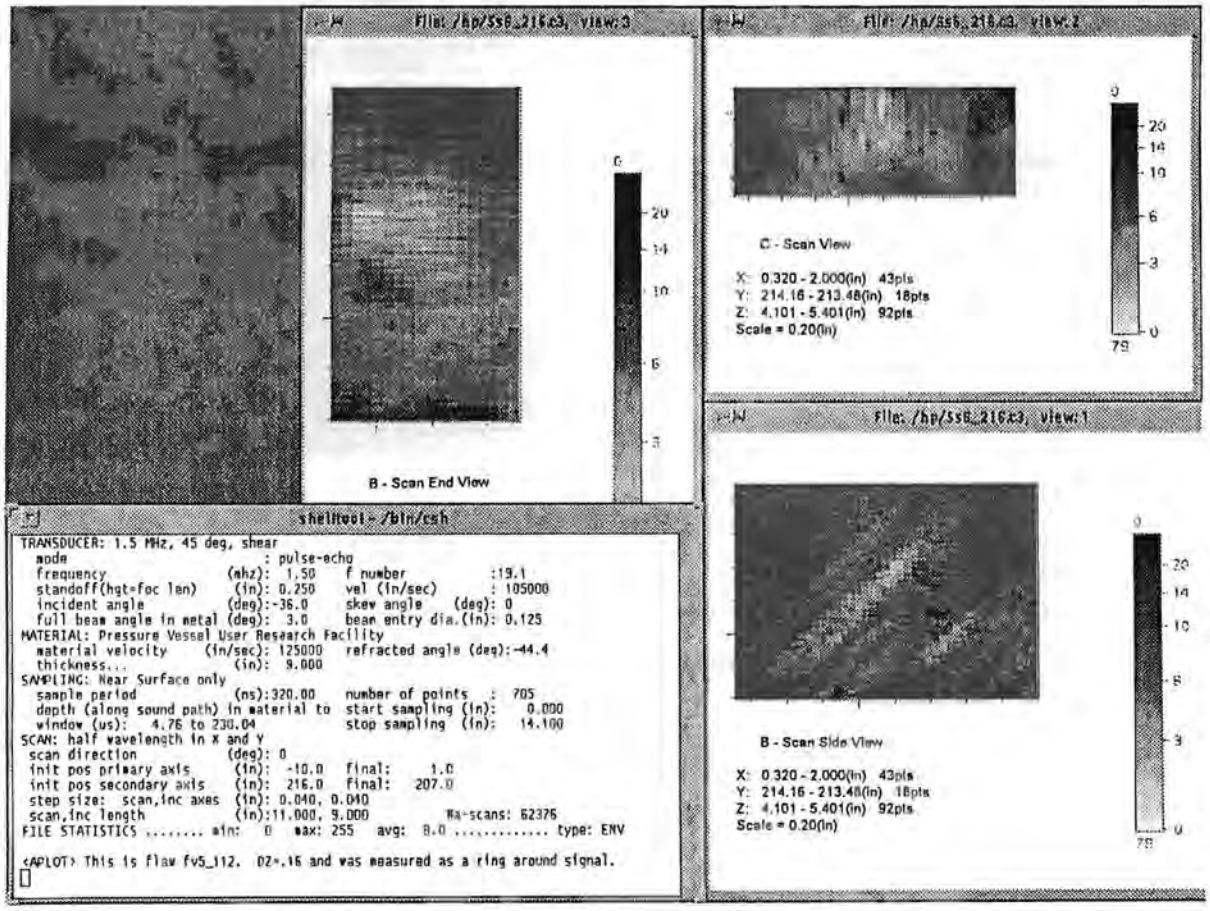

Figure A.111 - Volumetric indication #8 in the base metal below 25 mm: mode 6

Appendix B

Inspections of the Midland Vessel

Appendix B

Inspections of the Midland Vessel

This appendix contains the results of a nondestructive examination of nuclear reactor vessel weldment for the presence of fabrication defects. Sections of material, approximately 1219 mm (4 ft.) in length, were cut from an unused nuclear reactor vessel, the Midland Vessel, by Babcock and Wilcox (Booth 1998) and sent to the EPRI NDE Center. PNNL conducted a sequence of ispections using the Synthetic Aperture Focusing Technique for Ultrasonic Testing (SAFT-UT) on this vessel material under the sponsorship of the U.S. Nuclear Regulatory Commission for the purpose of detecting and characterizing the fabrication (preservice) defects. The results of these SAFT-UT inspections are the subject of this report.

Among the principle findings of this analysis is that the SAFT-UT data correlates with a destructive analysis of one block of the material. The results of this correlation demonstrate that the majority of the destructively analyzed flaws are ready apparent in the SAFT-UT data. The SAFT-UT inspections of approximately 1000 square inches of clad surface area show eight total defects at the clad to base metal interface. All of the eight defects are less than 2.2 mm in through-wall extent and in the range of 2 to 15 mm in lateral extent. In 164 linear inches of weld, 23 total defects were found in the weldment, heat-affected zone, and base metal. Of these 23 defects, 17 had a through-wall extent of 2 mm or less. The remaining 6 defects had a through-wall extent in the range of 5 to 18 mm. The lateral extent of the 23 base-metal defects was in the range of 5 to 36 mm. The size distribution of flaws as measured by SAFT-UT in the Midland blocks is estimated to be not measurably different in shape from that of the Marshall distribution; however, the overall density of flaws is estimated to be substantially larger than that of the Marshall distribution.

Recommendations are given in this appendix for gaining additional resolving power using SAFT-UT. The frequencies of transducers, scanning step sizes, and requisite data volumes for examining vessel material for fabrication defects are discussed. The use of material coordinates for inspection systems is recommended for efficiency in analysis and protecting the quality of the data.

Appendix B provides the reader with an understanding of the vessel material that was inspected and the kinds of inspections that were performed by SAFT-UT. A correlation of the SAFT-UT indications that were found in the data with a destructive analysis of a fraction of the material is also given. Finally, the detection methods, the sizes and types of the defects, and the distribution of those defects in important categories are documented in this Appendix.

1.0 Introduction

This report is part of a program, sponsored by the U.S. Nuclear Regulatory Commission (NRC), to develop a technical data base for fabrication flaws that exist in nuclear reactor pressure vessels (RPV). In this program, samples of RPV material are examined to detect and characterize the flaws introduced into the material when it was fabricated. The obtained flaw data can then be used to estimate rates of occurrences in a portion of the reactor population.

During the month of June 1989, the Midland blocks, consisting of material removed from the beltline region of the Midland reactor pressure vessel were examined using the Synthetic Aperture Focusing Technique for Ultrasonic Testing (SAFT-UT) developed by PNNL under sponsorship of the U.S. NRC. The SAFT-UT system provides very high-resolution images for use in reliably detecting flaws and accurately sizing the flaws detected. The SAFT-UT system was taken to the Electric Power Research Institute (EPRI) NDE Center in Charlotte, North Carolina, where the Midland blocks were sent after being cut from the reactor pressure vessel. Ultrasonic and radiographic test were performed by NDE Center staff and SAFT-UT examinations were performed by PNNL staff. The purpose of the SAFT-UT inspections was to obtain information on the population of fabrication flaws in the Midland vessel.

Data from a destructive analysis of a portion of the vessel material, obtained from the EPRI NDE Center, has been correlated with the SAFT-UT data. The destructively analyzed flaws have been used to confirm the sizing accuracy and adjust the detection and characterization method. The adjusted characterization method has been applied to all of the indications in the SAFT-UT data and a complete set of images are provided in the report. The distribution of flaws in important categories is provided in the report.

This report contains a description of the Midland blocks. The physical characteristics of the blocks, including the thickness of the cladding, are reported in Section 2. The details of the SAFT-UT inspections are given in Section 3. This section contains a description of what portion of each Midland block was inspected. It contains a specification for the transducers used. Section 4 contains the correlation of the SAFT-UT data with a destructive analysis of one of the Midland blocks. This section contains a description of the detection and sizing methods for SAFT-UT indications as supported by the destructive analysis. Section 5 contains a complete analysis of the indications of the fabrication defects found by SAFT-UT in the Midland blocks. The images of the indications are included in this section. Section 5 should be skipped by those who are not interested in the specifics of the SAFT-UT images. Section 6 contains the distribution of the fabrication flaws in important categories, and Section 7 describes the recommendations for use of SAFT-UT to conduct inspections of reactor pressure vessel material.

2.0 Description of Midland Blocks

Information obtained from Babcock and Wilcox indicated that this vessel was manufactured by piercing a large ingot of steel and then rolling it until a ring of the proper shape and size was obtained. The cladding was deposited using a multi-wire (either 3 or 6) process and then it was smoothed with a belt grinder. The cladding is nominally 6 mm (1/4-in.) thick with a minimum thickness of 4.8 mm (3/16 in.).

The blocks were nominally 224 mm (8.8 in.) thick and 762 mm (30 in.) wide. Block lengths varied but were about 1219 mm (48 in.) long. The reactor pressure vessel (RPV) circumferential weldment was centered in the blocks. Three of the blocks inspected by SAFT-UT were cut down in size so that they were only 305 mm (12 in.) wide, in preparation for subsequent machining into mechanical test specimens. The location, type, orientation, and size of all of the detected flaws were to be estimated. This information would provide guidance for machining the mechanical test specimens in order to avoid unintentionally including flawed material in the study of the mechanical properties of non-degraded and intentionally degraded reactor vessel material.

Blocks were removed from three circumferential welds as shown in Figure 2.1. The blocks were numbered with the weld number (1, 2, or 3) and then with the order of removal in the sequence as show in the figure. Block 1-8 is then the eighth block removed from weld number 1. Weld #1, sometimes referred to as the beltline weld, is the weld between the lower shell course and the intermediate shell course of the vessel.

A coordinate system was established for each of the blocks and fiducial marks were placed on the blocks for use in the NDE. The weld center line was marked and the distance along the weld was measured as either plus or minus a distance from a fiducial mark near the center of the block. Figure 2.2 shows the nominal cross section of the weld.

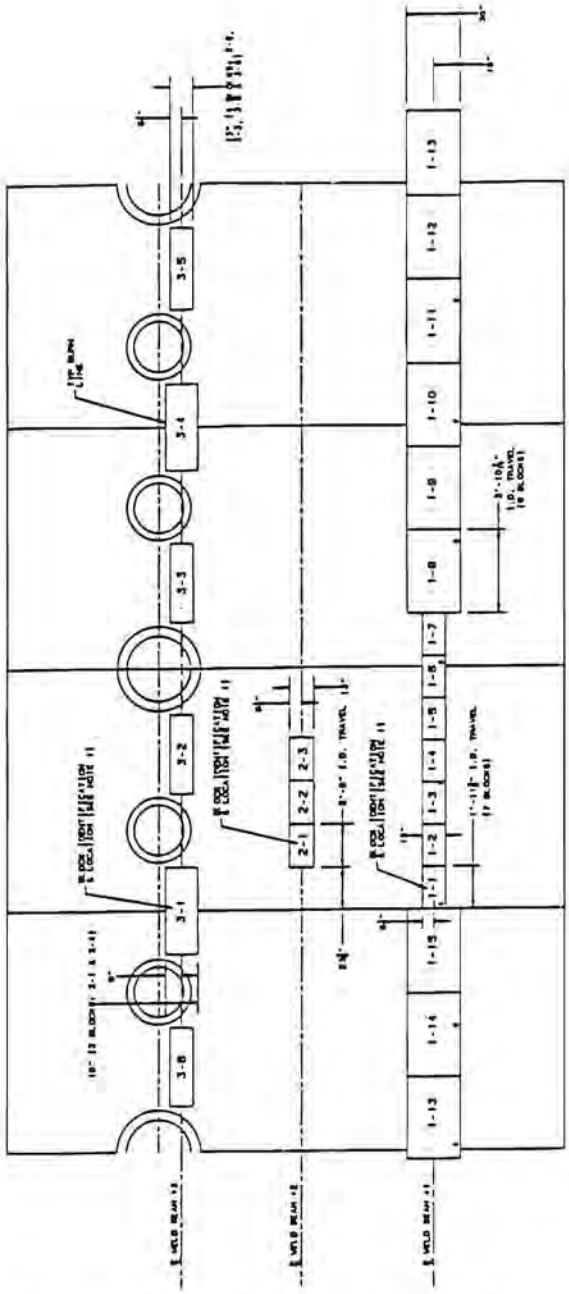

Figure 2.1 Diagram of Material Removed from the Midland Vessel
Source: Babcock & Wilcox Co. (1989)

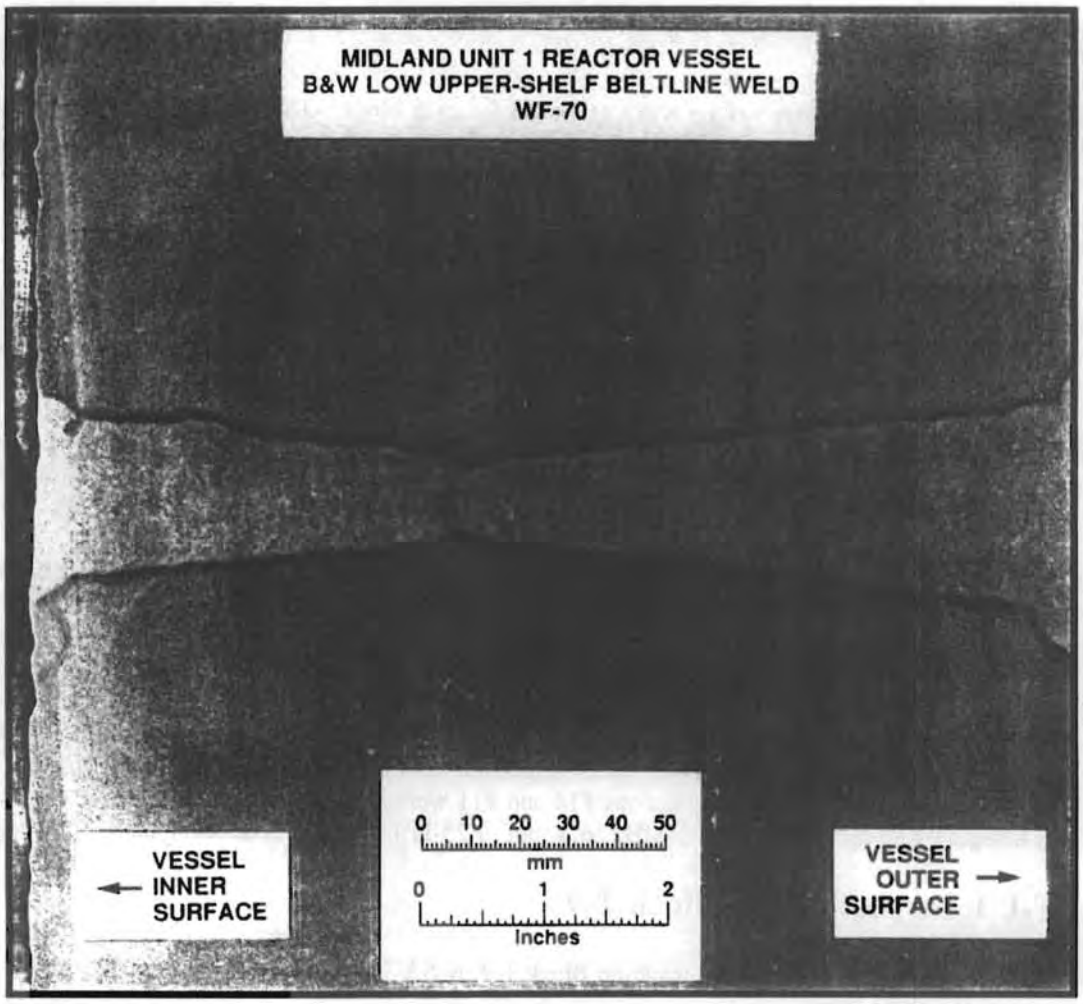

Figure 2.2 Photograph of Weld Cross Section
(Provided by Oak Ridge National Laboratory)

3.0 SAFT-UT Measurements

Four of the blocks that were cut from the beltline weld of the Midland vessel were inspected by SAFT-UT. The inspections covered a total of 4166 mm (164 in.) of circumferential weld length by collecting 155 files containing 650 Mbytes of data. Figure 3.1 shows some of the Midland blocks at the EPRI NDE Center when the SAFT-UT inspections were starting. Figure 3.2 shows the SAFT-UT system during the inspections. Figures 3.3 and 3.4 show the scanning configuration on Block 1-8.

As described in Section 2, a coordinate system was established for each block. The center line of the weld was marked and this line, replacing the circumferential axis of the vessel, is labeled the "Y" axis in this report. The distance across the weld, replacing the height axis of the vessel, is labeled the "X" axis in this report.

3.1 SAFT-UT Inspections of Midland Block 1-8

Block 1-8 was the first block inspected by SAFT-UT. This block was 224 mm (8.8 in.) thick, 1156 mm (45.5 in.) in circumferential length, and 722 mm (30.4 in.) high. Because of the scanner's geometry, a decision was made to scan the central 787 mm (31 in.) of the block and only return to the outer portions if time permitted.

Table 3.1 describes the inspections that were made on Block 1-8 by SAFT-UT. Block 1-8 received 45° shear wave inspections that were not made on the other three blocks. The other blocks received normal beam inspections from the top or bottom faces. These faces were not available on Block 1-8 when the SAFT-UT inspections were made.

Inspection #1 in the table was made with an RTD 88-255, L-wave, 2.0-MHz dual element normal beam probe on the clad surface. Inspection #2 was made with an RTD 1287-1156, L-wave, 2.0-MHz, dual element 45° probe from the clad surface. The direction of insonification was +X; that is, reflectors were illuminated from their -X side. Inspection #3 is a repeat of #2 where the insonification direction is -X. Inspections #4 and #5 were made from the clad side with an RTD 84-23, 70° L-wave, 2.0-MHz, dual element probe. Inspections #6 and #9 were full volume normal beam inspections using an Aerotech L07489, 2.25-MHz, 6.4 mm (0.25-in.) diameter, contact transducer on the clad surface. Inspections #7 and #8 were full volume 45° shear wave inspections from the clad side using a 1.0-MHz, 6.4 mm (0.25-in.) diameter transducer on a 45° wedge. Inspections #10 and #11 were full volume 45° shear wave inspections from the unclad side using an Aerotek K31358, 2.25-MHz, 6.4 mm (0.25-in.) diameter transducer on a 45° wedge.

3.2 SAFT-UT Inspections of Block 1-9

Table 3.2 describes the inspections that were made on Block 1-9 by SAFT-UT. This block was 305 mm (12 in.) wide and did not receive 45° shear wave inspections. Instead, normal beam inspections were made from the bottom face.

Inspection #1 was made with an RTD 84-23, 70° L-wave, 2.0-MHz, dual element probe where the direction of insonification was +X. Inspection #2 is a repeat of #1 where the insonification direction is -X. Inspections #3, #4, and #5 were full volume normal beam inspections using an Aerotech L07489, 2.25-MHz, 6.4 mm (0.25-in.) diameter, contact transducer.

3.3 SAFT-UT Inspections of Block 1-11

Table 3.3 describes the inspections that were made on Block 1-11 by SAFT-UT. This block was 305 mm (12 in.) wide and did not receive 45° shear wave inspections. Instead, normal beam inspections were made from top face.

Inspection #1 was made with an RTD 84-23, 70° L-wave, 2.0-MHz, dual element probe where the direction of insonification was +X. Inspection #2 is a repeat of #1 where the insonification direction is -X. Inspections #3, #4, and

#5 were full volume normal beam inspections using an Aerotech L07489, 2.25-MHz, 6.4 mm (0.25-in.) diameter, contact transducer.

Table 3.1 SAFT-UT Inspections on Block 1-8

Inspection No. / Type	Beam Direction	Frequency, MHz	Y Coverage, mm (in.)	X Coverage, mm (in.)
Near-Surface (Clad) Zone Inspections				
1 / Normal beam	N/A	2.0	-51 to 102 (-2.0 to 4.0)	-75 to 75 (-3.0 to 3.0)
2 / 45°L	+X	2.0	-51 to 102 (-2.0 to 4.0)	-75 to 75 (-3.0 to 3.0)
3 / 45°L	-X	2.0	-51 to 102 (-2.0 to 4.0)	-75 to 75 (-3.0 to 3.0)
4 / 70°L	+X	2.0	-560 to 535 (-22.0 to 21.0)	-152 to 152 (-6.0 to 6.0)
5 / 70°L	-X	2.0	-560 to 535 (-22.0 to 21.0)	-152 to 152 (-6.0 to 6.0)
Inspections of the Weld from the Clad Side				
6 / Normal beam	N/A	2.25	-432 to 381 (-17.0 to 15.0)	-317 to 330 (-12.5 to 13.0)
7 / 45°S	+X	1.0	-411 to 393 (-16.2 to 15.5)	-330 to 330 (-13.0 to 13.0)
8 / 45°S	+Y	1.0	-406 to 381 (-16.0 to 15.0)	-76 to 76 (-3.0 to 3.0)
Inspections of the Weld from the Unclad Side				
9 / Normal beam	N/A	2.25	-483 to 422 (-19.0 to 16.6)	-342 to 355 (-13.5 to 14.0)
10 / 45°S	+X	2.25	-483 to 406 (-19.0 to 16.0)	-356 to 229 (-14.0 to 9.0)
11 / 45°S	-X	2.25	-483 to 355 (-19.0 to 14.0)	-38 to 267 (-1.5 to 10.5)

Table 3.2 SAFT-UT Inspections on Block 1-9

Inspection No. / Type	Beam Direction	Frequency, MHz	Y Coverage, mm (in.)	X Coverage, mm (in.)
Near-Surface (Clad) Zone Inspections				
1 / 70°L	+X	2.0	-560 to 535 (-22.0 to 21.0)	-152 to 152 (-6.0 to 6.0)
2 / 70°L	-X	2.0	-560 to 535 (-22.0 to 21.0)	-152 to 152 (-6.0 to 6.0)
Inspections of the Weld from the Clad Side				
3 / Normal beam	N/A	2.25	-450 to 465 (-17.7 to 18.3)	-152 to 152 (-6.0 to 6.0)
Inspections of the Weld from the Unclad Side				
4 / Normal beam	N/A	2.25	-635 to 610 (-25.0 to 24.0)	-152 to 152 (-6.0 to 6.0)
Inspections of the Weld from Bottom Side				
5 / Normal beam	N/A	2.25	-457 to 400 (-18.0 to 15.7)	-152 to 152 (-6.0 to 6.0)

3.4 SAFT-UT Inspections of Block 1-12

Table 3.4 describes the inspections that were made on Block 1-12 by SAFT-UT. This block was 305 mm (12 in.) wide and did not receive 45° shear wave inspections. Instead, normal beam inspections were made from top face.

Inspection #1 was made with an RTD 84-23, 70° L-wave, 2.0-MHz, dual element probe where the direction of insonification was +X. Inspection #2 is a repeat of #1 where the insonification direction is -X. Inspections #3 and #4 were full-volume normal beam inspections using an Aerotech L07489, 2.25-MHz, 6.4 mm (0.25-in.) diameter, contact transducer.

Table 3.3 SAFT-UT Inspections on Block 1-11

Inspection No. / Type	Beam Direction	Frequency, MHz	Y Coverage, mm (in.)	X Coverage, mm (in.)
Near-Surface (Clad) Zone Inspections				
1 / 70°L	+X	2.0	-475 to 601 (-18.7 to 24.0)	-152 to 152 (-6.0 to 6.0)
2 / 70°L	-X	2.0	-475 to 601 (-18.7 to 24.0)	-152 to 152 (-6.0 to 6.0)
Inspections of the Weld from the Clad Side				
3 / Normal beam	N/A	2.25	-483 to 597 (-19.0 to 23.5)	-152 to 152 (-6.0 to 6.0)
Inspections of the Weld from the Unclad Side				
4 / Normal beam	N/A	2.25	-584 to 635 (-23.0 to 25.0)	-152 to 152 (-6.0 to 6.0)
Inspections of the from Top Side				
5 / Normal beam	N/A	2.25	-356 to 587 (-14.0 to 23.0)	-152 to 152 (-6.0 to 6.0)

Table 3.4 SAFT-UT Inspections on Block 1-12

Inspection No. / Type	Beam Direction	Frequency, MHz	Y Coverage, mm (in.)	X Coverage, mm (in.)
Near-Surface (Clad) Zone Inspections				
1 / 70°L	+X	2.0	-508 to 584 (-20.0 to 23.0)	-152 to 152 (-6.0 to 6.0)
2 / 70°L	-X	2.0	-508 to 584 (-20.0 to 23.0)	-152 to 152 (-6.0 to 6.0)
Inspections of the Weld from the Unclad Side				
3 / Normal beam	N/A	2.25	-584 to 610 (-23.0 to 24.0)	-152 to 152 (-6.0 to 6.0)
Inspections of the Weld from Top Side				
4 / Normal beam	N/A	2.25	-508 to 584 (-20.0 to 23.0)	-152 to 152 (-6.0 to 6.0)

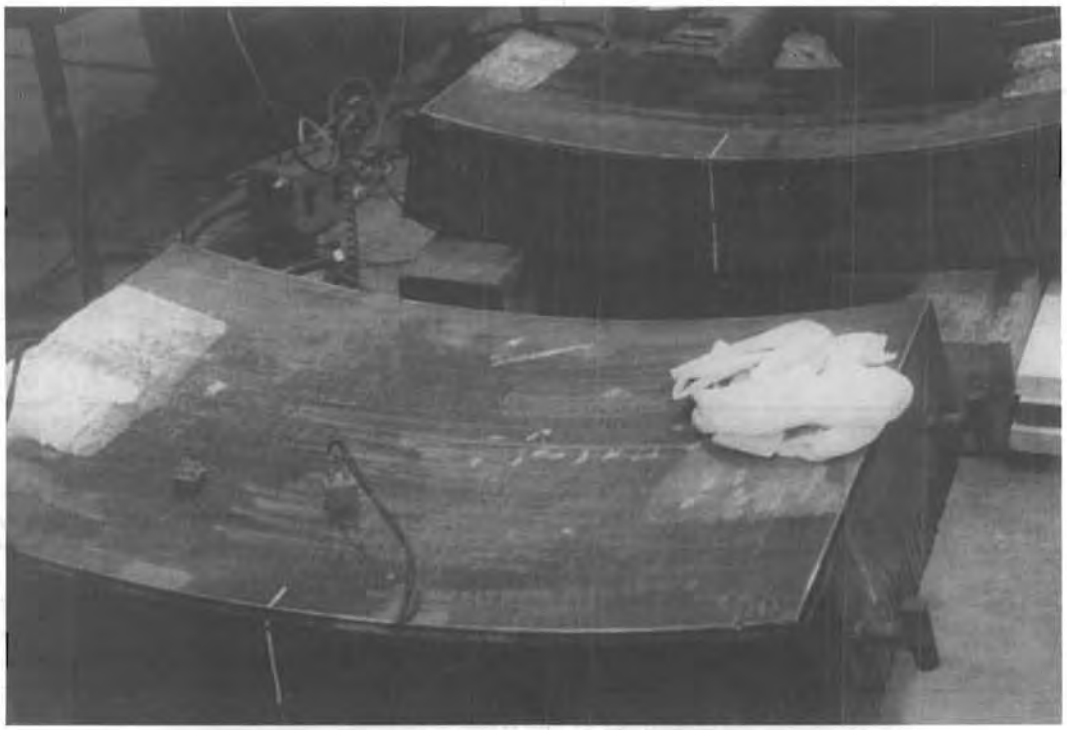

Figure 3.1 Photo of Material Removed from the Midland Vessel

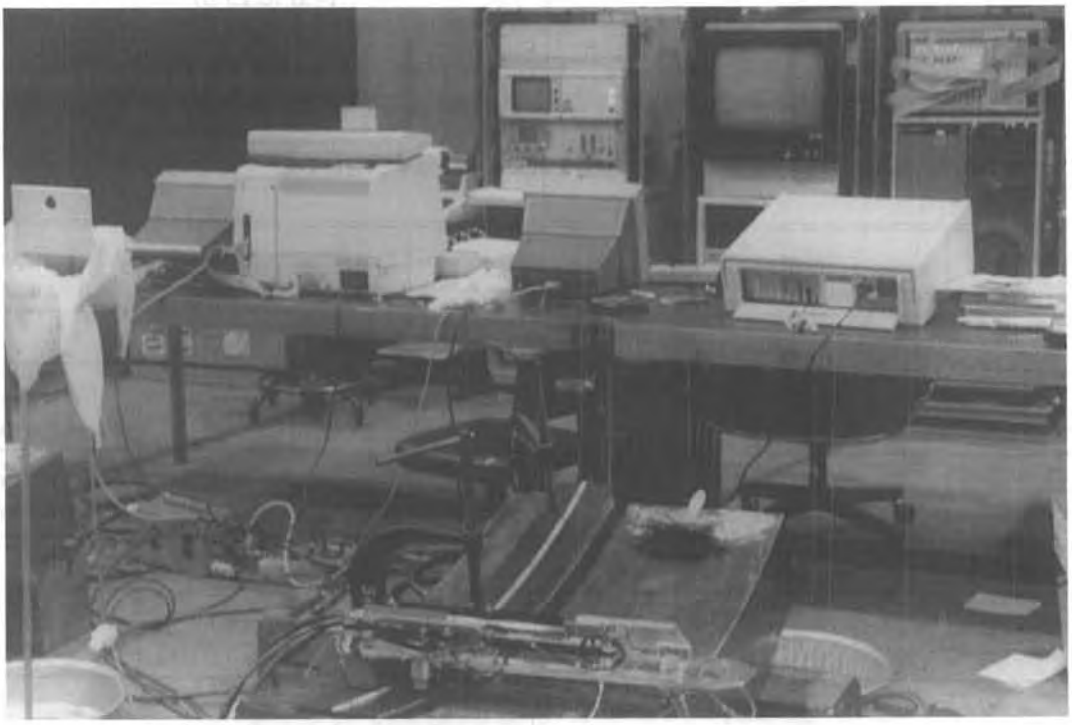

Figure 3.2 Photo of SAFT-UT System as Configured for Inspection of Midland Blocks

Figure 3.3 Photo of SAFT-UT Scanner Performing Inspections on the Clad Side of a Midland Block

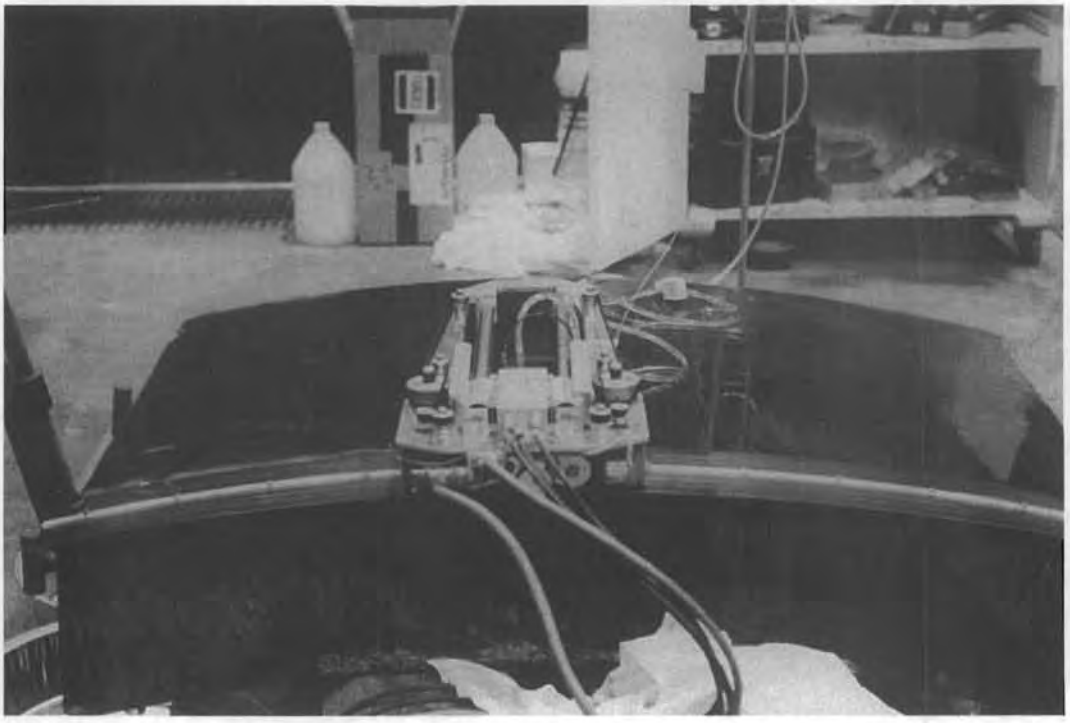

Figure 3.4 Photo of SAFT-UT Scanner Performing Inspections on the Unclad Side of a Midland Block

4.0 Correlation of SAFT-UT Data with Destructive Analysis of Block 1-8

In this section a comparison is made of SAFT-UT inspection results with a destructive analysis performed by the EPRI NDE Center on Block 1-8. The destructive analysis reported sizes for defects at the weld root and at the clad-to-base metal interface. The detection results for SAFT-UT are given for the weld root followed by the detection results for the clad-to-base metal interface.

4.1 Destructive Analysis of Indications

Tables 4.1 and 4.2 describe the results from the destructive analysis of 13 indications found by the (non-SAFT) ultrasonic testing (UT) performed by the staff at the EPRI NDE Center. Indications were found near the root of the weld and near the clad-to-base metal interface.

For the six indications in the base metal (Table 4.1), "Y" refers to the circumferential position (along the weld center line) for the indication as reported by the UT. "DY" is the extent of a flaw in circumferential direction as measured by the destructive analysis. If the indication was not found in the destructive analysis, then no value is given for "DY." "X" and "DX" are not given but the defects are reported to be in the weld root which inplies "X" = 0.0 $\pm$ 12 mm. "Z" refers tothedepth from the clad side of the block (inside of the vessel) as reported by the UT. "DZ" is the extent in the depth dimension as measured by the destructive analysis. The characteristics of the defects that were found in the destructive analysis are also given in Tables 4.1 and 4.2 along with a reference to the individual photographs of the defects.

For the seven indications near the clad-to-base metal interface (Table 4.2), "DY" is not reported by the destructive analysis. If the indication was not found in the destructive analysis, then no value is given for "DX."

Defects were not determined by the destructive analysis for indications 1, 4, 9, 12, and 13. Two defects were found for indications 3, 6, and 10. Figures 4.1 through 4.11 were provided by the Electric Power Research Institute's NDE Center, Charlotte, North Carolina.

4.2 Defects Found in the Weld Root

Table 4.3 shows the results of the analysis of SAFT-UT data for the detection of the weld root defects from the destructive test. The detection result is shown for each of the six different SAFT-UT inspections performed on Block 1-8. Two of the defects, #5 and #6, were readily apparent in the SAFT-UT data. One of the defects, #2, was not detected. It should be noted that none of the six defects were in the central 610 mm (24 in.) of the block. As a consequence of this, all of the defects were missed by at least one SAFT-UT inspection and one of the defects, #3, was not covered by any of the SAFT-UT inspections because this defect was located near the end of the block.

4.2.1 Description of Detection Method

The defects were small slag, typically 1-2 mm in diameter, and were located at the weld root, about 89 mm (3.5 in.) below the clad surface. In order to successfully detect the weak signals from these reflectors, the SAFT-UT data was analyzed by looking for the presence of distinguishing shapes amidst the surrounding background noise. The typical shape for a reflector in the 45° shear inspections is shown in Figure 4.12. This shape can be found only in the side view (B-scan) of the 45° shear data. The typical shape for a reflector in the normal beam data is shown in Figure 4.13.

This detection method leads to the identification of additional reflectors in the SAFT-UT data. These additional reflectors fall into two general categories. The first category are those that are found near the weld root, between 80 mm and 95 mm (3.25 and 3.75 in.) from the clad surface. There are two indications in this category and they are found by both 45° shear and normal beam inspections. The second category of additional base-metal indications found by

SAFT-UT are not found near the weld root. There are seven of these indications and most of these are only found by the normal beam inspections. All of the SAFT-UT data have been analyzed by this detection method. The data are reported in Section 5.0. All the summary results are covered in Section 6.0.

Table 4.1 Results from the Destructive Analysis of Indications in Block 1-8 (Weld Root Indications)

Indication No.	Y, mm (in.)	DY, mm (in.)	X, mm (in.)	DX, mm (in.)	Z, mm (in.)	DZ, mm (in.)	Characterization
1	-465 (-18.3)	-	-	-	100 (3.9)	-	Presence not determined by destructive test.
2	-445 (-17.5)	1 (0.04)	-	-	98 (3.8)	2 (0.08)	Slag. See destructive test results in Figure 4.1.
3t	470 (18.5)	0.75 (0.03)	-	-	74 (2.9)	1.25 (0.05)	Destructive test found 2 defects. Both were slag. See destructive test results of 3b in Figure 4.2.
3b	-	3 (0.12)	-	-		1.25 (0.05)	
4	420 (16.5)	-	-	-	91 (3.6)	-	Presence not confirmed by destructive test. See destructive test results in Figure 4.3.
5	380 (15.0)	5 (0.2)	-	-	89 (3.5)	2 (0.08)	Slag. See destructive test results in Figure 4.4.
6t	350 13.8	2 (0.08)	-	-	99 (3.9)	1.5 (0.06)	Destructive test found 2 defects, both slag. See destructive test results in Figures 4.5 and 4.6.
6b		3.5 (0.14)	-	-		2.5 (0.10)	

4.3 Defects Found Near the Clad-to-Base Metal Interface

Table 4.4 shows the results of the analysis of SAFT-UT data for the detection of the four clad-to-base metal defects from the destructive test. Only the four locations where the destructive analysis reported defects are considered in the table. One of the defects, #8, was readily apparent in the SAFT-UT data in that it had the proper shape in side-view B-scan and had considerable amplitude in both inspections. One of the defects, #7, was detected and had the proper shape from one inspection only. One of the defects, #11, was detected at a high amplitude, but shapeless spot. One of the defects, #10, was not detected by SAFT-UT.

4.3.1 Description of Detection Method

The five defects were small slag, typically 1-2 mm in depth and 2-5 mm in length, and were located at the interface between the clad and the base metal. In order to successfully detect the signals from these reflectors, the SAFT-UT data was analyzed in two steps. The first step was to look for the presence of distinguishing shapes. The second step was to look for high-amplitude signals that have some bulk, not just one hot pixel, where the amplitude is considerably above the background reflections from the clad-to-base metal interface. The typical shape for a reflector in the 70°L-wave

inspections is shown in Figure 4.14. This shape can be found only in the side view (B-scan) of the 70° L-wave data. The typical image for a reflector that is included based on amplitude alone is shown in Figure 4.15.

It is important to consider the number of additional flaws that this detection method leads to in the SAFT-UT data from Block 1-8. These additional reflectors fall into two general categories. The first category are those that have a distinguishing shape. There were no reflectors in this category in the data from Block 1-8. The second category are the reflectors that qualify based on amplitude. There are three reflectors in this category in the SAFT-UT data from Block 1-8. All of the SAFT-UT data have been analyzed by this detection method. The results are reported in Section 5.0.

Table 4.2 Results from the Destructive Analysis of Indications in Block 1-8 (Near-Surface Zone Indications)

Indication No.	Y, mm (in.)	DY, mm (in.)	X, mm (in.)	DX, mm (in.)	Z, mm (in.)	DZ, mm (in.)	Characterization
7	81 (3.2)	-	-22 (-0.8)	4 (0.16)	-	1 (0.04)	Clad-to-base metal interface slag. See destructive test results in Figure 4.7.
8	112 (4.4)	-	33 (1.3)	5 (0.2)	-	2 (0.08)	Clad-to-base metal interface slag. See destructive test results in Figure 4.8.
9	112 (4.4)	-	0 (0.0)	-	-	-	Presence not determined by destructive test.
10a	204 (8.0)	-	15 (0.6)	5 (0.2)	-	1 (0.04)	Clad-to-base metal interface. See destructive test results in Figure 4.9.
10b	-	-	-	2 (0.08)	-	1 (0.04)	1 mm below interface. See destructive test results in Figure 4.10.
11	235 (9.2)	-	-15 (-0.6)	1.5 (0.06)	-	0.5 (0.02)	Clad-to-base metal interface. See destructive test results in Figure 4.11.
12	235 (9.2)	-	12 (0.5)	-	-	-	Presence not determined by destructive test.
13	288 (15.3)	-	-11 (-0.4)	-	-	-	Presence not determined by destructive test.

Table 4.3 Detection by SAFT-UT of the Weld-Root Defects found in the Destructive Analysis of Midland Block 1-8

	#2	#6
Normal beam, clad side	No coverage	No detection
Normal beam, unclad side	No detection	No detection
45° shear, clad, dir = 0	No coverage	No detection
45° shear, clad, dir = 90	No detection	No coverage
45° shear, unclad, dir = 0	No detection	Detection
45° shear, unclad, dir = 180	No detection	Detection
Detection Results	Not detected	Detected (high S/N)
	#5	#3
Normal beam, clad side	Detection	No coverage
Normal beam, unclad side	No detection	No coverage
45° shear, clad, dir = 0	No coverage	No coverage
45° shear, clad, dir = 90	No detection	No coverage
45° shear, unclad, dir = 0	Detection	No coverage
45° shear, unclad, dir = 180	Detection	No coverage
Detection Result	Detected (high S/N)	No coverage

Table 4.4 Detection by SAFT-UT of the Clad-to-Base Metal Defects found in the Destructive Analysis of Midland Block 1-8

	#7	#8	#10	#11
70°, L-wave, dir = +X	Detection	Detection	No detection	No detection
70°, L wave, dir = -X	No detection	Detection	No detection	Detection
Detection Result	Detection	Detection	No detection	Detection

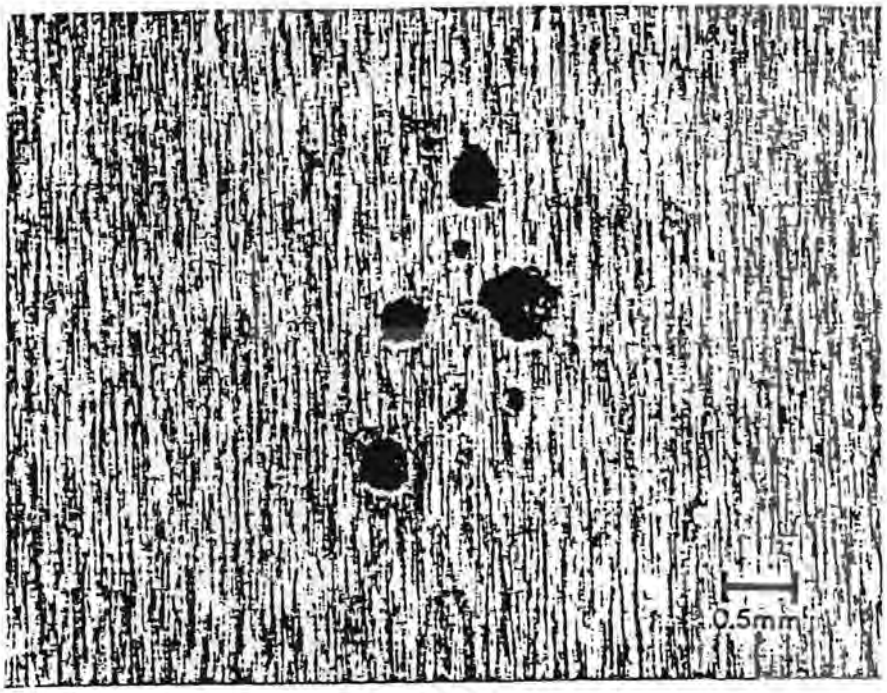

(a) Depth: 14.25 mm (0.561 in.), as machined

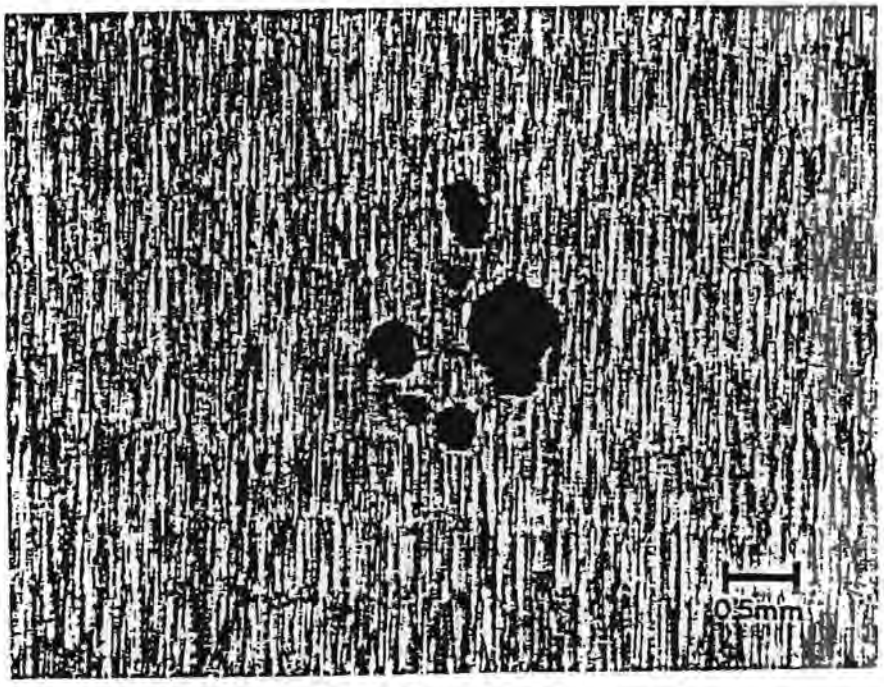

(b) Depth: 14.15 mm (0.557 in.), as machined

Figure 4.1 DA Photograph of Midland Flaw 1-8 #2
Photographs provided by the EPRI NDE Center

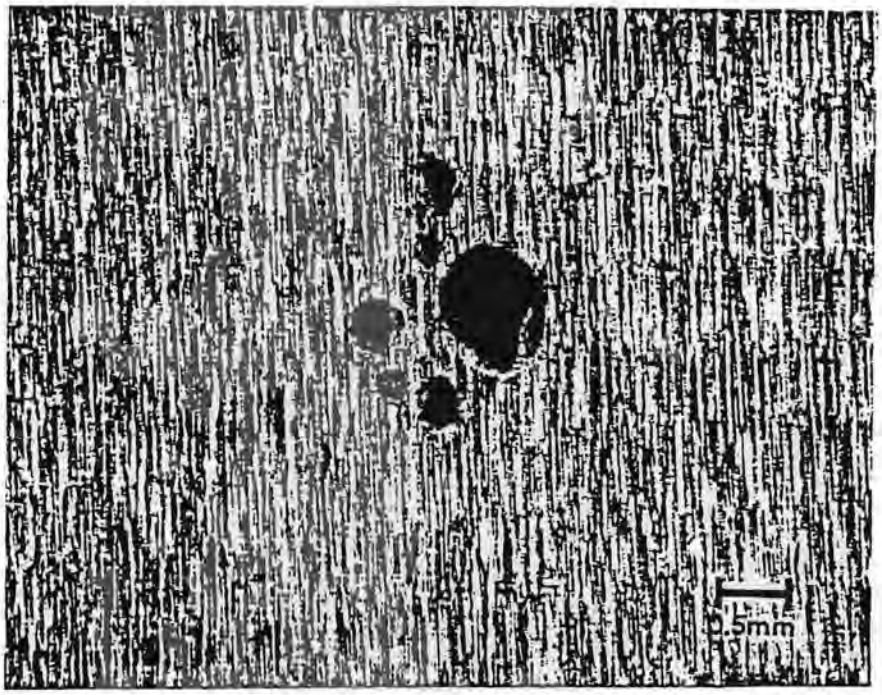

(c) Depth: 14.1 mm (0.555 in.), as machined

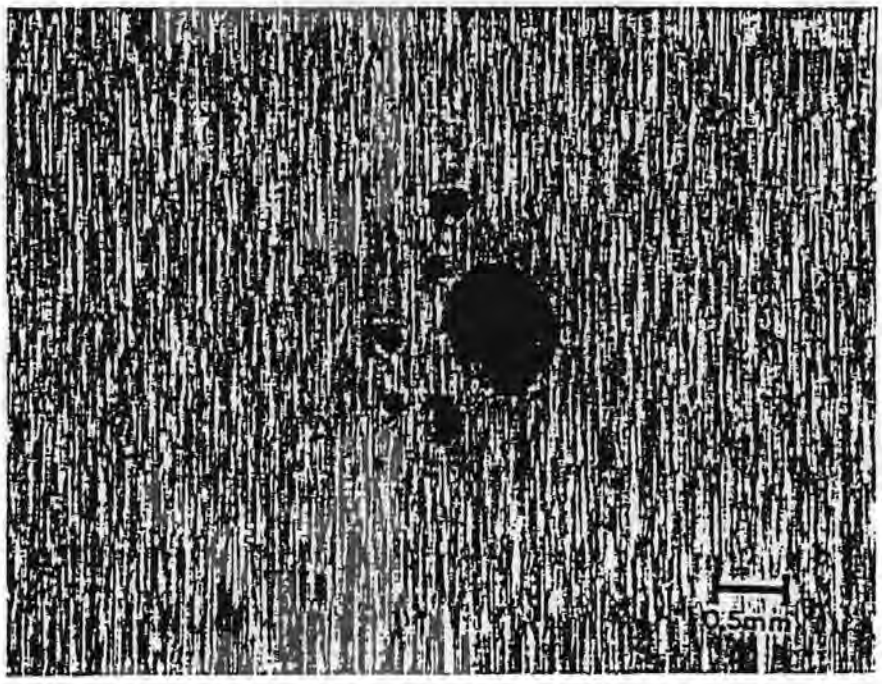

(d) Depth: 14.05 mm (0.553 in.), as machined

Figure 4.1 (cont'd)
Photographs provided by the EPRI NDE Center

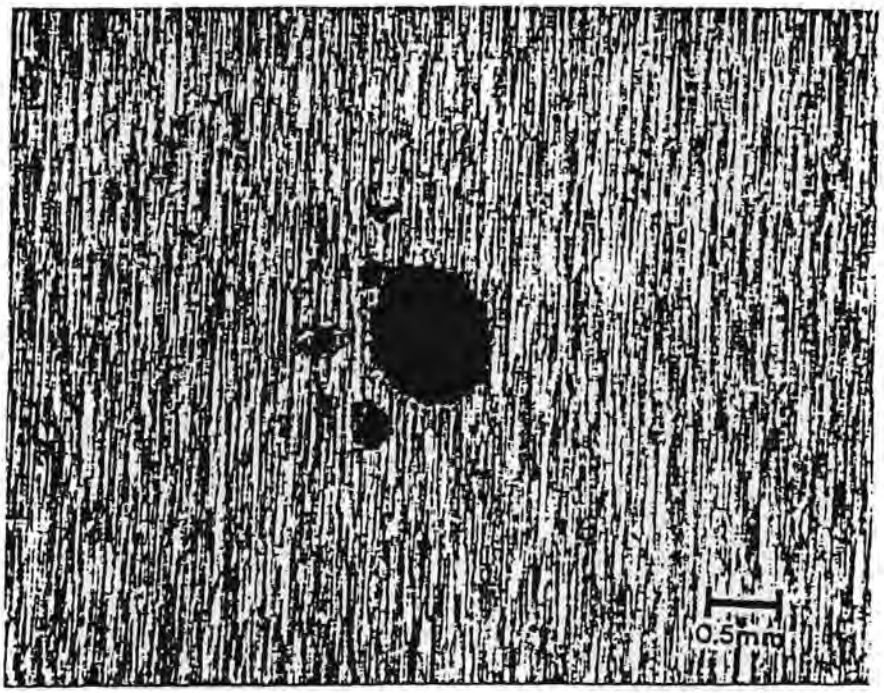

(e) Depth: 14.02 mm (0.552 in.), as machined

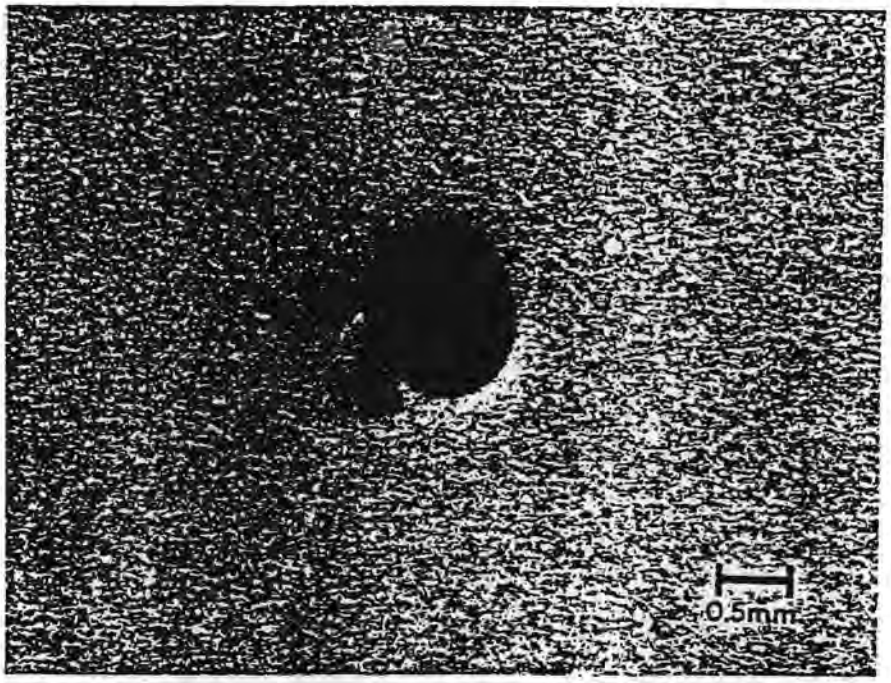

(f) Depth: 14.97 mm (0.550 in.), as polished and etched

Figure 4.1 (cont'd)
Photographs provided by the EPRI NDE Center

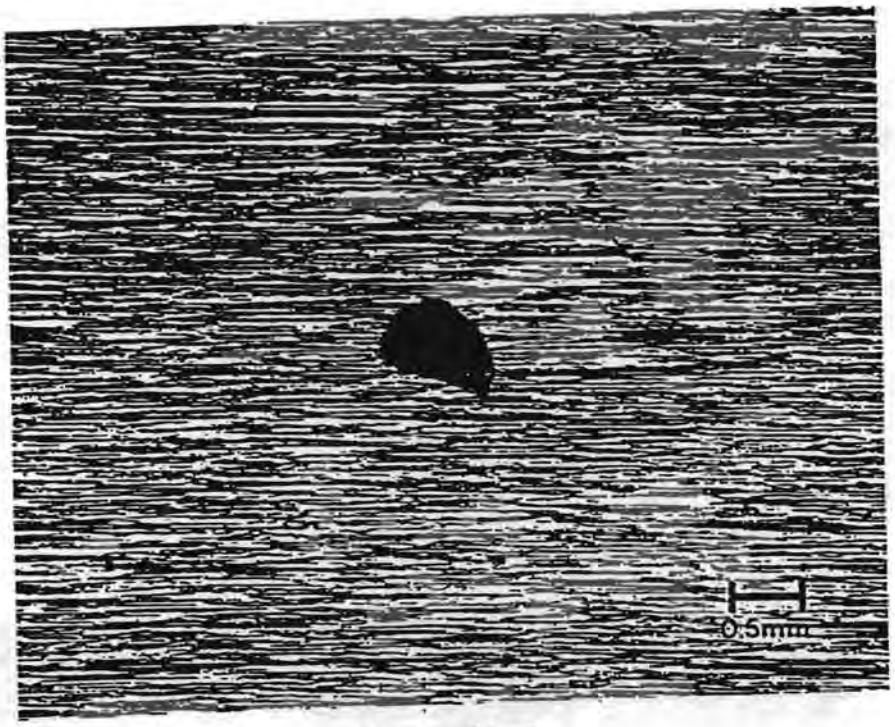

(a) As machined

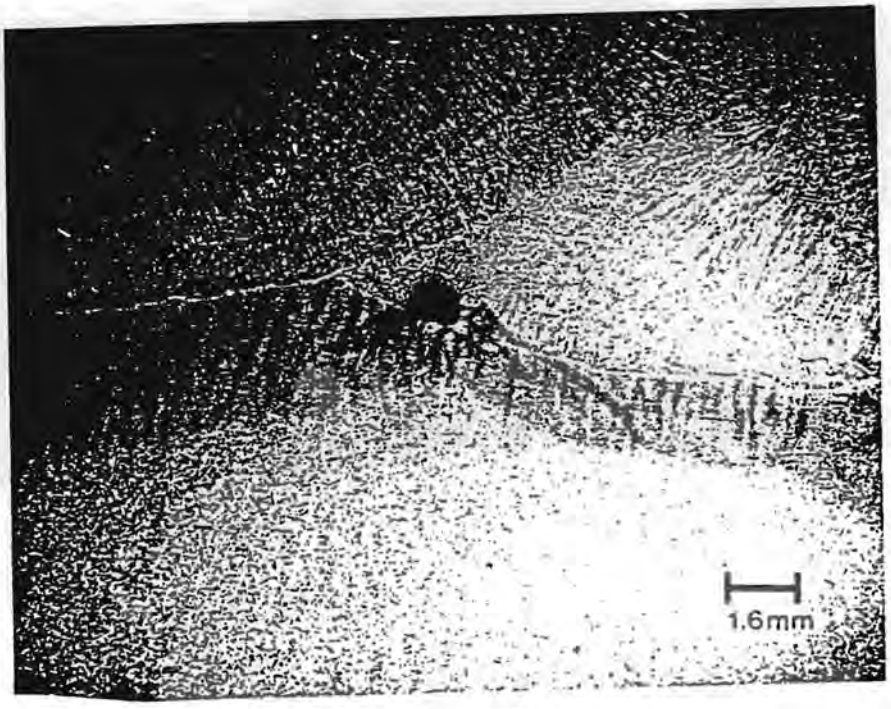

(b) Polished and etched

Figure 4.2 DA Photograph of Midland Flaw 1-8 #3b
Photographs provided by the EPRI NDE Center

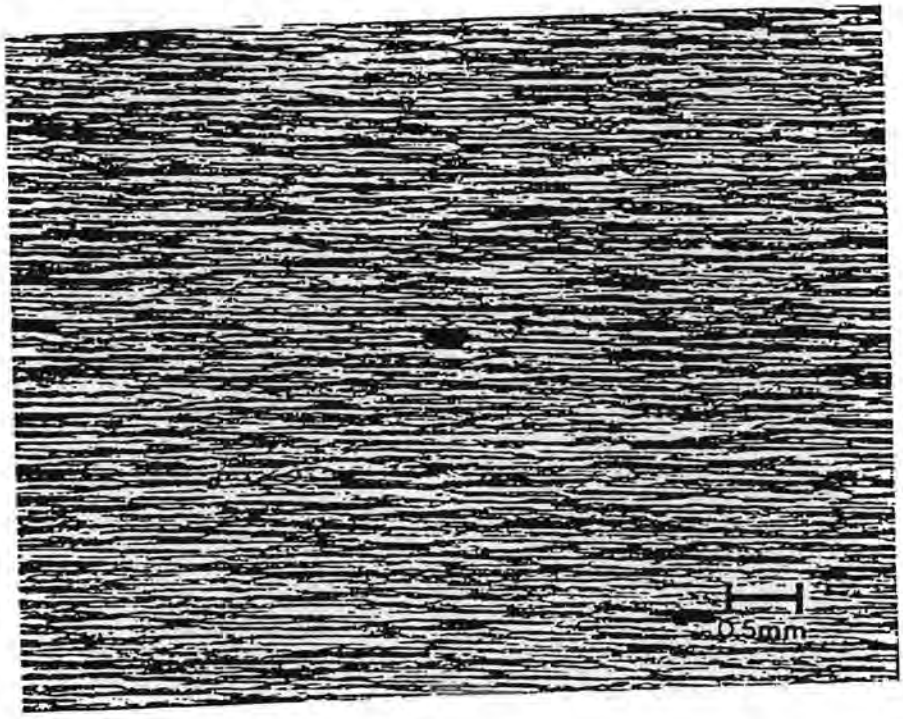

Figure 4.3 DA Photograph of Midland Flaw 1-8 #4b, as machined.
Photograph provided by the EPRI NDE Center

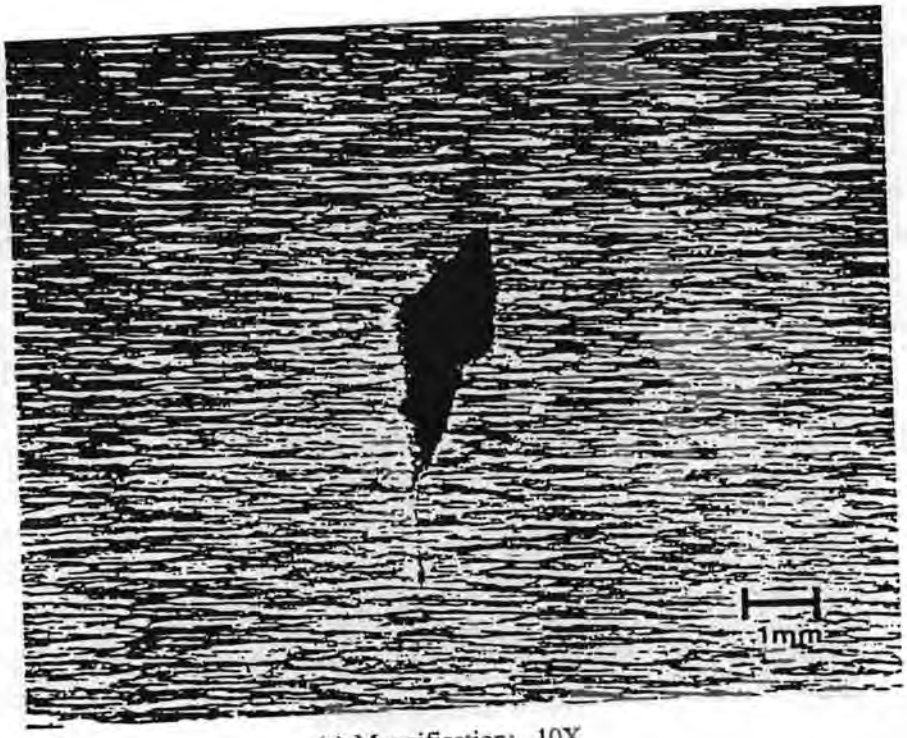

(a) Magnification: 10X

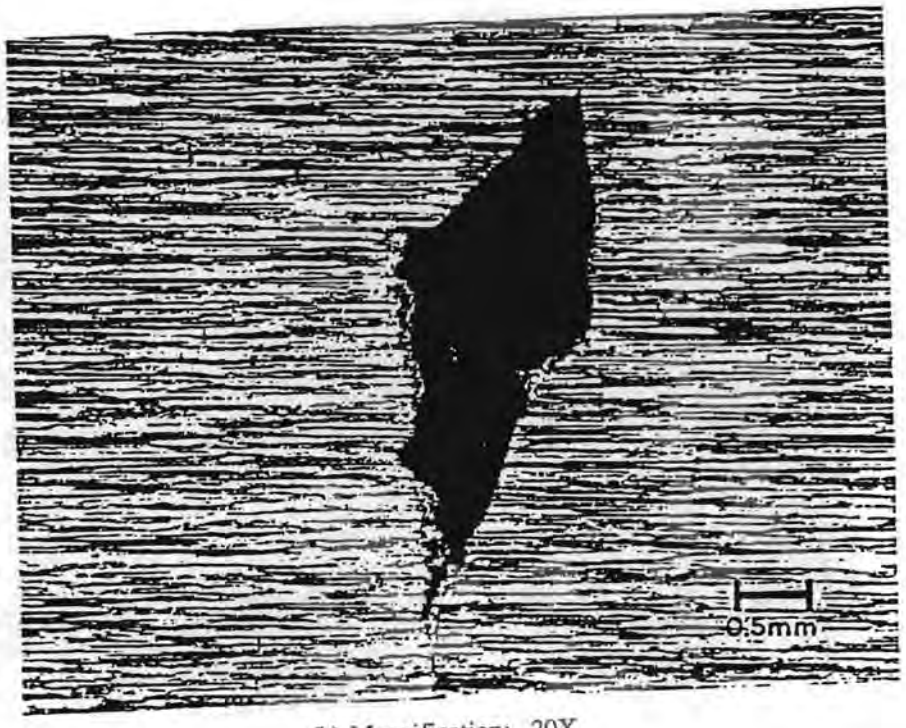

(b) Magnification: 20X

Figure 4.4 DA Photograph of Midland Flaw 1-8 #5t
Photographs provided by the EPRI NDE Center

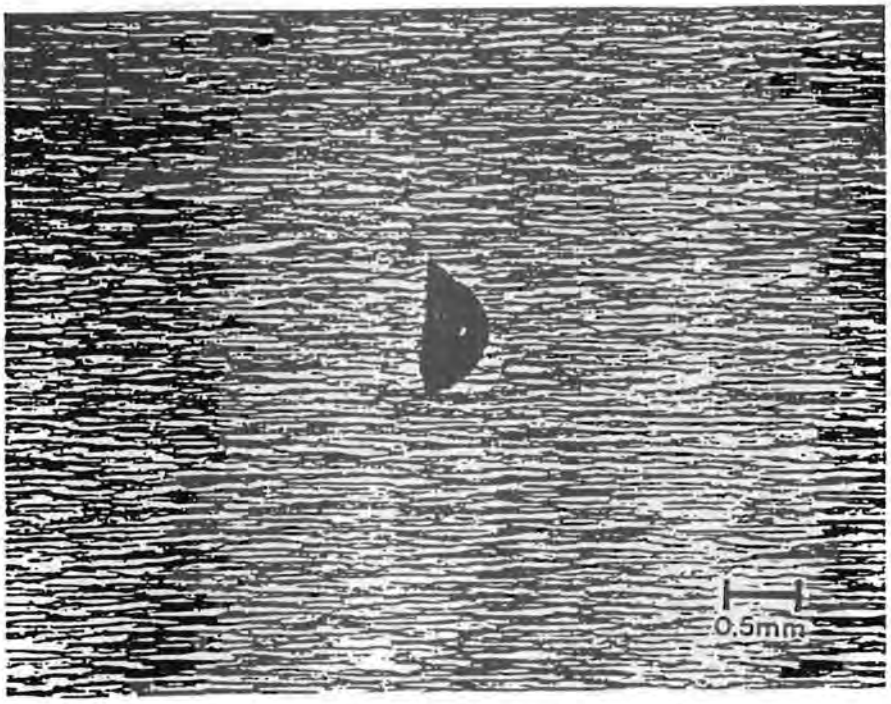

(a) Depth: 6.32 mm (0.249 in.), as machined

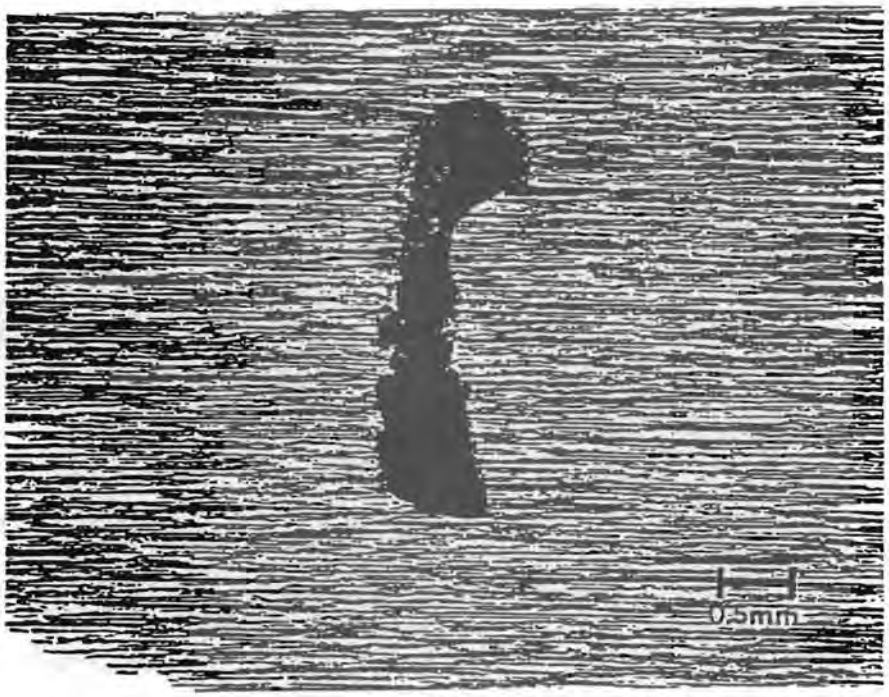

(b) Depth: 5.82 mm (0.229 in.), as machined

Figure 4.5 DA Photograph of Midland Flaw 1-8 #6b
Photographs provided by the EPRI NDE Center

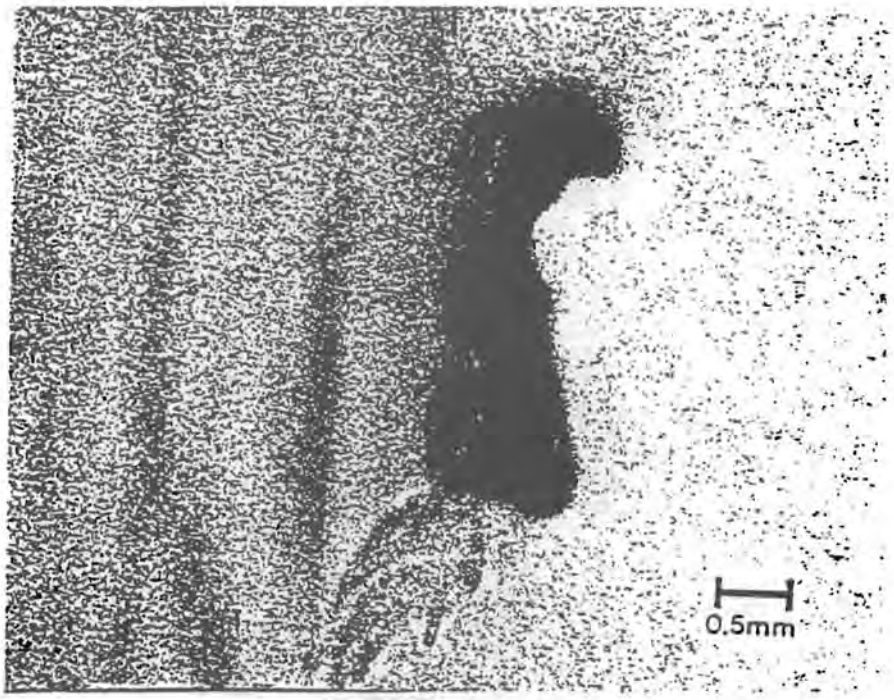

(c) As polished and etched, magnification: 20X

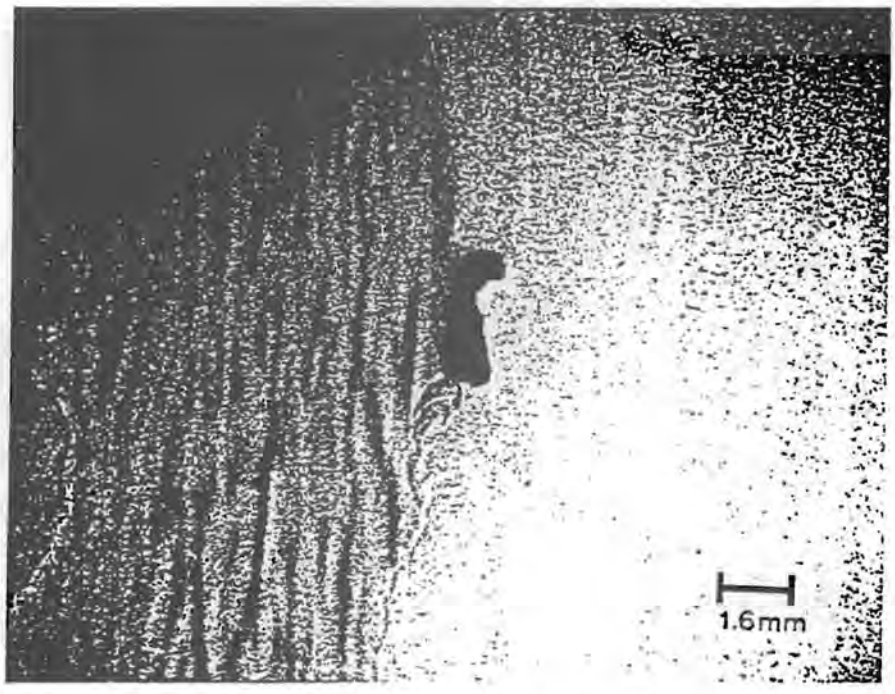

(d) As polished and etched, magnification: 6.3X

Figure 4.5 (cont'd)
Photographs provided by the EPRI NDE Center

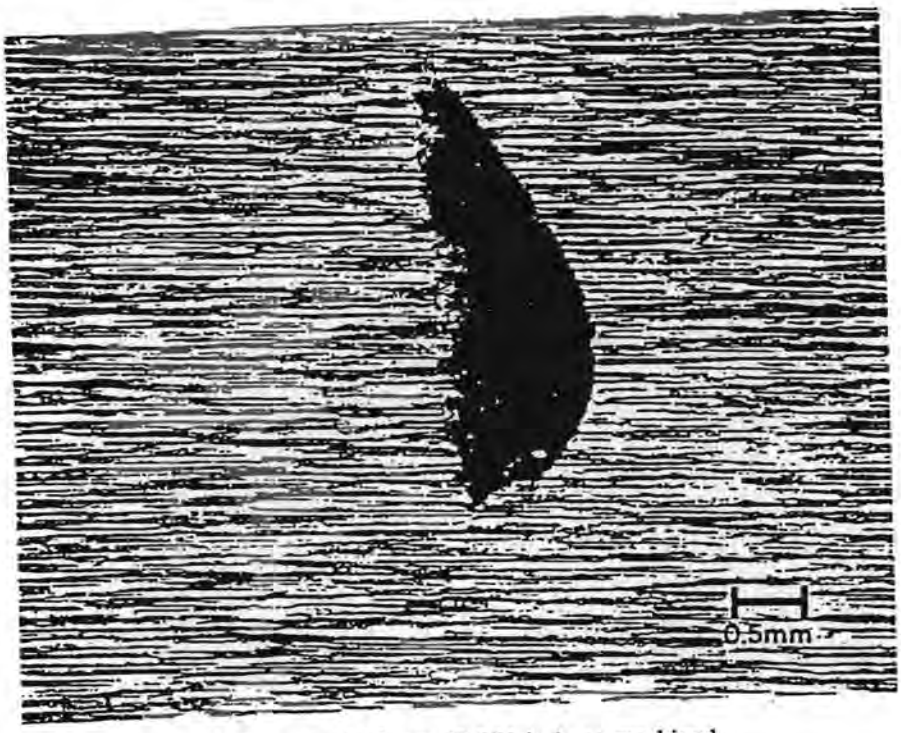

(a) Depth: 6.45 mm (0.254 in.), as machined

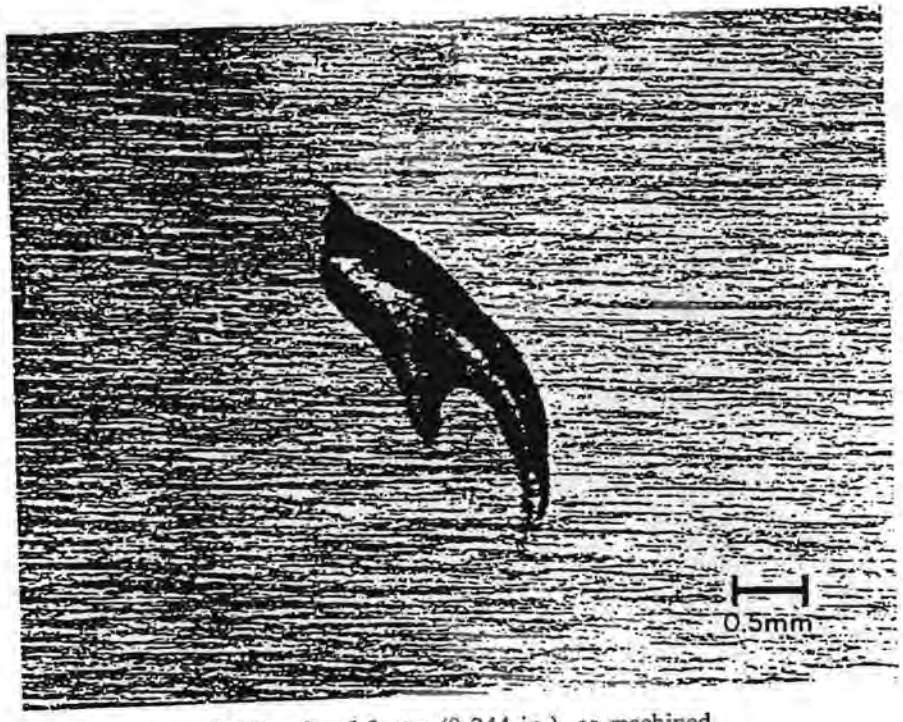

(b) Depth: 6.2 mm (0.244 in.), as machined

Figure 4.6 DA Photograph of Midland Flaw 1-8 #6t
Photographs provided by the EPRI NDE Center

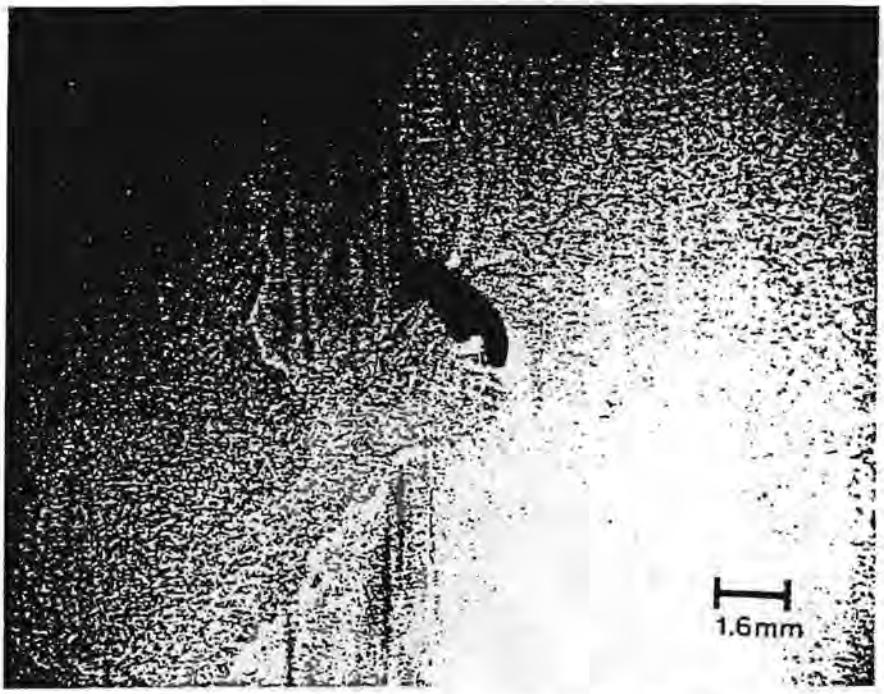

(c) As polished and etched, magnification: 6.3X

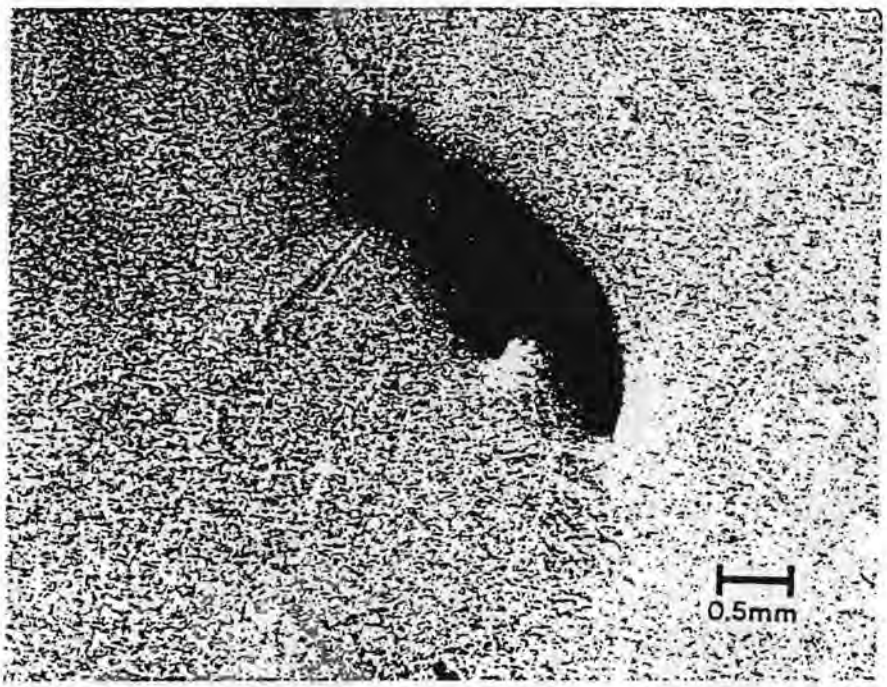

(d) As polished and etched, magnification: 20X

Figure 4.6 (cont'd)
Photographs provided by the EPRI NDE Center

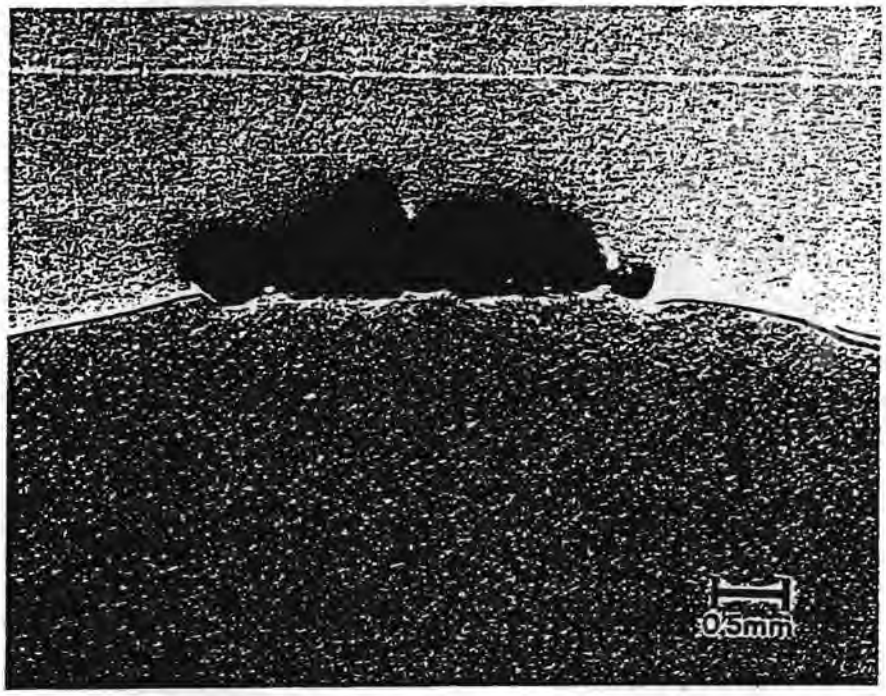

(a) As polished and etched, magnification: 20X

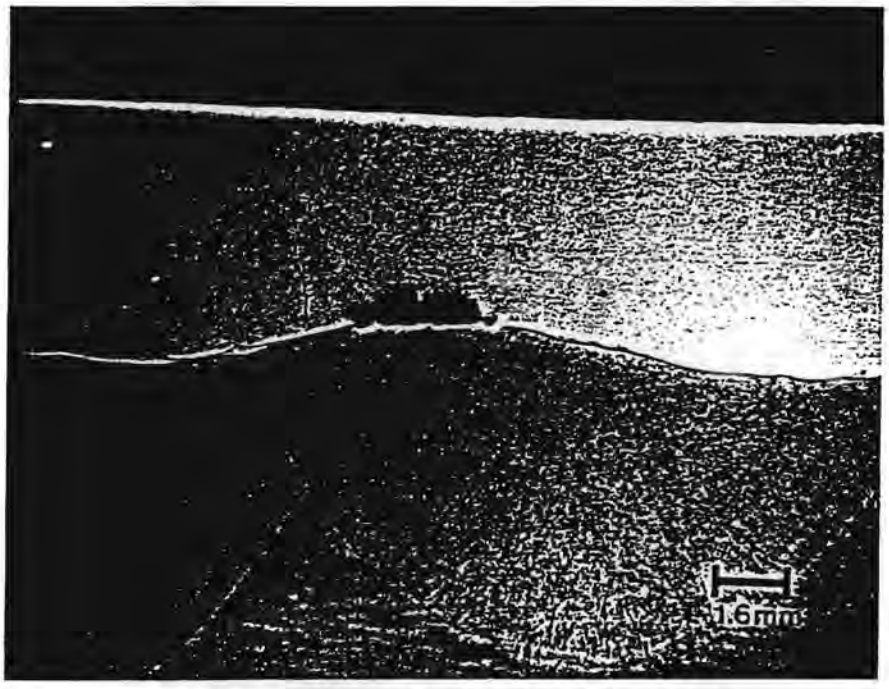

(b) As polished and etched, magnification: 6.3X

Figure 4.7 DA Photograph of Midland Flaw 1-8 #7b
Photographs provided by the EPRI NDE Center

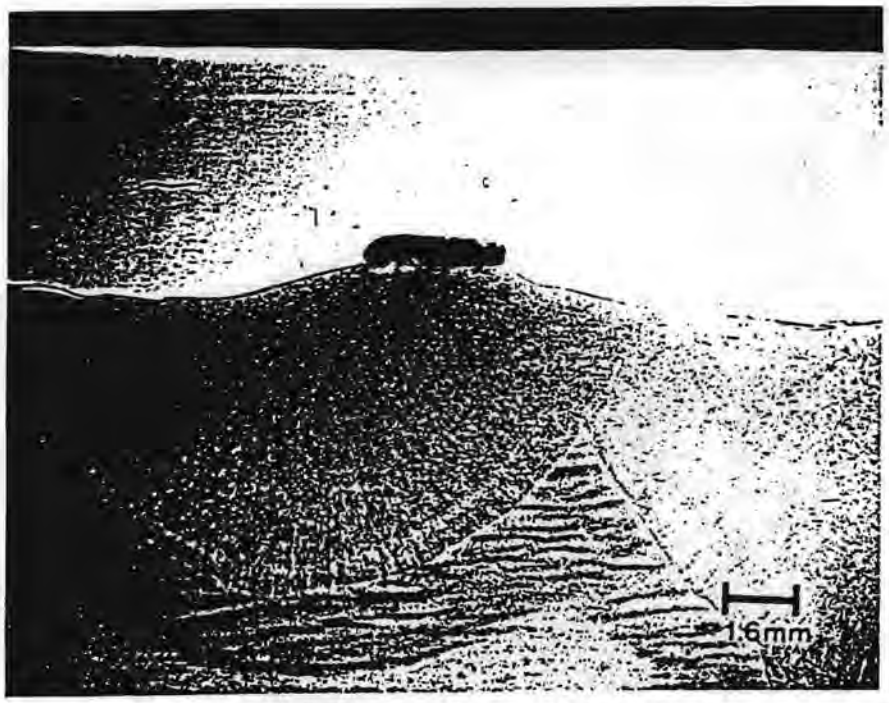

(a) As polished and etched, magnification: 6.3X

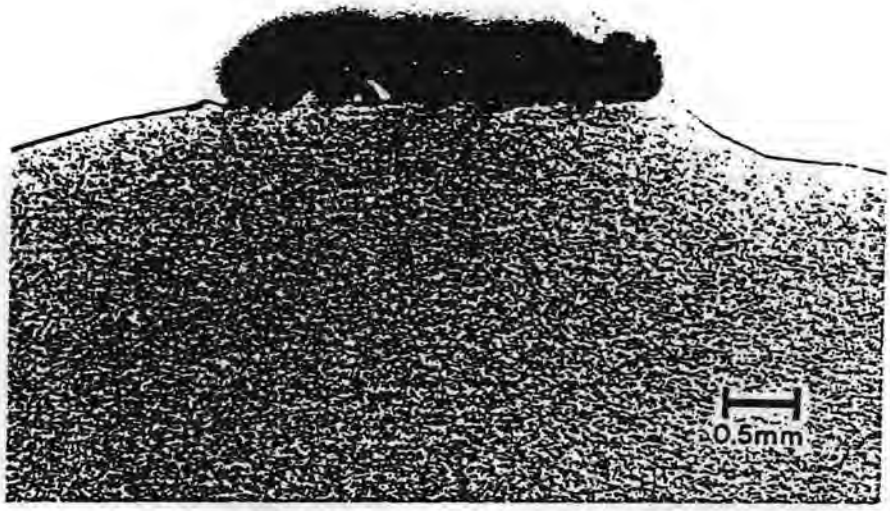

(b) As polished and etched, magnification: 20X

Figure 4.8 DA Photograph of Midland Flaw 1-8 #8
Photographs provided by the EPRI NDE Center

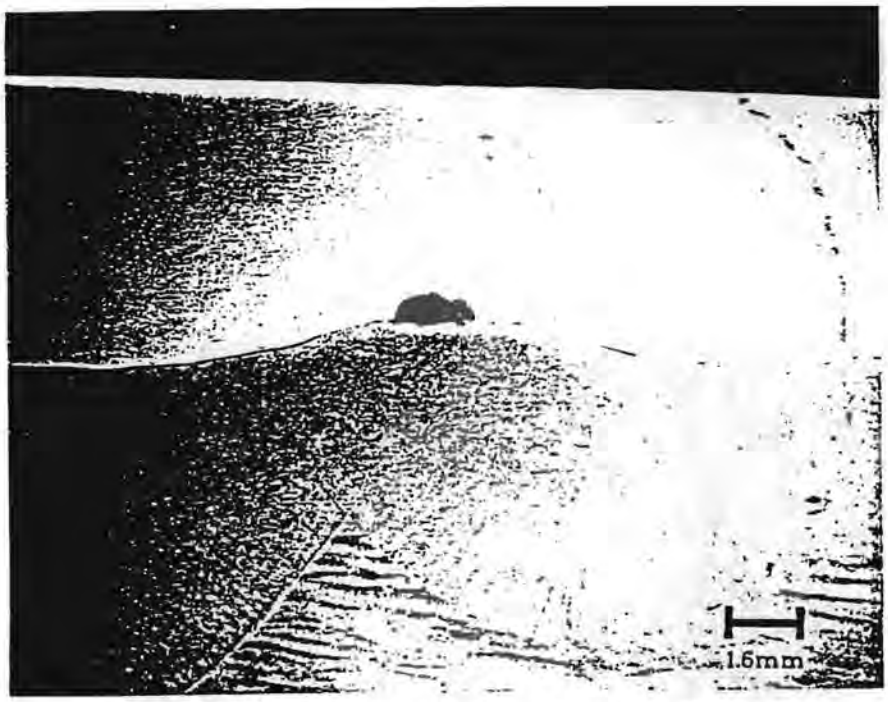

(a) As polished and etched, magnification: 6.3X

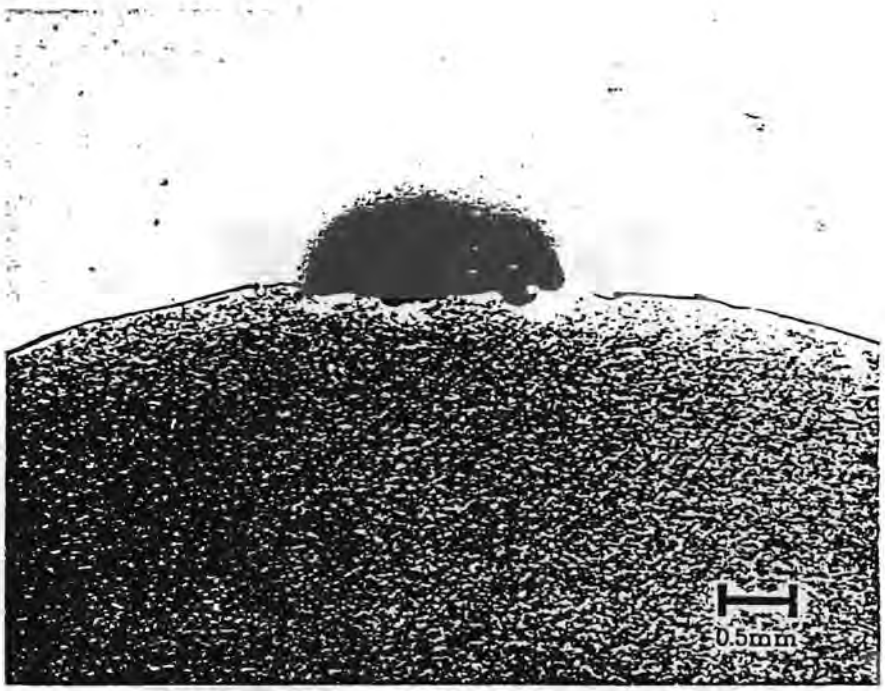

(b) As polished and etched, magnification: 20X

Figure 4.9 DA Photograph of Midland Flaw 1-8 #10a
Photographs provided by the EPRI NDE Center

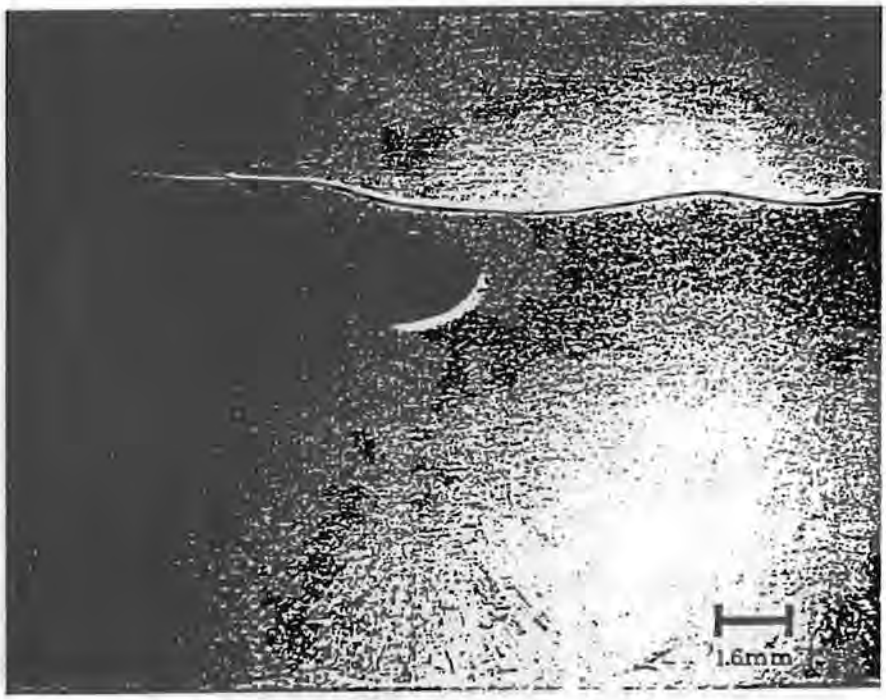

(a) As polished and etched, magnification: 6.3X

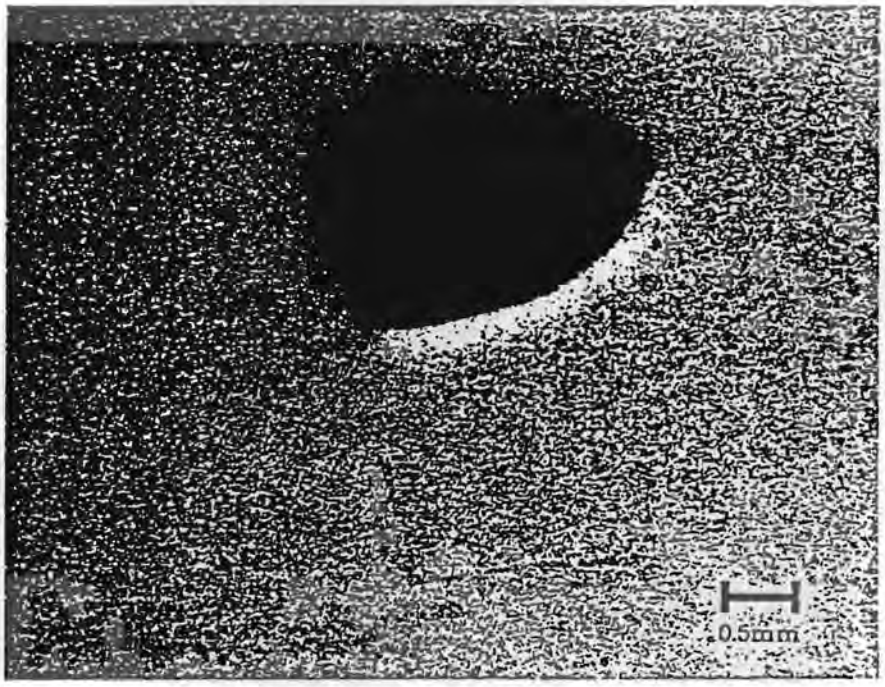

(b) As polished and etched, magnification: 20X

Figure 4.10 DA Photograph of Midland Flaw 1-8 #10b
Photographs provided by the EPRI NDE Center

(a) As machined

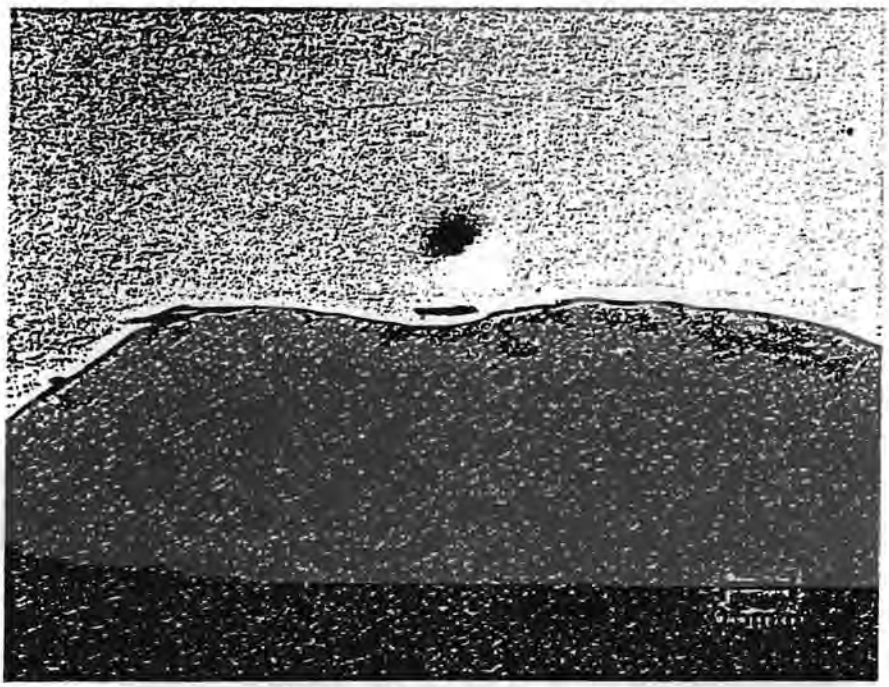

(b) As polished and etched

Figure 4.11 DA Photograph of Midland Flaw 1-8 #11
Photographs provided by EPRI NDE Center

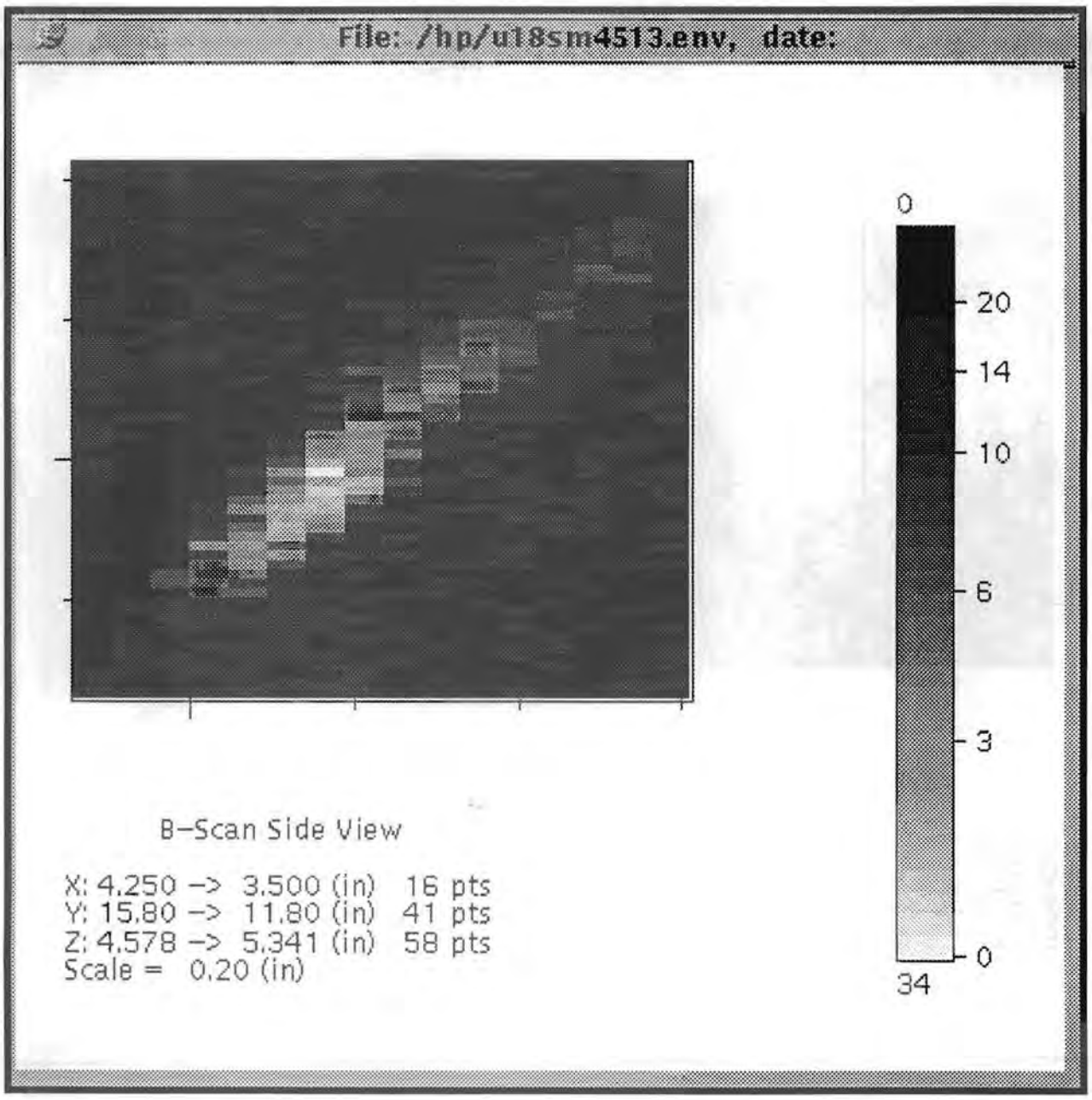

Figure 4.12 Typical Shape for a Reflector in the 45° Shear Inspections. Side View (XZ) of Base-Metal Indication in Block 1-8 at Y = 350 mm. 45° shear inspection from the unclad side. Beam direction is +X. Z values in the figure are measured from the unclad side.

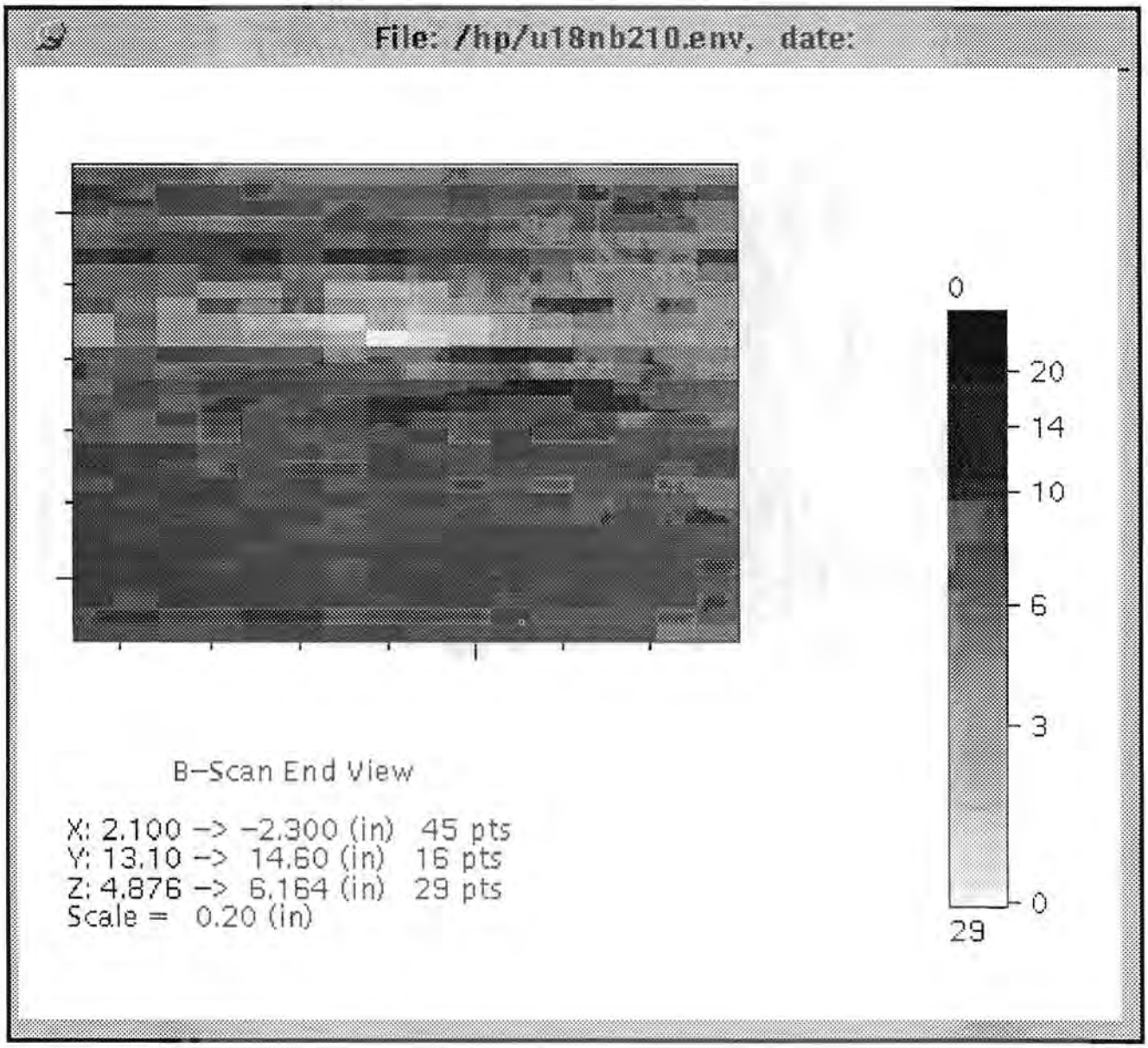

Figure 4.13 Typical Shape for a Reflector in the Normal Beam Data. Side View (XZ) of Base-Metal Indication in Block 1-8 at Y = 350 mm. Normal beam inspection from the unclad side. Z values in the figure are measured from the unclad side.

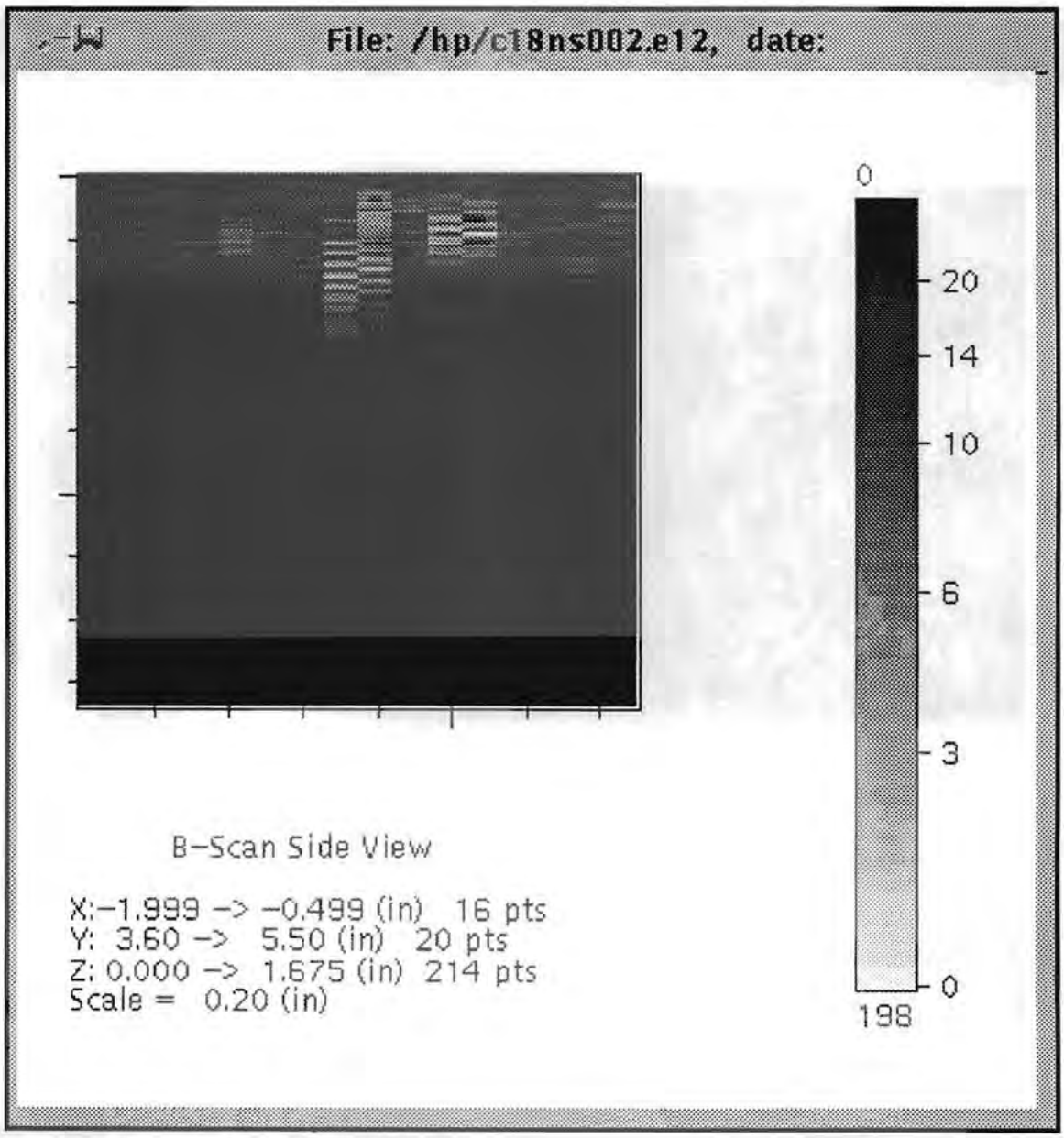

Figure 4.14 Typical Shape for a Reflector in the 70° L-Wave Inspections. Side View (XZ) of Clad to Base-Metal Indication in Block 1-8 at Y = 112 mm. 70° L-wave inspection with beam direction of +X.

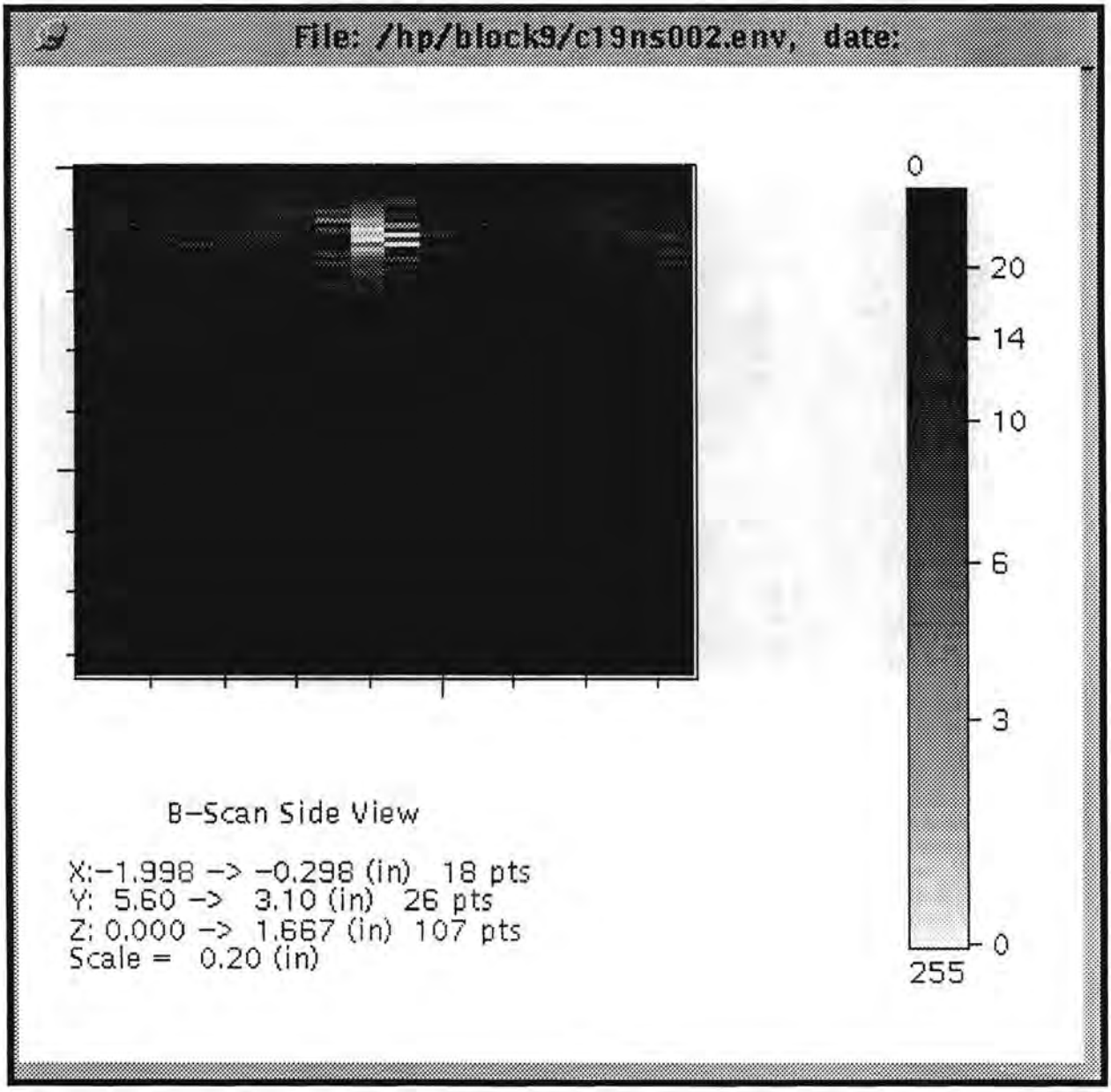

Figure 4.15 Typical Shapeless Image for a Bright Reflection in the 70° L-Wave Inspections. Side View (XZ) of Clad to Base-Metal Indication in Block 1-9 at Y = 117 mm. 70° L-wave inspection with beam direction of +X.

5.0 Analysis of SAFT-UT Data

In this section, the indications detected in the SAFT-UT data are characterized according to location, size, and flaw type. Images are presented in this section for all of the indications. Tables are provided for listing and describing the important attributes of the indications.

SAFT-UT images are presented in three engineering views: side view, end view, and C-scan view. The axes displayed in the images are the scanner's axes and the coordinates are scanner coordinates, not material coordinates. When the scanner axes differs from the material axis, an explanation is given in the figure caption.

The first of the three views in the figures is always the B-scan side view. In this view, the vertical axis is "Z" in scanner coordinates, with axis label given in the form of "Z: X.XXX - Y.YYY" where X.XXX is the coordinate at the top of the vertical axis and Y.YYY is the coordinate at the bottom of the axis. The horizontal axis is "X" in scanner coordinates, and the "Y" axis is perpendicular to the view. The scale given is the distance between the tick marks (minor tick marks included).

The second of the three views is always the B-scan end view. In this view, the vertical axis is "Z" and the horizontal axis is "Y." The third view is always the C-scan end view where the vertical axis is "Y" and the horizontal axis is "X."

The units in the images are given in inches, as determined by the software, and displays in metric units are not available at this time. Metric units are given in the text wherever possible. The tables give material coordinates for the location of the reflectors. Sizing in the tables uses the best available information from the inspections in which a reflector was detected.

For large flaws, a doublet set of time-of-flight (TOF) curves is expected. However, in analyzing the data, there were no cases where a doublet set of TOF curves was detected. The search for doublet TOF curves included exhaustive examination down to the background noise level of the data. Since no doublet TOF curves could be detected, it was postulated that the flaws were very small (no measurable extent along the line of insonification) and that the second TOF curve was merged with the first one.

Using this explanation, it then becomes important to be able to place an upper bound on the extent of a flaw that will cause the two TOF curves to collapse. There are a number of ways that this upper bound can be estimated. Two time-of-flight curves are said to be resolved when there is a 6-dB drop in amplitude between the two curves. This method yields a conservative result. A smaller amplitude drop, 3 dB, can be used to distinguish when a single TOF curve has greater effective ringdown due to the presence of a second curve. Flaws that have extent causing this broadening of the TOF curve can be sized to some degree and an effort should be made to do so.

The SAFT-UT data from the Midland blocks permits recognition that a TOF curve has increased in ringdown size. For the 45° shear inspections at 2.25 MHz, this criterion produces an upper bound flaw size of less than 1.3 mm (0.050 in.). In viewing the images of the responses from some of the indications, the responses tended to be tight packets. For indications imaged with the 70° probe, the upper bound flaw size was larger. For the 3 dB criterion, the upper bound flaw size was determined to be 2.24 mm (0.088 in.).

The lateral resolution of the system determines the minimum size in the plane perpendicular to the insonification direction for small reflectors. The resolution in this plane is on the order of 5.1 mm to 8.13 mm (0.2 in. to 0.32 in.) depending on the spatial sampling used for the various transducers and scans performed.

Since the indications in the Midland vessel had little measurable through-wall extent, it is difficult to characterize the indications as planar or volumetric. Still, it is important to use what features the data provides, and the following rules have been used in characterizing each reflector in the SAFT-UT data. For a reflector to be characterized as a planar flaw, it must be detected in an angle beam inspection or in normal beam from the bottom or top machined surfaces. And in addition, the

reflector must be not detected in a normal beam inspection from the clad or unclad surfaces where adequate coverage is provided by at least one such inspection. All remaining reflectors are considered to be volumetric flaws.

5.1 Indications In and Near the Weld

There were a total of 23 indications that were detected in the SAFT-UT data from the weld and base metal in the four Midland blocks. None of the 23 showed a doublet TOF curve but nine of them had measurable through-wall extent.

5.1.1 Estimation of Weld and Base-Metal Defects in Block 1-8

Twelve indications were found in the weld and base metal in Block 1-8 but none showed measurable broadening of the TOF curve. Table 5.1 shows a direct comparison of the sizes and locations of reflectors in the SAFT-UT data that correspond with flaws found in the destructive analysis. Table 5.2 shows the location and characterization of all indications in the weld and base metal of Block 1-8 that were detected and characterized by SAFT-UT.

Table 5.1. Comparison of SAFT-UT Results with the Destructive Analysis of Weld Root Indications in Block 1-8

Flaw #5	Y, mm (in.)	DY, mm (in.)	X, mm (in.)	DX, mm (in.)	Z, mm (in.)	DZ, mm (in.)	Notes
Destructive Data	380 (15.0)	5 (0.2)	--	--	89 (3.5)	2 (0.1)	X and DX not given but flaw is in the weldment so X is 0 ± 12.7 mm (0.5 in.). See Figure 4.4.
SAFT-UT	380 (15.0)	5 (0.2)	-5 (-0.2)	13 (0.5)	89 (3.5)	1.3 (0.05)	DZ is determined from 45°S inspection from the unclad side. See Figure 5.1d.
Flaw #6t & 6b	**Y, mm (in.)**	**DY, mm (in.)**	**X, mm (in.)**	**DX, mm (in.)**	**Z, mm (in.)**	**DZ, mm (in.)**	**Notes**
Destructive Data	350 (13.8)	2.0 (0.08) 3.5 (0.14)	--	--	99 (3.9)	1.5 (0.06) 2.5 (0.10)	See Figures 4.5 and 4.6.
SAFT-UT	350 (13.8)	10 (0.4)	-10 (-0.4)	18 (0.7)	91 (3.6)	1.3 (0.05)	DZ is determined from 45°S inspection from the unclad side. See Figure 5.2g.

Table 5.2. SAFT-UT Results from Weld and Base Metal of Block 1-8

Y, mm (in.)	DY, mm (in.)	X, mm (in.)	DX, mm (in.)	Z, mm (in.)	DZ, mm (in.)	Characterization
380 (15.0)	5 (0.2)	-5 (-0.2)	13 (0.5)	89 (3.5)	1.3 (0.05)	Detected by SAFT-UT in normal beam from the clad side and in two different 45°S files from the unclad side. See Figure 5.1. DZ is determined from data shown in Figure 5.1d. This is one or more small volumetric defects. Destructive analysis shows one defect labeled 5T. See Table 4.1 and Figure 4.4 for DA results.
351 (13.8)	20 (0.8)	-10 (-0.4)	18 (0.7)	91 (3.6)	1.3 (0.05)	Detected by SAFT-UT in 45°S files from the unclad side. See Figure 5.2. DZ is determined from data shown in Figure 5.2g. This is one or more small planar defects. Destructive analysis shows two small defects label 6t and 6b. See Table 4.1 and Figure 4.5 for DA results.
318 (12.5)	15 (0.6)	-10 (-0.4)	13 (0.5)	91 (3.6)	1.3 (0.05)	Detected by SAFT-UT in normal beam from the clad side and in a 45°S inspection from the clad side. See Figure 5.3. This is a volumetric defect. DZ is estimated from Figure 5.3d.
249 (9.8)	5 (0.2)	0.0 (0.0)	20 (0.8)	109 (4.3)	1.3 (0.05)	Detected by SAFT-UT in normal beam from clad and unclad side. Also detected in 45°S files from the clad side. See Figure 5.4. This is a small volumetric defect. DZ is estimated from Figures 5.4k and 5.4g. DX is estimated from Figure 5.4h, and DY is estimated from Figure 5.4e.
-127 (-5.0)	10 (0.4)	0.00 (0.0)	15 (0.6)	112 (4.4)	-	Detected by SAFT-UT in normal beam from the clad side. See Figure 5.5. No estimate is made for DZ since this reflector is only detected in normal beam from the clad side. This is one or more small volumetric defects.
-249 (-9.8)	10 (0.4)	13 (0.5)	8 (0.3)	79 (3.1)	-	Detected by SAFT-UT in normal beam from the clad side. See Figure 5.6. No estimate is made for DZ since this reflector is only detected in normal beam from the clad side. This is a small volumetric defect.
-391 (-15.4)	10 (0.4)	5 (0.2)	8 (0.3)	86 (3.4)	-	Detected by SAFT-UT in normal beam from the clad side. See Figure 5.7. No estimate is made for DZ since this reflector is only detected in normal beam from the clad side. This is a small volumetric defect.
-465 (-18.3)	15 (0.6)	20 (0.8)	-	109 (4.3)	1.3 (0.05)	Detected by SAFT-UT in 45°S from the unclad side. See Figure 5.8. DZ is estimated from Figure 5.8a. No estimate is made for DX. DY is estimated from Figure 5.8b. This is a small defect, possibly planar since it was not detected in normal beam. But, confidence is

Y, mm (in.)	DY, mm (in.)	X, mm (in.)	DX, mm (in.)	Z, mm (in.)	DZ, mm (in.)	Characterization
						limited by the lack of coverage from the clad side. An indication was reported at this location by NDE center UT. Destructive analysis did not find a defect.
-71 (-2.8)	15 (0.6)	-15 (-0.6)	10 (0.4)	183 (7.2)	-	Detected by SAFT-UT in normal beam from the clad side. See Figure 5.9. No estimate is made for DZ since this reflector is only detected in normal beam from the clad side. This is a small volumetric defect.
-185 (-7.3)	25 (1.0)	2.5 (0.1)	51 (2.0)	155 (6.1)	-	Detected by SAFT-UT in normal beam from the clad side. See Figure 5.10. No estimate is made for DZ since this reflector is only detected in normal beam from the clad side. This is probably multiple volumetric defects.
-254 (-10.0)	20 (0.8)	-13 (-0.5)	13 (0.5)	183 (7.2)	-	Detected by SAFT-UT in normal beam from the clad side. See Figure 5.11. No estimate is made for DZ since this reflector is only detected in normal beam from the clad side. This is probably multiple small volumetric defects.
-325 (-12.8)	19 (0.75)	38 (1.5)	13 (0.5)	208 (8.2)	-	Detected by SAFT-UT in normal beam from the clad side. See Figure 5.12. No estimate is made for DZ since this reflector is only detected in normal beam from the clad side. This is probably multiple small volumetric defects.

5.1.2 Indications of Weld and Base-Metal Defects in Block 1-9

Eight indications were found in the weld and base metal in Block 1-9. Four of the eight are within ± 1 in. of the weld center line and are considered to be associated with the weld. The other four are outside this zone and are considered to be indications from the parent material. Seven of the eight showed measurable depth extent. Table 5.3 shows the location and characterization of all indications in the base metal of Block 1-9 that were detected and characterized by SAFT-UT.

Table 5.3. SAFT-UT Results from Weld and Base Metal of Block 1-9

Y, mm (in.)	DY, mm (in.)	X, mm (in.)	DX, mm (in.)	Z, mm (in.)	DZ, mm (in.)	Characterization
Indications in and near the Weld of the Base Metal						
-582 (-22.9)	36 (1.4)	18 (-0.7)	-	178 (7.0)	18 (0.7)	Detected by SAFT-UT in normal beam from the bottom side. See Figure 5.13. This is probably multiple planar defects separated by 36 mm (1.4 in.) in Y.
-584 (-23.0)	23 (0.9)	-43 (-1.7)	-	145 (5.7)	<5 (<0.2)	Detected by SAFT-UT in normal beam from the bottom side. See Figure 5.14. This is either small planar defects separated by 23 mm (0.9 in.) in Y or a single planar defect of the size noted.
-597 (-23.5)	-	-66 (-2.6)	-	178 (7.0)	10 (0.4)	Detected by SAFT-UT in normal beam from bottom side. See Figure 5.15. Only part of the defect was insonified by SAFT-UT. This is probably a small planar defect of the size noted.
-221 (-8.7)	13 (0.5)	-30 (-1.2)	-	64 (2.5)	5 (0.2)	Detected by SAFT-UT in normal beam from the bottom side. See Figure 5.16. This is probably a single planar defect of the size noted.
-69 (-2.7)	13 (0.5)	2 (0.1)	-	114 (4.5)	5 (0.2)	Detected by SAFT-UT in normal beam from the bottom side. See Figure 5.17. This is a small planar defect.
183 (7.2)	25 (1.0)	-2 (-0.1)	-	121 (4.8)	8 (0.3)	Detected by SAFT-UT in normal beam from the bottom side. See Figure 5.18. This is a small planar defect.
203 (8.0)	10 (0.4)	0 (0.0)	5 (0.2)	119 (4.7)	-	Detected by SAFT-UT in normal beam from the clad side. See Figure 5.19. No estimate is made for DZ since this reflector is only detected in normal beam from the clad side. This is a small volumetric defect.
185 (7.3)	23 (0.9)	76 (3.0)	5 (0.2)	206 (8.1)	-	Detected by SAFT-UT in normal beam from the clad side. See Figure 5.20. No estimate is made for DZ since this reflector is only detected in normal beam from the clad side. This is a small volumetric defect.

5.1.3 Indications of Weld and Base-Metal Defects in Block 1-11

Two indications were found in the weld and base metal in Block 1-11. Both of the indications showed measurable depth extent. Table 5.4 shows the location and characterization of the two indications in the base metal that were detected and characterized by SAFT-UT.

Table 5.4. SAFT-UT Results from Block 1-11

Y, mm (in.)	DY, mm (in.)	X, mm (in.)	DX, mm (in.)	Z, mm (in.)	DZ, mm (in.)	Characterization
-152 (-6.0)	10 (0.4)	8 (0.3)	-	132 (5.2)	2 (0.1)	Detected by SAFT-UT in normal beam from the top side. See Figure 5.21. This is a small planar defect.
-140 (-5.5)	20 (0.8)	-13 (-0.5)	-	150 (5.9)	2 (0.1)	Detected by SAFT-UT in normal beam from the top side. See Figure 5.22. This is either small planar defects separated by 20 mm or a single planar defect of the size noted.

5.1.4 Indications of Weld and Base-Metal Defects in Block 1-12

One indications was found in the base metal in block 1-12. Table 5.5 shows the location and characterization of the indication.

Table 5.5. SAFT-UT Results from Block 1-12

Y, mm (in.)	DY, mm (in.)	X, mm (in.)	DX, mm (in.)	Z, mm (in.)	DZ, mm (in.)	Characterization
-96 (-3.8)	10 (0.4)	-13 (-0.5)	-	119 (4.7)	2 (0.1)	Detected by SAFT-UT in normal beam from the top side. See Figure 5.23. This is a small planar defect.

5.2 Indications Near the Clad-to-Base Metal Interface

Table 5.6 shows a direct comparison of the sizes and locations of the reflectors in the SAFT-UT data that correspond with flaws found in the destructive analysis. There were a total of eight indications that were detected in the SAFT-UT data from the clad-to-base metal interface in four Midland blocks. All of the SAFT-UT data were analyzed using the method described in Section 4.2.1.

Table 5.6. Comparison of SAFT-UT Results with the Destructive Analysis of Block 1-8 (Near-Surface Zone Indications)

Flaw #7	Y, mm (in.)	DY, mm (in.)	X, mm (in.)	DX, mm (in.)	Z, mm (in.)	DZ, mm (in.)	Notes
Destructive Data	81 (3.2)	--	-22 (-0.8)	4 (0.16)	7 (0.27)	1 (0.04)	See Figure 4.7.
SAFT-UT	89 (3.5)	5 (0.2)	8 (0.3)	5 (0.2)	8 (0.3)	<2.2 (<0.09)	See Figure 5.26. There is a sign difference between the destructive analysis and the SAFT-UT data for X. The origin of this difference is not known.
Flaw #8	**Y, mm (in.)**	**DY, mm (in.)**	**X, mm (in.)**	**DX, mm (in.)**	**Z, mm (in.)**	**DZ, mm (in.)**	**Notes**
Destructive Data	112 (4.4)	--	33 (1.3)	5 (0.2)	10 (0.4)	2 (0.08)	See Figure 4.8.
SAFT-UT	112 (4.4)	5 (0.2)	-33 (-1.3)	5 (0.2)	10 (0.4)	<2.2 (<0.09)	See Figure 5.27. There is a sign difference between the destructive analysis and the SAFT-UT data for X. The origin of this difference is not known.
Flaw #11	**Y, mm (in.)**	**DY, mm (in.)**	**X, mm (in.)**	**DX, mm (in.)**	**Z, mm (in.)**	**DZ, mm (in.)**	**Notes**
Destructive Data	235 (9.2)	--	-15 (-0.6)	1.5 (0.06)	6 (0.24)	0.5 (0.02)	See Figure 4.11.
SAFT-UT	236 (9.3)	5 (0.2)	18 (0.7)	5 (0.2)	5 (0.2)	<2.2 (<0.09)	See Figure 5.28. There is a sign difference between the destructive analysis and the SAFT-UT data for X. The origin of this difference is not known.

5.2.1 Estimation of Defects at the Clad-to-Base Metal Interface in Block 1-8

Six indications were found at the clad-to-base metal interface in Block 1-8. Table 5.7 shows the location and characterization of all indications in Block 1-8 that were detected and characterized by SAFT-UT.

Table 5.7. SAFT-UT Results from the Clad-to-Base Metal Interface of Block 1-8

Y, mm (in.)	DY, mm (in.)	X, mm (in.)	DX, mm (in.)	Z, mm (in.)	DZ, mm (in.)	Characterization
-526 (-20.7)	5 (0.2)	-20 (-0.8)	5 (0.2)	5 (0.2)	<2.2 (<0.09)	Detected by SAFT-UT in 70° L-wave inspection in the +X direction only. See Figure 5.24. This is a volumetric defect.
-211 (-8.3)	2 (0.1)	-20 (-0.8)	5 (0.2)	5 (0.2)	<2.2 (<0.09)	Detected by SAFT-UT in 70° L-wave inspection in the +X direction only. See Figure 5.25. This is a volumetric defect.
89 (3.5)	5 (0.2)	8 (0.3)	5 (0.2)	8 (0.3)	<2.2 (<0.09)	Detected by SAFT-UT in 70° L-wave inspection in the +X direction only. See Figure 5.26. This is a volumetric defect. Destructive analysis shows one small defect labeled #7. See Table 4.1 and Figure 4.6 for DA results.
112 (4.4)	5 (0.2)	-33 (-1.3)	5 (0.2)	10 (0.4)	<2.2 (<0.09)	Detected by SAFT-UT in 70° L-wave inspections in the +X and -X directions. See Figure 5.27. This is a volumetric defect. Destructive analysis shows one defect labeled #8. See Table 4.1 and Figure 4.7 for DA results. This indication had been conservatively called planar in Doctor (1991). DA confirms volumetric.
236 (9.3)	5 (0.2)	18 (0.7)	5 (0.2)	5 (0.2)	<2.2 (<0.09)	Detected by SAFT-UT in 70° L-wave inspection in the -X direction only. See Figure 5.28. This is a volumetric defect. Destructive analysis shows one small defect labeled #11. See Table 4.1 and Figure 4.10 for DA results.
442 (17.4)	15 (0.6)	-23 (-0.9)	5 (0.2)	5 (0.2)	<2.2 (<0.09)	Detected by SAFT-UT in 70° L-wave inspection in the +X direction. See Figure 5.29. This is a volumetric defect.

5.2.2 Estimation of Defects at the Clad-to-Base Metal Interface in Block 1-9

One indication was found at the clad-to-base metal interface in Block 1-9. Table 5.8 shows the location and characterization of the one indication found by SAFT-UT in Block 1-9 at the clad-to-base metal interface.

Table 5.8. SAFT-UT Results from the Clad-to-Base Metal Interface of Block 1-9

Y, mm (in.)	DY, mm (in.)	X, mmm (in.)	DX, mm (in.)	Z, mm (in.)	DZ, mm (in.)	Characterization
117 (4.6)	15 (0.6)	-30 (-1.2)	5 (0.2)	5 (0.2)	<2.2 (<0.09)	Detected by SAFT-UT in 70° L-wave inspection in the +X direction. See Figure 5.30. This is either two small volumetric defects or a larger defect of the size noted.

5.2.3 Estimation of Defects at the Clad-to-Base Metal Interface in Block 1-11

One indication was found at the clad-to-base metal interface in Block 1-11. Table 5.9 shows the location and characterization of one indications found by SAFT-UT in Block 1-11.

Table 5.9. SAFT-UT Results from the Clad-to-Base Metal Interface of Block 1-11

Y, mm (in.)	DY, Mm (in.)	X, mm (in.)	DX, mm (in.)	Z, mm (in.)	DZ, mm (in.)	Characterization
387 (15.3)	23 (0.9)	8 (0.3)	5 (0.2)	11 (0.45)	<2.2 (<0.09)	Detected by SAFT-UT in 70° L-wave inspection in the -X direction only. See Figure 5.31. This is the deepest of the 8 indications found in the near-surface zone. Because no destructive data exists to prove otherwise, this indication is conservatively assumed to be planar.

5.2.4 Estimation of Defects at the Clad-to-Base Metal Interface in Block 1-12

No indications were found at the clad-to-base metal interface in Block 1-12.

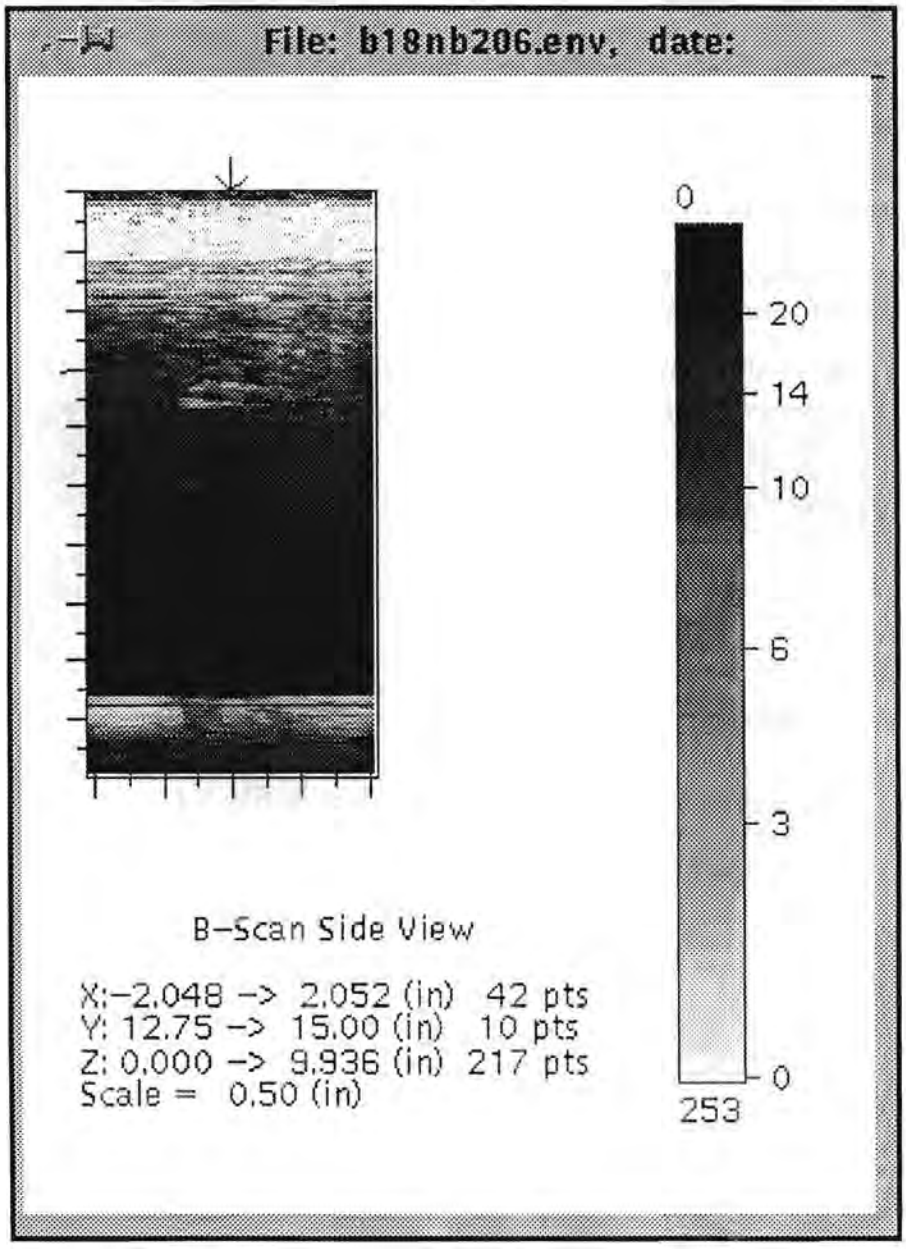

Figure 5.1a Side View (XZ) of Base-Metal Indication in Block 1-8 at Y = 381 mm (15.0 in.). Normal beam inspection from the clad side. This indication corresponds to flaw #5 in the destructive analysis.

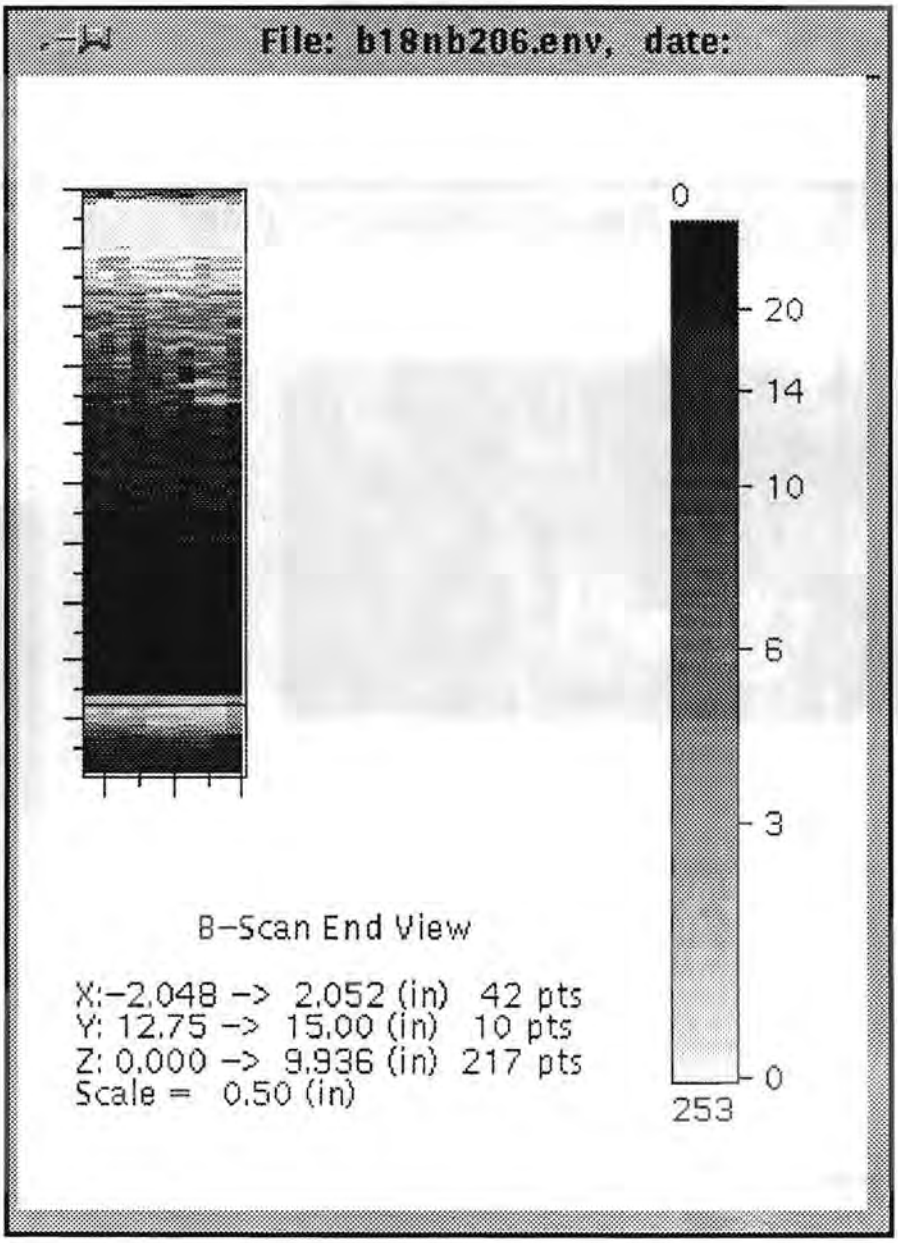

Figure 5.1b End View (YZ) of Base-Metal Indication in Block 1-8 at Y = 381 mm (15.0 in.). Normal beam inspection from the clad side. This indication corresponds to flaw #5 in the destructive analysis.

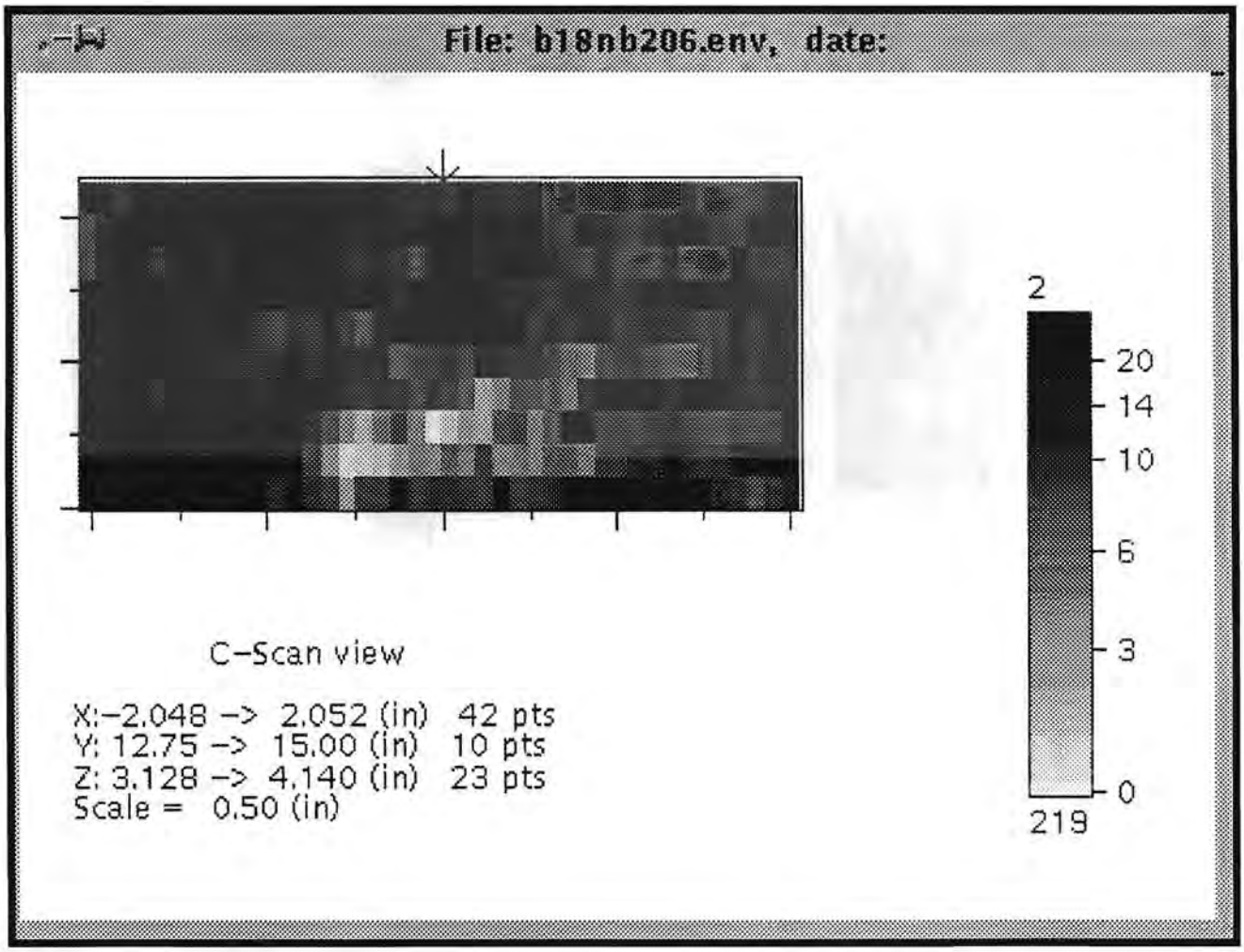

Figure 5.1c C-scan View (XY) of Base-Metal Indication in Block 1-8 at Y = 381 mm (15.0 in.). Normal beam inspection from the clad side. This indication corresponds to flaw #5 in the destructive analysis.

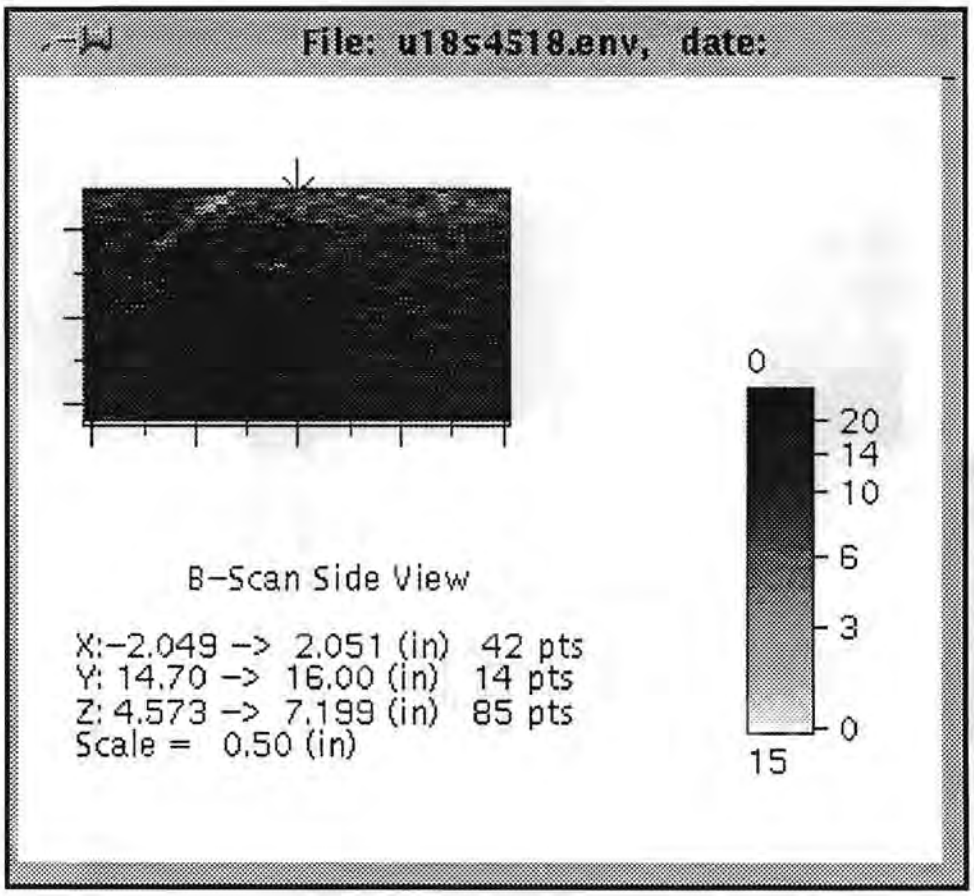

Figure 5.1d Side View (XZ) of Base-Metal Indication in Block 1-8 at Y = 381 mm (15.0 in.). 45° shear inspection from the unclad side. Beam direction is +X. Z values in the figure are measured from the unclad side. This indication corresponds to flaw #5 in the destructive analysis.

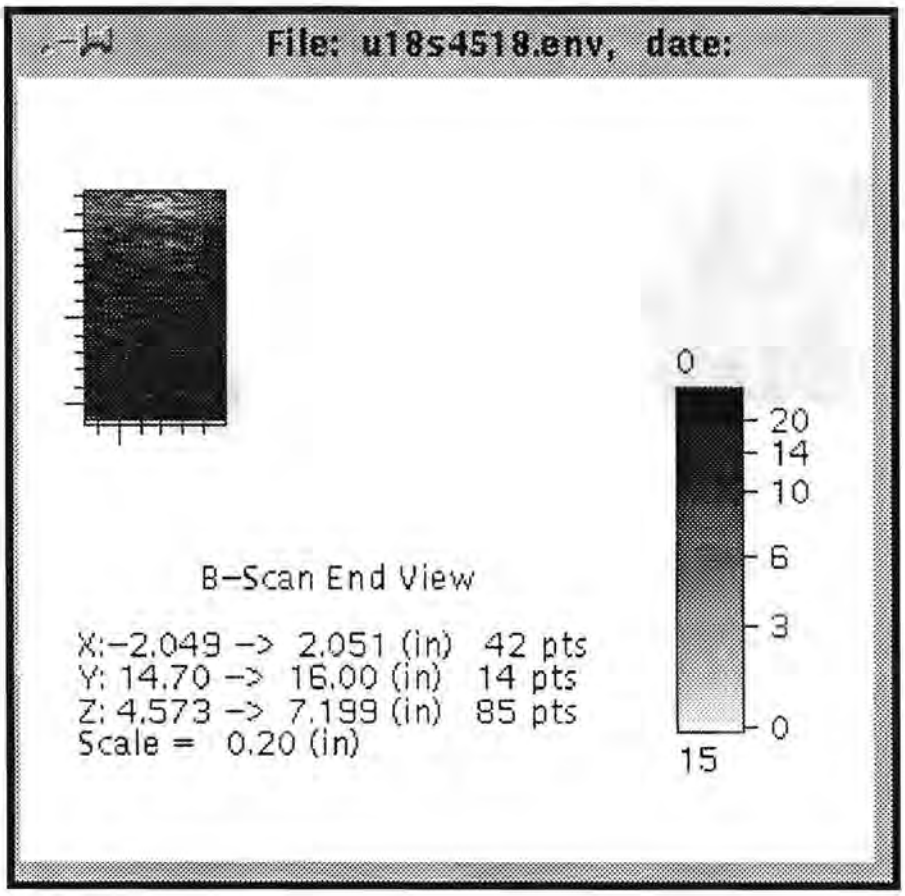

Figure 5.1e End View (YZ) of Base-Metal Indication in Block 1-8 at Y = 381 mm (15.0 in.). 45° shear inspection from the unclad side. Beam direction is +X. Z values in the figure are measured from the unclad side. This indication corresponds to flaw #5 in the destructive analysis.

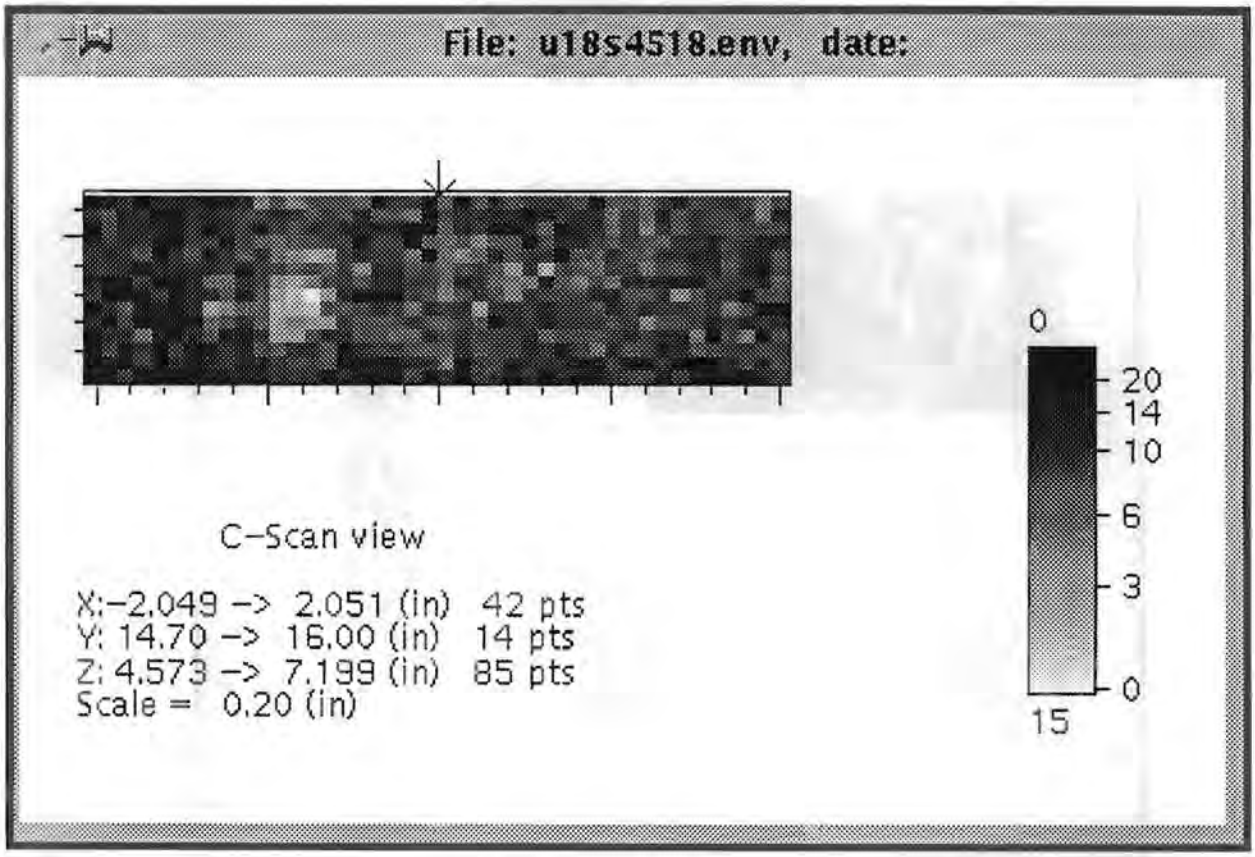

Figure 5.1f C-scan View (XY) of Base-Metal Indication in Block 1-8 at Y = 381 mm (15.0 in.). 45° shear inspection from the unclad side. Beam direction is +X. Z values in the figure are measured from the unclad side. This indication corresponds to flaw #5 in the destructive analysis.

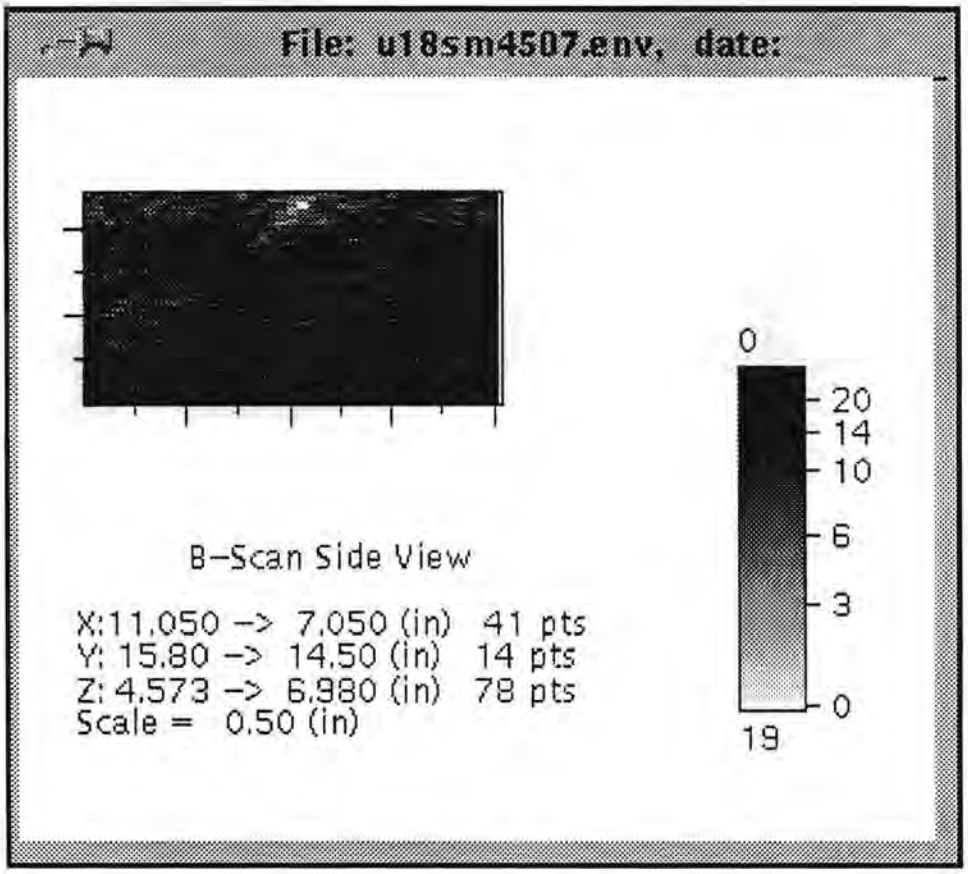

Figure 5.1g Side View (XZ) of Base-Metal Indication in Block 1-8 at Y = 381 mm (15.0 in.). 45° shear inspection from the unclad side. Beam direction is -X. Z values in the figure are measured from the unclad side. X values in the figure are +2 to -2 inches in material coordinates. This indication corresponds to flaw #5 in the destructive analysis.

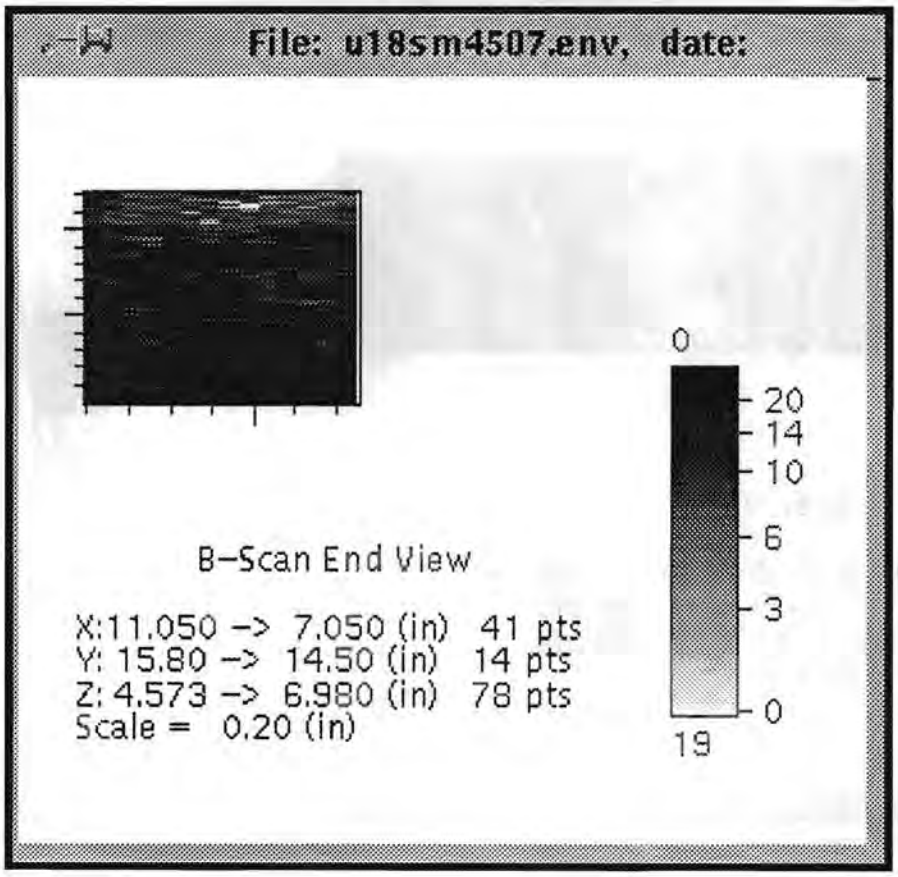

Figure 5.1h Side View (YZ) of Base-Metal Indication in Block 1-8 at Y = 381 mm (15.0 in.). 45° shear inspection from the unclad side. Beam direction is -X. Z values in the figure are measured from the unclad side. X values in the figure are +2 to -2 inches in material coordinates. This indication corresponds to flaw #5 in the destructive analysis.

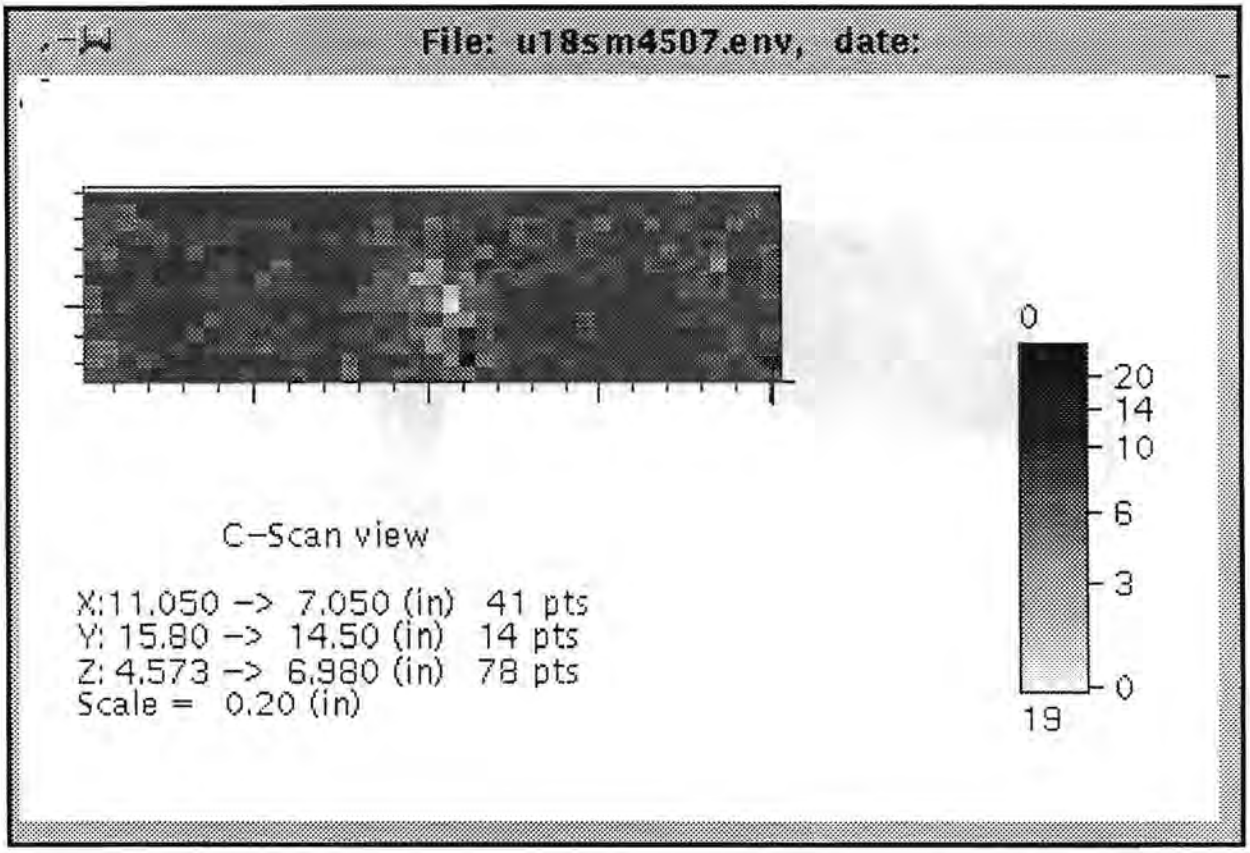

Figure 5.1i C-scan View (XY) of Base-Metal Indication in Block 1-8 at Y = 381 mm (15.0 in.). 45° shear inspection from the unclad side. Beam direction is -X. Z values in the figure are measured from the unclad side. X values in the figure are +2 to -2 inches in material coordinates. This indication corresponds to flaw #5 in the destructive analysis.

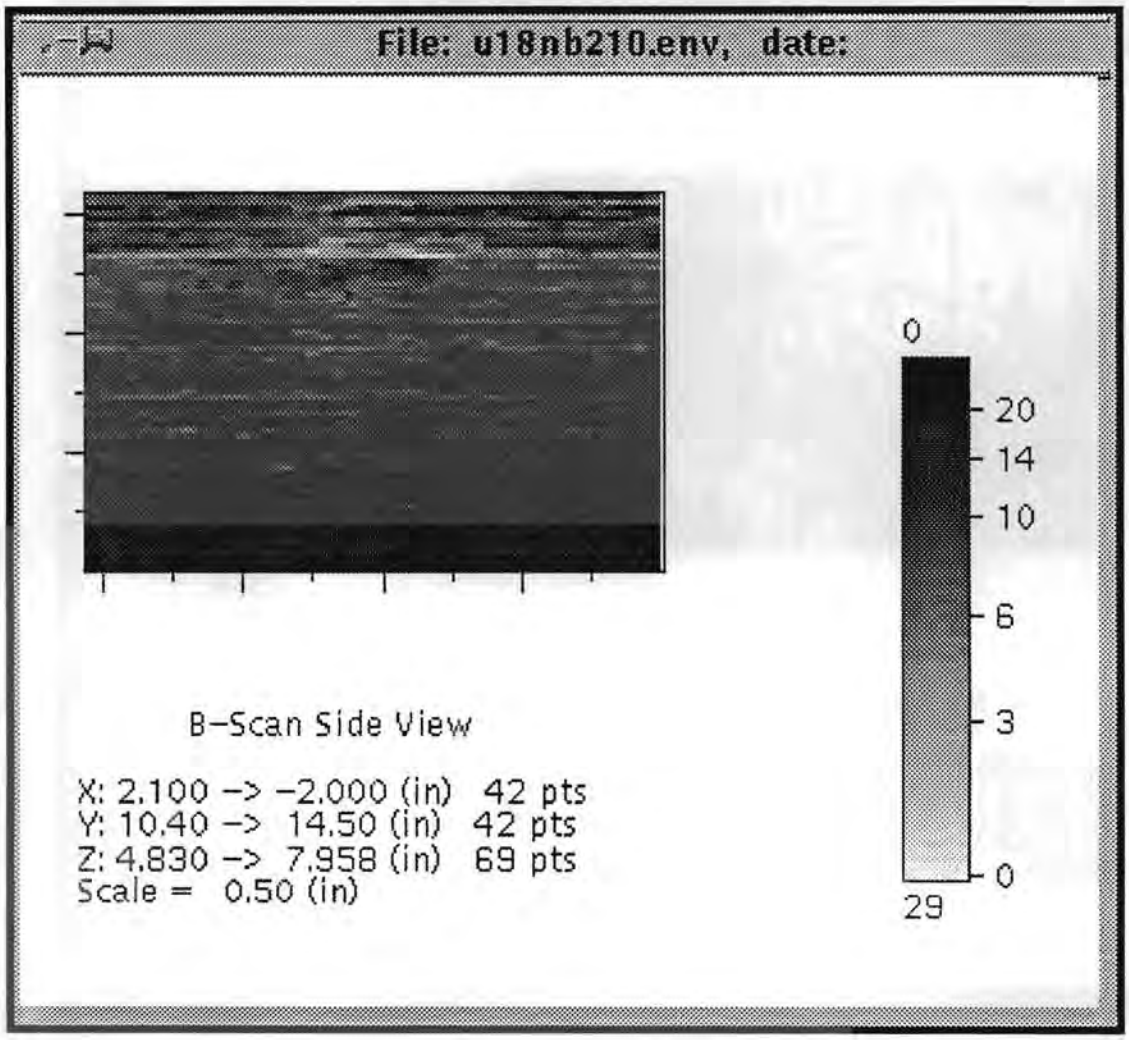

Figure 5.2a Side View (XZ) of Base-Metal Indication in Block 1-8 at Y = 351 mm (13.8 in.). Normal beam inspection from the unclad side. Z values in the figure are measured from the unclad side. This indication corresponds to flaw #6 in the destructive analysis.

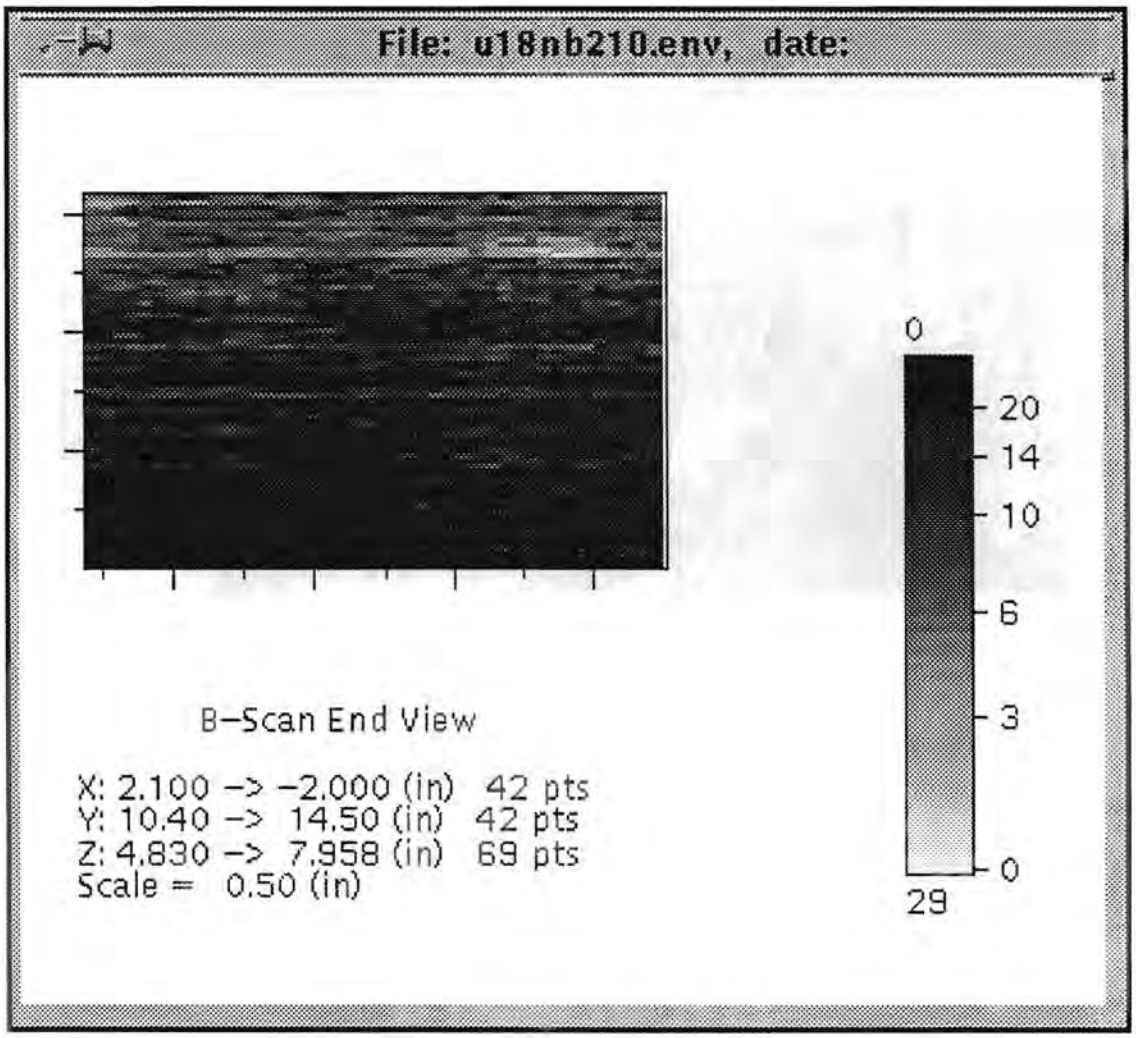

Figure 5.2b End View (YZ) of Base-Metal Indication in Block 1-8 at Y = 351 mm (13.8 in.). Normal beam inspection from the unclad side. Z values in the figure are measured from the unclad side. This indication corresponds to flaw #6 in the destructive analysis.

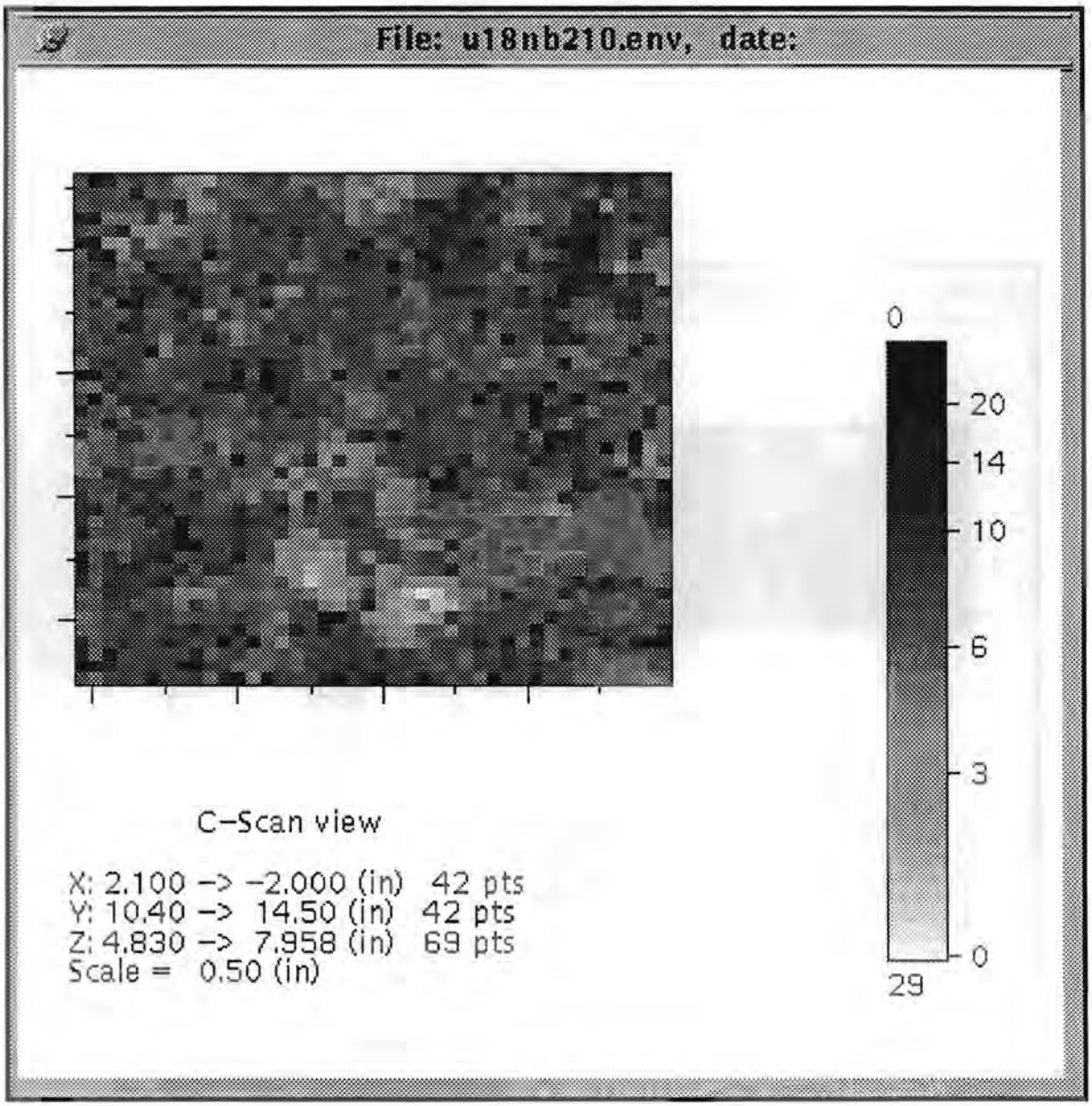

Figure 5.2c C-scan View (XY) of Base-Metal Indication in Block 1-8 at Y = 351 mm (13.8 in.). Normal beam inspection from the unclad side. Z values in the figure are measured from the unclad side. This indication corresponds to flaw #6 in the destructive analysis.

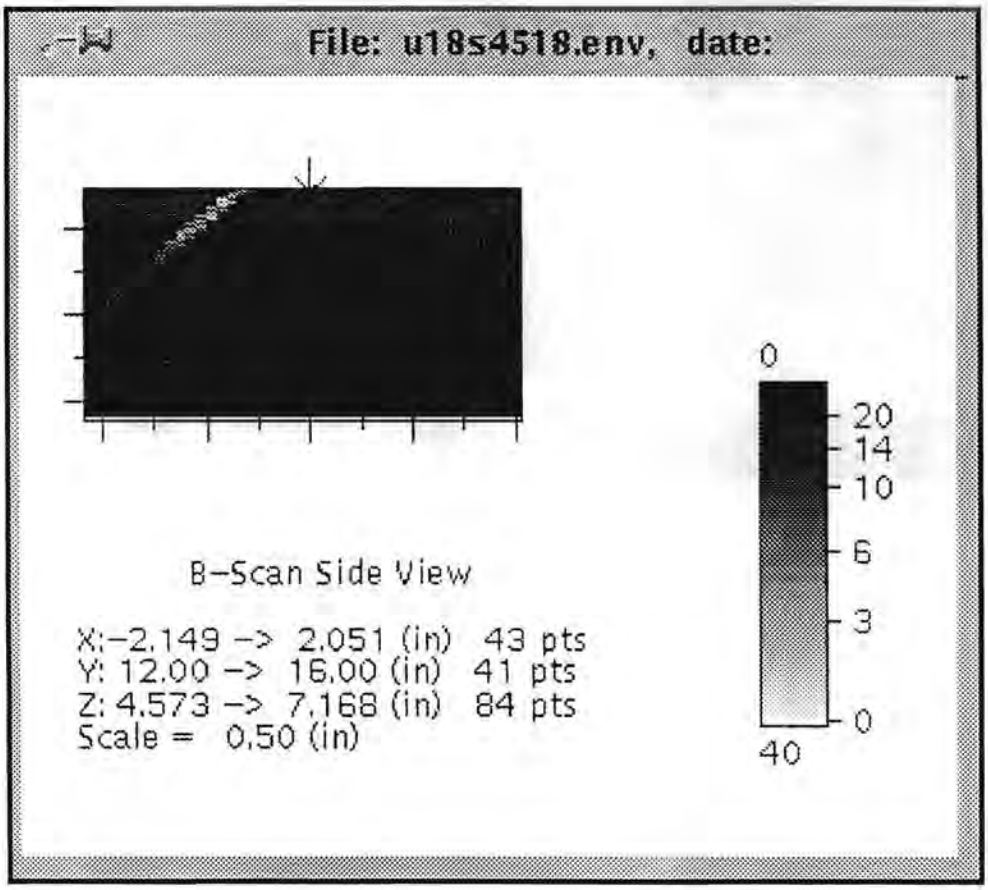

Figure 5.2d Side View (XZ) of Base-Metal Indication in Block 1-8 at Y = 351 mm (13.8 in.). 45° shear inspection from the unclad side. Beam direction is +X. Z values in the figure are measured from the unclad side. This indication corresponds to flaw #6 in the destructive analysis.

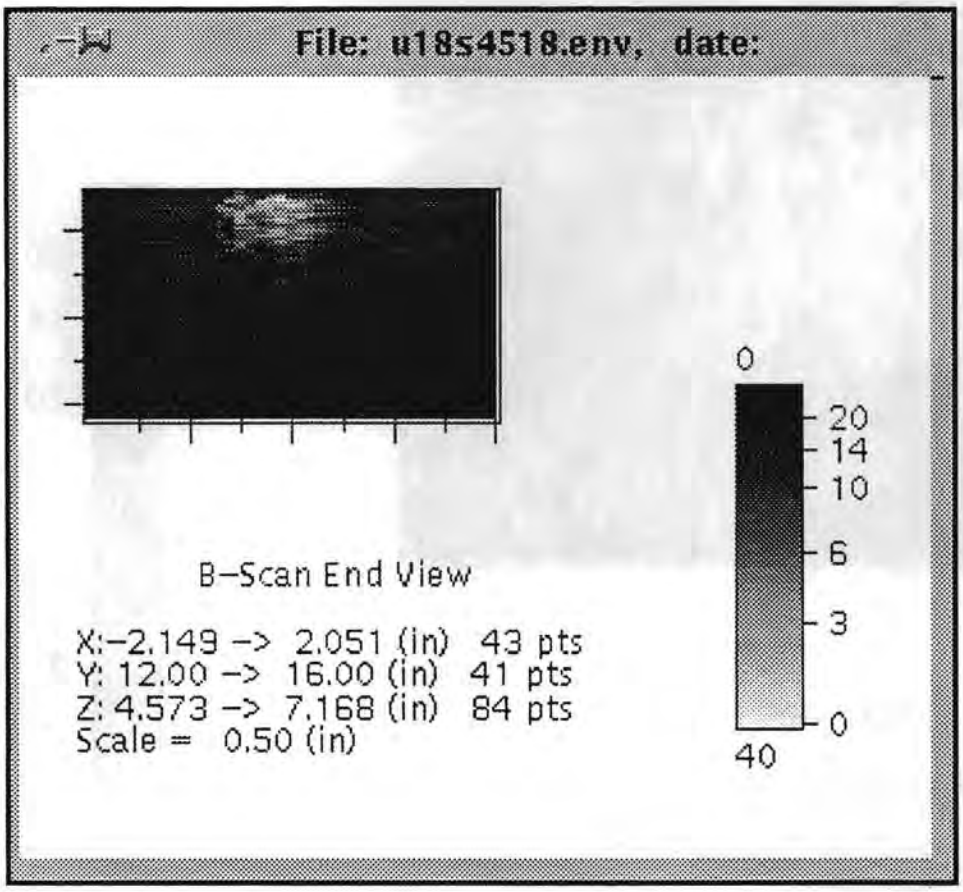

Figure 5.2e End View (YZ) of Base-Metal Indication in Block 1-8 at Y = 13.8 45° shear inspection from the unclad side. Beam direction is +X. Z values in the figure are measured from the unclad side. This indication corresponds to flaw #6 in the destructive analysis.

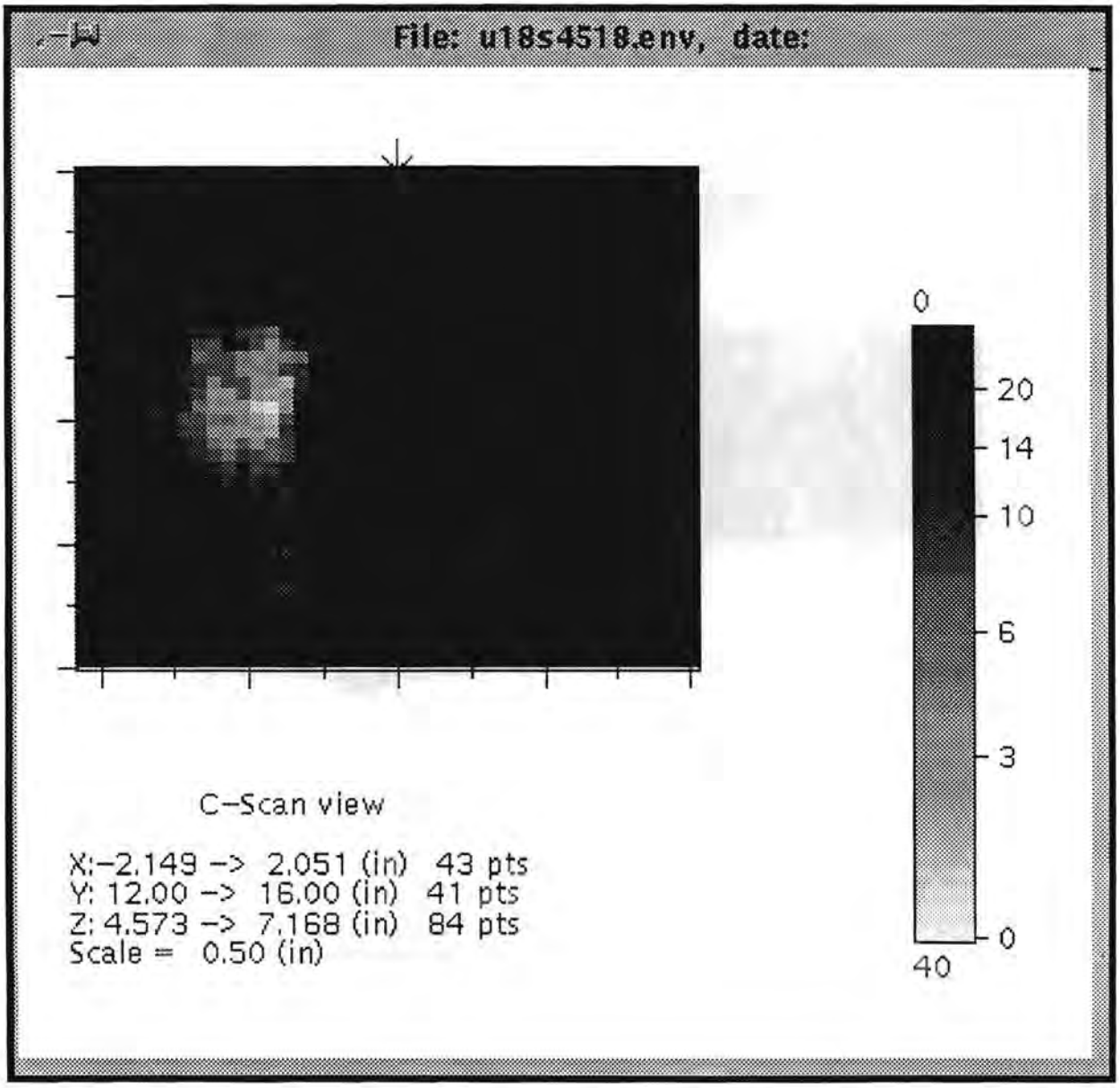

Figure 5.2f C-scan View (XY) of Base-Metal Indication in Block 1-8 at Y = 351 mm (13.8 in.). 45° shear inspection from the unclad side. Beam direction is +X. Z values in the figure are measured from the unclad side. This indication corresponds to flaw #6 in the destructive analysis.

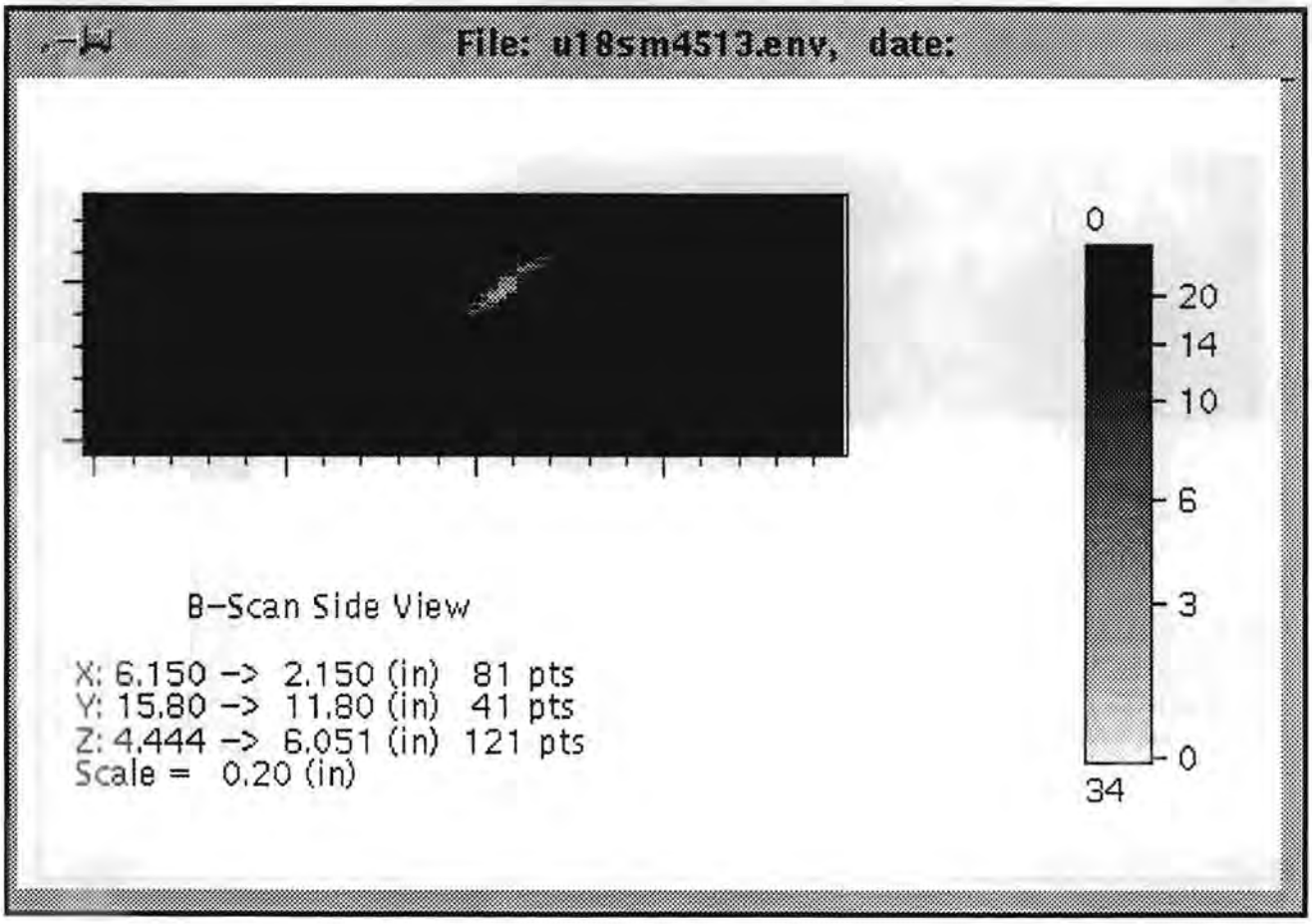

Figure 5.2g Side View (XZ) of Base-Metal Indication in Block 1-8 at Y = 351 mm (13.8 in.). 45° shear inspection from the unclad side. Beam direction is -X. Z values in the figure are measured from the unclad side. X values in the figure are +2 to -2 inches in material coordinates. This indication corresponds to flaw #6 in the destructive analysis.

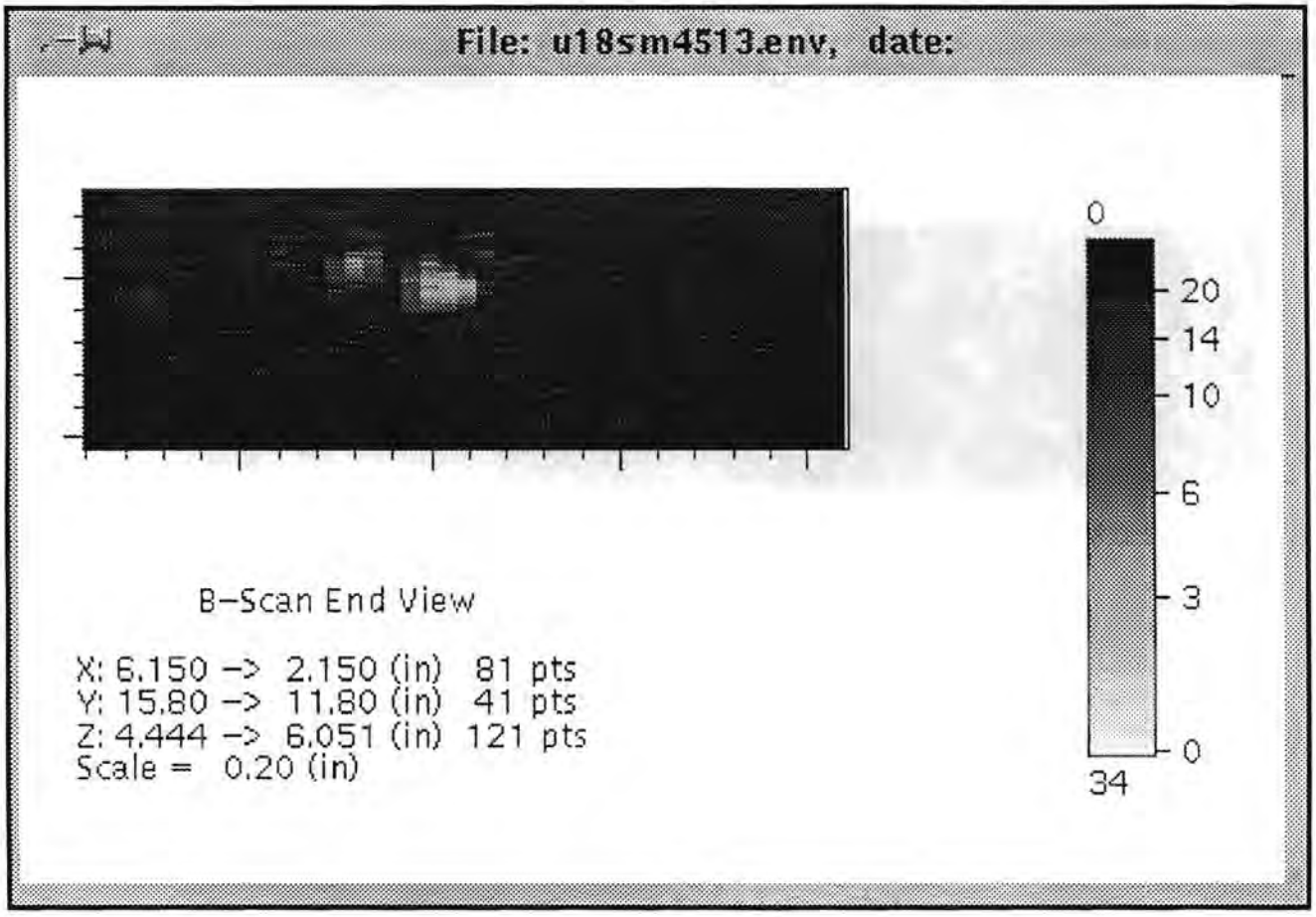

Figure 5.2h Side View (YZ) of Base-Metal Indication in Block 1-8 at Y = 351 mm (13.8 in.). 45° shear inspection from the unclad side. Beam direction is -X. Z values in the figure are measured from the unclad side. X values in the figure are +2 to -2 inches in material coordinates. This indication corresponds to flaw #6 in the destructive analysis.

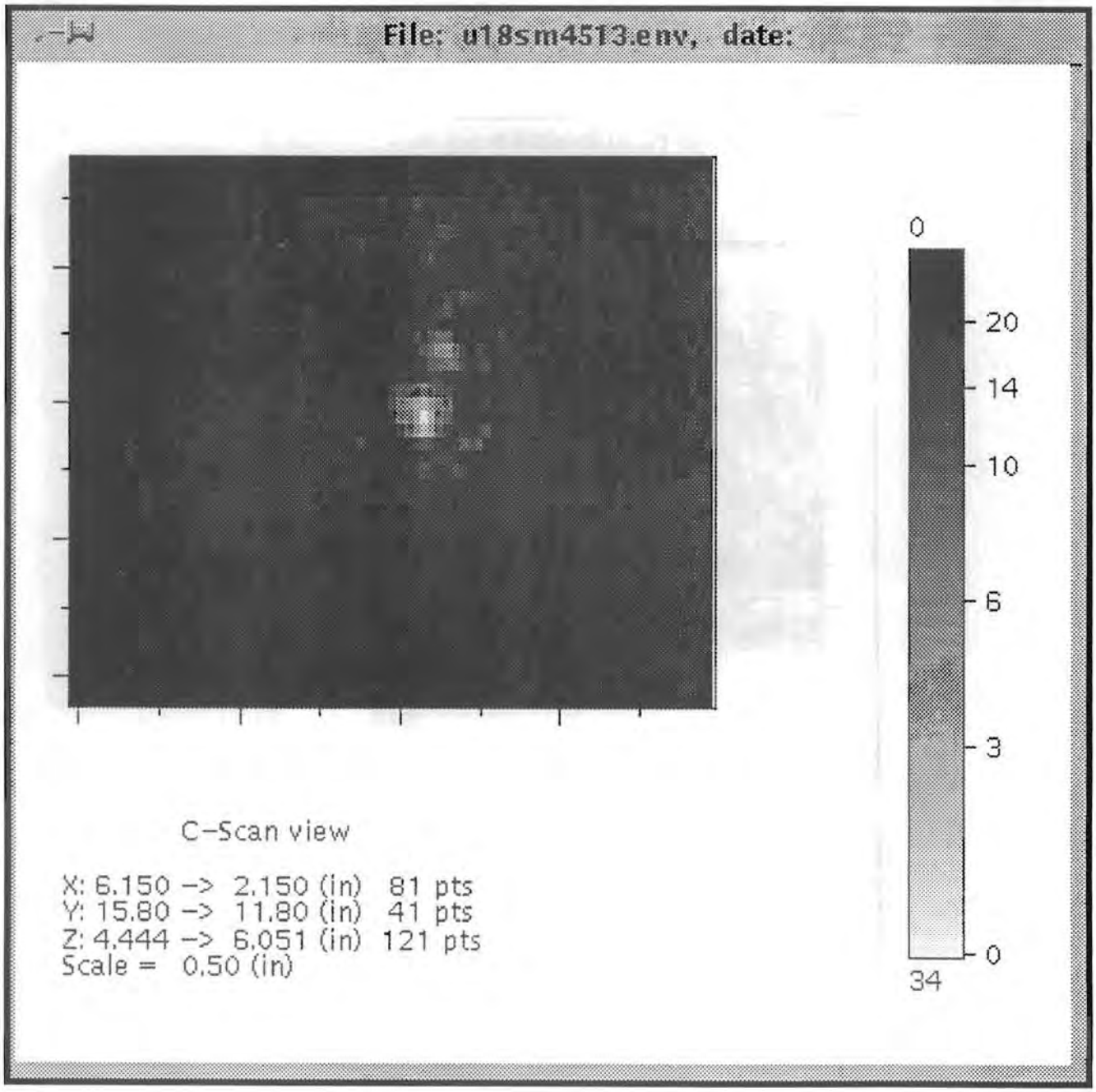

Figure 5.2i C-scan View (XY) of Base-Metal Indication in Block 1-8 at Y = 351 mm (13.8 in.). 45° shear inspection from the unclad side. Beam direction is -X. Z values in the figure are measured from the unclad side. X values in the figure are +2 to -2 inches in material coordinates. This indication corresponds to flaw #6 in the destructive analysis.

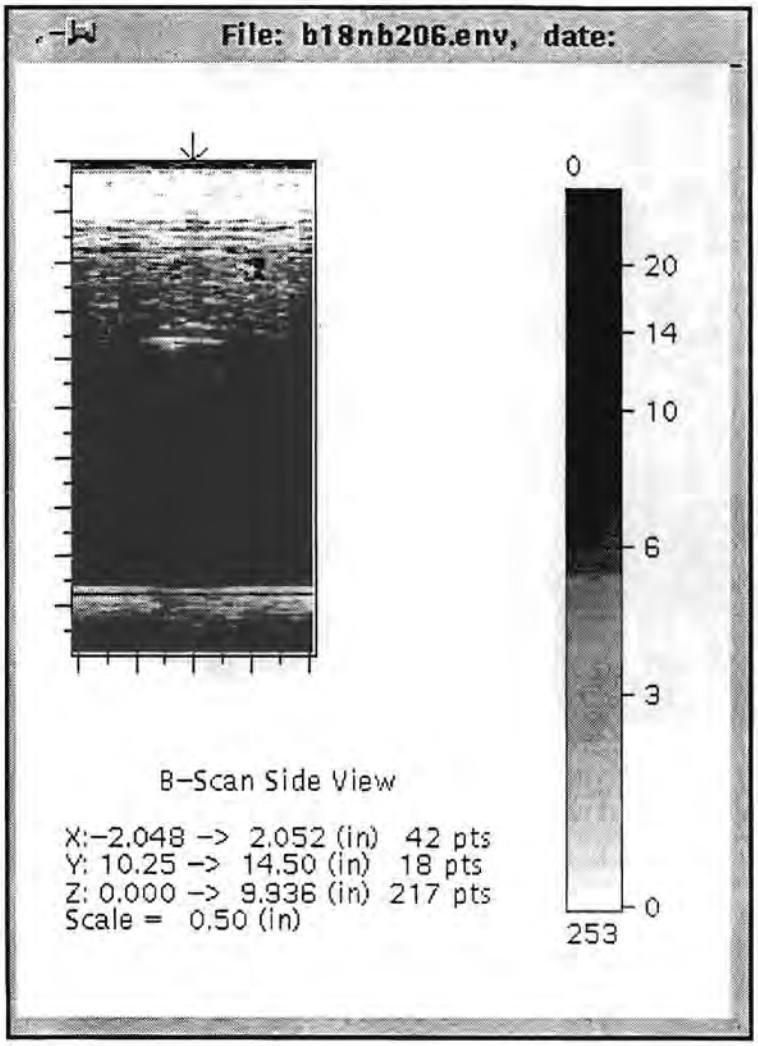

Figure 5.3a Side View (XZ) of Base-Metal Indication in Block 1-8 at Y = 318 mm (12.5 in.). Normal beam inspection from the clad side.

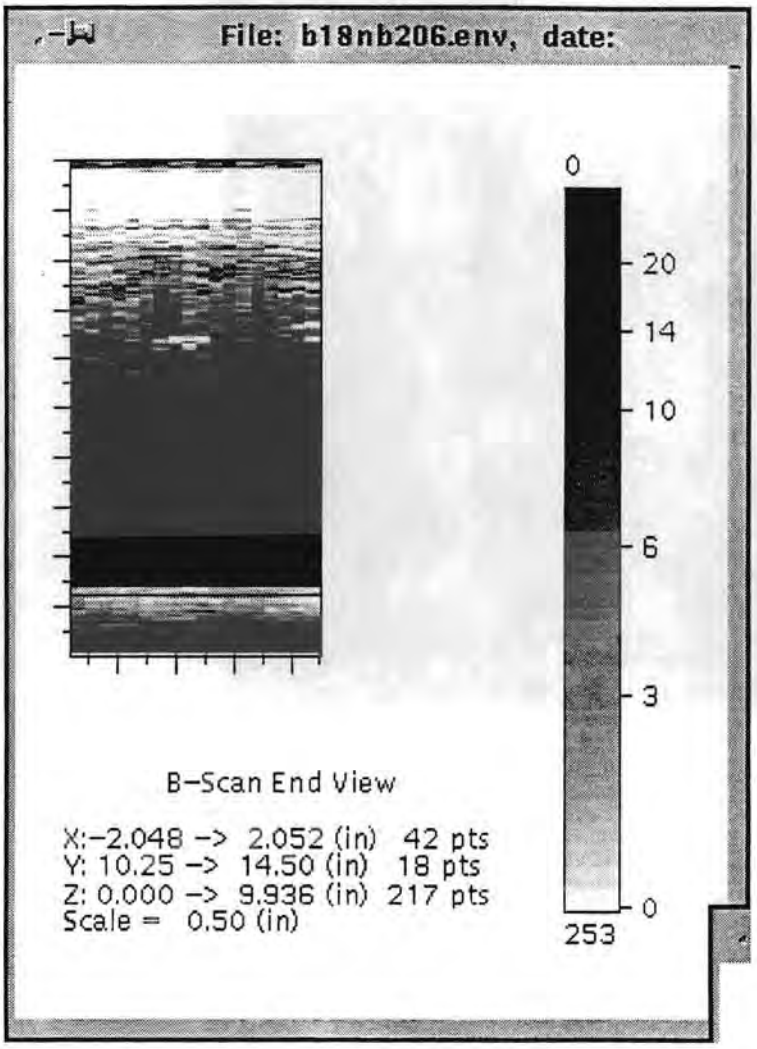

Figure 5.3b End View (YZ) of Base-Metal Indication in Block 1-8 at Y = 318 mm (12.5 in.). Normal beam inspection from the clad side.

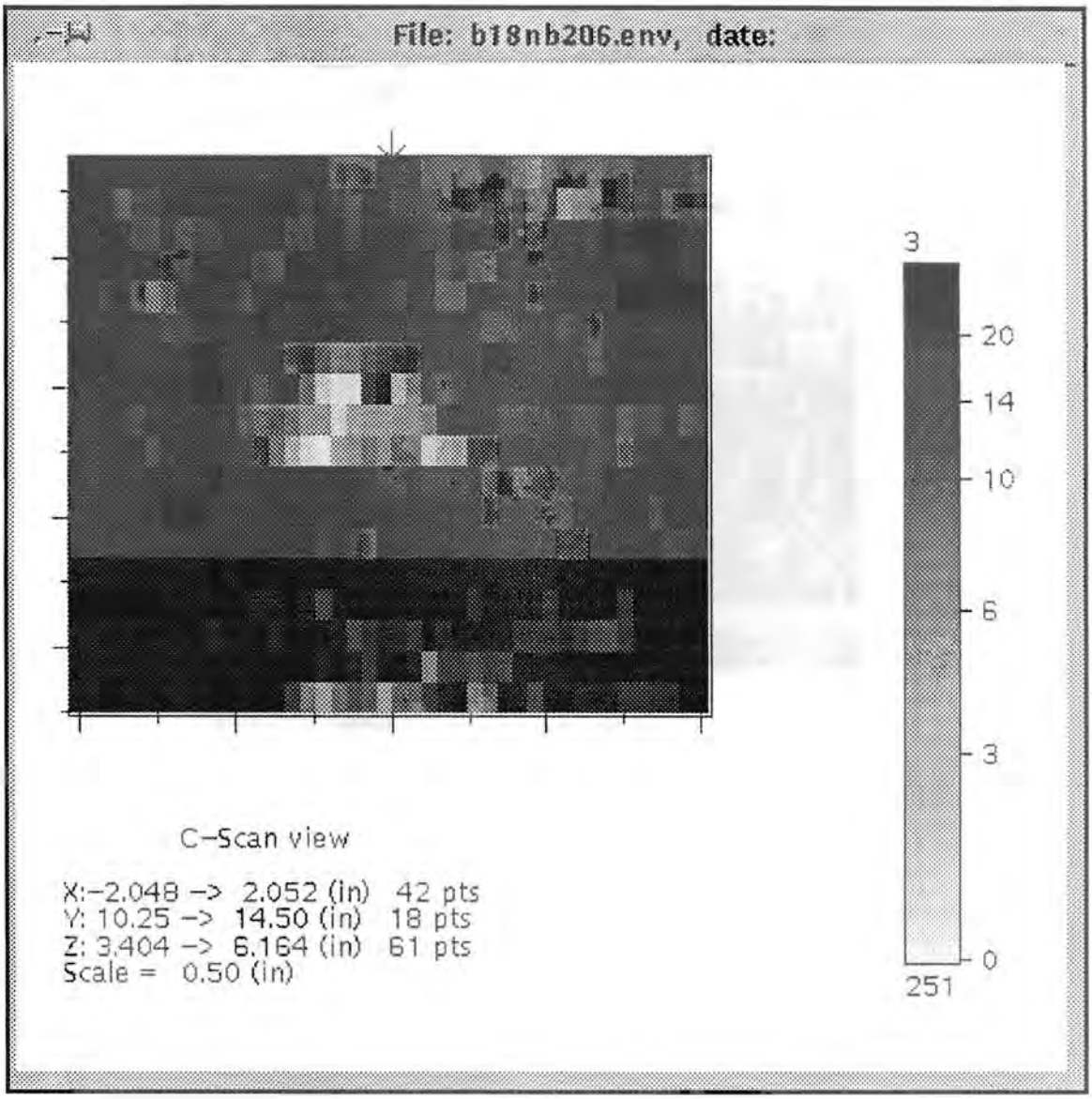

Figure 5.3c C-scan View (XY) of Base-Metal Indication in Block 1-8 at Y = 318 mm (12.5 in.). Normal beam inspection from the clad side.

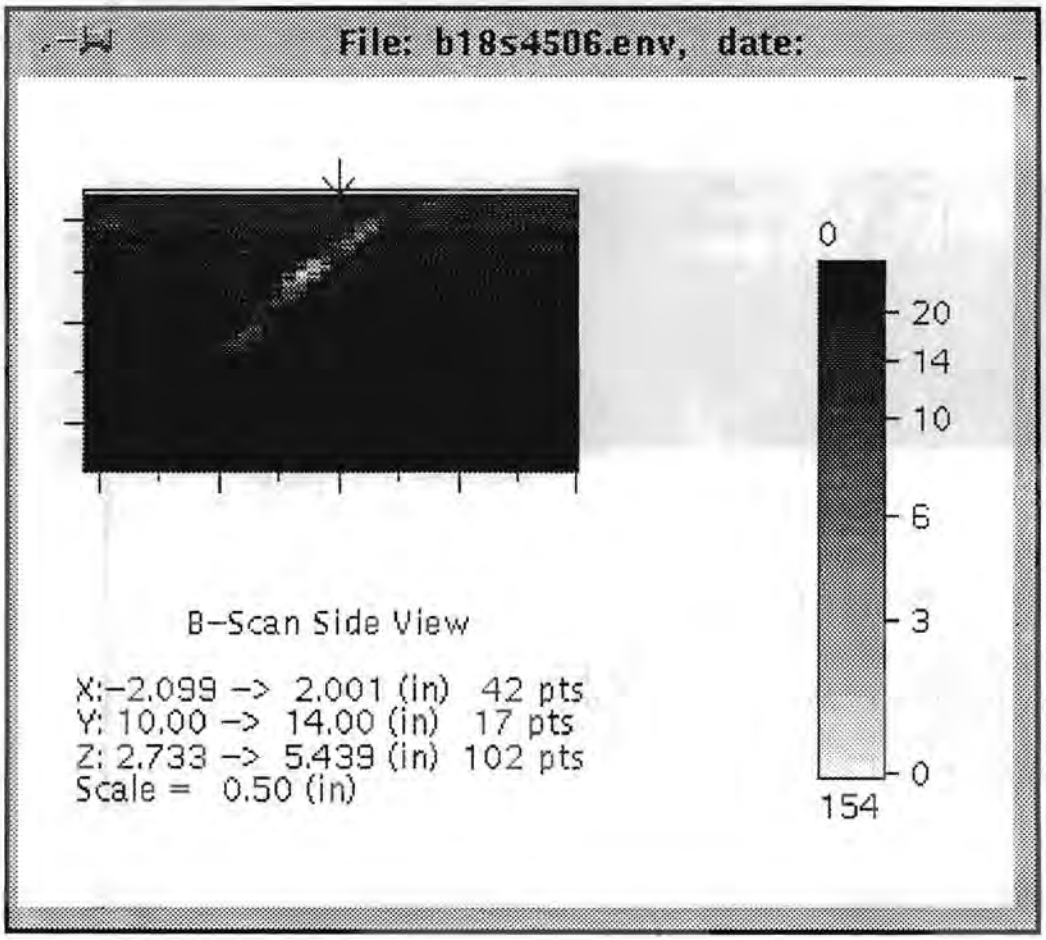

Figure 5.3d Side View (XZ) of Base-Metal Indication in Block 1-8 at Y = 318 mm (12.5 in.). 45° shear inspection from the clad side.

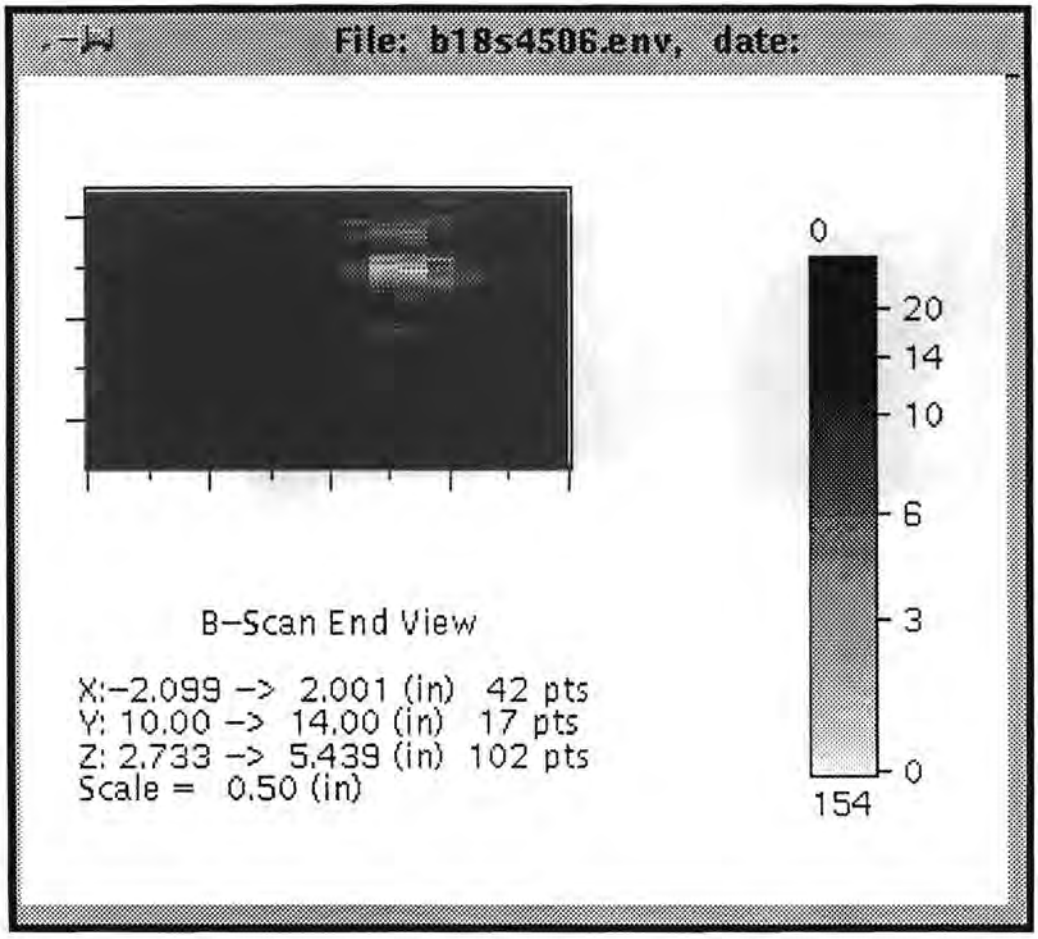

Figure 5.3e End View (YZ) of Base-Metal Indication in Block 1-8 at Y = 318 mm (12.5 in.). 45° shear inspection from the clad side.

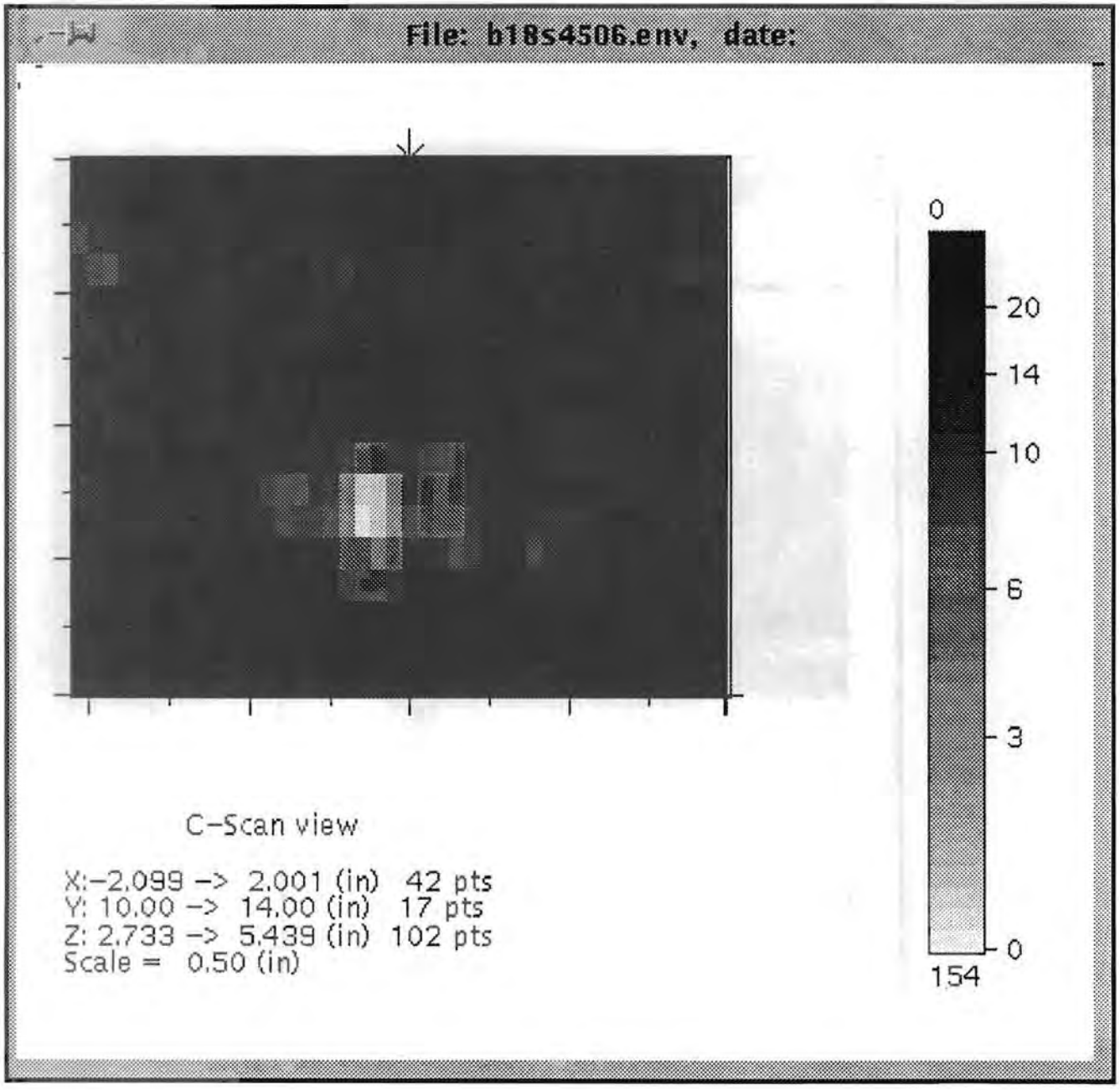

Figure 5.3f C-scan View (XY) of Base-Metal Indication in Block 1-8 at Y = 318 mm (12.5 in.). 45° shear inspection from the clad side.

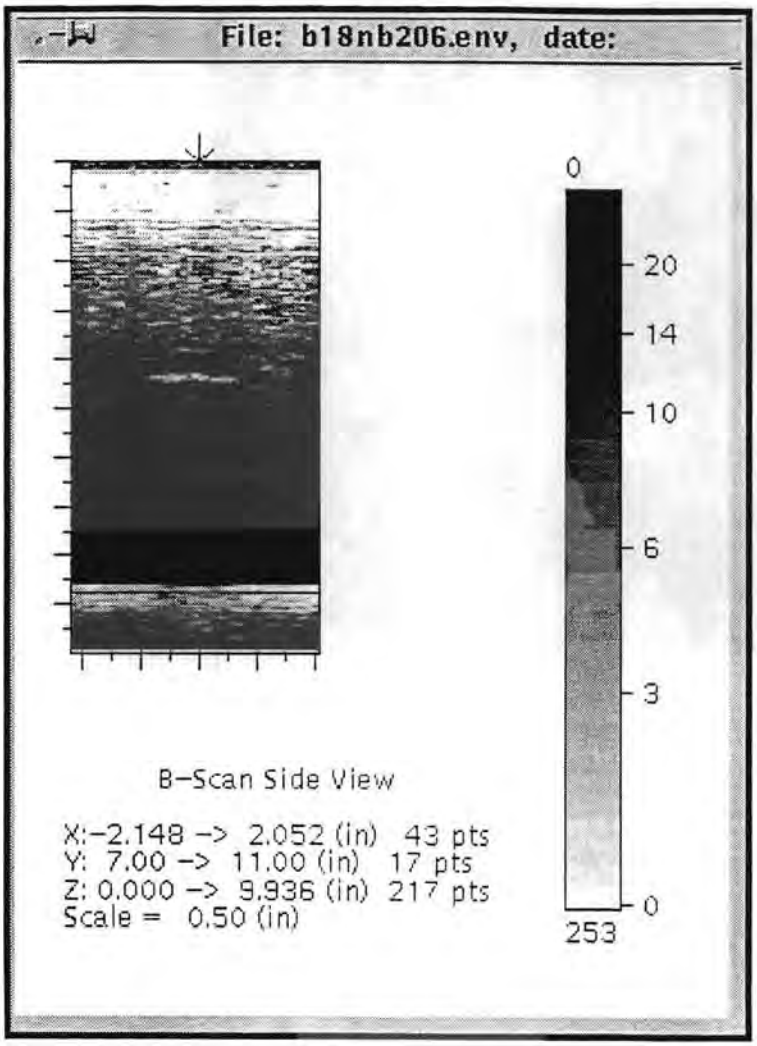

Figure 5.4a Side View (XZ) of Base-Metal Indication in Block 1-8 at Y = 249 mm (9.8 in.). Normal beam inspection from the clad side.

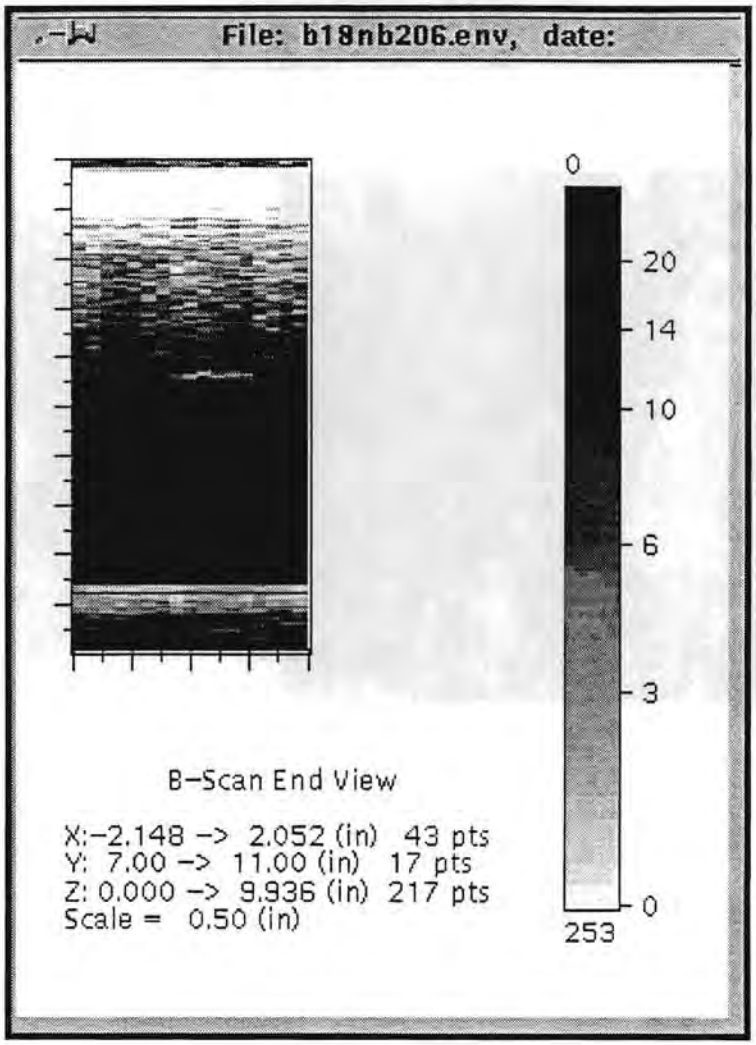

Figure 5.4b End View (YZ) of Base-Metal Indication in Block 1-8 at Y = 249 mm (9.8 in.). Normal beam inspection from the clad side.

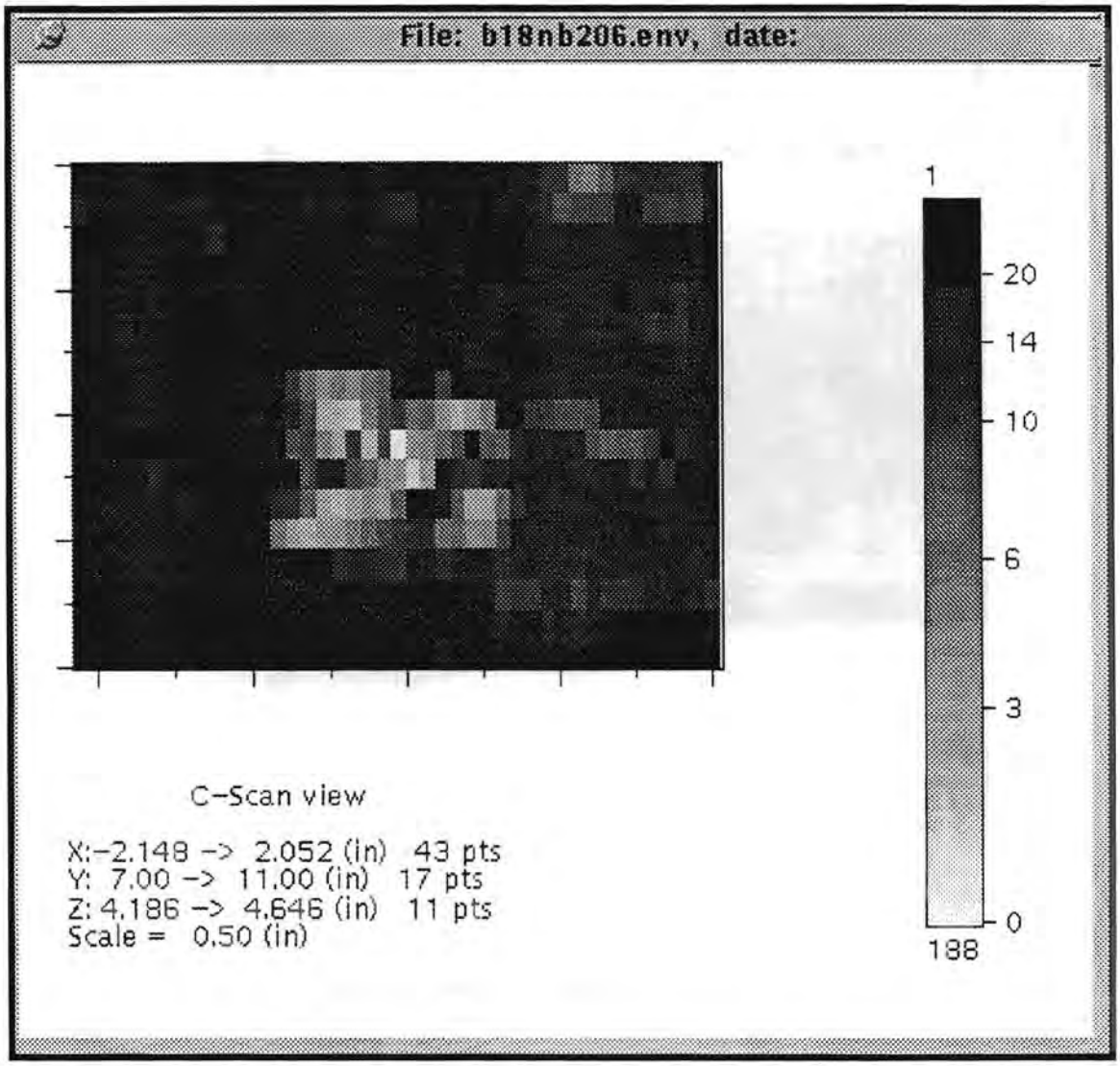

Figure 5.4c C-scan View (XY) of Base-Metal Indication in Block 1-8 at Y = 249 mm (9.8 in.). Normal beam inspection from the clad side.

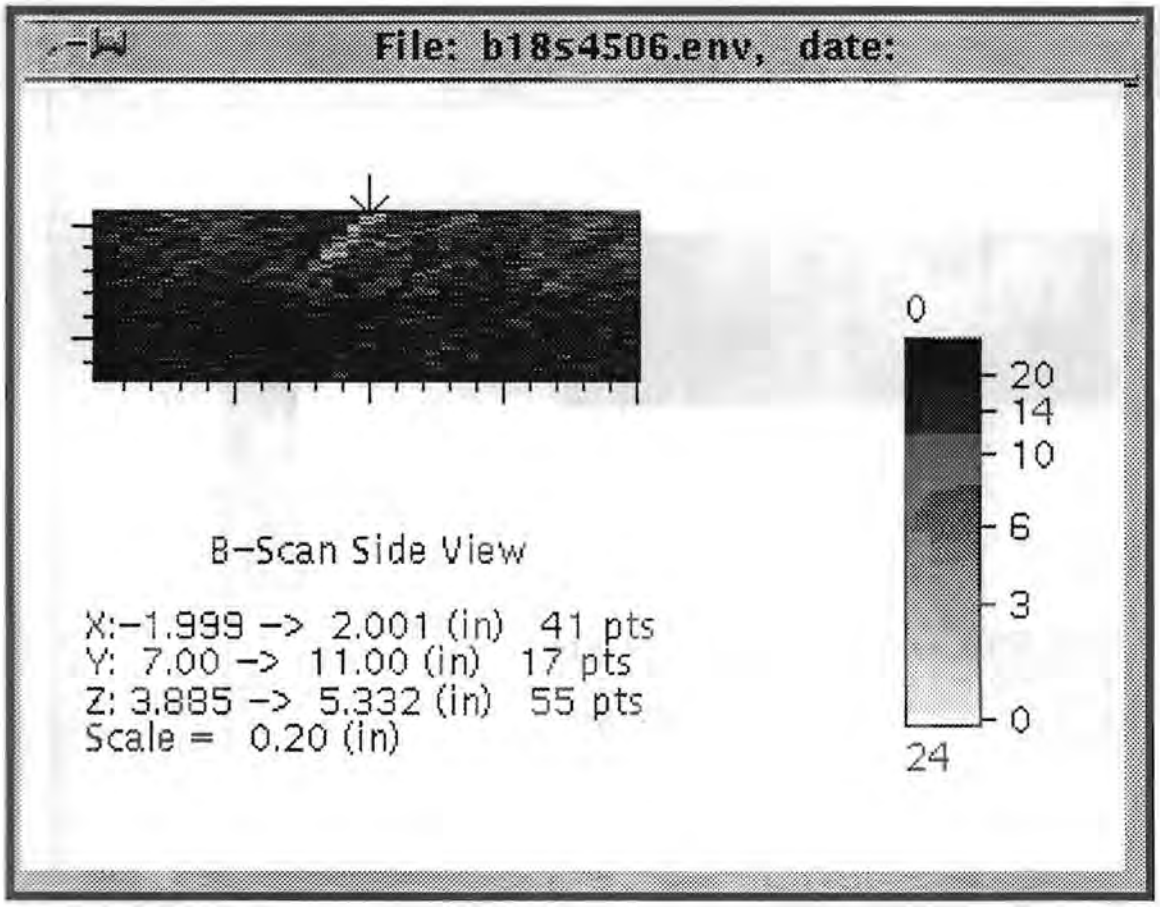

Figure 5.4d Side View (XZ) of Base-Metal Indication in Block 1-8 at Y = 249 mm (9.8 in.). 45° shear inspection from the clad side. Beam direction is +X.

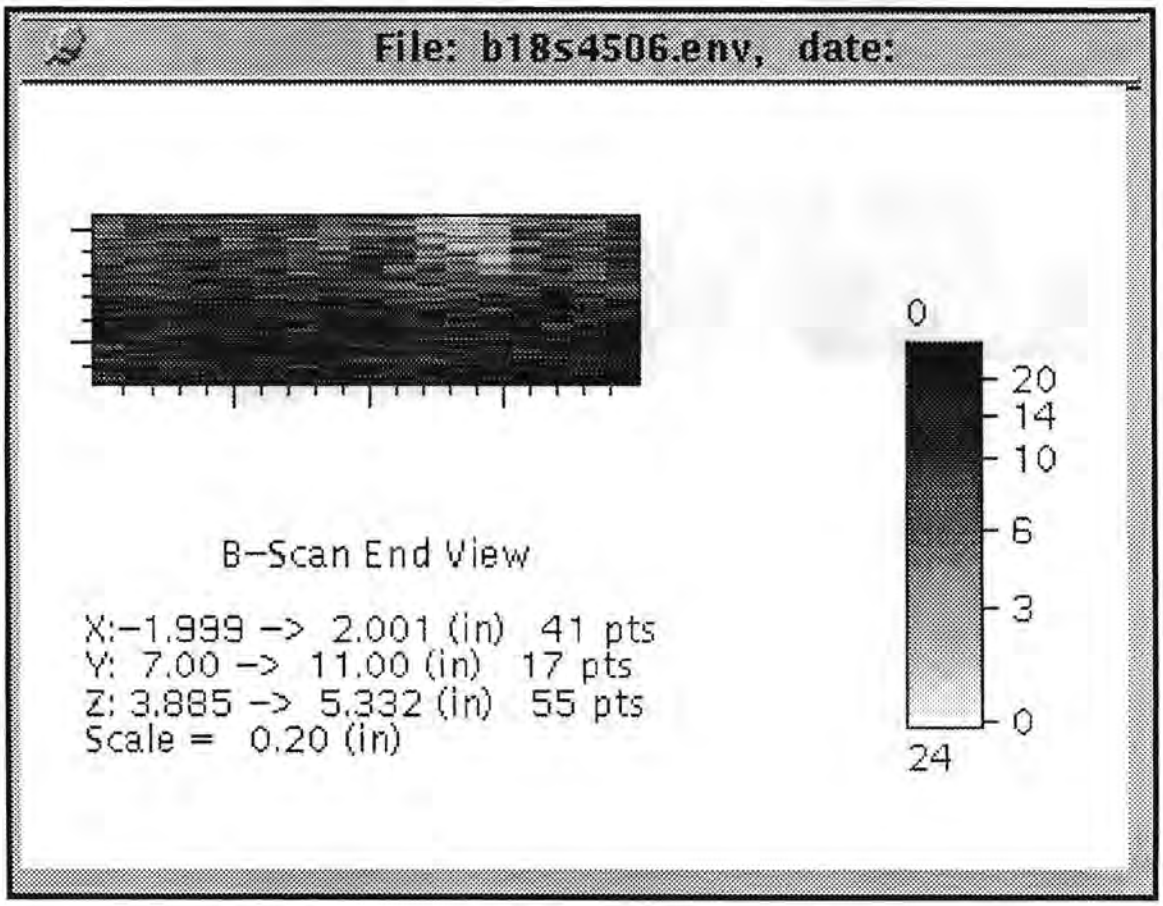

Figure 5.4e End View (YZ) of Base-Metal Indication in Block 1-8 at Y = 249 mm (9.8 in.). 45° shear inspection from the clad side. Beam direction is +X.

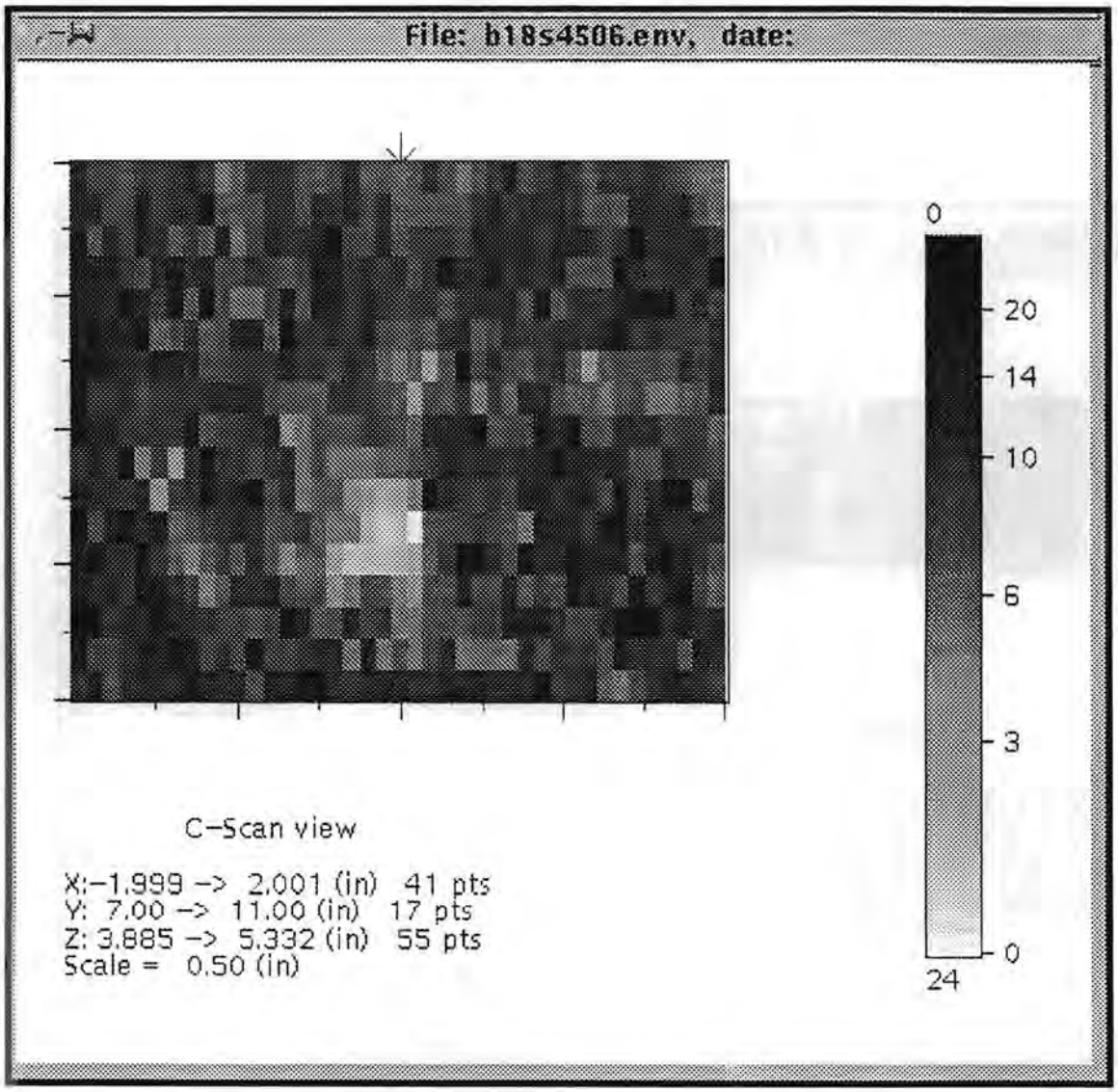

Figure 5.4f C-scan View (XY) of Base-Metal Indication in Block 1-8 at Y = 249 mm (9.8 in.). 45° shear inspection from the clad side. Beam direction is +X.

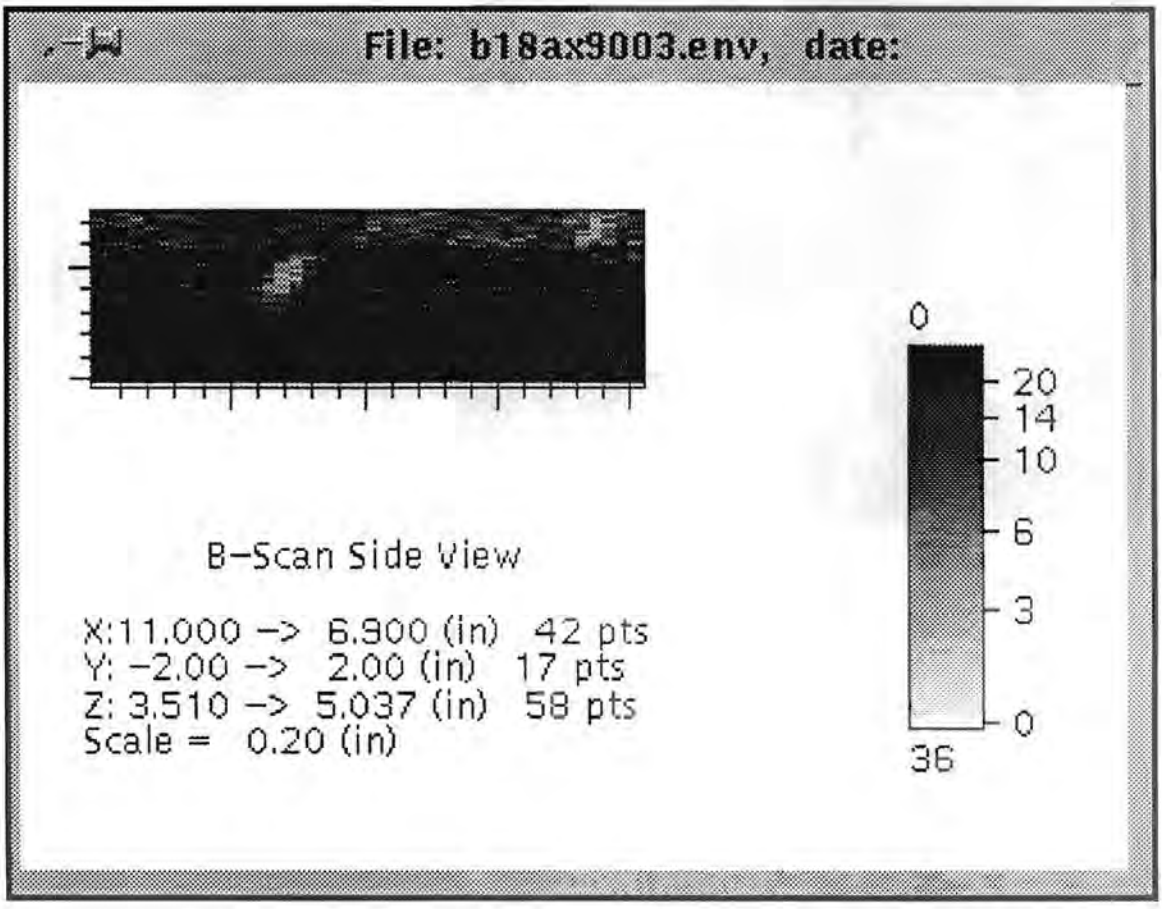

Figure 5.4g Side View (in scanner coordinates) of Base-Metal Indication in Block 1-8 at Y = 249 mm (9.8 in.). 45° shear inspection from the clad side. Beam direction is -Y. X coordinates shown in the figure correspond to Y material coordinates.

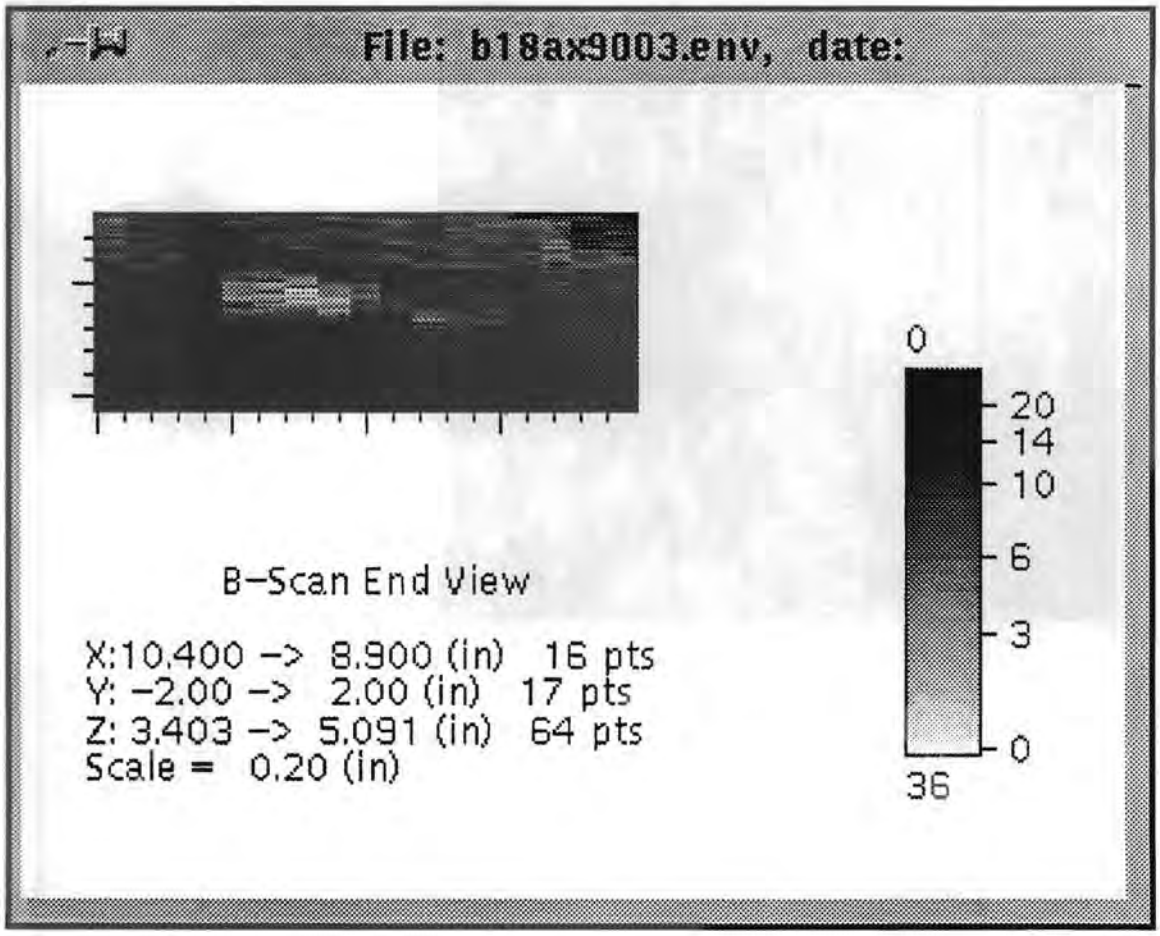

Figure 5.4h End View (in scanner coordinates) of Base-Metal Indication in Block 1-8 at Y = 249 mm (9.8 in.). 45° shear inspection from the clad side. Beam direction is -Y. Y coordinates shown in the figure correspond to X material coordinates.

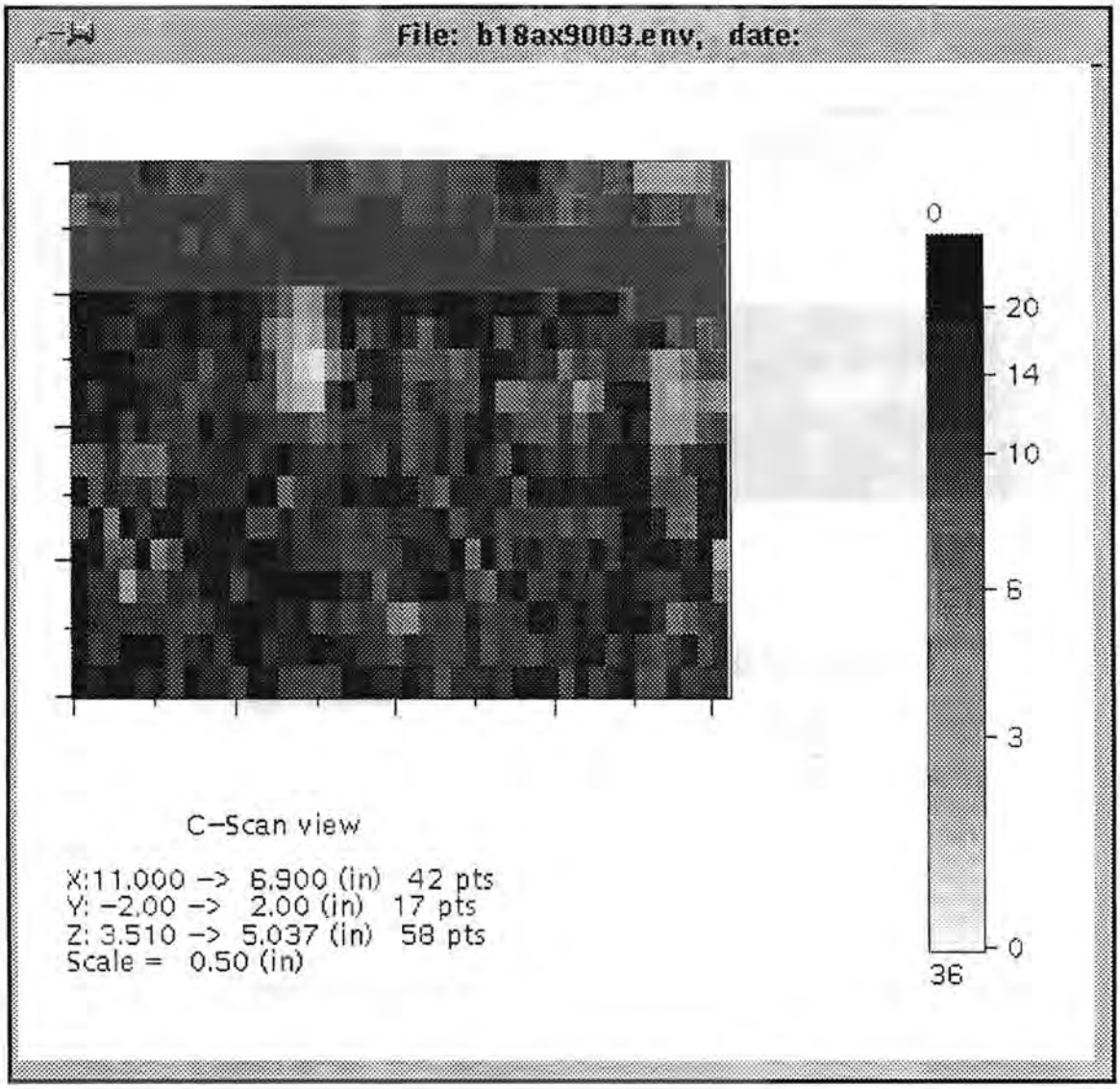

Figure 5.4i C-scan View (in scanner coordinates) of Base-Metal Indication in Block 1-8 at Y = 249 mm (9.8 in.). 45° shear inspection from the clad side. Beam direction is -Y. Y coordinates shown in the figure correspond to X material coordinates.

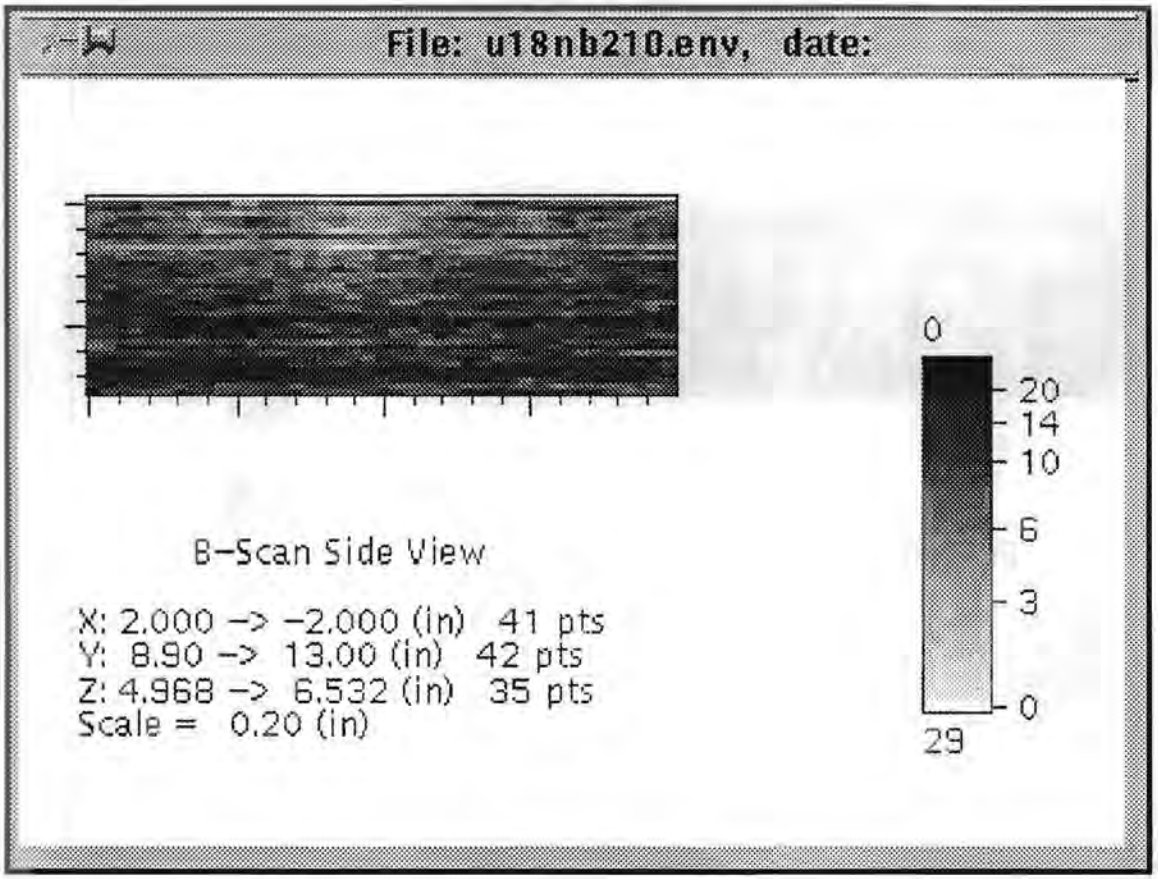

Figure 5.4j Side View (XZ) of Base-Metal Indication in Block 1-8 at Y = 249 mm (9.8 in.). Normal beam inspection from the unclad side. Z values shown in figure are measured from the unclad side.

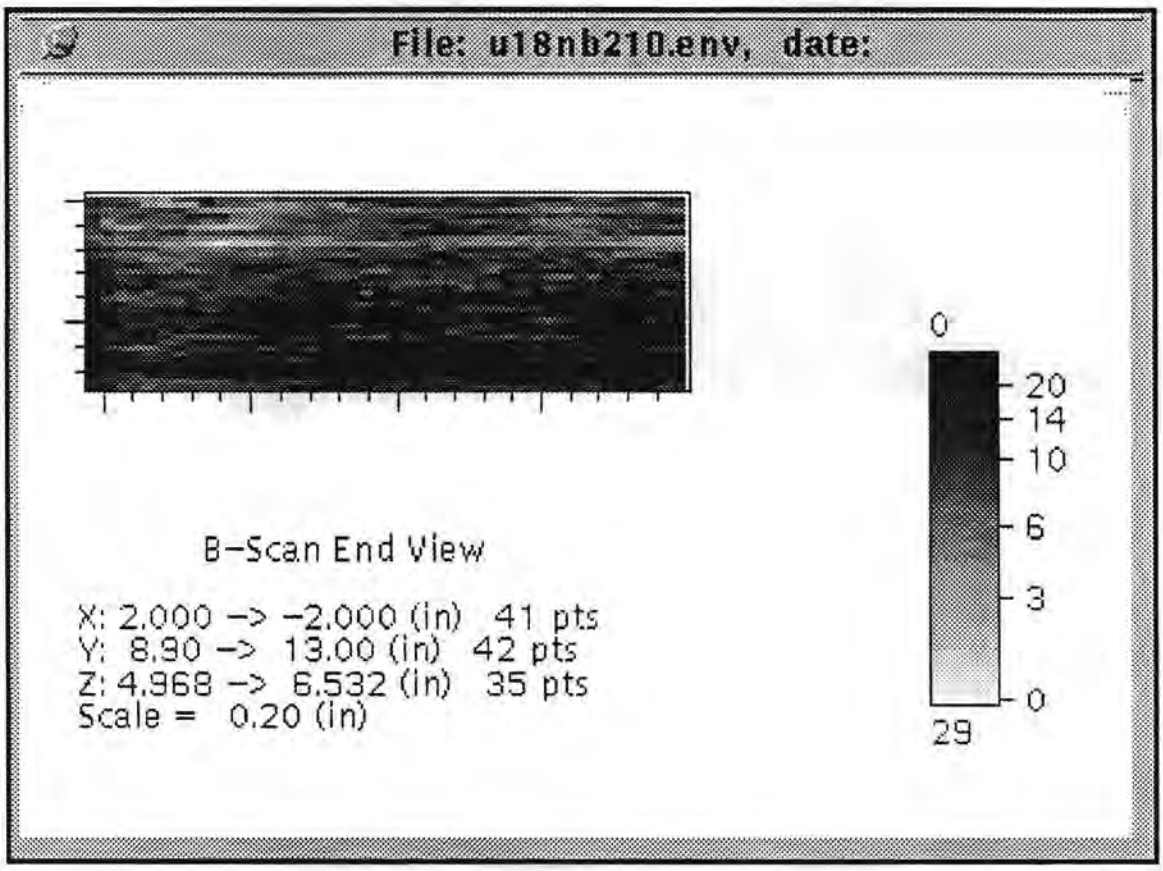

Figure 5.4k End View (YZ) of Base-Metal Indication in Block 1-8 at Y = 249 mm (9.8 in.). Normal beam inspection from the unclad side. Z values shown in figure are measured from the unclad side.

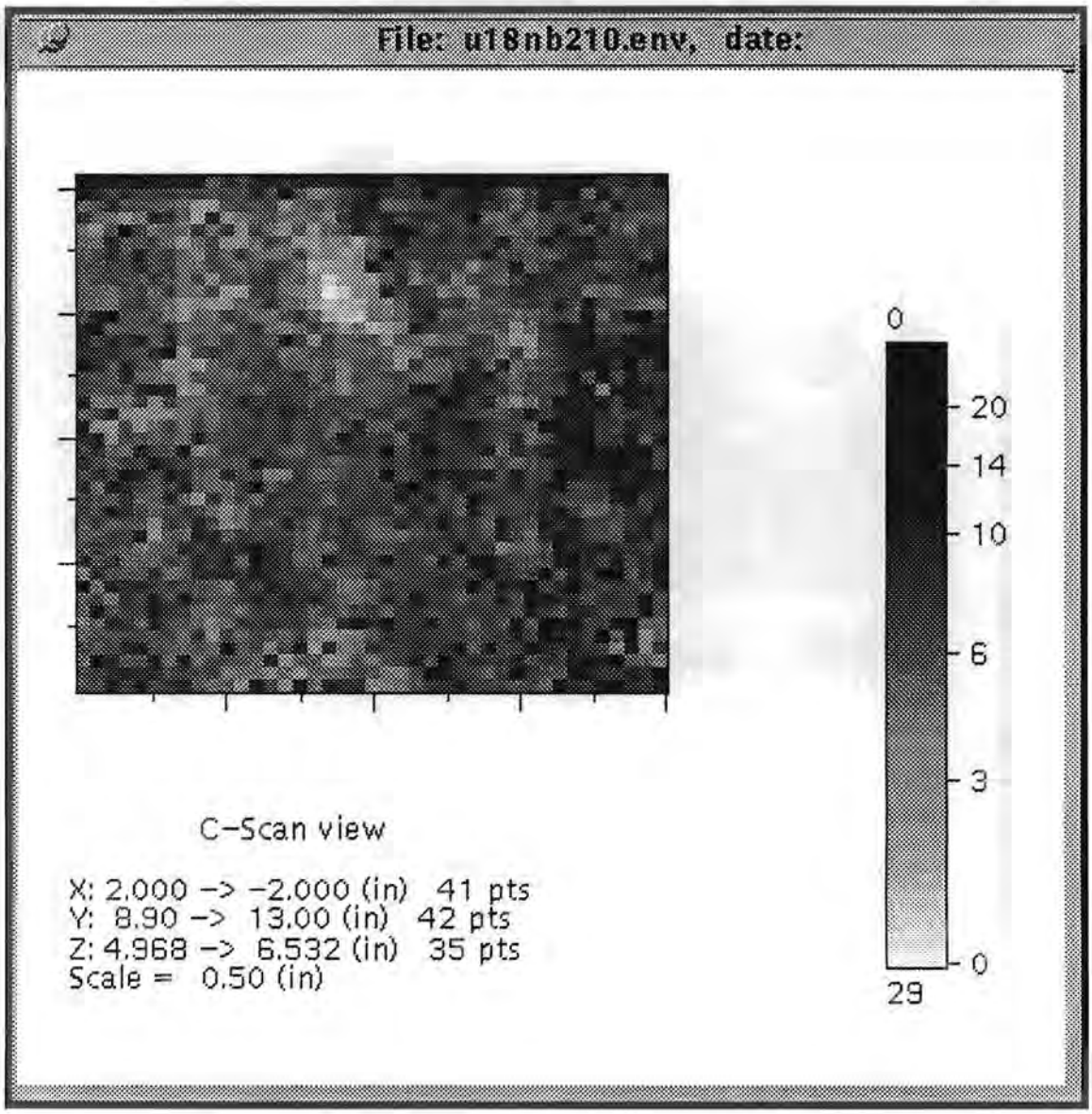

Figure 5.41 C-scan View (XY) of Base-Metal Indication in Block 1-8 at Y = 249 mm (9.8 in.). Normal beam inspection from the unclad side. Z values shown in figure are measured from the unclad side.

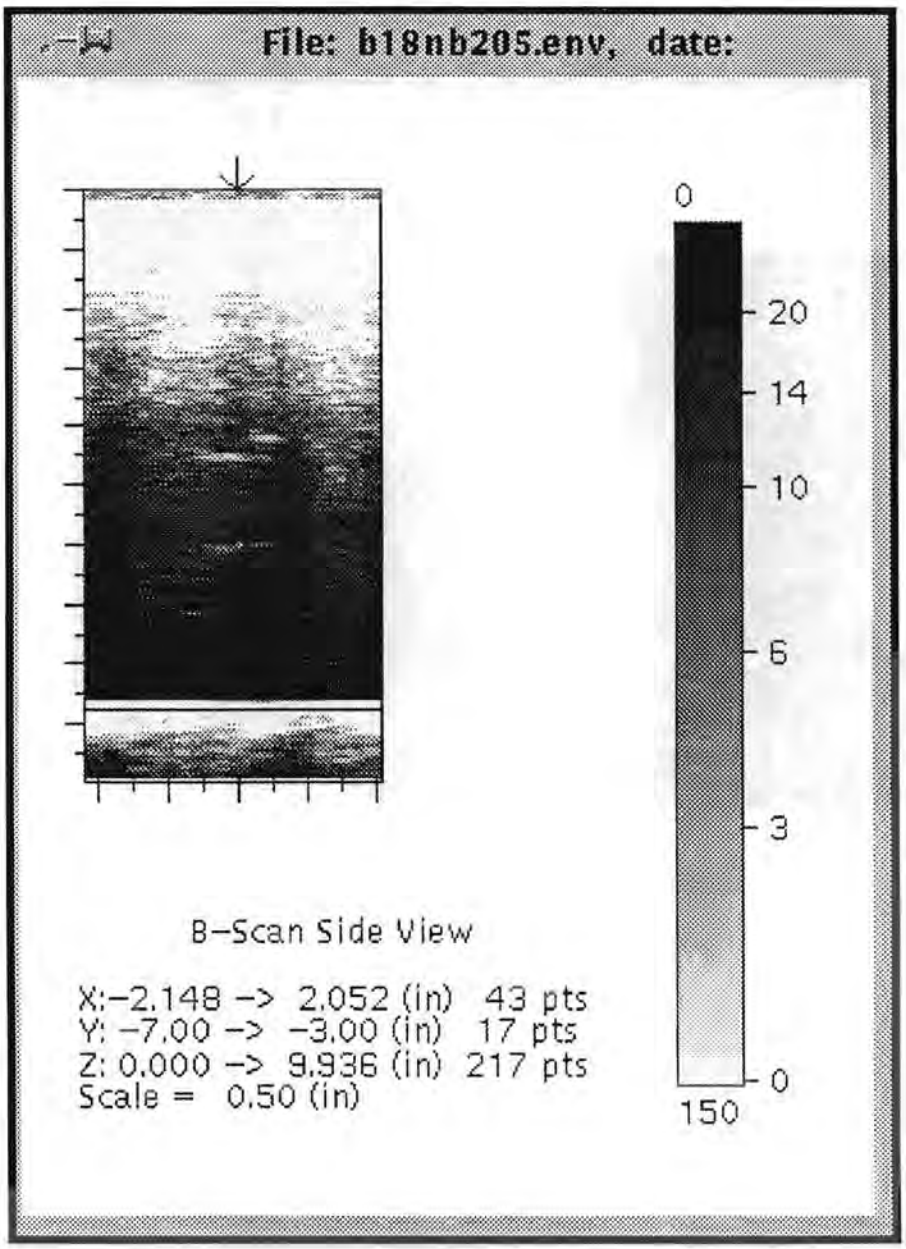

Figure 5.5a Side View (XZ) of Base-Metal Indication in Block 1-8 at Y = -127 mm (-5.0 in.). Normal beam inspection from the clad side.

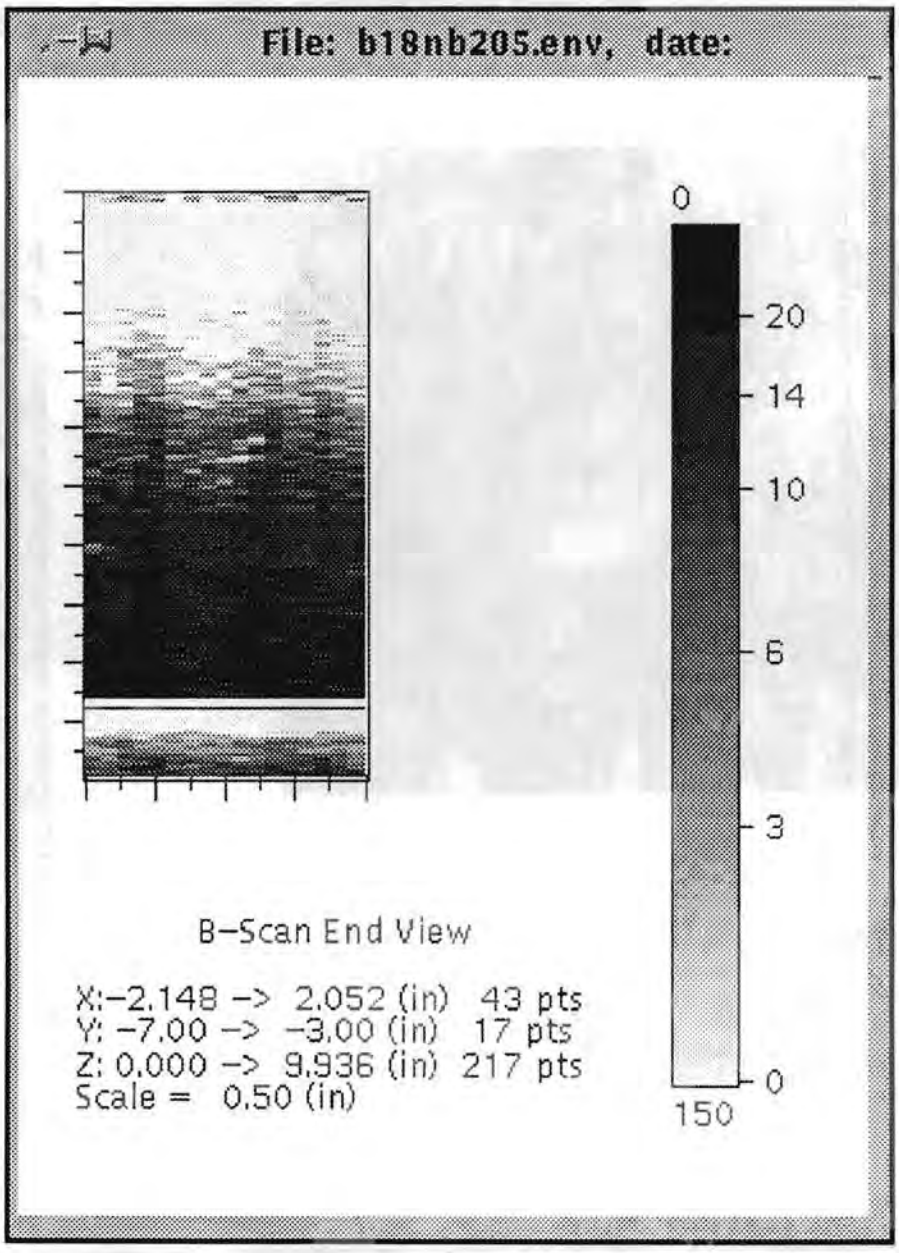

Figure 5.5b End View (YZ) of Base-Metal Indication in Block 1-8 at Y = -127 mm (-5.0 in.). Normal beam inspection from the clad side.

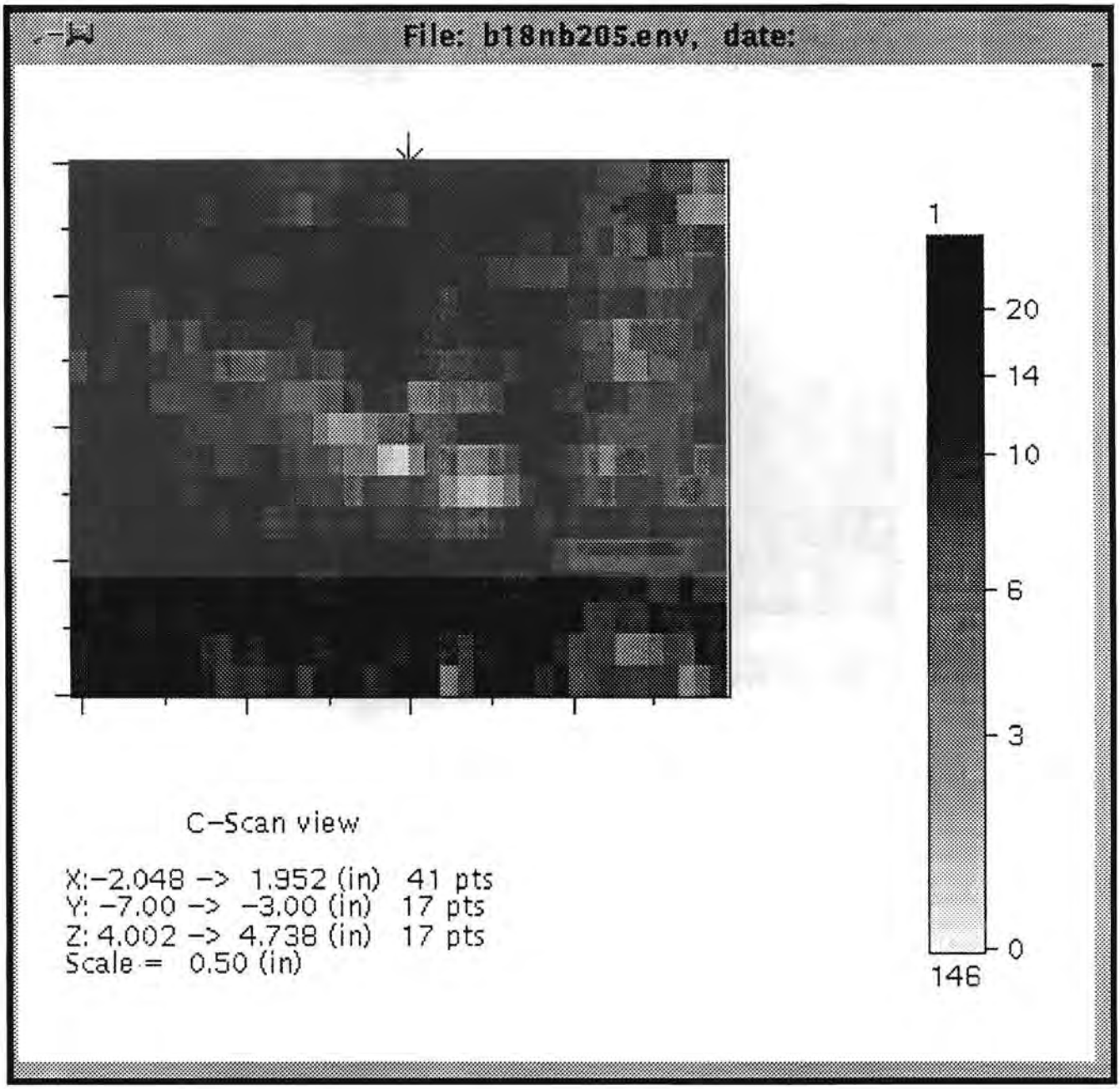

Figure 5.5c C-scan View (XY) of Base-Metal Indication in Block 1-8 at Y = -127 mm (-5.0 in.). Normal beam inspection from the clad side.

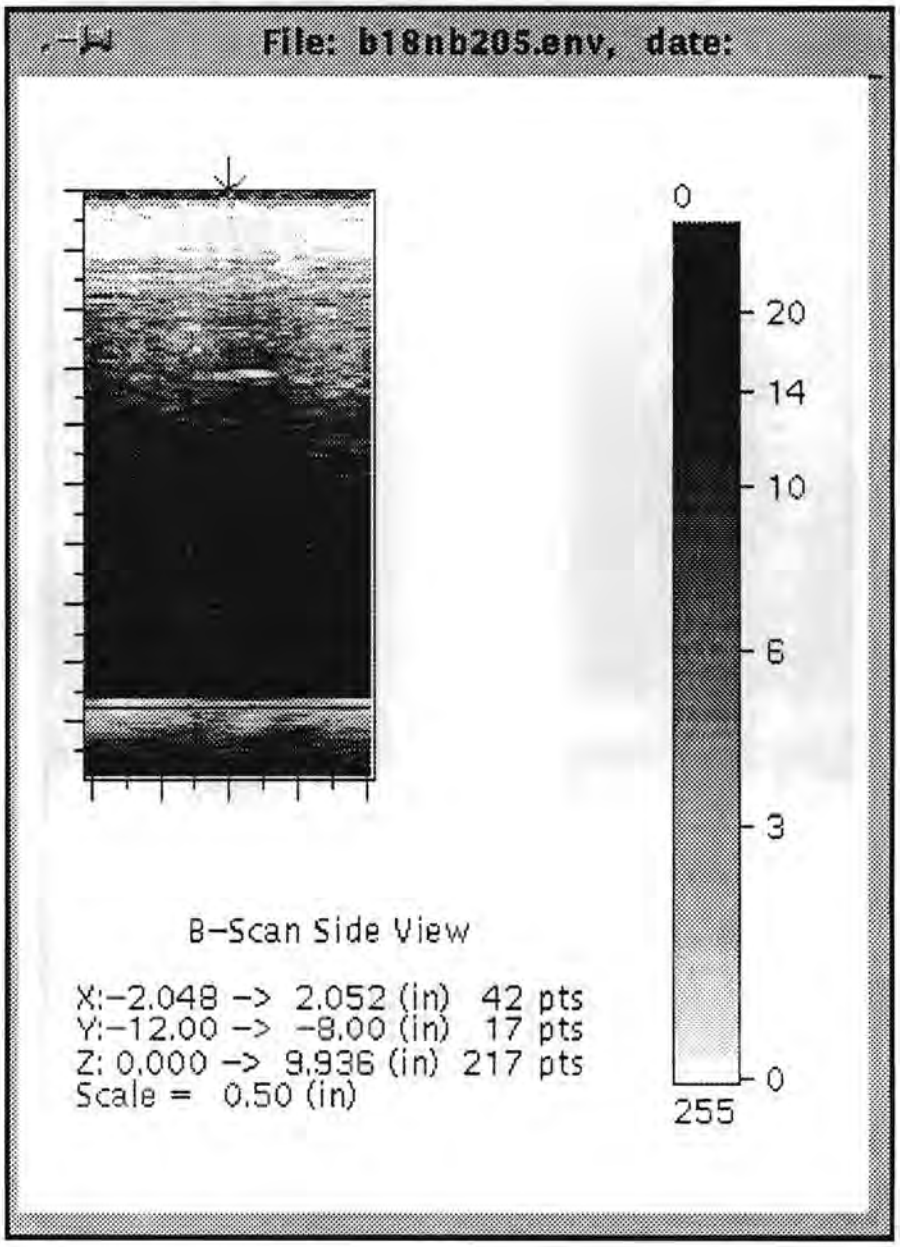

Figure 5.6a Side View (XZ) of Base-Metal Indication in Block 1-8 at Y = -249 mm (-9.8 in.). Normal beam inspection from the clad side.

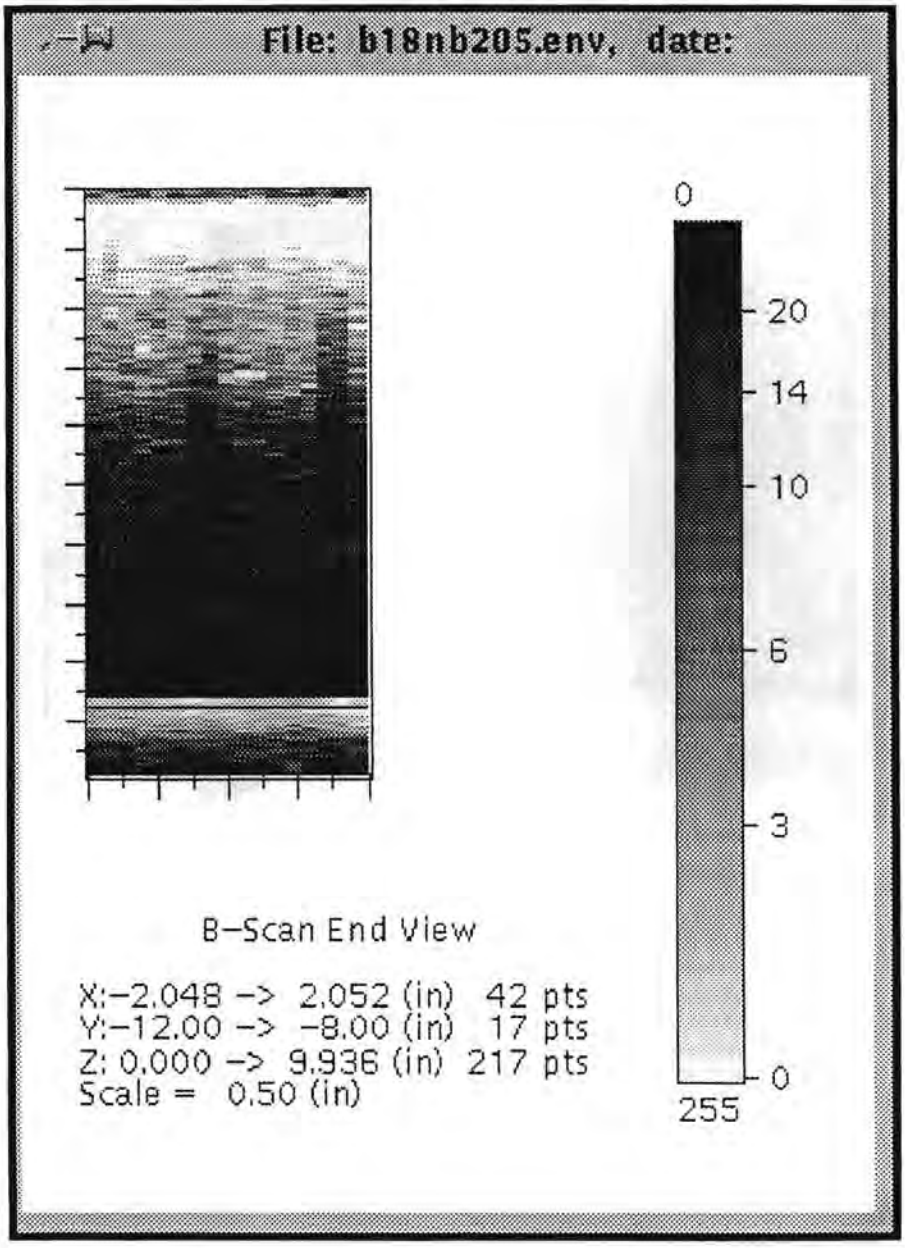

Figure 5.6b End View (YZ) of Base-Metal Indication in Block 1-8 at Y = -249 mm (-9.8 in.). Normal beam inspection from the clad side.

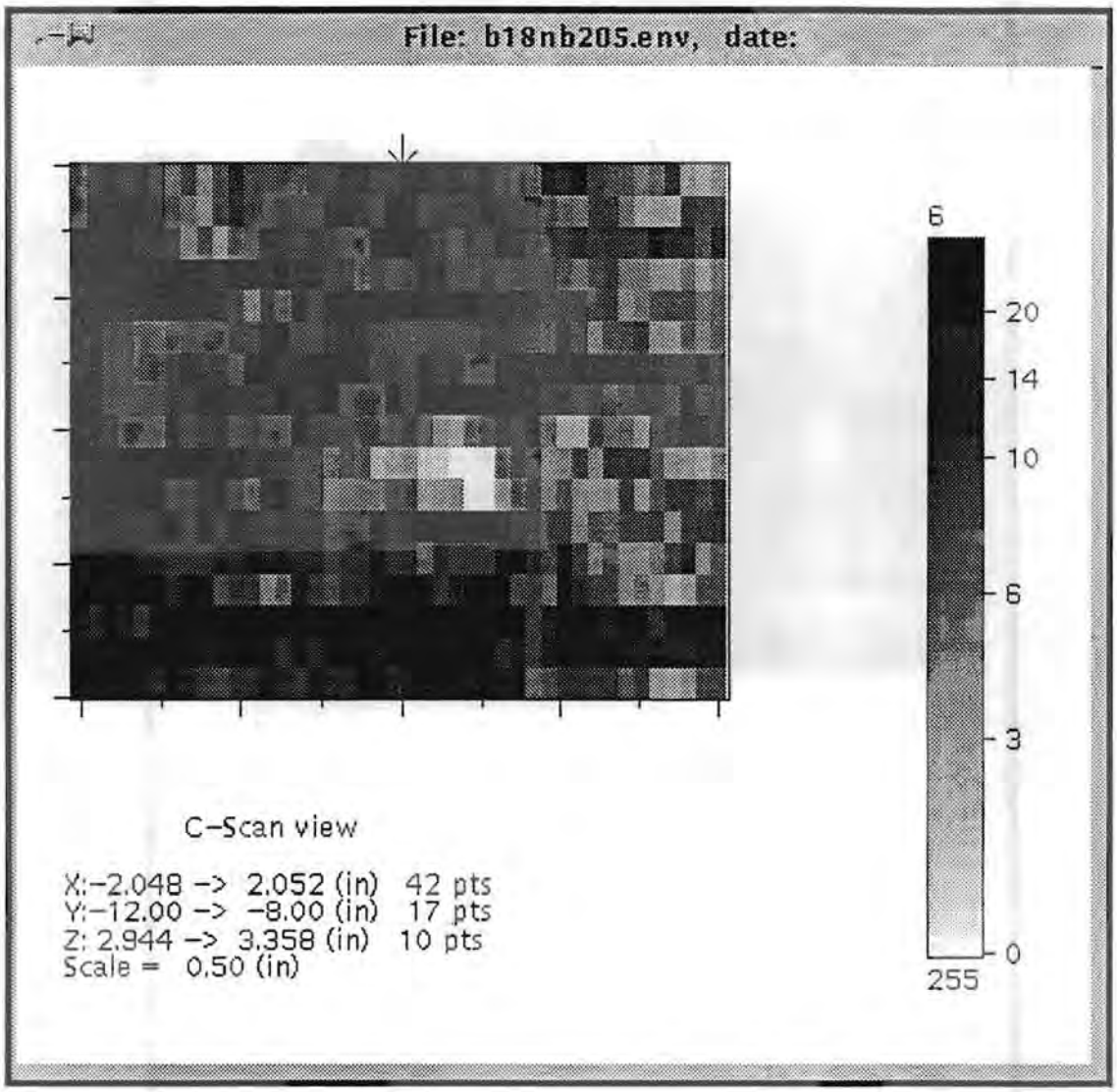

Figure 5.6c C-scan View (XY) of Base-Metal Indication in Block 1-8 at Y = -249 mm (-9.8 in.). Normal beam inspection from the clad side.

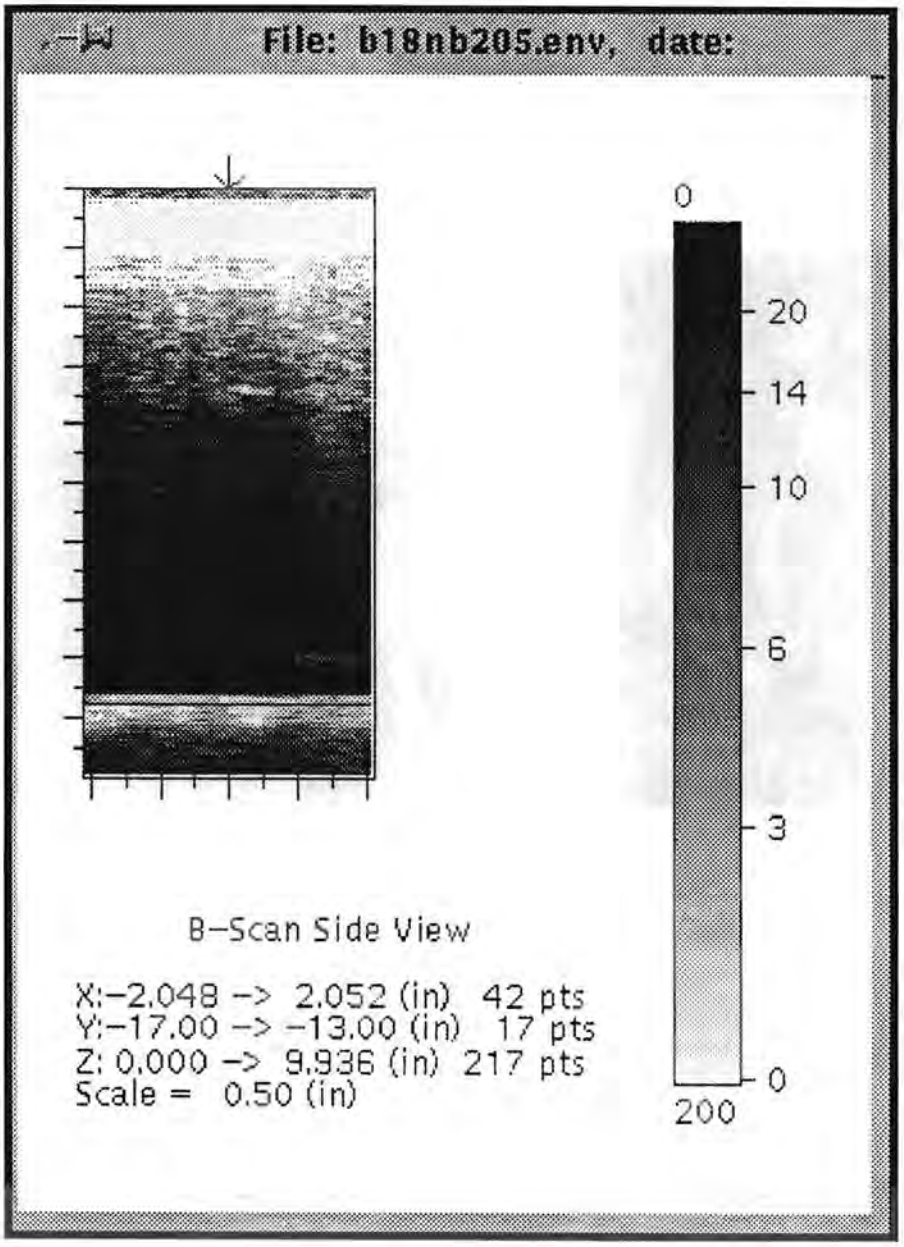

Figure 5.7a Side View (XZ) of Base-Metal Indication in Block 1-8 at Y = -391 mm (-15.4 in.). Normal beam inspection from the clad side.

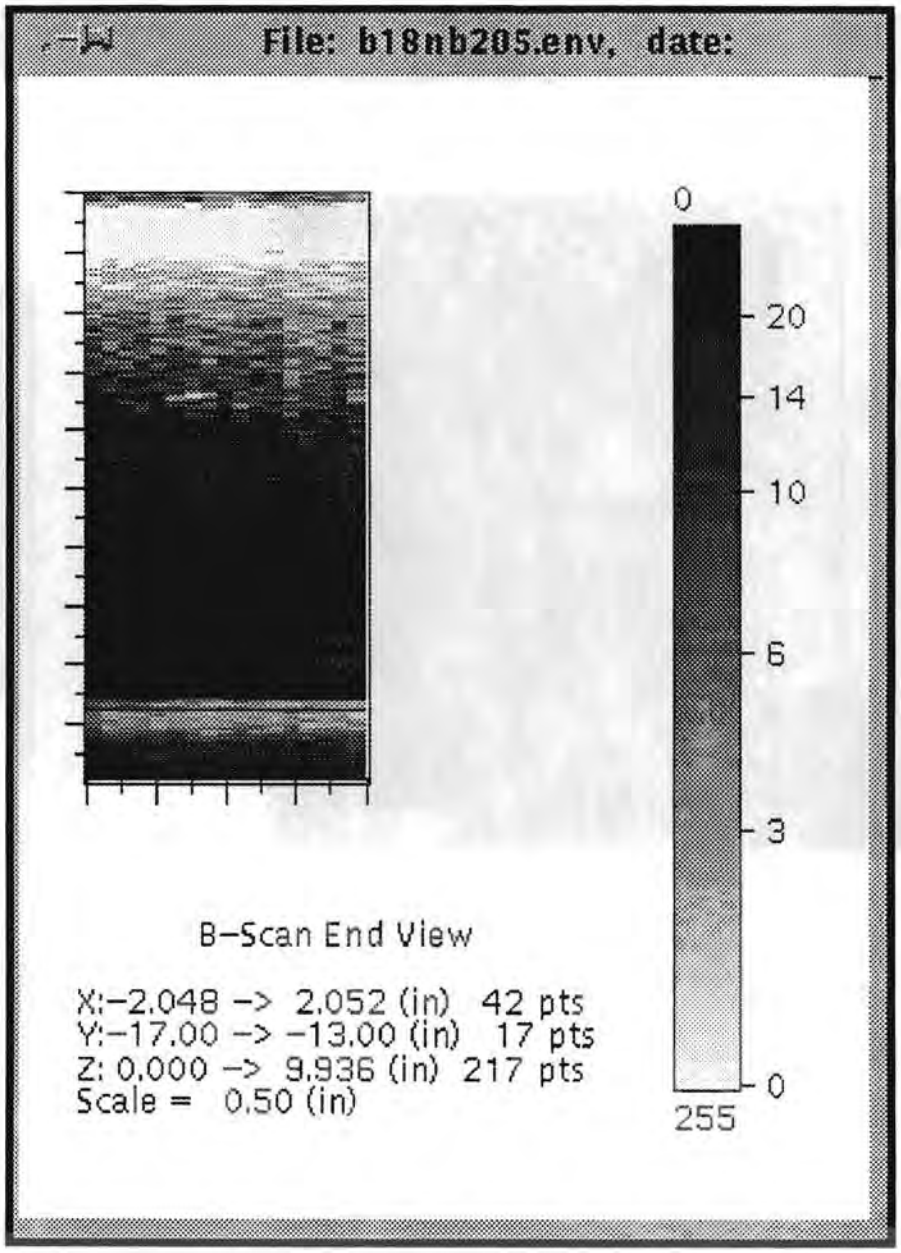

Figure 5.7b End View (YZ) of Base-Metal Indication in Block 1-8 at Y = -391 mm (-15.4 in.). Normal beam inspection from the clad side.

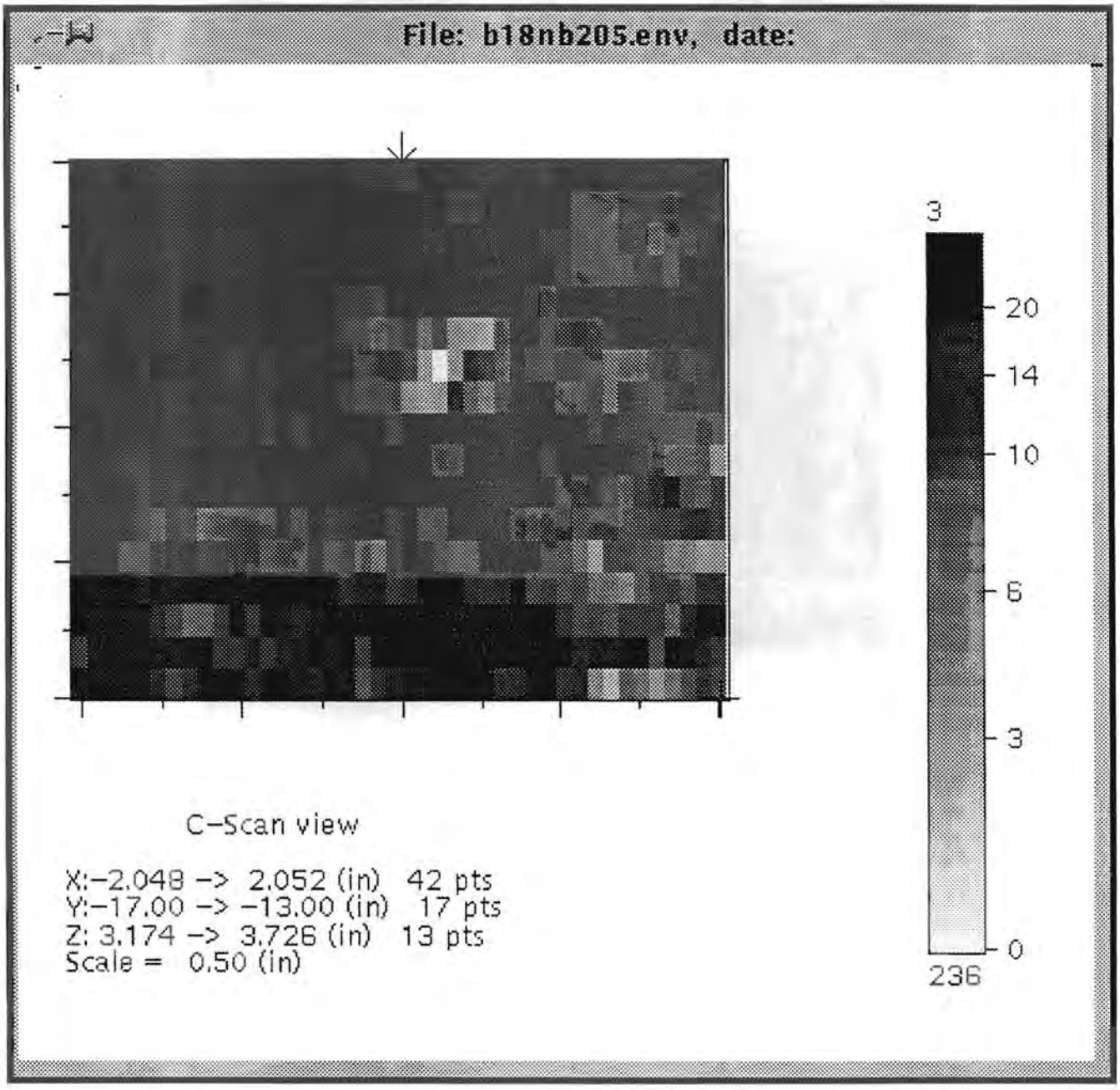

Figure 5.7c C-scan View (XY) of Base-Metal Indication in Block 1-8 at Y = -391 mm (-15.4 in.). Normal beam inspection from the clad side.

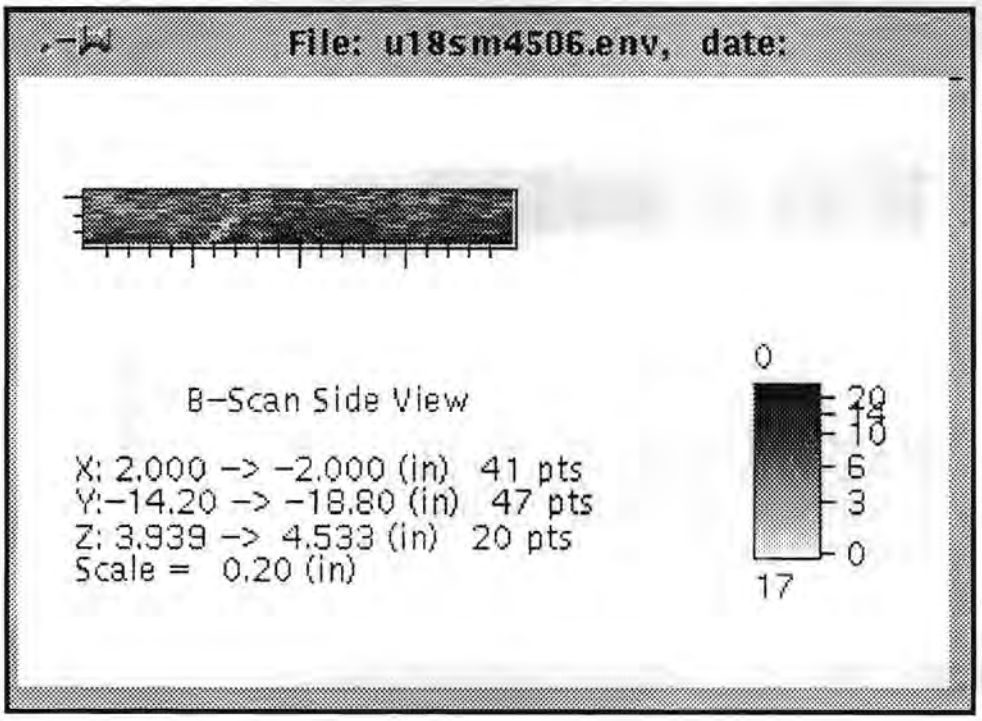

Figure 5.8a Side View (XZ) of Base-Metal Indication in Block 1-8 at Y = -465 mm (-18.3 in.). 45° shear inspection from the unclad side. Beam direction is -X. Z values in the figure are measured from the unclad side.

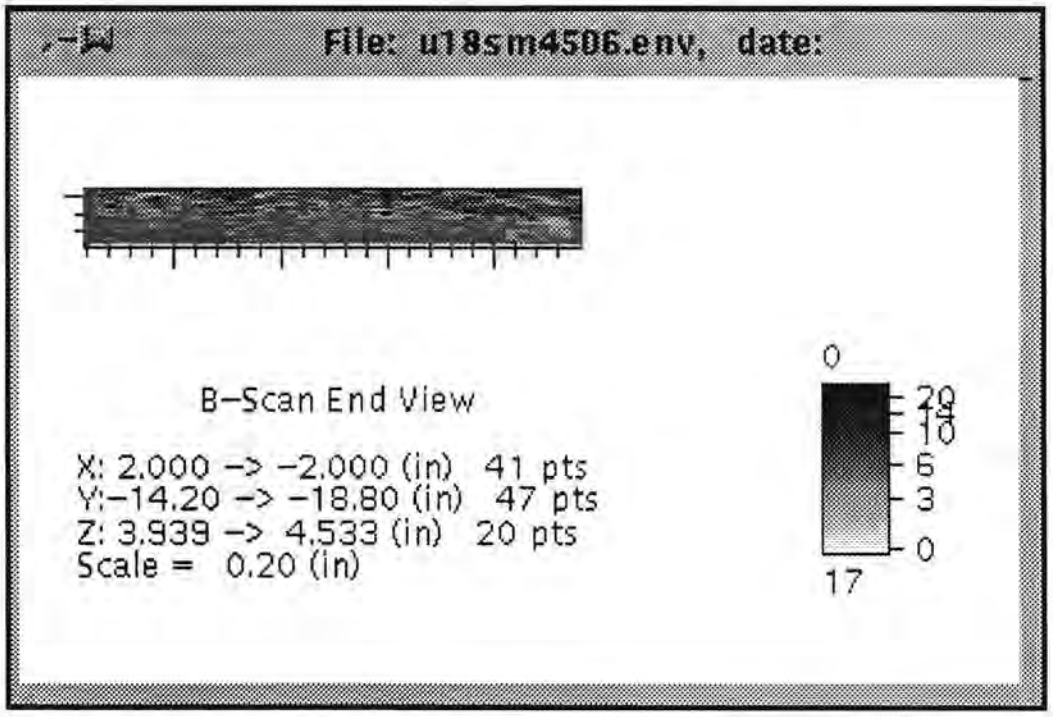

Figure 5.8b End View (YZ) of Base-Metal Indication in Block 1-8 at Y = -465 mm (-18.3 in.). 45° shear inspection from the unclad side. Beam direction is -X. Z values in the figure are measured from the unclad side.

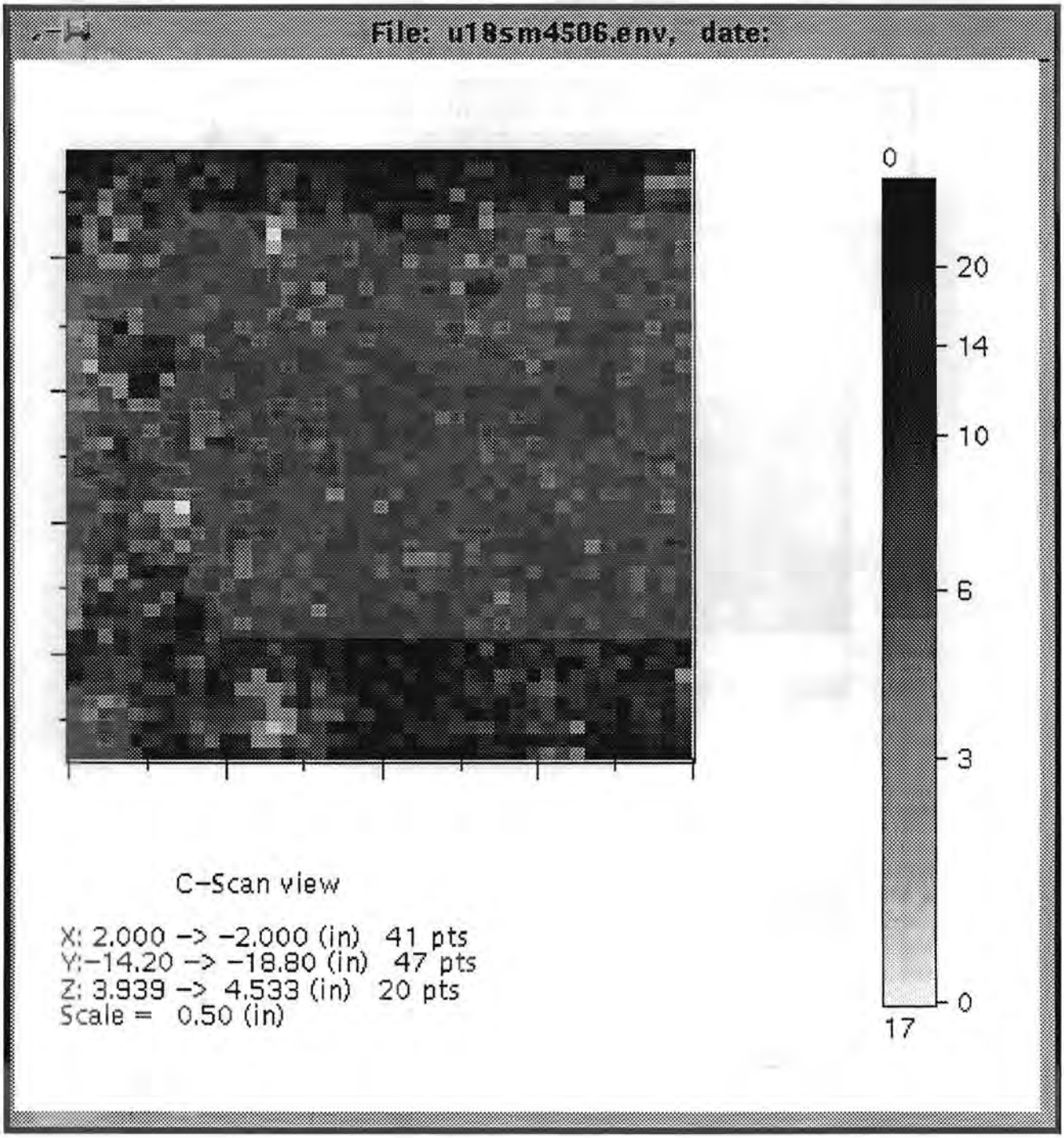

Figure 5.8c C-scan View (XY) of Base-Metal Indication in Block 1-8 at Y = -465 mm (-18.3 in.). 45° shear inspection from the unclad side. Beam direction is -X. Z values in the figure are measured from the unclad side.

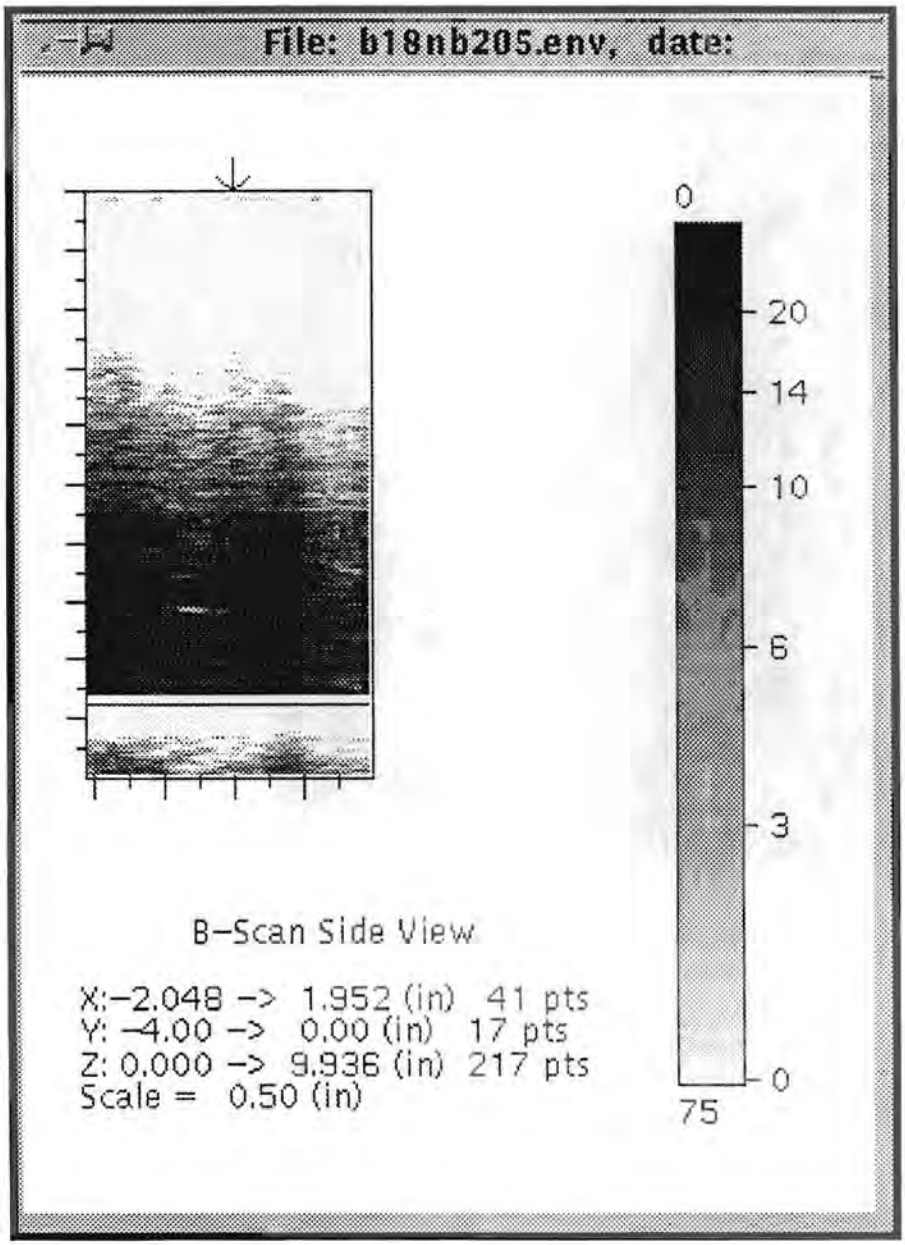

Figure 5.9a Side View (XZ) of Base-Metal Indication in Block 1-8 at Y = -71 mm (-2.8 in.). Normal beam inspection from the clad side.

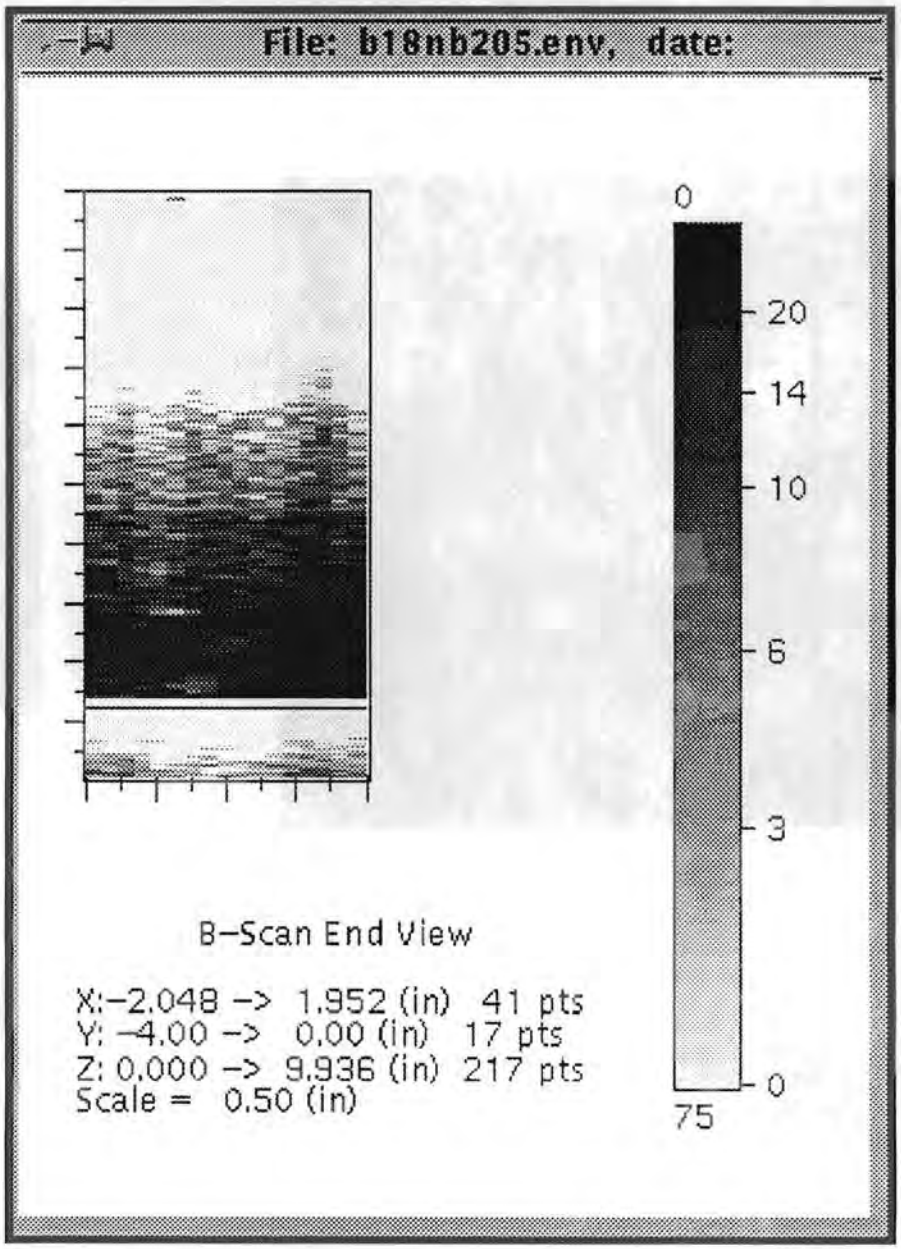

Figure 5.9b End View (YZ) of Base-Metal Indication in Block 1-8 at Y = -71 mm (-2.8 in.). Normal beam inspection from the clad side.

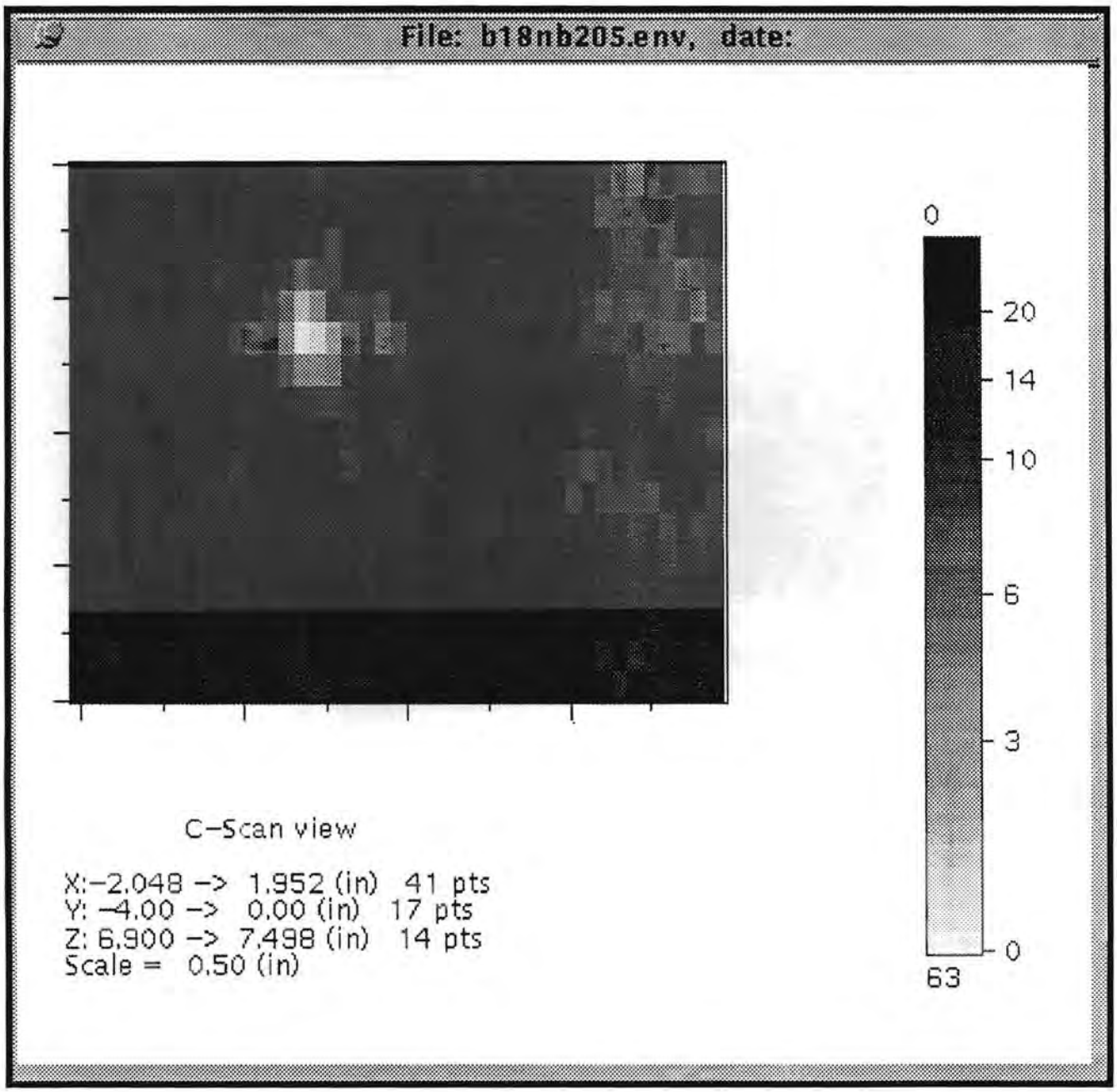

Figure 5.9c C-scan View (XY) of Base-Metal Indication in Block 1-8 at Y = -71 mm (-2.8 in.). Normal beam inspection from the clad side.

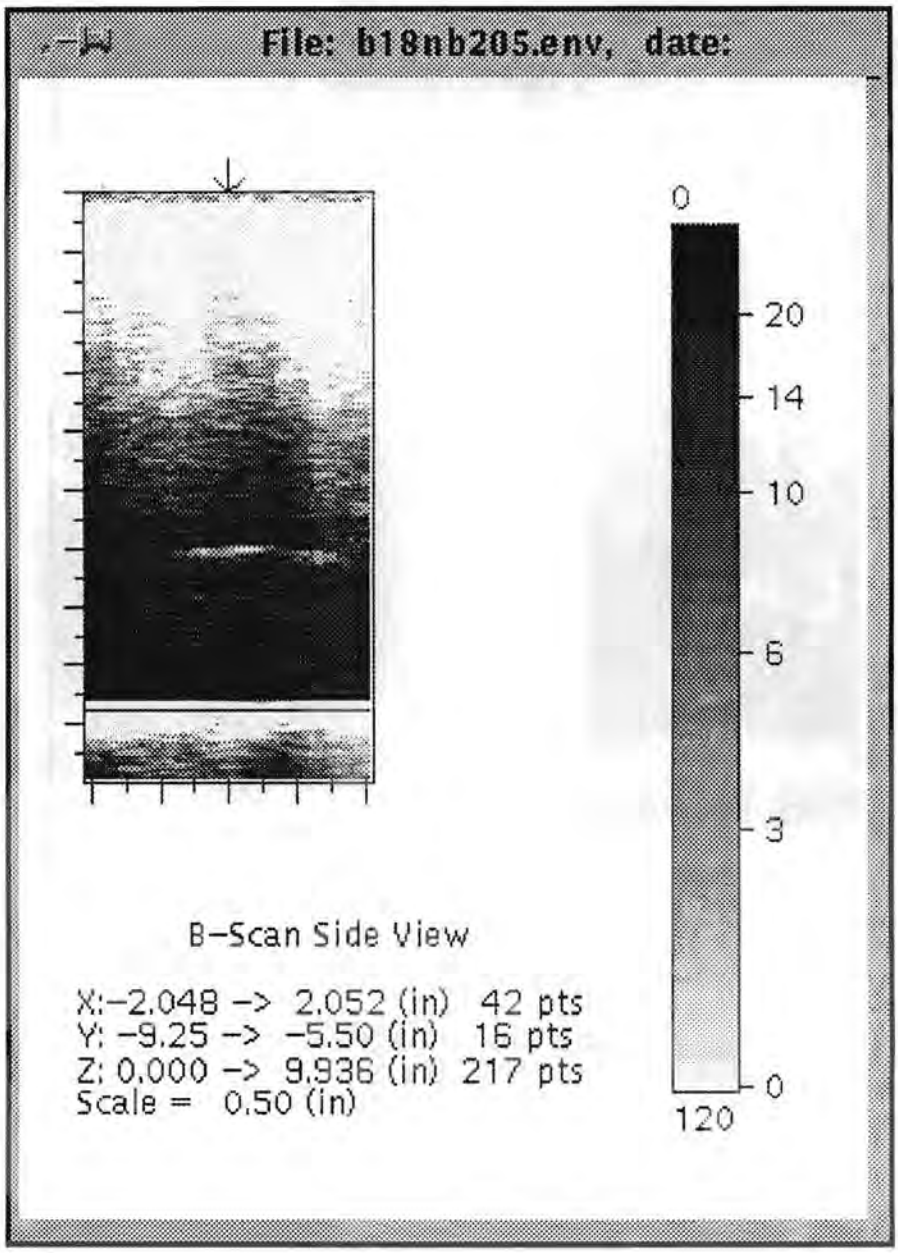

Figure 5.10a Side View (XZ) of Base-Metal Indication in Block 1-8 at Y = -185.4 mm (-7.3 in.). Normal beam inspection from the clad side.

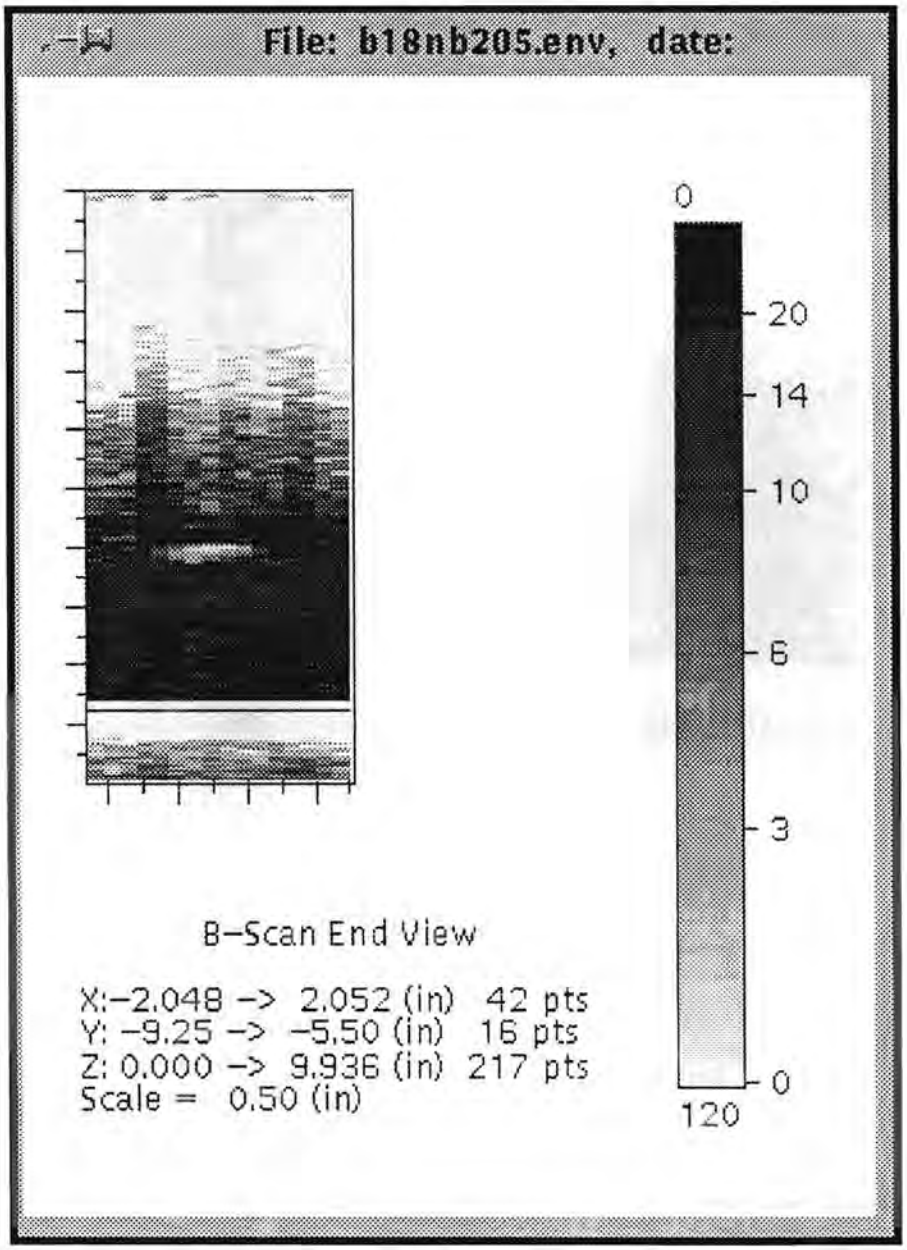

Figure 5.10b End View (YZ) of Base-Metal Indication in Block 1-8 at Y = -185.4 mm (-7.3 in.). Normal beam inspection from the clad side.

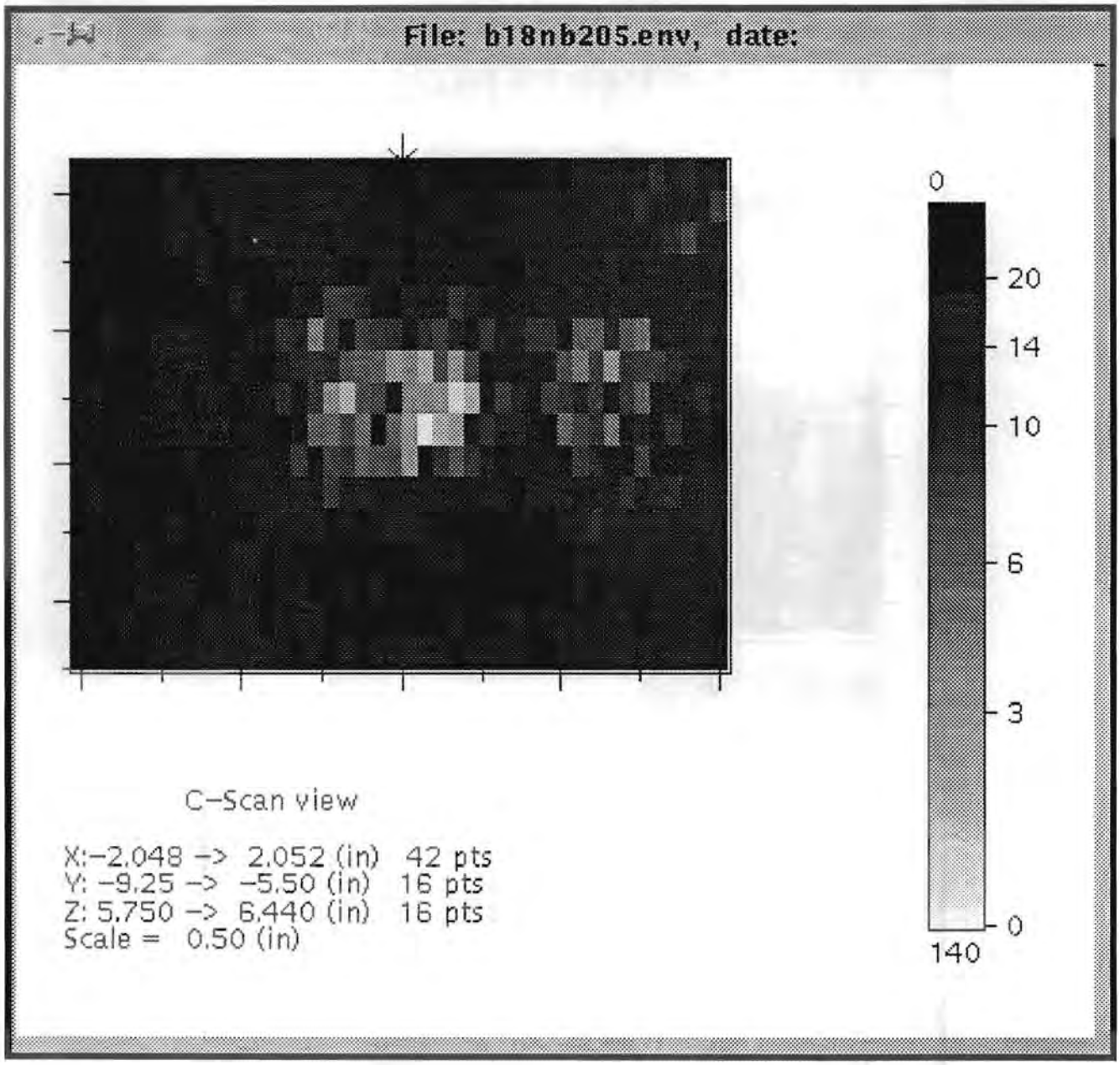

Figure 5.10c C-scan View (XY) of Base-Metal Indication in Block 1-8 at Y = -185.4 mm (-7.3 in.). Normal beam inspection from the clad side.

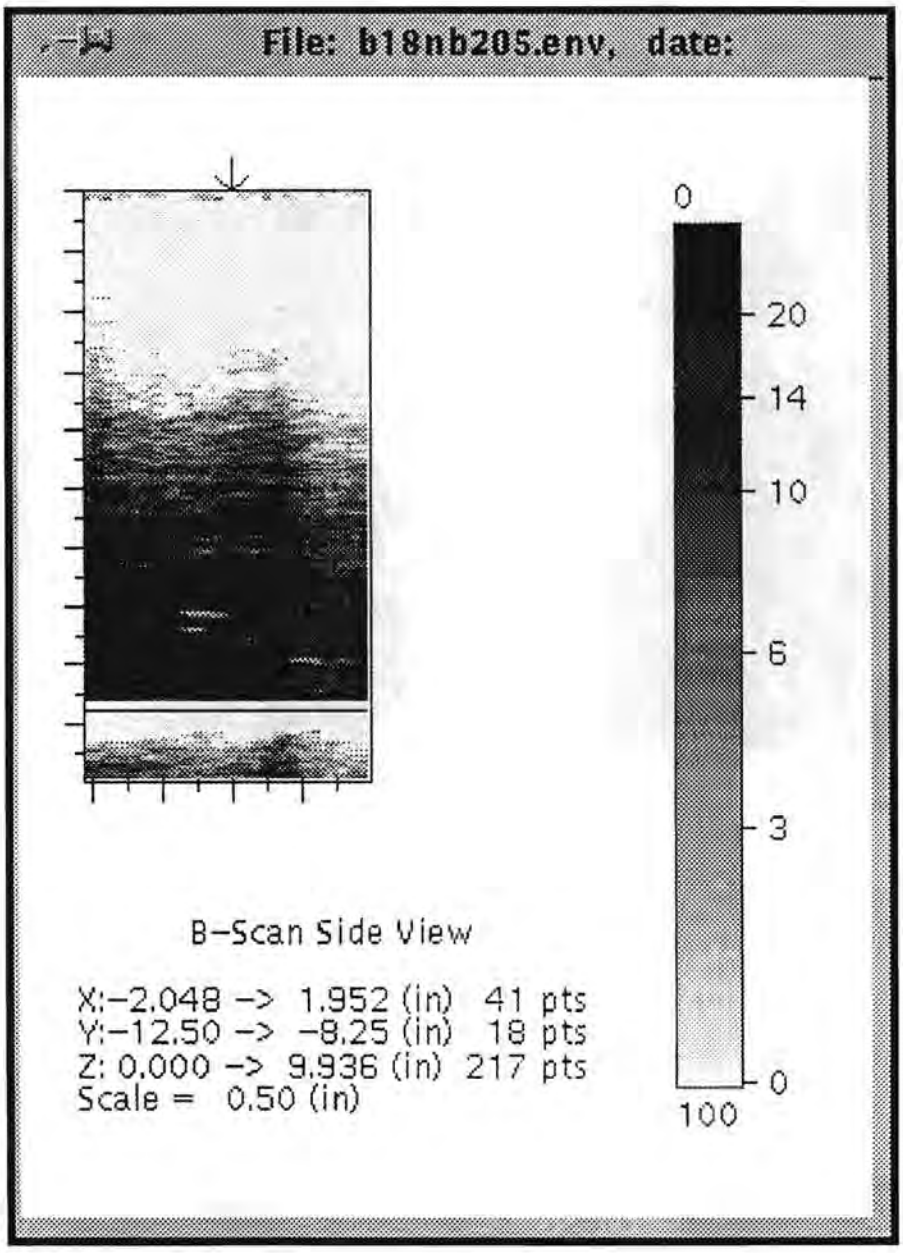

Figure 5.11a Side View (XZ) of Base-Metal Indication in Block 1-8 at Y = -254 mm (-10.0 in.). Normal beam inspection from the clad side.

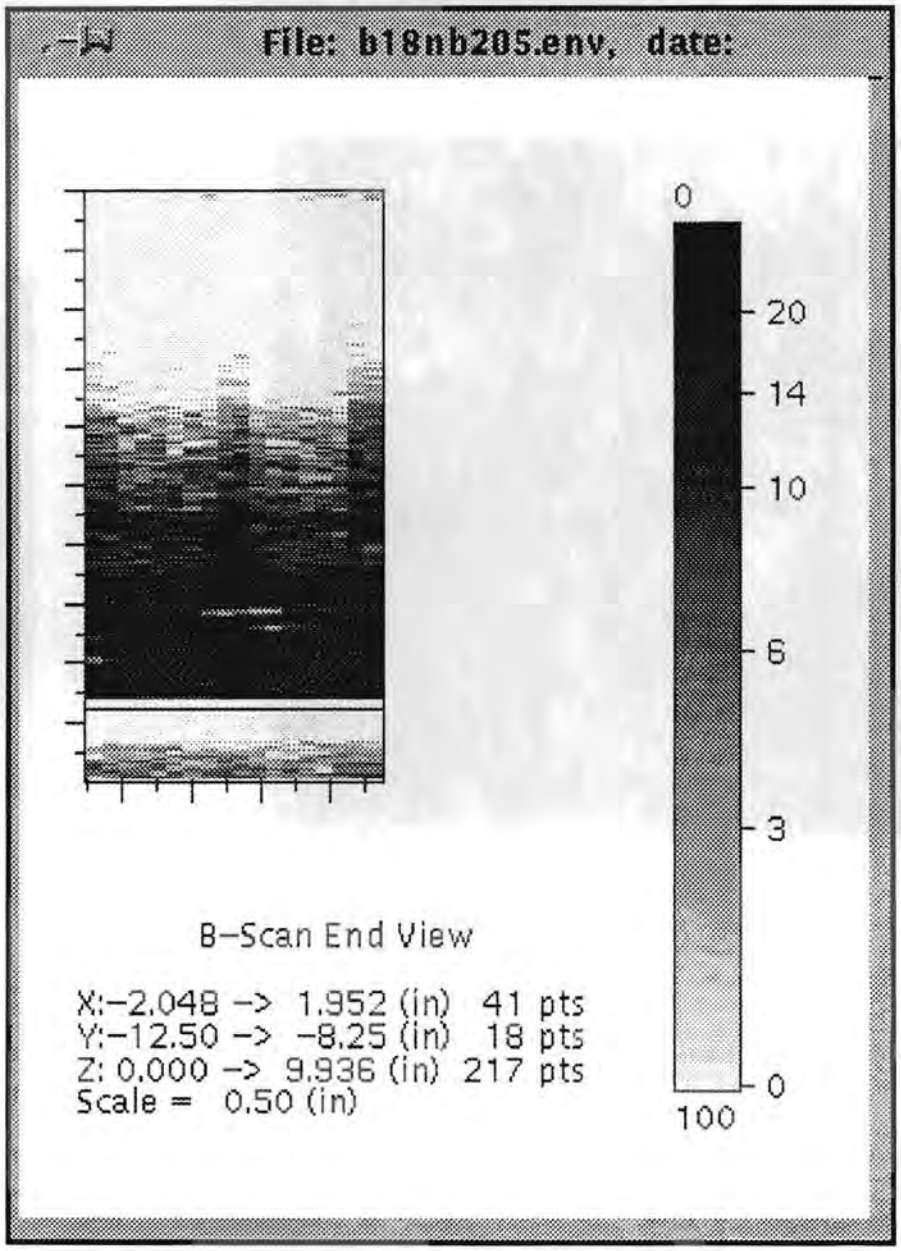

Figure 5.11b End View (YZ) of Base-Metal Indication in Block 1-8 at Y = -254 mm (-10.0 in.). Normal beam inspection from the clad side.

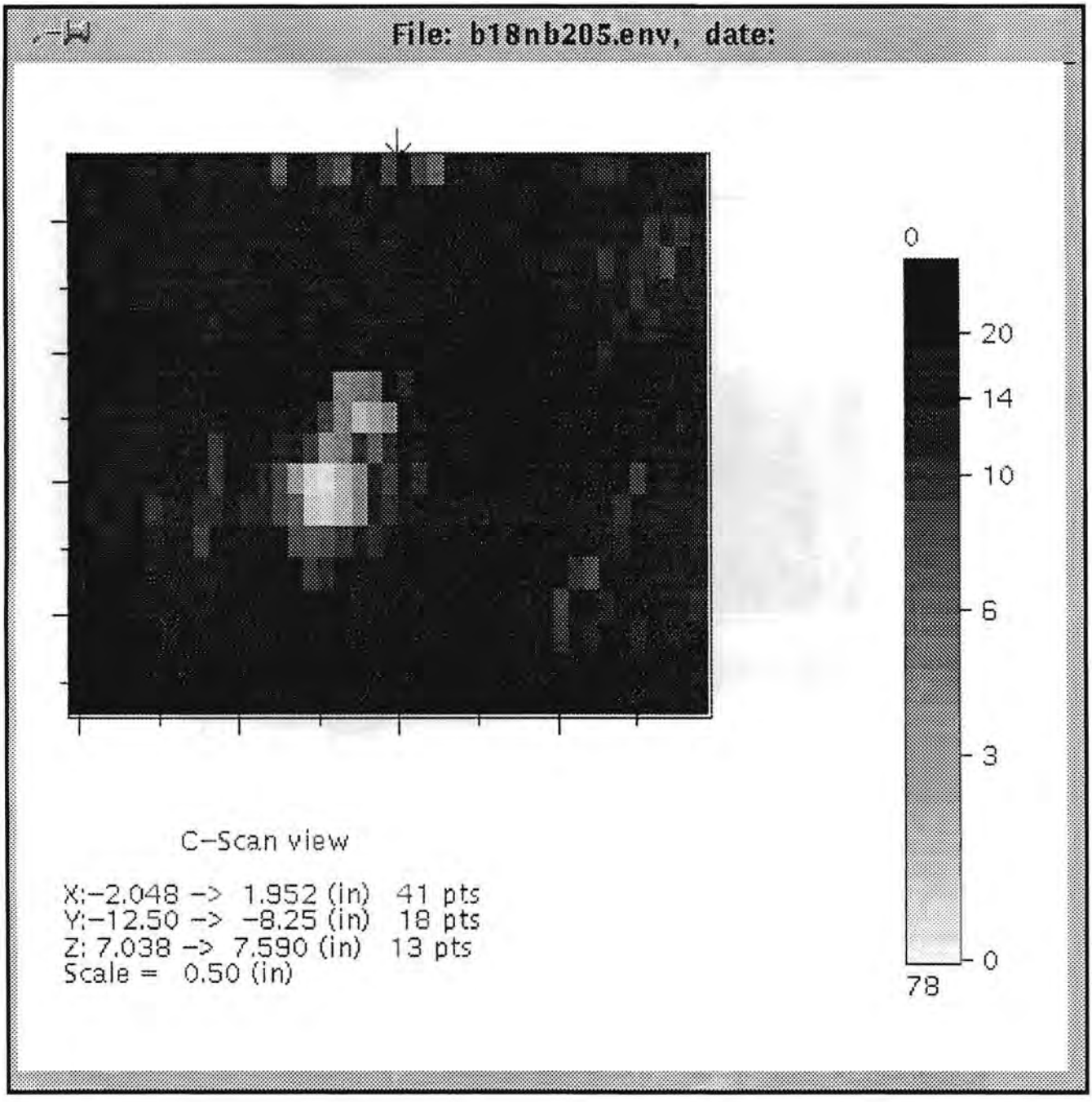

Figure 5.11c C-scan View (XY) of Base-Metal Indication in Block 1-8 at Y = -254 mm (-10.0 in.). Normal beam inspection from the clad side.

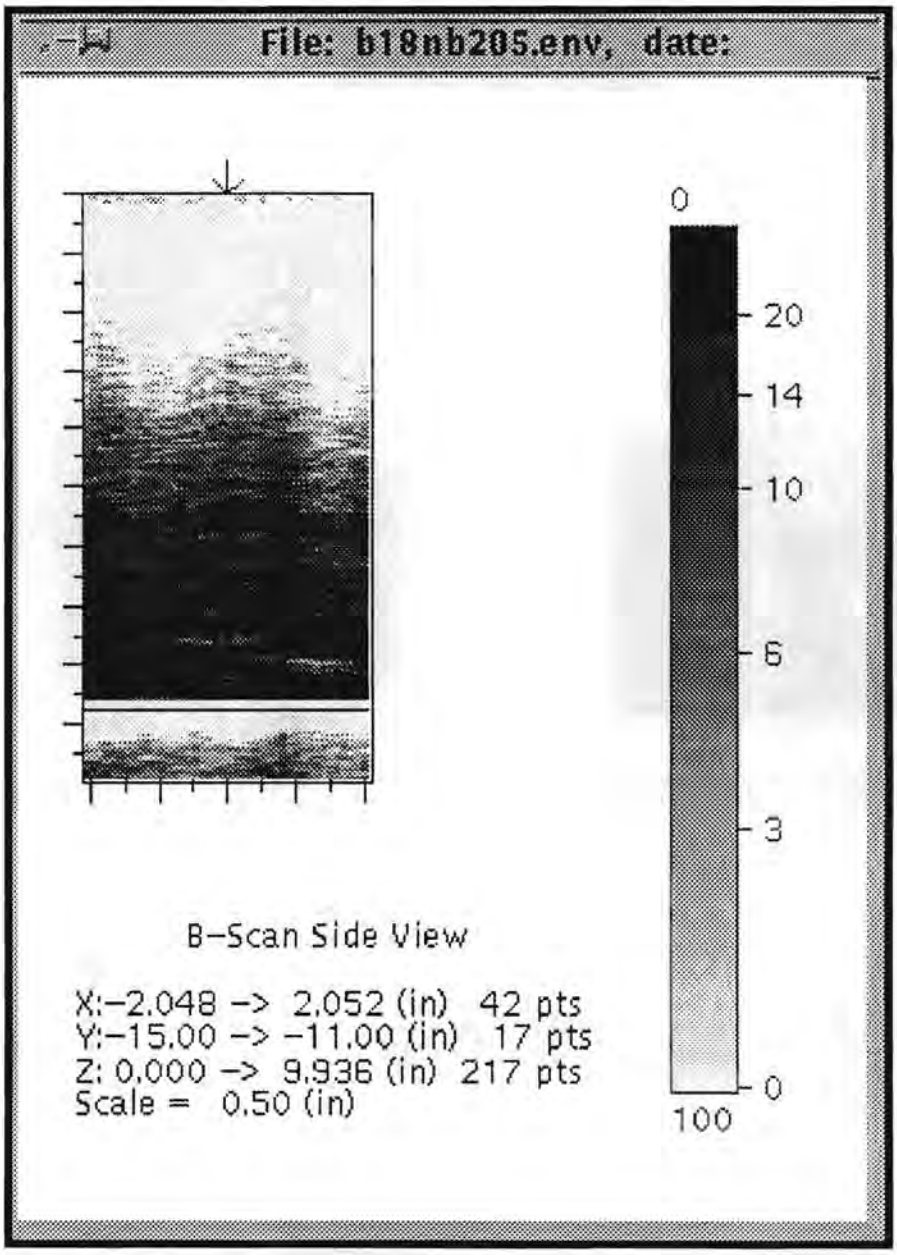

Figure 5.12a Side View (XZ) of Base-Metal Indication in Block 1-8 at Y = -325 mm (-12.8 in.). Normal beam inspection from the clad side.

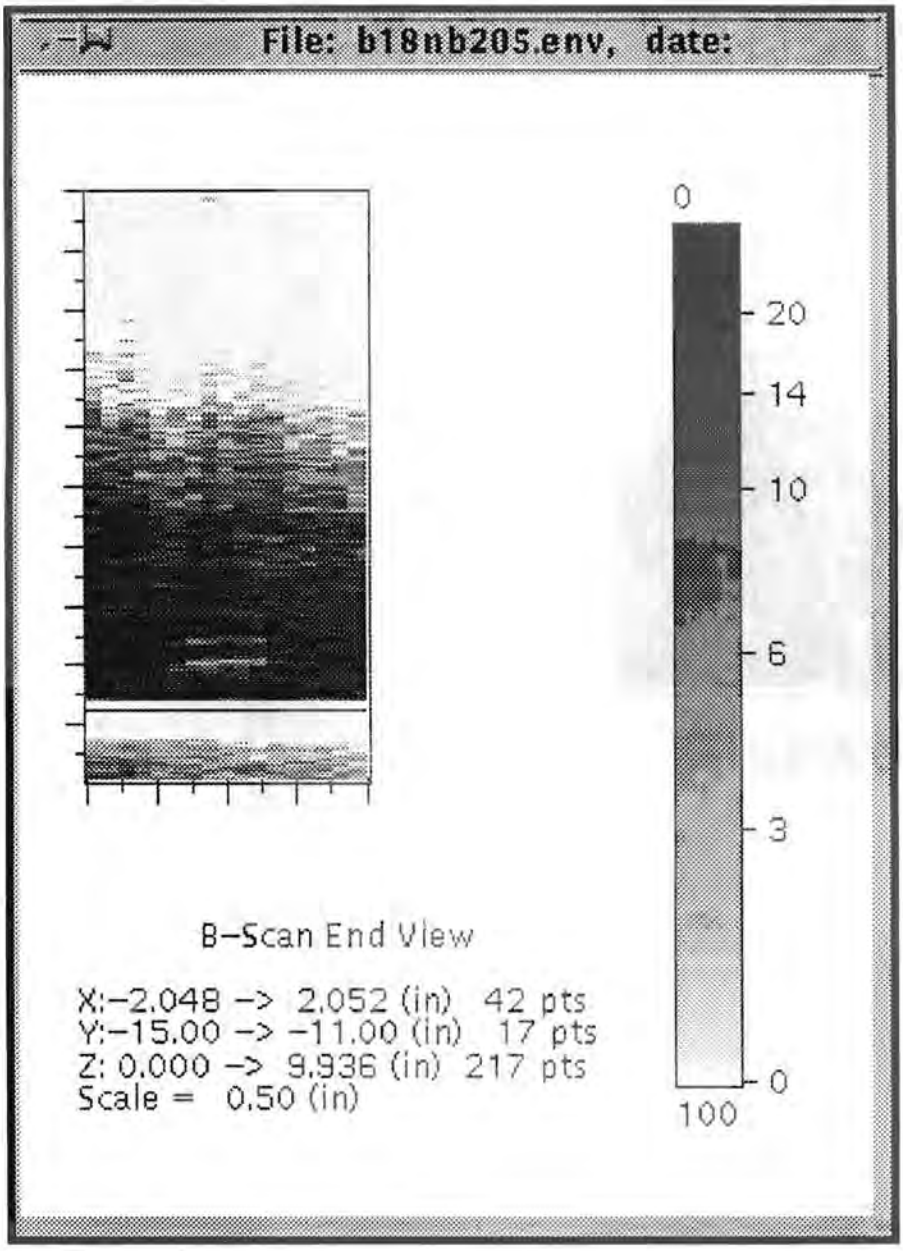

Figure 5.12b End View (YZ) of Base-Metal Indication in Block 1-8 at Y = -325 mm (-12.8 in.). Normal beam inspection from the clad side.

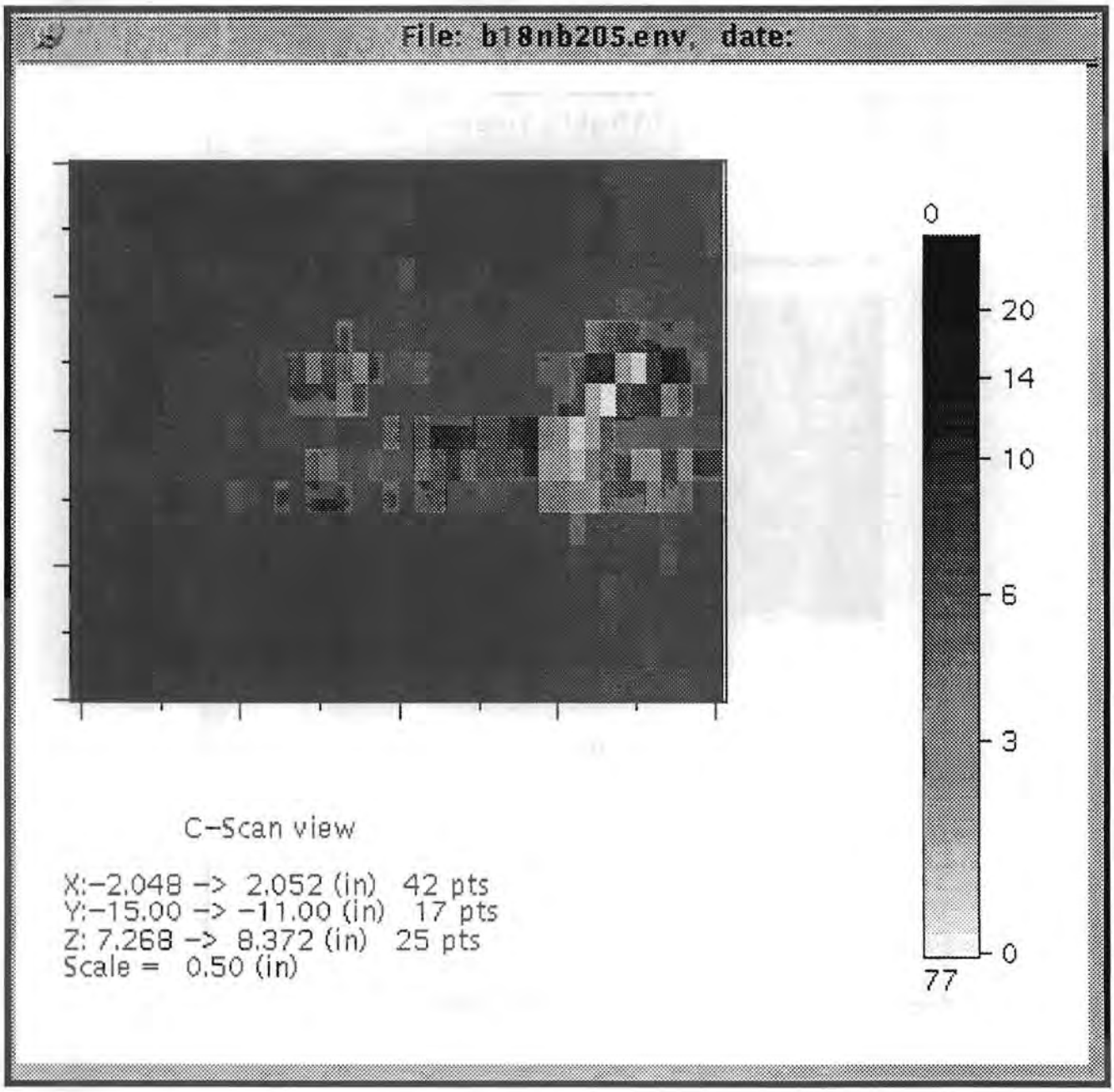

Figure 5.12c C-scan View (XY) of Base-Metal Indication in Block 1-8 at Y = -325 mm (-12.8 in.). Normal beam inspection from the clad side.

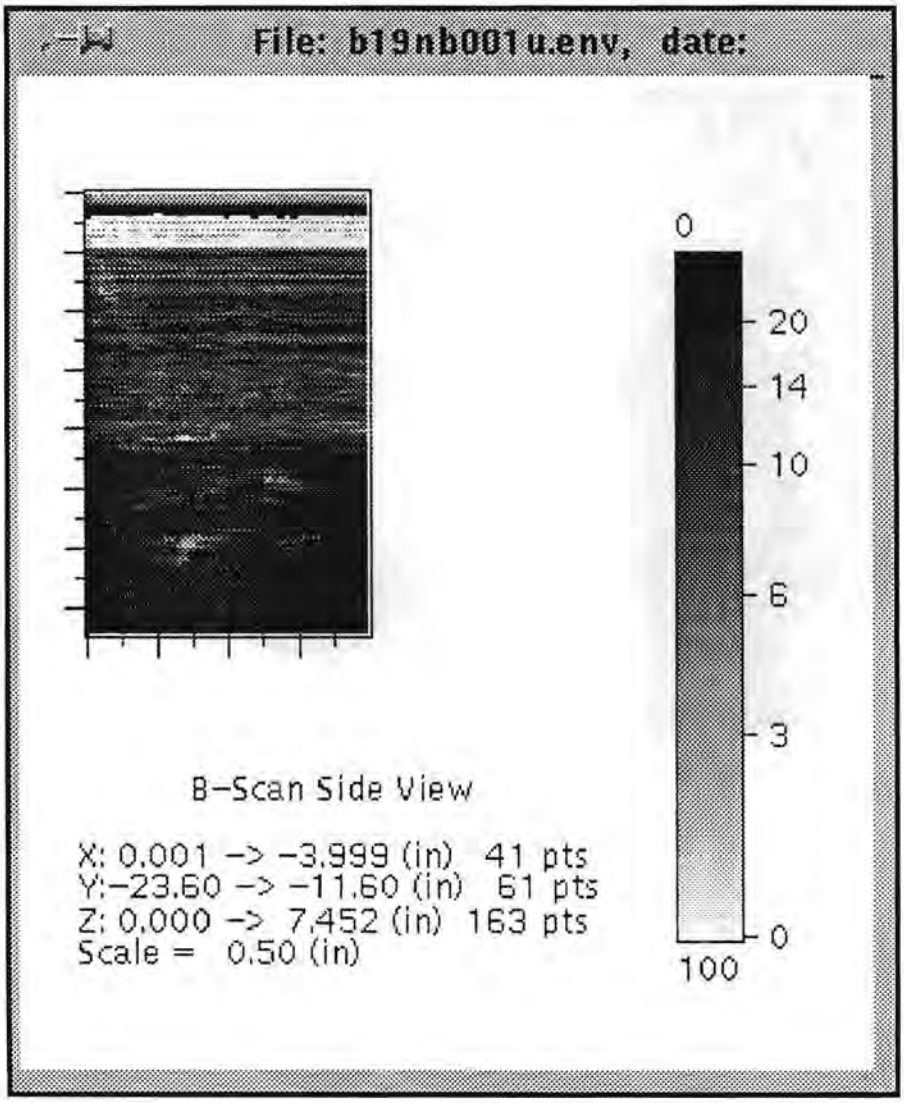

Figure 5.13a Side View (scanner coordinates xz) of Base-Metal Indication in Block 1-9 at Y = -582 mm (-22.9 in.). Normal beam inspection from the bottom side. Z in the figure corresponds to material coordinates of X from -152 mm (-6 in.) to +36.8 mm (+1.45 in.). X in the figure corresponds to material coordinates of Z from 216 mm (8.5 in.) to 114.3 (4.5 in.).

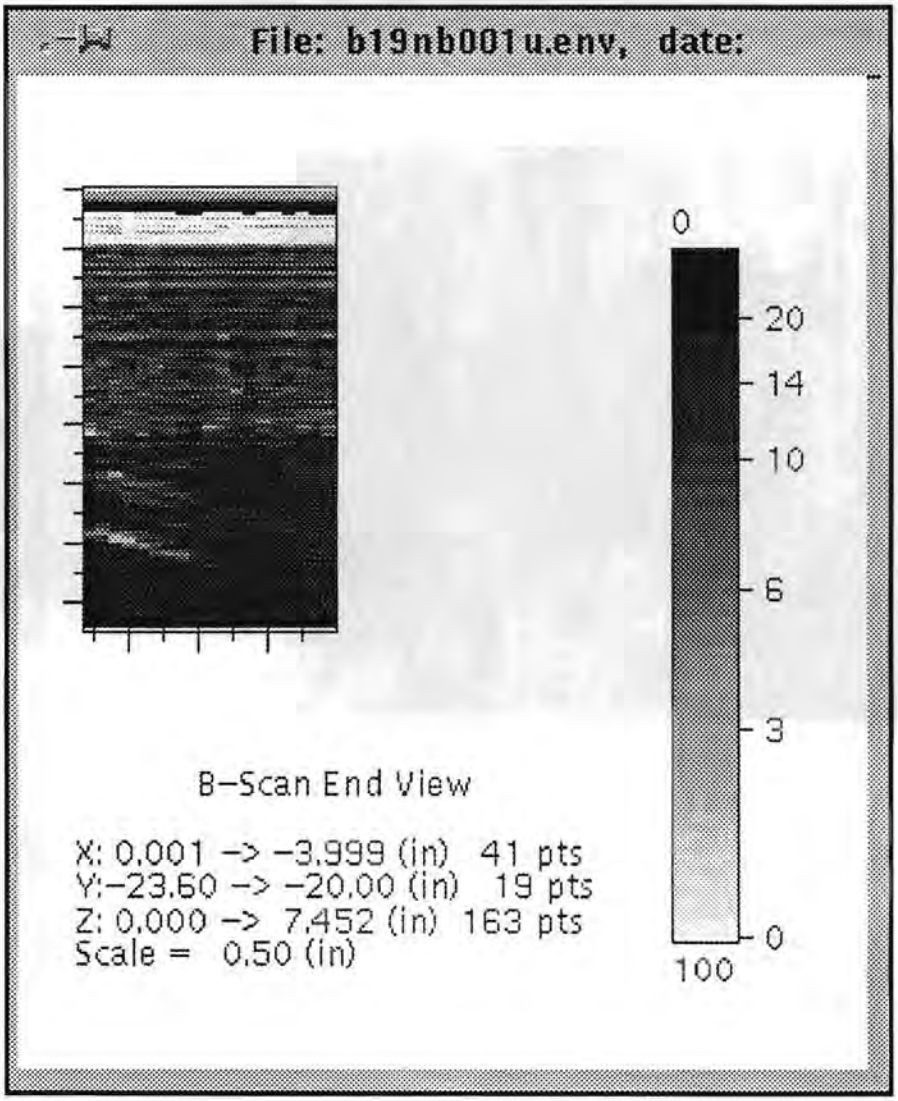

Figure 5.13b End View (scanner coordinates yz) of Base-Metal Indication in Block 1-9 at Y = -582 mm (-22.9 in.). Normal beam inspection from the bottom side. Z in the figure corresponds to material coordinates of X from -152 mm (-6 in.) to +36.8 mm (+1.45 in.). X in the figure corresponds to material coordinates of Z from 216 mm (8.5 in.) to 114.3 (4.5 in.).

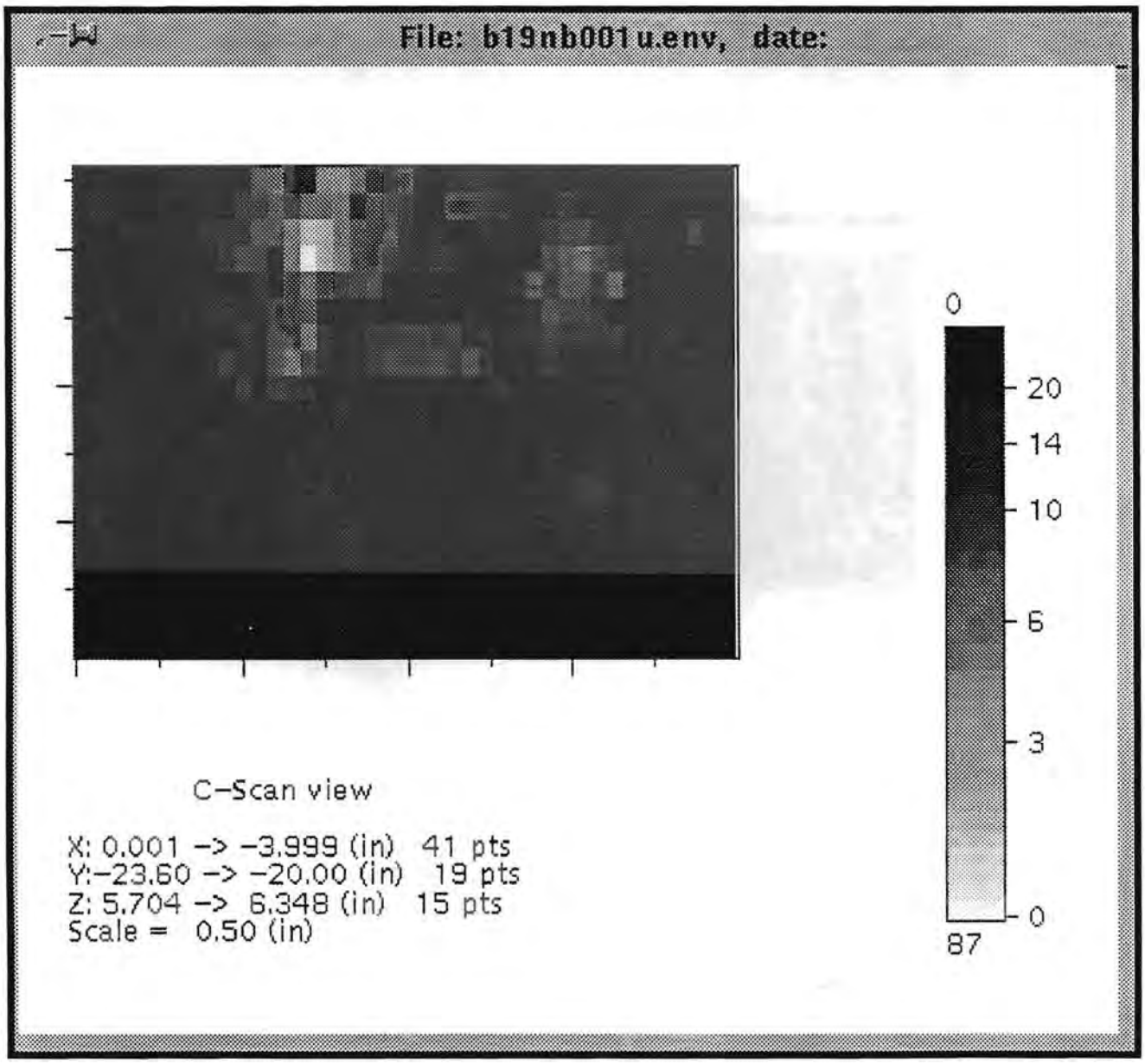

Figure 5.13c C-scan View (scanner coordinates xy) of Base-Metal Indication in Block 1-9 at Y = -582 mm (-22.9 in.). Normal beam inspection from the bottom side. Z in the figure corresponds to material coordinates of X from -152 mm (-6 in.) to +36.8 mm (+1.45 in.). X in the figure corresponds to material coordinates of Z from 216 mm (8.5 in.) to 114.3 (4.5 in.).

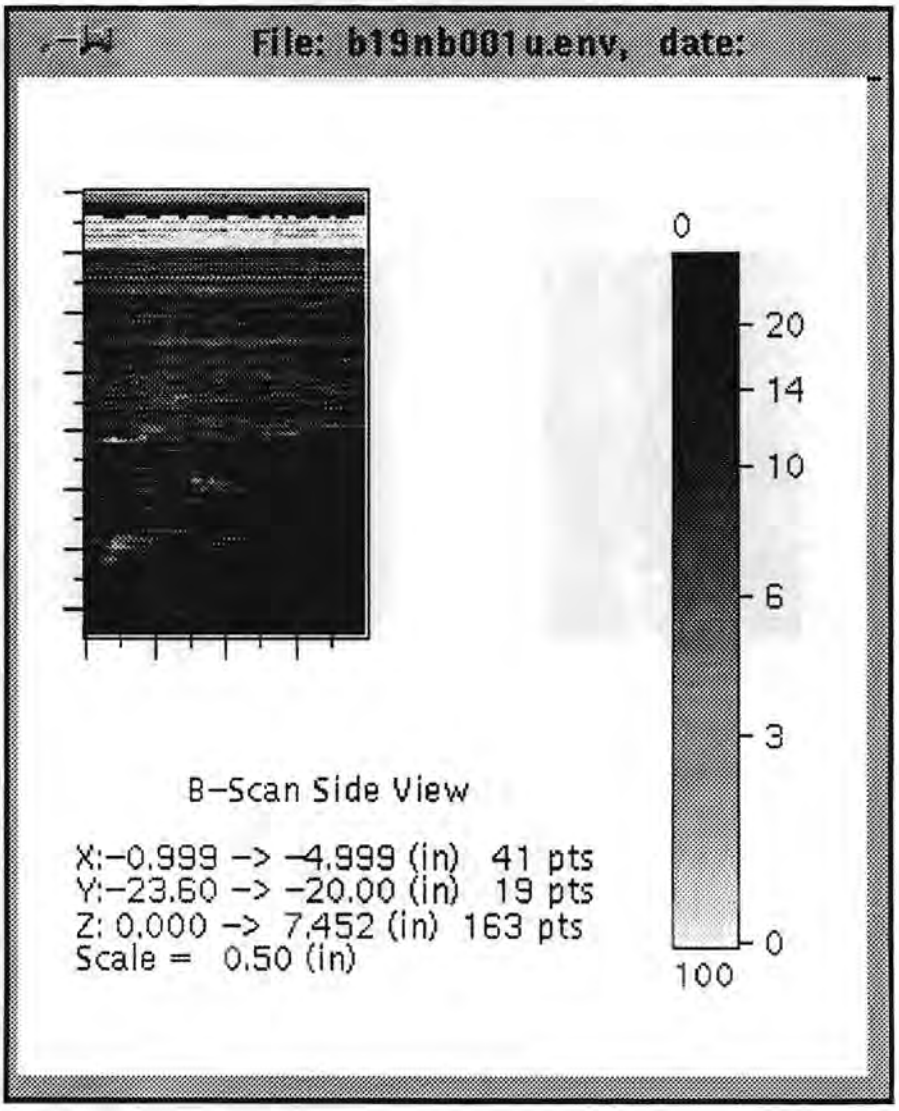

Figure 5.14a Side View (scanner coordinates xz) of Base-Metal Indication in Block 1-9 at Y = -584 mm (-23.0 in.).. Normal beam inspection from the bottom side. Z in the figure corresponds to material coordinates of X from -152 mm (-6 in.) to +368 mm (+1.45 in.). X in the figure corresponds to material coordinates of Z from 191 mm (7.5 in.) to 88.9 mm (3.5 in.).

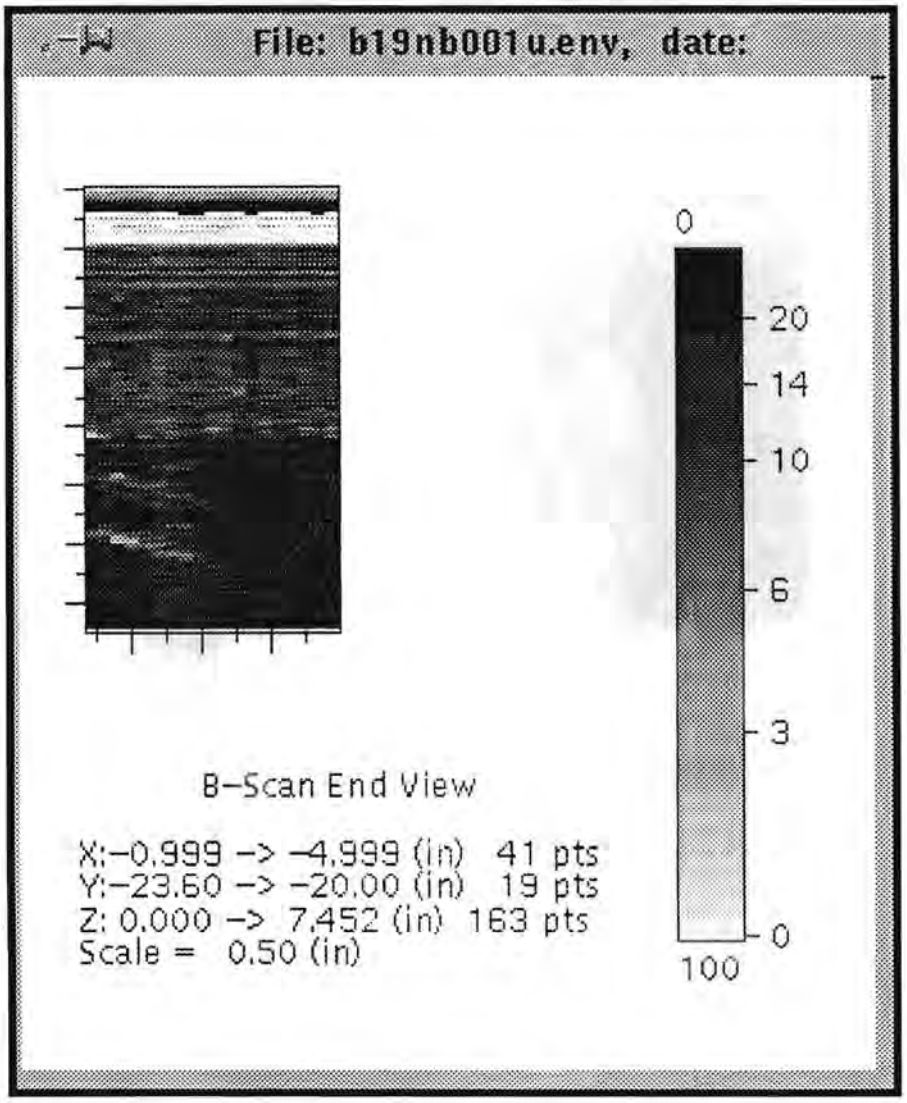

Figure 5.14b End View (scanner coordinates yz) of Base-Metal Indication in Block 1-9 at Y = -584 mm (-23.0 in.).. Normal beam inspection from the bottom side. Z in the figure corresponds to material coordinates of X from -152 mm (-6 in.) to +368 mm (+1.45 in.). X in the figure corresponds to material coordinates of Z from 191 mm (7.5 in.) to 88.9 mm (3.5 in.).

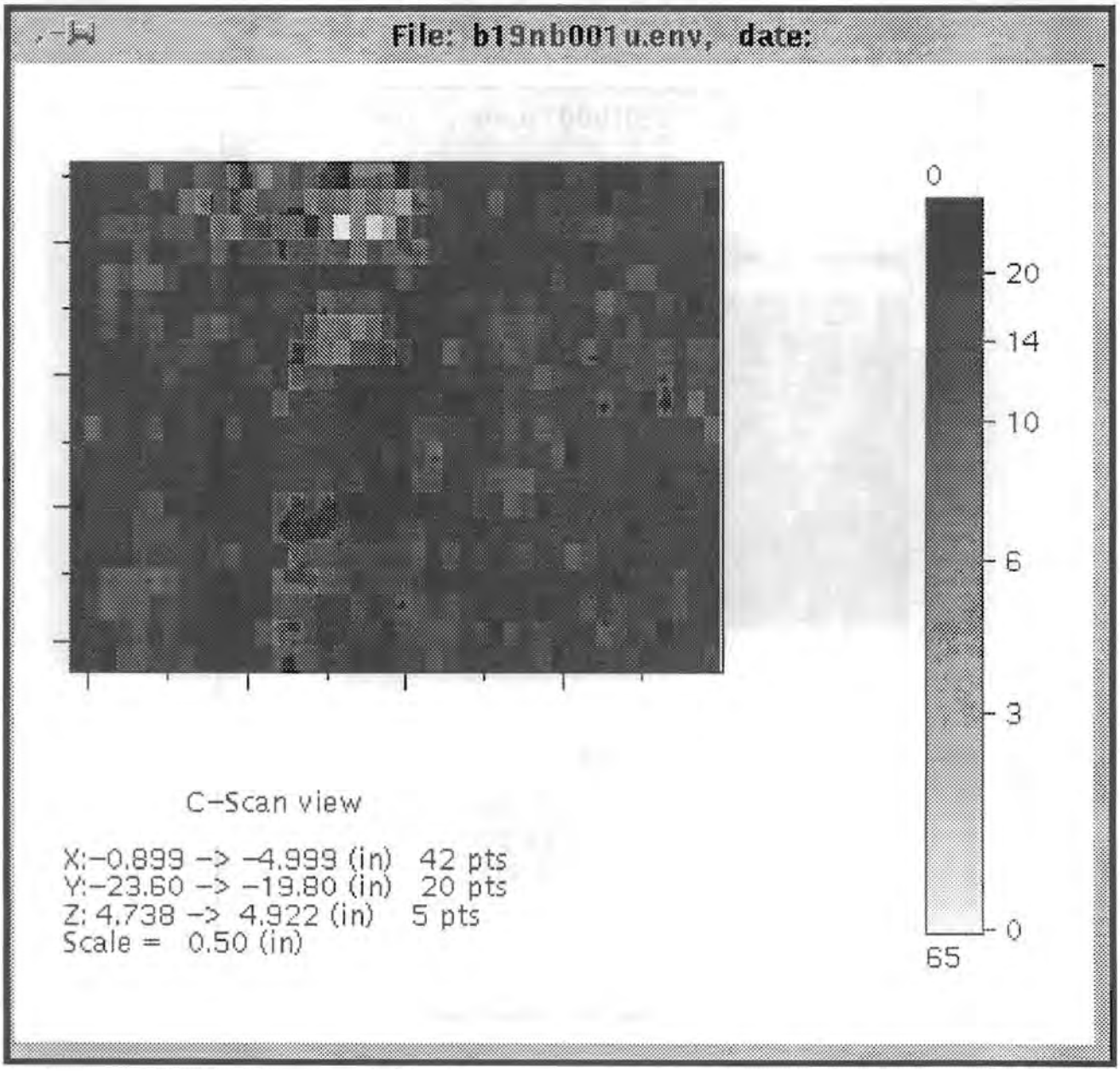

Figure 5.14c C-scan View (scanner coordinates xy) of Base-Metal Indication in Block 1-9 at Y = -584 mm (-23.0 in.).. Normal beam inspection from the bottom side. Z in the figure corresponds to material coordinates of X from -152 mm (-6 in.) to +368 mm (+1.45 in.). X in the figure corresponds to material coordinates of Z from 191 mm (7.5 in.) to 88.9 mm (3.5 in.).

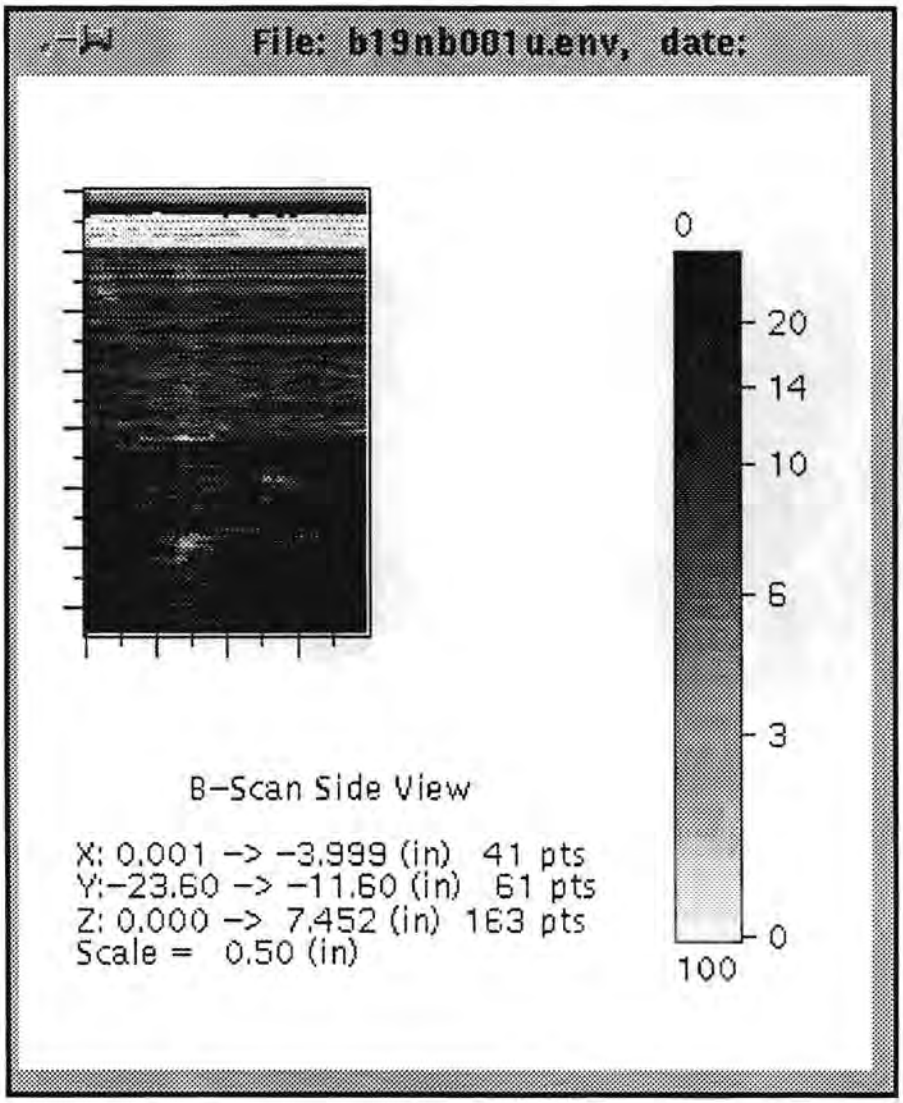

Figure 5.15a Side View (scanner coordinates xz) of Base-Metal Indication in Block 1-9 at Y = -597 mm (-23.5 in.). Normal beam inspection from the bottom side. Z in the figure corresponds to material coordinates of X from -152 mm (-6 in.) to +368 mm (+1.45 in.). X in the figure corresponds to material coordinates of Z from 216 mm (8.5 in.) to 114 mm (4.5 in.).

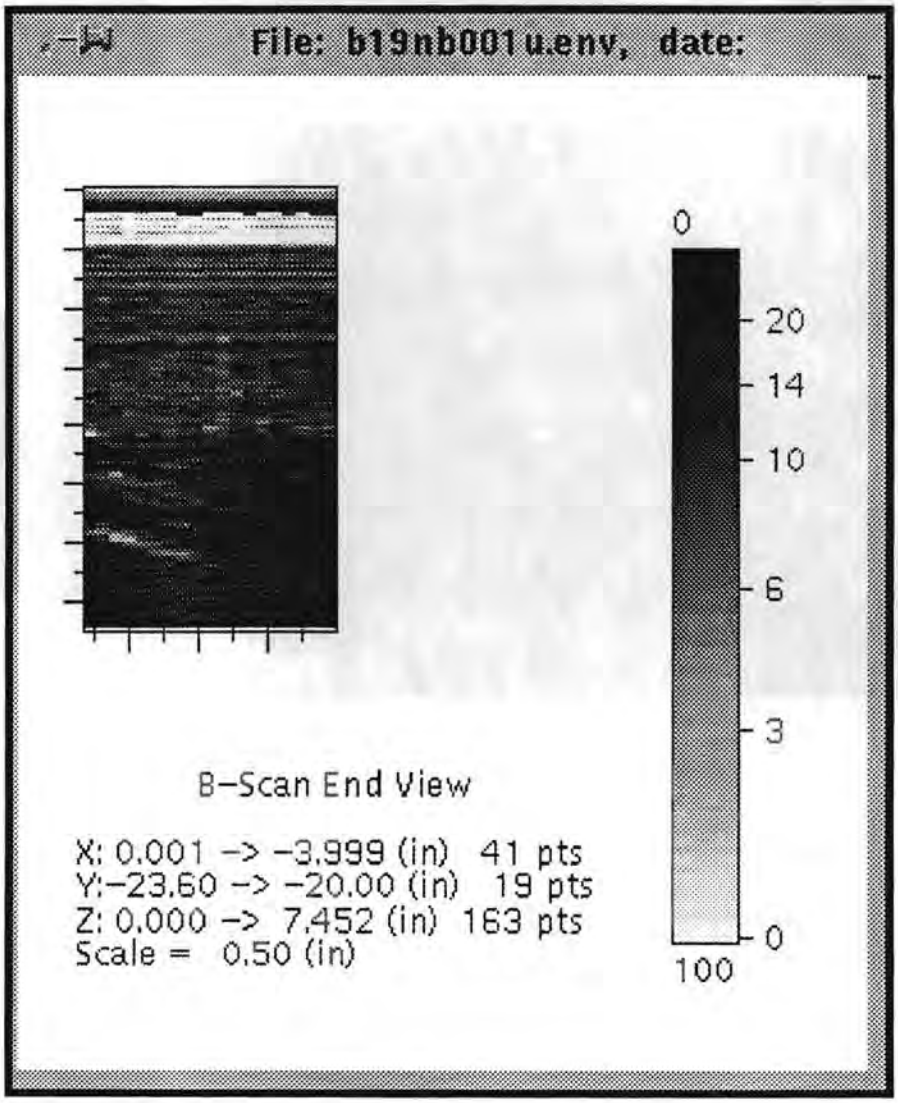

Figure 5.15b End View (scanner coordinates yz) of Base-Metal Indication in Block 1-9 at Y = -597 mm (-23.5 in.). Normal beam inspection from the bottom side. Z in the figure corresponds to material coordinates of X from -152 mm (-6 in.) to +368 mm (+1.45 in.). X in the figure corresponds to material coordinates of Z from 216 mm (8.5 in.) to 114 mm (4.5 in.).

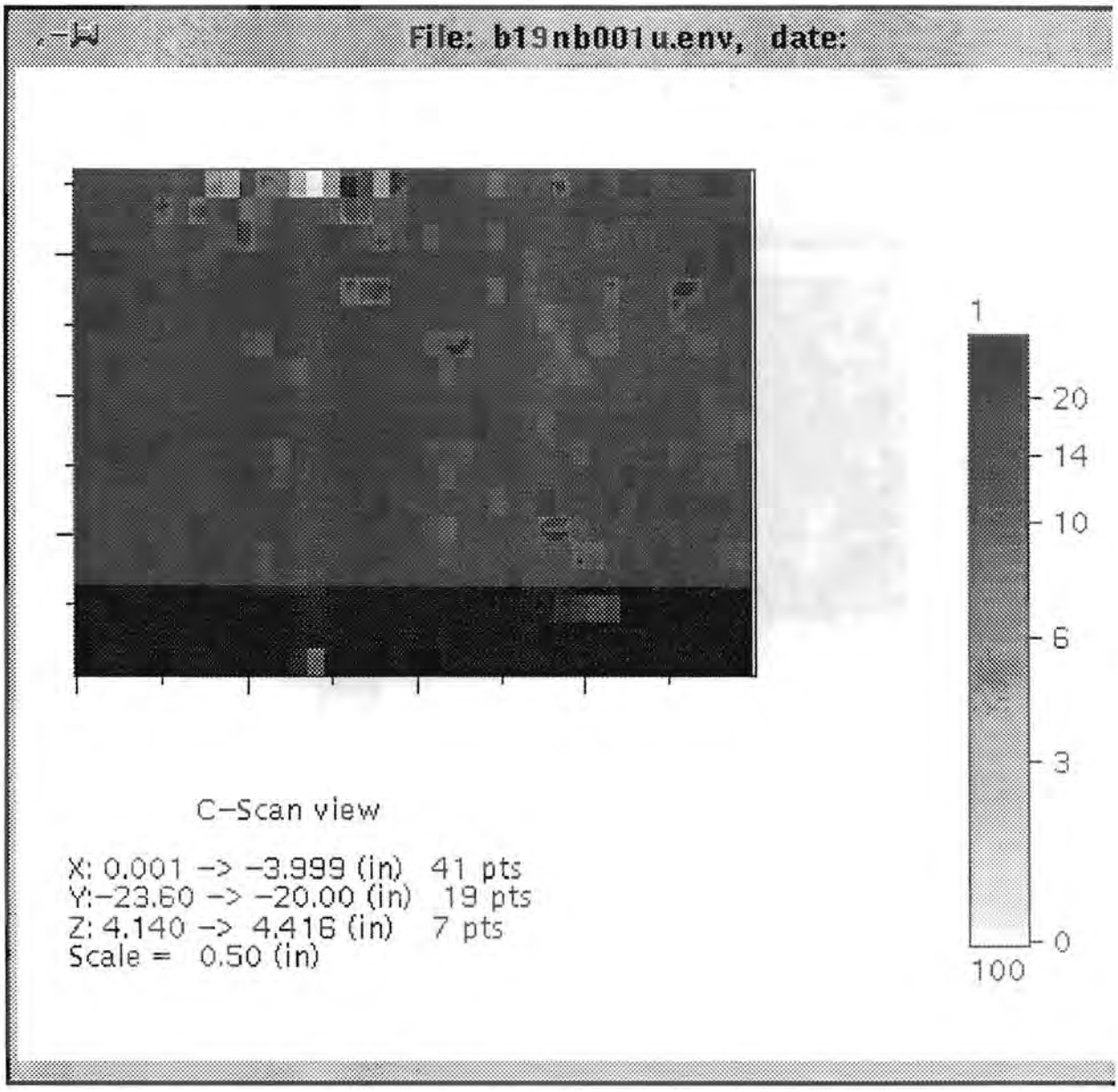

Figure 5.15c C-scan View (scanner coordinates xy) of Base-Metal Indication in Block 1-9 at Y = -597 mm (-23.5 in.). Normal beam inspection from the bottom side. Z in the figure corresponds to material coordinates of X from -48 mm (-1.9 in.) to -41 mm (-1.6 in.). X in the figure corresponds to material coordinates of Z from 216 mm (8.5 in.) to 114 mm (4.5 in.).

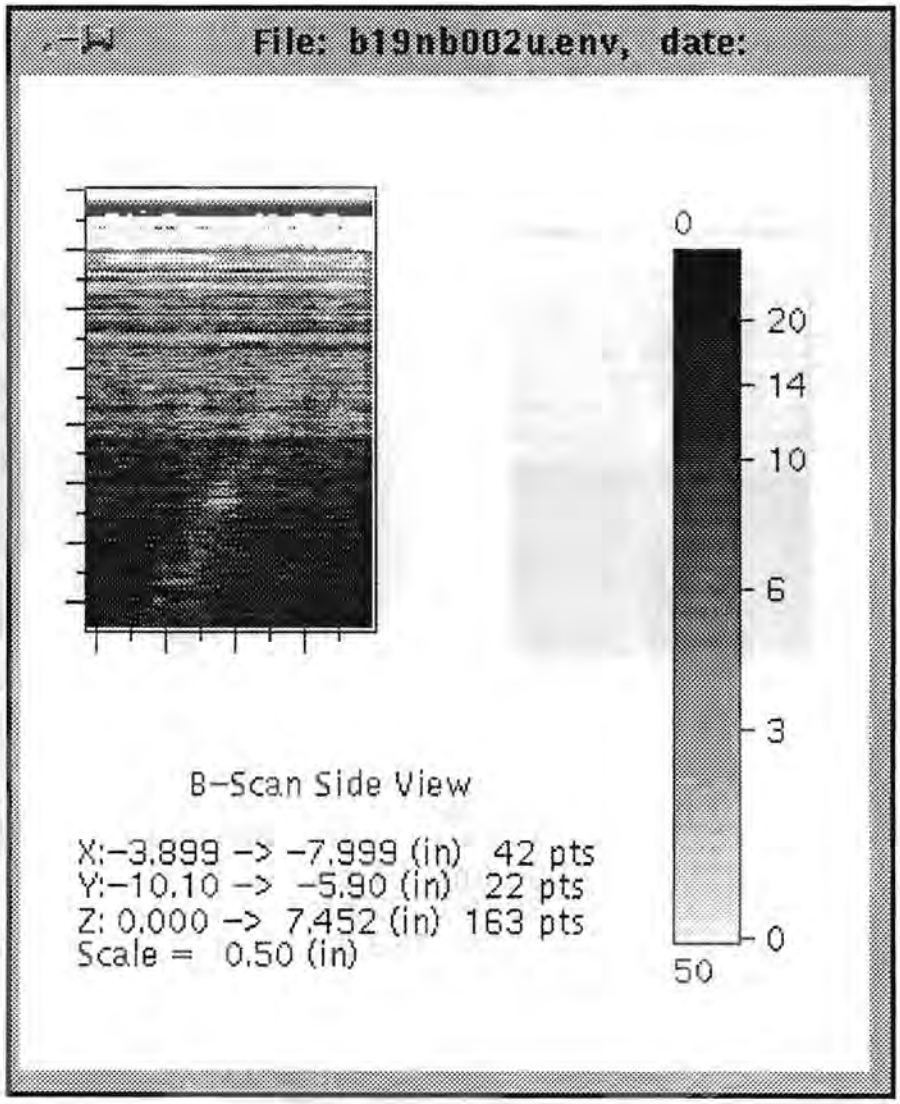

Figure 5.16a Side View (Scanner Coordinates XZ) of Base-Metal Indication in Block 1-9 at Y = -22.1 mm (-8.7 in.). Normal beam inspection from the bottom side. Z in the figure corresponds to material coordinates of X from -152 mm (-6 in.) to +368 mm (+1.45 in.). X in the figure corresponds to material coordinates of Z from 119 mm (4.7 in.) to 13 mm (0.5 in.).

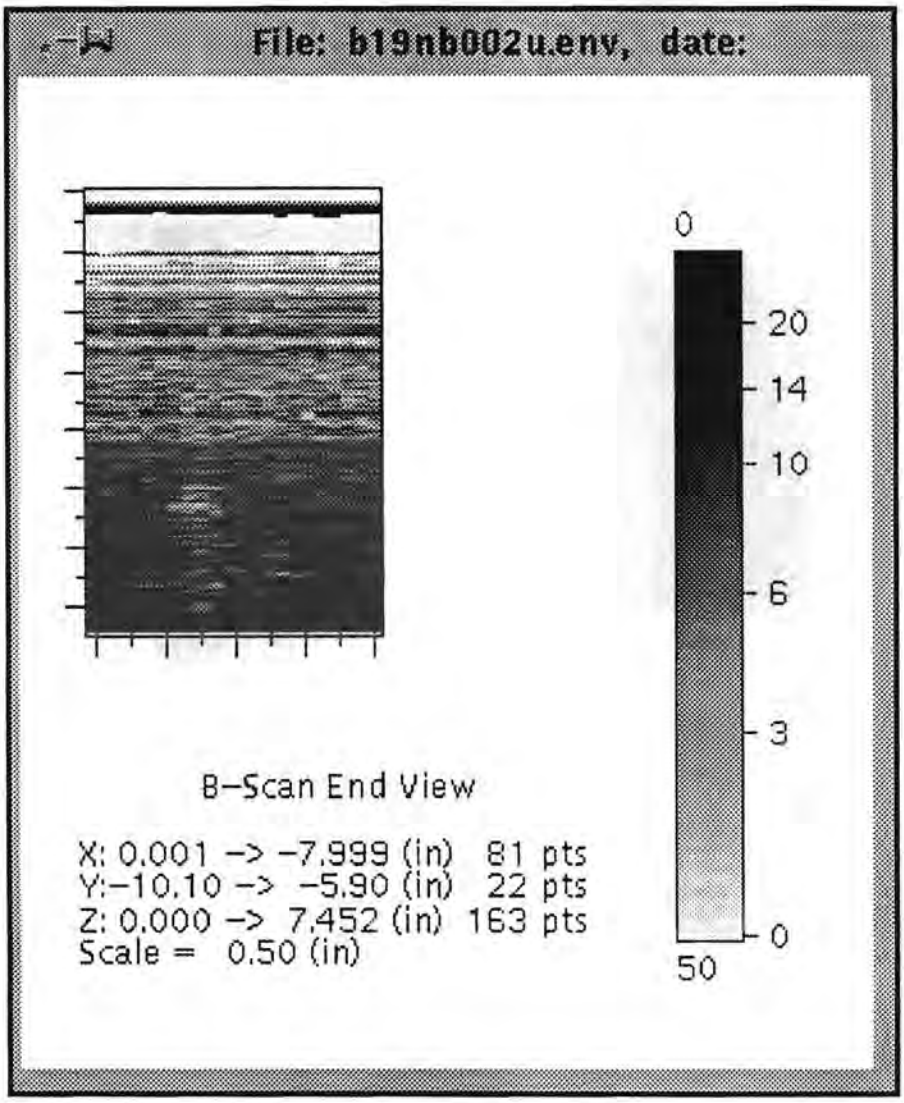

Figure 5.16b End View (Scanner Coordinates YZ) of Base-Metal Indication in Block 1-9 at Y = -22.1 mm (-8.7 in.). Normal beam inspection from the bottom side. Z in the figure corresponds to material coordinates of X from -152 mm (-6 in.) to 368 mm (1.45 in.).

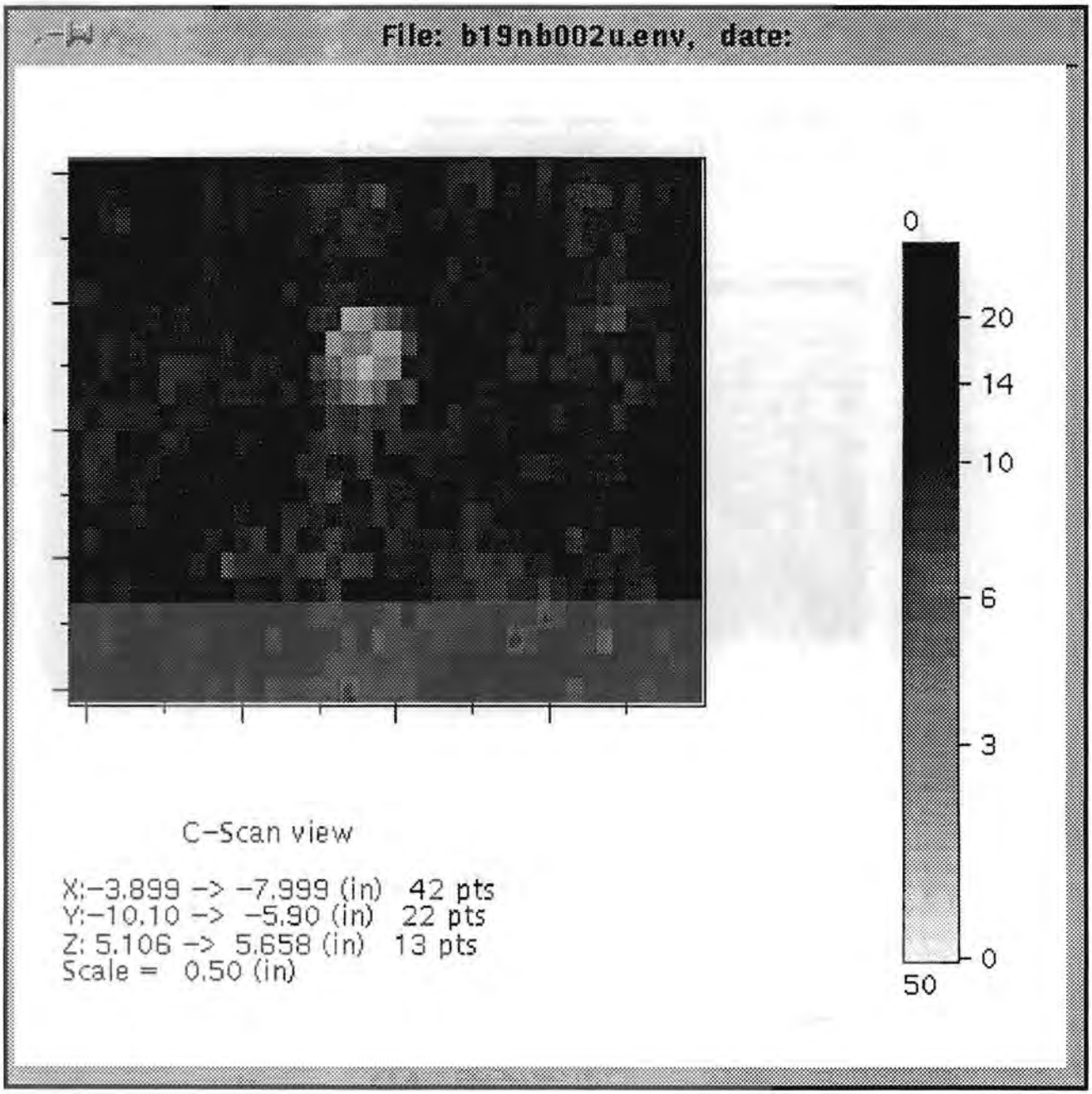

Figure 5.16c C-scan View (Scanner Coordinates XY) of Base-Metal Indication in Block 1-9 at Y = -22.1 mm (-8.7 in.). Normal beam inspection from the bottom side. X in the figure corresponds to material coordinates of Z from 119 mm (4.7 in.) to 13 mm (0.5 in.).

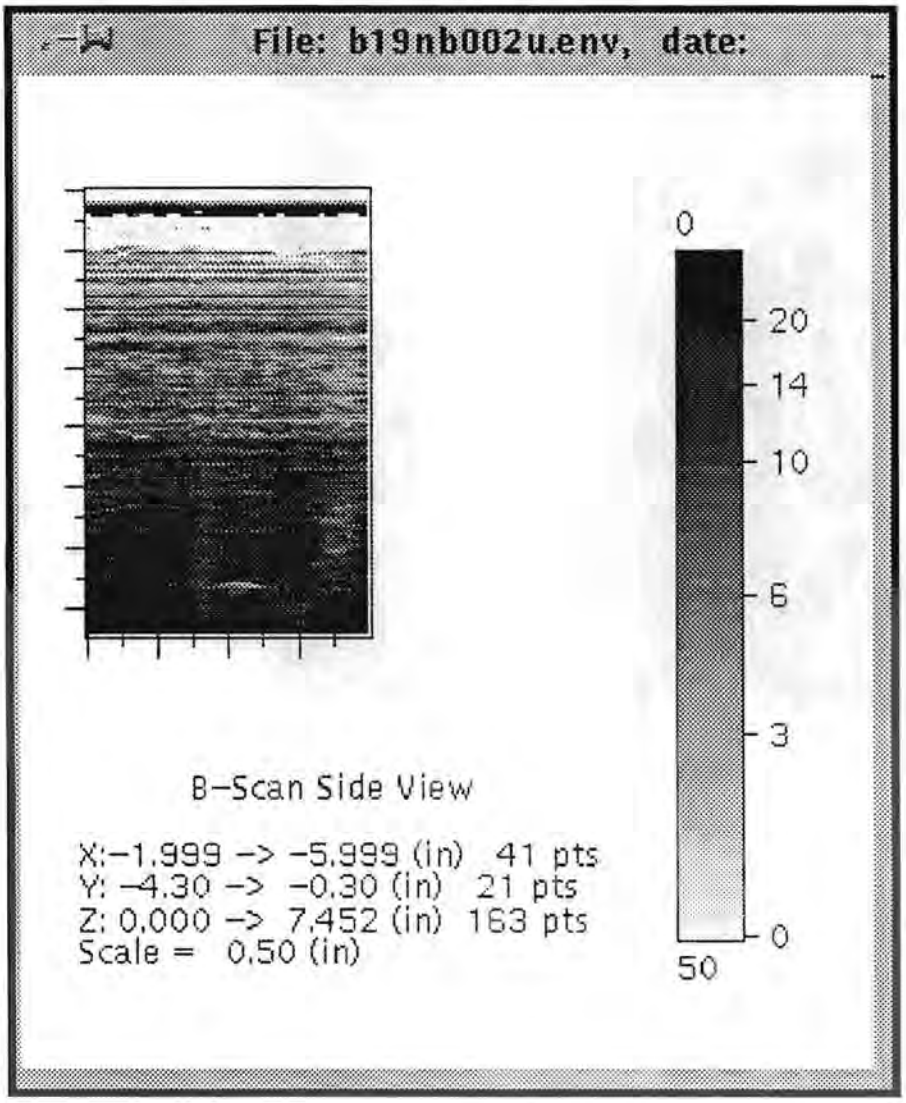

Figure 5.17a Side View (Scanner Coordinates XZ) of Base-Metal Indication in Block 1-9 at Y = -69 mm (-2.7 in.). Normal beam inspection from the bottom side. Z in the figure corresponds to material coordinates of X from -152 mm (-6 in.) to +368 mm (+1.45 in.). X in the figure corresponds to material coordinates of Z from 165 mm (6.5 in.) to 64 mm (2.5 in.).

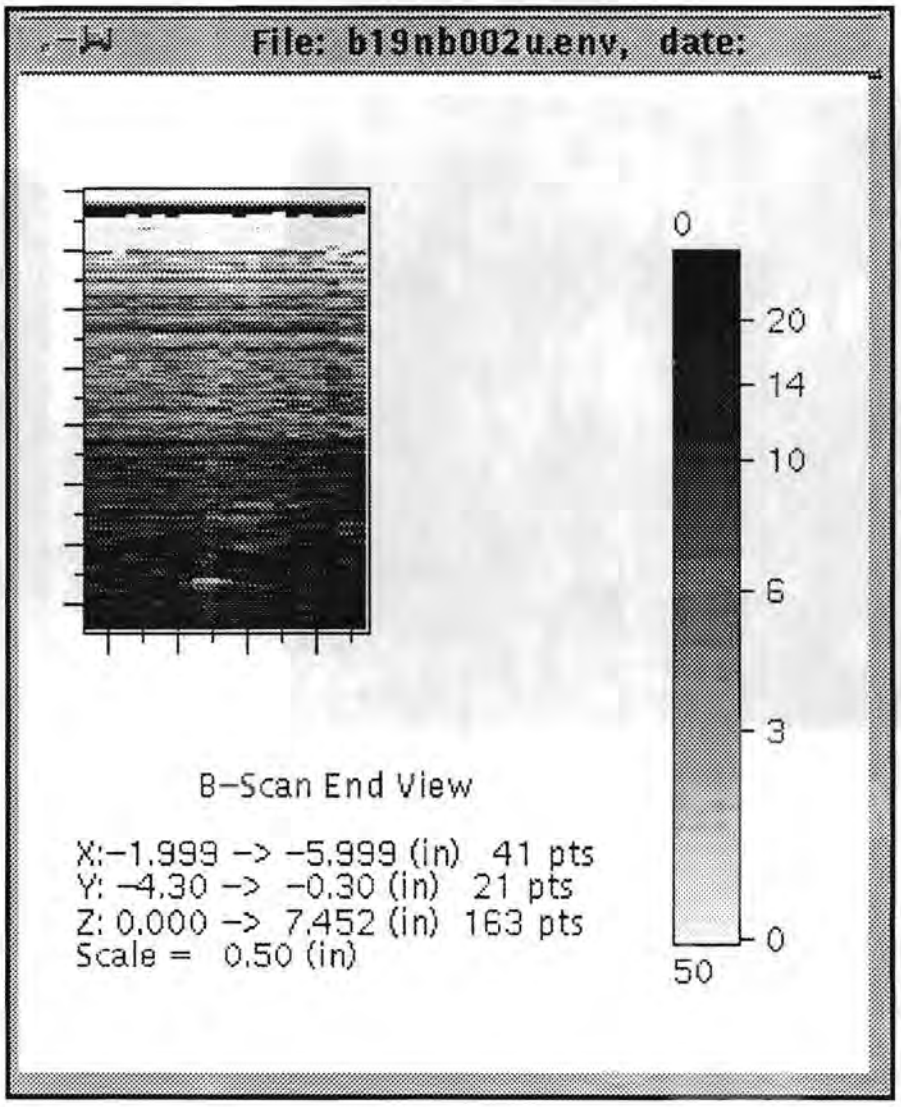

Figure 5.17b End View (Scanner Coordinates YZ) of Base-Metal Indication in Block 1-9 at Y = -69 mm (2.7 in.). Normal beam inspection from the bottom side. Z in the figure corresponds to material coordinates of X from -152 mm (-6 in.) to +368 mm (+1.45 in.).

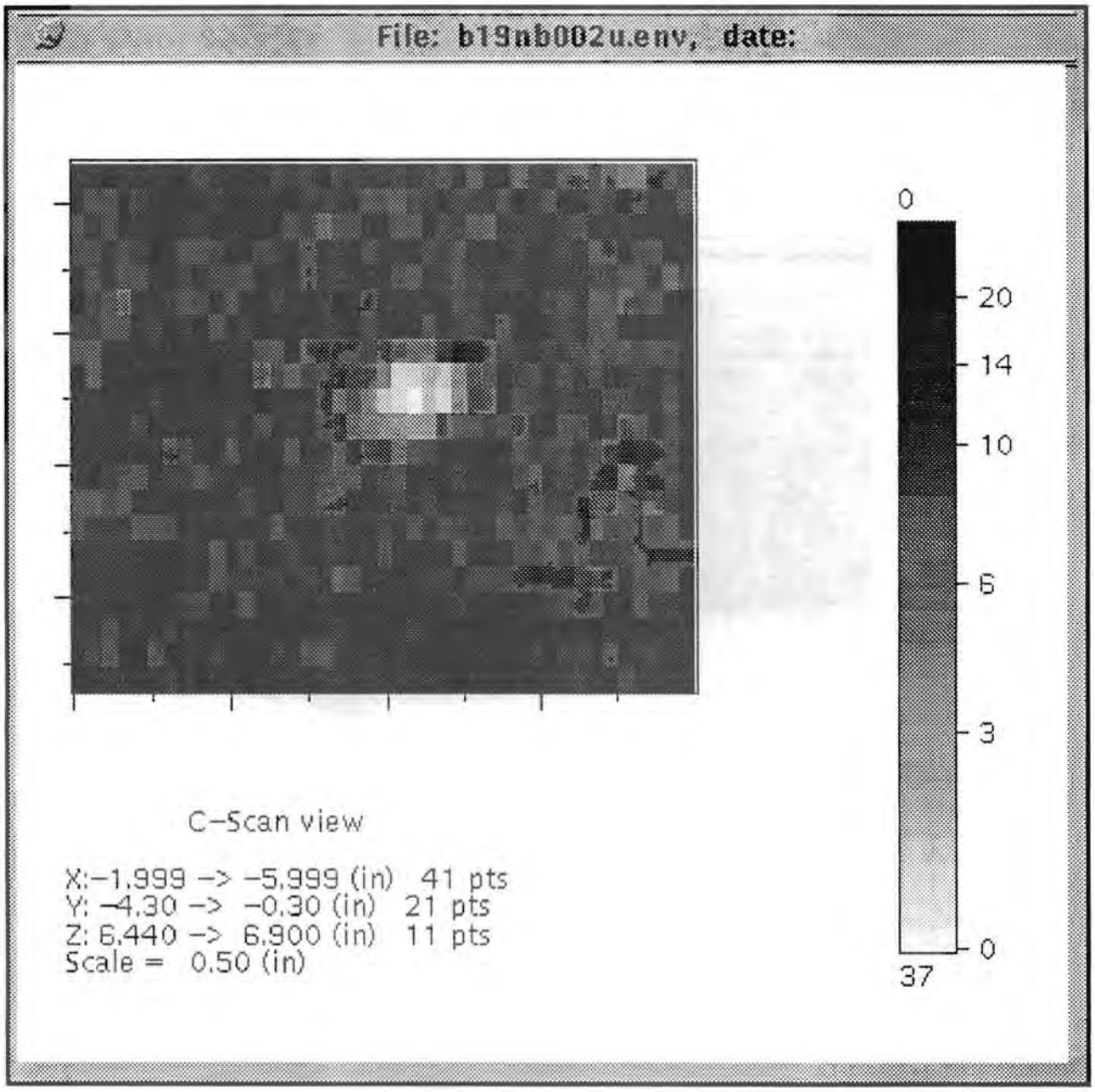

Figure 5.17c C-scan View (Scanner Coordinates XY) of Base-Metal Indication in Block 1-9 at Y = -69 mm (2.7 in.). Normal beam inspection from the bottom side. X in the figure corresponds to material coordinates of Z from 165 mm (6.5 in.) to 64 mm (2.5 in.).

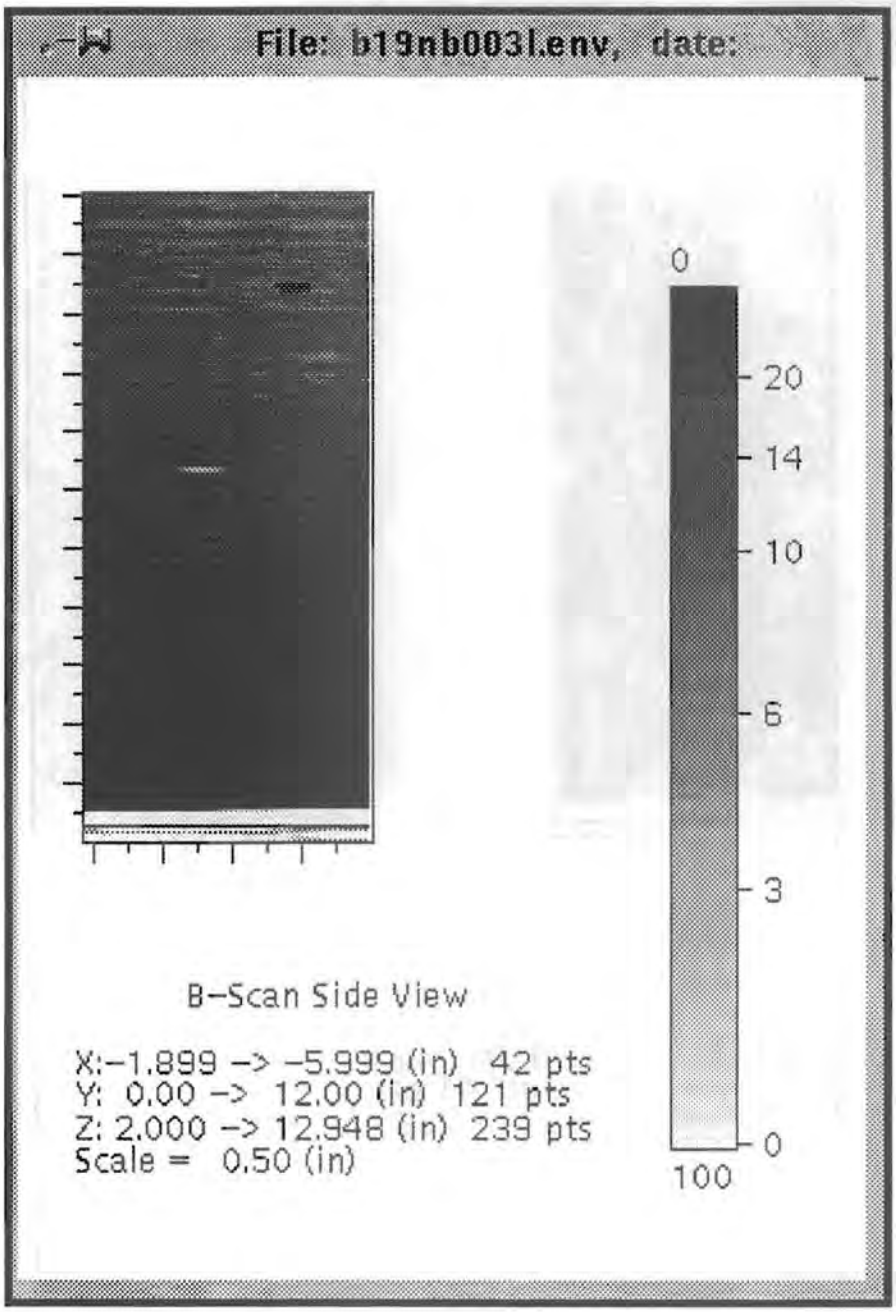

Figure 5.18a Side View (Scanner Coordinates XZ) of Base-Metal Indication in Block 1-9 at Y = 183 mm (7.2 in.). Normal beam inspection from the bottom side. Z in the figure corresponds to material coordinates of X from -102 mm (-4 in.) to 178 mm (7 in.). X in the figure corresponds to material coordinates of Z from 168 mm (6.6 in.) to 64 mm (2.5 in.).

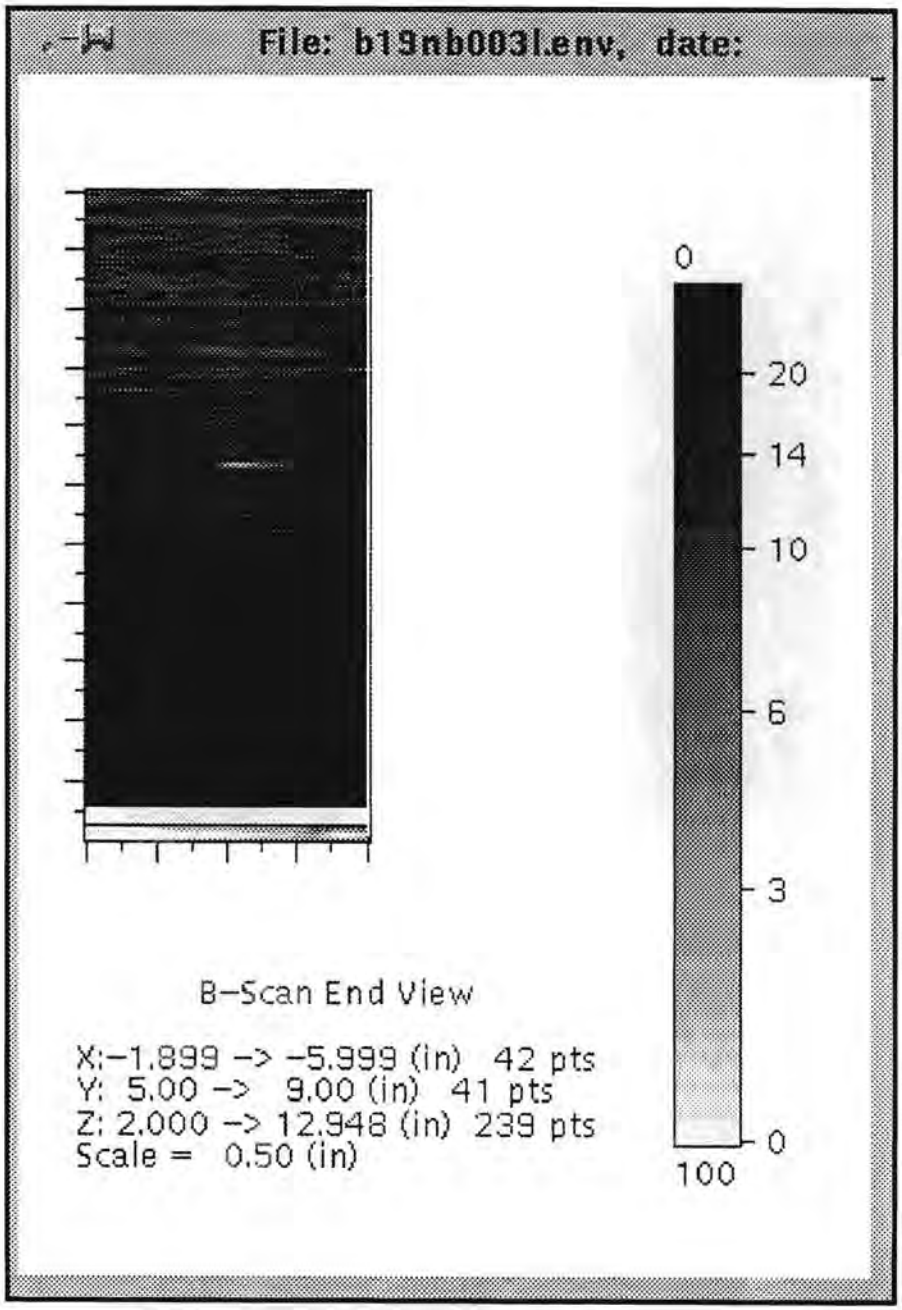

Figure 5.18b End View (Scanner Coordinates YZ) of Base-Metal Indication in Block 1-9 at Y = 183 mm (7.2 in.). Normal beam inspection from the bottom side. Z in the figure corresponds to material coordinates of X from -102 mm (-4 in.) to 178 mm (7 in.).

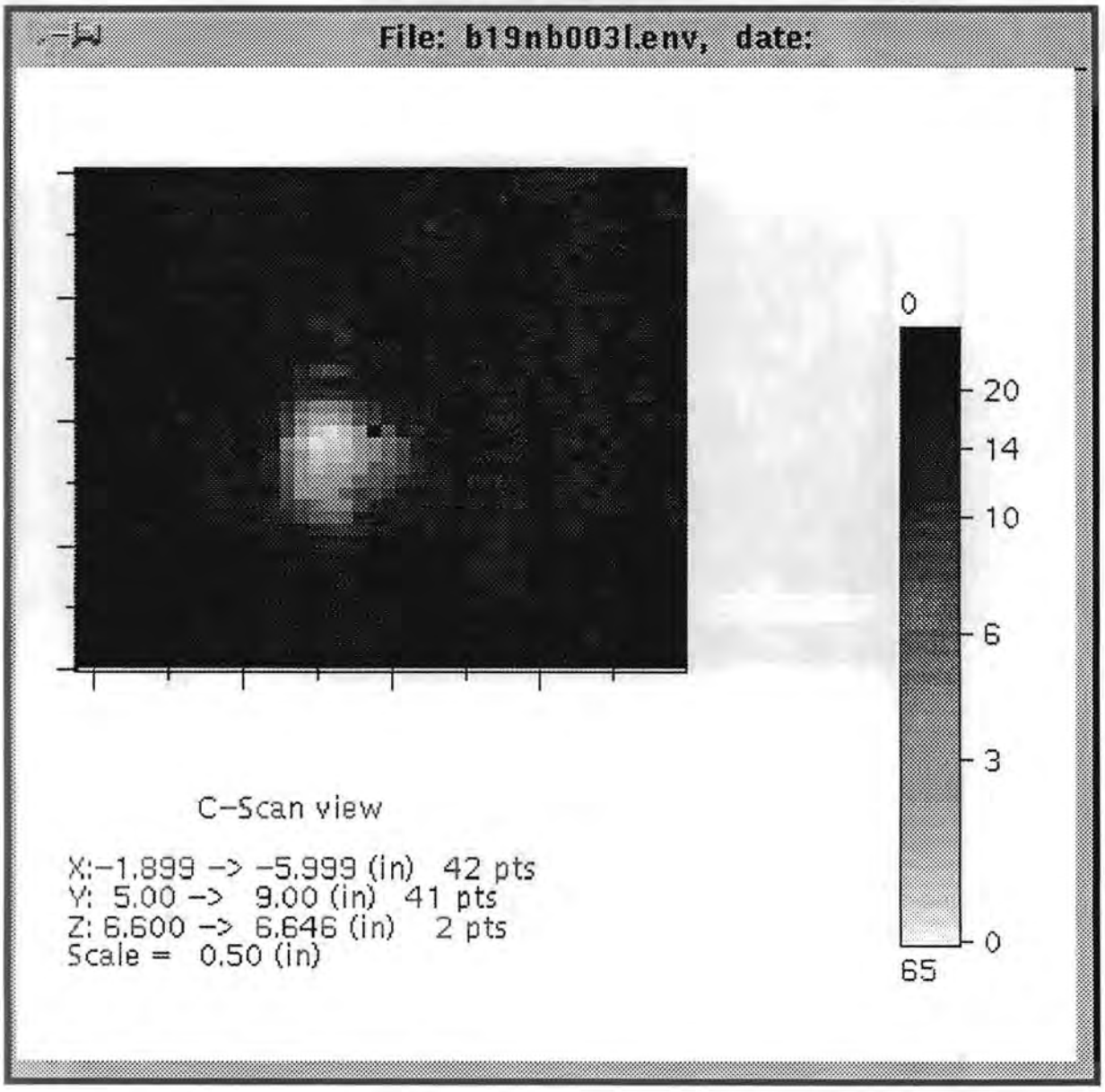

Figure 5.18c C-scan View (Scanner Coordinates XY) of Base-Metal Indication in Block 1-9 at Y = 183 mm (7.2 in.). Normal beam inspection from the bottom side. X in the figure corresponds to material coordinates of Z from 168 mm (6.6 in.) to 64 mm (2.5 in.).

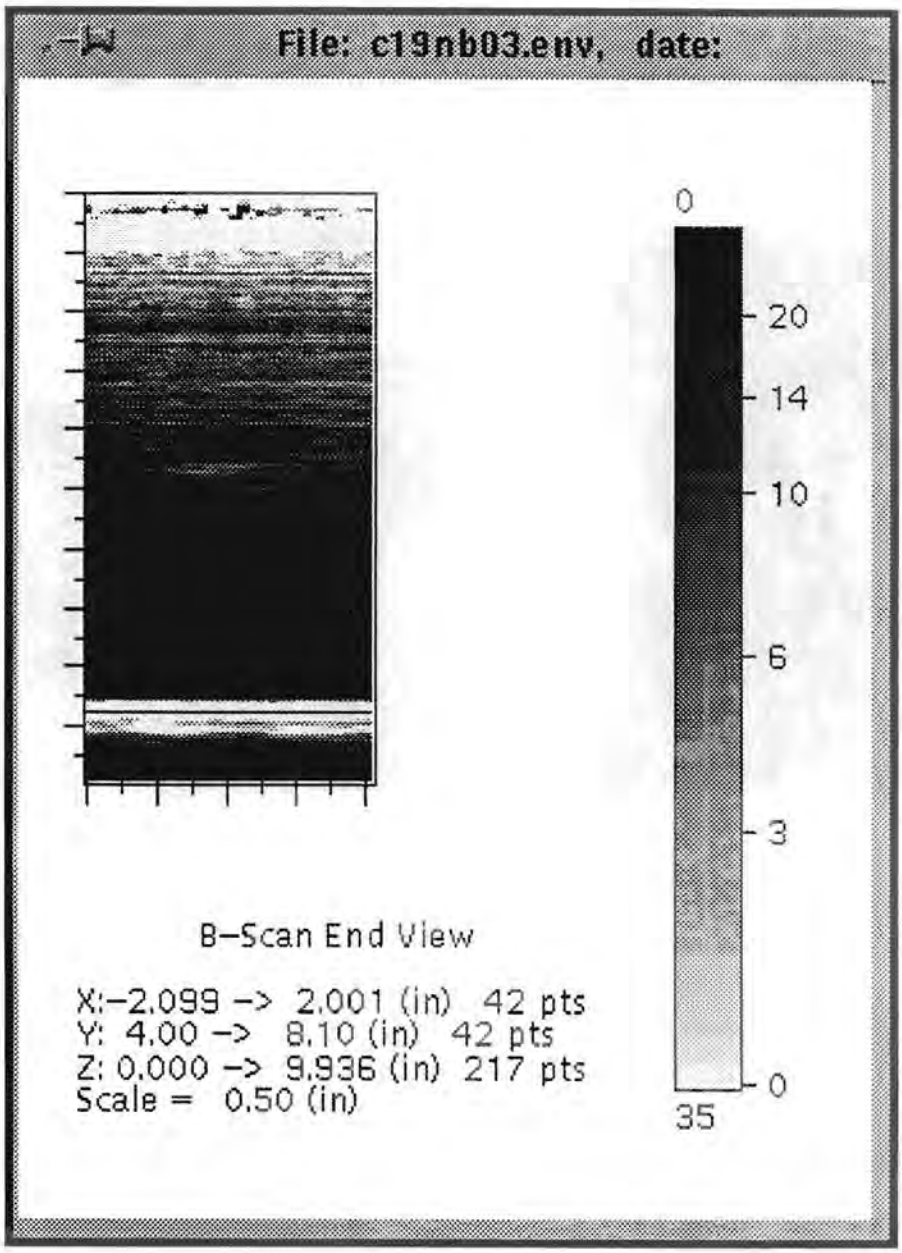

Figure 5.19a Side View (XZ) of Base-Metal Indication in Block 1-9 at Y = 203 mm (8.0 in.). Normal beam inspection from the clad side.

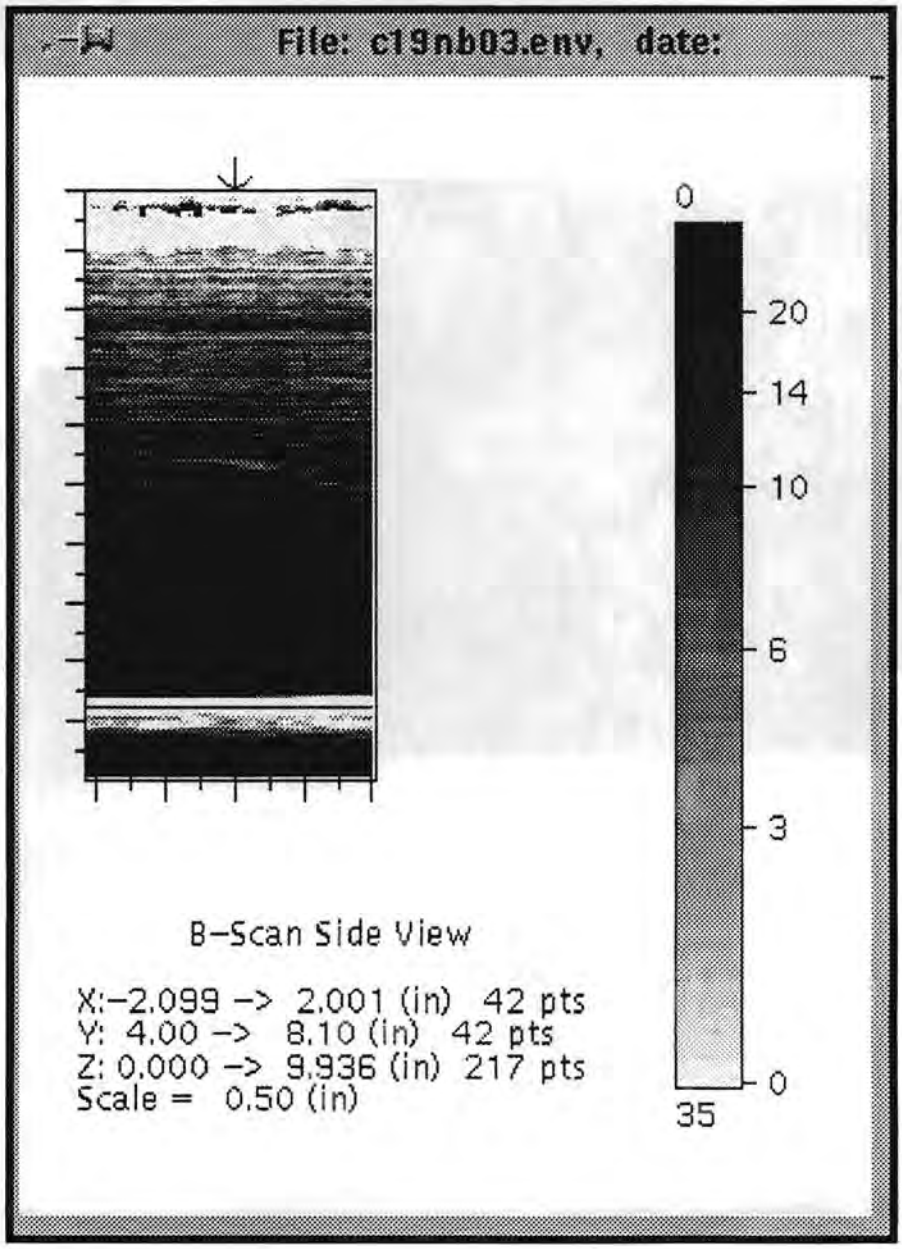

Figure 5.19b End View (YZ) of Base-Metal Indication in Block 1-9 at Y = 203 mm (8.0 in.). Normal beam inspection from the clad side.

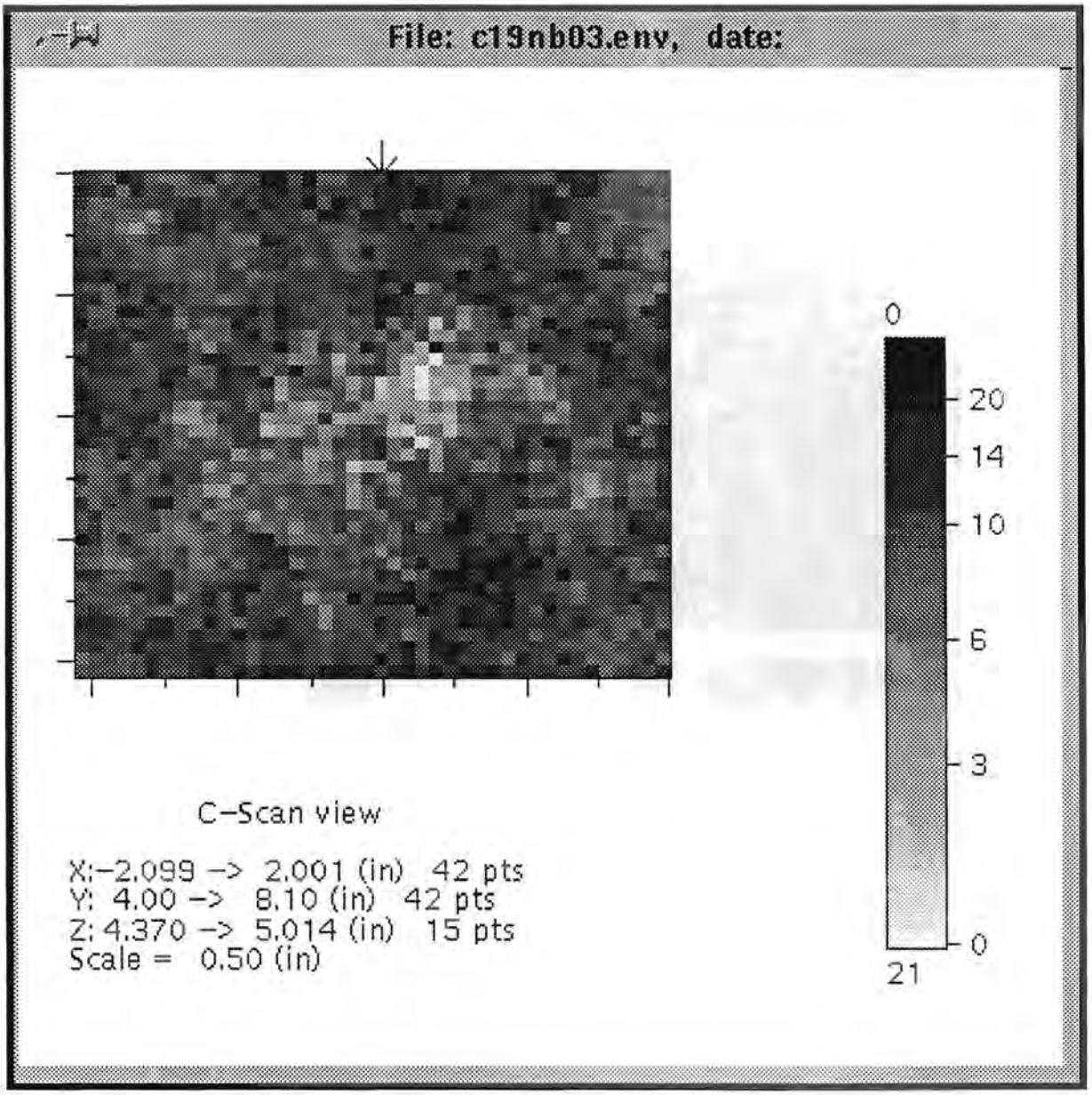

Figure 5.19c C-scan View (XY) of Base-Metal Indication in Block 1-9 at Y = 203 mm (8.0 in.). Normal beam inspection from the clad side.

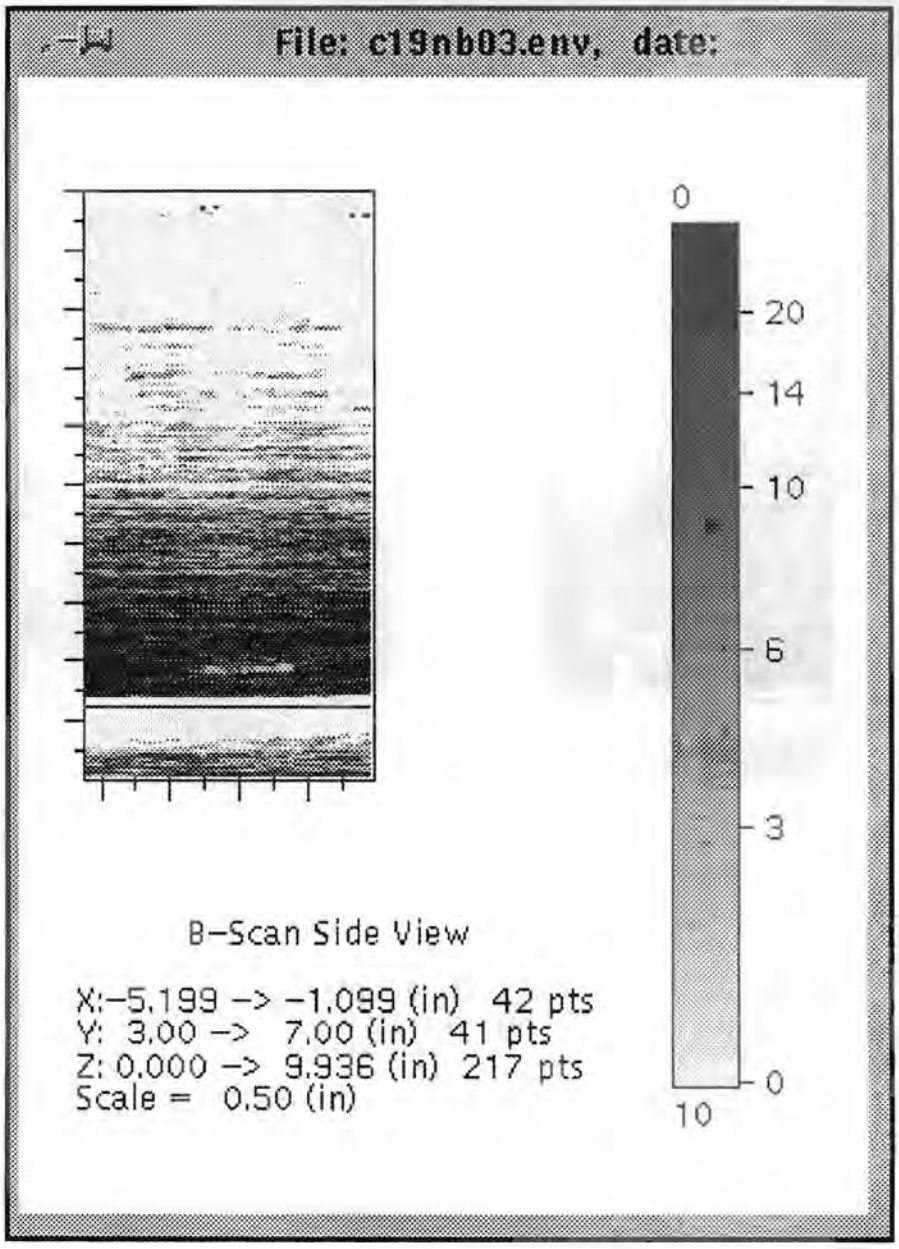

Figure 5.20a Side View (XZ) of Base-Metal Indication in Block 1-9 at Y = 185 mm (7.3 in.). Normal beam inspection from the clad side.

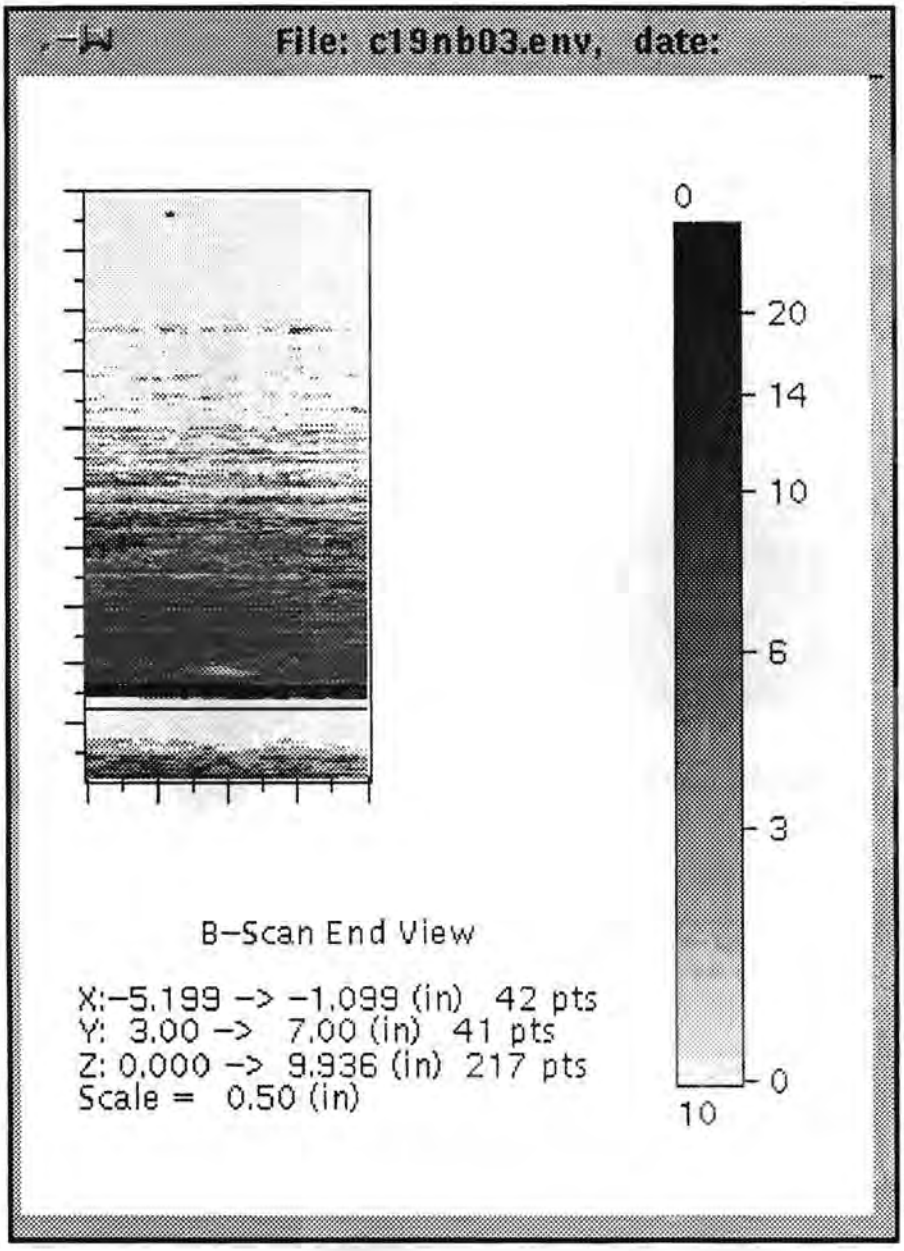

Figure 5.20b End View (YZ) of Base-Metal Indication in Block 1-9 at Y = 185 mm (7.3 in.). Normal beam inspection from the clad side.

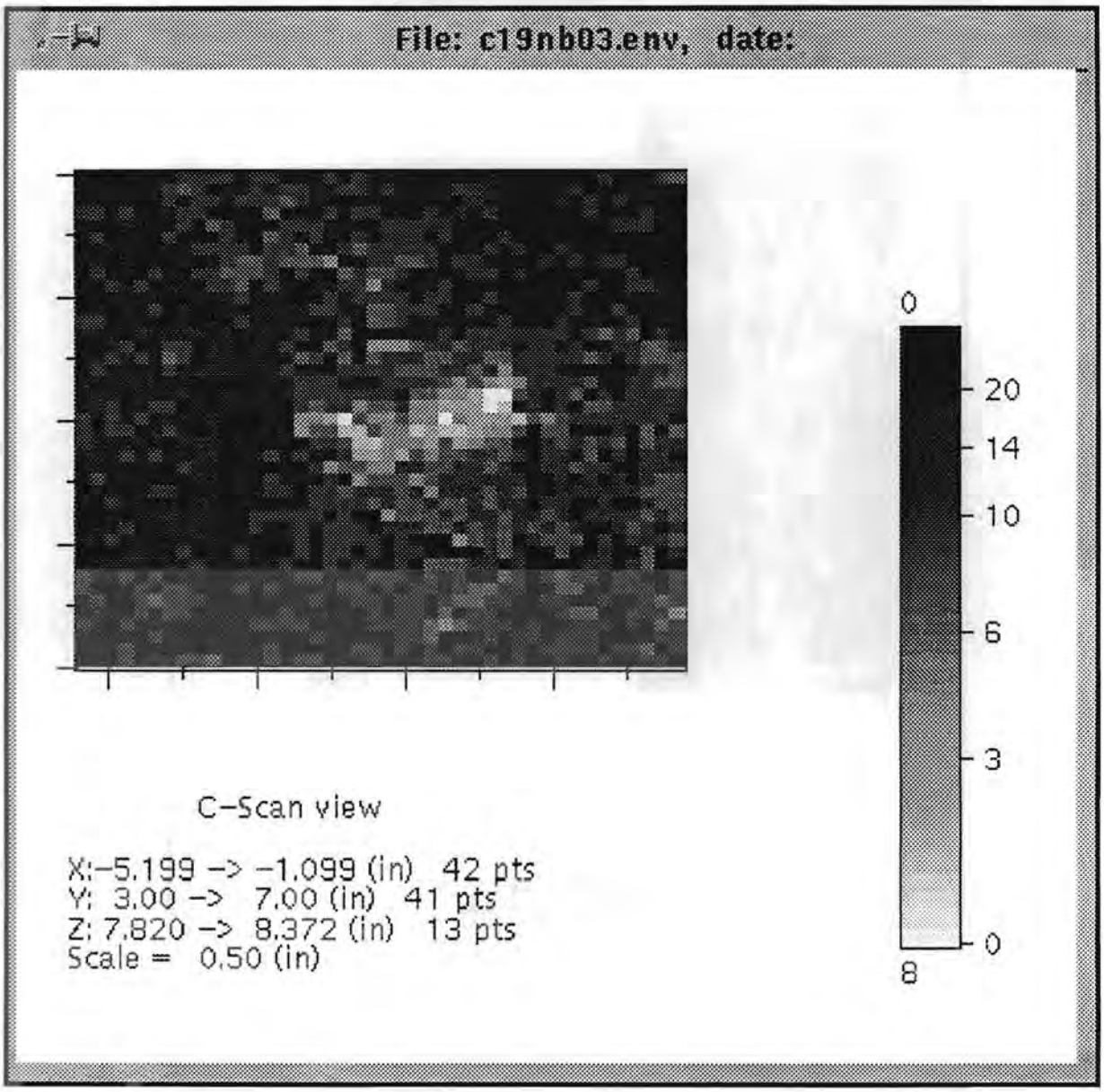

Figure 5.20c C-scan View (XY) of Base-Metal Indication in Block 1-9 at Y = 185 mm (7.3 in.). Normal beam inspection from the clad side.

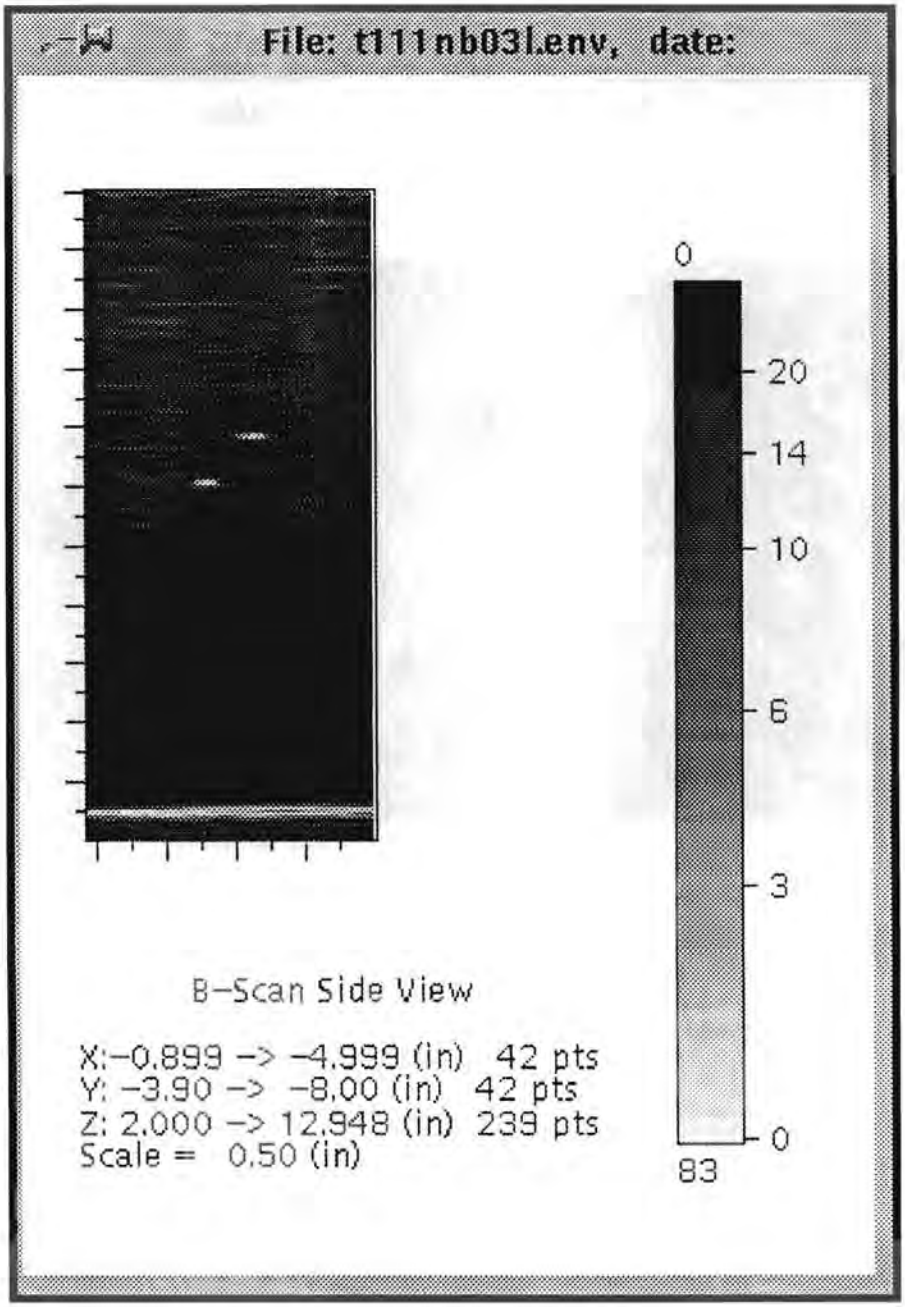

Figure 5.21a Side View (Scanner Coordinates XZ) of Base-Metal Indication in Block 1-11 at Y = -152 mm (-6.0 in.). Normal beam inspection from the top side. Z in the figure corresponds to material coordinates of X from -102 mm (-4 in.) to 178 mm (7 in.). X in the figure corresponds to material coordinates of Z from 188 mm (7.4 in.) to 84 mm (3.3 in.).

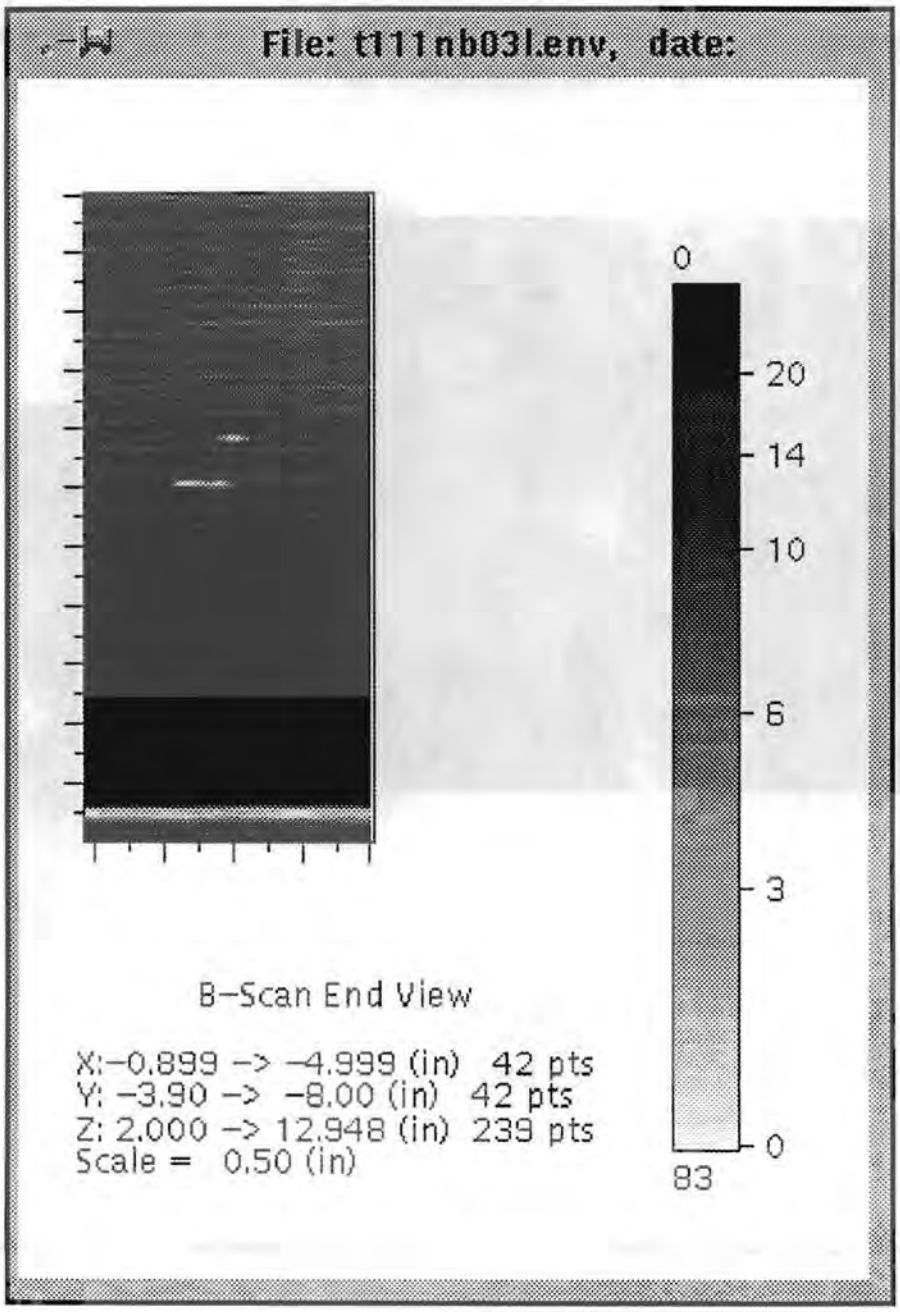

Figure 5.21b End View (Scanner Coordinates YZ) of Base-Metal Indication in Block 1-11 at Y = -152 mm (-6.0 in.). Normal beam inspection from the top side. Z in the figure corresponds to material coordinates of X from -102 mm (-4 in.) to 178 mm (7 in.).

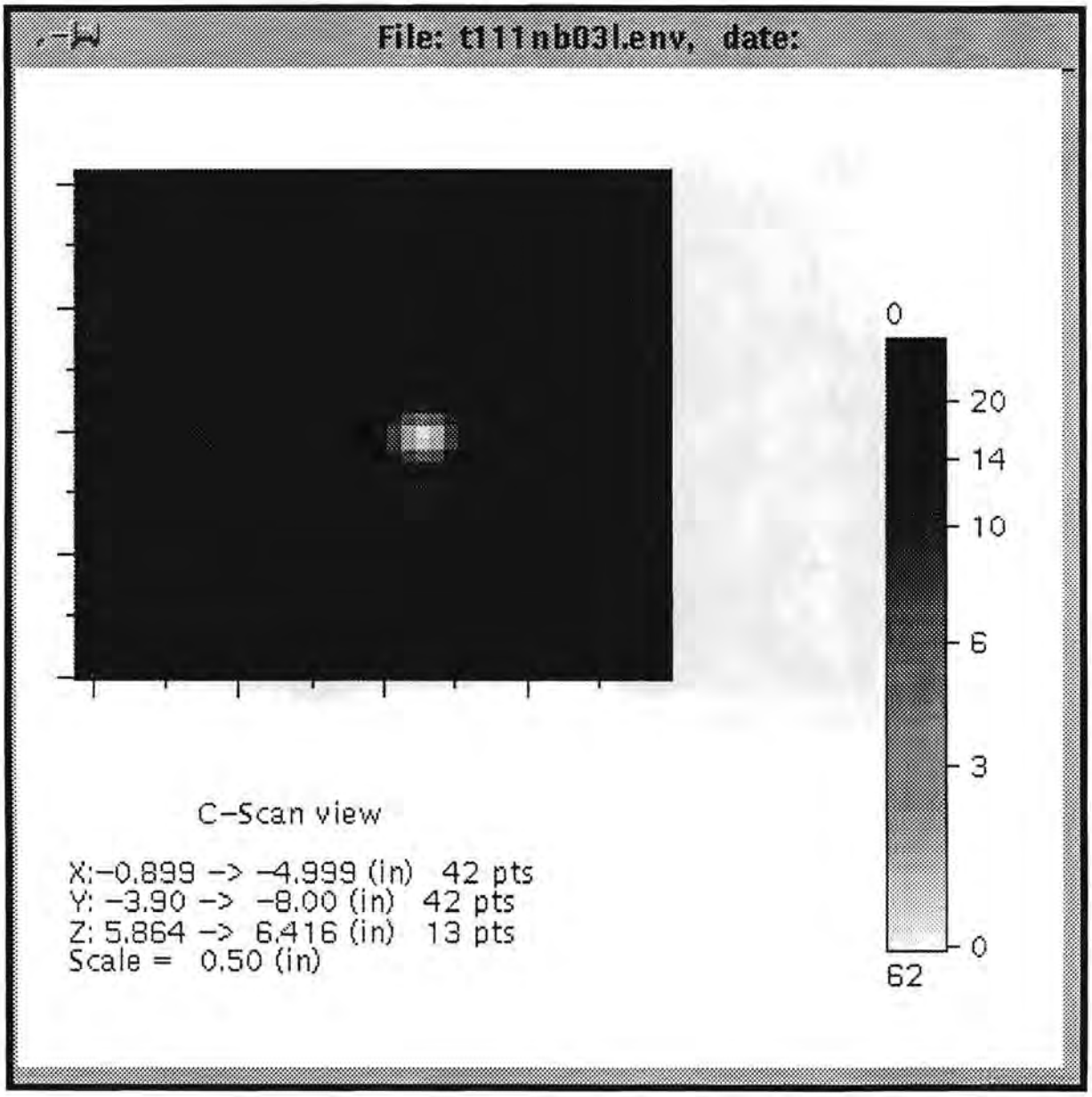

Figure 5.21c C-scan View (Scanner Coordinates XY) of Base-Metal Indication in Block 1-11 at Y = -152 mm (-6.0 in.). Normal beam inspection from the top side. X in the figure corresponds to material coordinates of Z from 188 mm (7.4 in.) to 84 mm (3.3 in.).

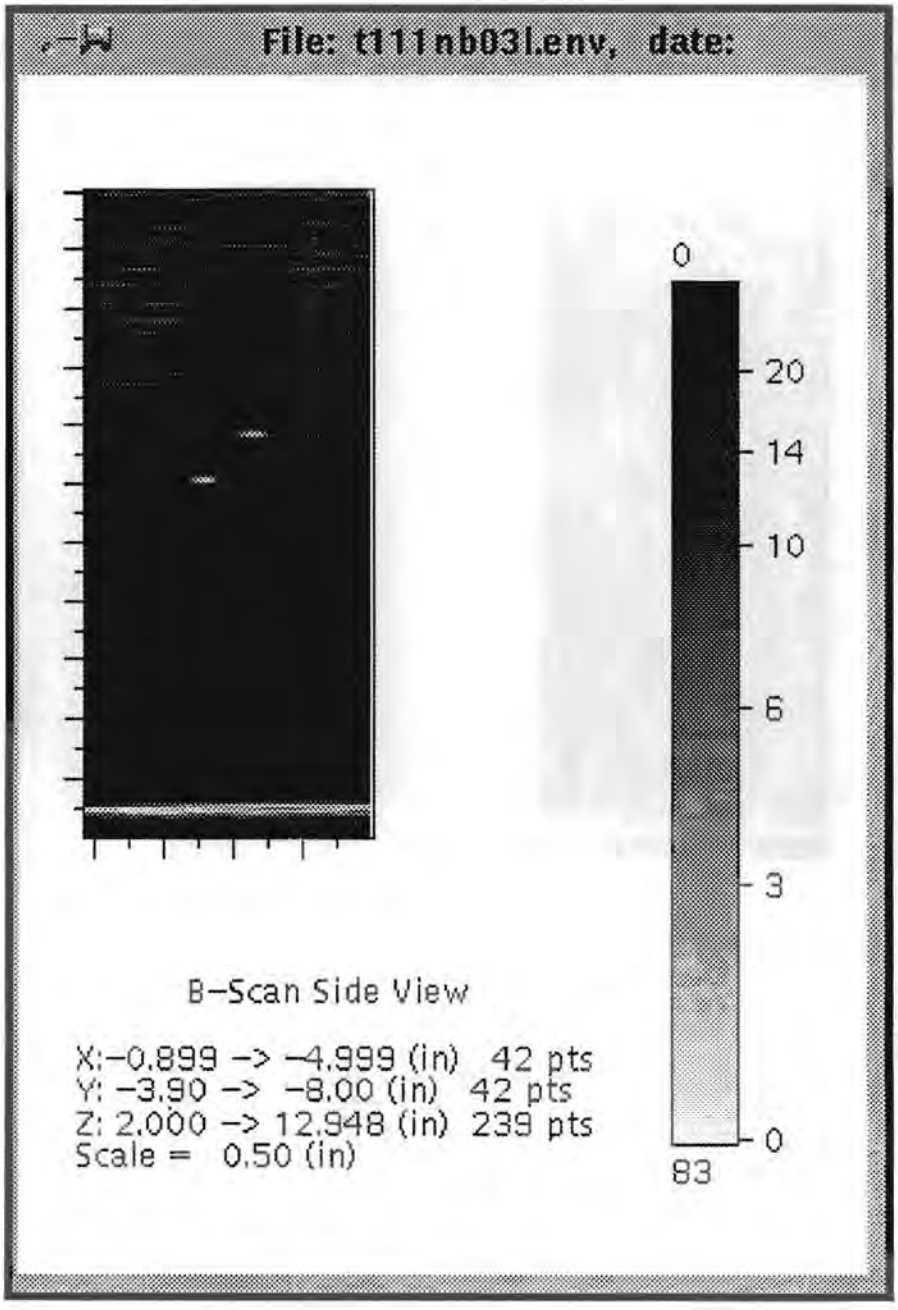

Figure 5.22a Side View (Scanner Coordinates XZ) of Base-Metal Indication in Block 1-11 at Y = -140 mm (-5.5 in.). Normal beam inspection from the top side. Z in the figure corresponds to material coordinates of X from -102 mm (-4 in.) to 178 mm (7 in.). X in the figure corresponds to material coordinates of Z from 188 mm (7.4 in.) to 84 mm (3.3 in.).

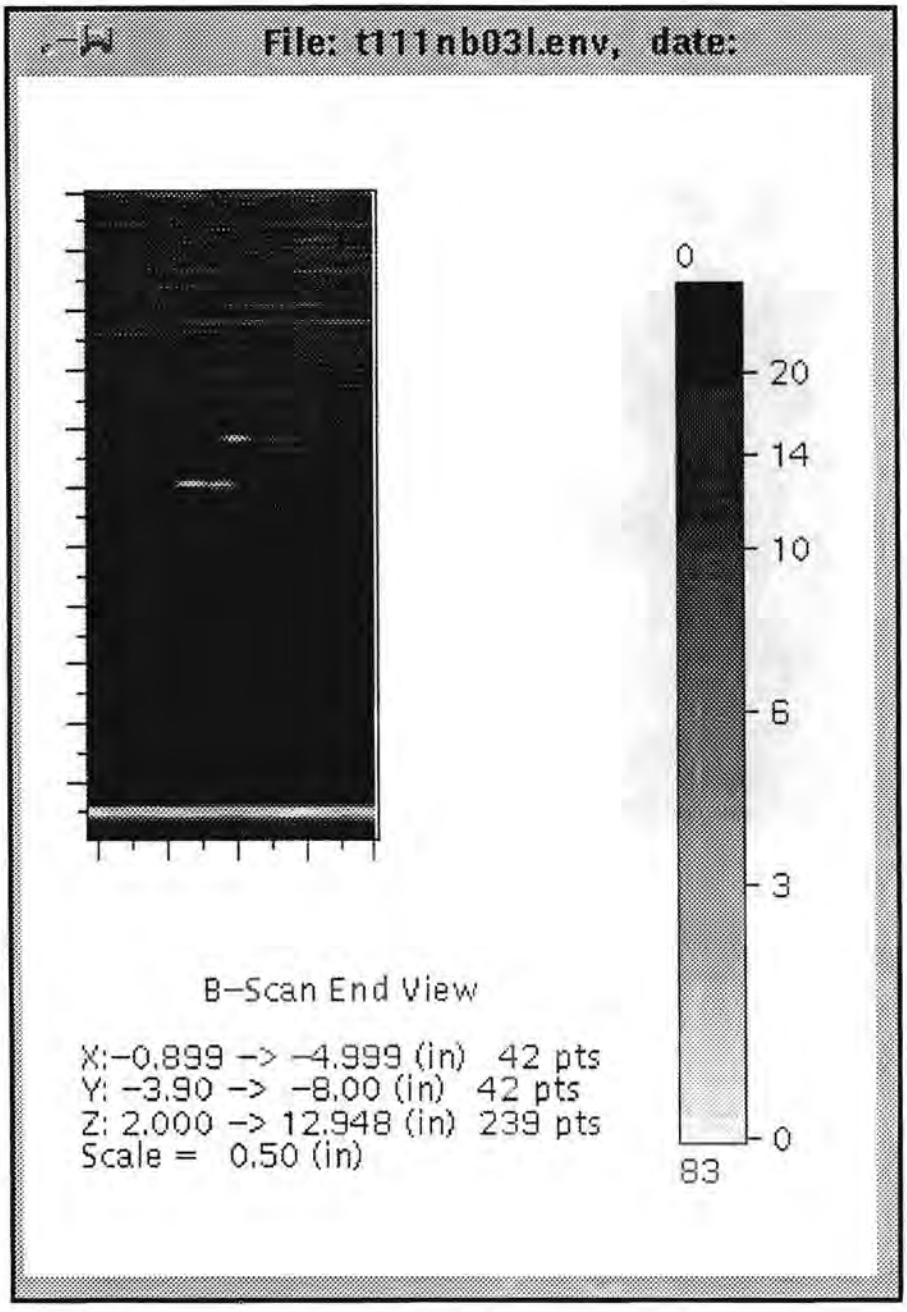

Figure 5.22b End View (Scanner Coordinates YZ) of Base-Metal Indication in Block 1-11 at Y = -140 mm (-5.5 in.). Normal beam inspection from the top side. Z in the figure corresponds to material coordinates of X from -102 mm (-4 in.) to 178 mm (7 in.).

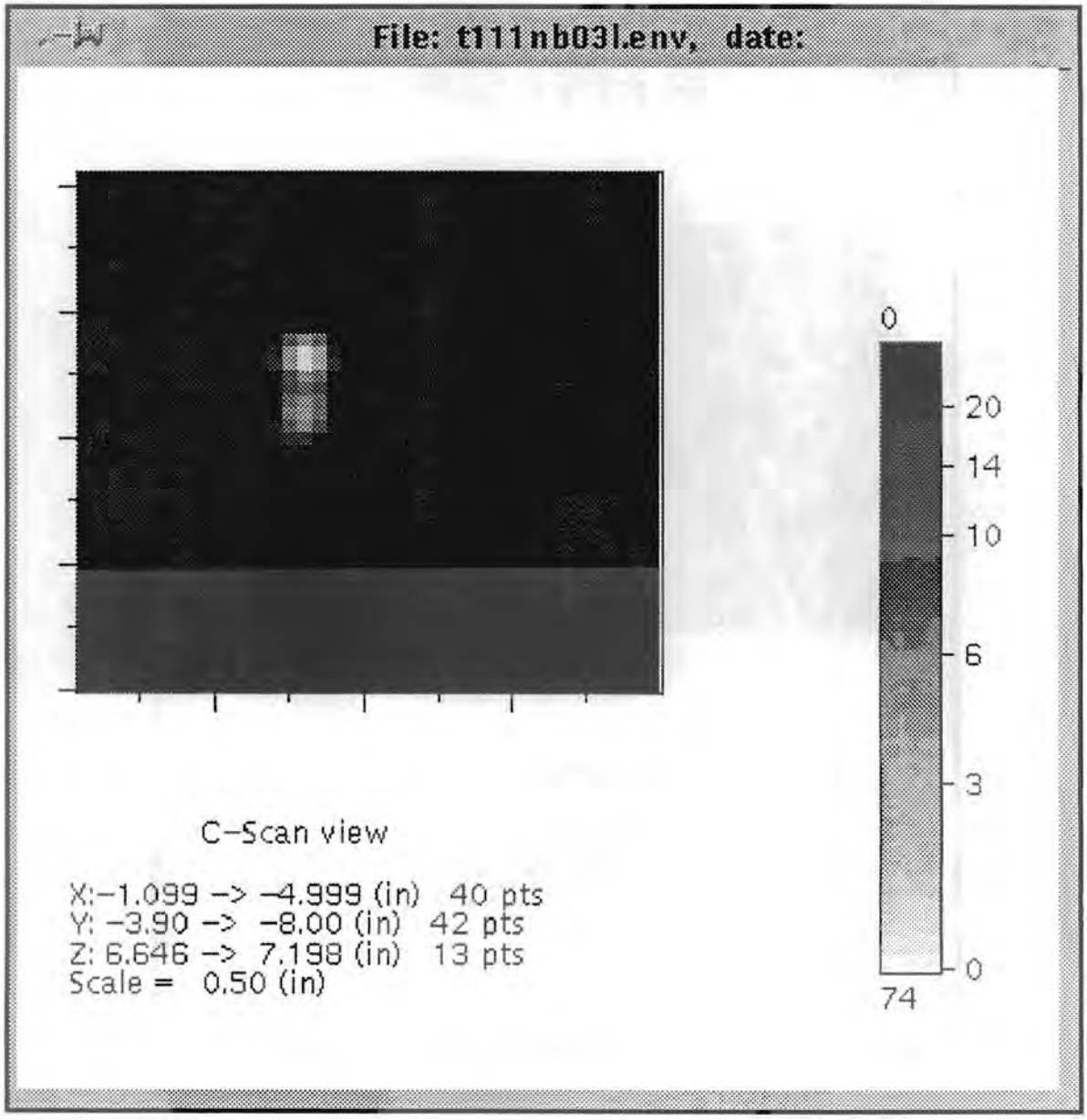

Figure 5.22c C-scan View (Scanner Coordinates XY) of Base-Metal Indication in Block 1-11 at Y = -140 mm (-5.5 in.). Normal beam inspection from the top side. X in the figure corresponds to material coordinates of Z from 188 mm (7.4 in.) to 84 mm (3.3 in.).

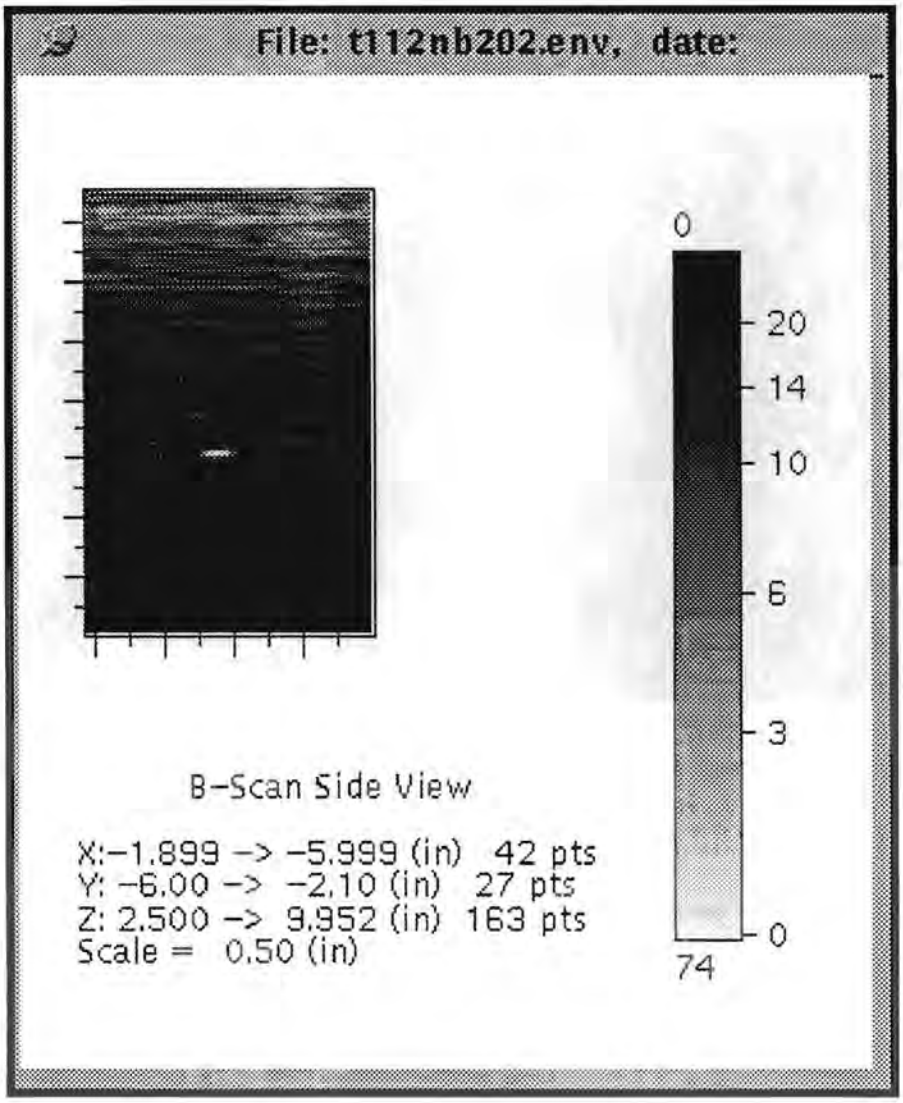

Figure 5.23a Side View (Scanner Coordinates XZ) of Base-Metal Indication in Block 1-12 at Y = -96 mm (-3.8 in.). Normal beam inspection from the top side. Z in the figure corresponds to material coordinates of X from 89 mm (3.5 in.) to 76 mm (3.0 in.). X in the figure corresponds to material coordinates of Z from 168 mm (6.6 in.) to 64 mm (2.5 in.).

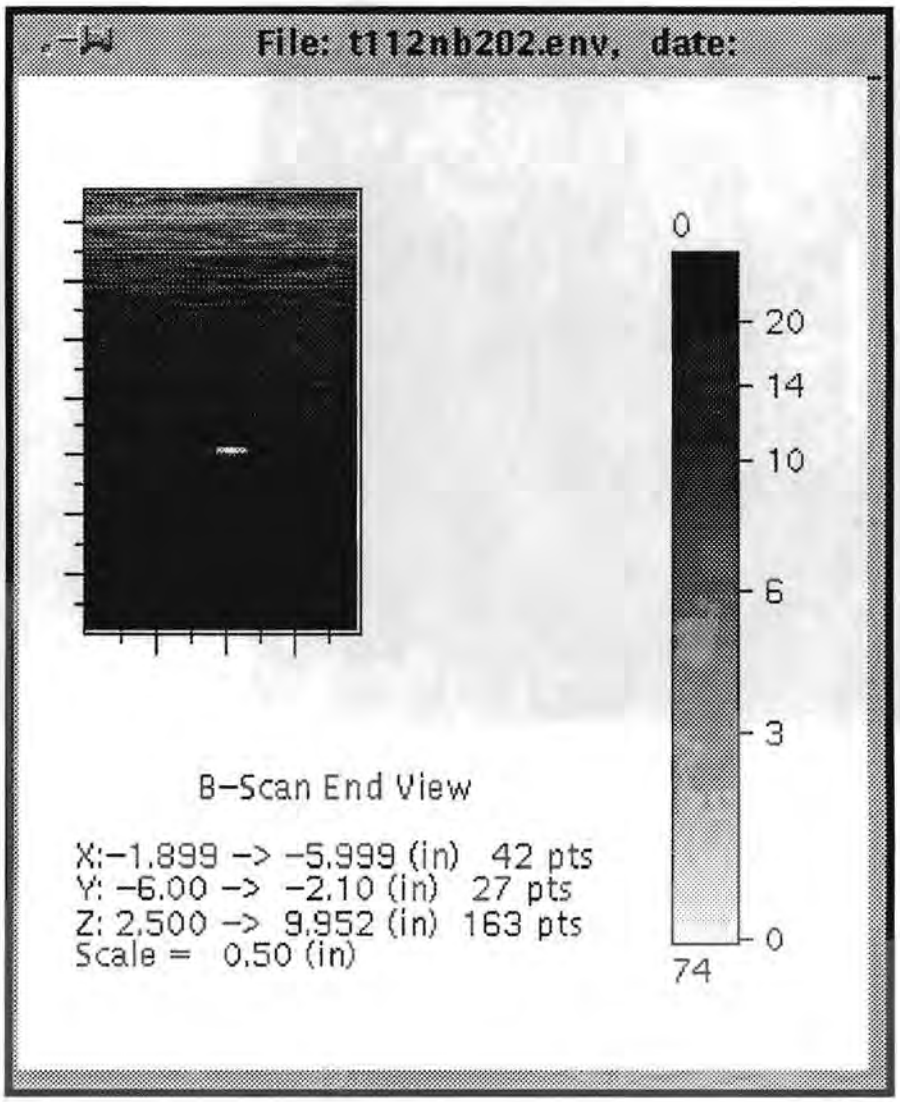

Figure 5.23b End View (Scanner Coordinates YZ) of Base-Metal Indication in Block 1-12 at Y = -96 mm (-3.8 in.). Normal beam inspection from the top side. Z in the figure corresponds to material coordinates of X from 89 mm (3.5 in.) to 76 mm (3.0 in.).

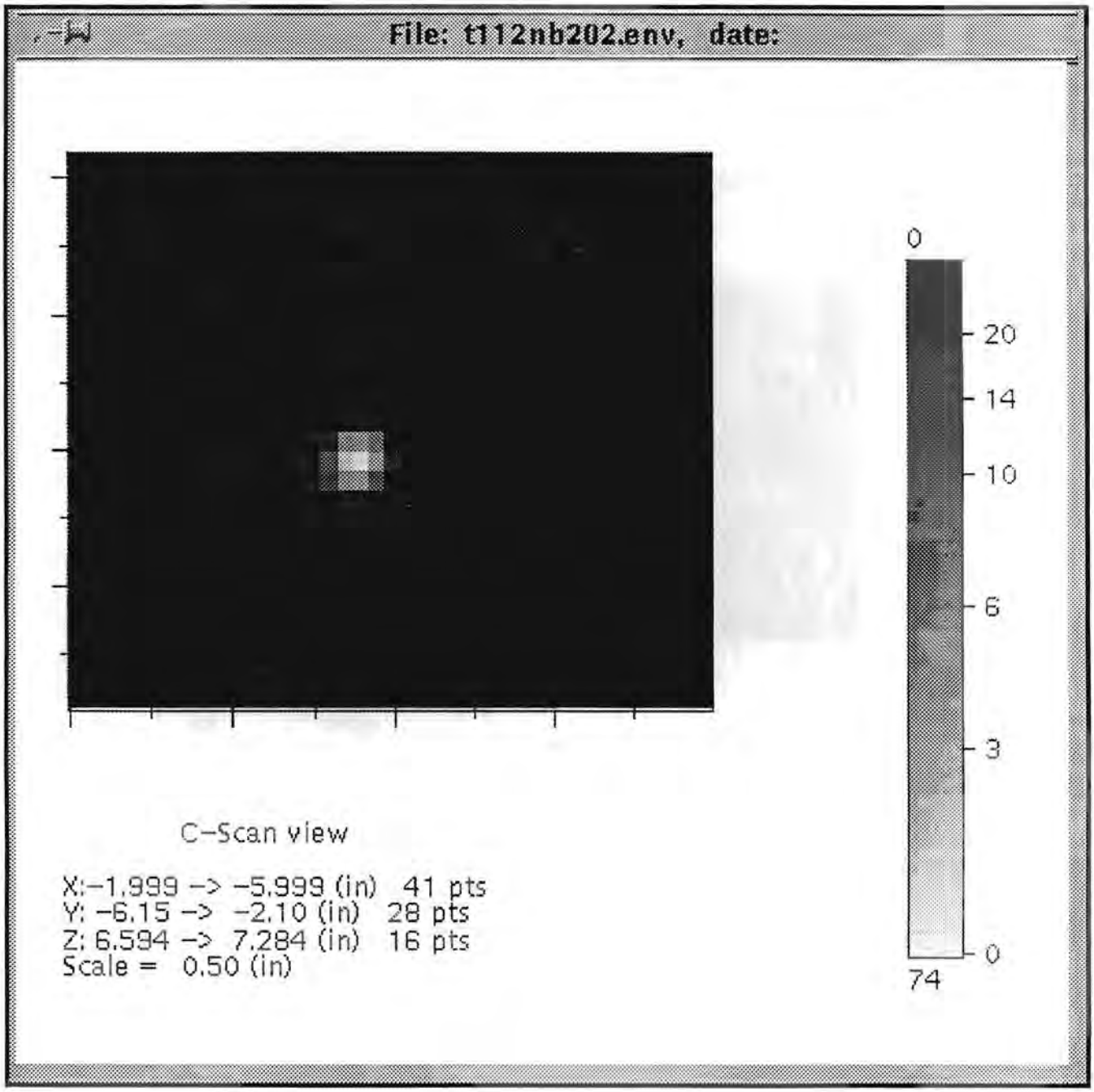

Figure 5.23c. C-scan View (Scanner Coordinates XY) of Base-Metal Indication in Block 1-12 at Y = -96 mm (-3.8 in.). Normal beam inspection from the top side. X in the figure corresponds to material coordinates of Z from 168 mm (6.6 in.) to 64 mm (2.5 in.).

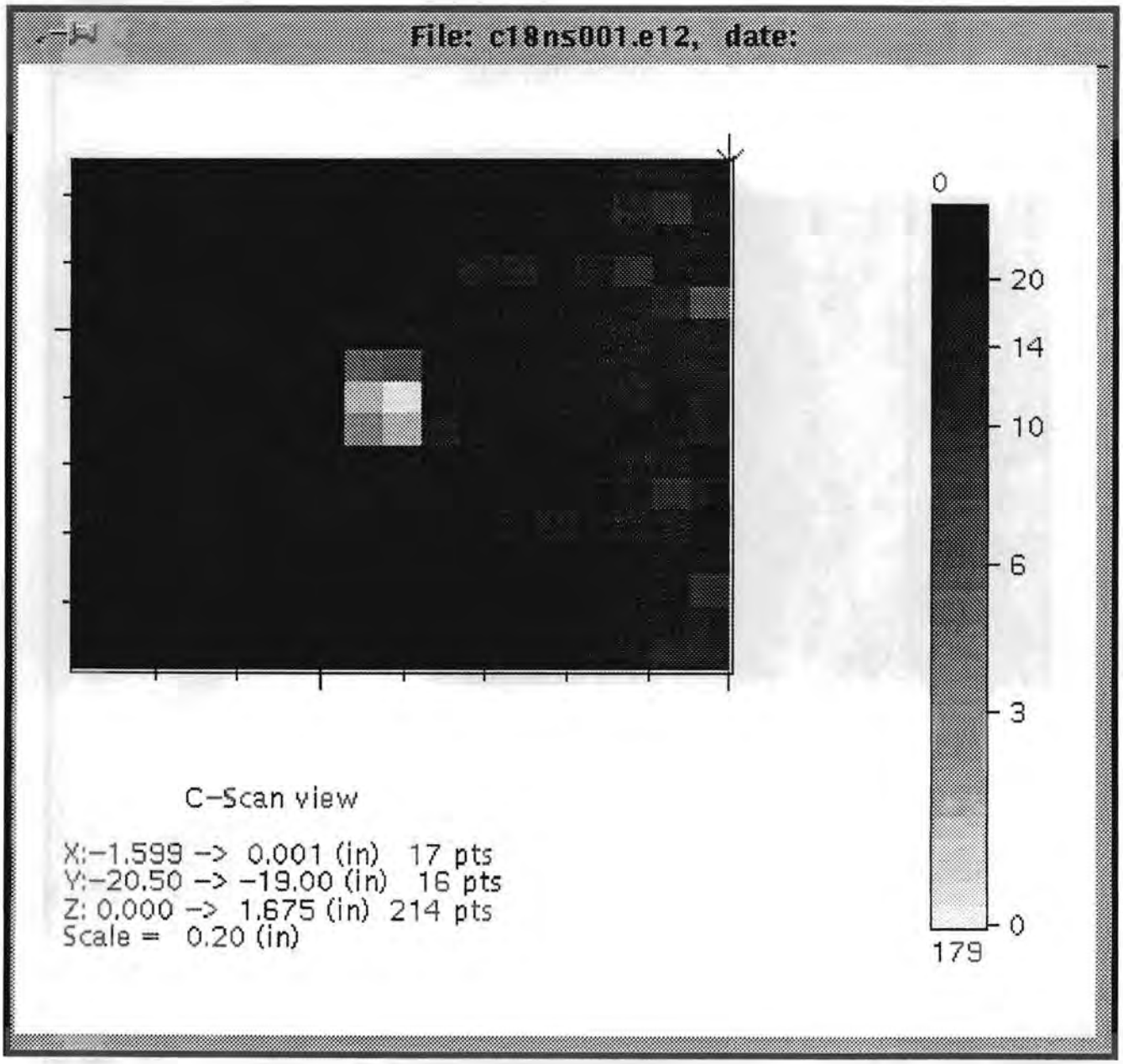

Figure 5.24c C-scan View (XY) of Clad to Base-Metal Indication in Block 1-8 at Y = -526 mm (-20.7 in.). 70° L-wave inspection with beam direction of +X.

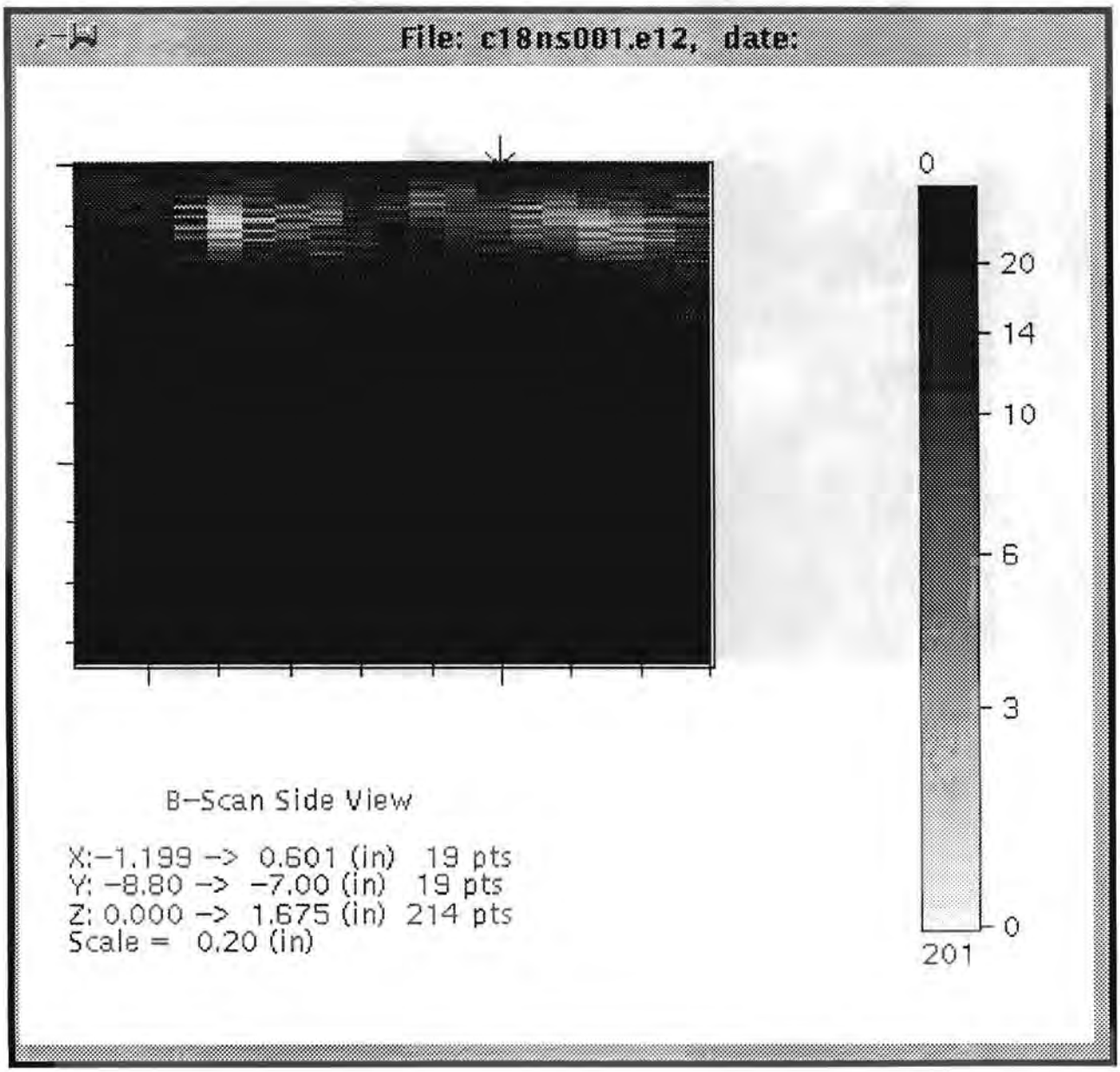

Figure 5.25a Side View (XZ) of Clad to Base-Metal Indication in Block 1-8 at Y = -211 mm (-8.3 in.). 70° L-wave inspection with beam direction of +X.

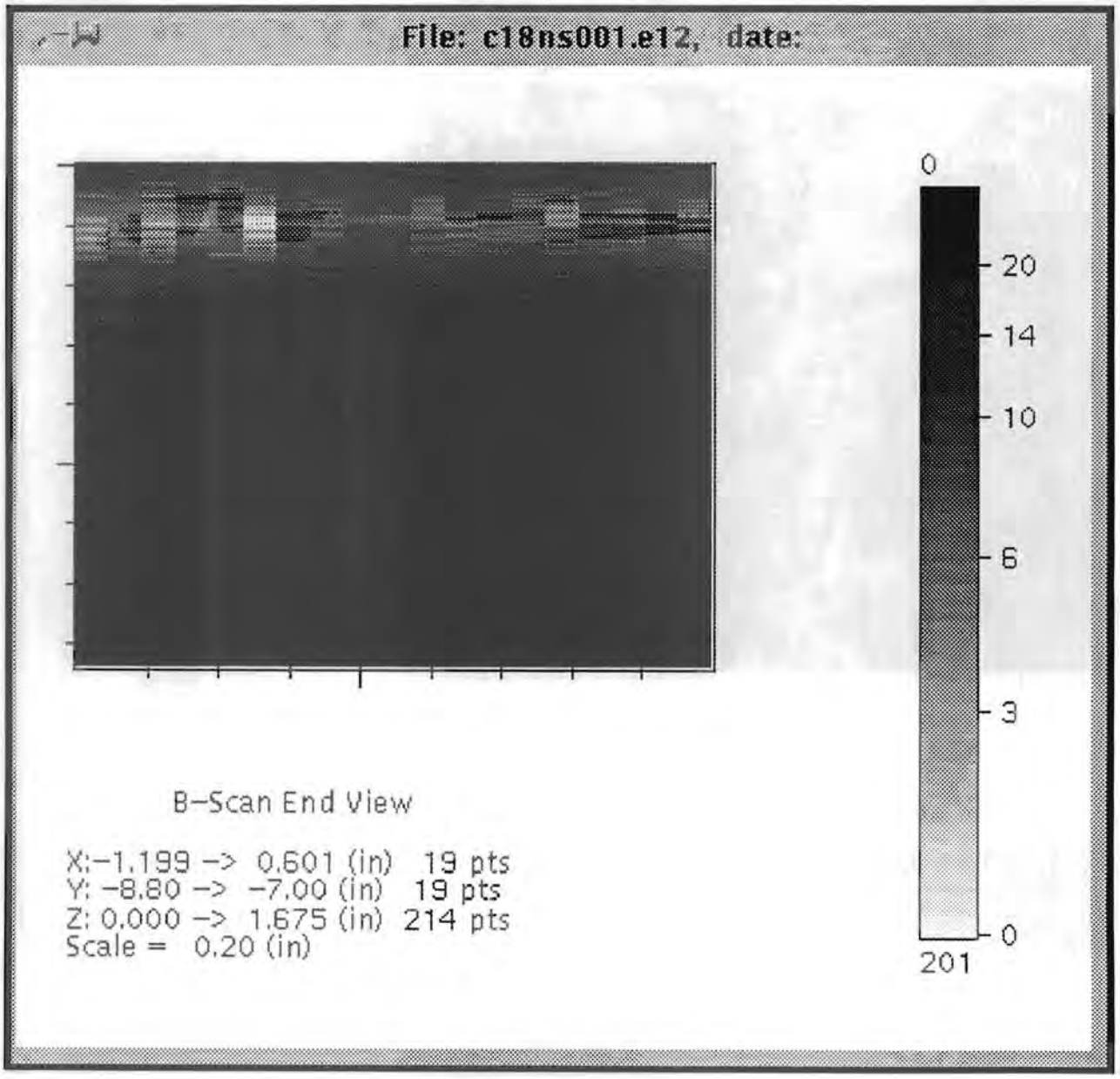

Figure 5.25b End View (YZ) of Clad to Base-Metal Indication in Block 1-8 at Y = -211 mm (-8.3 in.). 70° L-wave inspection with beam direction of +X.

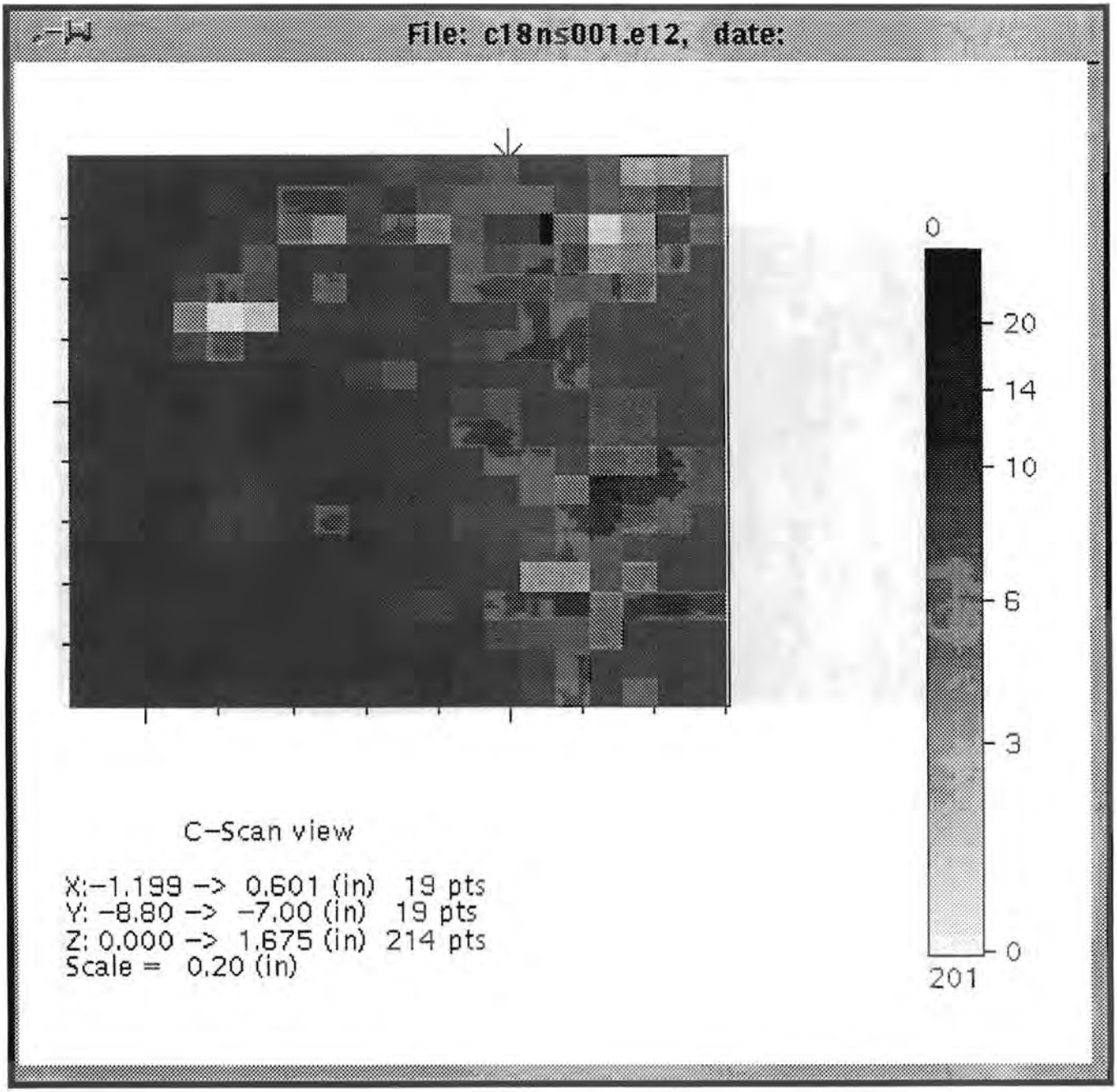

Figure 5.25c C-scan View (XY) of Clad to Base-Metal Indication in Block 1-8 at Y = -211 mm (-8.3 in.). 70° L-wave inspection with beam direction of +X.

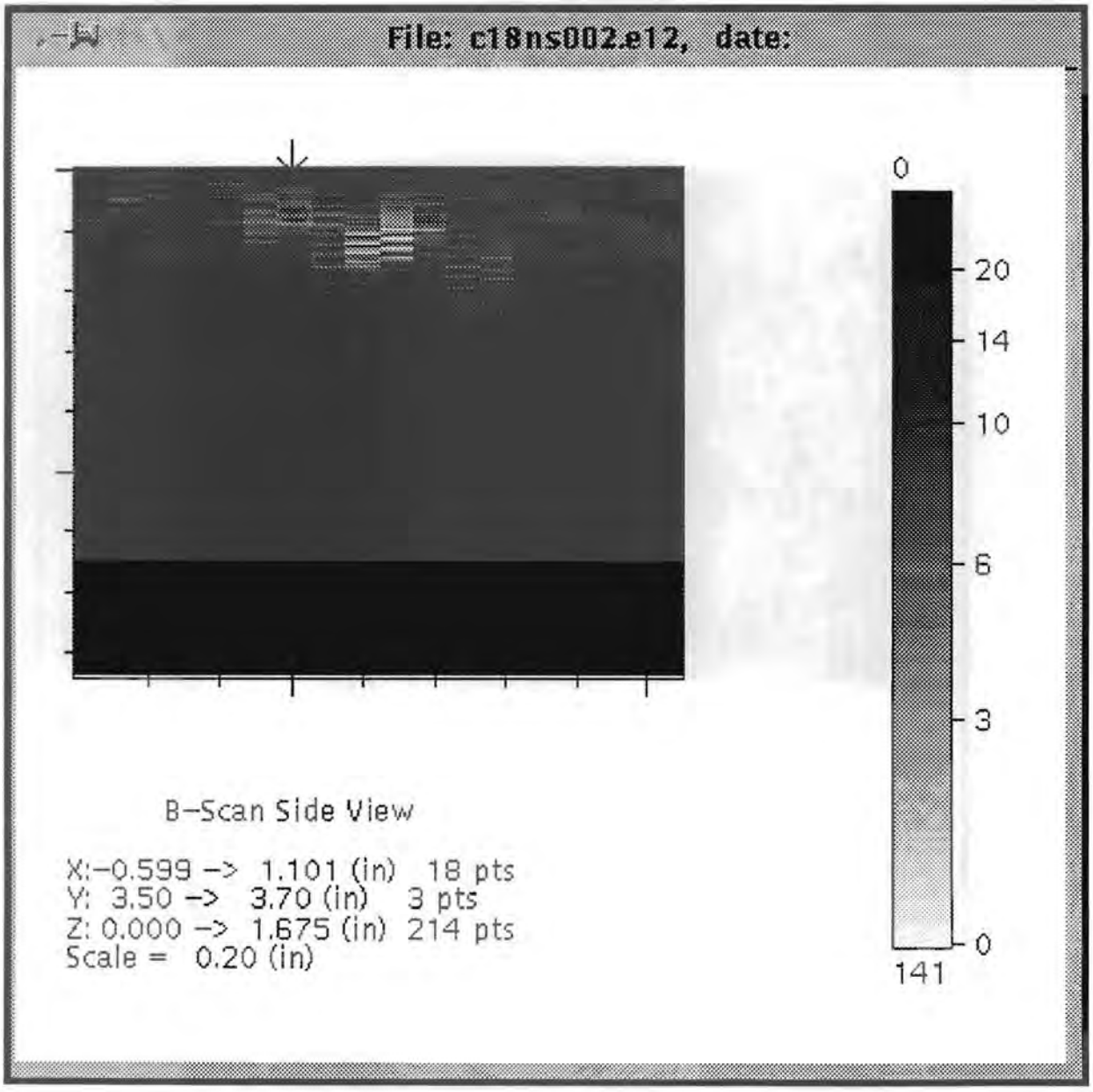

Figure 5.26a Side View (XZ) of Clad to Base-Metal Indication in Block 1-8 at Y = 89 mm (3.5 in.). 70° L-wave inspection with beam direction of +X. This indication corresponds to flaw #7 in the destructive analysis.

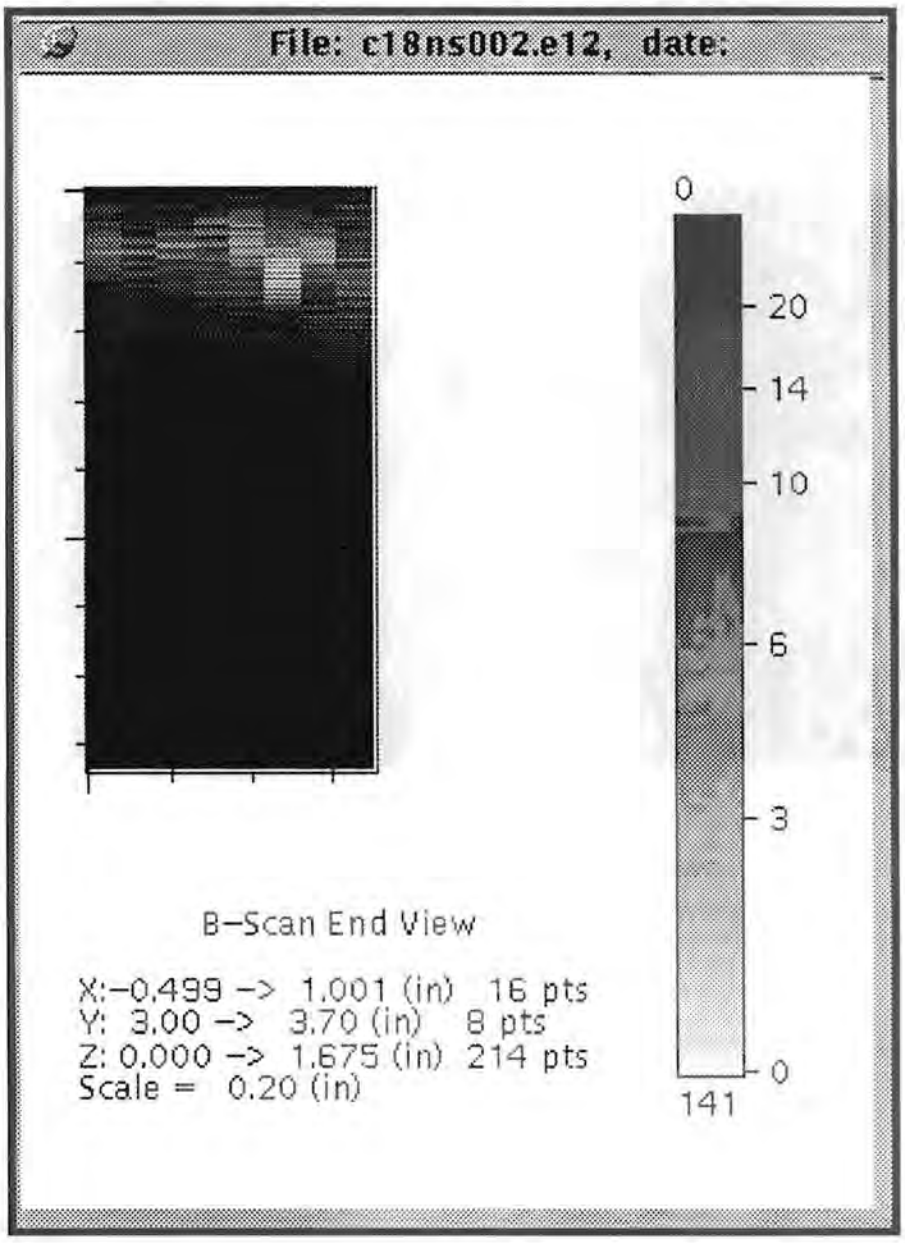

Figure 5.26b End View (YZ) of Clad to Base-Metal Indication in Block 1-8 at Y = 89 mm (3.5 in.). 70° L-wave inspection with beam direction of +X. This indication corresponds to flaw #7 in the destructive analysis.

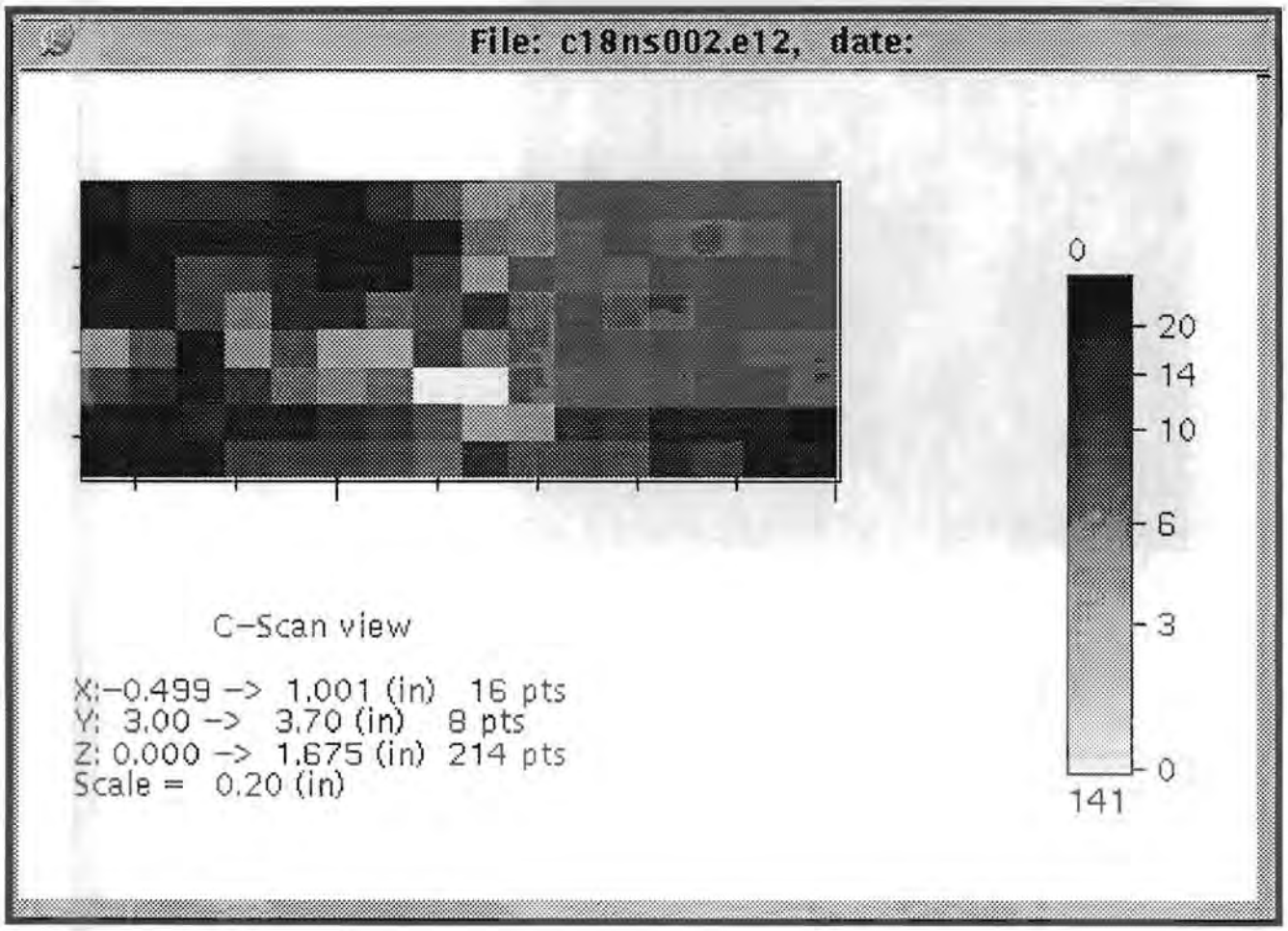

Figure 5.26c C-scan View (XY) of Clad to Base-Metal Indication in Block 1-8 at Y = 89 mm (3.5 in.). 70° L-wave inspection with beam direction of +X. This indication corresponds to flaw #7 in the destructive analysis.

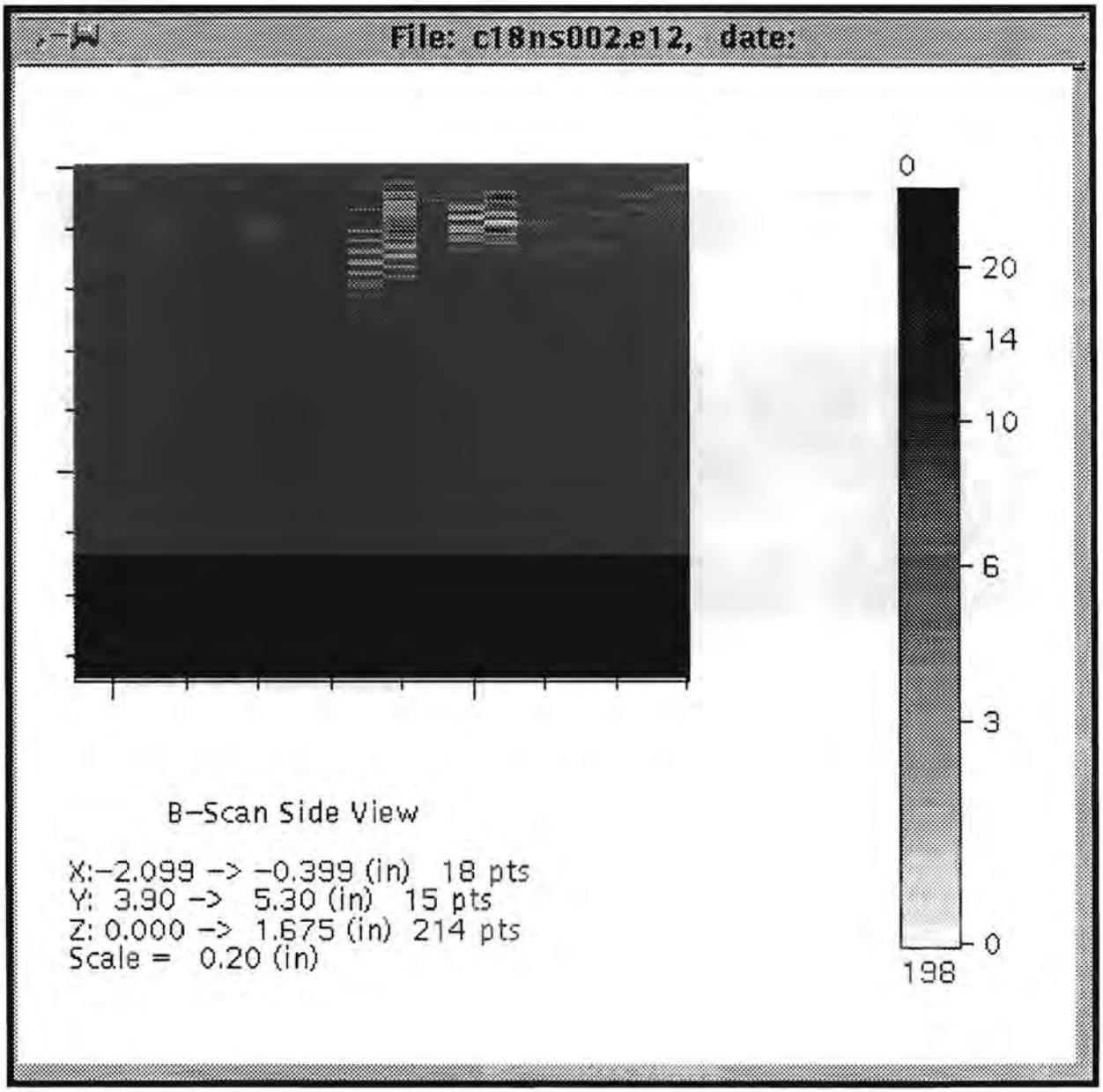

Figure 5.27a Side View (XZ) of Clad to Base-Metal Indication in Block 1-8 at Y = 112 mm (4.4 in.). 70° L-wave inspection with beam direction of +X. This indication corresponds to flaw #8 in the destructive analysis.

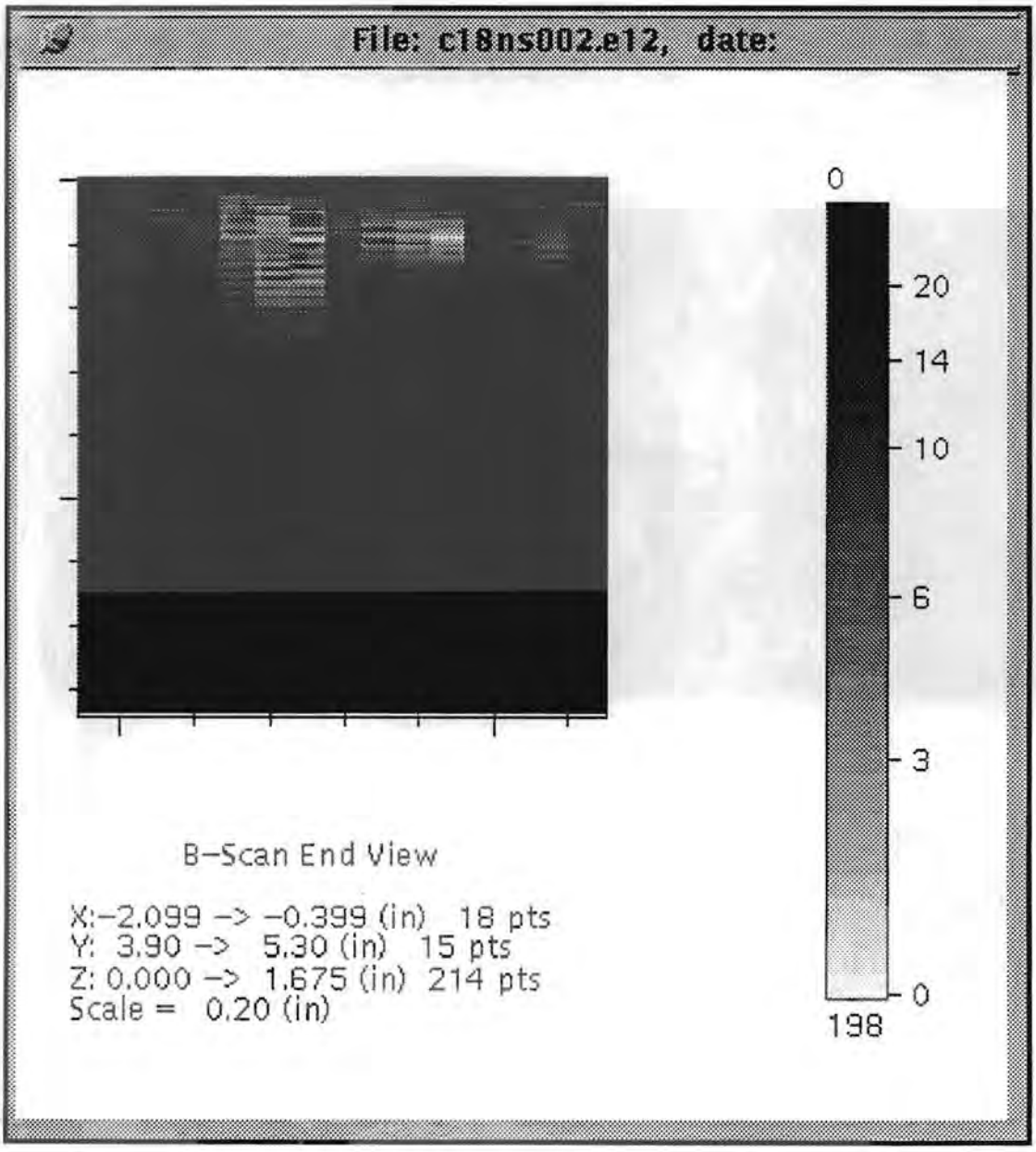

Figure 5.27b End View (YZ) of Clad to Base-Metal Indication in Block 1-8 at Y = 112 mm (4.4 in.). 70° L-wave inspection with beam direction of +X. This indication corresponds to flaw #8 in the destructive analysis.

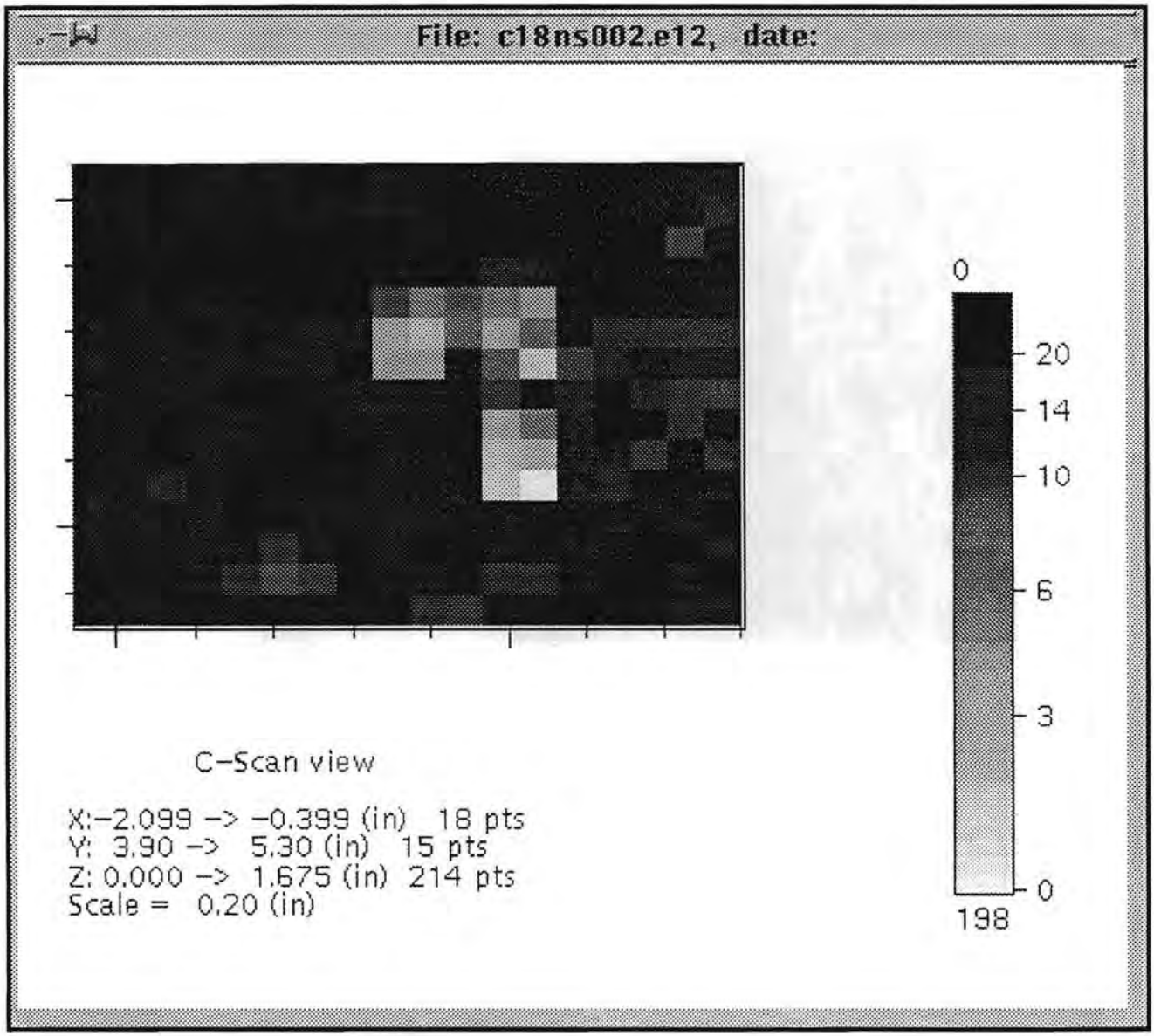

Figure 5.27c C-scan View (XY) of Clad to Base-Metal Indication in Block 1-8 at Y = 112 mm (4.4 in.). 70° L-wave inspection with beam direction of +X. This indication corresponds to flaw #8 in the destructive analysis.

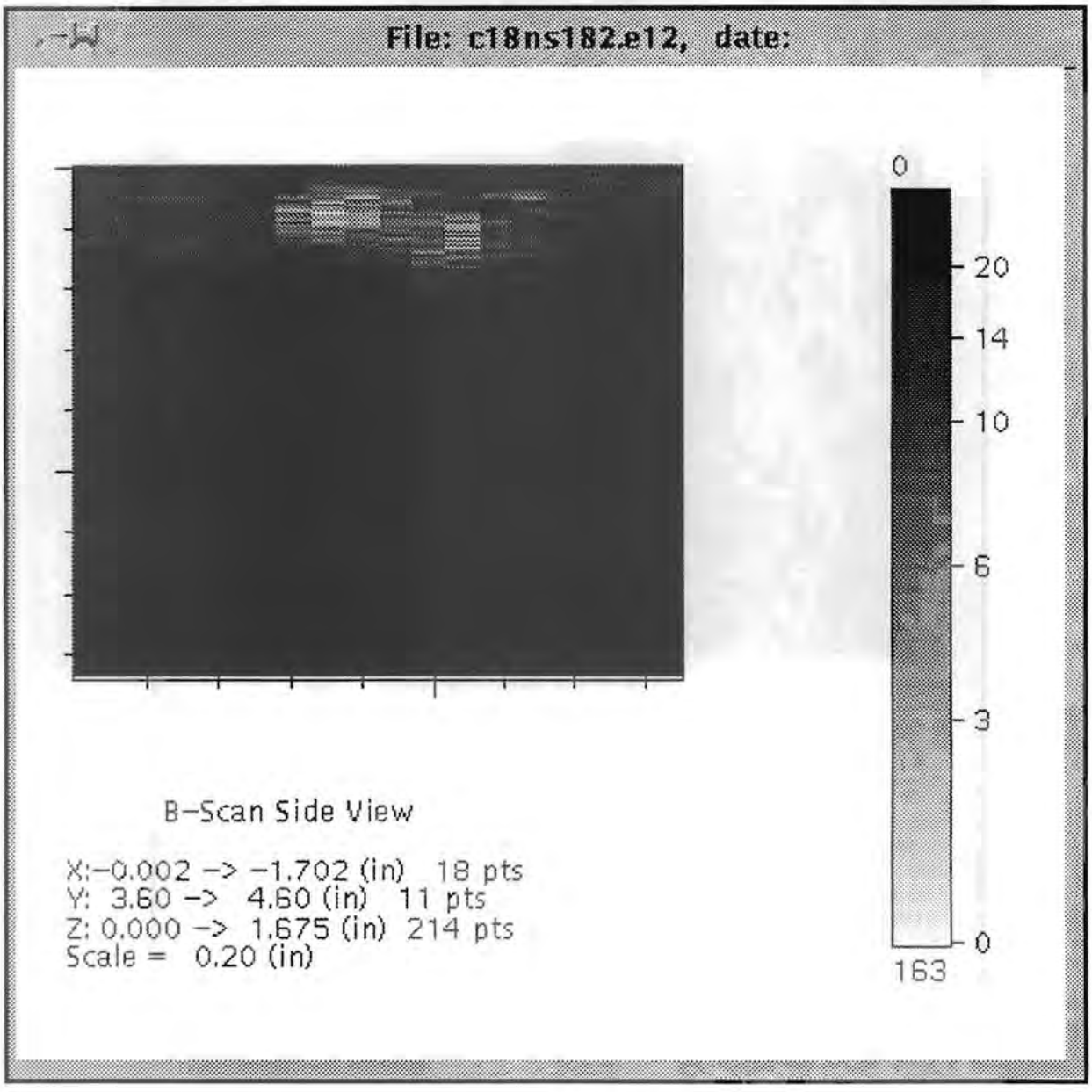

Figure 5.27d Side View (XZ) of Clad to Base-Metal Indication in Block 1-8 at Y = 112 mm (4.4 in.). 70° L-wave inspection with beam direction of -X. This indication corresponds to flaw #8 in the destructive analysis.

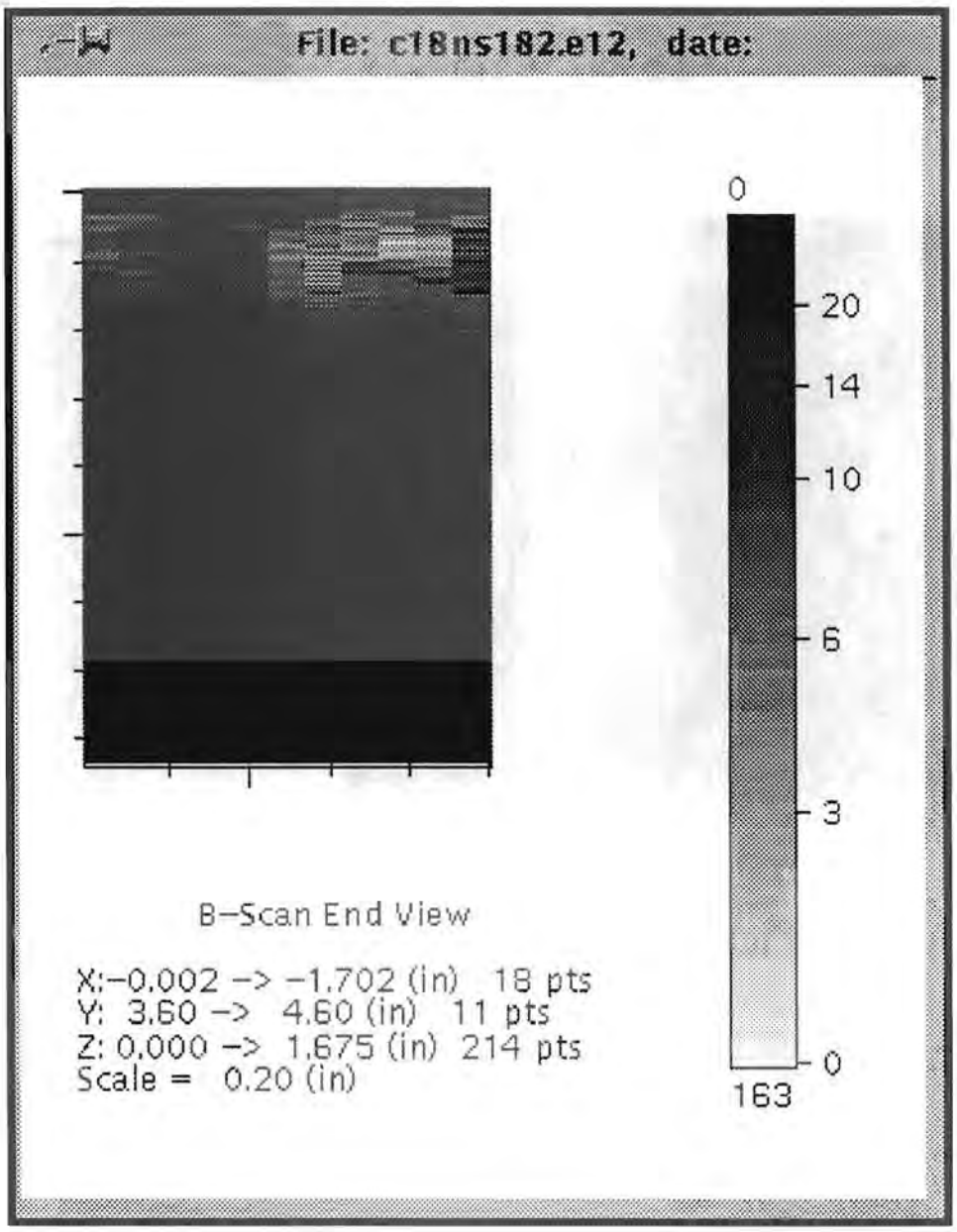

Figure 5.27e End View (YZ) of Clad to Base-Metal Indication in Block 1-8 at Y = 112 mm (4.4 in.). 70° L-wave inspection with beam direction of -X. This indication corresponds to flaw #8 in the destructive analysis.

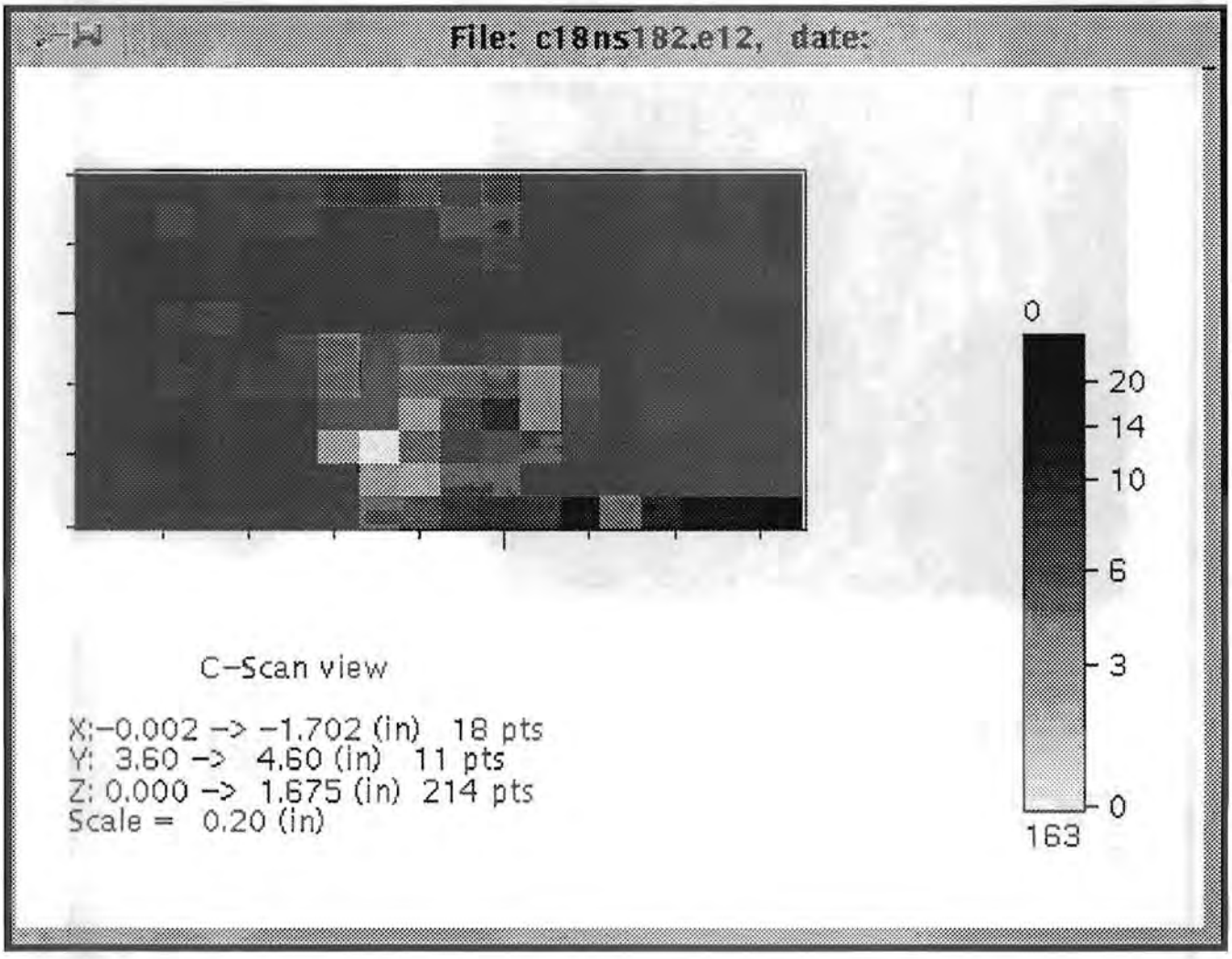

Figure 5.27f C-scan View (XY) of Clad to Base-Metal Indication in Block 1-8 at Y = 112 mm (4.4 in.). 70° L-wave inspection with beam direction of -X. This indication corresponds to flaw #8 in the destructive analysis.

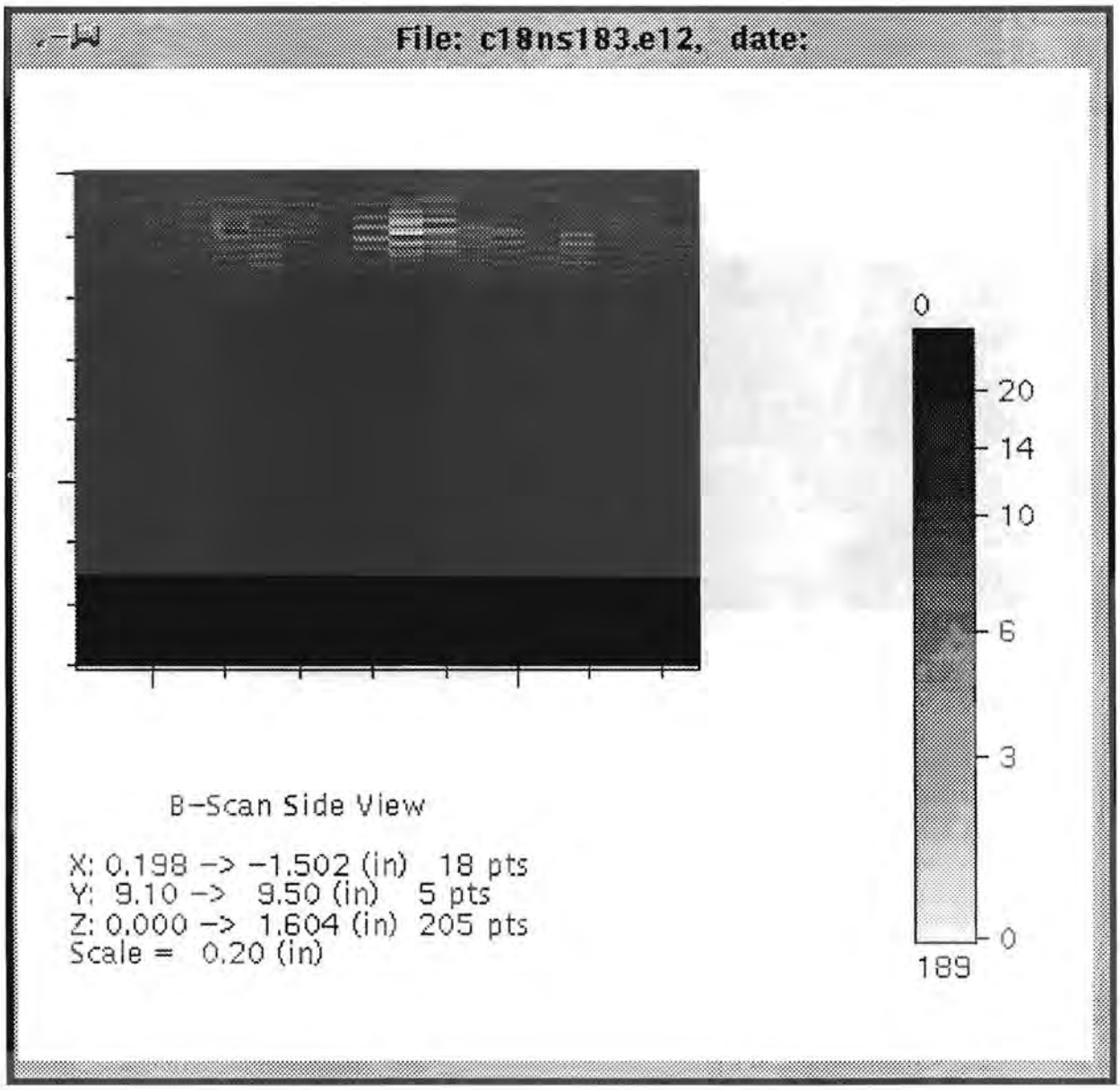

Figure 5.28a Side View (XZ) of Clad to Base-Metal Indication in Block 1-8 at Y = 236 mm (9.3 in.). 70° L-wave inspection with beam direction of -X. This indication corresponds to flaw #11 in the destructive analysis.

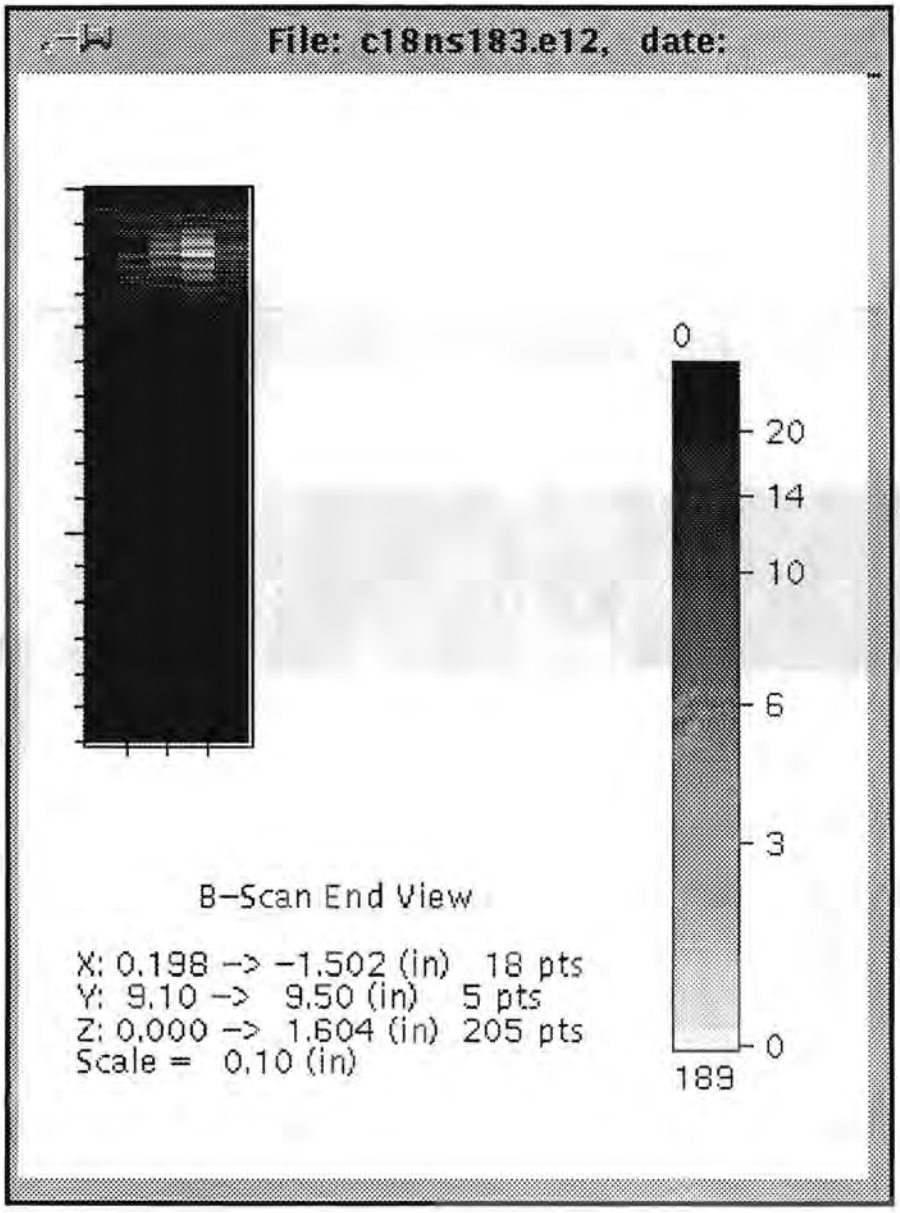

Figure 5.28b End View (YZ) of Clad to Base-Metal Indication in Block 1-8 at Y = 236 mm (9.3 in.). 70° L-wave inspection with beam direction of -X. This indication corresponds to flaw #11 in the destructive analysis.

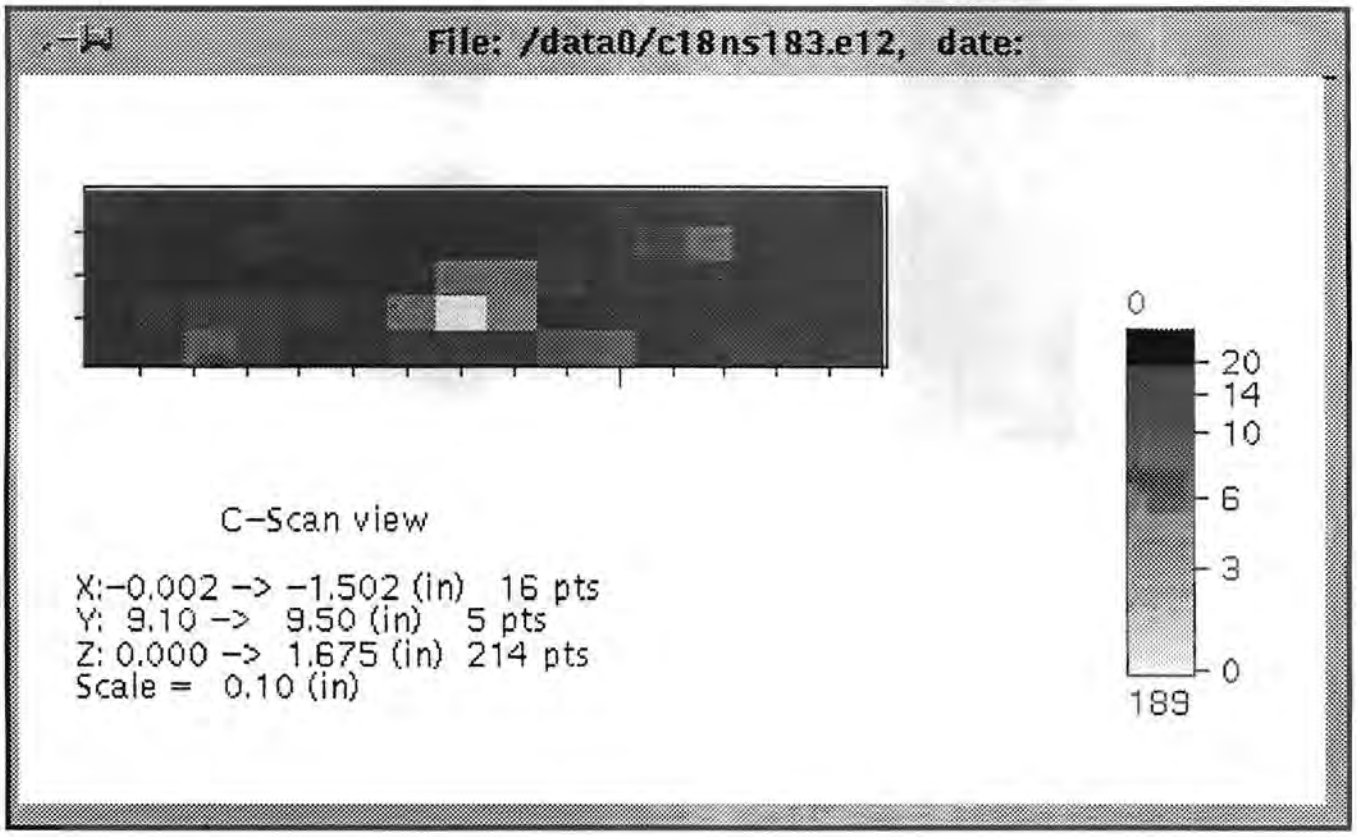

Figure 5.28c C-scan View (XY) of Clad to Base-Metal Indication in Block 1-8 at Y = 236 mm (9.3 in.). 70° L-wave inspection with beam direction of -X. This indication corresponds to flaw #11 in the destructive analysis.

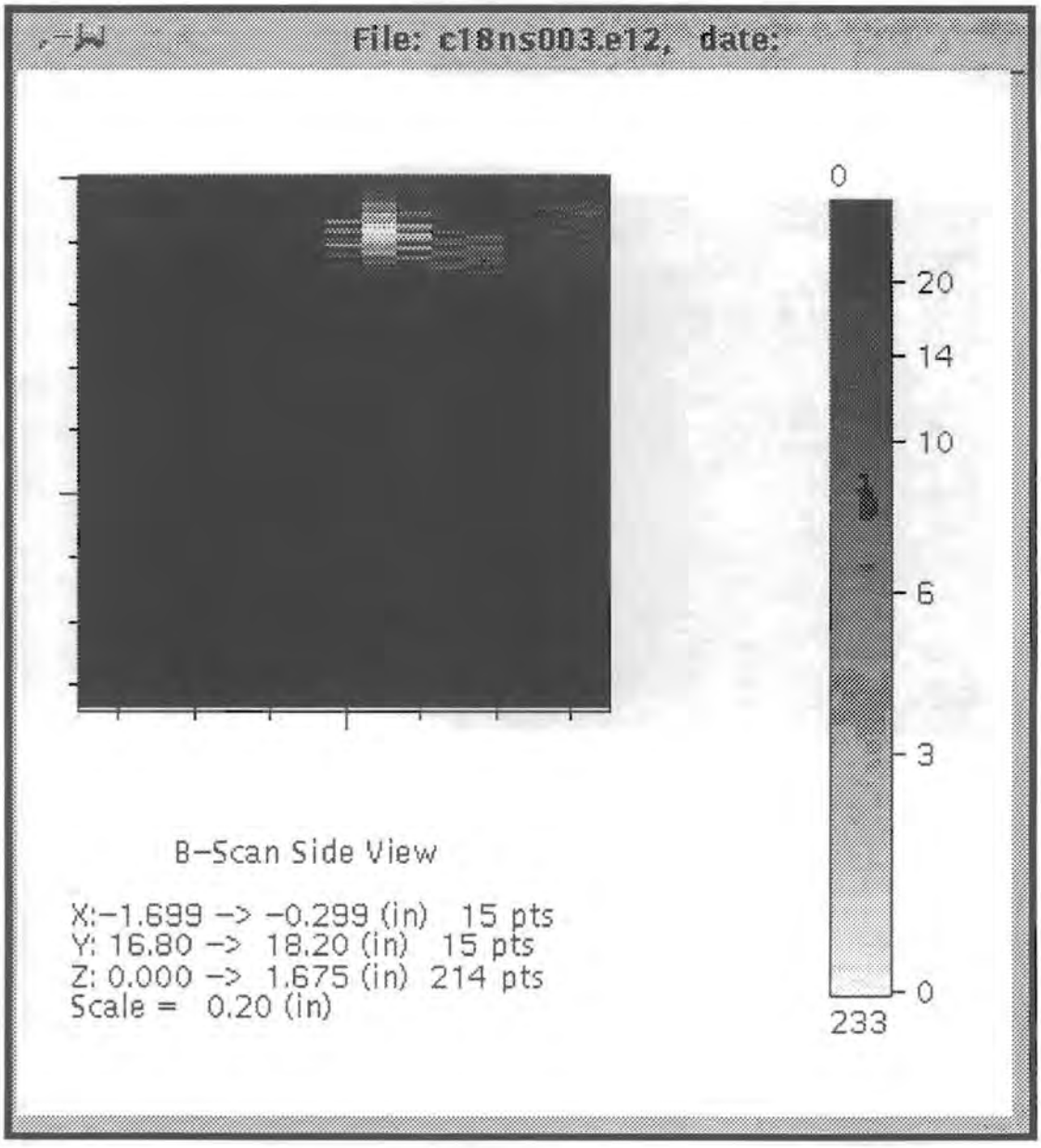

Figure 5.29a Side View (XZ) of Clad to Base-Metal Indication in Block 1-8 at Y = 442 mm (17.4 in.). 70° L-wave inspection with beam direction of +X.

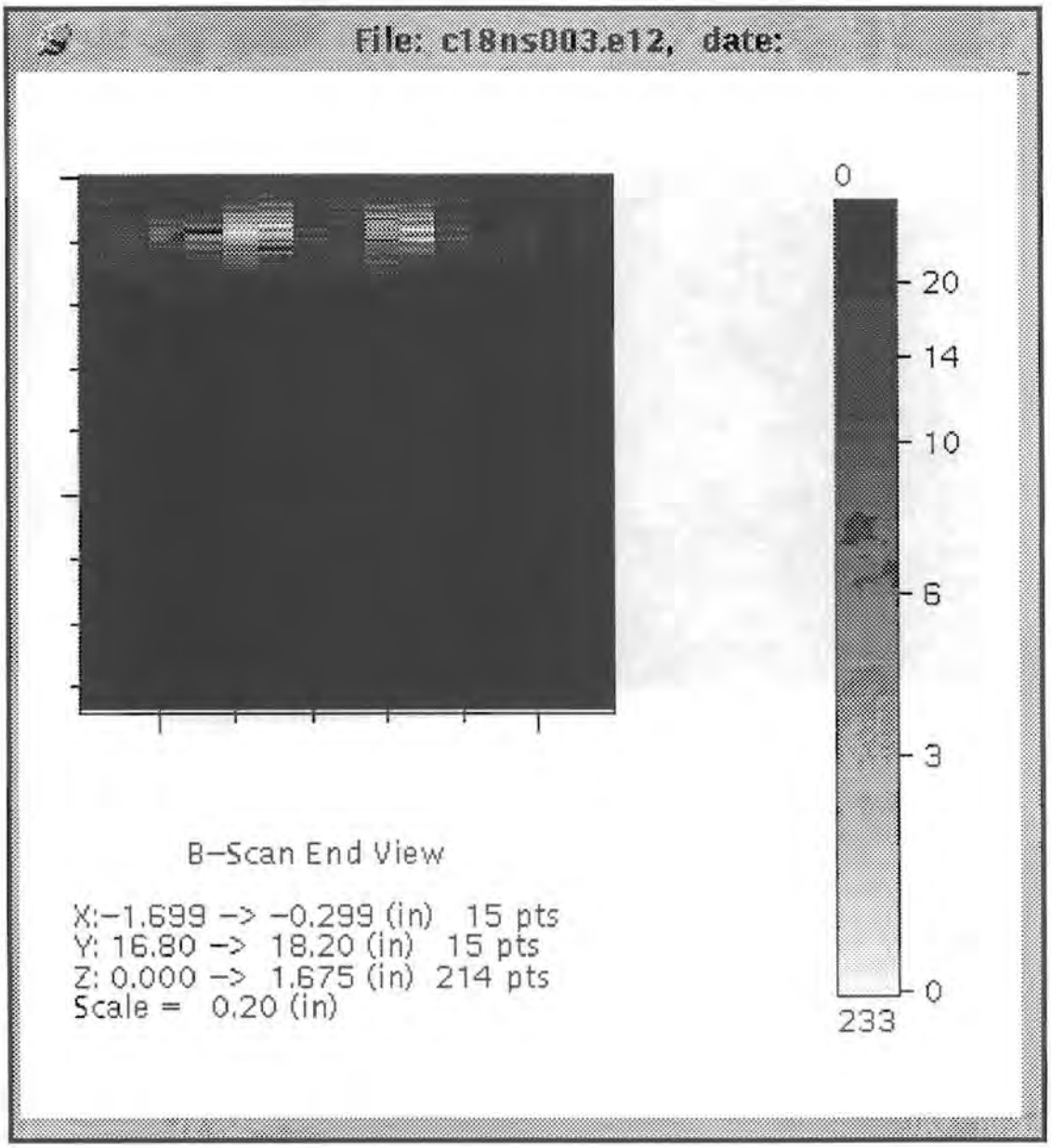

Figure 5.29b End View (YZ) of Clad to Base-Metal Indication in Block 1-8 at Y = 442 mm (17.4 in.). 70° L-wave inspection with beam direction of +X.

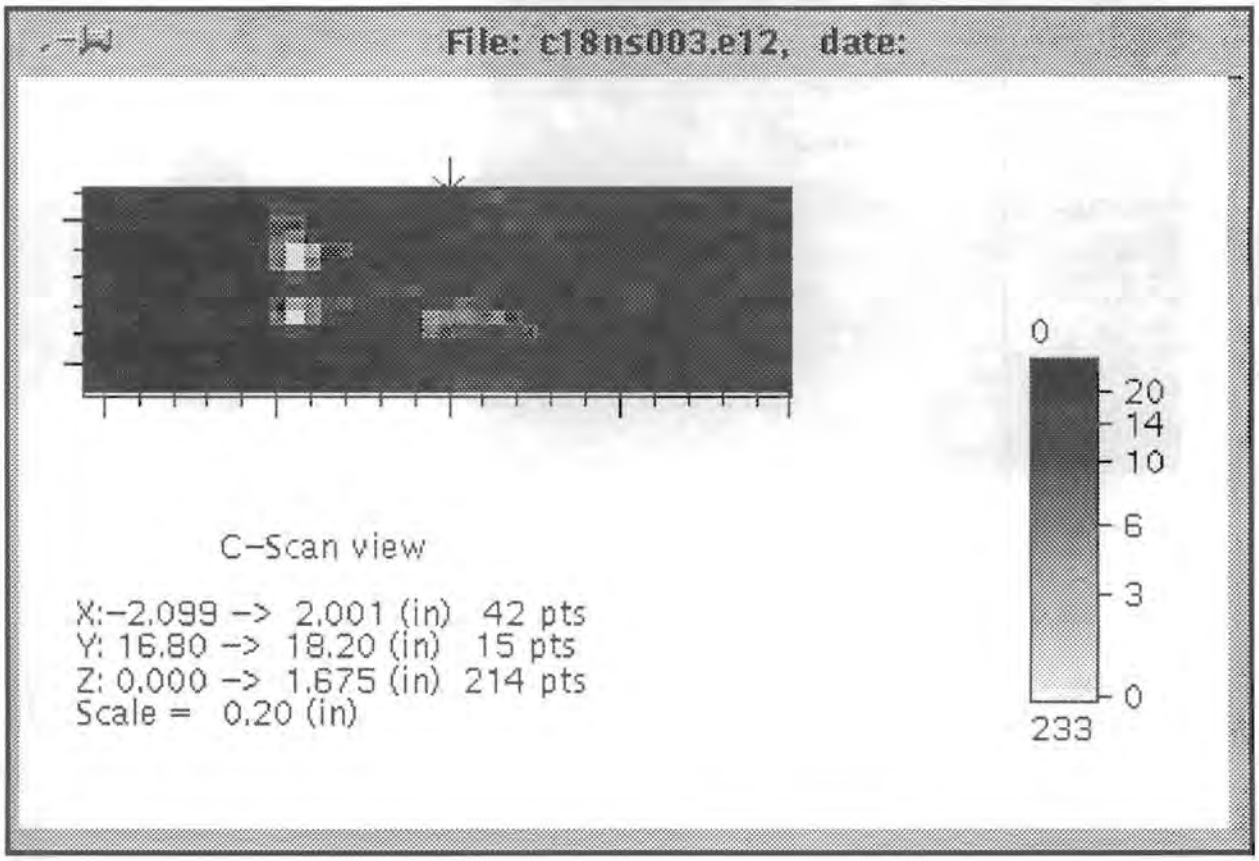

Figure 5.29c C-scan View (XY) of Clad to Base-Metal Indication in Block 1-8 at Y = 442 mm (17.4 in.). 70° L-wave inspection with beam direction of +X.

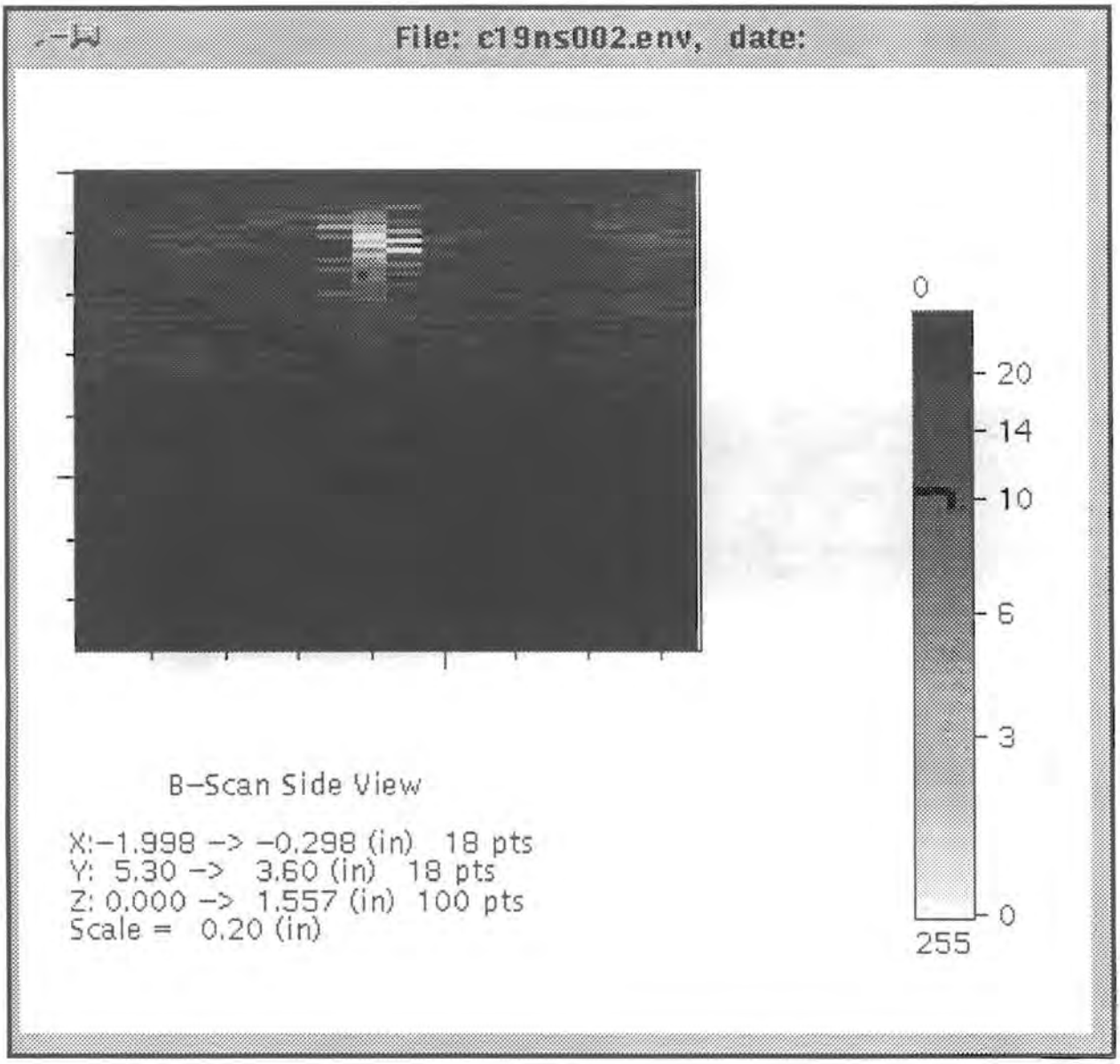

Figure 5.30a Side View (XZ) of Clad to Base-Metal Indication in Block 1-9 at Y = 117 mm (4.6 in.). 70° L-wave inspection with beam direction of +X.

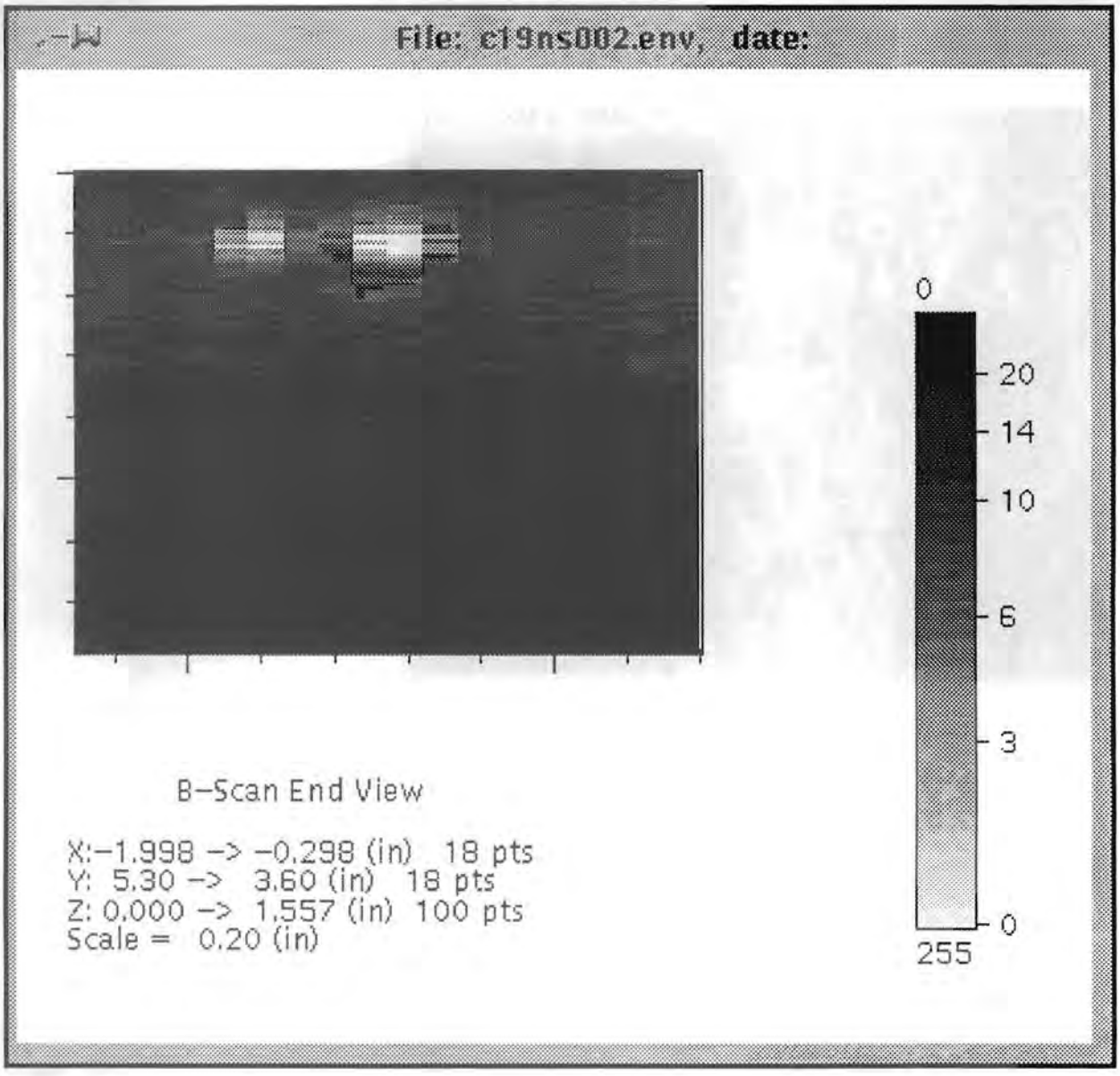

Figure 5.30b End View (YZ) of Clad to Base-Metal Indication in Block 1-9 at Y = 117 mm (4.6 in.). 70° L-wave inspection with beam direction of +X.

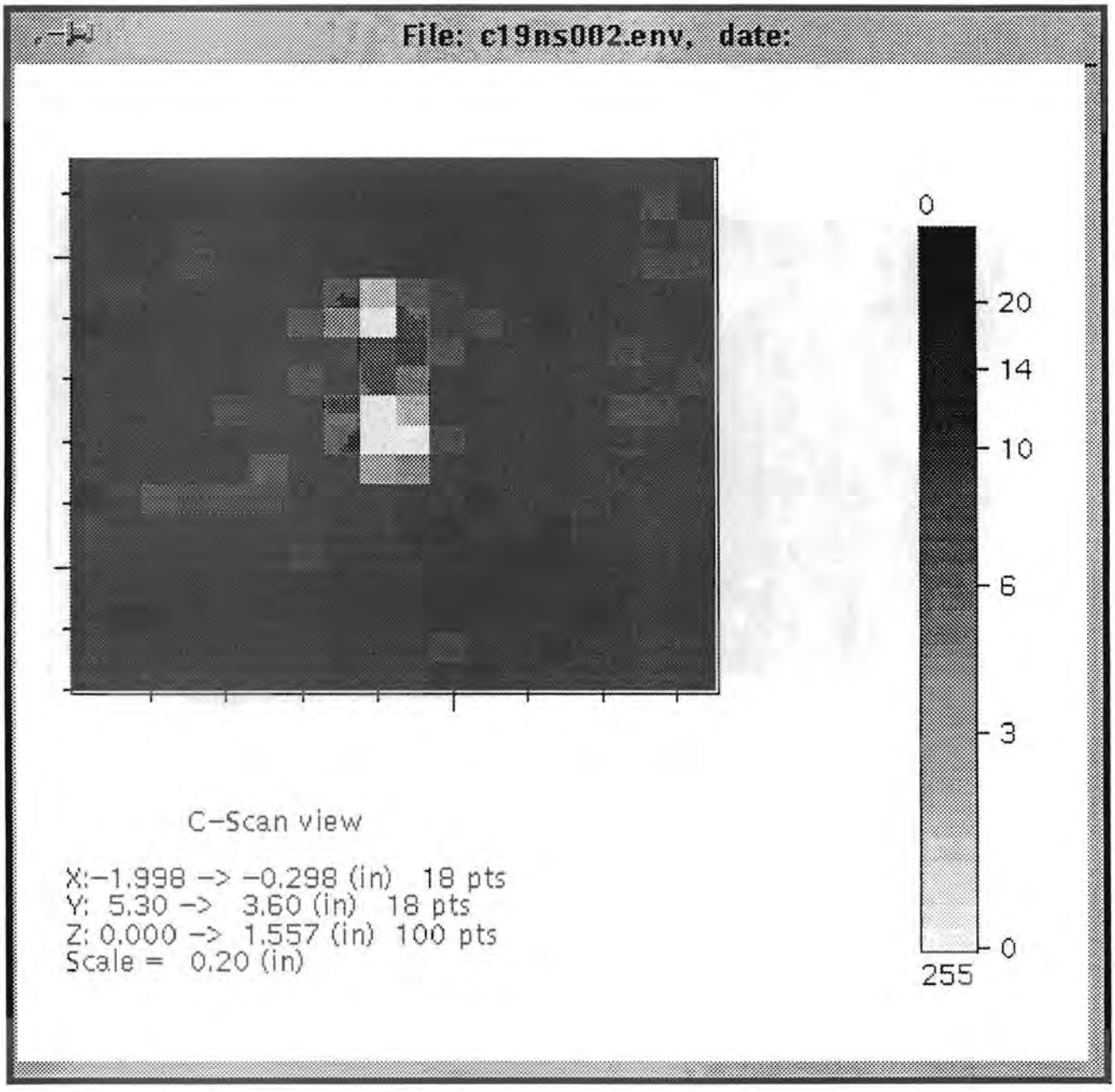

Figure 5.30c C-scan View (XY) of Clad to Base-Metal Indication in Block 1-9 at Y = 117 mm (4.6 in.). 70° L-wave inspection with beam direction of +X.

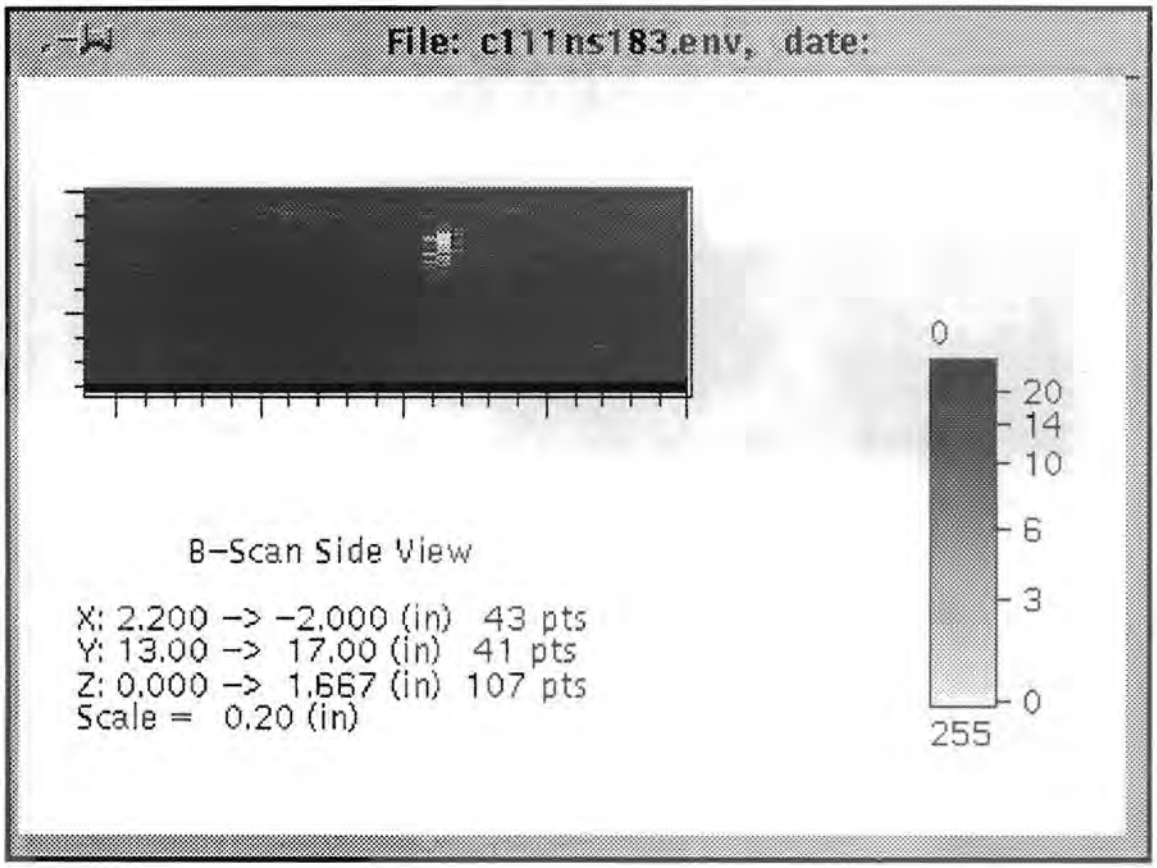

Figure 5.31a Side View (XZ) of Clad to Base-Metal Indication in Block 1-11 at Y = 387 mm (15.3 in.). 70° L-wave inspection with beam direction of -X.

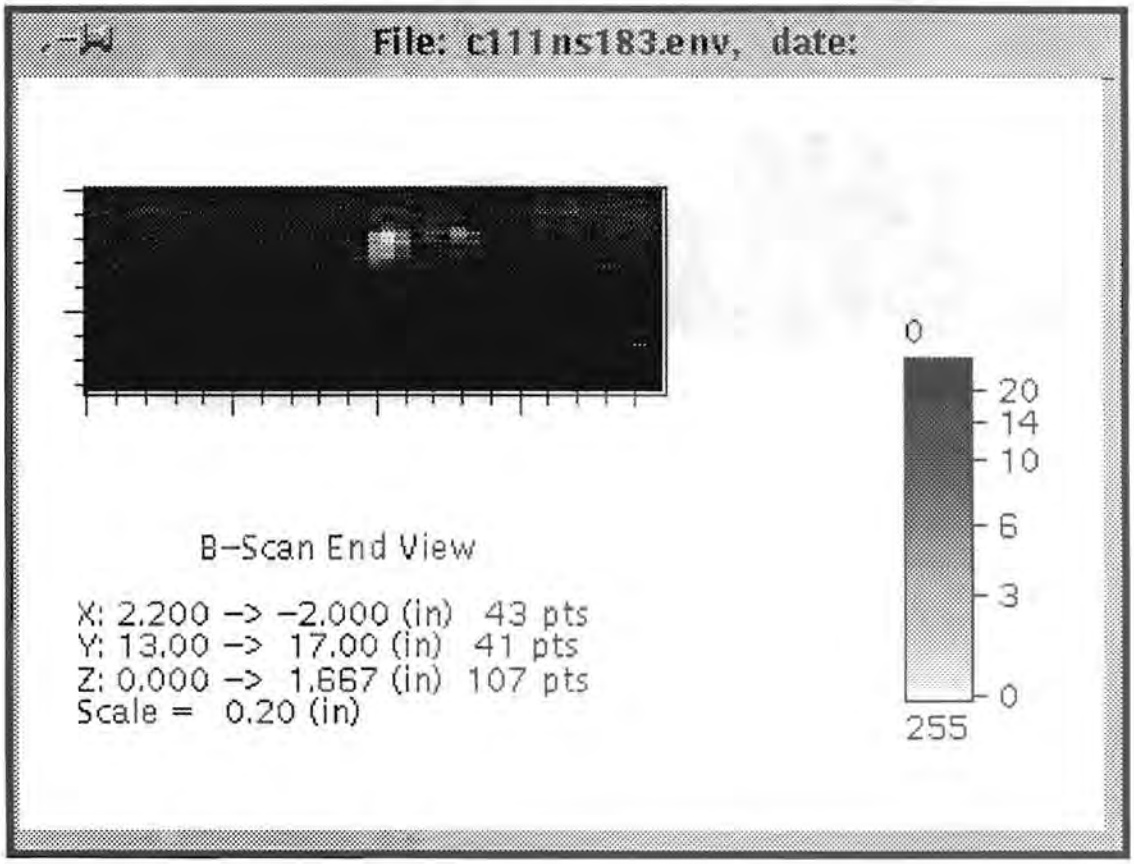

Figure 5.31b End View (YZ) of Clad to Base-Metal Indication in Block 1-11 at Y = 387 mm (15.3 in.). 70° L-wave inspection with beam direction of -X.

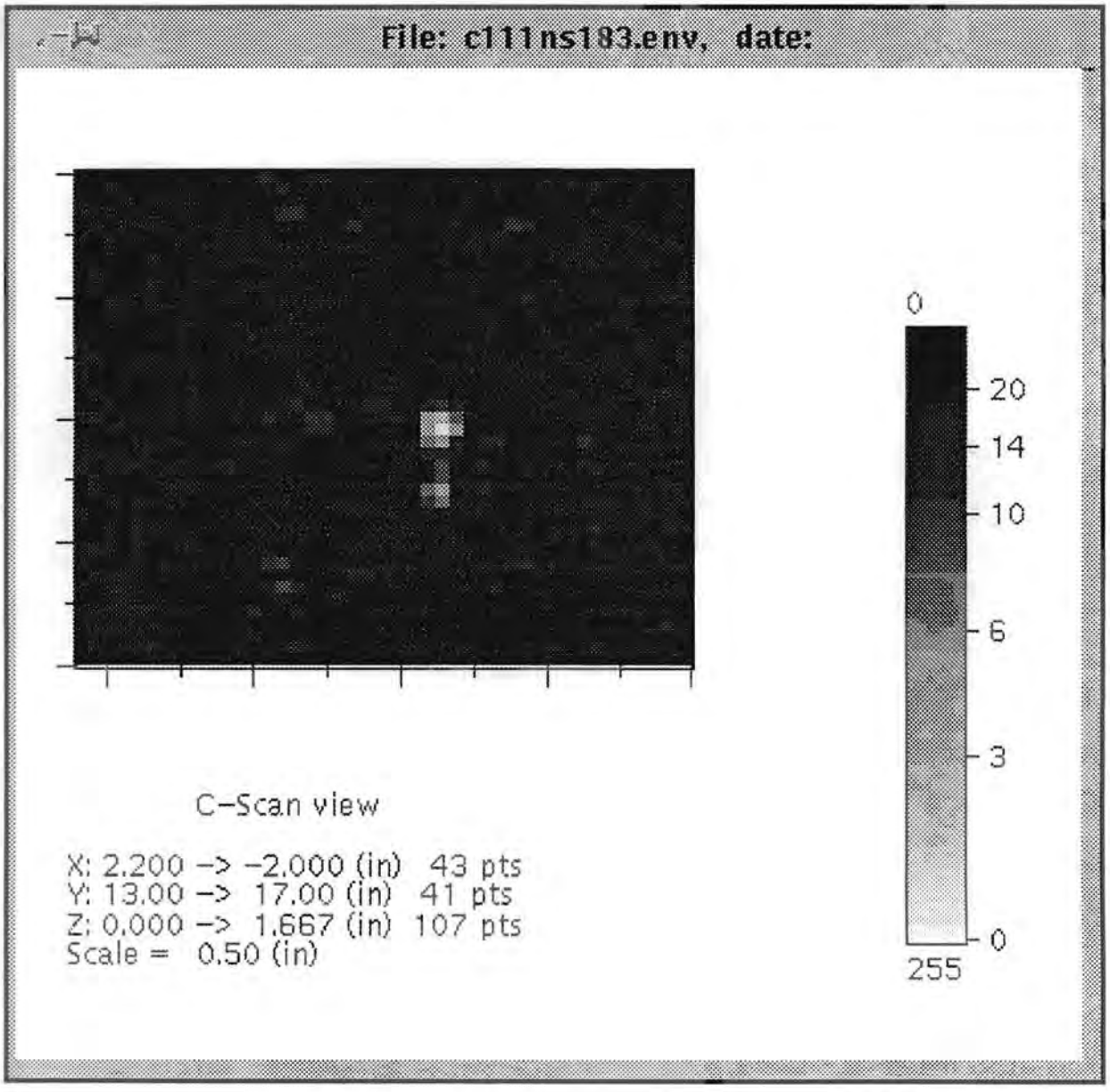

Figure 5.31c C-scan View (XY) of Clad to Base-Metal Indication in Block 1-11 at Y = 387 mm (15.3 in.). 70° L-wave inspection with beam direction of -X.

6.0 Distribution of Flaws in the Midland Blocks

Characteristics of the fabrication flaws in reactor pressure vessels are necessary inputs to the application of fracture mechanics calculations for assessments of reactor pressure vessel integrity. The features of the indications found by SAFT-UT in four Midland blocks have been extracted from the data. The flaws are distributed across the important feature types (location, type, and size). SAFT-UT Probability of Detection (POD), False Call Probability (FCP), and sizing error are estimated in this section. Flaw rates are estimated in this section without adjustment for POD, FCP, or sizing error.

6.1 Features of SAFT-UT Indications

Tables 6.1 and 6.2 show the location, type, and size for the 31 flaws found in the SAFT-UT data from the inspections of the Midland blocks. These tables are summaries of the detailed information contained in Section 5 of this report.

6.1.1 Location

Five categories were defined for classifying the location of indications in the Midland blocks: the near-surface zone (including the clad-to-base metal interface), weld root, weld, weld fusion zone, and base metal. In the first category are the indications at the clad-to-base metal interface. The near-surface zone is defined as the inner 25 mm of the vessel. Eight indications were found in this category. In the second category are indications near the weld root; four indications were found in this category, between 80 and 95 mm below the clad surface and within ± 12 mm of the weld centerline. In the third category are the indications within the weld. Ten indications were found in this category, where the weld cross section shown in Figure 2.2 was used for the location of the weld material. In the fourth category are indications in the weld fusion zone. Four indications were found in this zone, where the fusion zone was assumed to extend 6 mm beyond the weld-metal cross section shown in Figure 2.2. In the last category are indications in the base metal. Five indications were found in this category.

6.1.2 Type

The 31 flaws found in the Midland blocks have been categorized as either planar or volumetric. Planar flaws in this categorization are meant to include those flaws that are most important to calculations of vessel integrity such as vertically oriented cracks, lack of fusion in the weld, etc. Volumetric flaws in this categorization are meant to include flaws such as inclusions, pores, and laminations. The method used to determine the flaw type is described in Section 5.

6.1.3 Size

Tables 6.1 and 6.2 show both through-wall extent and circumferential extent of the 31 flaws.

6.2 Number of Flaws in the Categories

Table 6.3 shows the distribution of the 31 flaws as a function of through-wall extent, location, and type. The table also shows some interesting features of the flaw distribution, such as, the flaws found in the near-surface zone, weld root, and HAZ are all less than 2.2 mm in through-wall extent.

6.3 Probability of Detection, False Call Probability, and Sizing Error

In order to use the SAFT-UT results in an estimation procedure for flaw rates, it is necessary to determine the detection and sizing capabilities of SAFT-UT. Some valuable detection and sizing information can be obtained from this data set; that is, the SAFT-UT inspections of the Midland blocks and the destructive analysis of Midland Block 1-8. Additional information can be extracted from other tests that SAFT-UT has been used in and from the PISC II program.

6.3.1 Probability of Detection (POD)

The results from the PISC II program have shown that three distinct defect types should be considered when quantifying the POD of defects in heavy section steel (Crutzen, 1988). Smooth, planar defects (e.g., thermal fatigue cracks) are the most difficult to detect, rough planar defects are easier to detect, and volumetric defects such as slag inclusions and porosity have significantly higher POD than the other two defect types.

In the PISC II exercises, advanced UT techniques were used to inspect extensive amounts of pressure vessel material. Using these inspection data, the POD estimates shown in Table 6.4 were obtained from a logistic curve fit (Heasler 1993). As one can see from the table, the advanced procedures do best with volumetric defects.

The SAFT-UT probability of detection for volumetric defects with through-wall extent in the range of 1 to 2 mm can be estimated at 0.7 for both near-surface and sub-surface defects in the Midland blocks. This estimate uses the SAFT-UT detection results, reported in Section 4, of three detections for four defects inspected in the near-surface zone and two indications for three defects inspected in the weld root.

Since three of the Midland blocks (1-9, 1-11, and 1-12) received SAFT-UT inspections from the top or bottom machined face of the blocks, the POD for vertically oriented planar reflectors is increased and assumed to be the same as for volumetric flaws. The POD for SAFT-UT in the inspections of Midland blocks is estimated in Table 6.5.

6.3.2 False Call Probability

The results of the advanced method inspections of the PISC II program give an upper limit for FCP of 0.12 (0.08 clad) for volumetric flaws in thick section material. This value was reported in Heasler (1993) and was calculated from the number of detections in material without known flaws. But this number is only an upper limit because no destructive test was made to confirm that the material was blank.

The Midland destructive test results do not directly apply to a calculation of false call probability for SAFT-UT. The destructive test was performed to examine selected indications in the EPRI NDE Center UT data (Foulds 1993). The selection of the locations for destructive analysis was reported to be biased toward the more significant indications (the larger ones) in the UT data.

6.3.3 Sizing Error

SAFT-UT was used in the PISC III Full Scale Vessel (FSV) test located in Stuttgart, Germany at the Materialprufungsanstalt (MPA) Laboratory that involved the characterization of 12 indications in a full-scale reactor pressure vessel (PISC III report, 1993). The flaws in that FSV test had a range of 6 to 110 mm in through-wall extent; the statistical results for sizing error showed that SAFT-UT tended to undersize the flaws by 3.7 mm and the standard deviation of the SAFT-UT results from the true state was 4.7 mm (Doctor et al. 1994).

destructive analysis for defects numbers 1, 4, 9, 11, and 12 and, for this reason, no comparison can be made to a SAFT-UT estimate. Two defects (numbers 2 and 10) were not detected in the SAFT-UT data. One defect (number 3) was not inspected by SAFT-UT because it was at the end of the block.

The two small defects in the weld root (numbers 5 and 6) were undersized by SAFT-UT. The three small defects at the clad-to-base metal interface were oversized by SAFT-UT.

6.4 Flaw Rate Estimates

A parametric form for the flaw rate function, a two-parameter Weibull function, has been used to represent the rate of occurrence of flaws as a function of through-wall extent as follows:

$$\Lambda_o(s) = \beta_o \exp\left(-\left(\frac{s}{\alpha}\right)^{\beta_1}\right)$$

where $\Lambda_o(s)$ is the number of flaws with through-wall extent greater than s, per unit of weld length;
β_o is the total number of flaws per unit of weld length;
s is the through-wall extent of a flaw; and
α and β_1 are the two parameters of Weibull function that are to be fit to the empirical data.

In this report, we fit the raw data in Tables 6.1 and 6.2 to the Weibull model. The resulting estimate shows what the results are when detection or sizing errors are not included. This approach gives the most "optimistic" result that can be obtained from the data, because the introduction of detection and sizing error will increase the flaw rate function and also widen the confidence bounds.

Figures 6.1 and 6.2 present the results of a maximum likelihood Weibull fit to the SAFT-UT data for the 31 flaws. Figure 6.1 displays the estimates and confidence bounds for the parameters α and β_1, which determine the shape of the cumulative flaw rate function. This plot shows the 50%, 80%, 90%, and 95% confidence bounds on these parameters. Figure 6.2 presents a plot of $\Lambda(s)$, surround by 95% confidence bounds.

Tables 6.8 shows five different flaw rate parameters set for the Weibull model that have been published (Found et al. 1993) including the data in this report. The Marshall estimates for parameters α and β_1 fall somewhat outside the 95% confidence region produced by the maximum likelihood fit to the SAFT-UT data. The significance of this discrepancy is not great because the confidence bounds on the Marshall distribution would show significant overlap with the SAFT-UT distribution. The estimate for β_0 for Marshall distribution does not agree with the SAFT-UT results. According to the maximum likelihood fit to the SAFT-UT data, a 95% confidence bound on β_0 is (3.5 to 14.4) flaws/m; much higher than the Marshall Committee estimate of 0.003 to 0.3 flaw/m (0.4 to 40 flaws/m^3), where we have used a narrow gap weld cross section of 0.008 m^2.

In summary, the SAFT-UT data from the four Midland blocks does not support the assumption of a Marshall distribution of flaws in this material. The most significant differences between the two distributions is that the total flaw density as measured by SAFT-UT is higher than that assumed in the Marshall distribution. The other published flaw density estimates shown in Table 6.8 have that property as well. But the number of flaws that support these estimates of the flaw rate function is small.

Table 6.1 Summary of Base Metal Defects found by SAFT-UT

Block	Depth, mm	Depth Extent, mm	Circum. Extent, mm	Defect Type	Material
1-8	89	1.3	5	Volumetric	Root
	91	1.3	20	Planar	Root
	91	1.3	15	Volumetric	Root
	109	1.3	5	Volumetric	Weld
	112	-	10	Volumetric*	Weld
	79	-	10	Volumetric*	Weld
	86	-	10	Volumetric*	Root
	109	1.3	10	Planar	Fusion
	183	-	15	Volumetric*	Weld
	155	-	15	Volumetric*	Base
	183	-	20	Volumetric*	Fusion
	208	-	20	Volumetric*	Weld
1-9	178	18	36	Planar	Weld
	145	5	23	Planar	Base
	178	10	-	Planar	Base
	64	5	13	Planar	Base
	114	5	13	Planar	Weld
	121	8	25	Planar	Weld
	119	-	10	Volumetric*	Weld
	206	-	23	Volumetric*	Base
1-11	132	2	10	Planar	Weld
	150	2	20	Planar	Fusion
1-12	119	2	10	Planar	Fusion

* These defects were only detected in normal beam from the clad or unclad side. For this reason, they are estimated to be volumetric in nature without measurable through-wall extent.

Table 6.2 Summary of Clad-to-Base Metal Defects found by SAFT-UT

Block	Depth, mm	Depth Extent, mm	Circum. Extent, mm	Defect Type	Location
1-8	5	<2.2	5	Volumetric	Near-surface
	5	<2.2	2	Volumetric	Near-surface
	8	<2.2	5	Volumetric	Near-surface
	10	<2.2	5	Volumetric	Near-surface
	5	<2.2	5	Volumetric	Near-surface
	5	<2.2	15	Volumetric	Near-surface
1-9	5	<2.2	15	Volumetric	Near-surface
1-11	11	<2.2	23	Planar	Near-surface

Table 6.3 Midland: Number of Flaws in Categories

	Through-Wall Extent of Flaw											
	<2.2 mm		5 mm		8 mm		10 mm		18 mm		Total	
Flaw Location	V*	P**	V	P	V	P	V	P	V	P	V	P
Near Surface	8	0	0	0	0	0	0	0	0	0	8	0
Root	3	1	0	0	0	0	0	0	0	0	3	1
Weld	6	1	0	1	0	1	0	0	0	1	6	4
Fusion (HAZ)	1	3	0	0	0	0	0	0	0	0	1	3
Base	2	0	0	2	0	0	0	1	0	0	2	3
Total	20	5	0	3	0	1	0	1	0	1	20	11

* Volumetric
** Planar

Table 6.4 POD for Advanced Procedures from Fits to PISC-II Data

Flaw Type	Material	POD (2 mm*)	POD (6 mm*)	POD (12 mm*)
Smooth Planar	Base	**	0.19	0.23
	Clad	**	0.19	0.25
Rough Planar	Base	**	0.35	0.60
	Clad	**	0.16	0.40
Volumetric	Base	0.30	0.84	0.99
	Clad	0.18	0.60	**

* Through-Wall Extent of Defect
** No estimation

Table 6.5. Estimated POD for SAFT-UT Inspections of the Midland Blocks

Through-Wall Extent	1-2 mm	6 mm	12 mm
POD for Near-Surface	0.7	--	--
POD for Weld and Base Metal	0.7	0.84	0.99

Table 6.7 True-State Table for Through-Wall Extent

EPRI NDE Center Indication Number	True State from Destructive Analysis	SAFT-UT Estimate	Material
1	Not determined	Not applicable	Root
2	1 mm	Not detected	Root
3t 3b	0.75 mm 3 mm	Not inspected	Root
4	Not determined	Not applicable	Root
5	2 mm	1.3 mm	Root
6t 6b	2 mm* 3.5 mm	1.3 mm	Root
7	1 mm	< 2.2 mm	CBI**
8	2 mm	< 2.2 mm	CBI
9	Not determined	Not applicable	CBI
10a 10b	1 mm 1 mm	Not detected	CBI
11	0.5 mm	< 2.2 mm	CBI
12	Not determined	Not applicable	CBI
13	Not determined	Not applicable	CBI

* Two defects found and sized but no data provided on spatial relationship.
** Clad-to-Base Interface zone

Table 6.8 Flaw Rate Function Parameters

Data Set	α, mm^{-1} ($in.^{-1}$)	β_1	β_0, Flaws/m (Flaws/ft.)	95% Confidence Bounds on β_0, Flaws/m (Flaws/ft.)
Marshall Distribution[a]	6.25 (0.246)	1	0.003 to 0.3 (0.02)	
SAFT-UT, 31 flaws[b]	3.81 (0.15)	1.39	7.4 (2.30)	3.5 to 14.4 (1.06 to 4.41)
SAFT-UT, 11 flaws[c]	7.11 (0.28)	1.49	2.1 (0.66)	1.9 to 13.2 (0.59 to 4.02)
SAFT-UT, Sandia Report[d]	1.27 (0.05)	0.61	11.0 (3.4)	
EPRI NDE Center UT, Sandia Report	4.70 (0.185)	1.30	3.0 (0.93)	

(a) Marshall, 1982.
(b) Data from this report. SAFT-UT inspections of four Midland blocks without adjustment for POD or sizing error.
(c) Data reported in Doctor (1991). SAFT-UT inspection results without correlation with destructive analysis and without adjustment for POD or sizing error.
(d) Data reported in Foulds (1993).

Table 6.9 Estimates of Cumulative Flaw Rates

Data Set	Λ (2.5 mm) Flaws/m	Λ (5 mm) Flaws/m	95% Confidence Bounds on β_0, Flaws/m (Flaws/ft.)
Marshall[a]	.02 - .2	0.0013 - 0.13	0.0004 - .04
SAFT-UT, 31 flaws[b]	4.2	1.7	0.054
SAFT-UT, 11 flaws[c]	1.7	1.2	0.24
SAFT-UT, Sandia Report[d]	2.4	1.1	0.21
EPRI NDE Center UT, Sandia Report	1.9	1.0	0.10

(a) The flaw distribution for preservice condition of vessels recommended in U.S. Nuclear Regulatory Guide 1.154 for use in probabilistic fracture mechanics analysis of PWR vessel integrity under pressurized thermal shock.

(b) Data from this report. SAFT-UT inspections of four Midland blocks without adjustment for POD or sizing error.

(c) Data reported in Doctor (1991). SAFT-UT inspection results without correlation with destructive analysis and without adjustment for POD or sizing error.

(d) Data reported in Foulds (1993).

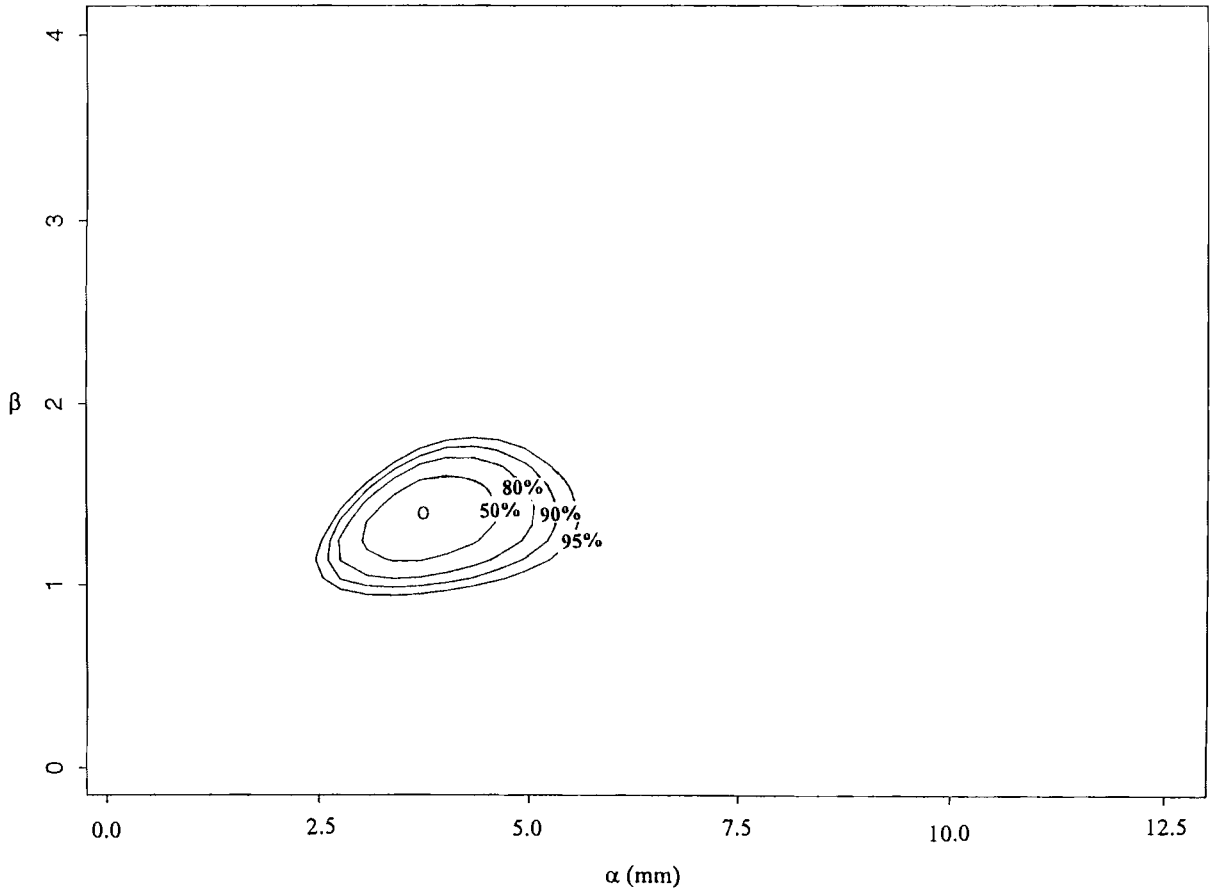

Figure 6.1 Parameter Estimates with Confidence Bounds for Simple Weibull Fit to the SAFT-UT Data of 31 Flaws

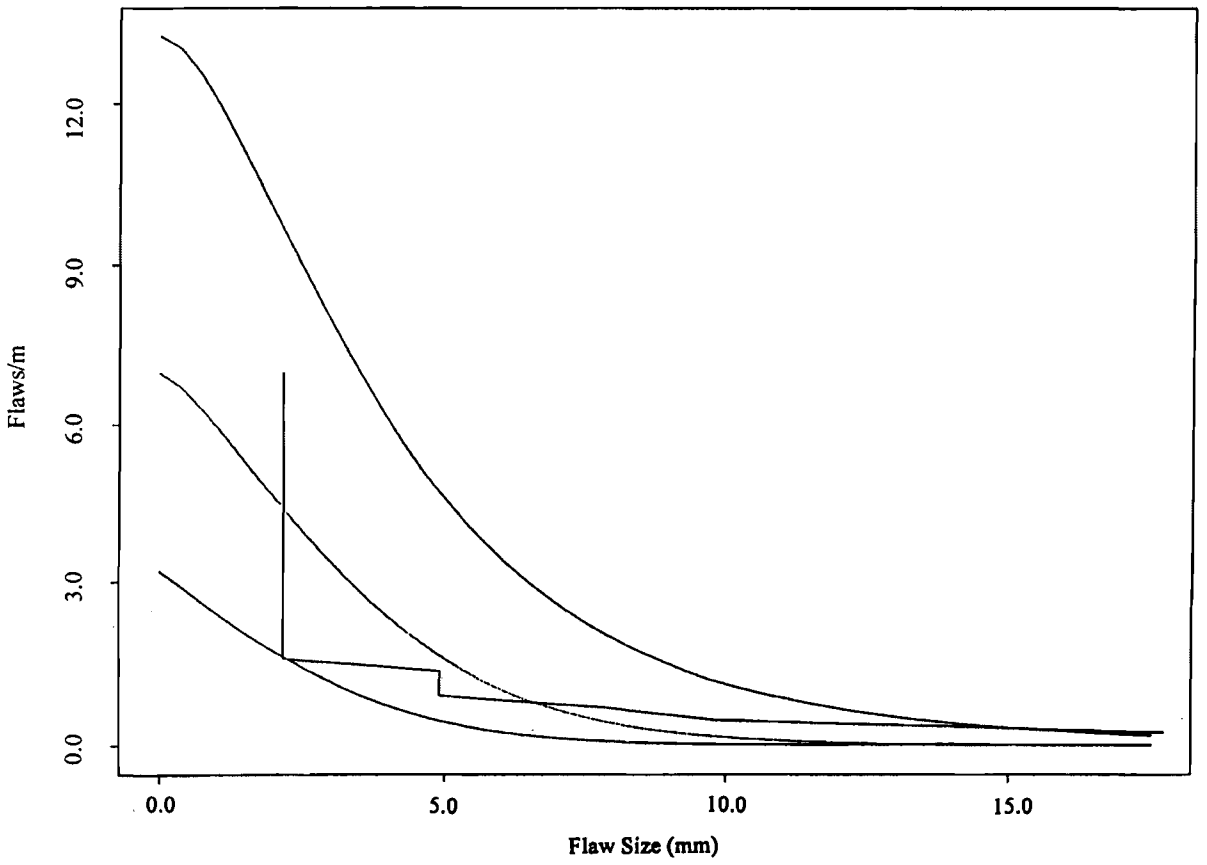

Figure 6.2 Estimate of Cumulative Flaw Rate Function with 95% Confidence Interval for Simple Weibull Fit to the SAFT-UT Data of 31 Flaws

7.0 Recommendations for the Use of SAFT-UT on Vessel Material

The SAFT-UT field system was designed to provide a spatial sampling that would provide high-resolution images for defects that are of potential importance to structural integrity. It was in this configuration that the SAFT-UT system was used for the inspection of the Midland blocks. In general, the flaws found by SAFT-UT were small. Destructive analysis of Block 1-8 found mainly slag inclusions that were sometimes less than 1 mm (0.04 in.) in extent in one or more dimensions. After the SAFT-UT system was used on the Midland blocks, improvements were made to the system to permit more accurate characterization of these small fabrication defects. The changes to the SAFT-UT system are described in this section.

The SAFT-UT normal beam inspections of the Midland blocks were made with a 2.25 MHZ transducer. A 5.0 MHZ transducer is recommended for the inspection of small fabrication defects in the base metal of vessel material in order to gain better performance in measuring lateral extent.

The inspections of the clad-to-base metal interface are composed mostly of 70°, 2.0-MHZ, L-wave inspections. An inspection of this type has a wavelength in the metal of 3 mm (0.12 in.). Objects greater than 2.2 mm in depth extent will show some measurable size. Unfortunately, the use of a higher frequency for the 70° L-wave inspections is not recommended. The clad-to-base metal region is a difficult medium for the propagation of higher frequencies. But because of the occurrence of volumetric indications (slag inclusions) at the clad-to-base metal interface, the use of a 4.0-MHZ dual-element, normal beam, near-surface transducer is recommended to supplement the 70°, 2.0 MHZ SAFT-UT inspections.

The above discussion of minimum measurable lateral extent has not considered the spacial sampling intervals that must accompany the SAFT-UT scanning process. For the inspections of the Midland blocks most of the data were taken with 2.5 mm steps in X and Y. Because the spatial sampling locations are made randomly with respect to the location of the small fabrication defects, the minimum measurable lateral extent must be increased by one step size interval. This significantly increases the minimum measurable lateral extent, and we recommend that step sizes in X and Y be set to one-half wavelength for SAFT-UT inspections. This is 0.64 mm (0.025 in.) for 5 MHZ normal beam and 1.5 mm (0.060 in.) for 70° L-wave inspections.

The implications of the above recommendations, where one wants to detect and accurately size very small indications, on the computer methods are significant. File sizes for RF data will exceed 100 MBytes. The SAFT-UT system was not configured to acquire, process, or display inspections with such large data sizes when the Midland blocks were inspected. Even on the present SAFT-UT system, based on an 80 MIP processing CPU, the SAFT focusing can require more than 24 hours when the use of high gain causes large amounts of both signal and noise to be present in the RF (raw) data. For analyzing small indications, the data must be taken with very high density. The reality is that, for these kinds of inspections, the file sizes can become so large that some difficulties remain for fieldable systems. We expect that the implementation of the above recommendations will become more manageable as computer methods advance.

A significant additional recommendation regards the use of material coordinates in the acquisition of SAFT-UT data. The SAFT-UT system used scanner coordinates for its computer records (file header information) and for display purposes when the Midland data was taken. A recommendation for the analysis of multiple inspections of vessel material is that all of the images be presented in material coordinates and that the material coordinates should be documented as a computer record when the data is taken. Such presentation simplifies the interpretation of inspections from different angles and from different sides of the vessel, instills confidence in the interpretation, and reduces ambiguity.

8.0 References

Booth, D. L. 1989. *Material Documentation Report for the Weld Material Removed from the Consumers Power (Midland) Reactor Vessel (620-0012-51),* BAW-2070. The Babcock .& Wilcox Company, Lynchburg, Virginia.

Doctor, S. R., et al. 1991. "Progress in Evaluation and Improvement in Nondestructive Examination Reliability for Inservice Inspection of Light Water Reactors (LWRS) and Characterizing Fabrication Flaws in Reactor Pressure Vessels," Proc. US *NRC 19th Water Reactor Safety Information Meeting, Vol. 1,* NUREG/CP-0 119. U.S. Nuclear Regulatory Commission, Washington, D.C.

Doctor, S. R., L. J. Angel, A. A. Diaz, R. V. Harris, Jr., F. A. Simonen, and G. J. Schuster. 1994 (in press). "Reliability of NDE - Cast Stainless Steel, SAFT-UT Performance, PISC III Program Status, and Evaluation of Computer-Based UT/ISI Systems," in Proc. *of 21st Water Reactor Safety Information Meeting,* Nuclear Regulatory Commission, Washington D.C.

Foulds, J. R. and E. L. Kennedy. 1993. *Midland Reactor Pressure Vessel Flaw Distribution,* SAND93-7064. Failure Analysis Associates, Inc., Menlo Park, California.

Hall, T. E., L. D. Reid, and S. R. Doctor. 1988. *The SAFT-UT Real-Time Inspection System - Operational Principles and Implementation,* NUREG/CR-5075. Prepared for the U.S. Nuclear Regulatory Commission, Washington, DC.

Evaluation of the Sizing Results of 12 Flaws of the Full Scale Vessel Installation. 1993. PISC III Report No. 26 -Action 2, Phase 1. EUR 15371 EN. Prepared for Programme for the Inspection of Steel Components. Commission of the European Communities, Brussels, Luxembourg.

Marshall, W. 1982. "An Assessment of the Integrity of PWR Pressure Vessels, Summary Report," first report of a study group under the Chairmanship of Sir Walter Marshall, CBE FRS, UDAEA, London.

NRC FORM 335 (2-89) NRCM 1102, 3201, 3202

U.S. NUCLEAR REGULATORY COMMISSION

BIBLIOGRAPHIC DATA SHEET

(See instructions on the reverse)

1. REPORT NUMBER (Assigned by NRC, Add Vol., Supp., Rev., and Addendum Numbers, if any.)

NUREG/CR-6471, Vol. 1
PNNL-11143

2. TITLE AND SUBTITLE

Characterization of Flaws in U.S. Reactor Pressure Vessels

Density and Distribution of Flaw Indications In PVRUF

3. DATE REPORT PUBLISHED

MONTH	YEAR
November	1998

4. FIN OR GRANT NUMBER

L1099, W6275

5. AUTHOR(S)

G.J. Schuster, S.R. Doctor, P.G. Heasler

6. TYPE OF REPORT

Technical

7. PERIOD COVERED *(Inclusive Dates)*

8. PERFORMING ORGANIZATION - NAME AND ADDRESS *(If NRC, provide Division, Office or Region, U.S. Nuclear Regulatory Commission, and mailing address; if contractor, provide name and mailing address.)*

Pacific Northwest National Laboratory
Richland, WA 99352

9. SPONSORING ORGANIZATION - NAME AND ADDRESS *(If NRC, type "Same as above"; if contractor, provide NRC Division, Office or Region, U.S. Nuclear Regulatory Commission, and mailing address.)*

Division of Engineering Technology
Office of Nuclear Regulatory Research
U.S. Nuclear Regulatory Commission
Washington, DC 20555-0001

10. SUPPLEMENTARY NOTES

D.A. Jackson, NRC Project Manager

11. ABSTRACT *(200 words or less)*

Characterization of Flaws in U.S. Reactor Pressure Vessels is a multi-volume report. Volume 1, this document, provides the results of a nondestructive examination conducted at the Oak Ridge National Laboratory's Pressure Vessel Research User Facility (PVRUF) on a vessel fabricated for a canceled nuclear power plant. Volume 2, in preparation, will document the results of Pacific Northwest National Laboratory's (PNNL) destructive validation of the flaw rates in the PVRUF evaluation. Twenty linear meters of weldment were inspected by SAFT-UT including the entire circumferential beltline weld of the vessel. There were 2500 detectable indications in the SAFT-UT inspections of the PVRUF vessel. The largest number of these, 982, were found at the clad-to-base metal interface, but 978 of these were less than 2mm (0.08 in.) in size. In the near surface zone, the weld metal contained 98 detectable planar indications. The density of indications was four times higher in the weldment than in the base metal. The distribution of the empirical data provided enough information to apply a parametric model of the cumulative flaw rate to six different subsets of the data, and to obtain reasonable confidence bounds on the results. Recommendations are given for validating the indication rates by selective destructive analysis to provide the necessary high quality flaw statistics for use in fracture mechanics calculations such as those used in pressurized thermal shock (PTS) analysis.

12. KEY WORDS/DESCRIPTORS *(List words or phrases that will assist researchers in locating the report.)*

Ultrasonic Testing, Inservice Inspection, Nondestructive Testing, Nondestructive Examination, Nondestructive Evaluation, Reactor Pressure Vessels, Fabrication Flaw

13. AVAILABILITY STATEMENT

unlimited

14. SECURITY CLASSIFICATION

(This Page)
unclassified

(This Report)
unclassified

15. NUMBER OF PAGES

16. PRICE